Design and Fabrication of a Novel Large-area, High-efficiency Cosmic Ray Veto Detector for the Mu2e Experiment

Steven Boi
Saint Charles, Illinois

Bachelor of Science, Northern Illinois University, 2014

A Dissertation submitted to the Graduate Faculty
of the University of Virginia in Candidacy for the Degree of
Doctor of Philosophy

Department of Physics

University of Virginia

April, 2021

This dissertation is approved by the following committee members:

Edmond Craig Dukes (Advisor)

Robert Craig Group

P.Q. Hung

Mark Williams

"I dedicate this work to my sister, Dr. Shannon K. Boi, whose hard work, dedication, and achievements were the inspiration to embark on this long and treacherous journey."

Acknowledgements

I would like to thank my advisor, Craig Dukes, for his unwaivering guidance, support, and expertise that was invaluable throughout my Doctorate. My success would not have been possible without Craig Group, whose wisdom and enthusiasm was greatly appreciated. A special thanks to Yuri Oksuzian, Ralf Ehrlich, Sten Hansen, Davit Chokheli, and Akram Artikov, for their unfettered support. I would like to thank my friend and peer, Matthew Joyce, who suffered alongside me throughout my graduate studies. I would like to thank my friend Thomas Anderson, whose technical prowess was critical to the success of many projects. I would like to thank my sister, Shannon Boi, and my family for their immense support and unending encouragement. I would also like to thank Eric Fernandez and Wayne Farrell, whose technical skill was indispensable for many projects. And lastly, I would like to thank my crew at Station 12 and ACFR, for their encouragement and brotherhood while writing this dissertation. I would like to extend my deepest apologies to anyone I may have missed as you are still greatly appreciated.

Abstract

The Muon to Electron Conversion (Mu2e) experiment is a high-precision experiment being mounted at Fermilab, which will search for coherent, neutrino-less muon-to-electron conversion in the presence of an atomic nucleus. Such a process would exhibit charged lepton flavor violation (CLFV), which has not yet been observed. Mu2e is designed to improve the sensitivity by four orders of magnitude over the present limits. In the search for beyond the standard model (BSM) physics, Mu2e is uniquely sensitive to a wide range of models and indirectly probes mass scales up to the energy scale of 10^4 TeV. By design, the backgrounds for the experiment will be well understood and kept at a sub-event level, which in the event of the observation of muon-to-electron conversion, will be direct confirmation of BSM physics.

A significant background comes from processes initiated by cosmic-ray muons, which will produce approximately one CLFV-like event per day. In order to reduce this rate to less than one event over the lifetime of the experiment, a large and highly efficient cosmic-ray veto (CRV) detector is needed. The overall efficiency must be no less than 99.99 %, a requirement that must be maintained in the presence of intense backgrounds produced by proton and muon beams. A novel detector was designed that employs long scintillator strips with embedded wavelength shifting fibers, read out using silicon photomultipliers. The combination of a high-light yield scintillator and state-of-the-art photosensors results in a compact, highly efficient detector that is easy to manufacture and whose design is being used or considered for use in a host of other planned experiments. The design, fabrication, and performance of the CRV is presented.

Contents

Acronyms

ASIC Application Specific Integrated Circuit

BR Branching Ratio

BSM Beyond-the-Standard Model

CLFV Charged Lepton Flavor Violation

CMB Counter Motherboard

CMOS Complimentary Metal-oxide-semiconductor

CRTS Cosmic Ray Test Stand

CRV Cosmic Ray Veto

CRV-Cryo CRV Cryo Sector

CRV-D CRV Downstream Sector

CRV-DS CRV Downstream Short Sector

CRV-L CRV Left Sector

CRV-R CRV Right Sector

CRV-T CRV Top Sector

CRV-TS CRV Top TS Sector

CRV-TS-Ext CRV Top TS Extension Sector

CRV-U CRV Upstream Sector

CSC Cathode Strip Chamber

DAQ Data Acquisition

DCR Dark Count Rate

DIO Decay-in-Orbit

DS Detector Solenoid

DTC Data Transfer Controller

FEB Front End Board

FEBE Front End Board Enclosure

FGB Fiber Guide Bar

FPGA Field Programmable Gate Array

FTBF Fermilab Test Beam Facility

FWHM Full Width at Half Maximum

HDMI High-Definition Multimedia Interface

LED Light Emitting Diode

LFV Lepton Flavor Violation

LINAC Linear Accelerator

LPDDR Low Power Double Data Rate (RAM)

MPPC Multipixel Photon Counter

Mu2e Muon-to-Electron Conversion

MWPC Multi-Wire Proportional Chamber

PDE Photon Detection Efficiency

PE Photoelectron

PLL Phase Lock Loop

PMT Photomultiplier Tube

PS Production Solenoid

RAM Random-Access Memory

RMC Radiative Muon Capture

ROC Readout Controller

ROM Read-Only Memory

RPC Radiative Pion Capture

SCB SiPM Carrier Board

SiPM Silicon Photomultiplier

SMB SiPM Mounting Block

SUSY Supersymmetric

TS Transport Solenoid

UVa University of Virginia

VCXO Voltage-Controlled Crystal Oscillator

WLS Wavelength Shifting

List of Figures

List of Tables

Chapter 1.

Introduction

1.1. Particle Physics and the Standard Model

To first understand charged lepton flavor violation and its significance within the field of physics, it is good to begin with some fundamentals. Particle physics, in its most basic form, is the branch of physics that studies fundamental particles and their interactions. Since physics is a broad and deep ocean of knowledge, it is best to avoid re-describing all of physics and instead focus on the topics that are pertinent to particle physics and how these relate to the search for charged lepton flavor violation and new physics. An obvious place to start is the Standard Model.

Since its inception, the Standard Model has been an excellent description for three of the four fundamental forces and the classification of known elementary particles. Succinctly, the four forces of nature include the strong and weak, electromagnetic, and gravitational forces, the last of which has yet to be reconciled with the Standard Model. Interactions between particles are handled by mediators of the forces, also known as bosons. Previously postulated and recently discovered (2012) [1, 2], the Higgs boson is attributed to providing mass to the fundamental particles. The fabric of the Standard Model is a non-abelian gauge theory woven with quantum field theory and its extensions, quantum electrodynamics (QED) and quantum chromodynamics (QCD). It is based upon the gauge symmetry group $SU(3)_C \times SU(2)_L \times U(1)_Y$, where C denotes color, L indicates that $SU(2)$ only acts on left-chiral fermions, and Y is hypercharge.

1.1.1. Bosons

Currently, there are four bosons that mediate the interactions between the fundamental and composite particles of nature and one which gives rise to particle mass and explains the origin of $U(1)_{EM}$ through spontaneous symmetry breaking of the $SU(2)_L \times SU(1)_Y$ electroweak sector (Fig. 1.1). One of the distinct properties of bosons is that they possess integer or zero spin, obeying Bose-Einstein statistics, which includes mesons (quark-antiquark composite particles). The force carriers have integer spin and are either massive or massless. Massless bosons include the photon, γ, which mediates the electromagnetic interaction, and the eight gluons, g, which mediate the strong interaction. Massive bosons include the W^+, W^-, and Z^0 gauge bosons, which mediate the weak interaction. The Higgs is not a force carrier, but a massive, spin-0 scalar boson that provides the mechanism through which the fermions and massive bosons acquire mass.

It is expected that this list is incomplete as there are a variety of phenomena that are unexplained such as the origin or mediator of gravity, neutrino mass, flavor structure, or dark matter/energy and baryogenesis.

1.1.2. Fermions

There are three generations of matter, known as fermions, that fall into two different categories: the quarks and leptons (Fig. 1.1). Unlike the spin-0 or spin-1 bosons, fermions

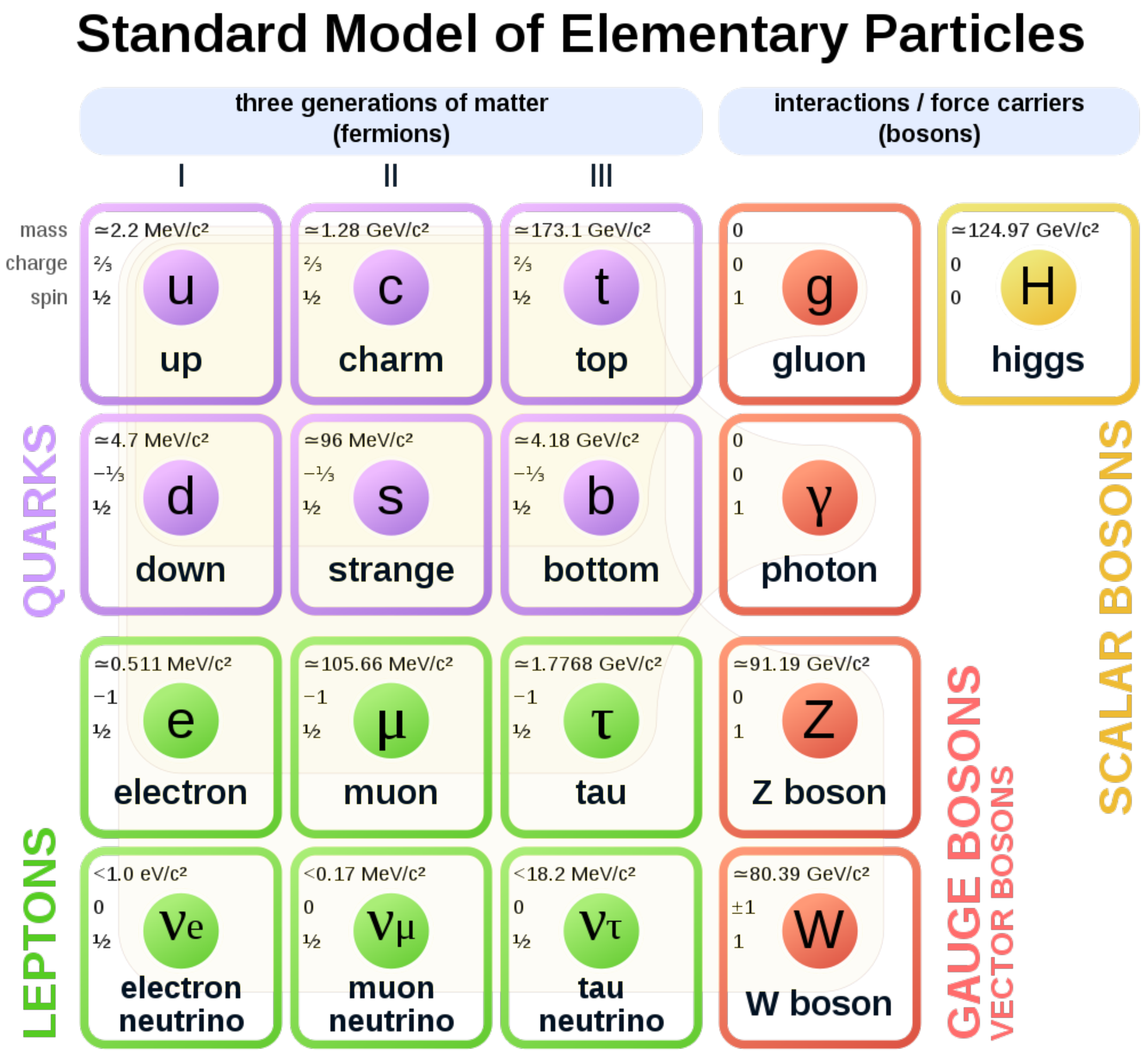

Figure 1.1.: Standard Model of elementary particles showing the organization of fermions into two types, quarks and leptons, and three generations, along with the five fundamental bosons.

are spin-1/2 particles and obey Fermi-Dirac statistics, and hence the Pauli exclusion principle. The three generations of fermions are arranged according to their mass, among other properties, with particles being more massive in higher generations. Generations II and III (Fig. 1.1) are known to be unstable and decay to particles in the first generation.

The quarks, in order of increasing generation, are the up (u) and down (d), the strange (s) and charm (c), and the top (t) and bottom (b) quarks, and their antiparticle forms. Quarks possess color charge and interact with each other via the strong force through the exchange of gluons. Due to color confinement, free quarks are never observed. Quark-based composite particles, or hadrons, are color-neutral and fall into one of two categories: baryons and mesons. Baryons contain an odd number of quarks, at least three, and include familiar particles like the neutron (udd) and proton (uud) along with exotic hadrons like tetra and pentaquarks. Mesons contain an even number of quarks, at least two, and are comprised of quark-antiquark pairs. Due to quarks being spin-1/2, mesons are classified as bosons since they are integer/zero-spin particles. In addition to color-charge, quarks have electric charge and weak isospin, allowing them to interact with other fermions through the weak and electromagnetic interactions.

The leptons, in order of increasing generation, are the electron (e) and its neutrino partner the electron-neutrino (ν_e), the muon (μ) and muon-neutrino (ν_μ), and the tau (τ) and tau-neutrino (ν_τ), along with their antiparticle forms. Leptons do not carry color charge, so they do not interact strongly. As a result, the entire collection of leptons interacts weakly, with only the charged leptons (e, μ, τ) having the additional ability to interact via the electromagnetic interaction. This means neutrinos are neutral, known experimentally to be massive, and only interact weakly, which makes them very difficult to detect. Among the charged leptons, the muon and tau are unstable and will decay into other particles and neutrinos, and conserve what is referred to as lepton flavor number, L_e, L_μ, L_τ. Lepton number is a conserved quantity denoting the number of leptons and antileptons of a specific flavor, e, μ, and τ, which includes their neutrino partners. Each lepton has a value of 1 and each antilepton a value of -1, while all other particles have a value of 0. Observed experimentally, one of the properties of neutrinos is their ability to oscillate, or convert, between flavors. Not only does this imply the existence of neutrino mass, which is not currently described by the Standard Model, but leads to an apparent non-conservation of lepton flavor. This indicates that, while the Standard Model is a very good description for the fundamental particles and their interactions, there must be physics beyond the Standard Model, so-called New Physics, which provides a more adequate explanation for such phenomena. One way to search for this new physics is to look carefully for processes that violate charged lepton flavor.

1.2. Muon-to-electron Conversion

1.2.1. Charged Lepton Flavor Violation Theory

Within the Standard Model, lepton flavor changing processes are forbidden due to conservation of charged lepton flavor numbers L_e, L_μ, L_τ. Through a variety of experimental observations, it is known that weak interactions, namely charge-current interactions, create neutrinos in three flavors: ν_e, ν_μ, ν_τ, corresponding to each of the charged leptons, e, μ, τ, respectively. For reasons yet to be explained by modern physics, neutrinos of each flavor state exhibit mixing with three states of definite mass for which only the difference in the square of their masses are known [3]. As a result, neutrinos propagating through space can possess a flavor state that is different from its original flavor. One of the yet irreconcilable issues of the Standard Model is that it does not predict any masses or the oscillatory behavior of neutrinos, which is itself a lepton flavor violating (LFV) process. In an extension of the Standard Model, one that accounts for neutrino oscillations, non-conservation of charged lepton flavor number is permissible, but highly

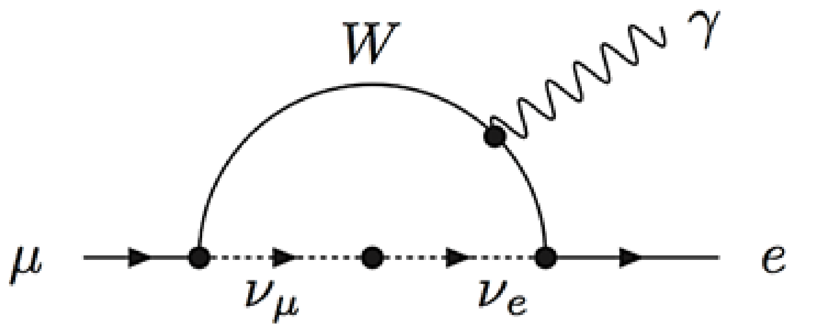

Figure 1.2.: Example of non-conservation of lepton flavor in $\mu^+ \to e^+\gamma$ due to neutrino oscillation, a process permitted by extension of the Standard Model to include neutrino masses.

suppressed. Figure 1.2 shows an example of a charged LFV process, $\mu \to e\gamma$, which has an exceedingly small branching ratio (BR):

$$BR(\mu \to e\gamma) = \frac{3\alpha}{32\pi}\left|\sum_{i=2,3} U^*_{\mu i} U_{ei} \frac{\Delta m^2_{1i}}{M^2_W}\right|^2 < 10^{-54}. \tag{1.1}$$

The rate for neutrino-based charged LFV processes is constrained by the mixing parameters outlined above, however for non-neutrino-based charged lepton flavor violating (CLFV) processes the rate is highly model-dependent. While neutrino oscillations depend only on the mixing angles and masses, measurement of these parameters does not lend insight to the rates of CLFV processes due to the dependence of CLFV processes on the underlying mechanisms that generate neutrino masses and lepton mixing. A minimal extension of the Standard Model, by introduction of three right-handed SU(2) singlet fields and Yukawa couplings, generates neutrino masses and accounts for oscillations, while also allowing CLFV processes. A CLFV process such as $\mu^- N \to e^- N$, only occurs through loop diagrams with amplitudes proportional to the ratio of the square of the neutrino mass differences and the mass of the W boson: $(\Delta m^2_{ij}/M^2_W)^2$. The rate is effectively unobservable, on the order of 10^{-50}, due to the disparity in size between Δm_{ij} and M_W. Beyond-the-Standard Model (BSM) physics, such as the Littlest Higgs

Table 1.1.: "DNA" of flavor physics effects for the most interesting observables in a selection of SUSY and non-SUSY BSM models. "★★★" signals large effects, "★★" visible but small effects, and "★" implies that the given model does not predict sizable effects in that observable. A "?" indicates there is no prediction for the given observable [6].

	AC	RVV2	AKM	δLL	FBMSSM	LHT	RS
$D^0 - \bar{D}^0$	★★★	★	★	★	★	★★★	?
ϵ_K	★	★★★	★★★	★	★	★★	★★★
$S_{\psi\phi}$	★★★	★★★	★★★	★	★	★★★	★★★
$S_{\phi K_S}$	★★★	★★	★	★★★	★★★	★	?
$A_{CP}(B \to X_s\gamma)$	★	★	★	★★★	★★★	★	?
$A_{7,8}(B \to K^*\mu^+\mu^-)$	★	★	★	★★★	★★★	★★	?
$A_9(B \to K^*\mu^+\mu^-)$	★	★	★	★	★	★	?
$B \to K^{(*)}\nu\bar{\nu}$	★	★	★	★	★	★	★
$B_s \to \mu^+\mu^-$	★★★	★★★	★★★	★★★	★★★	★	★
$K^+ \to \pi^+\nu\bar{\nu}$	★	★	★	★	★	★★★	★★★
$K_L \to \pi^0\nu\bar{\nu}$	★	★	★	★	★	★★★	★★★
$\mu \to e\gamma$	★★★	★★★	★★★	★★★	★★★	★★★	★★★
$\tau \to \mu\gamma$	★★★	★★★	★	★★★	★★★	★★★	★★★
$\mu N \to eN$	★★★	★★★	★★★	★★★	★★★	★★★	★★★
d_n	★★★	★★★	★★★	★★	★★★	★	★★★
d_e	★★★	★★★	★★	★	★★★	★	★★★
$(g-2)_\mu$	★★★	★★★	★★	★★★	★★★	★	?

model with T-parity (LHT) [4] or Ross, Velasco-Sevilla, and Vives (RRV) [5] model, predicts enhancements to CLFV processes that have effects measurable by next-generation experiments. A process like $\mu^- N \to e^- N$, for instance, is uniquely sensitive to a host of supersymmetric (SUSY) and non-SUSY BSM physics models [6]. One of the advantages of probing the $\mu \to e$ conversion channel is, beyond the discovery of BSM physics, that it acts as a litmus test for the validity of many new-physics models. A comparison of various observables and their sensitivity to a variety of models is presented in Table 1.1.

Of the different probes for new physics, muons have the advantage of being readily produced in intense beams, offering improved search sensitivity in comparison with rare kaon and tau decays. Three muon processes in particular offer the greatest sensitivity to the effects of new physics: $\mu^+ \to e^+\gamma$, $\mu^+ \to e^-e^+e^+$, and $\mu^-N \to e^-N$. As explained earlier, the rate of CLFV processes are inherently model-dependent, however one can estimate the sensitivity of a process by constructing a model-independent magnetic-moment-type and contact-type effective LFV operators in a simplified Standard Model Lagrangian [7]:

$$\mathscr{L}_{CLFV} = \frac{m_\mu}{(1+\kappa)\Lambda^2}\bar{\mu_R}\sigma_{\mu\nu}e_L F^{\mu\nu} + \frac{\kappa}{(1+\kappa)\Lambda^2}\bar{\mu_L}\gamma_\mu e_L \left(\sum_{q=u,d} \bar{q_L}\gamma^\mu q_L\right). \tag{1.2}$$

In Eq. 1.2, the subscripts L, R indicate the chirality of the different SM fermion fields, $F^{\mu\nu}$ is the photon field strength, and m_μ is the mass of the muon. Additionally, there are two independent constants Λ and κ, which parameterize the operator coefficients. The first parameter Λ is a the effective mass scale of new physics (with dimension of mass), and the second parameter, κ is dimensionless and governs the relative contribution of each operator. It is important here to clarify that Λ is only an effective mass scale. For the magnetic moment interaction it is related to the mass of new particles via a loop factor and a coupling term for the new interactions, for example $1/\Lambda^2 \propto g^2e/(16\pi^2M^2)$ where M is the mass of the new particles, g is the coupling strength for the new interaction, and e is the electric charge. For the contact operator, Λ is more closely related to the mass of new particles, i.e. $1/\Lambda^2 \propto g^2/M^2$. The first term, the magnetic-moment-type operator, mediates all three processes and is generated by an emitted photon that is real or virtual. The second term, the four-fermion contact-type operators, mediates $\mu^-N \to e^-N$ conversion at the leading order and the other two processes at the one-loop level, and includes processes not resulting in an on-mass-shell photon. At $\kappa \gg 1$, the four-fermion operators dominate, while at $\kappa \ll 1$, the magnetic-moment operator dominates.

Unique to $\mu^- N \to e^- N$ and $\mu^+ \to e^- e^+ e^+$ is their sensitivity to new physics regardless of κ. Unfortunately, discovery of $\mu^- N \to e^- N$ does not allow for the determination of Λ or κ independently. Other CLFV observables would be required in order to learn more about the new physics. An advantage that the search for CLFV has is that it probes mass scales higher than what is possible with current direct searches performed at the LHC. As seen in Fig. 1.3, increased sensitivity in the search for CLFV sets lower limits for the scale at which new physics exists. Currently excluded by the MEG ($\mu \to e\gamma$) and SINDRUM-II ($\mu^- N \to e^- N$ on Au) is much of the region where new physics would exist at or below 10^3 TeV. With an increase in sensitivity four orders of magnitude over the limits set by SINDRUM-II for $\mu^- N \to e^- N$, effective mass scales up to 10^4 TeV would be explored.

1.2.2. Charged Lepton Flavor Violation in New Physics Models

Supersymmetric SO(10) Type I See-saw Grand Unified Model

In an attempt to answer some of the yet unexplained phenomena of physics such as the gauge hierarchy problem, leptogenesis, neutrino masses, etc, supersymmetric versions of the Standard Model with weak-scale SUSY breaking parameters have been hypothesized. Many of these models predict enhanced rates for CLFV processes. In particular, within the context of an SO(10) SUSY Grand Unified Theory model, assumptions for the Dirac Yukawa couplings for heavy, right-handed neutrinos being either PMNS-like or CKM-like, allows one to predict a non-zero rate of a CLFV process like $\mu^- N \to e^- N$ in terms of SUSY breaking parameters. A recent study, which took into consideration the observed value of θ_{13} and the light Higgs mass, calculated the rate of $\mu^- N \to e^- N$ in titanium using SUSY breaking parameters [8] and is shown in Fig. 1.4 for two different values of the SUSY parameter tanβ, where β is the ratio of Higgs doublet vacuum expectation

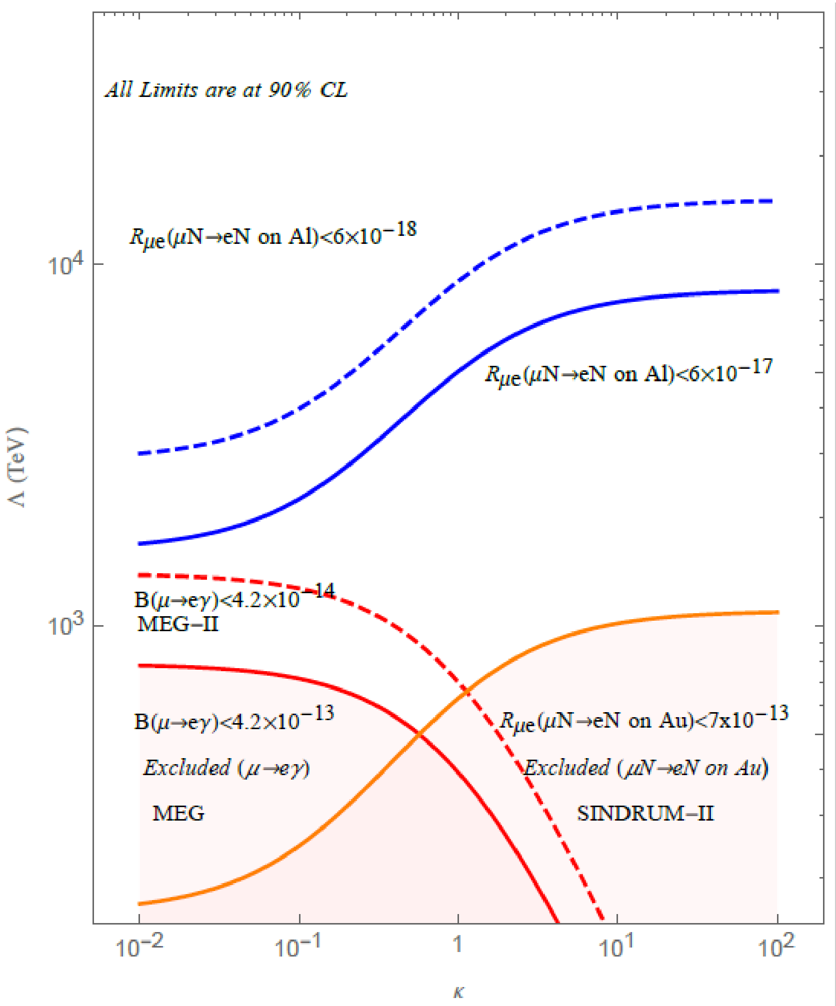

Figure 1.3.: Sensitivity to the mass scale of new physics for $\mu^- N \to e^- N$ and $\mu^+ \to e^+\gamma$ as a function of the relative strength of operators in Eq. 1.2. The solid orange line and shaded region represents the excluded region of new physics phase space set by SINDRUM-II. The solid (dashed) blue line represents the limits that would be set by a $\mu^- N \to e^- N$ search (Mu2e) at a sensitivity of $<6 \times 10^{-17}$ ($<6 \times 10^{-18}$). The solid red line and shaded region represent the excluded region set by MEG, with the dashed line representing the region that would be excluded by an increase in sensitivity with the MEG-II upgrade [7].

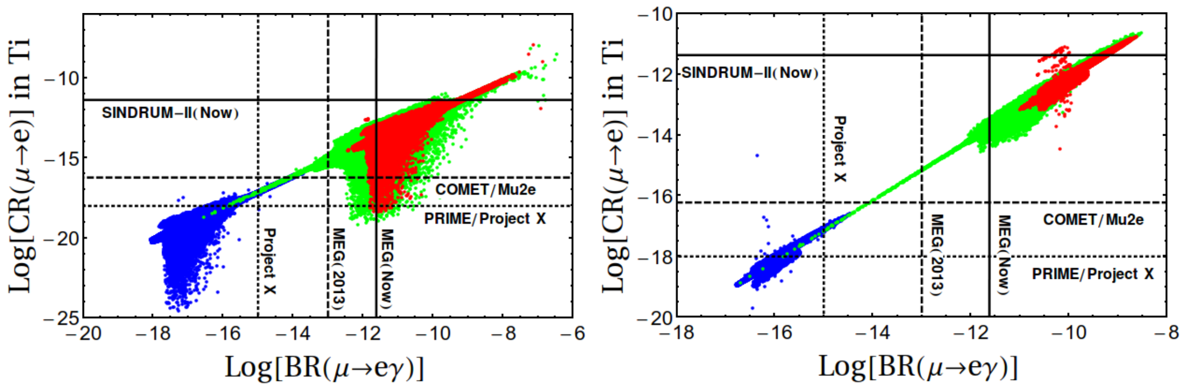

Figure 1.4.: Predictions of the branching ratio for $\mu \to e\gamma$ and $\mu \to e$ conversion in titanium for two types of mixing: the CKM case (blue), the PMNS case in mSUGRA (red), and the Non-Universal Higgs Mass (green), for tan$\beta = 10$(left), 40(right). The various horizontal and vertical lines, solid and dashed, correspond to the limits set by current and proposed experiments, respectively [8].

values ($\beta = H_u/H_d$). The most prominent feature of these plots is the capability for next generation experiments like the MEG upgrade and Mu2e to probe a majority of the PMNS-like parameter space, for large β, and part of the CKM-like space.

Scalar Leptoquarks

Physics models that extend the Standard Model through the addition of one scalar representation of $SU(3) \times SU(2) \times U(1)$ and exhibit an unusual enhancement the top mass, by generation of scalar leptoquarks at the TeV mass scale, can enhance the muon-to-electron conversion rate and branching ratio of $\mu \to e\gamma$, while conforming to currently known experimental constraints imposed by collider and quark-flavor physics [9]. Figure 1.5, shows the relationship between the coupling strength (λ) and the range of scalar leptoquark masses for the $\mu^- N \to e^- N$ rate in aluminum with the proposed sensitivity of Mu2e experiment, and the branching ratio for $\mu^+ \to e^+\gamma$ at the proposed sensitivity of the MEG upgrade.

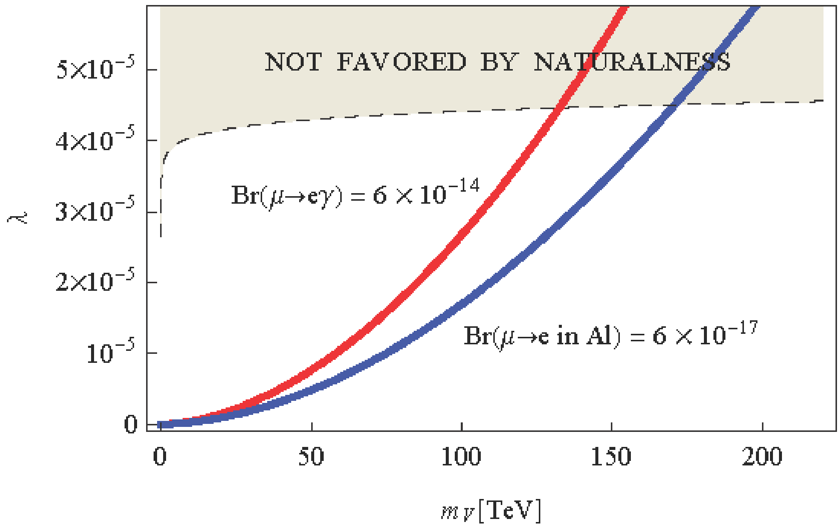

Figure 1.5.: Coupling strength λ as a function of leptoquark mass for $\mu \rightarrow e$ conversion in Al at the proposed Mu2e sensitivity and the branching ratio for $\mu \rightarrow e\gamma$ at the proposed MEG upgrade sensitivity. The shaded region is excluded due to not satisfying a naturalness condition [9].

Littlest Higgs Model with T-Parity

In addition to SUSY theories hypothesized for electroweak symmetry breaking, composite Higgs models where the Higgs boson emerges as a pseudo-Nambu-Goldstone boson are strong contenders. More specifically, the Littlest Higgs model with T-parity (LHT) provides a calculable framework from the lowest orders up to scales on the order of 10 TeV. Such a property is attributed to the collective symmetry breaking mechanism that prevents the Higgs mass from being subject to quadratic divergences at the single-loop level. Due to T-parity, a discrete symmetry analogous to R-parity in the Minimal Supersymmetry Standard Model (MSSM), tree-level contributions from heavy gauge bosons to observables involving only Standard Model particles are explicitly forbidden [4]. The advantage of this is that it relaxes the precision electroweak constraints, both direct and indirect, that Littlest Higgs models (without T-parity) previously suffered from [10]. Variation of LHT model parameters provides a measurable correlation for the branching ratio of $\mu^- N \rightarrow e^- N$ in titanium to $\mu^+ \rightarrow e^+\gamma$, as seen in Fig. 1.6 [11]. The blue line in the figure is the contribution of the MSSM dipole operator, the yellow line is

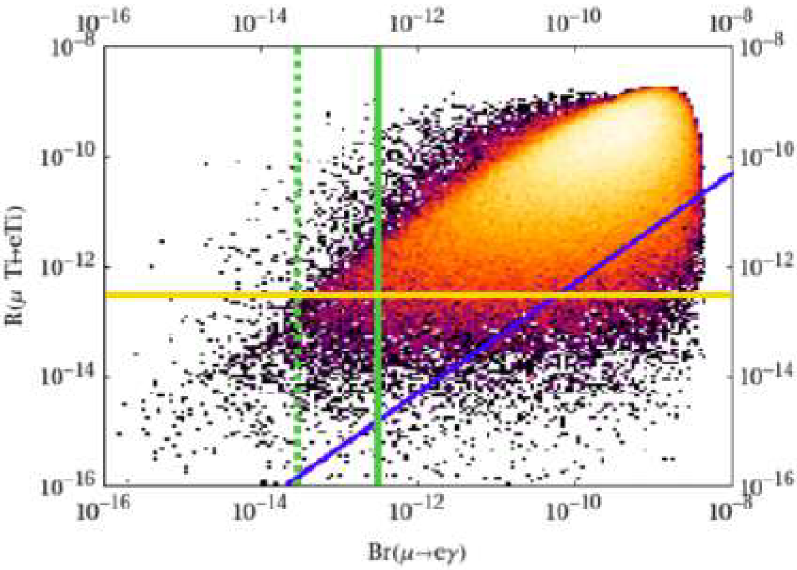

Figure 1.6.: Predictions of the branching ratios for $\mu \to e\gamma$ and $\mu \to e$ conversion in titanium for a selection of LHT model parameters [11]. The blue line represents the contribution of the MSSM dipole operator. The yellow line represents the upper limit set by SINDRUM-II. The green lines, dashed and solid, represent the expected and current upper limits, respectively, set by MEG.

the upper limit set by SINDRUM-II, and the green lines, dashed and solid, represent the expected and current upper limits, respectively, set by MEG.

Left-Right Symmetric Models

Among the features of left-right symmetric models are the restoration of parity and retention of remnants of grand unification at short and very-short distances. In addition, it lays the framework for developing testable neutrino-mass models. With a assumption that the breaking scale is around 5 TeV, the predicted rates for $\mu \to e$ conversion in various nuclei, and the branching ratio for $\mu \to e\gamma$, lie within the proposed sensitivities for the Mu2e and MEG experiments, respectively, as shown in Table 1.2. The predictions of the branching ratios for $\mu \to e\gamma$ and $\mu \to e$ conversion rate in gold are shown in Fig. 1.7. The predictions for different branching ratios and conversion rates for various LFV

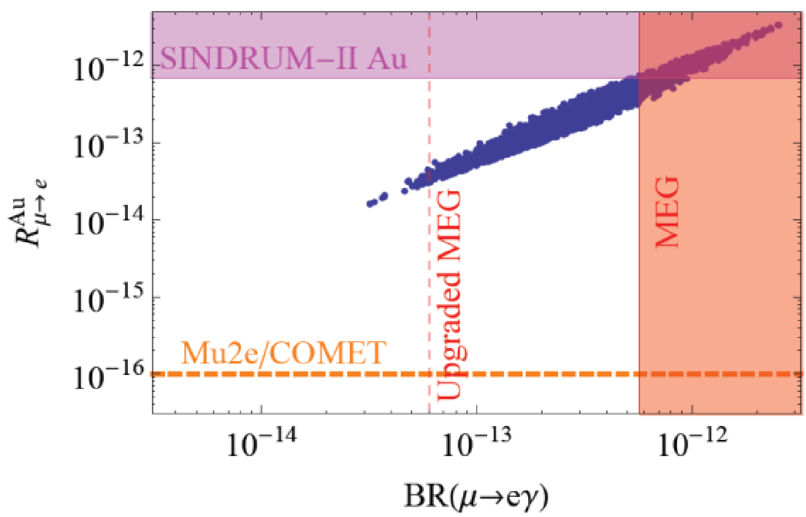

Figure 1.7.: Predictions for $\mu \to e\gamma$ and the $\mu \to e$ conversion rate in gold in a left-right symmetric model. The shaded regions are constraints imposed by the SINDRUM-II [14] and MEG [13] experiments. The dashed lines represent the limits expected to be set by the MEG upgrade, Mu2e, and COMET experiments.

observables by varying the parameters for a left-right symmetric model, and current experimental limits, are presented in Table 1.2.

Table 1.2.: Left-right symmetric model predictions for different charged LFV processes $\ell_i \to \ell_j\gamma$ and $\mu \to e$ conversion ($\mathrm{R}^*_{\mu\to\mathrm{e}}$) in various nuclei. The best-fit and range values correspond to the values obtained from various model parameters. Current experimental limits @ 90% CL are shown for comparison [12].

LFV Observable	Best-Fit Value	Range	Experimental Limit
BR($\mu \to e\gamma$)	4.86×10^{-13}	$(3.2 \times 10^{-14} - 2.6 \times 10^{-12})$	$< 4.2 \times 10^{-13}$ [13]
BR($\tau \to e\gamma$)	1.08×10^{-12}	$(9.7 \times 10^{-14} - 5.1 \times 10^{-12})$	$< 3.3 \times 10^{-8}$
BR($\tau \to \mu\gamma$)	6.37×10^{-13}	$(3.7 \times 10^{-14} - 3.7 \times 10^{-12})$	$< 4.4 \times 10^{-8}$
$R^{Ti}_{\mu\to e}$	4.26×10^{-13}	$(2.1 \times 10^{-14} - 3.3 \times 10^{-12})$	$< 4.3 \times 10^{-13}$ [13]
$R^{Au}_{\mu\to e}$	3.80×10^{-13}	$(1.6 \times 10^{-14} - 3.4 \times 10^{-12})$	$< 7.0 \times 10^{-13}$
$R^{Pb}_{\mu\to e}$	2.60×10^{-13}	$(1.1 \times 10^{-14} - 2.4 \times 10^{-12})$	$< 4.6 \times 10^{-11}$

Flavor-violating Higgs Decays

Since its discovery by the ATLAS [1] and CMS [2] experiments in 2012, the Higgs boson has potentially provided an additional pathway for LFV processes. A flavor violating Higgs that couples to leptons and quarks arises in many frameworks and can be a valuable probe for new physics [15]. Searches for CLFV have imposed constraints on non-standard, flavor-violating Higgs decays, such as $h \to e\mu, e\tau, \mu\tau$, that are tighter than the sensitivities achievable at current collider experiments. The current limit on muon-to-electron conversion (Fig. 1.8) implies $\sqrt{|Y_{\mu e}|^2 + |Y_{e\mu}|^2} < 4.6 \times 10^{-5}$, where $|Y_{\mu e}|$ and $|Y_{e\mu}|$ are the Yukawa coupling strengths. Mu2e is expected to be sensitive to $\sqrt{|Y_{\mu e}|^2 + |Y_{e\mu}|^2} > few \times 10^{-7}$. The process $\mu^- N \to e^- N$ is the most sensitive channel to study the Yukawa couplings. A list of the various channels, their couplings, and the current bounds is presented in Table 1.3.

1.3. Signal and Backgrounds for $\mu N \to eN$ Experiments

For all of the CLFV processes involving muon parents, the electron plays an important role in allowing experiments to distinguish backgrounds from the CLFV processes they search for. Therefore, it is important to know what properties the electron will have for a given CLFV process. Considering only the case of the neutrino-less conversion of a muon into an electron in the presence of a nucleus, the process largely parallels that of a simple two-body decay. A muon stopping in an atom rapidly cascades down to the 1S state [16], where it undergoes nuclear capture, decay, or conversion. The rate of capture and decay in orbit (DIO) for a muon bound to a nucleus (Fig. 1.9) depends on the number of protons in the target nucleus. For low-Z materials, most muons decay

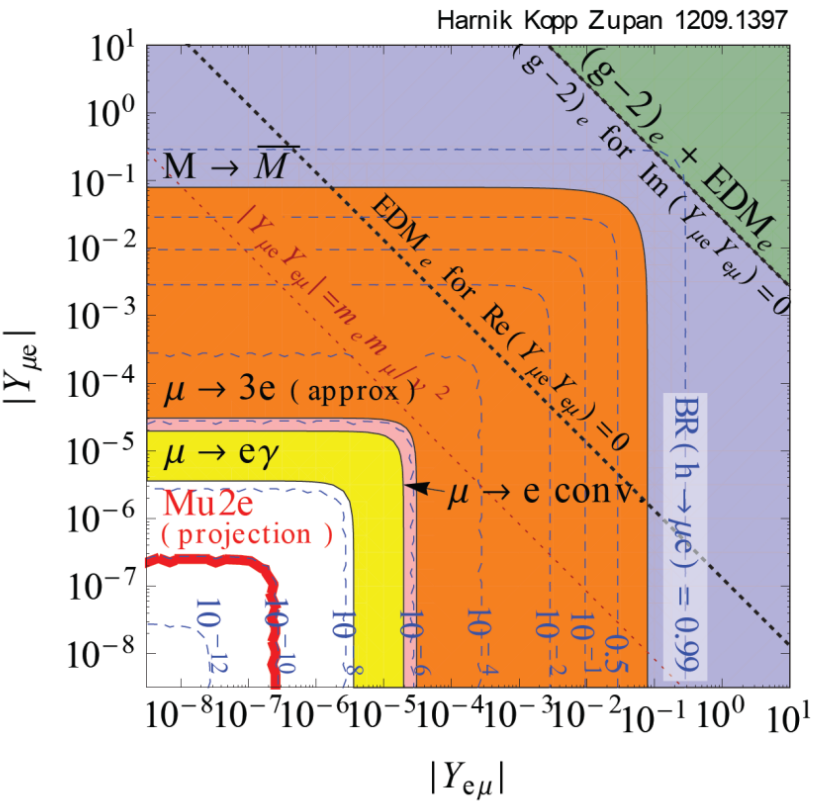

Figure 1.8.: Constraints on the flavor-violating couplings, $|Y_{\mu e}|$ and $|Y_{e\mu}|$, for a 125 GeV/c^2 Higgs boson [15]. The diagonal couplings are approximated by their SM values. The dashed lines are contours of constant $h \to \mu e$. The red line represents the limit expected to be set by Mu2e.

Table 1.3.: Constraints on flavor-violating Higgs couplings to e, μ, τ for a Higgs mass $m_h = 125\,\text{GeV}$ and assuming flavor-diagonal Yukawa couplings are equal to the Standard-Model values [15].

Channel	Coupling	Bound
$\mu \to e\gamma$	$\sqrt{\lvert Y_{\mu e}\rvert^2 + \lvert Y_{e\mu}\rvert^2}$	$< 3.6 \times 10^{-6}$
$\mu \to 3e$	$\sqrt{\lvert Y_{\mu e}\rvert^2 + \lvert Y_{e\mu}\rvert^2}$	$\lesssim 3.1 \times 10^{-5}$
electron $g-2$	$\mathrm{Re}(Y_{e\mu} Y_{\mu e})$	$-0.019...0.026$
electron EDM	$\lvert\mathrm{Im}(Y_{e\mu} Y_{\mu e})\rvert$	$< 9.8 \times 10^{-8}$
$\mu \to e$ conversion	$\sqrt{\lvert Y_{\mu e}\rvert^2 + \lvert Y_{e\mu}\rvert^2}$	$< 1.2 \times 10^{-5}$
$M - \bar{M}$ oscillations	$\lvert Y_{\mu e} + Y^*_{e\mu}\rvert$	< 0.079
$\tau \to e\gamma$	$\sqrt{\lvert Y_{\tau e}\rvert^2 + \lvert Y_{e\tau}\rvert^2}$	< 0.014
$\tau \to 3e$	$\sqrt{\lvert Y_{\tau e}\rvert^2 + \lvert Y_{e\tau}\rvert^2}$	$\lesssim 0.12$
electron $g-2$	$\mathrm{Re}(Y_{e\tau} Y_{\tau e})$	$[-2.1...2.9] \times 10^{-3}$
electron EDM	$\lvert\mathrm{Im}(Y_{e\tau} Y_{\tau e})\rvert$	$< 1.1 \times 10^{-8}$
$\tau \to \mu\gamma$	$\sqrt{\lvert Y_{\tau\mu}\rvert^2 + \lvert Y_{\mu\tau}\rvert^2}$	0.016
$\tau \to 3\mu$	$\sqrt{\lvert Y_{\tau\mu}\rvert^2 + \lvert Y_{\mu\tau}\rvert^2}$	$\lesssim 0.25$
muon $g-2$	$\mathrm{Re}(Y_{\mu\tau} Y_{\tau\mu})$	$(2.7 \pm 0.75) \times 10^{-3}$
muon EDM	$\mathrm{Im}(Y_{\mu\tau} Y_{\tau\mu})$	$-0.8...1.0$
$\mu \to e\gamma$	$(\lvert Y_{\tau\mu} Y_{e\tau}\rvert^2 + \lvert Y_{\mu\tau} Y_{\tau e}\rvert^2)^{1/4}$	$< 3.4 \times 10^{-4}$

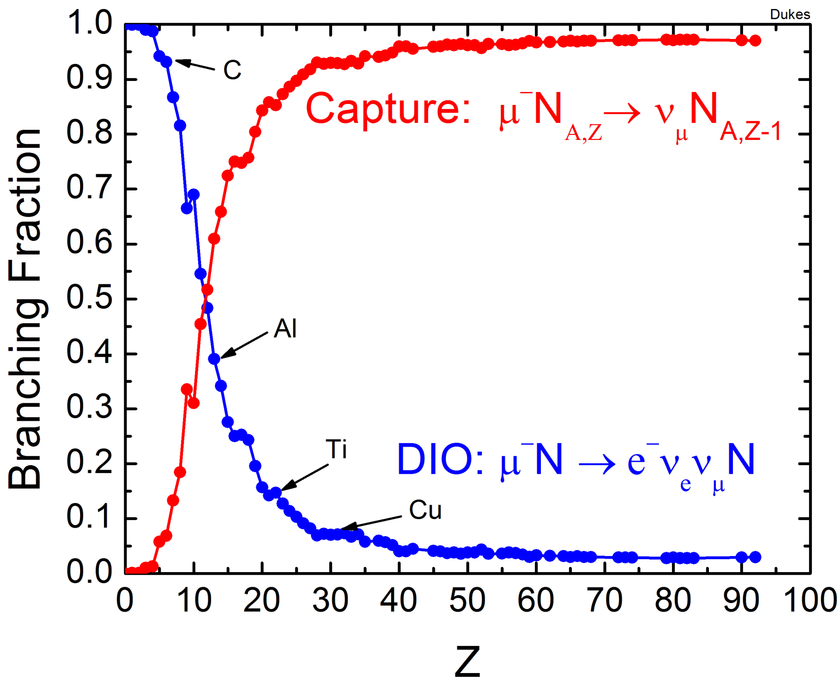

Figure 1.9.: The branching fraction of nuclear capture and decay in orbit for a muon bound to different nuclei. For very low-Z materials, most muons decay in orbit. For higher-Z materials, muons are mostly captured by the nucleus.

in orbit, however as Z increases the majority of muons are captured by the nucleus. Similarly, the lifetime of a muon in a material (Fig. 1.10) is also dependent upon Z and can be as long as 2 μs for low-Z materials or as short as 70 ns for high-Z materials [17]. Due to the large difference between the mass of the nucleus and the electron, the energy lost to nuclear recoil is small and is approximately $E_{rec} \approx m_\mu^2/2m_{nucleus}$ [18]. Additional energy is lost due to the atomic binding energy for the muon ($E_B \approx Z^2\alpha^2 m_\mu/2$) [18], the energy that is required to remove it from the 1S state in the atom. Thus, the resulting signal for a muon-to-electron conversion process in the presence of a nucleus is a coherent, monoenergetic electron, herein referred to as a conversion-electron, with an energy slightly less than the rest mass of the muon, as shown in Eq. 1.3:

$$E_e = m_\mu c^2 + E_{recoil}(A) + E_{binding}(Z), \tag{1.3}$$

where A and Z are the number of nucleons and protons in the nucleus, respectively.

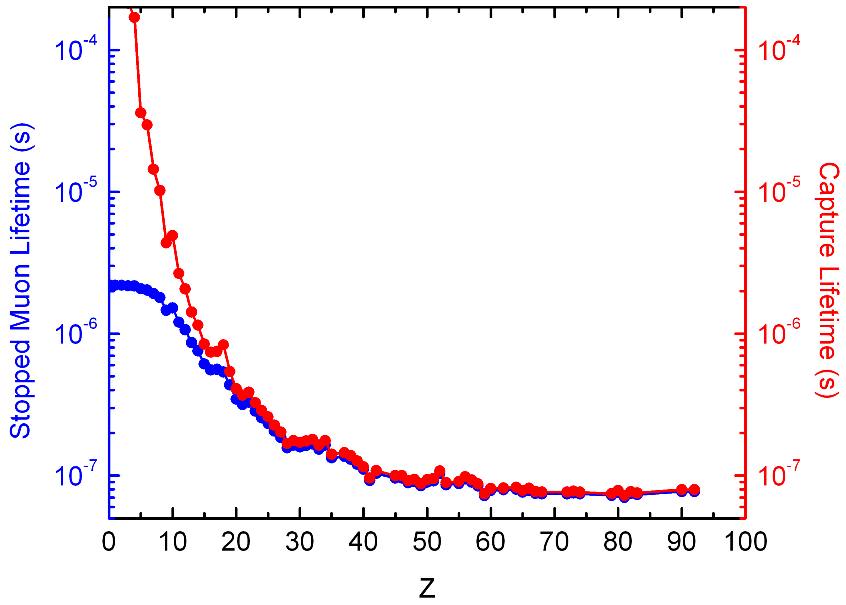

Figure 1.10.: Shown in blue is the mean lifetime of a muon bound to the nucleus of different elements (decay in orbit). Shown in red is the mean lifetime of a bound muon before being captured by the nucleus.

Considering the signal energy is very near the rest mass of the muon, it is distinct from the energy of electrons that are the result of free muon decay, as described by the Michel spectrum, where the most probable electron energy is half the rest mass of the muon (52.8 MeV), shown in Fig. 1.11. The lifetime of the muon in aluminum, the stopping target used in Mu2e, is 864 ns and the conversion-electron energy is 104.97 MeV [17]. While the delayed appearance of a large energy conversion-electron is distinct, the signature is not completely free of backgrounds. For modern experiments searching for CLFV through muon-to-electron conversion there are several sources of background that drive the design. These include:

1. Processes intrinsic to the search for muon-to-electron conversion that scale with beam intensity, including:

   a) Prompt beam processes

   b) Delayed beam processes

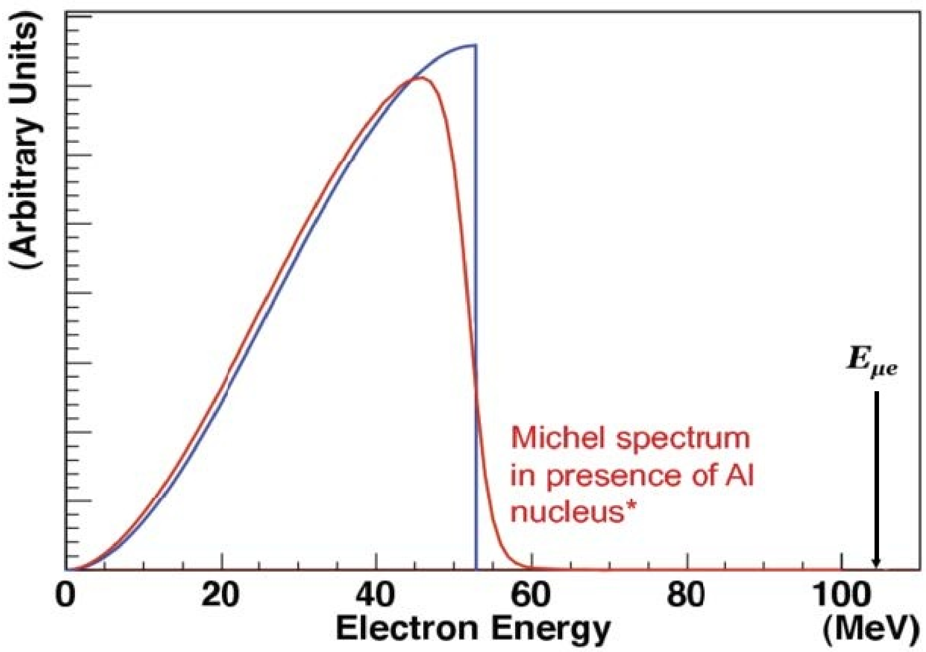

Figure 1.11.: The electron energy spectrum from free muon decay (blue), which has a sharp cutoff at half the rest mass of a muon. Shown in red is the energy spectrum from the decay of a muon bound to an aluminum nucleus. The energy of the mono-energetic conversion electron is shown in black.

2. Cosmic ray induced processes
3. Reconstruction Errors

1.3.1. Processes intrinsic to the search for muon-to-electron conversion that scale with beam intensity

The first background type, which is common to any $\mu^- N \to e^- N$ search, are processes that are intrinsic to stopping muons in a target. The two most prominent are muons that decay in orbit (DIO) and radiative muon capture (RMC).

For free muons decaying via $\mu \to e\nu_\mu\bar{\nu}_e$, the maximal electron energy is less than half the rest mass of the muon. However, in the case of a muon decaying while bound to a nucleus, the energy spectrum for the emitted electron is modified by the addition of a tail that extends above half the rest mass of the muon (Fig. 1.11). In the case where the neutrinos are at rest in the decay frame and the electron recoils off the nucleus, the energy of the electron is very close to the energy one would expect for a conversion-electron. While this is not particularly probable, as the probability of such high-energy electrons falls approximately as $(\mathrm{E}_{\mathrm{endpoint}} - \mathrm{E}_{\mathrm{e}})^5$, this high-energy tail is a background for conversion experiments. While this background is intrinsic to the search of $\mu^- N \to e^- N$, it can be suppressed by precise measurements of electron energy. Experimentally, the uncertainties on the measured endpoint energy are large, however, theoretical analyses employing $O(\alpha)$ radiative corrections place the uncertainty in the endpoint spectrum at 2.5% [19]. Special consideration of the target material can reduce DIO backgrounds from muons stopping in foreign nuclei, such as the stopping target support structure or contaminants in the target material. Shown in Fig. 1.12, the DIO endpoint energy is highest for low-Z materials. The choice of a low-Z target material is preferred to reduce the background of DIO electrons coming from other materials in the apparatus. For example, the maximal energy for a DIO electron coming from a tungsten target support falls below the maximal DIO electron and conversion-electron energies for an aluminum target.

Much like DIO, radiative muon capture (RMC) has the ability to produce electrons of energies similar to conversion-electrons. The process of RMC can generate high-energy photons ($\mu^- N \to \nu_\mu \gamma (N-1)$) that create secondary electron-positron pairs through interactions in the stopping target and surrounding materials. The endpoint energy for RMC electrons is shifted away from the conversion-electron energy due to mass differences between the initial and final nuclear states. An appropriate choice of stopping target material can be made such that the mass of the daughter nuclei is several MeV/c^2 greater or greater than stopping target mass, which forces the endpoint energy to fall below the conversion-electron energy. For an aluminum stopping target the daughter nucleus is

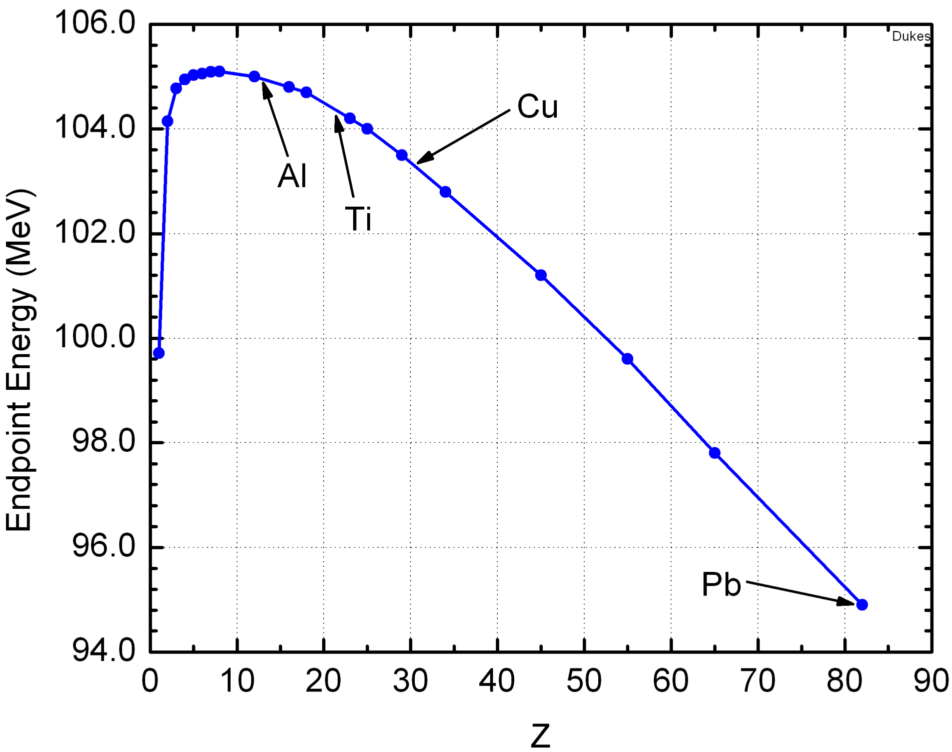

Figure 1.12.: The endpoint energy for decay in orbit electrons for different Z elements.

magnesium whose endpoint energy for RMC is 101.9 MeV [20], which is 3.1 MeV below the conversion-electron energy.

1.3.2. Prompt Beam Processes

Prompt processes are processes where the detected electron is almost coincident in time with the arrival of beam particles at the stopping target. The largest contributor to this is radiative pion capture (RPC). The generation of intense muon beams involves the creation of pions that decay into muons. As such, muon beams initially contain significant pion contamination. Pions that reach and stop in the stopping target are quickly captured by the nucleus and can produce real or virtual high-energy photons, which can convert into electrons with an energy very close to the conversion-electron energy. The lifetime of a stopped pion is much shorter than the lifetime of a stopped muon: 26 ns [21] and 864 ns, respectively. This background can be suppressed by the use of a pulsed beam structure for pion production. By producing pions at discrete intervals, sufficient time can pass for the pions to decay before opening the live window.

1.3.3. Delayed Beam Processes

Delayed processes are those due to particles that travel slowly down the beam line. The generation of a muon beam results in the creation of slow moving antiprotons. Antiprotons that arrive at the stopping target during the experiment's live window can annihilate and produce conversion-like electrons. The solution, which comes at a minor loss of muons stopping in the stopping target, is the addition of low-Z materials in the muon beam line to capture antiprotons and reduce their impact as a background.

1.3.4. Cosmic Ray Induced Processes

Cosmic rays are another background to $\mu^- N \to e^- N$ searches, as cosmic muons can decay or interact with material in the apparatus generating conversion-like electrons. As opposed to the other backgrounds, the background due to cosmic rays scales with the live time of the experiment. Cosmic rays incident on the apparatus, especially those near the stopping target, have the potential to create conversion-like electrons whose reconstructed track appears to originate from the stopping target. This can occur through normal muon decay ($\mu^- \to e^- \nu_\mu \bar{\nu}_e$) or from their interaction with materials, producing high energy delta electrons. The most effective solution to suppressing this background is the implementation of a detector that can reject conversion-like events that are in coincidence with cosmic rays entering the apparatus.

1.3.5. Reconstruction Errors

While many of the above backgrounds can be suppressed through accurate measurements or the employment of specialized detectors, errors in reconstruction, inherent to any experiment, can lead to enhancements in backgrounds or the misinterpretation/identification of conversion-like events. Muon capture can result in the emission of photons or neutrons. Captured neutrons can result in additional photons. All of these contribute to the possibility of generating tracks within the tracking detectors, due to pair- or photo-production, or Compton scattering. Electrons from these various process have the ability to travel through low-mass tracking detectors, creating conversion-like tracks. The most difficult tracks to reject are those caused by electrons that are the product of pair-production from photons generated through neutron interactions. Careful design of the tracking detector(s) and determination of the quality of the tracks through them can help mitigate errors in track reconstruction.

1.4. Historical Searches for Charged Lepton Flavor Violation

Since the 1940s, there have been extensive searches for CLFV processes, so far with only tighter constraints being placed on the upper branching fractions [22]. These searches have been in many sectors, with searches in the muon sector being the most promising (Fig. 1.13). Experiments in the muon sector can be divided into three main search categories: coherent muon to electron conversion in the presence of a nucleus ($\mu^- N \to e^- N$), muons decaying into an electron and photon ($\mu^+ \to e^+\gamma$), and muons decaying into three electrons ($\mu^+ \to e^- e^+ e^+$). The upper limits for these processes are shown in Table 1.4. These searches possess complimentary sensitivity to new physics

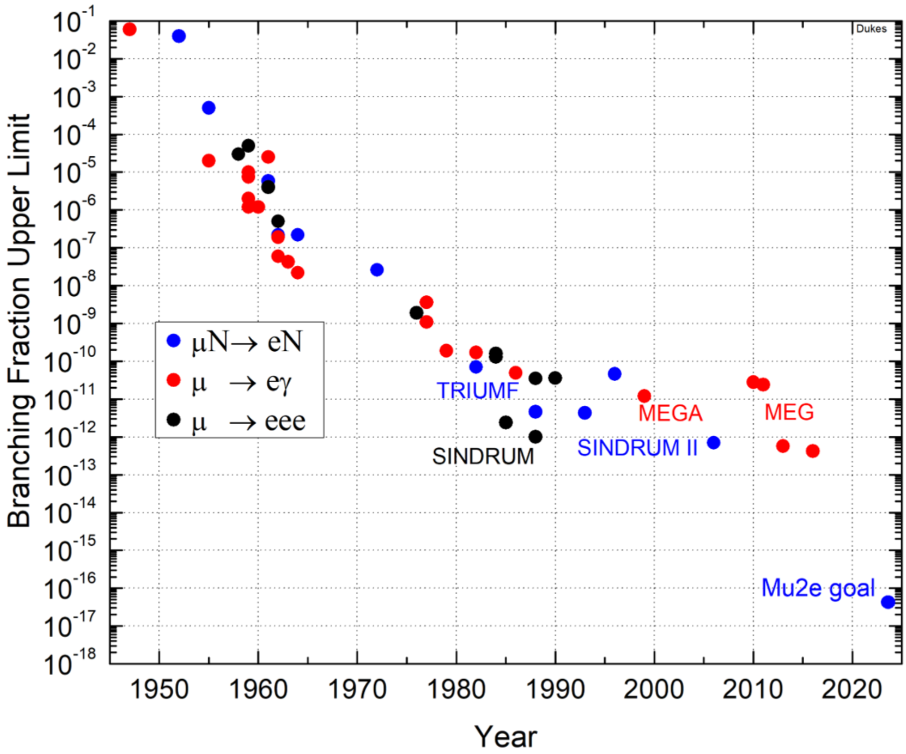

Figure 1.13.: Historical searches for CLVF in the muon sector. The target sensitivity for the Mu2e experiment is four orders of magnitude higher than the current limit set by SINDRUM-II.

effects and a signal found in several would be useful in untangling the underlying physics responsible for CLFV. While there have been a great number of experiments searching for CLFV, the most notable experiments that have had an influence on the next-generation of muon-to-electron conversion experiments, like Mu2e, are SINDRUM-II and a search at TRIUMF. Both experiments have demonstrated that experimental backgrounds can be kept to a sub-event level, which makes the observation of CLFV an unambiguous sign of new physics.

There are many next-generation muon experiments that are being built to search for rare CLFV processes involving muon parents. Those include an upgrade to the MEG experiment called MEG-II, which continues the search for $\mu^+ \rightarrow e^+\gamma$ with a design sensitivity of 6×10^{-14} [24], and Mu3e, which will search for $\mu^+ \rightarrow e^-e^+e^+$ with a design

Table 1.4.: The upper limits for muon sector CLFV searches.

$\Gamma(\mu \to e) < 7 \times 10^{-13}$ (in Au, 90% CL)[14]
$Br(\mu \to e\gamma) < 4.2 \times 10^{-13}$ (90% CL)[13]
$Br(\mu \to eee) < 1 \times 10^{-12}$ (90% CL)[23]

sensitivity of 2×10^{-15} [25]. There are several $\mu \to e$ experiments such as DeeMe, which will search for $\mu \to e$ in graphite (SES 1×10^{-13}) or silicon carbide (SES 2×10^{-14}) [26], and Mu2e and COMET, which will search for $\mu^- N \to e^- N$ using an aluminum stopping target with design sensitivities of 3×10^{-17} [27] and 3×10^{-15} (Phase-I) [28], respectively.

Chapter 2.

The Muon to Electron Conversion Experiment

2.1. Introduction to Mu2e

The Muon-to-electron Conversion Experiment (Mu2e) at Fermilab proposes to determine the ratio of the measured coherent, neutrino-less muon to electron conversion rate, in the field of a nucleus, to the rate of muon captures on the nucleus:

$$R_{\mu e} = \frac{\Gamma(\mu^- + A(Z,N) \to e^- + A(Z,N))}{\Gamma(\mu^- + A(Z,N) \to \nu_\mu + A(Z-1,N))}. \tag{2.1}$$

The rate of muon captures on the nucleus is the normalization factor for the conversion events. The charged lepton flavor violating conversion of a muon to an electron in the presence of a nucleus results in a monoenergetic electron whose energy is very close to the rest mass of the muon, with minor energy lost due to recoil of the nucleus and its binding energy:

$$E_e = m_\mu c^2 + E_{recoil}(A) + E_{binding}(Z), \tag{2.2}$$

where the recoil and binding energy depend on A and Z, the number of nucleons and protons in the nucleus, respectively. Due to a balance between muon-capture rates and the muonic-atom lifetime, as well as the need for the smallest possible binding energy and a daughter atom that is more massive, aluminum was selected as the stopping target material. In aluminum the emission energy of a conversion-electron is 104.97 MeV with a mean muon lifetime of 864 ns [17]. Observation of this process would be an unambiguous sign of new physics beyond the Standard Model. Currently, the best experimental limit on muon-to-electron conversion is set by the SINDRUM II experiment, $R_{\mu e}$ <7×10^{-13} (@ 90% CL) [14]. Mu2e intends to surpass this limit by four orders of magnitude, achieving a single event sensitivity of 3×10^{-17}. To reach this sensitivity, the backgrounds to muon-to-electron conversion need to be well-understood and kept to a sub-event level over the three-year run time of the experiment.

2.2. Mu2e Experimental Operation

The basic operation of Mu2e can be reduced to a short list of tasks: generate a muon beam, stop muons in a target, and look for conversion events. The actual operation of Mu2e, however, is slightly more complicated. In its attempt to achieve a four order of magnitude increase in sensitivity over the present limit set by SINDRUM-II, Mu2e will employ several novel features: implementation of a high-intensity, highly efficient, solenoid-based muon beam, a cutting-edge, low-mass spectrometer, and utilization of a pulsed beam structure from Fermilab's powerful and flexible accelerator complex.

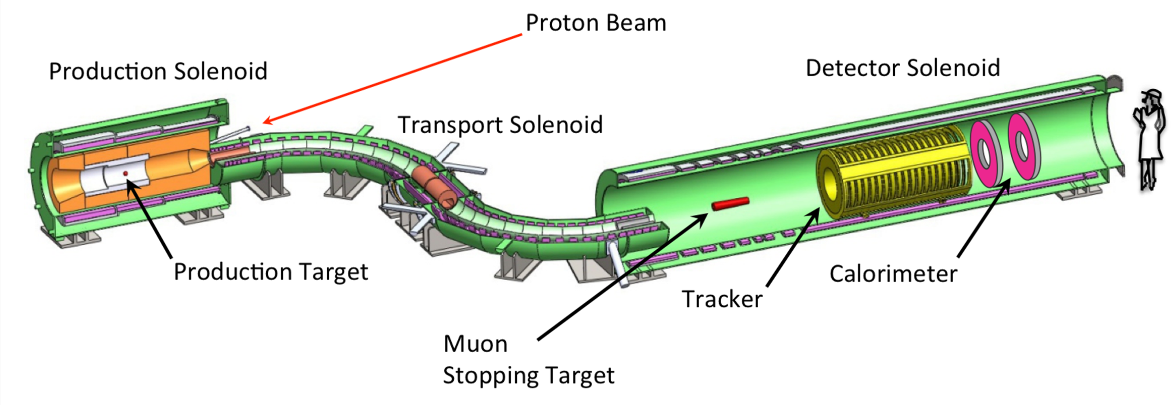

Figure 2.1.: Overview of the Mu2e apparatus.

Shown in Fig. 2.1, the basic design of Mu2e consists of an array of three superconducting solenoids: the Production Solenoid (PS), the Transport Solenoid (TS), and the Detector Solenoid (DS). An intense, pulsed beam of 8 GeV protons, delivered by the accelerator complex, is directed at a tungsten target in the PS, generating pions. A gradient in the magnetic field (Fig. 2.2) sweeps the pions into the TS as they decay to muons. Utilizing an S-shape and an asymmetric collimator midway through the solenoid, the TS allows for momentum and sign selection of the muons, respectively, as they move towards the DS. The S-shape is also used to eliminate line-of-sight between the PS and the stopping target to avoid neutral particles impacting the stopping target. Sufficient path-length is provided by the TS to allow most of the pions to decay before reaching the DS.

The Mu2e experiment will make use of only low-energy negative muons. Located in the upstream section of the DS is the stopping target, which is comprised of many thin aluminum foils. Approximately half of the muon beam will stop in the target. After a short period of time, enough for beam-induced backgrounds to dissipate, a fraction of the bound muons will decay and eject electrons that will spiral down the DS. The combination of a low-mass, straw-tube tracking detector and crystal calorimeter are used to measure the energy of the electrons and reject background events. Surrounding the

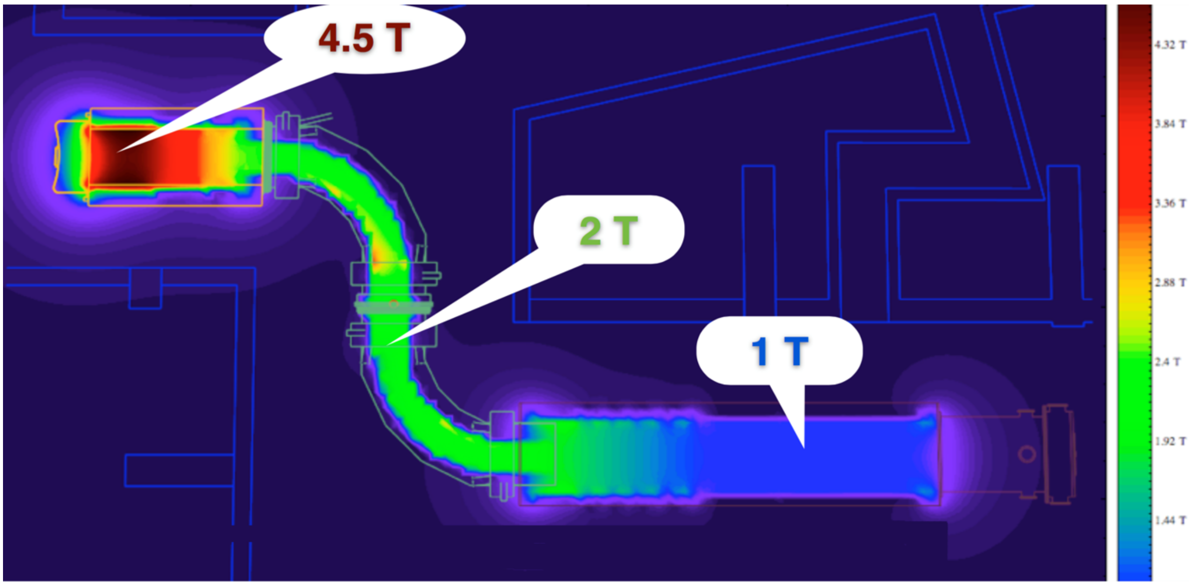

Figure 2.2.: Magnetic field values in the Mu2e apparatus.

entirety of the DS and half of the TS is a large-area, high-efficiency cosmic-ray veto detector. The purpose of this detector is to identify and reject events where cosmic ray muons impinge upon the DS, possibly producing fake conversion-like signals.

A key aspect in the search for muon-to-electron conversion at Mu2e is hinged upon the proton beam delivered to the experiment. Unlike its predecessor, SINDRUM-II, Mu2e will take advantage of a pulsed beam structure that provides adequate time for beam-induced backgrounds to diminish. Prompt backgrounds associated with the arrival of the proton beam are known as the beam flash. The decay or interaction of pions in the beamline would be a significant background if a non-pulsed beam structure was used. Radiative pion capture is largely eliminated by having a delayed search window that is well-timed to the lifetime of a muon bound to aluminum (864 ns). The accelerator complex at Fermilab, including the re-purposed Debuncher ring (Delivery ring), employs slow-resonant extraction to deliver a pulse of 8 GeV protons every 1695 ns. As shown in Fig. 2.3, after a proton pulse the search for $\mu \rightarrow e$ conversion is delayed by 700 ns so that the secondary-beam particles from the beam flash are minimal and pion captures by the stopping target have been reduced by 10^9. Shortly before the arrival of the next proton

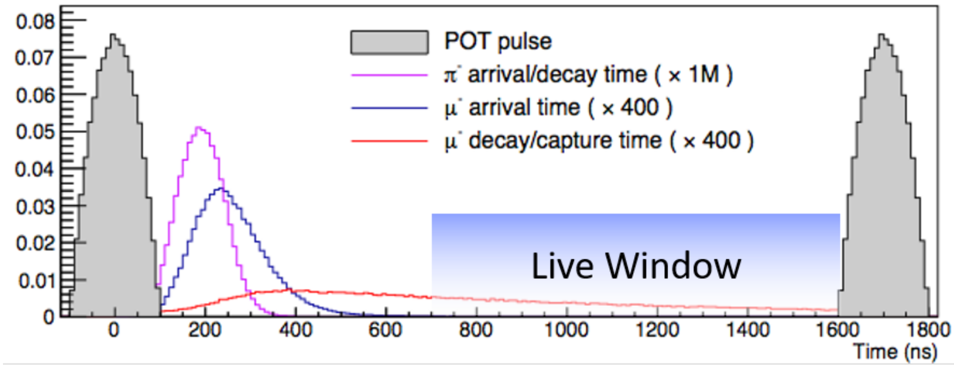

Figure 2.3.: The time structure in which protons are delivered to the Mu2e apparatus, and the time in which resulting pion capture backgrounds, muon capture and decay times occur with respect to the delayed live-window in which the search for $\mu \to e$ conversion will take place.

pulse, the signal window closes. Beam extinction, defined as the ratio of the number of protons arriving out-of-time with respect to the beam pulse to the number of protons within the pulse, must be kept to a minimum so as to reduce the effects of out-of-time protons reaching the production target.

During the signal window, muons decaying or undergoing CLFV conversion expel electrons isotropically from the stopping target. Because of the gradient magnetic field near the stopping-target region (Fig. 2.2), there is an increased acceptance for conversion-like electrons as those emitted in the upstream direction are reflected back downstream. Beam-related backgrounds are also easier to reject due to a change in pitch of their trajectory when passing through the gradient field, resulting in tracks not consistent with conversion-electrons. The downstream region of the DS has a uniform magnetic field and contains a calorimeter and tracking detector. Both the Tracker and Calorimeter are designed as hollow cylinders centered along the beam axis. This allows an overwhelming majority of electrons produced by DIO to pass through the center of both detectors without creating hits. Only electrons with transverse momentum greater than 90 MeV/c have radii large enough to create hits in the detectors (Fig. 2.4).

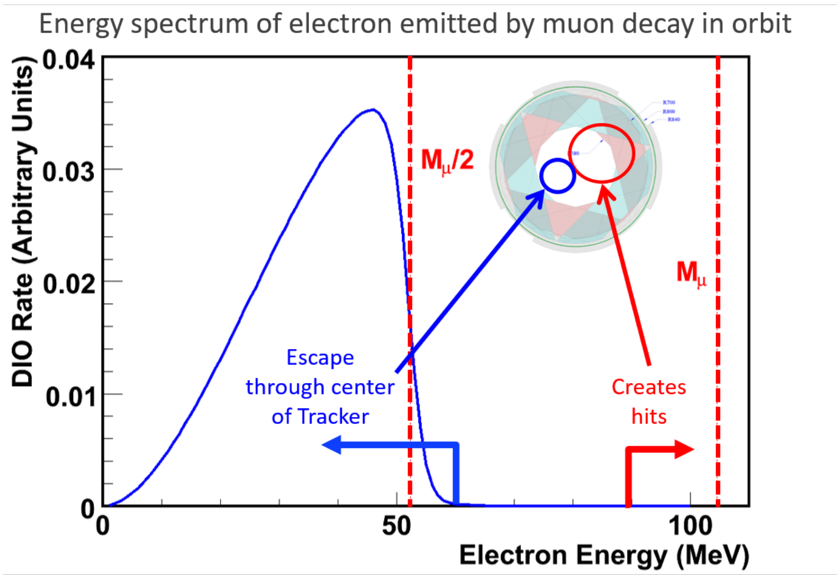

Figure 2.4.: Most of the DIO electrons pass through the center of the tracker and calorimeter (inset). Only electrons with transverse momentum greater than 90 MeV/c are able to create hits in the detectors.

The main purpose of the stopping target is to maximize the number of stopped muons while minimizing the amount of material conversion-electrons need to traverse while propagating towards the instrumentation. Careful selection of the stopping target material for the experiment was required, a decision made with several considerations. First, the sensitivity to $\mu \to e$ conversion is roughly proportional to Z, which implies Z should be maximized[†]. For heavier elements, the DIO endpoint energy decreases [18] and the lifetime of muonic atom decreases [17]. The shorter lifetime makes it difficult to have an appropriately timed live window that maximizes the acceptance for the signal while minimizing contamination from backgrounds. Also dependent on the mass of the nucleus is the background from radiative muon capture: $\mu^- \mathrm{Al} \to \nu_\mu \gamma \mathrm{Mg}$. The mass of the target nuclei should be less than that of the daughter nuclei to keep the photon energy well below the conversion-electron energy. An additional consideration is the purity and mechanical strength of the target material as both are important factors in avoiding muons stopping in foreign nuclei, which could introduce backgrounds. With these considerations aluminum

[†]This is only true up to a Z of around 40.

proves to be the ideal candidate for the stopping-target material [29]. The stopping target should be thick enough in the beam axis direction so as to stop at least 40% of incident muons to reach the desired sensitivity level, however, the target should not be so thick as to result in additional backgrounds from beam or cosmic-ray induced processes, such as scattering of beam electrons or delta-rays from cosmic ray muons. In addition the thickness should not adversely affect the momentum resolution. The chosen configuration of the stopping target is 37 thin, 0.10 ± 0.05 mm, concentric 100.0 ± 0.5 mm disks with a 43.0 ± 0.5 mm hole in the center and 22.2 ± 1.0 mm of inter-disk spacing, all supported by 3-mil gold plated tungsten wires [29], shown in Fig. 2.5.

To determine the ratio of the measured coherent, neutrino-less muon-to-electron conversion rate to the rate of muon captures on the nucleus (Eq. 2.1) the rate of muon captures will be measured by a special detector downstream of the DS, called the Stopping Target Monitor, with an accuracy of 10 % at the $1\,\sigma$ level over the lifetime of the experiment [30].

2.3. Accelerator and Beamline

A total of 3.6×10^{20} protons incident on the production target are needed over the run time of the experiment in order to achieve the desired sensitivity. These protons are to be delivered in well defined pulses, both spatially and temporally, separated by a time interval that is greater than the lifetime of a muon captured by an aluminum target (864 ns). Since protons incident on the production target between beam pulses contribute to experiment backgrounds, the ratio of out-of-time to in-time beam particles, also known as beam extinction, must be less than one part in 1×10^{10}. A summary of the beam design specifications are listed in Table 2.1 and the beam time profile is shown in Fig. 2.6.

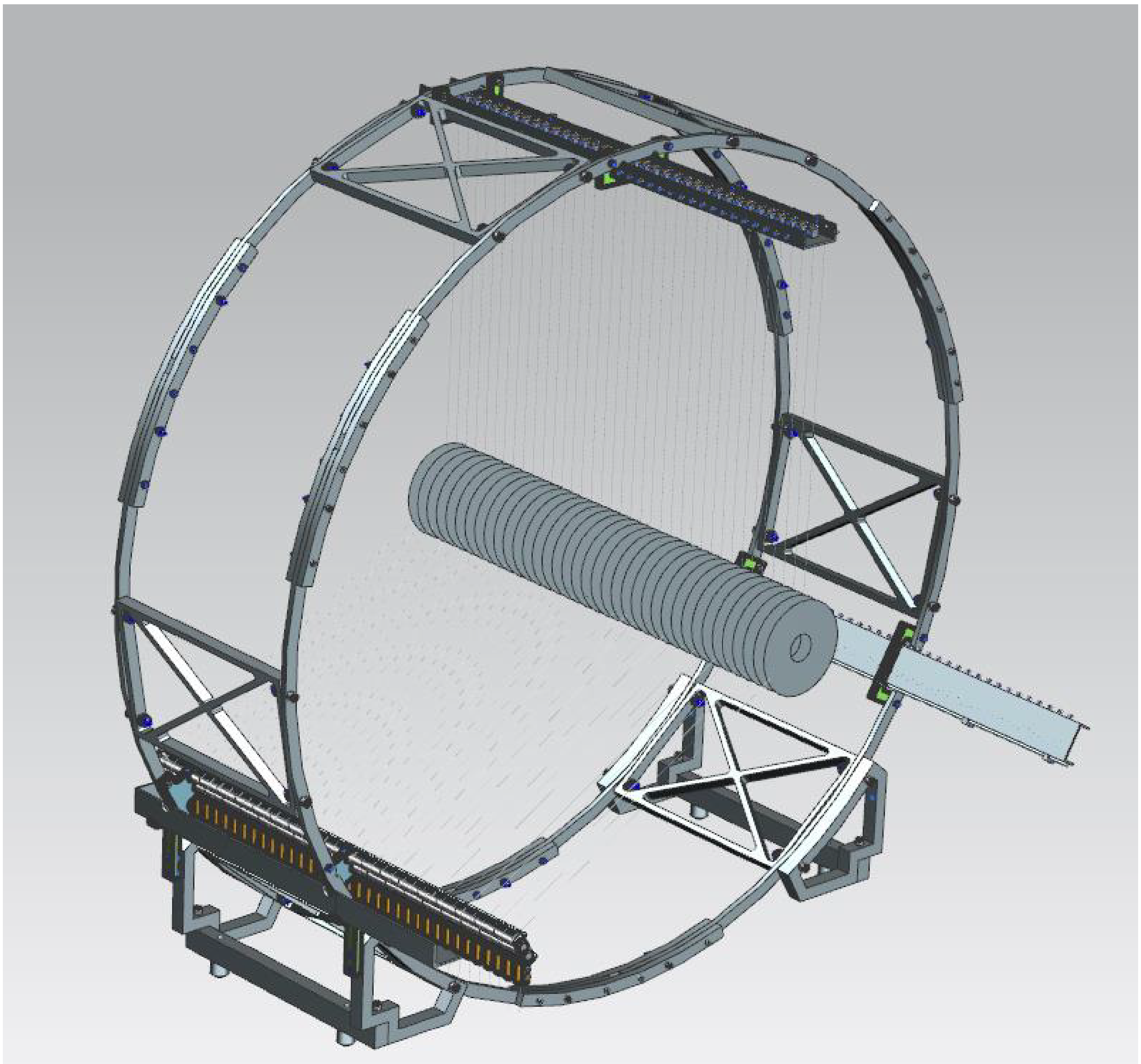

Figure 2.5.: The muon stopping target showing the 37 thin aluminum foils supported by tungsten wires, tensioned by bronze weights that are shown in the lower-left of the image.

Table 2.1.: Summary of the design specifications of the proton beam delivered to Mu2e.

Parameter	Design Value	Unit
Total protons on target	3.6×10^{20}	protons
Time between beam pulses	1695	ns
Maximum variation in pulse separation	<1	ns
Spill duration	54	ms
Beamline transmission window	230	ns
Transmission window jitter (rms)	5	ns
Out-of-time extinction factor	10^{-10}	
Average proton intensity per pulse	3.1×10^{7}	protons/pulse
Maximum pulse to pulse intensity variation	50	%
Minimum target spot size (rms)	1	mm
Maximum target spot size (rms)	1	mm
Target beam divergence (rms)	0.5	mrad

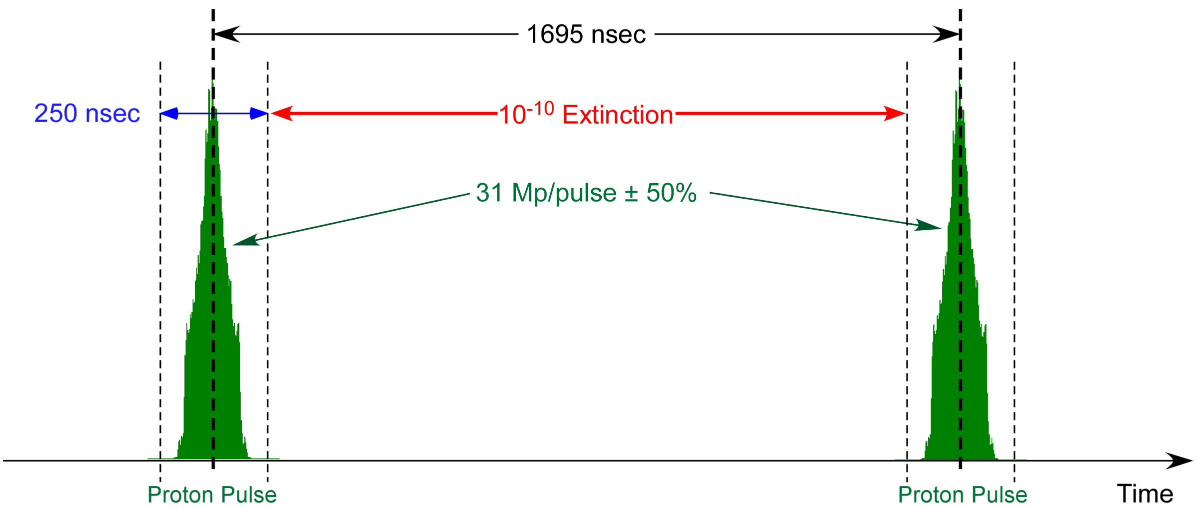

Figure 2.6.: The intensity of the pulsed proton beam (height in this graphic) with respect to time (x-axis in this graphic), required by the Mu2e experiment. Listed here are the intensity, extinction, and pulse period requirements.

Much of the accelerator infrastructure that will be used to deliver protons to Mu2e already exists. While this reduces the effort needed to commission beam to the experiment, special consideration must be taken to minimize the impact to existing users, such as the NOνA experiment. At the beginning of the beamline are a pair of 35 KeV H^- ion sources. The H^- ions are accelerated up to 400 MeV through the existing Linear Accelerator (LINAC) and stripped of electrons before delivery to the Booster ring. In the Booster, the protons are accelerated to 8 GeV/c before being injected into the Recycler where they are grouped into bunches and later sent to the Debuncher/Delivery Ring where they undergo slow resonant extraction and are sent to the Muon Campus (Figs. 2.7, 2.8).

2.3.1. Solenoids

Three superconducting solenoids form the muon beamline and house the experiment's detectors. Gradients in the magnetic fields in specific regions of the solenoids allow for the efficient collection and transport of muons and conversion-electrons. In the region where the detectors are located, the magnetic field is uniform and allows for precision measurements of the electron momentum. The solenoids that generate this complex field configuration are comprised of three distinct magnets: the Production Solenoid, the Transport Solenoid, and the Detector Solenoid. To minimize the backgrounds from muons that might stop in gaseous atoms, to reduce the effects of multiple scattering for low-momentum particles, and to prevent sparking of the Tracker's straw tubes, the inner bores of the solenoids are evacuated to 1×10^{-4} Torr.

Production Solenoid

The first in the chain of Mu2e solenoids is the Production Solenoid (PS) (Fig. 2.9). Containing the tungsten production target, the PS is a relatively high-field solenoid

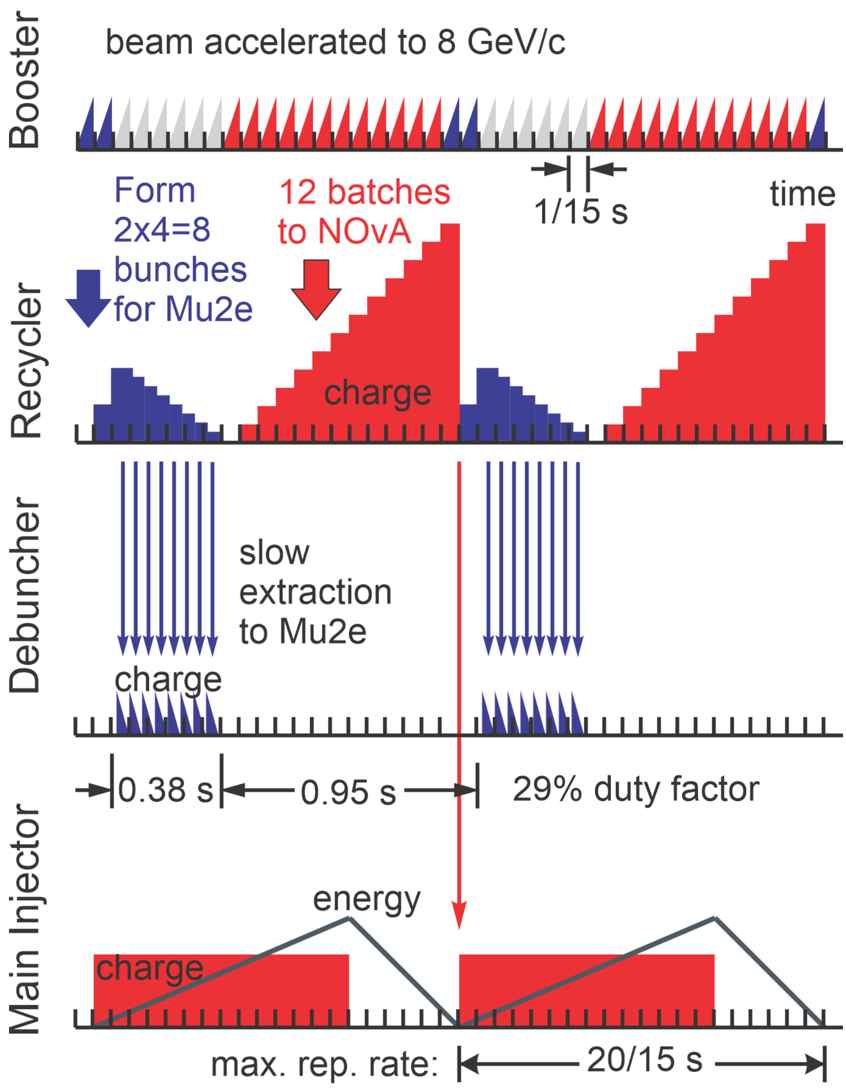

Figure 2.7.: Plot showing the batch timeline as shared by the Mu2e and NOνA experiments. The blue and red bars correspond to the proton batches used by the Mu2e and NOνA experiments respectively. Mu2e beam manipulations are performed in the first eight 15 Hz ticks. NOνA uses the remaining twelve 15 Hz ticks to slip stack proton batches. The total length of a Main Injector cycle is 20 ticks = 1.333 sec, with one tick being 1/15 sec = 66.7 ms. The Main Injector timeline concerns only NOνA and is shown here only for completeness.

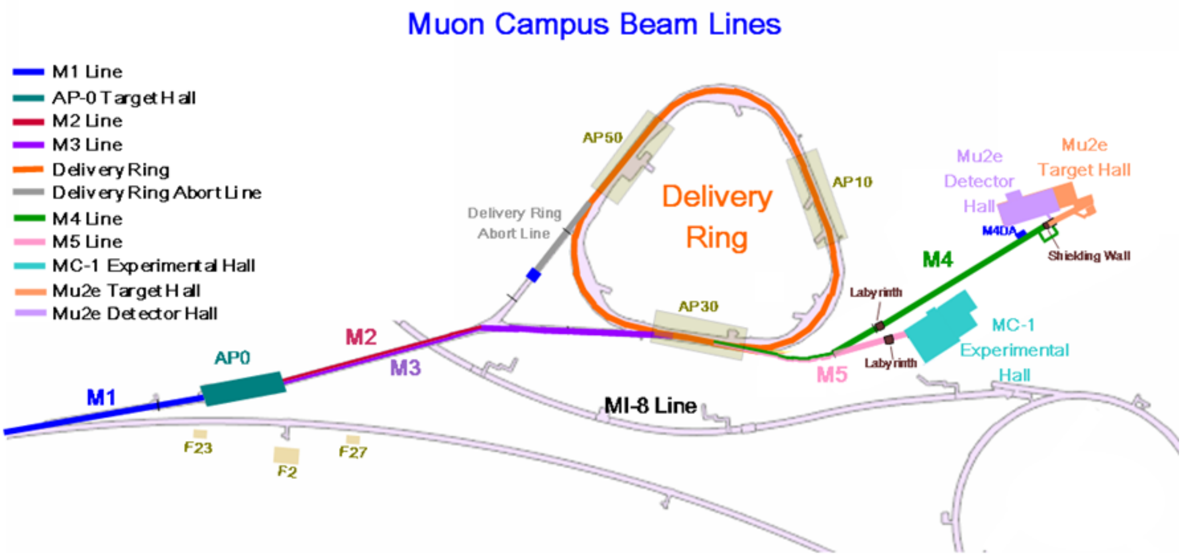

Figure 2.8.: Muon Campus beamlines. Protons are transferred from the Recycler Ring (not shown) to the Delivery Ring where they are slow extracted and delivered to the Mu2e experiment via the M4 beamline.

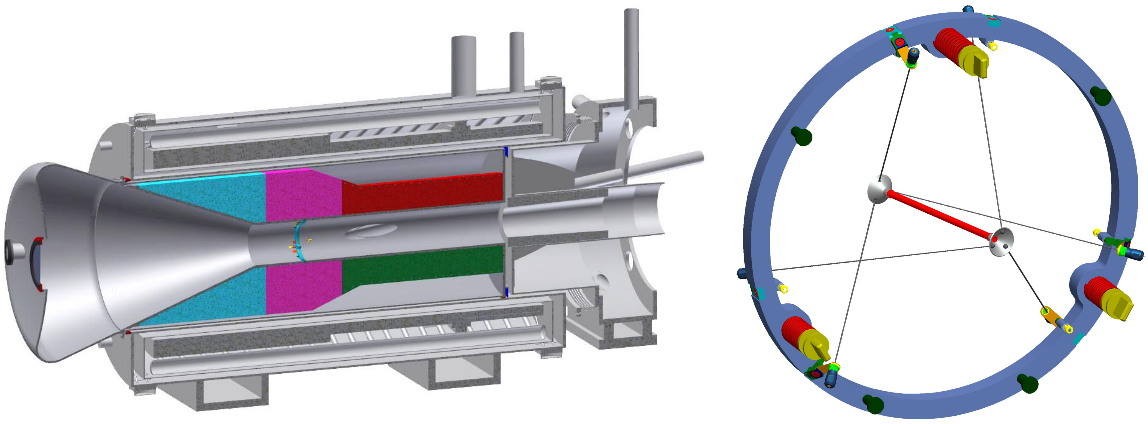

Figure 2.9.: Production Solenoid (PS) assembly (left) that houses the production target (right).

with an axial gradient that varies from 4.6 T to 2.5 T in the downstream direction. The gradient of the field reverses the direction of some charged particles produced in the upstream direction and pushes charged particles downstream, resulting in a greater collection and transport of pions.

Transport Solenoid

Directly downstream of the PS is the Transport Solenoid (TS), shown in Fig. 2.10. The TS is comprised of five sections, listed from the most upstream to the most downstream:

1. TS1: Straight section that interfaces with the Production Solenoid and contains a stationary collimator (COL1).
2. TS2: First 90° toroidal section.
3. TS3: Straight section that houses a collection of collimators (COL3u/d), the antiproton stopping window, and forms the junction between the toroidal sections TS2 and TS4.
4. TS4: Second 90° toroidal section.
5. TS5: Straight section that interfaces with the Detector Solenoid and contains the last collimator (COL5).

The two 90° bends in the TS fulfill several purposes. First, neutrons and photons that could produce backgrounds upon impact with the stopping target no longer have a direct path from the PS to the stopping target and can be attenuated by shielding. Second, charged particles are momentum and sign selected by the pair of asymmetric collimators (COL3u/d) located between the two bends of the TS. The separation of charges is a result of a displacement due to their propagation through the curved solenoidal field (curvature drift). The vertical displacement midway through the TS is described by:

$$D[m] = -\frac{Q}{e}\frac{\pi}{0.6B[T]}\frac{P_L^2 + 0.5P_T^2}{P_L[GeV/c]}, \tag{2.3}$$

where Q is the charge of the particle, e is the magnitude of the charge of the electron, B is the strength of the field, and P is the magnitude of the momentum, with components along P_L, or transverse to P_T, the magnetic field. Having an offset aperture in this middle collimator allows the passage of only one type of charge. The bend in the opposite direction returns the singly charged beam back to the beamline center. Particles propagating through the TS also execute fast gyrations with radius described by:

$$r[m] = \frac{P_T[GeV/c]}{0.3B[T]}, \tag{2.4}$$

where an appropriately placed aperture in the collimator allows for the transmission of only low-momentum particles that cannot scatter in the stopping target to mimic a conversion-electron.

Located between the COL3u/d collimators is the antiproton absorber. In addition to providing a physical barrier between the upstream and downstream sections of TS vacuum, inhibiting the downstream flow of radioactive molecules from activated materials near the PS, the antiproton stopping window is designed to remove antiprotons that can produce a serious physics background for the experiment, while not substantially degrading the muon yield or causing additional backgrounds [31].

Detector Solenoid

The last of the superconducting solenoids is the Detector Solenoid (DS), which houses the stopping target, tracker, and calorimeter. In the stopping target region, which is the upstream portion of the DS, the magnetic field has a gradient that reflects upstream-going electrons back towards the detectors, greatly increasing the acceptance of conversion-elections. In the downstream region of the DS where the tracker and calorimeter are located, the magnetic field is uniform to allow for precision measurement of electron momentum. At the end of the DS is the muon beam stop (MBS). The calorimeter, tracker, and stopping target are attached to the MBS, and the entire assembly is supported by a rail system inside the DS bore. The bulkhead is removable to allow the detectors to be

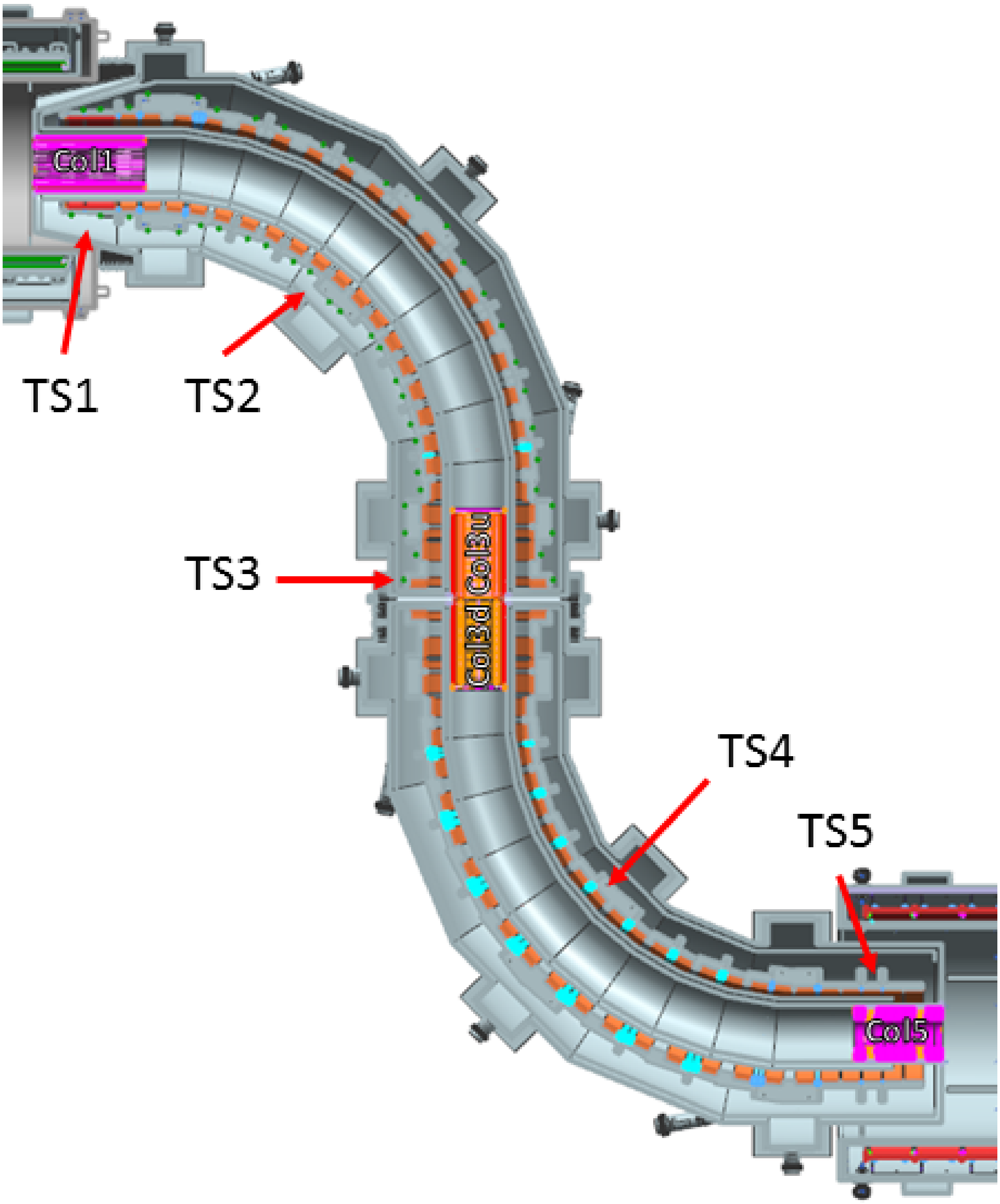

Figure 2.10.: The Transport Solenoid with sections and collimators identified.

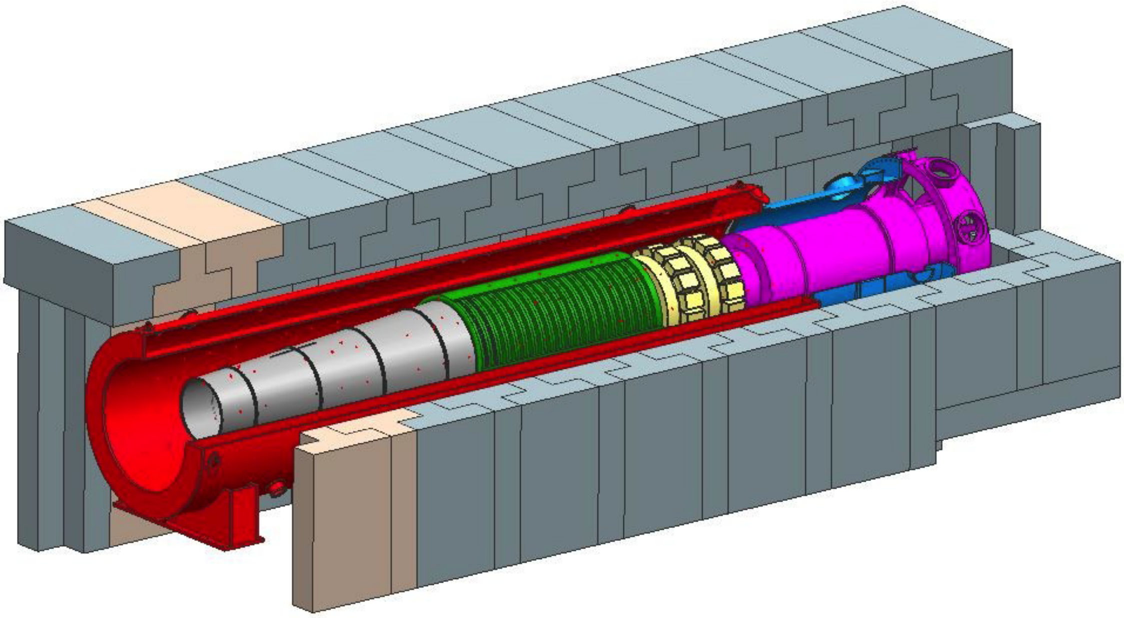

Figure 2.11.: Cutaway view of the complete Detector Solenoid assembly and concrete shielding blocks. The cryostat (red), stopping target support (gray), tracking detectors (green), calorimeter (yellow), and muon beam stop and cryostat bulkhead (purple) are visible.

serviced. Surrounding the DS, and part of the TS, are concrete shielding blocks. Shown in Fig. 2.11 is a cutaway of the DS assembly and shielding. The purpose of the concrete is to shield the Cosmic Ray Veto detector from particles coming from the beamline. The Cosmic Ray Veto, discussed later, surrounds the DS, outside of the shielding blocks. The downstream end of the shielding is movable, called the end-cap, which allows the inner-bore assembly to be removed for servicing (Fig. 2.12).

2.4. Detector Systems

At the heart of the Mu2e apparatus is a precision spectrometer designed to accurately measure the electron momentum while minimizing the impact of physics backgrounds. The two main components used to accomplish this goal is a low-mass tracking detector

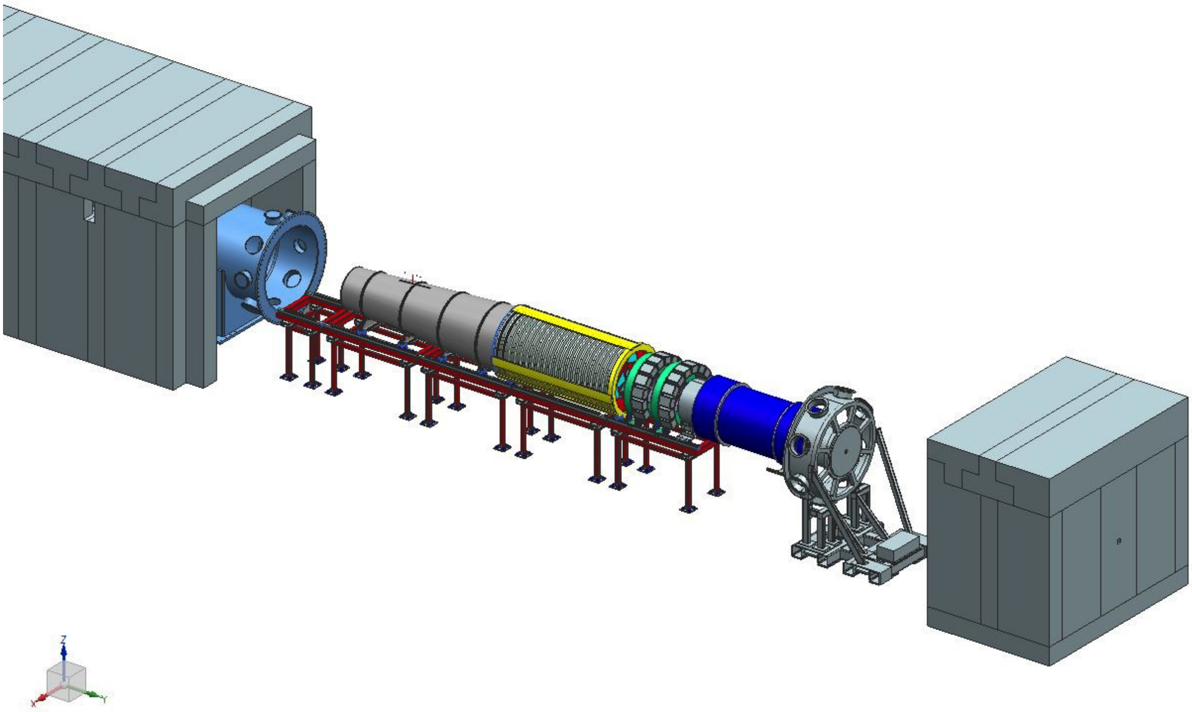

Figure 2.12.: View of the components which reside in the Detector Solenoid removed from the magnet bore. Also shown is the movable shielding end-cap.

and an electromagnetic calorimeter. An additional detector, the Cosmic Ray Veto, identifies and vetoes muon-induced backgrounds. Together these detectors will allow Mu2e to reach the designed sensitivity.

2.4.1. Tracker

The purpose of the Tracker is to precisely measure the momentum of electrons coming from the stopping target. The ability to perform this task is highly dependent on the design and environment in which the Tracker resides. Mentioned in the previous section, the Tracker is housed in the Detector Solenoid in a uniform 1 T field and high vacuum (1×10^{-4} Torr). The design of the Tracker must be such that it contains very little mass so as to reduce the effects of multiple-scattering, which is the main source of reconstruction errors, while still being extremely efficient with good tracking resolution.

The Tracker should have good acceptance of conversion-like electrons while not being overwhelmed by DIO electrons. Additionally, the Tracker must be able to survive the intense and prompt backgrounds associated with the beam flash.

To satisfy the general requirements, which are documented in more detail in Ref. [32], a drift straw tube detector was developed [33]. Consisting of 23,040 straw tubes placed circumferentially transverse to the beam axis, the region central to the beam axis is uninstrumented. Each straw tube is 5 mm in diameter, made of two layers of 6 μm spiral wound Mylar, with a 3 μm adhesive between the layers. The inner cathode surface has 500 Å of aluminum overlaid with 200 Å of gold. The outer surface has 500 Å of aluminum that acts as an electrostatic shielding and reduces the gaseous leak rate of the straw. Concentric to each tube is a 25 μm gold-plated tungsten sense wire. The drift gas is an 80% Argon 20% CO_2 mixture, run at a maximum operating voltage of 1500 V. Supported only at their ends, the 334 mm to 1174 mm long straws are arranged into 96-straw semi-circular panels. Each panel is comprised of two staggered layers of straws, which improves efficiency and aids in reducing the left-right ambiguity in tracking. Three panels, spanning 120° each, form one half of a tracking plane; the second half is another three panels rotated by 30°. A pair of planes, rotated 180° relative to one another, forms a tracking station. There are 18 stations, each separated by 46 mm, forming the entirety of the Tracker. The active region of the Tracker spans a radius from 380 mm to 700 mm, leaving the central region of the uninstrumented. This makes it blind to the bulk of the DIO spectrum (p $<$53 MeV), shown in Fig. 2.14. The Tracker is required to have a momentum resolution of at least 180 KeV, with very little high-side tail, which would contribute to background events by boosting DIO electrons into the signal region, as shown in Fig. 2.15.

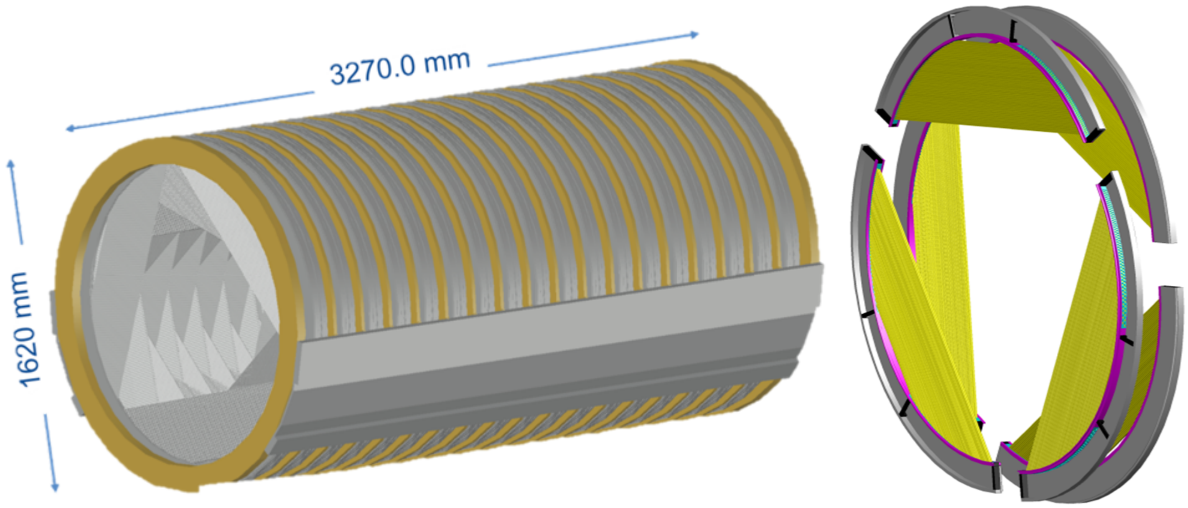

Figure 2.13.: Left: Rendering of the Tracker assembly showing the 18 stations. Right: Exploded view of a Tracker station, showing the panels of drift straw tubes that make up each plane.

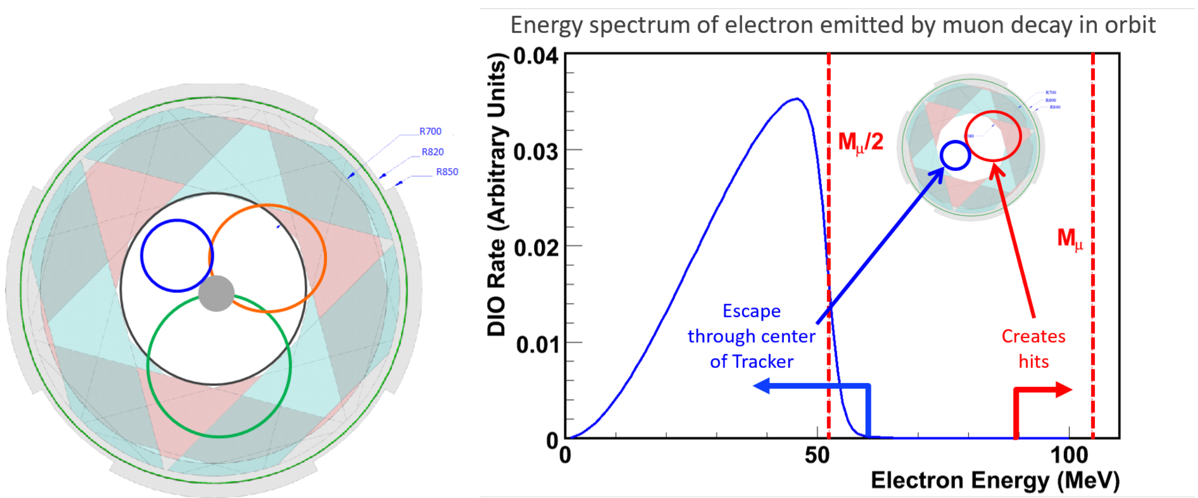

Figure 2.14.: Left: Example of a track which passes undetected through the center of the Tracker (blue) and two tracks that create hits in the Tracker (orange and green). Right: The majority of DIO electrons passes through the center of the Tracker, while only electrons with sufficient transverse momentum are able to create hits in the detector, such as conversion-electrons.

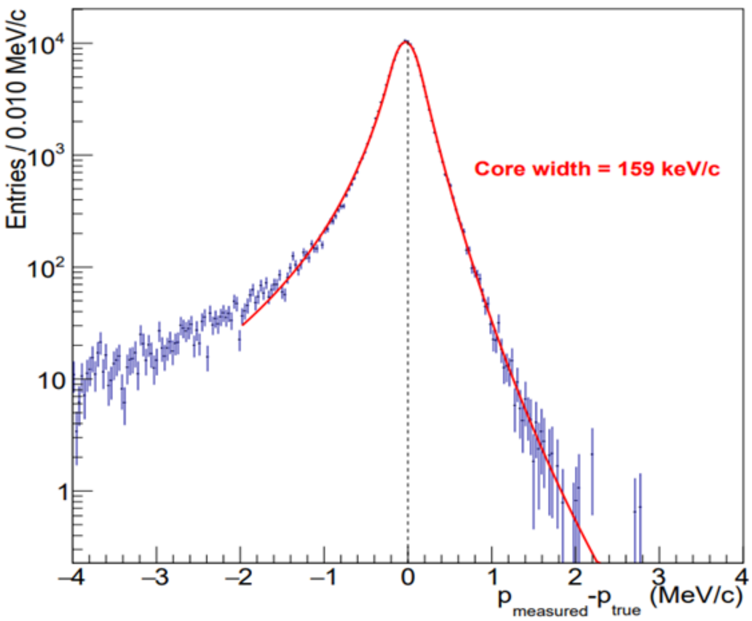

Figure 2.15.: Momentum resolution of the Tracker for conversion-electrons. Of particular importance is the lack of a high-side tail which would contribute to physics background by boosting high-energy DIO electrons into the signal region.

2.4.2. Calorimeter

The primary purpose of the Calorimeter is to provide a measurement which is complimentary to information ascertained by the Tracker. The Calorimeter is able to reduce backgrounds by obtaining timing and energy measurements of particles mimicking the conversion-electrons, for example: backwards going positrons that appear in the Tracker as forward going electrons. The requirements for the Calorimeter include: a 10% or better energy resolution to confirm the electron momentum measurement from the Tracker, a timing resolution better than 500 ps, which ensures any energy deposition in the Calorimeter is in time with reconstructed trajectories in the Tracker, a position resolution better than 1 cm, which is used to compare extrapolated trajectories from the Tracker to reconstructed tracks, provide trigger information, and reject muons at better than a 1/200 level [34]. Muon rejection is important to eliminate cosmic-ray muons that escape detection by the Cosmic Ray Veto and are reconstructed as electrons by

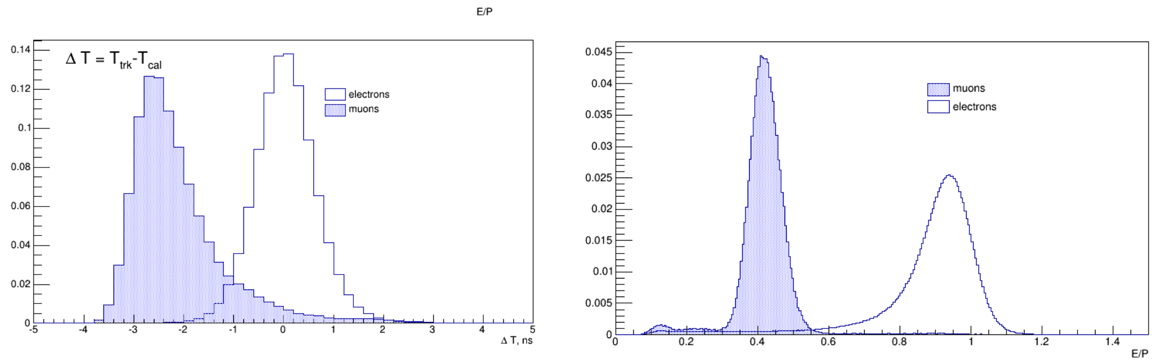

Figure 2.16.: Time difference, Δt, between the track seen in the Tracker and the energy deposition cluster in the Calorimeter (left) and E/P (right) for 105 MeV/c muons and electrons. [27]

the Tracker. The ability to distinguish between muons and electrons is determined from the time difference between particle tracks and Calorimeter clusters along with E/p measurements, both of which have clear separations, shown in Fig. 2.16.

The design of the Calorimeter, shown in Fig. 2.17, employs identical two disks, with an inner (outer) radius of 37 cm (66 cm) spaced 70 cm apart, comprised of pure Cesium Iodide (CsI) crystal scintillators. Each scintillating crystal has a 3.4 cm square profile and is 20 cm long, is wrapped with 150 μm Tyvek [35] for increased light collection and read out by a pair of silicon photomultipliers (SiPMs). There are 674 crystal bars in each disk, for a total of 1348 in the entire detector.

The design of the Calorimeter was optimized to maximize the the acceptance of conversion-electrons. The separation distance of the two disks is a half-pitch of the helical trajectory a 100 MeV electron. The length of each crystal is approximately 10 radiation lengths, but the helical trajectory electrons take results in an effective length of 15 radiation lengths. The energy and time resolution of the Calorimeter is $\sigma_E/E = O(5\%)$ and σ_t <500 ps (Fig. 2.18) at 100 MeV.

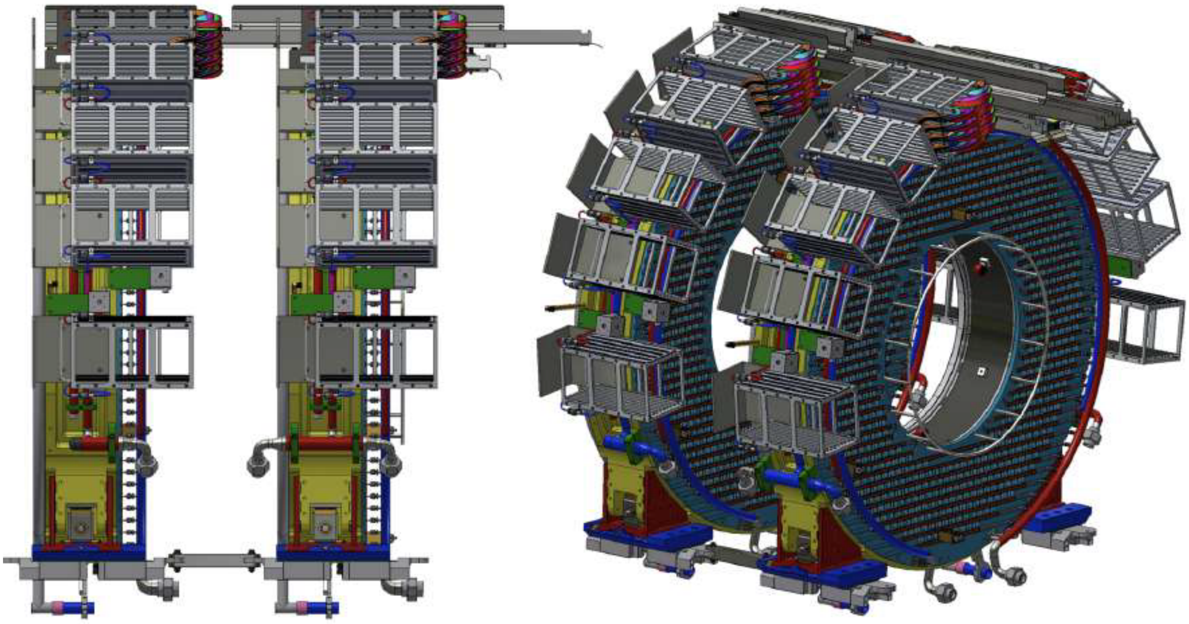

Figure 2.17.: Elevation and isometric views of the crystal-based electromagnetic calorimeter assembly.

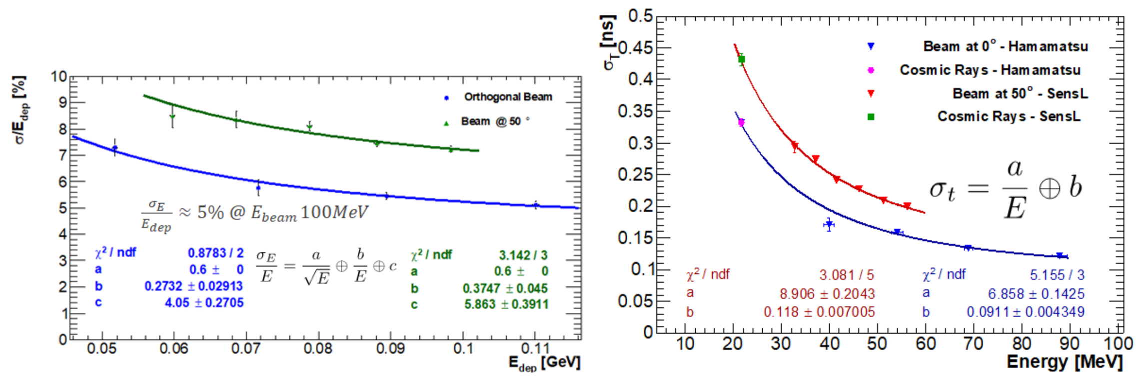

Figure 2.18.: Measured energy (left) and timing (right) resolution for the Mu2e Calorimeter, determined through testing of a prototype detector using an electron beam of known energy.

2.4.3. Cosmic Ray Veto

In order for the Mu2e experiment to reach the desired sensitivity, one of the largest backgrounds to the experiment must be well controlled: cosmic rays. A number of processes generated by cosmic rays can mimic conversion-electrons coming from the stopping target, including from the decay of cosmic muons, the secondary production of delta electrons produced from interactions with materials in the DS, and the misidentification of muons as electrons. Reduction of these background events is accomplished through implementation of a highly efficient Cosmic Ray Veto system, which will be discussed at length in the next chapter. It is expected that fake conversion-like events produced by cosmic ray muons will occur at a rate of approximately one per day. The task of the Cosmic Ray Veto detector is to detect, with very high efficiency, muons entering the apparatus that are in coincidence with a conversion-like electron identified by the Tracker and Calorimeter.

2.5. Backgrounds to the Conversion-Electron Signal

A number of processes can imitate a muon-to-electron conversion signal. It is understanding and controlling these background sources that drives the design of Mu2e. These backgrounds include:

1. Muon Decay In Orbit
2. Radiative Pion Capture (RPC)
3. Radiative Muon Capture (RMC)
4. Antiprotons
5. Muon Decay In Flight

6. Pion Decay In Flight
7. Beam Electrons
8. Cosmic Rays

These backgrounds were discussed in Ch. 1.3. Here an estimate for the total number of events for each background type is provided in the context of the Mu2e experiment.

2.5.1. Muon Decay In Orbit

Muons are able to decay while bound to the nucleus, a process also known as decay in orbit (DIO). This is an irreducible background for the Mu2e experiment. Using a detailed simulation of the experimental apparatus, realistic reconstruction of DIO electrons generated with energies consistent with the spectrum described in Ref. [18], and a momentum selection between 103.75 MeV/c to 105 MeV/c, we estimate a background of 0.14 ± 0.11 events with a single event sensitivity of $(2.6 \pm 0.07) \times 10^{-17}$ (Fig. 2.19). The uncertainties are attributed to limited Monte Carlo statistics, excluding corrections for particle-ID and cosmic-ray veto requirements. One of the issues with the DIO spectrum from Ref. [18] is that it does not include higher-order radiative effects, which affect the shape of the spectrum near the signal window and can change the background estimate. In lieu of better higher-order calculations, the systematic uncertainty associated with the predicted DIO spectrum is set to follow closely with radiative effects observed in Kaon physics which estimates the DIO background yield increasing by no more than 20 %, or no more than 0.04 events [36].

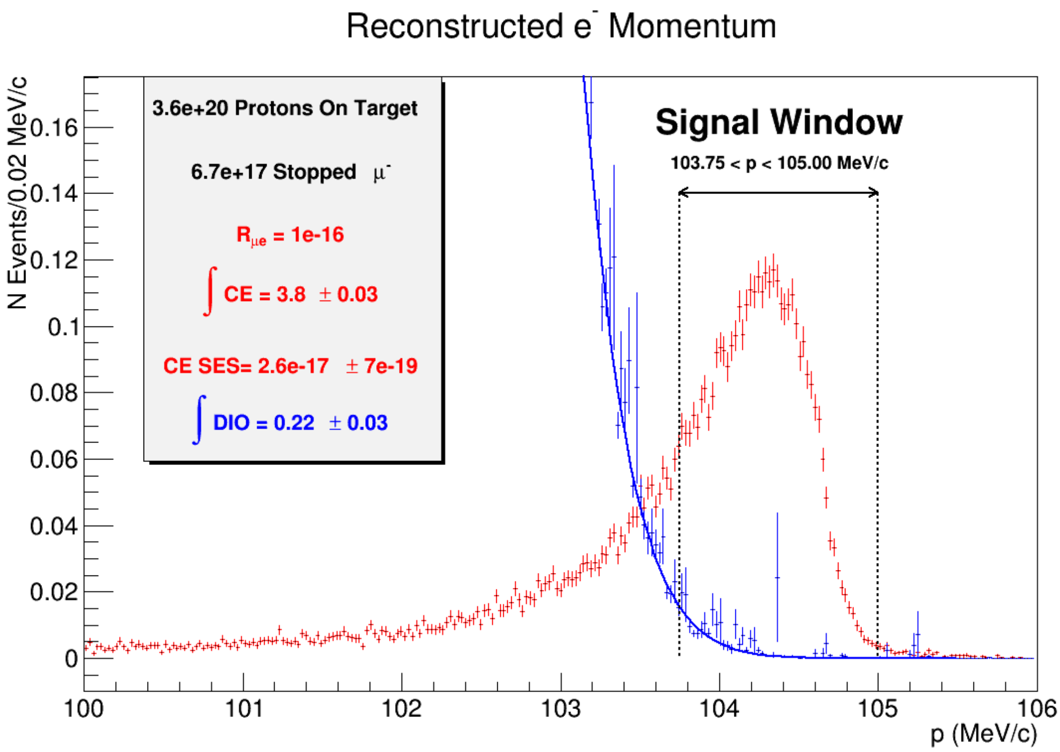

Figure 2.19.: Simulated reconstructed momentum spectrum for DIO (blue) and conversion-electrons (red) assuming a conversion rate of $R_{\mu e} = 10^{-16}$. The distributions are normalized to the total number of muon stops expected for 3.6×10^{20} protons on target.

2.5.2. Radiative Pion Capture

The background contribution of RPC was estimated through simulation, which treated the internal and external sources separately due to the radiated photon energy spectrum of a pion captured in aluminum having never been experimentally measured. Instead, the energy spectrum and rate is assumed to be that of RPC in magnesium. During simulation of the radiative process, photons were isotropically produced using the magnesium spectrum described in Ref. [37], with the time and position of creation sampled randomly from the expected stopped-pion position and time distributions. Internally produced e^+e^- pairs were simulated in the same manner, with their momentum sampled from the double-differential formula described in Ref. [38]. Shown in Fig. 2.20 is the expected background contribution of RPC electrons as a function of time. The vertical dashed line represents the start of the live window. It was found that for a live gate between $700 < t_0 < 1695$ ns (995 ns) the background contribution of RPC, with a proton beam extinction of 10^{-10}, was 0.025 ± 0.003. Contributions from radiative and internal-conversion processes were 51% and 49% respectively [36].

2.5.3. Radiative Muon Capture

For an aluminum target, the maximal energy for the external photon is $k_{max} = 101.9$ MeV, which is approximately 3 MeV lower than the DIO endpoint energy. While there are theoretical descriptions for external photon conversion [20, 39, 40], descriptions for the internal process do not currently exist. Hence, estimation of the background contribution from the internal conversion process utilizes the spectrum measured for aluminum from Refs. [41] and [42]. The estimated background from RMC is expected to be zero events with an upper limit of 0.004 for a live-window from 700 ns to 1695 ns, normalized to

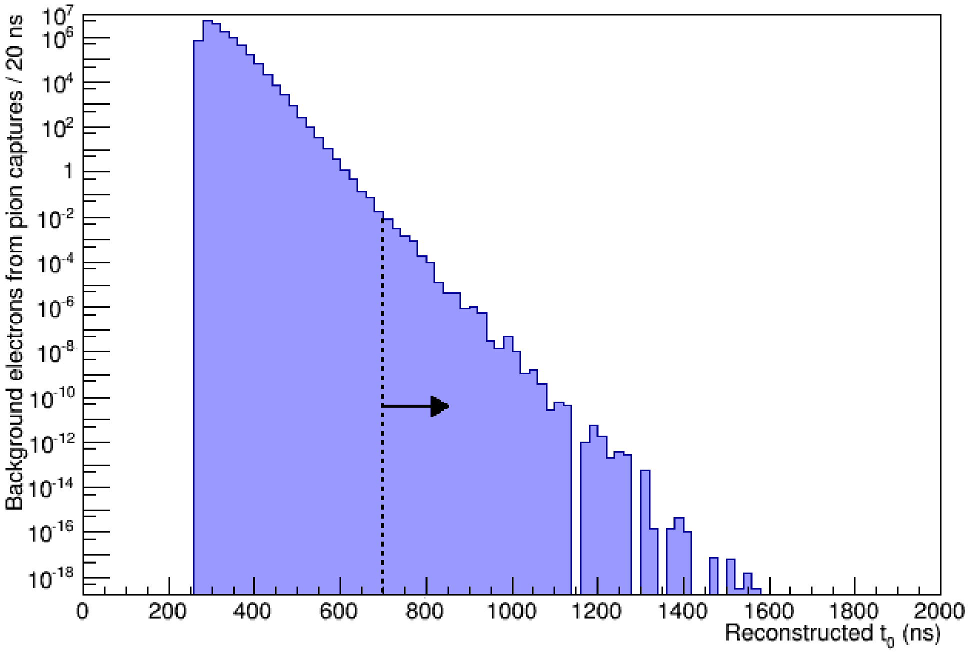

Figure 2.20.: In-time contribution of RPC background as a function of the start of the live gate. The black dotted line shows the start of a live-gate at 700 ns.

3.6×10^{20} protons on target, and includes on-shell and internal-conversion contributions with a kinematic endpoint of 101.9 MeV [36].

2.5.4. Antiproton Induced Backgrounds

A result of muon beam production is the production of antiprotons in the production target ($p + \mathrm{W} \to (\mathrm{W}^* + \bar{p}) + X$). A prominent feature of antiprotons is that they do not decay and carry negative electric charge. Antiprotons with momenta less than 100 MeV/c are not only able to propagate through the Transport Solenoid but do so slowly, which can take several microseconds to reach the Detector Solenoid. The flux of antiprotons is expected to be approximately constant in time, which means that the pulsed beam structure and delayed live window are not useful in suppressing this background. Antiprotons incident on matter within the Detector Solenoid can produce secondary particles, including electrons that may be indistinguishable from conversion-electrons. To reduce the effects of antiprotons, a series of absorbers were added to the Transport Solenoid section of the muon beamline. As a result, the estimated antiproton-induced background, which includes contributions from unabsorbed antiprotons reaching the stopping target (0.022), pion-captures (0.021), and high energy electron production due to antiproton annihilation (0.005), is 0.047 ± 0.024 events for 3.6×10^{20} protons on target [36]. The statistical uncertainty is low (3%) while the systematic uncertainty (50%) is largely driven by uncertainties in the antiproton production cross section.

2.5.5. Muon Decay In Flight

As out-of-time muons are transported through the beamline a fraction of them decay: $\mu \rightarrow \nu\bar{\nu}e$. Electrons that are produced from these muons can have the same energy as conversion-electrons. For these electrons to be consistent with the trajectory and momentum of a conversion-electron through the apparatus, the muons must have a momentum large enough to produce electrons of 105.6 MeV (>75 MeV/c), decay in the DS volume, and have enough transverse momentum to make it to the Tracker. Electrons produced upstream in the beamline (before the DS) are categorized as beam electrons and are suppressed by collimators in the TS. The gradient magnetic field in the upstream region of the DS changes the helical pitch of these particles and makes it inconsistent with the helical pitch of conversion-electrons emitted from the stopping target. The estimated background of muon-DIF for muons from in-time protons is negligible. The estimated background of muon-DIF due to out-of-time protons is <0.003 events for 3.6×10^{20} protons on target with a beam extinction of 10^{-10} [36].

2.5.6. Pion Decay In Flight

In addition to muons, pions that propagate through the beamline can decay into electrons: $\pi \rightarrow \nu e$. Background due to pion-DIF is defined here as only the electrons emitted by pions that decay in the DS, which require momenta of at least 58 MeV/c to produce 105 MeV electrons. Due to the pulsed proton beam structure and the short lifetime of the pion (26 ns), the estimated background of pion-DIF from pions produced from in-time protons is negligible within the signal window. The estimated background from pions produced by out-of-time protons is approximately zero events, with an upper limit uncertainty of <0.001 events, for 3.6×10^{20} protons on target and a beam extinction of 10^{-10} [36].

2.5.7. Beam Electrons

Several sources of electrons exist within the Production and Transport Solenoids. These electrons, produced through π^0 decays in the production target, antiproton annihilations, muon and $\pi^{\pm}$ decays in flight, and other interactions of beam particles in the upstream regions, have the ability to create false conversion-like events. For the purpose of this section, contributions due to antiprotons are excluded to avoid double counting. The TS collimators are designed to transport particles with momenta below 100 MeV/c, which helps attenuate beam electrons that possess momenta similar to conversion-like electrons. Additionally, the gradient magnetic field in the upstream region of the DS changes the pitch of the helical motion of beam particles, making them distinguishable from isotropically generated stopping-target particles during track reconstruction. There is a very limited acceptance for high-momentum beam electrons that exhibit a helical trajectory consistent with conversion-electrons and any electrons that satisfy this are prompt (150 ns) and are greatly reduced due to the pulsed beam structure and delayed live-window. The estimated background for beam electrons produced from out-of-time protons is $(2.6 \pm 1.4) \times 10^{-3}$ events for 3.6×10^{20} protons on target with a beam extinction of 10^{-10} [36].

2.5.8. Cosmic Rays

An inherent background that largely cannot be reduced through any other means except by detection is that produced by cosmic rays. Cosmic-ray muons that decay or interact in the DS volume can create conversion-like electrons. Near the stopping target, these electrons can be indistinguishable from conversion-electrons emitted from the stopping target. Additionally, shallow-angle cosmic-ray muons that enter the TS can scatter in a collimator, producing electrons that propagate into the DS. It is expected that there will be a conversion-like electron produced by cosmic rays for every four hours of live time. To be discussed in the next chapter, implementation of a high-efficiency Cosmic Ray Veto detector allows the rejection of conversion-like events that have cosmic rays entering the apparatus. It is expected that the background due to cosmic rays will be 0.13 ± 0.05 events for a three-year run time of the experiment.

Chapter 3.

The Cosmic Ray Veto

3.1. Overview

It is expected that cosmic-ray muons will produce roughly one conversion-like electron for every four hours of experiment live time, or once per day. Because it is impractical to stop these particles using shielding, a detector that identifies and vetoes this background must be employed: a cosmic ray veto (CRV). To satisfy this requirement, a novel, large-area, high-sensitivity detector was designed and is currently being fabricated. What makes this detector novel is the use of state-of-the-art photosensors and high light-yield scintillator that forms a compact, high-efficiency detector that is easy to manufacture. Additionally, the fundamental design has applications beyond the Mu2e experiment.

The basic design of the CRV is four layers of rectangular plastic scintillator extrusions read out by silicon photomultipliers (see Ch. 3.3.1), separated by aluminum absorbers. A compact detector was required due to space limitations within the experiment detector hall and it was desired that there be minimal gaps in the detector. While other technologies, such as cathode strip chambers, could satisfy only one of the constraints, plastic scintillator

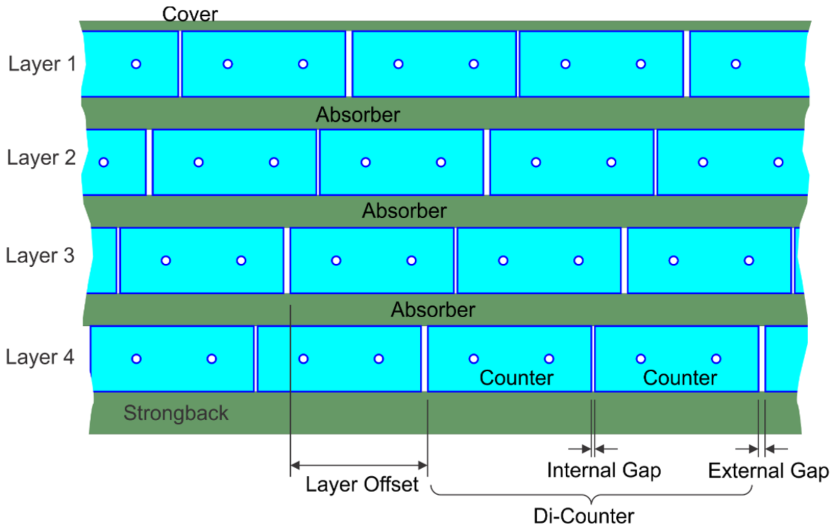

Figure 3.1.: Cross section of part of a typical module of the CRV. In this cartoon, the length of the module (and extrusions/counters) is running into the page. There are eight pairs of counters, known as dicounters, per layer of a module. Each layer is separated by an aluminum absorber and the entire stack is bonded to a thick aluminum strongback. The module is attached to the support structure by the strongback.

read out by silicon photomultipliers was the only solution that satisfied both constraints. A collection of 64 scintillator extrusions, as short as 1 m and as long as 7 m, with 16 per layer, form a module, the fundamental mechanical entity of the CRV. The cross section of part of a module is shown in Fig. 3.1. Both ends of a module are read out, except in certain areas of the CRV. Having double ended readout improves efficiency through redundancy and provides hit positions to within 15 cm along the length of the extrusions.

Collections of modules form sectors of the CRV (see Table 3.2 for module details). Shown in Fig. 3.2, the CRV is divided into several sectors that cover the top and sides of the Detector Solenoid (DS) and part of the Transport Solenoid (TS). The sectors of the CRV are the: upstream sector (CRV-U), which is furthest upstream, with the length of the modules oriented horizontally, the downstream sector (CRV-D), which is furthest downstream and also oriented horizontally, the left and right sectors (CRV-L and CRV-R, respectively), which are oriented vertically and extend the full length of the DS, and the top sections (CRV-T, CRV-TS, and CRV-TS-Ext, T denoting Top, TS indicating the part that sits above the TS, and TS-Ext denoting an extension of CRV-TS), which are oriented horizontally. An additional section (not pictured), CRV-Cryo-Outer (CRV-Cryo), surrounds a cryogenic pipe that passes through CRV-R. Every effort is made to minimize gaps in the CRV. The space between modules is minimized to reduce the effects of muons passing through projective gaps, which is further reduced by offsetting the layers in a module. Gaps between scintillator extrusions are also minimized.

Between the CRV and the solenoids is 36″ of concrete shielding (shown in red in Fig. 3.2) that limits exposure of the CRV to radiation sources in the beam line.

3.2. Mechanical Design

3.2.1. Dicounter Design

Rectangular plastic scintillator extrusions of lengths between 1m and 7m form the active volume for the detector, as the passage of charged particles through the plastic generates light. In each extrusion there are two co-extruded holes that contain wavelength shifting (WLS) fibers. The fibers are inserted into the holes but no adhesive, or filler, is used to bond them to the scintillator. Due to the length of the counters and the short attenuation length of the scintillator, the fibers are used to absorb light from the scintillator and pipe it to silicon photomultipliers (SiPMs) where it is converted to an electrical signal. A single extrusion outfitted with a pair WLS fibers and SiPMs forms the base unit of the detector: a counter. Pairs of counters are bonded together using epoxy (3M DP420 [43]) to form a dicounter.

At each end of a dicounter there are Fiber Guide Bars (FGBs) that hold the WLS fibers in a fixed position and form a mechanical interface for the SiPM readout and

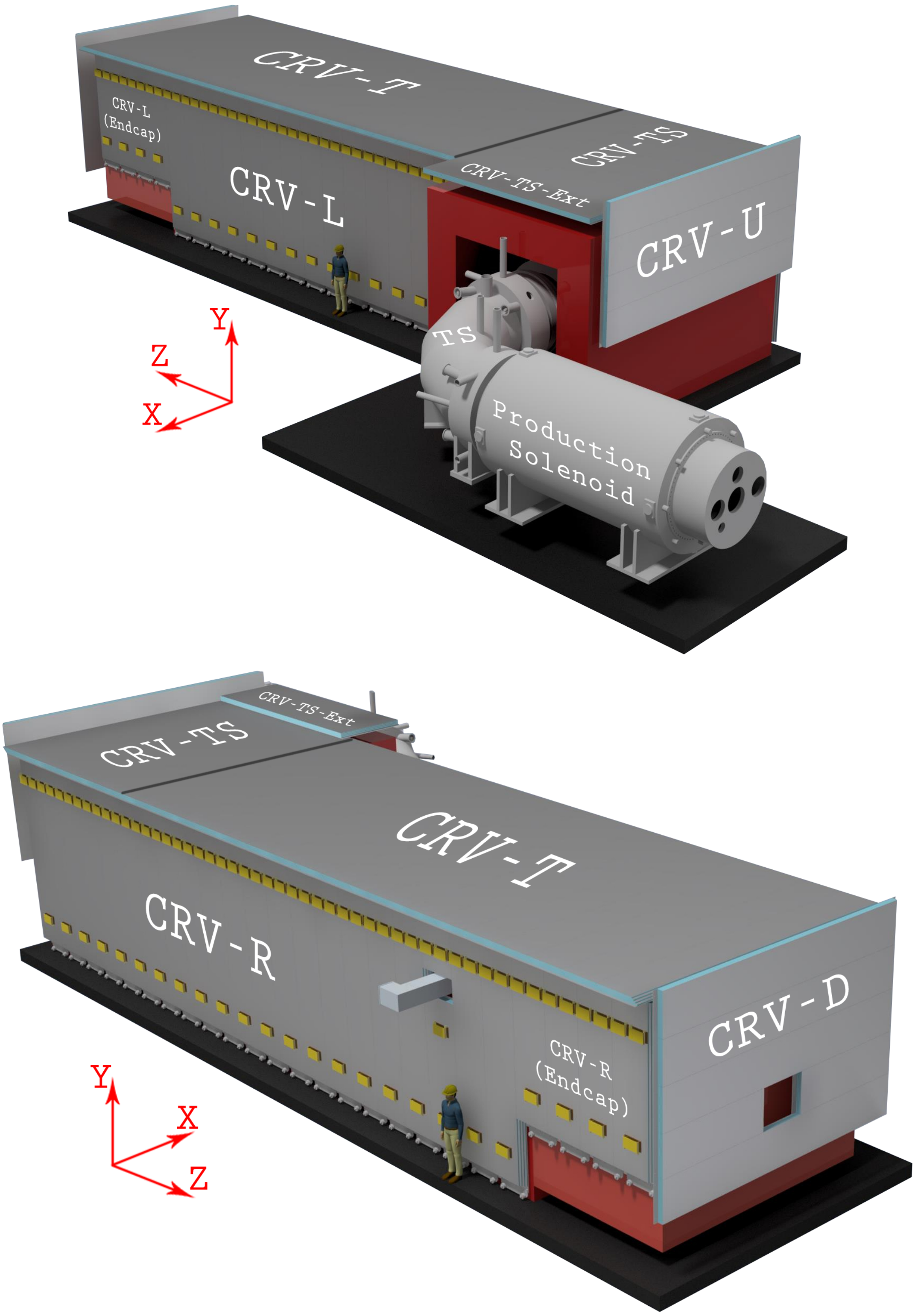

Figure 3.2.: Rendering of the Cosmic Ray Veto detector, with the sectors identified. The production and part of the transport solenoids are shown. The detector solenoid and remainder of the transport solenoid are hidden beneath the shielding (red) and the CRV.

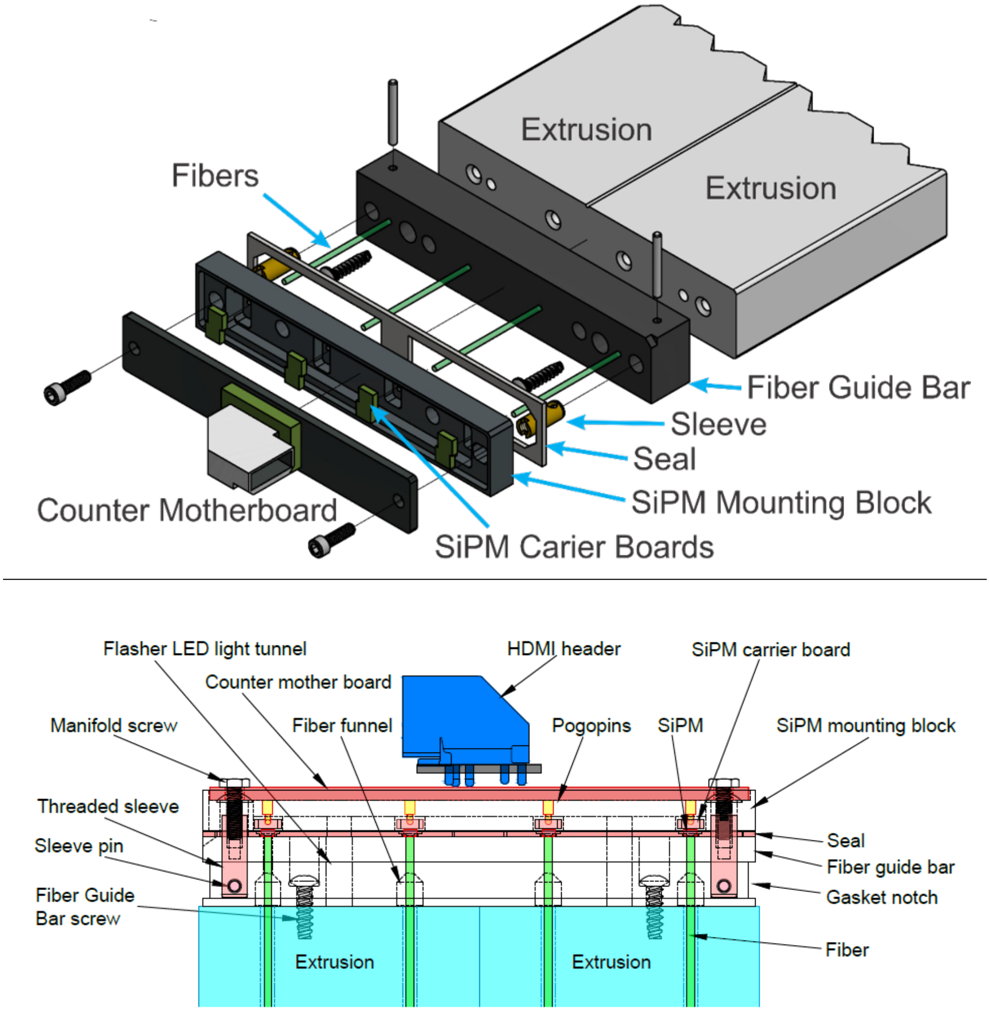

Figure 3.3.: Top: Exploded diagram of the mechanical design of a dicounter end and the readout electronics, known as a manifold. Bottom: X-ray view of the manifold assembly. Two types of manifolds are used: those with 90 deg HDMI headers, shown in the figures, and those with straight HDMI headers (not shown).

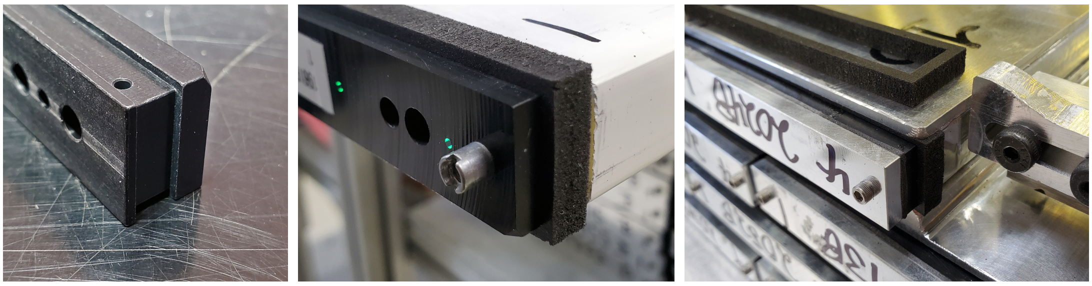

Figure 3.4.: A channel around the perimeter of the Fiber Guide Bar (left) retains a neoprene gasket (middle) used to prevent light from entering the dicounter when assembled in a module (right).

associated electronics (Fig. 3.3). These FGBs are attached to the scintillator by both epoxy (3M DP100 [44]) and #4-20 thread-forming screws [45]. Fibers embedded in the scintillator are fixed to the FGBs using epoxy within four counterbored holes. Because the position of the fibers is not well constrained in the scintillator, and to aid the installation of the FGB, chamfers within each counterbore funnel the fiber into the fiber hole. Two holes in the FGB allow light from LED flashers on the Counter Motherboard to enter the scintillator for calibration. Along the perimeter of each FGB is a channel that retains a neoprene seal to prevent light from entering the dicounter (Fig. 3.4).

The face of the FGB that is in contact with the scintillator is painted with BC-620 titanium dioxide reflector paint [46], which improves light yield by 70 % near the dicounter ends, decreasing the unavoidable drop-off that is a result of the FGB absorbing light that escapes the counter end [47]. Other materials and configurations were considered, a comparison of the change in light yield near the dicounter end is listed in Table 3.1. The selection of BC-620 over other materials, such as VM2000 [48], was made due to the ease of application. All FGBs were machined and inspected by C.H. Krammes & Co. [49]. Several samples in groups of 100 of the 5376 total FGBs were evaluated by the Fermilab Alignment and Metrology Department [50]. Additionally, FGBs are checked upon receipt at the University of Virginia using a go/no-go jig before use. All three layers of quality control were to ensure correct hole sizing and position for proper registration of WLS

Table 3.1.: Several materials were tested to improve the light yield at the end of a dicounter. Reflective white paint, BC-620 [46], was applied to both the FGB and to the end of the extrusion, yielding similar results. Two additional materials, VM2000 [48] and Tyvek [35], were placed between the FGB and extrusion interface that also improved light yield. Due to ease of application, BC-620 applied to the FGB was the selected material for improving light yield near the dicounter end [47].

Configuration	$\bar{\Delta}_{\mathrm{LightYield}}$
BC-620 on FGB	1.7
BC-620 on Extrusion	1.7
VM2000	1.9
Tyvek	1.7

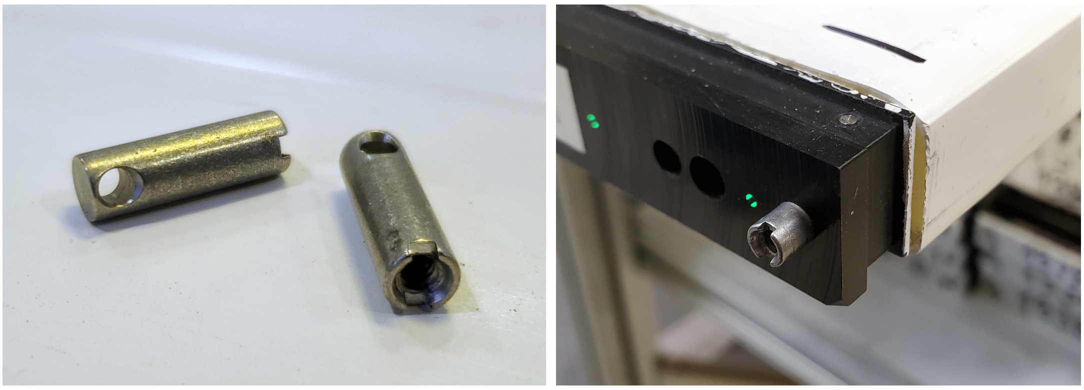

Figure 3.5.: A custom-made sleeve (left), inserted and pinned in the Fiber Guide Bar (right), is used to attach the readout manifold to the dicounter end.

fibers to the photodetectors. A custom-made threaded sleeve, also machined by C.H. Krammes & Co., (Fig. 3.5) is installed on each end of the FGB and fixed in place using a press-fit dowel pin. The threaded hole in each pin allows the Counter Motherboard, which serves as the top of the manifold, to be attached using screws.

The electronics serving each dicounter, shown in Fig. 3.6, are comprised of a Counter Motherboard (CMB) and four silicon photomultipliers (SiPMs), each mounted on a SiPM Carrier Board (SCB). All are contained in an anodized aluminum manifold known as a SiPM Mounting Block (SMB). As shown in Fig. 3.7, the SMB has four wells that hold the 2 mm × 2 mm SiPMs and ensure their proper positioning relative to the WLS fiber.

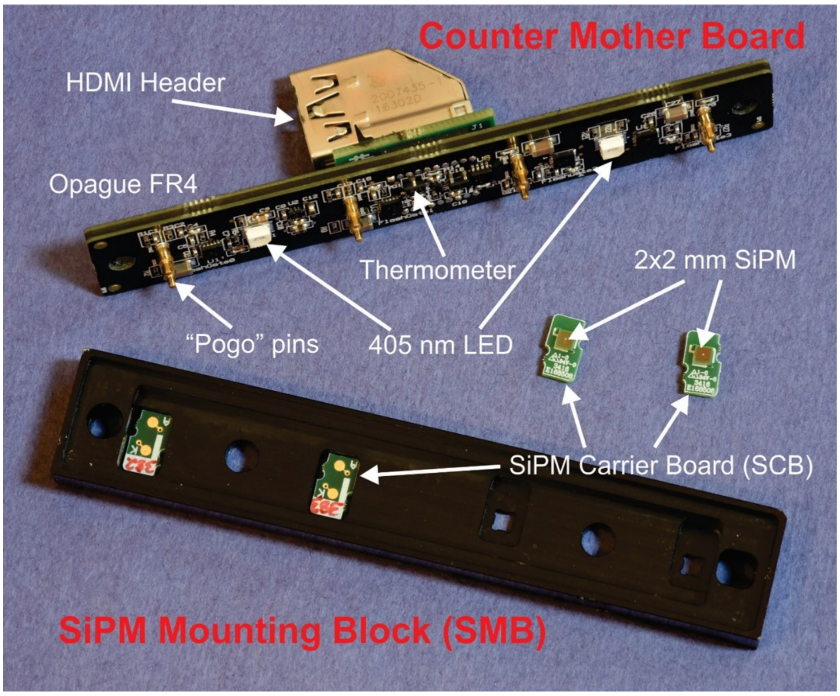

Figure 3.6.: The dicounter Manifolds are comprised of a Counter Motherboard (CMB) that interfaces to the silicon photomultipliers (SiPMs) through small SiPM Carrier Boards (SCBs). The SiPMs are retained in wells of the SiPM Mounting Block (SMB), and the entire assembly is sealed using Geocel-3300 RTV [51] to make it light tight.

The SiPMs are offset on the SCB to prevent incorrect polarity when installed in the SMB, which allows the CMB to be oriented in either direction. Additionally, the SCBs provide an interface between the SiPMs and the CMB via pogo pins on the CMBs that gently press the SiPMs flush against the fiber ends. For adequate light collection the SiPM needs to be centered on the WLS fiber within 0.3 mm (Fig. 3.8). Two holes on either end of the SMB mate it to the sleeves of the FGB and fix the locations for all other features of the SMB. Much like the FGB, there are two holes aligned with LED flashers on the CMB that allow light into the scintillator. An adhesive-backed neoprene gasket is applied to the SiPM side of the SMB that makes the interface between the SMB and FGB light-tight.

The Counter Motherboard, discussed in detail in Ch. 3.3.2, forms the top of the readout manifold. Fabricated from opaque, black FR4, the Counter Motherboard is

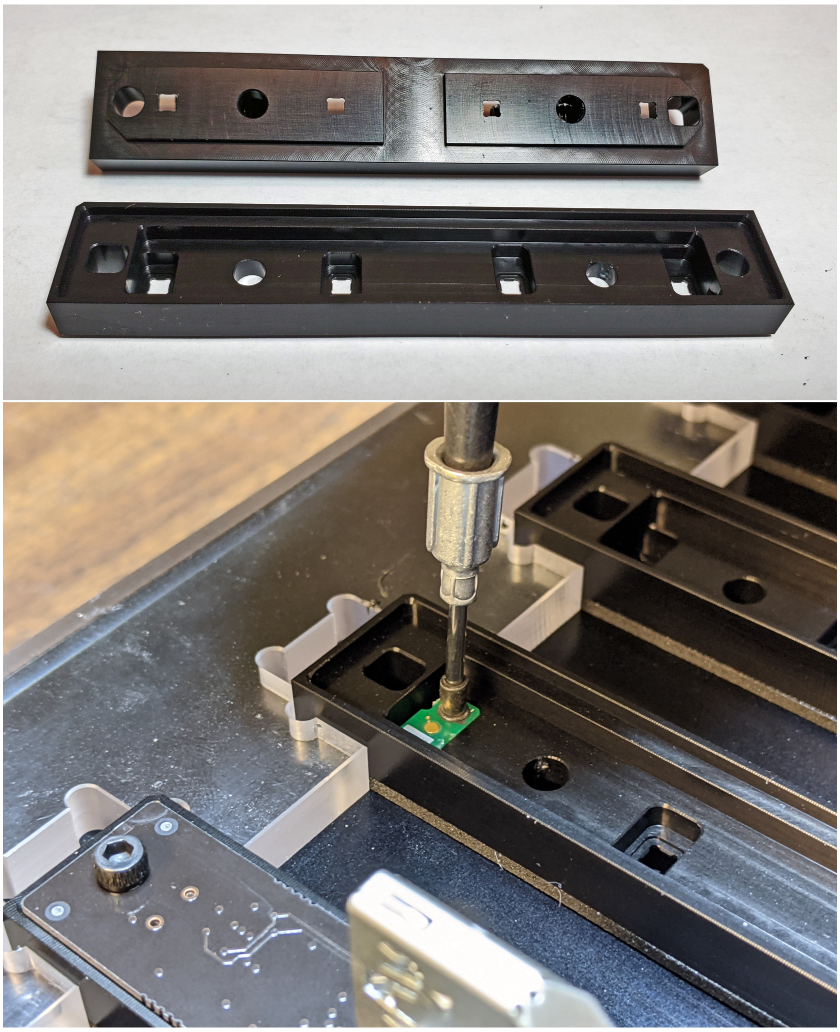

Figure 3.7.: The SiPM Mounting Block (SMB) is shown at the top. Wells in the SMB contain the SiPMs that are used to read out the WLS fibers. A SiPM being loaded into one of these wells is shown in the image on the bottom. Additional holes are used to align the SMB on the FGB and allow light from the Counter Motherboard to pass into the scintillator. A seal located on the FGB-side of the SMB prevents light leaks.

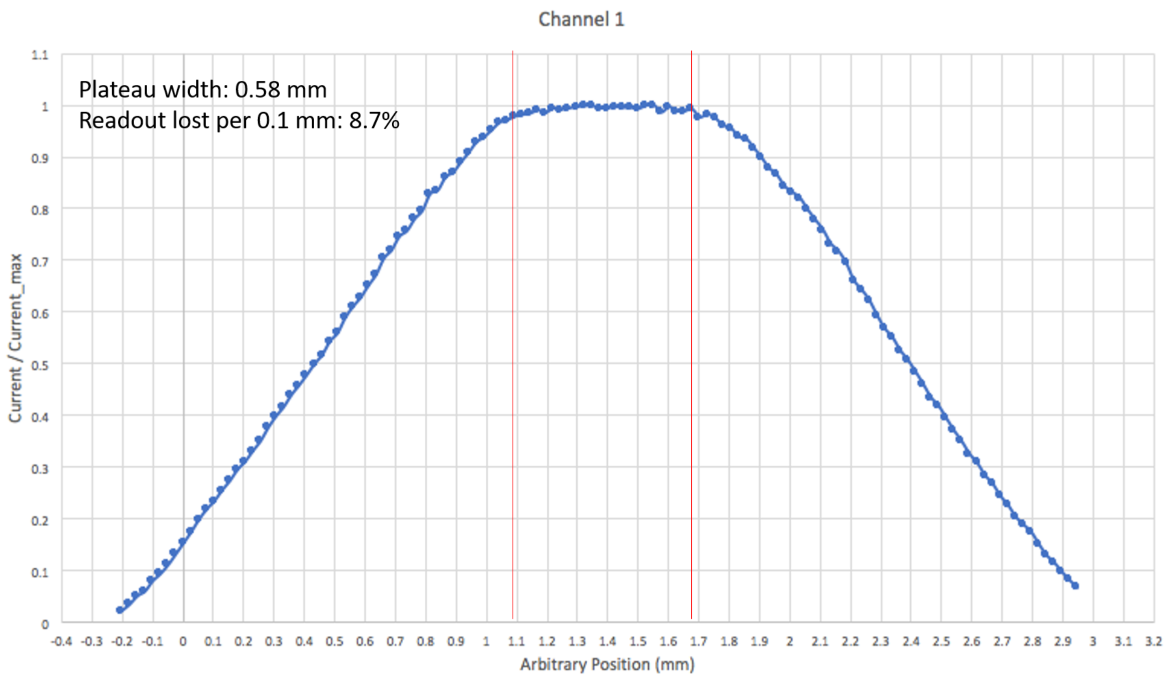

Figure 3.8.: Light yield, in arbitrary units, versus fiber position relative to the SiPM face. The red vertical lines indicate the width of the plateau at 98 % of the maximal response. The average width of the plateau was found to be 0.61 mm and the falloff rate was 8.55 % per 0.1 mm of misalignment. The plot was made using a 1.4 mm fiber.

Figure 3.9.: Placed into a special jig, opaque Geocel-3300 RTV [51] is used to seal the manifold assembly. Manifolds to the left in the figure are sealed.

not susceptible to light leaks. The entire assembly is mounted to the FGB using #4-40 machine screws. In addition to being inspected by the manufacturer [49], every SMB is checked upon receipt at the University of Virginia for feature size and position using a go/no-go jig.

3.2.2. Scintillator Extrusions

There are 5376 scintillator extrusions that form the active volume for the CRV. Each extrusion has a 19.8 mm x 51.3 mm rectangular profile with a co-extruded 0.25 mm thick 30 % rutile titanium dioxide (TiO_2) coating and two nominally 2.6 mm diameter holes, shown in Fig. 3.10. A drawing of the nominal profile can be found in Appendix A. The extrusion profile is a compromise between the low-aspect ratio preference of the extrusion process and the desire for high detector efficiency that favors a wide counter that reduces inefficiencies due to inter-counter gaps. The plastic is general purpose polystyrene (DOW Styron 665W [52]) doped with 1 % 2,5-diphenyloxazole (PPO) and 0.03 % 1,4-

bis(5-phenyloxazol-2-yl) benzene (POPOP) fluorescent additives. The co-extruded fiber channels are made by the injection of dry nitrogen into the semi-molten plastic during the extrusion process. All scintillator extrusions are made at the FNAL/NICADD extrusion facility at Fermilab [53]. The choice of plastic scintillator was based on previous use in MINOS [54] and MINERvA [55], for which the manufacturing infrastructure and tooling already existed. Scintillator production began January 16, 2018, with all 31,114 m of extrusions finished by May 16, 2018. Quality control processes and results are presented in Ch. 5.1.

3.2.3. Fibers

Embedded in each of the two channels of a counter is a 1.4 mm diameter Kuraray Y-11 (175 ppm), non-S-type, double-clad wavelength shifting fiber. The relative indices of refraction are 1.59, 1.49 and 1.42 for the core, inner, and outer cladding respectively [56]. This fiber was selected due to good light yield and attenuation length properties, and a similar fiber was previously used in the MINOS [54], MINERvA [55], and NOvA [57] experiments. The Y-11 fiber absorbs light in the $375-475$ nm (blue) region and re-emits it in $450-600$ nm (green) region [58], as shown in Fig. 3.11. The absorption spectrum is well matched to the scintillator emission spectrum. The emission spectrum of the fiber is well matched to the photon detection efficiency spectrum of the SiPMs (see Ch. 3.3.1). Because the length of each counter is on the order of meters, the long attenuation length > 3.5 m [58] was important. Fibers of 1.0, 1.4 and 1.8 mm diameter were tested at the Fermilab Test Beam Facility (FTBF) [59], and using a custom-built fiber scanner whose results are shown in Fig. 3.12 [60]. The 1.4 mm fiber† was ultimately chosen as a compromise between its light yield, attenuation properties, and overall cost.

†Recently 1.8 mm diameter fiber was acquired for use in 17 CRV-T modules in order to improve their light yield.

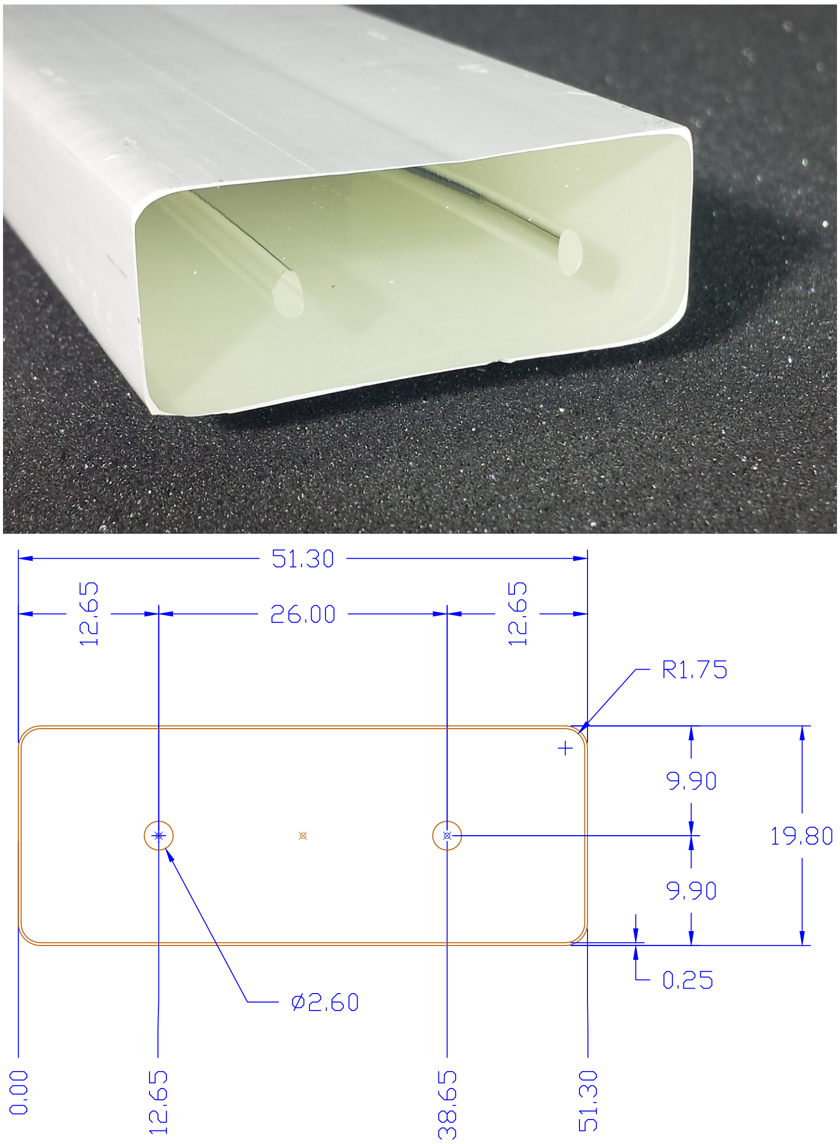

Figure 3.10.: Profile of the scintillator extrusions.

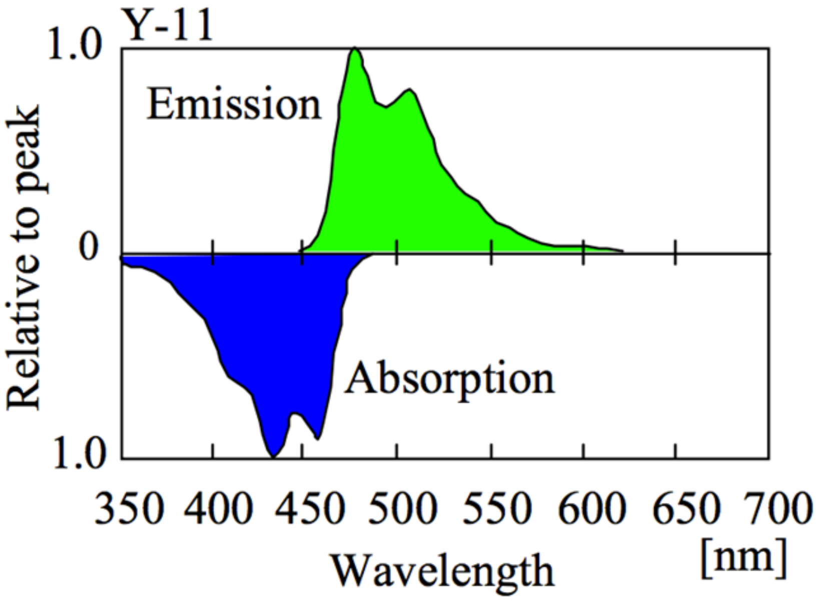

Figure 3.11.: Absorption and reemission spectra for Y11 WLS fiber [58].

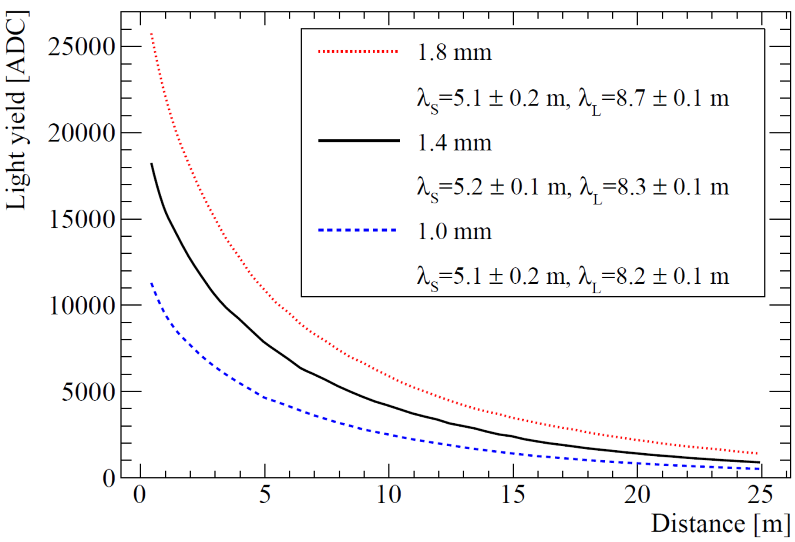

Figure 3.12.: Light yield measurements for 1.0, 1.4 and 1.8 mm Kuraray Y11 WLS fiber, using a custom-made fiber scanner (see Ch. 5.1) [60].

3.2.4. Module Design

All modules are similar in width, but have different lengths. A collection of 32 dicounters forms the basis for a detector module. A module consists of three layers of aluminum absorbers between four layers of dicounters. Each layer contains eight dicounters and most modules have layers offset by 42 mm to minimize the effects of projective gaps, shown in the top of Fig. 3.13. If there were no offset between layers, vertical muons could pass through these gaps with minimal path length, if any, through the scintillator. In the CRV-U and CRV-D sectors of the CRV, an offset between layers is not necessary as the projective gaps point to the horizon where the muon flux is effectively zero. The profile of a module with no offset is shown in the bottom of Fig. 3.13.

Adjacent dicounters within each layer are shimmed (typically with four 0.51 mm thick shims) to keep the overall layer width uniform and the spacing between the dicounters consistent. The nominal thickness of an aluminum absorber is 9.525 mm. Its purpose within the module is two-fold: it provides mechanical rigidity and it reduces the number of electrons produced from gamma interactions from traversing multiple dicounter layers, which would create spurious coincidences. All of the aluminum plates and dicounter layers are bonded together using Devcon HP-250 epoxy [61]. The modules are supported by a 12.7 mm thick strongback. The strongback is designed such that its width is 1.0 mm wider than the width of a row of dicounters in a layer. As a result the inter-module spacing (shown in red in Fig. 3.14) is expected to be no less than 2 mm, as adjacent modules only make contact along the strongback edge to prevent damage to the scintillator. Also shown in Fig. 3.14, absorbers are milled down on each edge to allow adjacent modules to mesh together without interference.

Before fabrication, dicounter surfaces along the edges (terraces, for modules with an offset between layers) are covered using a light-tight aluminum tape. After fabrication, the aluminum tape is protected using a low-friction, Teflon coated, fiberglass tape [62].

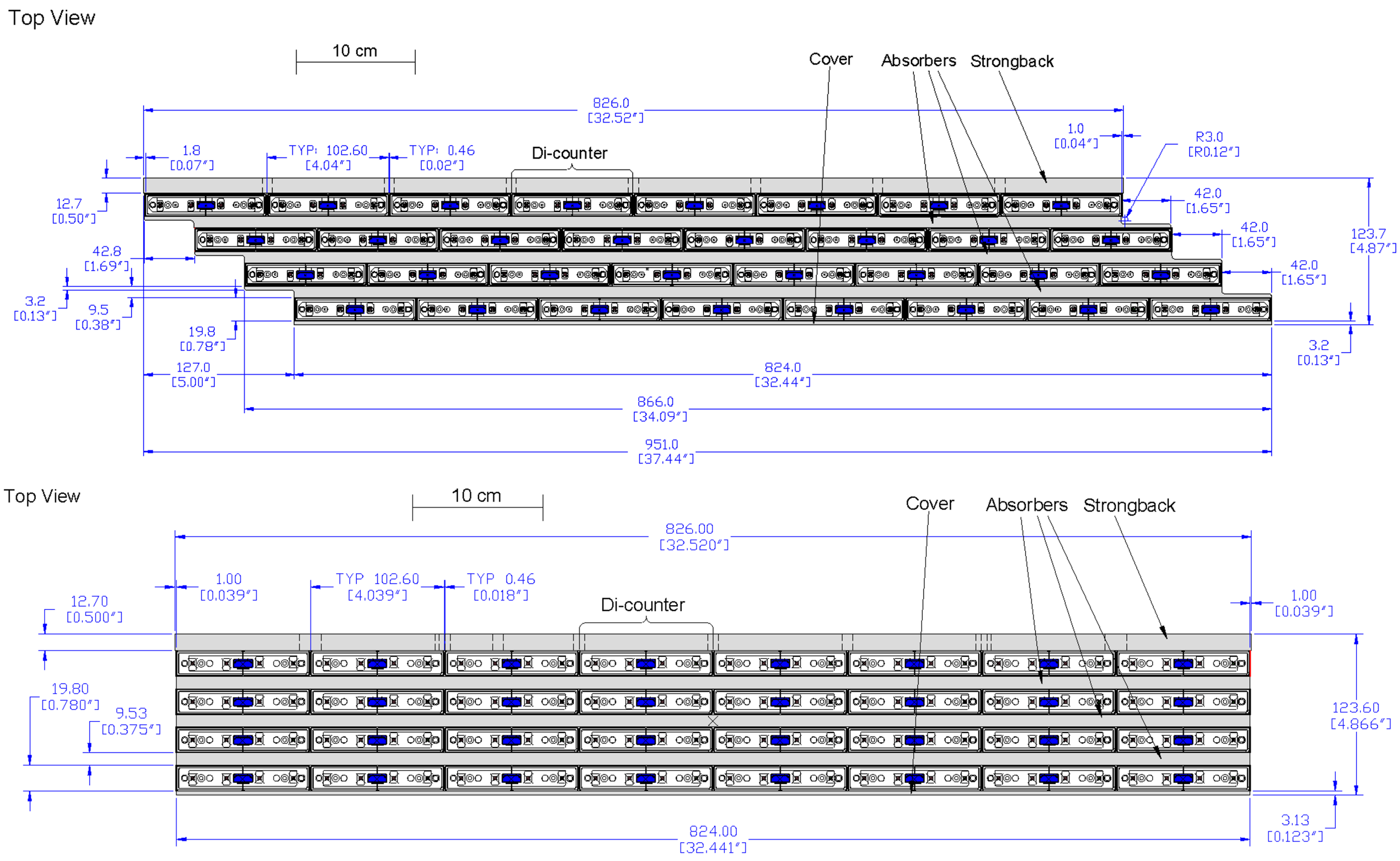

Figure 3.13.: Top: End view of a module with a 42 mm offset between layers to minimize the effects of projective gaps. Bottom: End view of a module with no offset, used in the CRV-U, CRV-D, and CRV-Cryo-Outer sectors. Due to the orientation of the modules, no layer offset is needed as projective gaps point to the horizon where the muon flux is effectively zero.

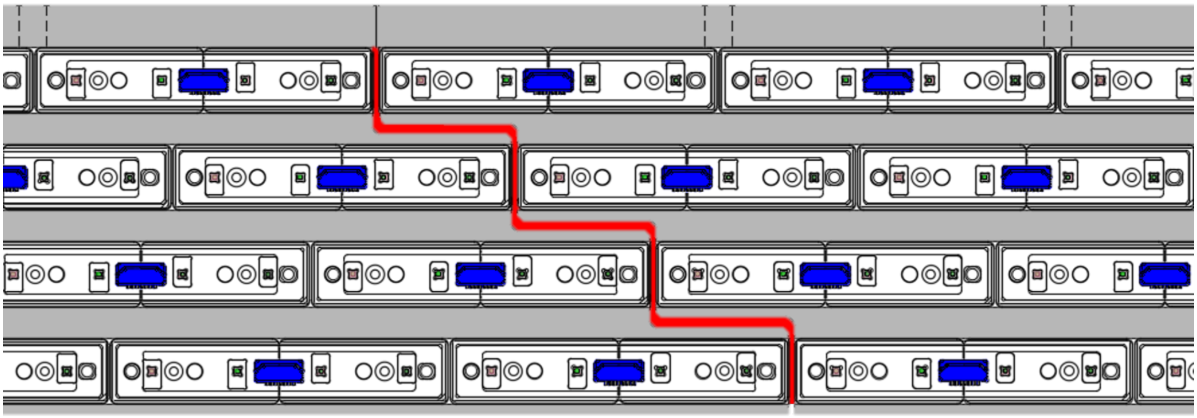

Figure 3.14.: End view of the intersection of two modules. Shown in red is the gap between modules set by contact of the strongbacks. The absorbers are milled to allow adjacent modules to mesh together without interference.

The outer perimeter of each layer is made light-tight using black RTV [51]. On the outer surface of the module, a thin 3.175 mm aluminum cover sheet protects the outer layer of dicounters. Side modules have several aluminum plates epoxied to the cover used for mounting of special magnetic-shielding enclosures that house the front-end electronics (Appendix J). Features on the strongback for upstream, downstream, and side modules allow for the modules to interface with the support structure components. A detailed analysis of the mechanical properties of the module design, including key items such as epoxy strength parameters and deflection when supported, is presented in Ref. [63].

Due to large radiation doses near the Production Solenoid, and the inability to access manifolds, CRV-TS, CRV-U, and CRV-TS-Ext feature single-ended readout, with reflectors or absorbers on the opposite end. Reflectors on the end of long modules, CRV-TS, CRV-TS-Ext, and CRV-U, are used to improve light collection. Short modules, CRV-DS and CRV-Cryo-Outer, have black absorbers on the far end, as these modules do not benefit from additional light collection.

In total, there are 83 modules, broken down into 13 different types, with the quantities and type-specific parameters listed in Table 3.2. CRV-Cryo-Outer is a special design that has 12 dicounters, of two different lengths, per layer. The use of two different length dicounters is to create a jog in the module that interfaces with the cryogenic pipe. Detailed drawings of each module type and their respective components are presented in Appendices B – H. The first five pilot modules, which were CRV-T modules, have covers and absorbers that are 5 mm shorter than the lengths specified in the drawings. The CRV-TS modules are identical to the CRV-T modules, except that one end has reflectors.

3.2.5. Module Support Structure

The module support structures are attached to the shielding blocks, except for a set of guide rails for the side modules that are affixed to the floor. Because the shielding block positions are not well defined, the module support structure is designed to accommodate changes in attachment positions in the event the blocks are removed and replaced due to servicing of the apparatus. Additionally, the shielding endcap is movable so the downstream section of the CRV-T, CRV-L/R (CRV-L/R-Endcap), and CRV-D support structures are designed to move with the endcap.

Attached to the bottom of the strongback of each side module is a wheel truck that supports the modules (Fig. 3.16). Each truck rides on an inverted v-shaped rail that allows the modules to roll along the length of the shielding for installation. By inserting shims under the wheels, the roll (vertical orientation) of each module can be adjusted. The rails that support the side modules at the downstream end of the shielding are attached to the endcap, as shown in Fig. 3.15. The side module below the cryogenic pipe uses the same rail on the floor but uses a series of slots to interface with attachment points on the shielding blocks (Fig. 3.17). The module that sits above the cryogenic pipe rests on a set of wheels that can be adjusted vertically and horizontally away from the shielding blocks (Fig. 3.17). Shown in Fig. 3.18, adjustments to the pitch and yaw of a

Table 3.2.: List of module types and their respective parameters.

	CRV-T	CRV-TS	CRV-TS-Ext	CRV-L	CRV-R	CRV-L-Endcap	CRV-R-Endcap	Cryo-R-Top	Cryo-R-Bot	CRV-U	CRV-D	CRV-DS	Cryo-Outer (Long)	Cryo-Outer (Short)
Quantity	20	5	2	15	20	4	4	1	1	4	4	2	1	-
Layers	4	4	4	4	4	4	4	4	4	4	4	4	4	4
Counter length (mm)	6,000	6,000	5,000	4,550	4,550	3,200	3,200	1,045	3,015	6,900	5,700	2,370	1,500	1,144
Module width overall (mm)	951.0	951.0	826.0	951.0	951.0	951.0	951.0	951.0	951.0	826.0	826.0	826.0	1238.2	207.7
Scintillator layer width (mm)	824.00	824.00	824.00	824.00	824.00	824.00	824.00	824.00	824.00	824.00	824.00	824.00	1236.18	205.73
Module overall length (mm)	6,100	6,100	5,100	4,738	4,738	3,388	3,388	1,115	3,203	7,100	5,900	2,570	1,570	1,214
Module thickness (mm)	123.65	123.65	123.65	123.65	123.65	123.65	123.65	123.65	123.65	123.65	123.65	123.65	104.60	123.65
Strongback surface area (m^2)	5.04	5.04	4.21	3.91	3.91	2.80	2.80	0.92	2.65	5.86	4.87	2.12	1.94	0.25
Scintillator surface area layer (m^2)	4.94	4.94	4.12	3.75	3.75	2.64	2.64	0.86	2.48	5.69	4.70	1.95	1.85	0.24
Inner gap (mm)	0.01	0.01	0.01	0.01	0.01	0.01	0.01	0.01	0.01	0.01	0.01	0.01	0.01	0.01
Outer gap (mm)	0.37	0.37	0.37	0.37	0.37	0.37	0.37	0.37	0.37	0.37	0.37	0.37	0.37	0.37
Layer offset (mm)	42	42	0	42	42	42	42	42	42	0	0	0	0	0
Number of fibers	128	128	128	128	128	128	128	128	128	128	128	128	176	80
Total module WLS fiber length (m)	771	771	643	586	586	413	413	137	389	886	733	307	268	94
Fiber ends read out	2	1	1	2	2	2	2	1	2	1	2	1	1	1
Fiber diameter	1.40	1.40	1.40	1.40	1.40	1.40	1.40	1.40	1.40	1.40	1.40	1.40	1.40	1.40
Dicounters/layer	8	8	8	8	8	8	8	8	8	8	8	8	11	2
Counters/layer	16	16	16	16	16	16	16	16	16	16	16	16	22	10
Counters total	64	64	64	64	64	64	64	64	64	64	64	64	88	40
Di-counters total	32	32	32	32	32	32	32	32	32	32	32	32	44	20
Single counter mass (kg)	6.5	6.5	5.4	4.9	4.9	3.4	3.4	1.1	3.2	7.4	6.1	2.6	1.6	1.2
Total counter mass/module (kg)	414	414	345	314	314	221	221	72	208	476	393	163	142	49
Absorber length (mm)	6,015	6,015	5,015	4,565	4,565	3,215	3,215	1,055	3,025	6,915	5,715	2,385	1,510	1,154
Absorber overall width (mm)	866.0	866.0	824.0	866.0	866.0	866.0	866.0	866.0	866.0	824.0	824.0	824.0	1236.2	205.7
Absorber thickness (mm)	9.525	9.525	9.525	9.525	9.525	9.525	9.525	9.525	9.525	9.525	9.525	9.525	3.175	9.525
Absorber bevel thickness (mm)	3.0	3.0	0.0	3.0	3.0	3.0	3.0	3.0	3.0	0.0	0.0	0.0	0.0	0.0
Absorber length extension, each end (mm)	7.5	7.5	7.5	7.5	7.5	7.5	7.5	5.0	5.0	7.5	7.5	7.5	5.0	5.0
Absorber mass (kg)	125	125	106	95	95	67	67	22	63	147	121	51	15	6
Strongback length (mm)	6,100	6,100	5,100	4,738	4,738	3,388	3,388	1,115	3,203	7,100	5,900	2,570	1,570	1,214
Strongback width (mm)	826.0	826.0	826.0	826.0	826.0	826.0	826.0	826.0	826.0	826.0	826.0	826.0	1238.2	207.7
Strongback thickness (mm)	12.700	12.700	12.700	12.700	12.700	12.700	12.700	12.700	12.700	12.700	12.700	12.700	12.700	12.700
Strongback side extension, each side (mm)	1.0	1.0	1.0	1.0	1.0	1.0	1.0	1.0	1.0	1.0	1.0	1.0	1.0	1.0
Strongback length extension: end 1 (mm)	50.0	50.0	50.0	50.0	50.0	50.0	50.0	50.0	50.0	100.0	100.0	100.0	50.0	50.0
Strongback length extension: end 2 (mm)	50.0	50.0	50.0	138.0	138.0	138.0	138.0	20.0	138.0	100.0	100.0	100.0	20.0	20.0
Strongback mass (kg)	173	173	144	134	134	96	96	32	91	201	167	73	66	9
Cover thickness (mm)	3.175	3.175	3.175	3.175	3.175	3.175	3.175	3.175	3.175	3.175	3.175	3.175	3.175	3.175
Cover length (mm)	6,015	6,015	5,015	4,565	4,565	3,215	3,215	1,055	3,025	6,915	5,715	2,385	1,510	1,154
Cover width (mm)	824.0	824.0	824.0	824.0	824.0	824.0	824.0	824.0	824.0	824.0	824.0	824.0	1236.2	205.7
Cover mass (kg)	42	42	35	32	32	23	23	7	21	49	40	17	15	2
FEBE mount mass (kg)	-	-	-	6	6	6	6	2	4	-	-	-	-	-
Total Al mass (kg)	590	590	499	451	451	319	319	105	301	690	571	241	127	29
Total module mass (kg)	1,004	1,004	843	771	771	546	546	179	513	1,165	964	405	348	-
Total module mass (lbs)	2,214	2,214	1,860	1,700	1,700	1,203	1,203	394	1,130	2,569	2,125	892	766	-
CMBs (90 degrees)	64	32	0	64	64	64	64	32	32	0	64	32	44	20
CMBs (straight)	0	0	32	0	0	0	0	0	32	32	0	0	0	0
CMBs (total)	64	32	32	64	64	64	64	32	64	32	64	32	44	20
Counter reflector manifolds	0	32	32	0	0	0	0	0	0	32	0	0	0	0
Counter absorber manifolds	0	0	0	0	0	0	0	32	0	0	0	32	44	20
Channels per Front End Board	64	64	32	64	64	64	64	64	64	32	64	64	64	64
Front End Boards	4	2	4	4	4	4	4	2	4	4	4	2	4	-
FEB enclosures (on module)	2	1	0	2	2	2	2	1	2	0	0	0	0	-
FEB enclosures (off module)	0	0	1	0	0	0	0	0	0	1	2	1	2	-
FEB enclosures (total)	2	1	2	2	2	2	2	1	2	2	2	1	2	-
Light transit time (ns)	34.5	34.5	28.7	26.1	26.1	18.4	18.4	6.0	17.3	39.7	32.8	13.6	8.6	6.6

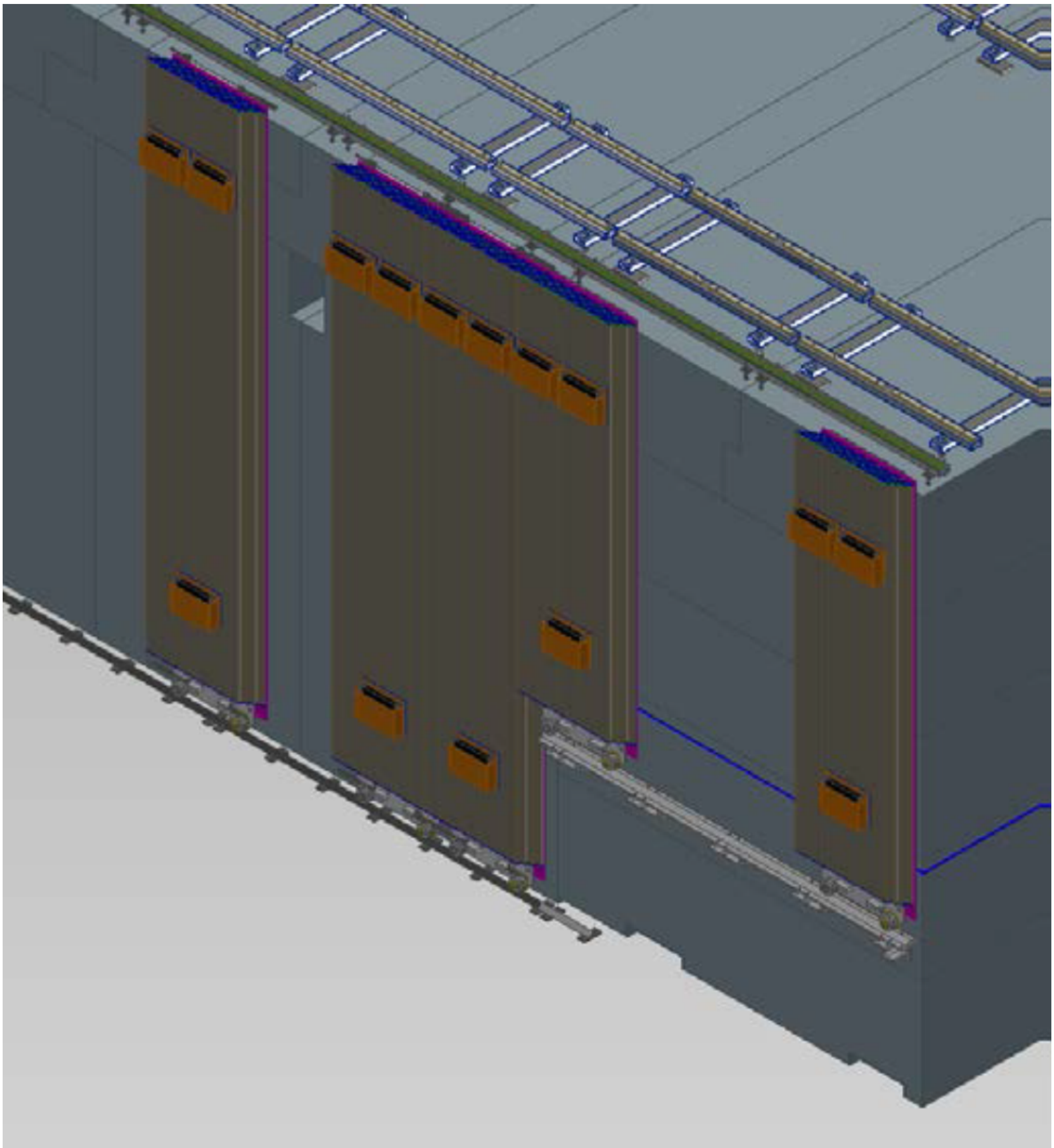

Figure 3.15.: Rendering showing a portion of the top and side module support structure at the endcap.

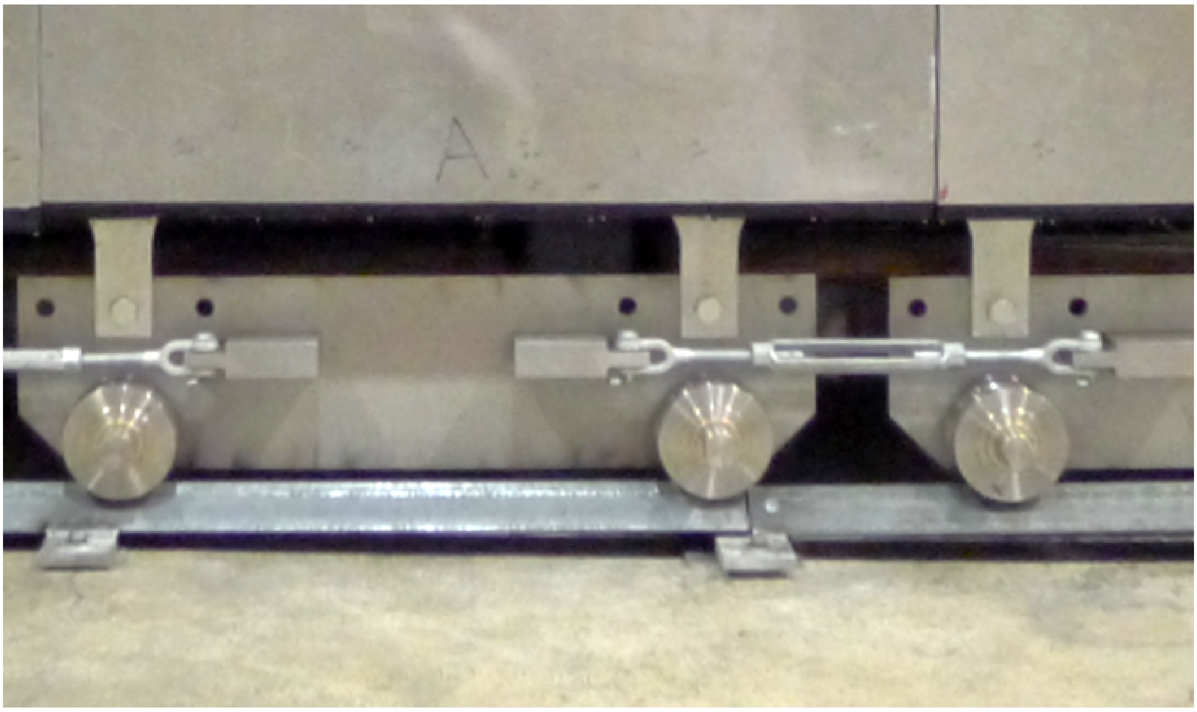

Figure 3.16.: Mounted to the bottom of the strongback of the side modules are wheel trucks that ride along an inverted v-shaped rail that is affixed to the floor. Shims placed under the wheels are used to adjust the vertical orientation of a module. Adjacent modules are pulled together using turnbuckles.

side module can be made through adjustment of turnbuckles that connect the top of the side module to a track mounted to the shielding blocks. The entire assembly is able to roll along this track. Side modules are brought together through the use of turnbuckles at the top and bottom of the strongbacks. The module that sits above the cryogenic pipe makes use of the same track assembly at the top of the shielding blocks.

The top modules, CRV-T and CRV-TS, lie flat on a series of frames, shown in Fig. 3.19. Low friction plastic on the frames allow modules to be slid into place. The frame height can be adjusted to keep the gap between the bottom of the top modules and the top of the side scintillator to a designed 90 mm. The modules are held in position without the use of fasteners between the modules and the frames. Similar to the side modules, turnbuckles are used to pull adjacent modules together. The frames that

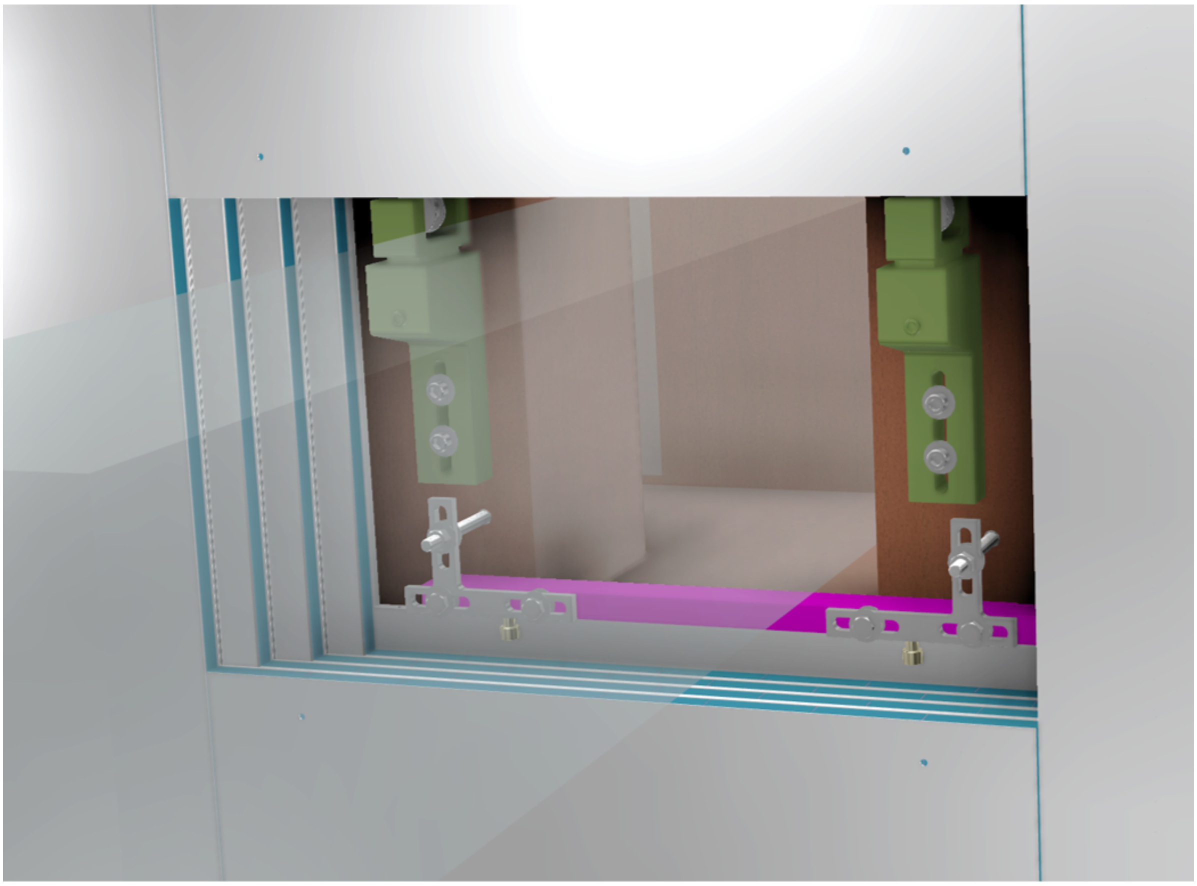

Figure 3.17.: An adjustable anchor and set of wheels supports the upper and lower sections of the modules above and below the cryogenic pipe. These modules make use of the same lower rail and upper track as the rest of the side modules.

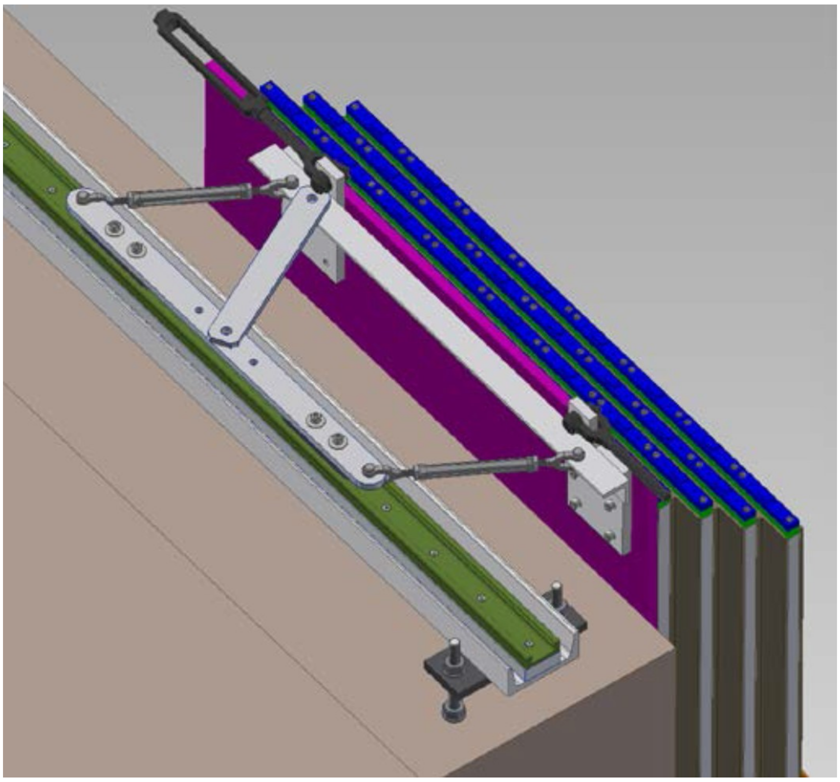

Figure 3.18.: Rendering of the upper assembly of the side support structure. Control of the pitch and yaw is made through turnbuckles on either end of the module.

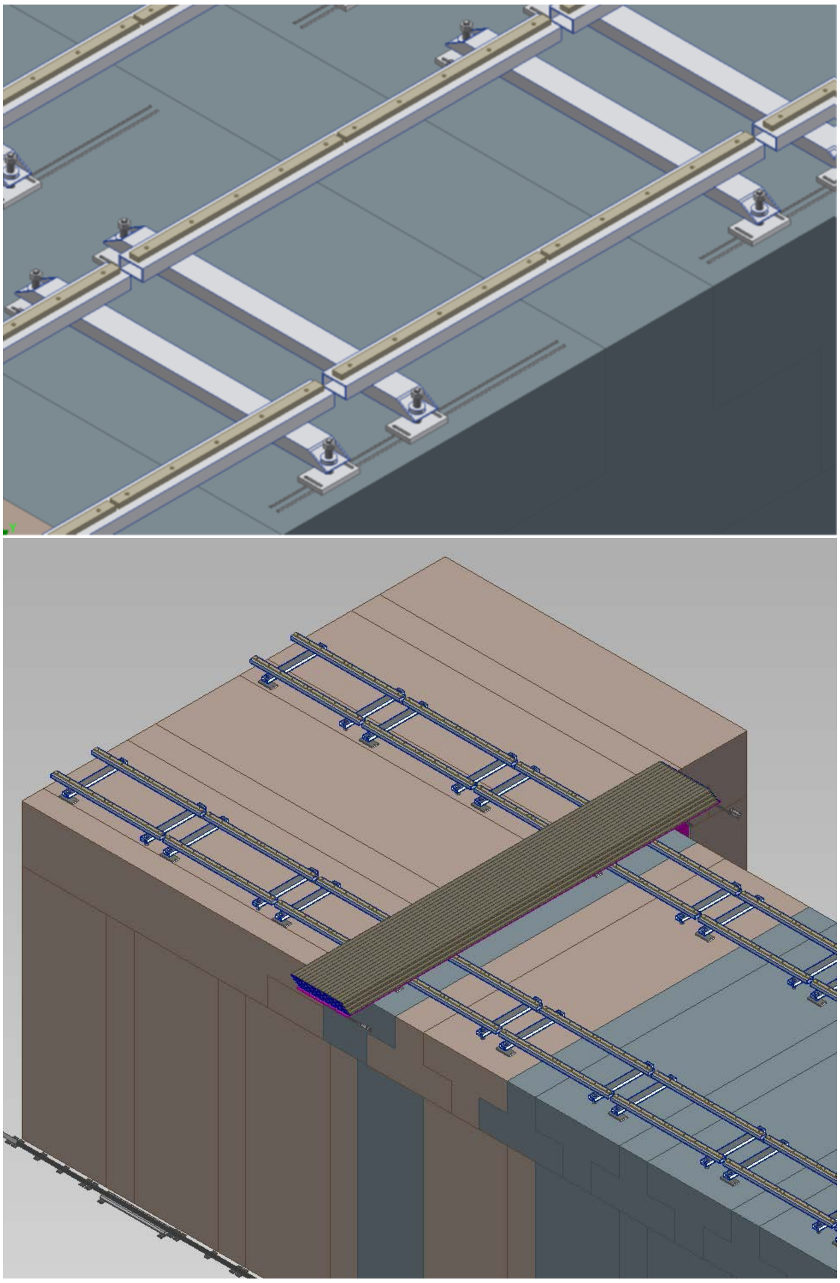

Figure 3.19.: The adjustable frames used to support the top modules (CRV-T/TS) without the use of fasteners. Low friction plastic allows the modules to be slid into place. Turnbuckles are used to join adjacent modules.

support CRV-TS-Ext are similar in design and attached to shielding blocks at a position higher than CRV-T/TS, as shown in Fig. 3.20.

CRV-U modules are attached to a frame assembly that sit on pedestal blocks separate from the shielding (Fig. 3.21). The the top of the frame assembly is connected to the

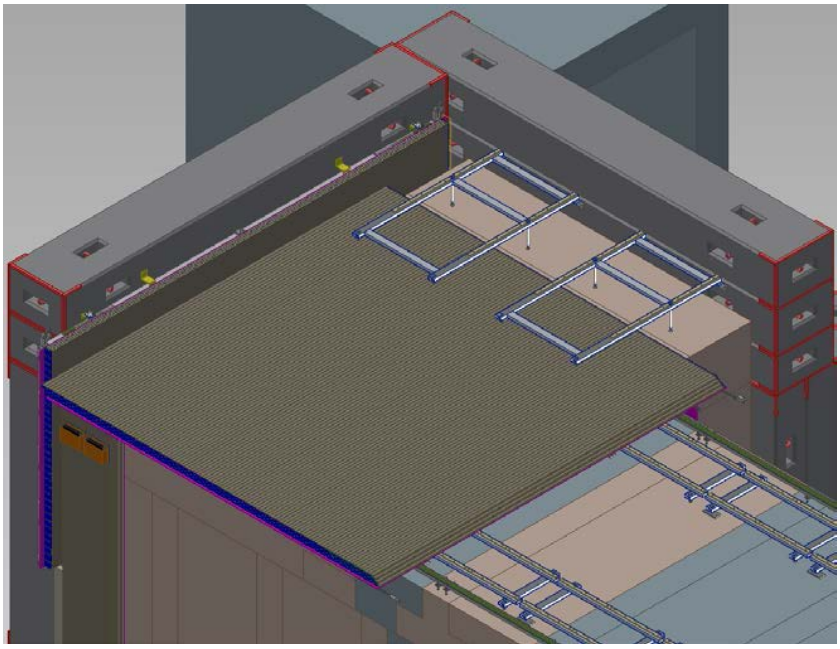

Figure 3.20.: The frames used to support the top extension modules (CRV-TS-Ext) without the use of fasteners. Low friction plastic allows the modules to be slid into place. Turnbuckles are used to join adjacent modules.

shielding blocks by tracks that allow horizontal movement. The base of the frame rests on another set of tracks and a leadscrew provides horizontal translation of the entire CRV-U assembly. Due to close proximity to the production solenoid, the radiation dose seen by these modules will be high. In the event the rates in CRV-U are higher than expected, the assembly can be moved away from the PS using the leadscrew.

Similar to CRV-U, CRV-D modules are attached to a frame assembly (Fig. 3.22). The entire frame assembly is mounted on brackets that attach to the endcap.

CRV-Cryo-Outer uses a track that is mounted to the wall of the building and does not need any special adjustments. As shown in Fig. 3.23, the module assembly hangs from a track. A second track captures the wheels of the assembly to prevent it from being bumped off the lower track.

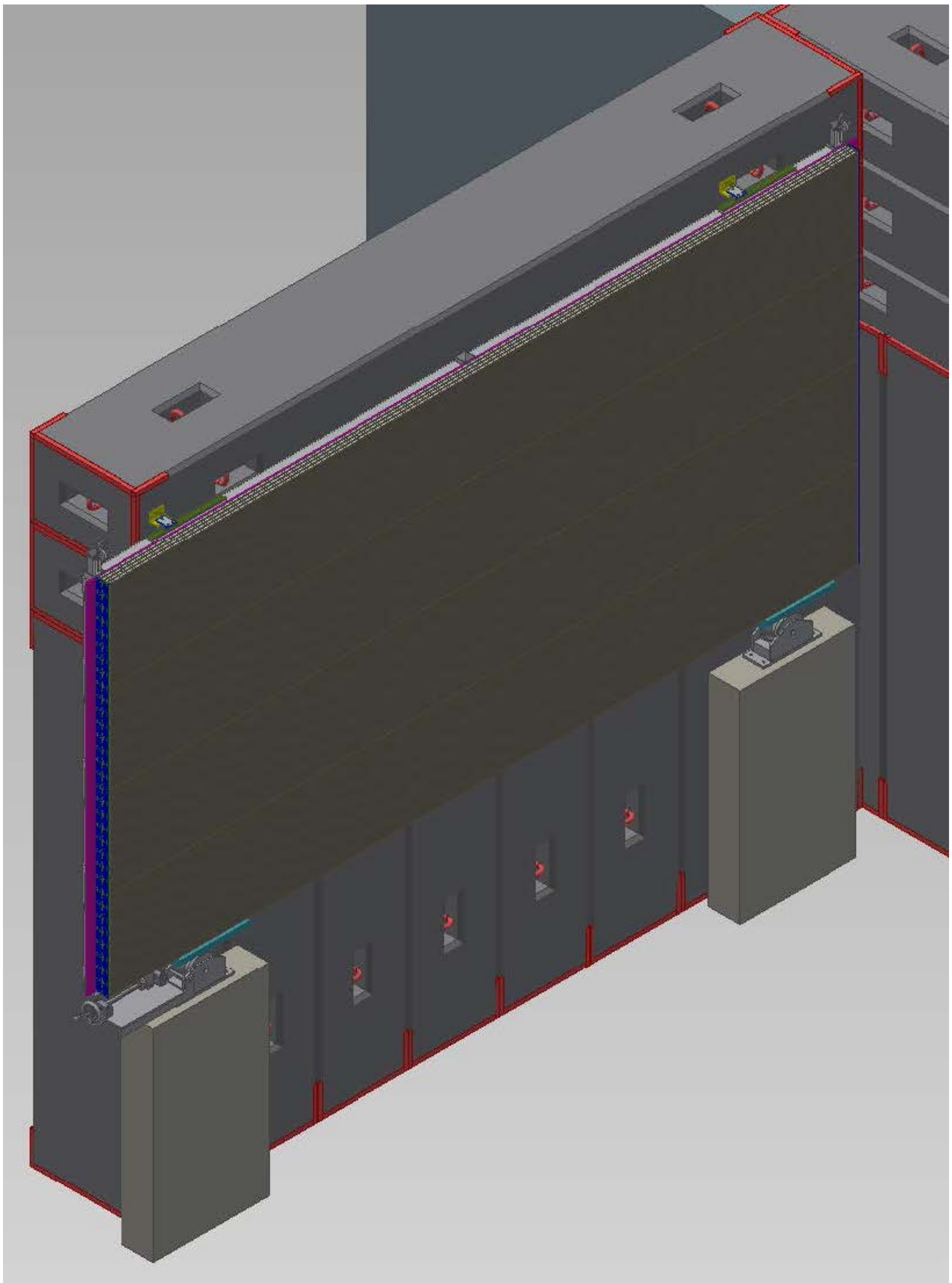

Figure 3.21.: CRV-U modules are attached to a frame assembly that rests on a set of tracks attached to special pedestals. A leadscrew provides horizontal translation of the entire CRV-U assembly (lower left). The top of the assembly is connected to the shielding blocks along special tracks that allow horizontal movement. Should the detector-end closest to the PS receive radiation doses that are higher than expected, CRV-U can be moved further away using the leadscrew.

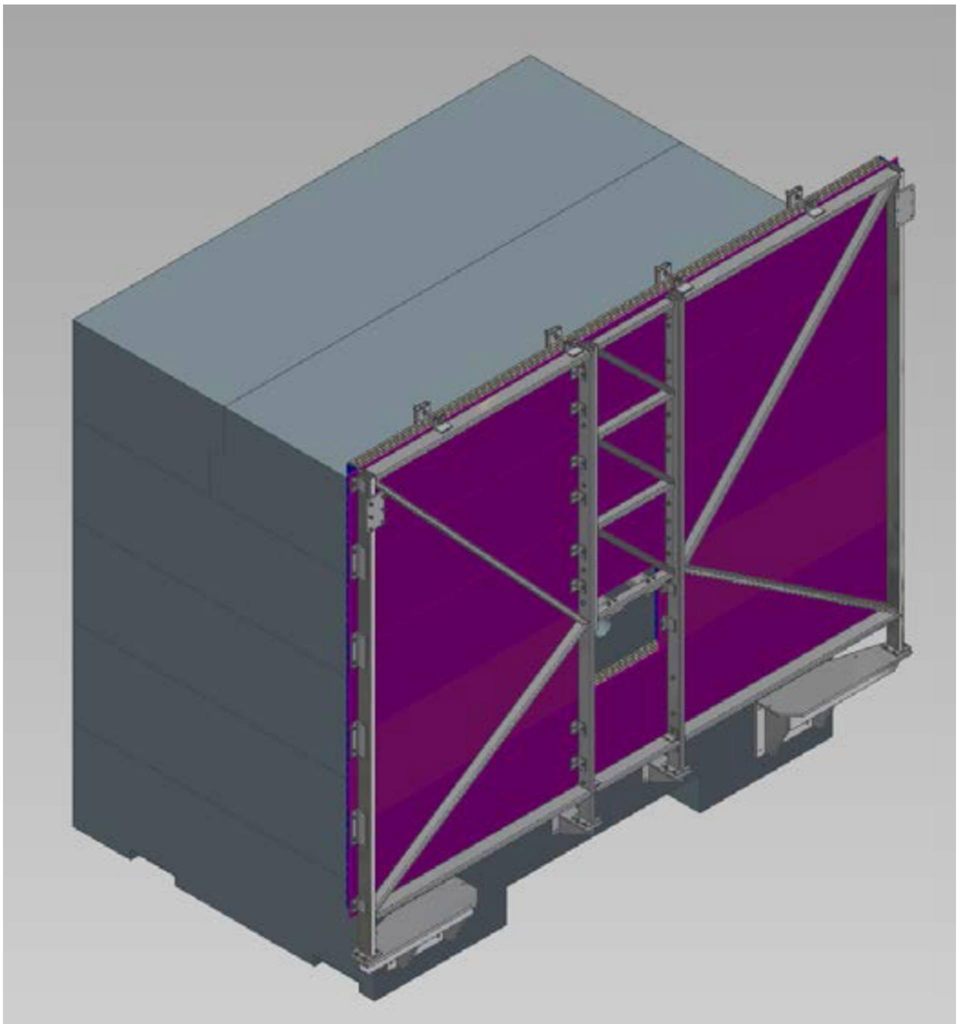

Figure 3.22.: CRV-D modules are attached to a frame assembly before being lowered as a single unit into the detector pit for installation. The CRV-D frame is attached to the movable shielding endcap.

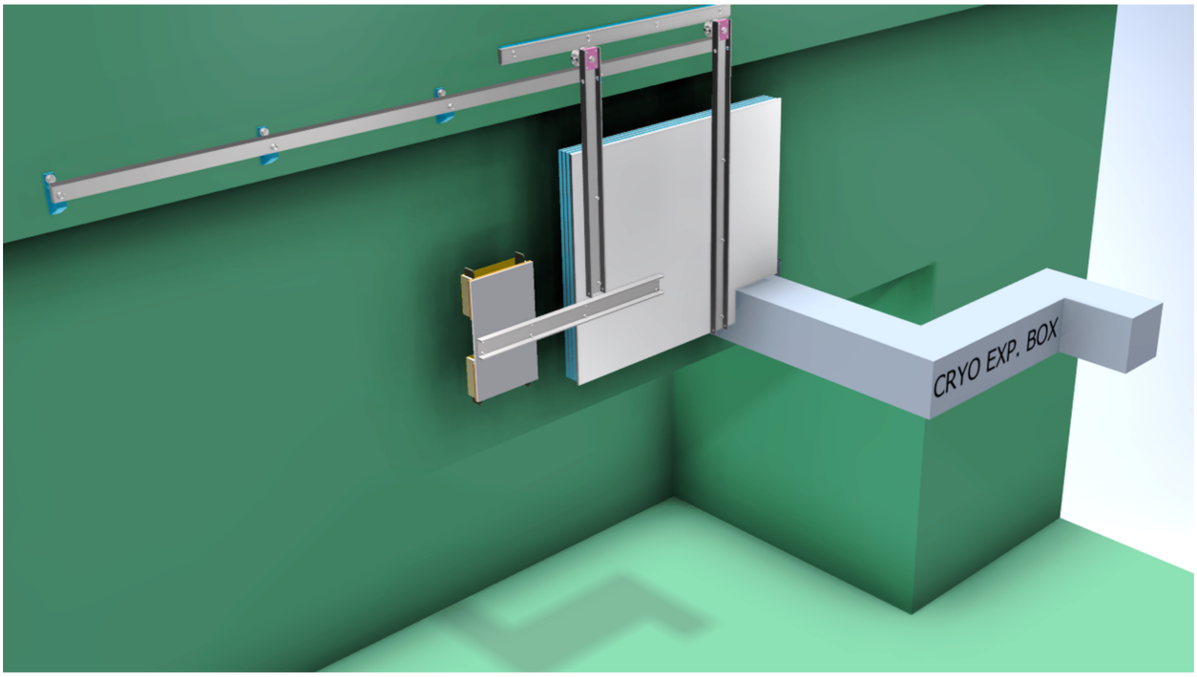

Figure 3.23.: The CRV-Cryo-Outer module hangs from a track mounted to the wall of the building (shown in green). A second track captures the wheels of the module assembly to prevent it from being bumped off the lower track. Enclosures for the front-end electronics are shown to the left of the module.

3.3. The Electronics Readout System

The electronics readout is a triggered system designed to: provide bias voltage to, and digitize signals, in amplitude and time, from the silicon photomultipliers, read out data at a high rate, and buffer an entire supercycle (2.56×10^5 μbunches) worth of data. To reduce costs, the electronics avoid the use of custom components such as ASICs and are assembled from off-the-shelf components. The readout electronics consist of several components (Fig. 3.24): silicon photomultipliers (SiPMs) on their SiPM Carrier Boards (SCBs), Counter Motherboards (CMBs), Front End Boards (FEBs), and Readout Controllers (ROCs).

The SiPMs convert light from the fibers into electrical signals, and are interfaced with the CMBs. In addition to shaping the signals from four SiPMs, the CMBs bias the SiPMs, flash the counters with LEDs, and measure the temperature of the manifold.

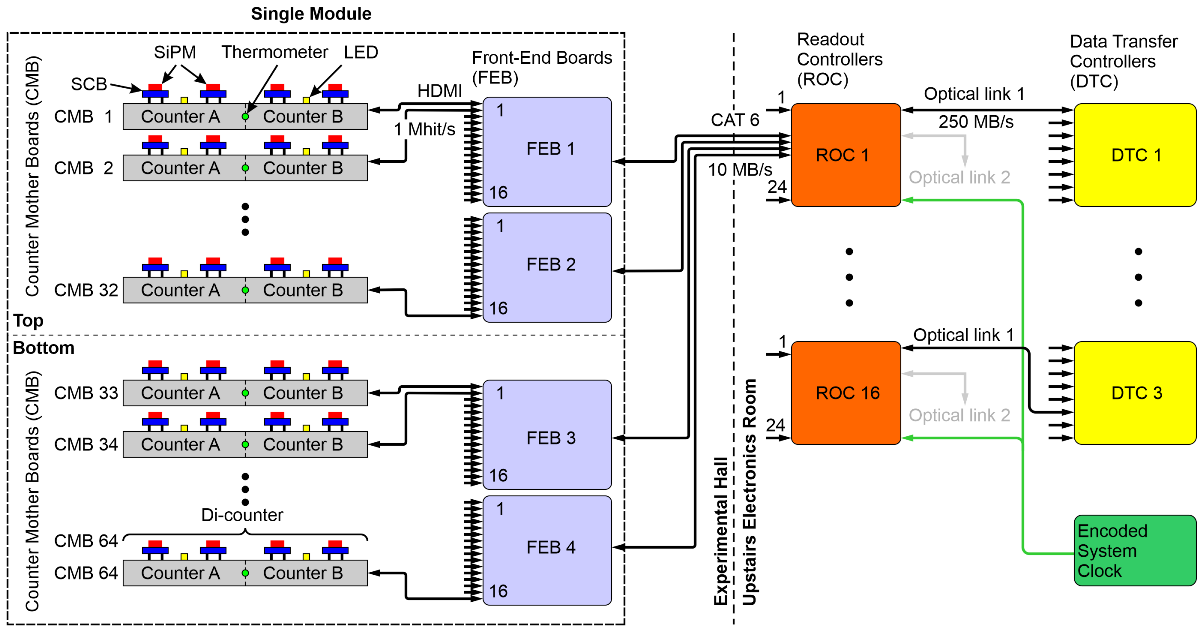

Figure 3.24.: A block diagram showing each of the components and their interconnects of the readout electronics for the CRV. Components to the left of the vertical dashed line are within the detector hall while components to the right are in the experiment's counting room.

The Front End Boards fulfill a variety of tasks that are vital to the read out of the CRV. In addition to being responsible for the receipt and digitization of SiPM signals from the CMBs, the FEB is tasked with supplying power to the CMBs and their associated SiPMs, buffering all of the data taken in a supercycle, aggregating and delivering zero-suppressed event data, and sending status information to the ROCs. Two FEBs are required to read out each module end. The ROCs aggregate data from up to 24 FEBs and act as an intermediary between the experiment's Data Transfer Controllers (DTCs) and the FEBs. They also send status, control, and timing information to multiple FEBs. Events that are collated by the ROCs are sent to the DTCs. The DTCs are the hardware front-end of the experiment's DAQ. There are a total of 19,456 SiPMs, 4864 CMBs, 316 FEBs, and 16 ROCs in the entire CRV system.

3.3.1. Silicon Photomultipliers

Due to the high detection efficiency required by the CRV, the collection of light from the scintillator must meet similarly strict requirements. At a minimum there are two photodetectors at each counter end, and readout at both ends when possible. This not only provides redundancy but is needed to obtain the required photostatistics and for calibration purposes. Having readout at both ends of the counter allows for longitudinal hit determination within 15 cm, and facilitates a constant energy threshold over the entire counter. The sum of the two photodetectors at an end is used in order to achieve the desired detection efficiency [64].

The photodetector selected to meet these requirements is a Hamamatsu multi-pixel photon counter (MPPC), part number S13360-2050VE [65], shown in Fig. 3.25. The device specifications are presented in Table 3.3. This device is a solid-state silicon-based photomultiplier (SiPM) that is comprised of a high density matrix of single-photon avalanche diodes (SPADs) connected in parallel. Each SPAD has a high internal gain that makes it sensitive to single photons. Operating in Geiger mode, a reverse-bias mode at a given voltage over the breakdown voltage, a photon incident on a pixel, the series combination of a SPAD and a quenching resistor, knocks loose an electron that is accelerated by the electric field due to reverse biasing of the diode. The fraction of photons incident on the device that are detected is known as photon detection efficiency (PDE), which depends on wavelength, bias, temperature, and the pixel packing fraction. Electrons that are liberated cause impact ionization within the SPAD, generating a measurable current. Because the current generated is discrete and the pixels are in parallel, the output of the SiPM is a superposition of current pulses generated by each detected photon. These discrete pulses are commonly referred to as photoelectrons (PEs). Even in the absence of light, photoelectrons are seen due to thermal noise, commonly referred to as dark counts. The rate of dark counts (DCR) depends on the temperature,

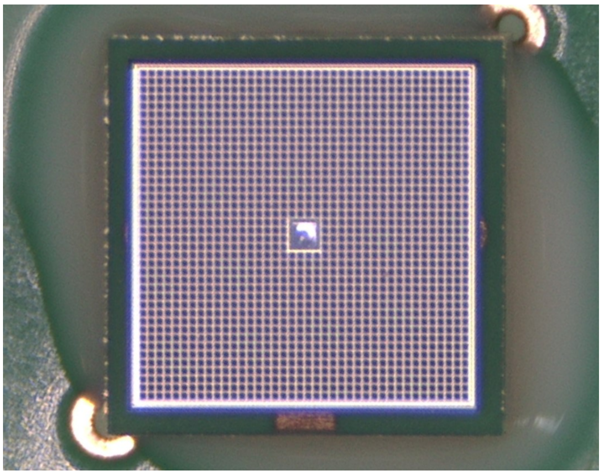

Figure 3.25.: Image of a Hamamatsu S13360-2050VE silicon photomultiplier used in the CRV. The active area is 2 mm × 2 mm with 1584, 50 μm pixels. The square in the center of the sensor is the through-silicon via (TSV).

Table 3.3.: Specifications for the Hamamatsu S13360-2050VE multi-pixel photon counter used in the CRV, at a bias that is 2.5 V higher than the breakdown voltage at 25 °C.

2 mm × 2 mm, 50 μm pixel
Surface-mount, TSV packaging
PDE >33 % (520 nm)
Gain >1.25 × 10^6
Pulse rise time <5 ns
DCR <300 kHz @ 0.5 PE threshold
Cross-talk (inter-pixel) <3.5 %
Bias spread: ±0.75 V
Temperature dependence 54 mV/°C

overvoltage, the size of the active area (number of pixels times pixel size), and radiation damage [66]. Cross-talk caused by discharge in a neighboring cell has a probability dependent on the overvoltage. At sufficiently high dark count rates, resolution of single photon counts becomes difficult.

Selection of the 50 μm pixel size was based on several considerations. First, the capacitance of the device is proportional to the pixel size, so a larger pixel delivers more charge. Smaller pixel size results in a higher dynamic range but can make single PEs difficult to resolve and the dynamic range can exceed the range of the 12-bit ADC that is used in the FEB. The trench size between pixels is fixed, so larger pixels results in a higher packing fraction and larger PDE. The TSV packaging, while introducing a small dead region in the center of the sensor, was chosen because of its thin epoxy layer, which improves acceptance of light from the fiber. The TSV does not significant impact light collection due to a majority of the light from the fiber being emitted at the outer perimeter of the fiber face. While cooling the SiPM reduces the dark count rate, implementing a cooling system was not feasible in the design of the dicounter manifold. The gain of the SiPMs varies with temperature, which can skew the determined number of PEs and impact the overall detection efficiency of the CRV. The temperature at the manifold is measured and corrections to the bias voltage of each device are made periodically through slow control (Ch. 3.3.4). Temperature excursions within the experimental hall are expected to be small and change over a long period of time. A nominal operating voltage of only 2.5 V above the breakdown voltage was chosen to be compatible with a feature on the FEB that can quickly lower the voltage by 3 V, to a bias below the breakdown voltage during the beam flash, making the devices insensitive to the blast of radiation that occurs. Additionally, this operating voltage keeps the DCR and crosstalk rates low, which increase greatly with radiation damage and higher bias voltages.

The SiPMs are mounted on a SiPM Carrier Board (SCB), shown in Fig. 3.26. The $4.9\,\mathrm{mm} \times 8.4\,\mathrm{mm}$ SCB provides a serialized, and more manageable, package for each device. A SiPM is surface mounted (by Hamamatsu) onto one side of the board while pads on the reverse side make contact with spring-loaded pins (pogo pins) on the CMBs. The rectangular shape and offset SiPM location prevents the device from being inserted into the manifold assembly with the polarity reversed. The SiPMs, on their carrier boards, are delivered in a 4×4 array called a waffle pack that is more suitable for shipping and quality control testing.

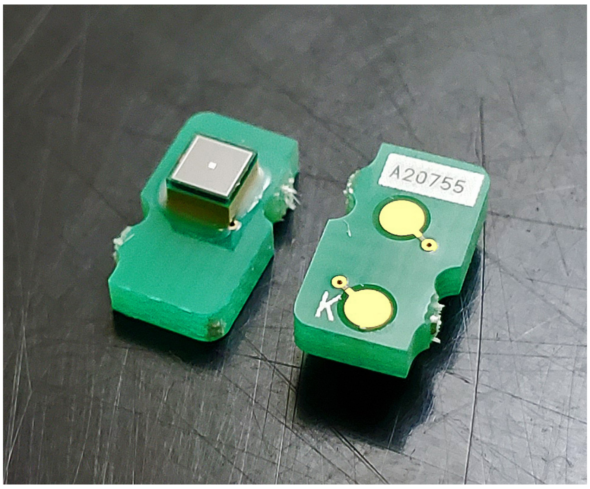

Figure 3.26.: SiPMs attached to carrier boards. Shown is the sensor, pads, and serial number.

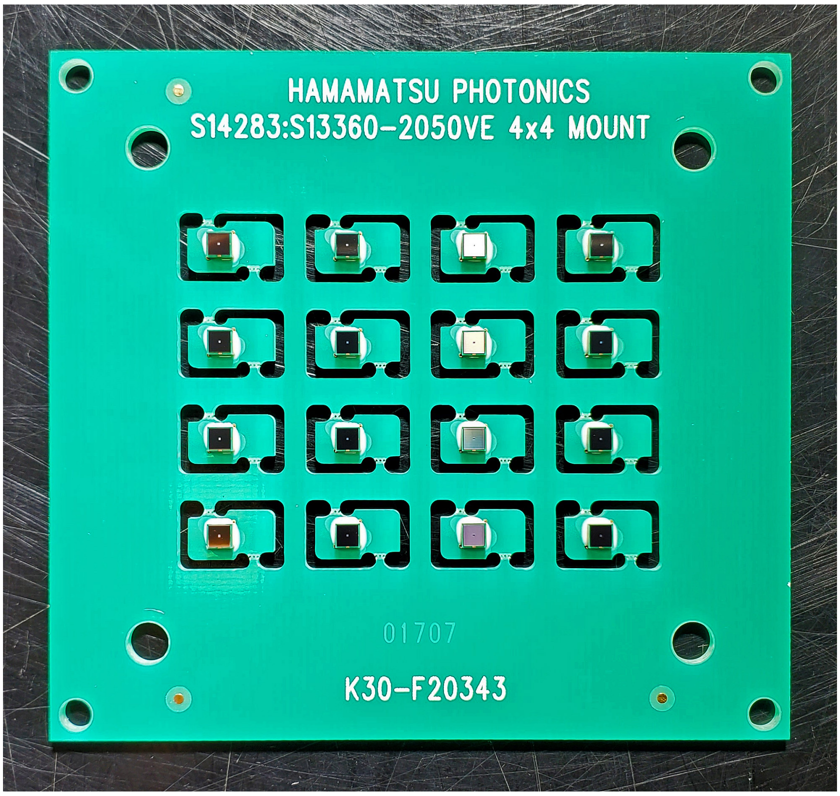

Figure 3.27.: Panel (waffle pack) of 16 SiPMs on their SCBs, as delivered from the manufacturer. Having the SiPMs in this configuration made quality control testing easier. Serial numbers are on the reverse side.

Quality Control

A total of 24,576 SiPMs were delivered on their Carrier Boards in 1536 4×4 waffle packs. Only 19,456 SiPMs are to be used, so the remainder serve as replacements. Each waffle pack of 16 SiPMs had its dark count rate, cross talk probability, and the breakdown voltage measured at Northern Illinois University using a special board that was fabricated for interfacing with the FEB [67]. These measurements were performed using a dark box in which the devices were exposed to a short pulse of light (5 ns) from a 405 nm LED at the far end, during which 1695 ns of digitized waveform data was collected (12.5 ns/sample) and thousands of such waveforms recorded.

The breakdown voltage was calculated using two methods: from the current as a function of voltage, and by plotting the gain versus voltage, and extrapolating the fit to zero gain. The two methods produced similar results. The requirement is that the breakdown voltage must be between ± 0.75 V across all devices. All devices had breakdown voltages between 51.0 V to 51.7 V, with a mean of 51.3 V (Fig. 3.28).

The gain (ADC/PE) was determined by putting the peak ADC values per waveform into a histogram and identifying the photoelectron peaks and computing the number of ADC counts between adjacent peaks. Calculation of the gain was performed at an operating voltage of 2.5 V over the breakdown voltage. An example of the PE spectrum generated by this method is shown in Fig. 3.29 [64]. The average gain was 14.1 ADC/PE, shown in Fig. 3.30 [64]. Adjustments will be made to the FEB amplifier settings to set the gain to $\sim$10 ADC/PE during normal detector operation.

The dark count rate (DCR) was determined by measuring the frequency of photoelectron peaks above a 0.5 PE threshold (Fig. 3.31 [64]) at a bias voltage of 2.5 V higher than the breakdown voltage. To conform with the specification listed in Table 3.3, the DCR

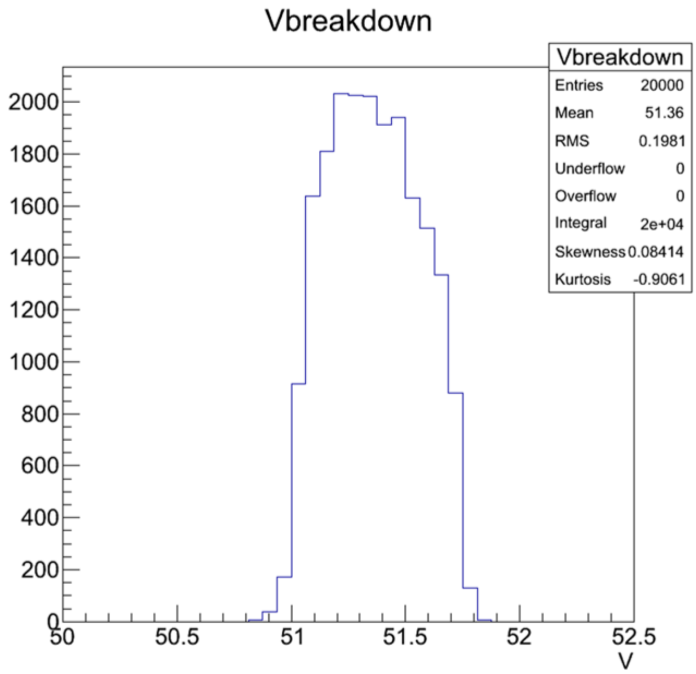

Figure 3.28.: Breakdown voltage measured for 20,000 SiPMs using the gain method.

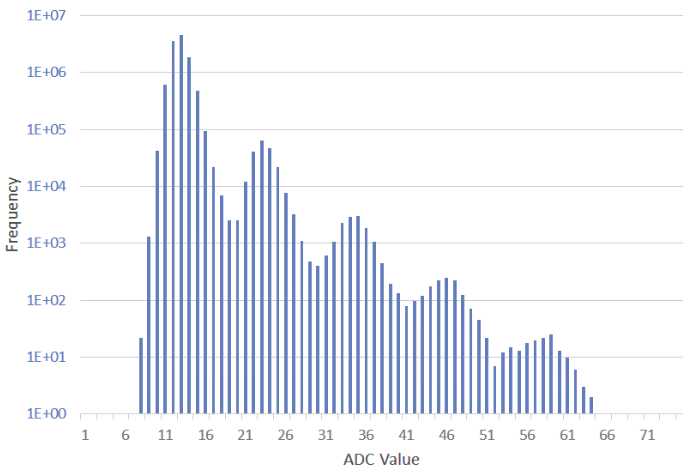

Figure 3.29.: Typical histogram showing the frequency of peak ADC values of the SiPM waveforms. The first peak is a single PE, the second peak is two PEs, and so on. The gain (ADC/PE) is computed from the difference in ADC counts for adjacent PEs.

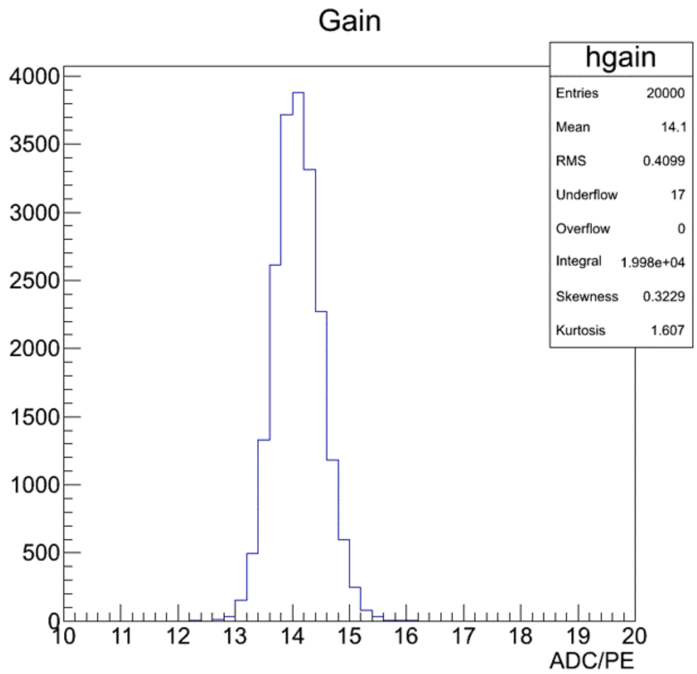

Figure 3.30.: Gain measured at 2.5 V above the operating voltage for 20,000 SiPMs.

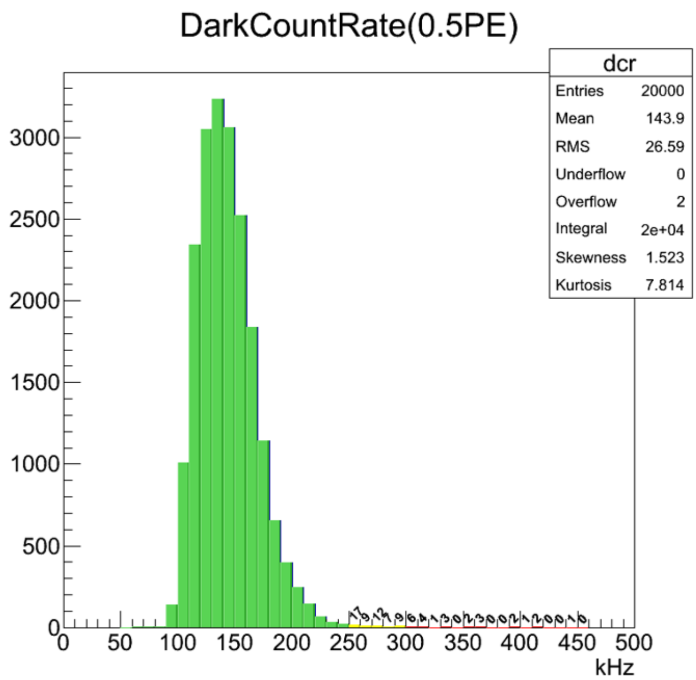

Figure 3.31.: Dark count rate above 0.5 PE threshold for 20,000 SiPMs.

must be below 300 KHz. Only 0.1 % of devices were rejected for having DCRs above the specified value.

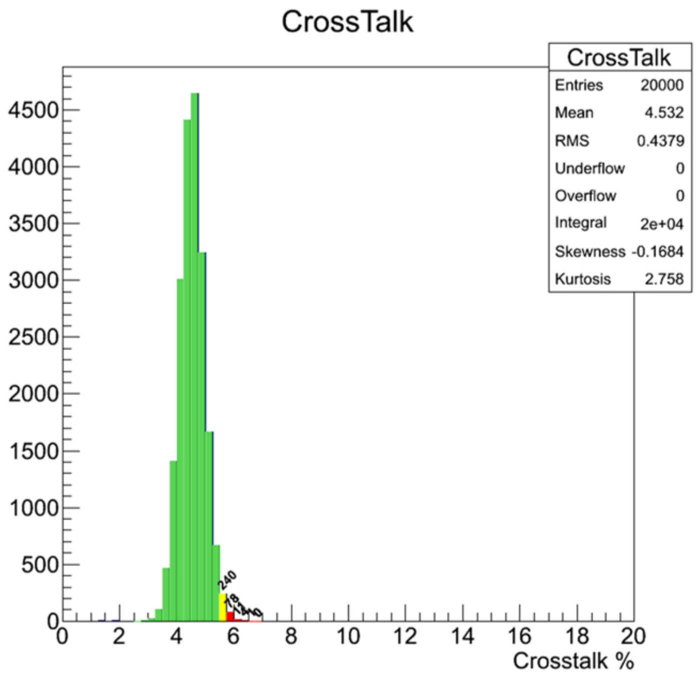

Figure 3.32.: Crosstalk probability, before application of the 2 % correction factor, for 20,000 SiPMs.

The cross-talk probability was determined by taking the ratio of the DCR at 1.5 PE to the DCR at 0.5 PE (Fig. 3.32 [64]) at a bias voltage of 2.5 V higher than the breakdown voltage. The requirement on cross-talk probability is that it must be less than 3.5 %. Using this method, the calculated cross-talk probability is 2 % higher than determined using a transimpedence amplifier by Hamamatsu. Accounting for this systematic increase, only 0.45 % of devices were rejected due to high cross-talk probabilities.

A sample of 176 SCB-mounted SiPMs was inspected using a coordinate mesauring machine at Fermilab's SiDet facility. The sensor position and Carrier Board dimensions (Fig. 3.33) were measured and found to be within 100 μm of specification, which is consistent with the tolerance of ± 0.1 mm.

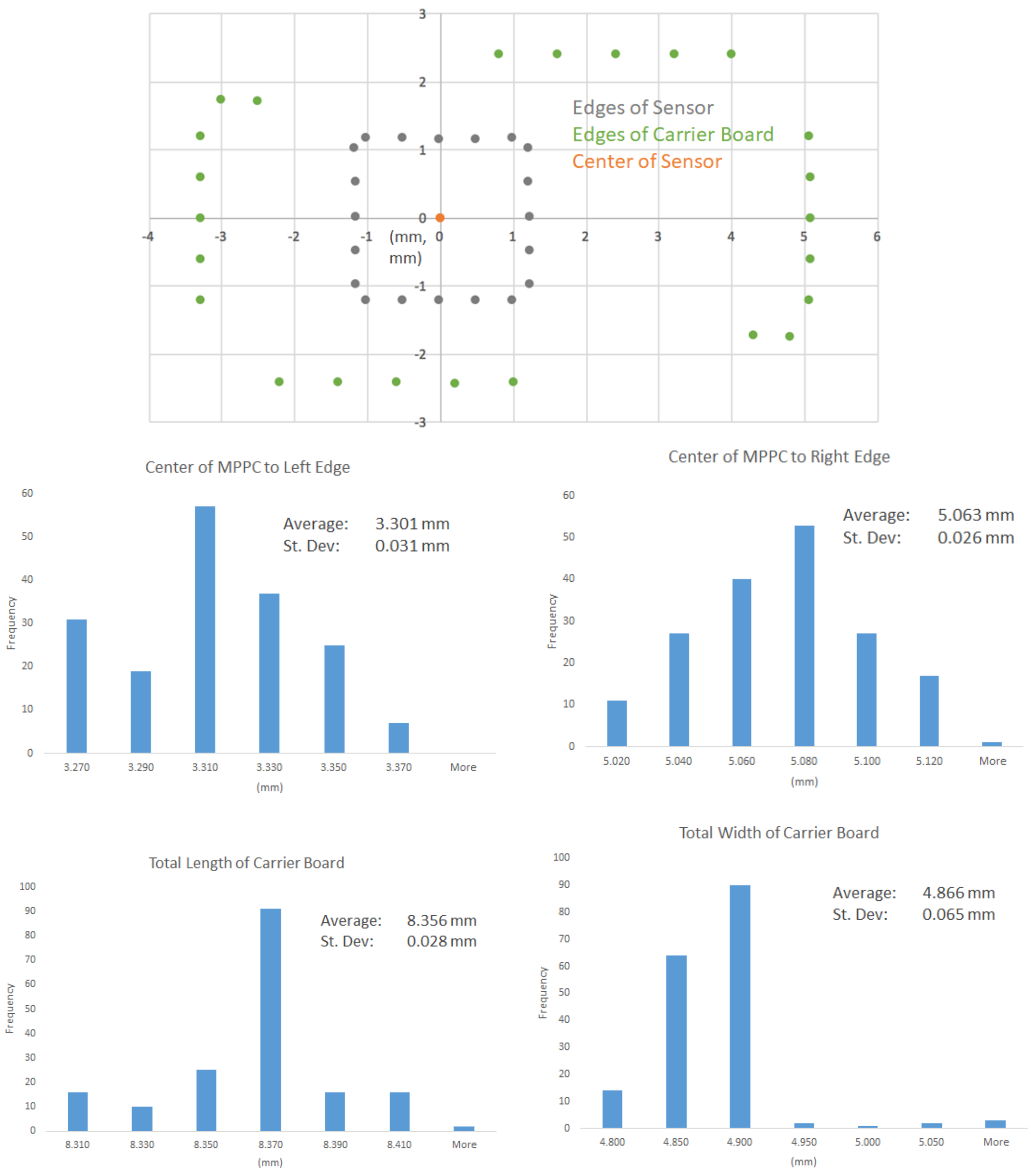

Figure 3.33.: Measurement of SiPM locations and SiPM Carrier Board dimensions. The top plot shows the edge points determined by a coordinate measuring machine. The upper left (right) histogram shows the distance of the left (right) edge of the SiPM to the left (right) edge of the Carrier Board. The lower left (right) histogram shows the length (width) of the Carrier Board. All measurements were within the ± 0.1 mm tolerance.

Gain Monitoring

Due to the temperature dependence of the operating point of the SiPMs, the bias voltage supplied to the devices will be modified in response to temperature variations. A thermometer present on each Counter Motherboard (see next section) measures the temperature at the SiPMs. Instead of applying the known temperature/operating-voltage corrections, which may not be valid due to the effects of radiation damage of the SiPMs, the gain of every device (ADC/PE) will be determined periodically and the bias voltage adjusted appropriately. The breakdown voltage will be determined by measuring the current as a function of voltage, in situ. To determine the gain, the FEBs will histogram the noise signals from each SiPM, and hence the first few photoelectron peaks.

Radiation Tolerance

Radiation damage in SiPMs occurs in two forms, bulk damage and surface damage. Bulk damage is a result of non-ionizing energy loss caused by neutrons, protons, and electrons (>300 KeV) propagating through the silicon. This results in displacements to the lattice structure and forms new energy states as a result of changing semiconductor donor/acceptor energy levels. Surface damage is induced by photons and electrons (<300 KeV) and results in the accumulation of charge or charge vacancies in the oxide layer. This changes the electric field in the device and results in additional surface currents. For the CRV the primary concern is bulk damage that largely impacts the detection efficiency and the ability to resolve PE peaks in the SiPM. In order to properly determine the PE thresholds, individual PEs must be able to be resolved at the highest radiation dose expected of 1×10^{10} n/cm^2 (Fig. 3.34), so that a reliable energy threshold can be set [64]. Only 3.9 % of devices are expected to receive fluences over 5×10^9 neutrons/cm^2 †. Using 200 MeV protons (1 MeV neutron equivalent [68]) at the Northwestern Medicine cyclotron

† All doses from here on are given in terms of 1 MeV neutron equivalent.

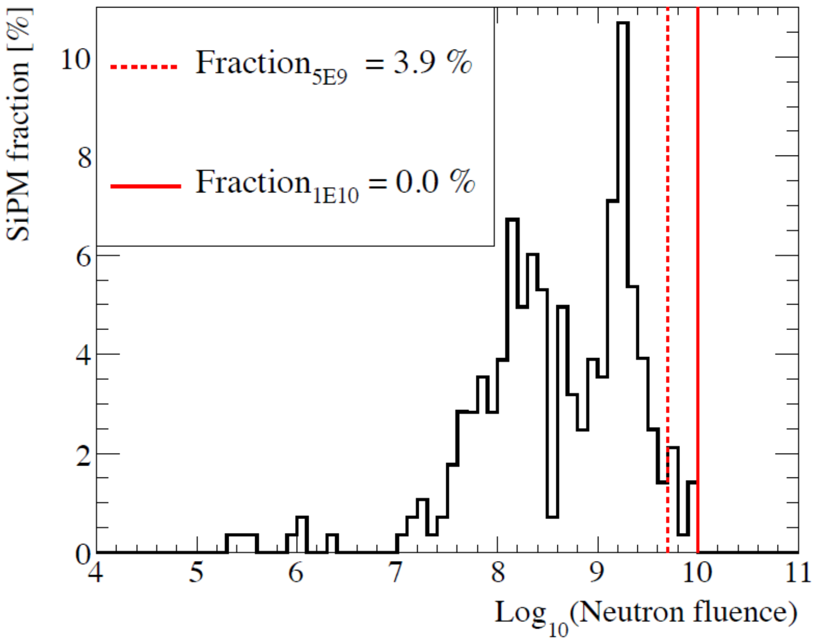

Figure 3.34.: Simulation showing the fraction of SiPMs mounted in the CRV receiving a specified neutron fluence. The fraction of SiPMs receiving doses greater than 5×10^9 neutrons/cm^2 is 3.9 %, the threshold represented by the dotted red line. The maximal fluence, 1×10^{10} neutrons/cm^2, is represented by the sold red line.

[69], four sets of 8 SiPMs were irradiated to varying fluences up to 1×10^{10} p/cm^2 [70]. The gain, breakdown voltage, and DCR were measured before and after irradiation. It was determined that the breakdown voltage and gain did not substantially change up to the highest tested irradiation levels. While the DCR increased with the dose, single PEs are still visible (Fig. 3.35) and a higher PE threshold can be set to keep the rate into the front-end electronics below the 1 MHz limit while still meeting the CRV efficiency requirement. The DCR rate as a function PE of threshold and overvoltage is shown in Fig. 3.36. At the nominal overvoltage of 2.5 V, a modest threshold of $\geq$4 PE keeps the DCR below the 1 MHz limit.

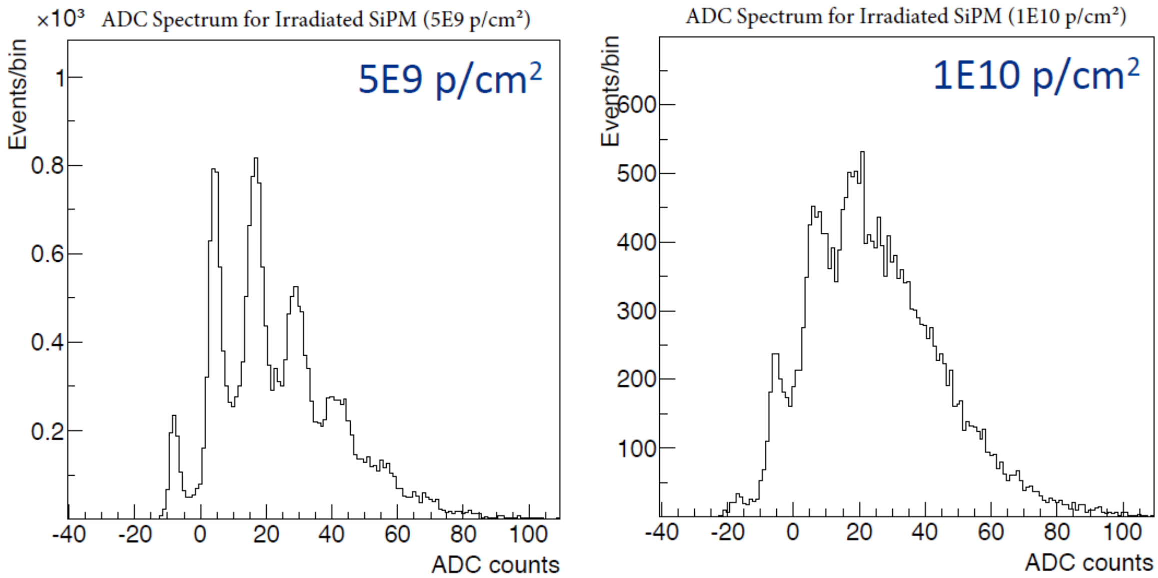

Figure 3.35.: LED response in ADC counts for SiPMs irradiated to a fluence of 5×10^9 p/cm^2 (left) and 1×10^{10} p/cm^2 (right). In both plots, individual PEs are still visible.

3.3.2. Counter Motherboards

Counter Motherboards (CMBs) are the interface between the SiPMs and the FEBs and are attached directly to the end of a dicounter (Fig. 3.37). Each CMB serves four SiPM channels, has passive shaping components, two LED flashers, four CMOS switches for fast lowering of the bias, a temperature sensor, and a unique electronic serial number. The connection to each SiPM Carrier Board is made using a set of spring-loaded contacts (pogo pins) that gently presses the SiPM flush against the face of the WLS fiber. Connection to the FEB is made using Type-A HDMI (with Ethernet) cables. Due to space constraints within the detector hall, two versions of the CMB exist: one with the HDMI header at 90° and the other with the header at 0°, relative to the surface of the CMB. A schematic of a CMB is shown in Appendix K.

Two 405 nm LEDs on the board are used for calibration purposes, illuminating the SiPMs on the other end of a dicounter to provide timing information and a heartbeat test. One LED services a counter, but both LEDs flash simultaneously when triggered.

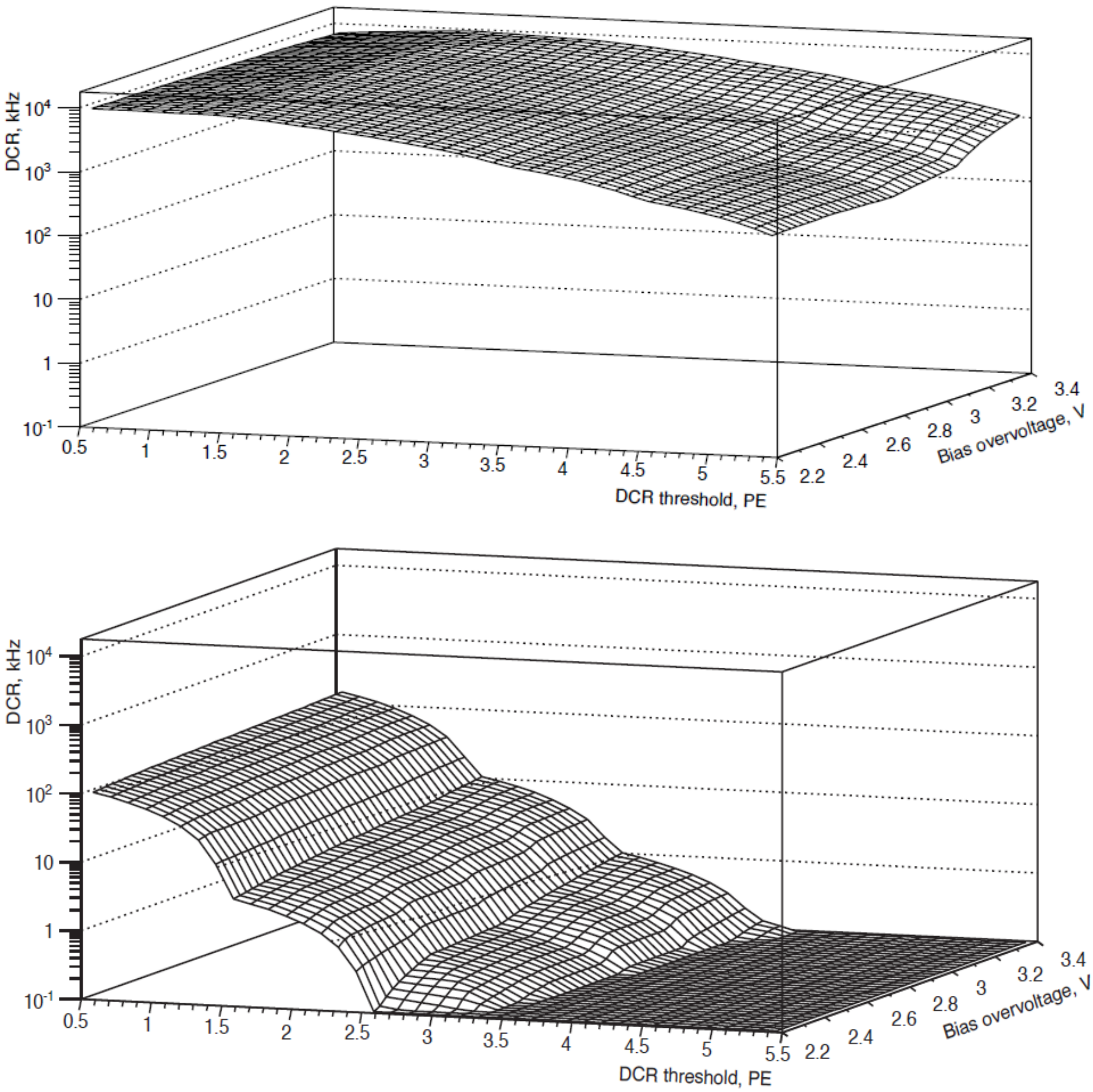

Figure 3.36.: Dark count rate for SiPMs irradiated (top) to a fluence of 1×10^{10} p/cm^2 (1 MeV neutron equivalent) as a function of the PE threshold and overvoltage. The same plot for a non-irradiated device is shown on the bottom.

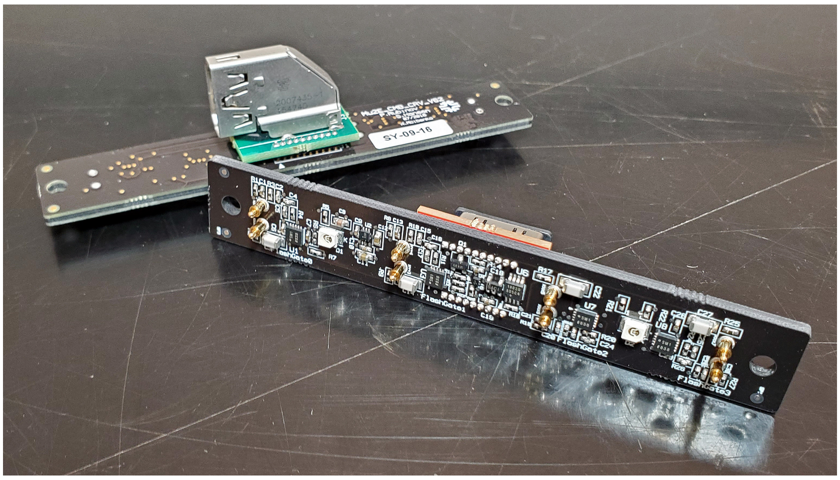

Figure 3.37.: Image of two Counter Motherboards (CMBs) showing the HDMI header and pogo pins.

Flasher intensity and duration is controlled by the FEB and has adjustments from 0 V to 14 V and 0 ns to 1695 ns in 6.25 ns (160 Mhz) steps. The LED flashers and flash gate, which are discussed in the next paragraph, cannot operate simultaneously as they share the same trigger line from the FEB, along with the same duration setting.

A set of four CMOS switches, one for each channel, allows for fast lowering of the SiPM bias by changing the ground reference. This feature, called the flash gate, lowers the SiPM's bias voltage below the breakdown voltage during the proton beam arrival (the first 450 ns in a 1695 ns microbunch) to make the SiPM insensitive to the prompt radiation associated with the beam (beam flash). Just prior to the signal window the bias voltage is brought back above the breakdown voltage. An example of the suppression of signals associated with the beam flash through activation of the flash gate is shown in Fig. 3.38.

Each CMB is equipped with a temperature sensor that is used as an input for adjustments in the bias voltage due to temperature fluctuations. In addition to providing the CMB temperature, each sensor has a unique electronic serial number that is used for identification. This serial number is linked to information about its location within the

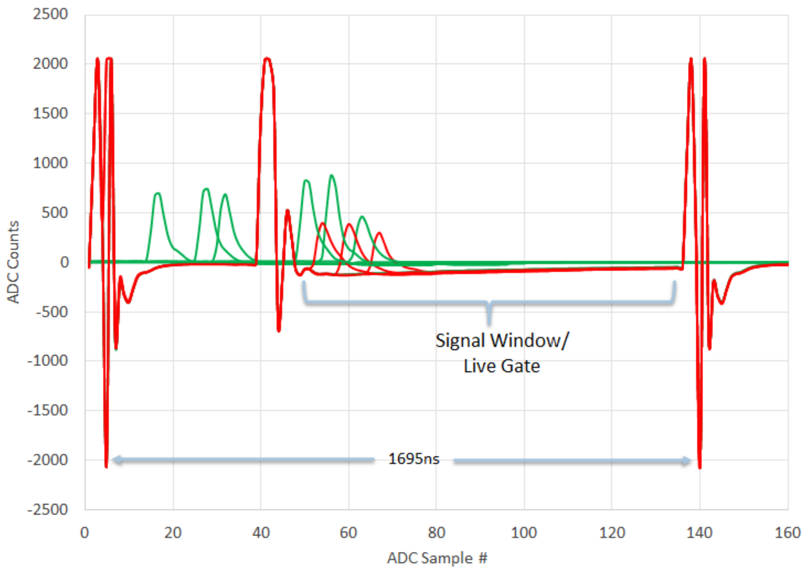

Figure 3.38.: By quickly lowering the bias voltage of the SiPMs below the breakdown voltage using the flash gate, the signals associated with the beam flash can be suppressed. The green line shows the SiPM response without use of the flash gate and shows pulses associated with the beam flash in the pre-signal window region. The red line shows the SiPM response with the flash gate. The pre-signal window pulses are absent. The large excursions are switching noise.

CRV (e.g., which dicounter end in which module) and the SiPMs that it is connected to. Figure 3.39 shows the pinout of the HDMI header.

Quality Control

All CMBs underwent quality control testing at UVa before being inserted into manifolds. These tests included an operational check of the temperature sensor and serial number readback, evaluation of a connected SiPM's response to light, and operational tests of the flash gate and LEDs. A special apparatus was designed and built for testing of up to 16 CMBs. Fabricated of aluminum, the apparatus has two columns of eight manifolds, shown in Fig. 3.40, and contains an unchanging set of SiPMs. Dividers separate each column of CMBs into a left and right half. This allowed for the separate evaluation of LEDs, as they both flash simultaneously when triggered. A pair of external 405 nm LEDs

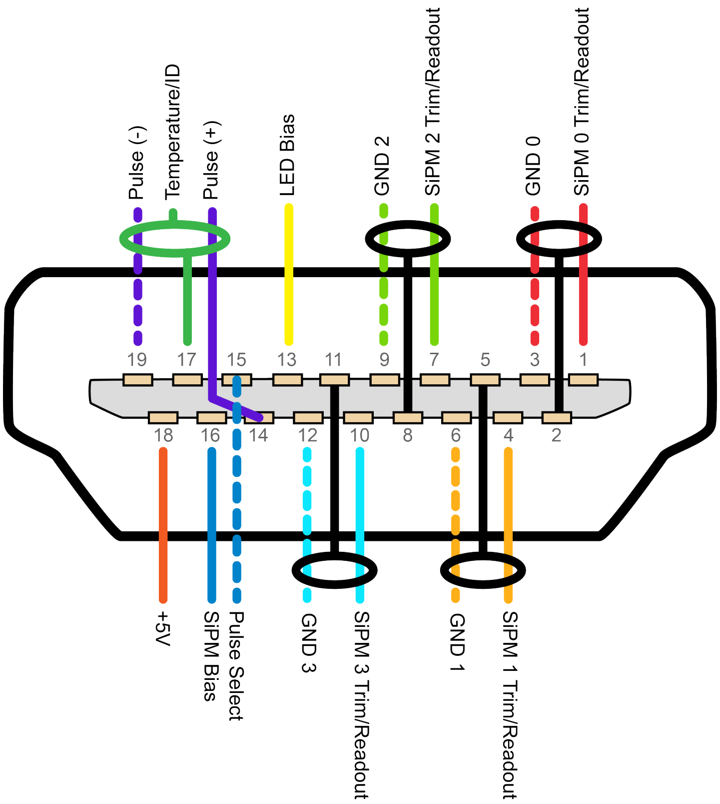

Figure 3.39.: Pinout of the HDMI Header. The same-colored solid and dashed lines indicate twisted pairs. The numbered grounds for each SiPM readout channel are connected to the flash gate. The loops indicate twisted-pair shielding. The black lines are ground.

Figure 3.40.: The CMB testing jig. Two columns of eight manifolds each containing a set of four SiPMs read out by the CMBs being tested. Two CMBs are shown for reference.

located on the base of each chamber illuminates the SiPMs. An exposed view of one of the four compartments in the testing jig is shown in Fig. 3.41. The LEDs are driven by a Tektronix PSPL2600C pulser [71] triggered by a FEB. Each CMB is loaded into a SMB and connection to the SiPMs is made by pressure exerted on the CMBs by a thick foam affixed to the hinged cover (Fig. 3.42). The entire apparatus is contained within a dark box that has HDMI and BNC feedthroughs for the CMBs and LEDs, respectively.

The temperature sensor is the first item evaluated for each CMB. Complete temperature sensor operation is confirmed by reading the serial number and temperature. Counter Motherboards with invalid serial numbers or temperatures are set aside for repair.

Since the same set of SiPMs are always used, the CMB response to the LEDs allows variations in the CMB response to be detected. All SiPM response tests are carried out at the same bias voltage. The response of each channel is determined by histogramming, within the FEB's FPGAs, ADC samples taken over a four-second period. During this time window, the LEDs are flashed at a rate of 189 KHz with a 3 ns duration, with the pulser's 48 V amplitude attenuated by 16 dB (due to the splitting needed to fan out the

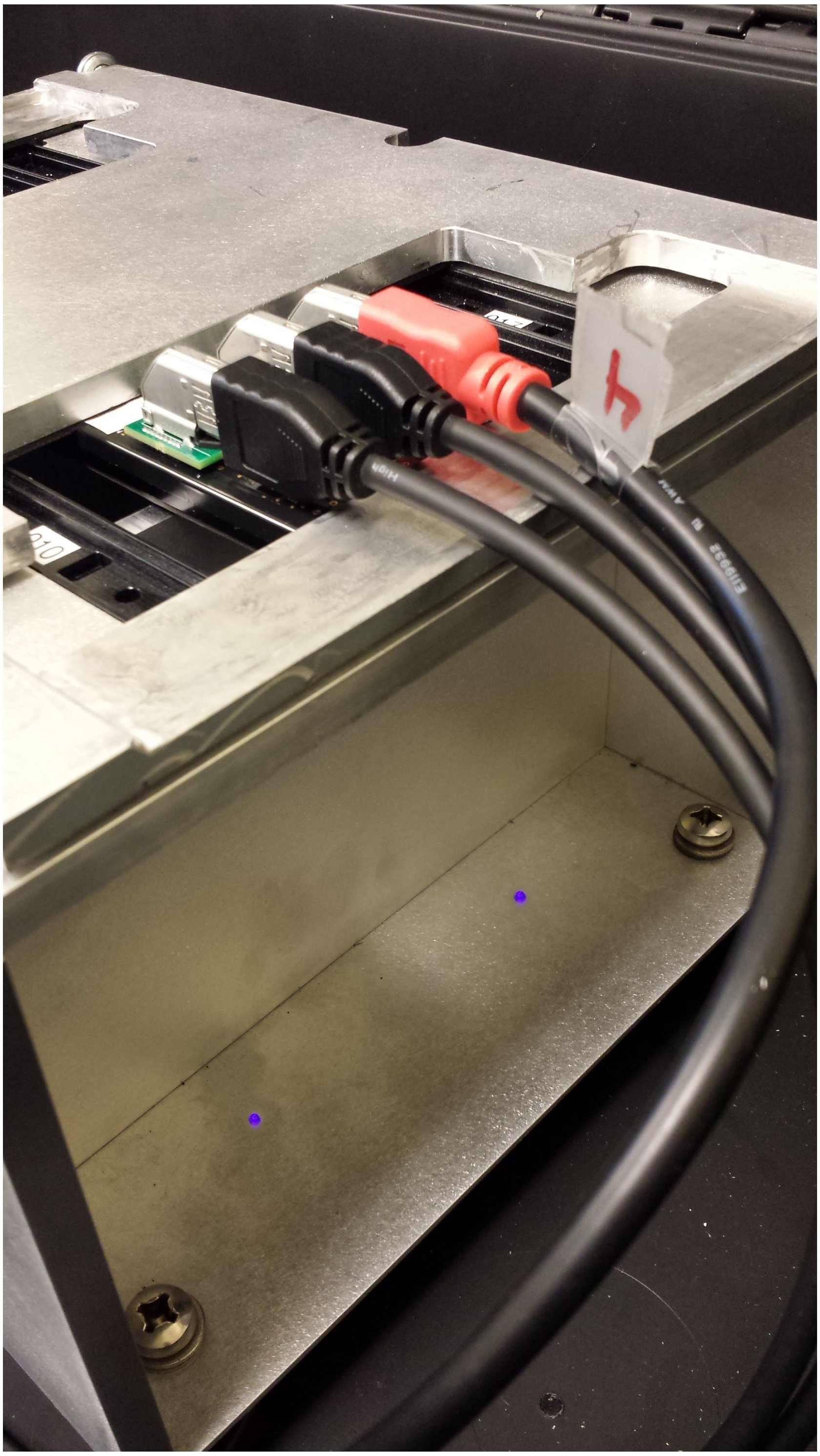

Figure 3.41.: An exposed view of one of the four compartments in the CMB testing jig. The two LEDs on the base that illuminate the SiPMs are visible in the image.

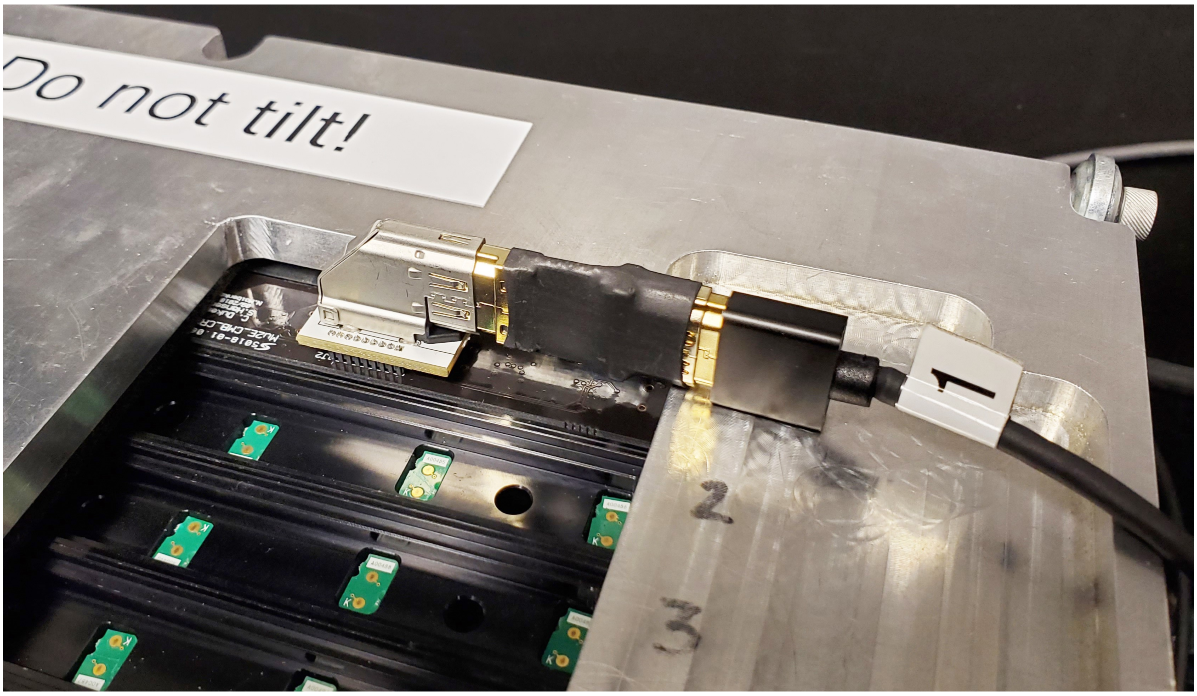

Figure 3.42.: CMB loaded into the CMB testing apparatus. The hinged plate retains the CMB in the manifold and exterts pressure on the CMB to make contact between the SiPMs and pogo pins. The HDMI cable is shown here.

pulser signal). Because the LEDs are not on continuously, both the dark count and LED response are visible, shown in Fig. 3.43. The peaks to the right of the pedestal are used to compute the gain (ADC/PE). The distribution in the center of the histogram is the response of the SiPM to the LED, characterized by the multiple photoelectron peaks on top of the bulk of the distribution. The CMB response is evaluated by integrating all counts above a 5.5 PE threshold. Contributions from dark counts are negligible. The effects of temperature variations are negligible due to the room's climate control ($\pm 0.5\,^{\circ}$C). The expected response and variation was computed by recording the response for each SiPM with a set of 16 known-working CMBs. Counter Motherboards that have more than a $1\,\sigma$ deviation from the average response are flagged and set aside for repair.

The flash gate operation is evaluated by verifying that the SiPMs did not respond to the flash of the external LEDs, verified by the absence of ADC counts above a 5.5 PE threshold using the same method described in the paragraph above.

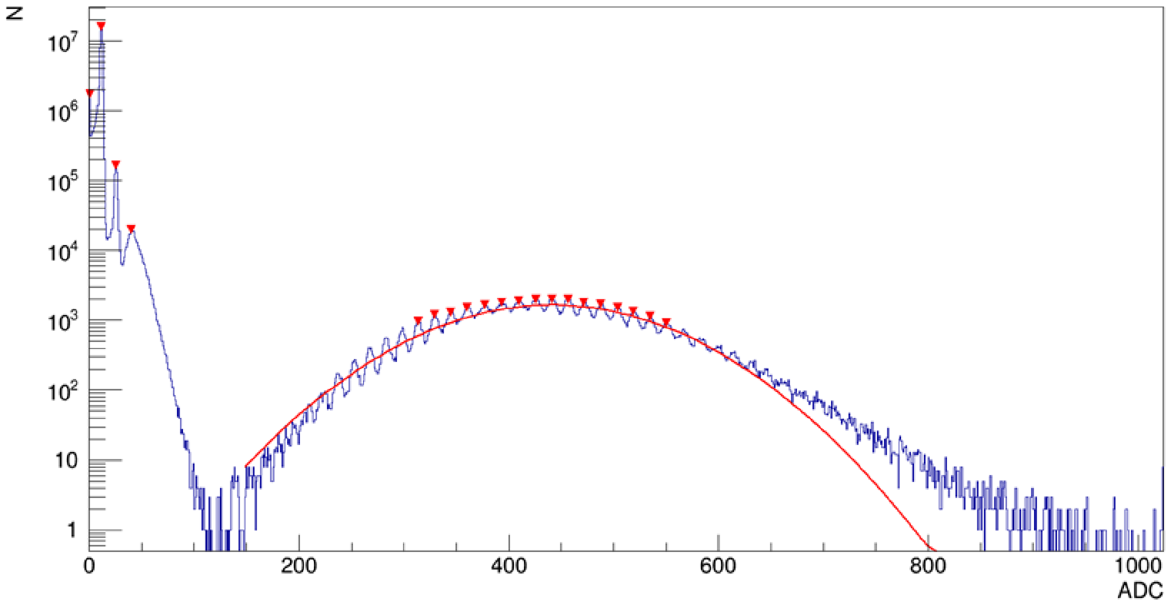

Figure 3.43.: Typical histogram for a SiPM illuminated by an external LED. The tallest peak (at left) is the pedestal value: the ADC value associated with the electronic baseline (absence of signal). The pedestal value is adjusted to be above zero so it is visible in the histogram. The peak at zero is underflow caused by undershoot. The peaks immediately to the right of pedestal are the first few photoelectrons. The bulk of the distribution in the center of the histogram are the multiple photoelectrons from being flashed by the LED. The red line is a Gaussian fit, while the red markers are detected peaks.

The on-board LEDs could only be verified to be operational by recording their response using adjacent CMBs, due to electronic noise generated on the CMB whose LEDs are flashed. As such, it was required that the adjacted CMBs did not have any known fault with their SiPM responses. Evaluation of the LEDs is done in a similar method as described in the preceding paragraph, but there is no requirement that the integrated response be within $1\,\sigma$ of the expected response, only that the integral was non-zero and multiple PEs peaks could be found.

While the flash gate and LED flashers share the same trigger circuitry, component-level issues could inhibit the operation of either function. Failure of both the flash gate and LED flashers are indicative of an issue with this trigger circuity.

Radiation Tolerance

Radiation tolerance of the CMB was studied using a 200 MeV proton beam at the Northwestern Medicine proton therapy cyclotron. Four CMBs, three powered and one un-powered, were exposed to a fluence of $1 \times 10^{11}\,\mathrm{cm}^{-2}$ without any measurable change in behavior or performance during, or after, irradiation [72].

3.3.3. Front End Boards

The Front End Board (FEB), shown in Fig. 3.44, is a 64 channel device that fulfills a variety of functions. Board power and data link is established through a single Cat6 power over Ethernet (PoE) connection to a Readout Controller. Connections to the CMBs are made using low-cost, high-bandwith HDMI cables. There are 16 HDMI headers on each FEB since each CMB has four SiPM channels. Eight Texas Instruments AFE5807 octal ultrasound analog front end chips [73] are used. Each ultrasound chip has eight channels of low-noise preamplification, variable gain amplification, low pass filters, and samples each channel at 80 MHz using 12 bit ADCs. A block diagram of a single channel is shown in Fig. 3.46. ADC samples are spaced in time by 12.5 ns. Groups of 16 channels are serviced by a Xilinx Spartan-6 FPGA [74], for a total of four FPGAs. An on-board bias generator (shown in Appendix L) supplies the SiPMs with a bias voltage of up to 80 V. A total of sixteen 12 bit DACs per FPGA provides ± 4.096 V of voltage adjustment, in 1 mV steps, for each SiPM, about the common bias. The current of each SiPM can be measured with 100 pA resolution, one channel at a time, using a single 24 bit ADC and a network of multiplexers (shown in Appendix L). This allows in situ I-V curves to be taken for SiPM calibration. It is also used to measure the response of counters to radioactive sources and for light leak testing.

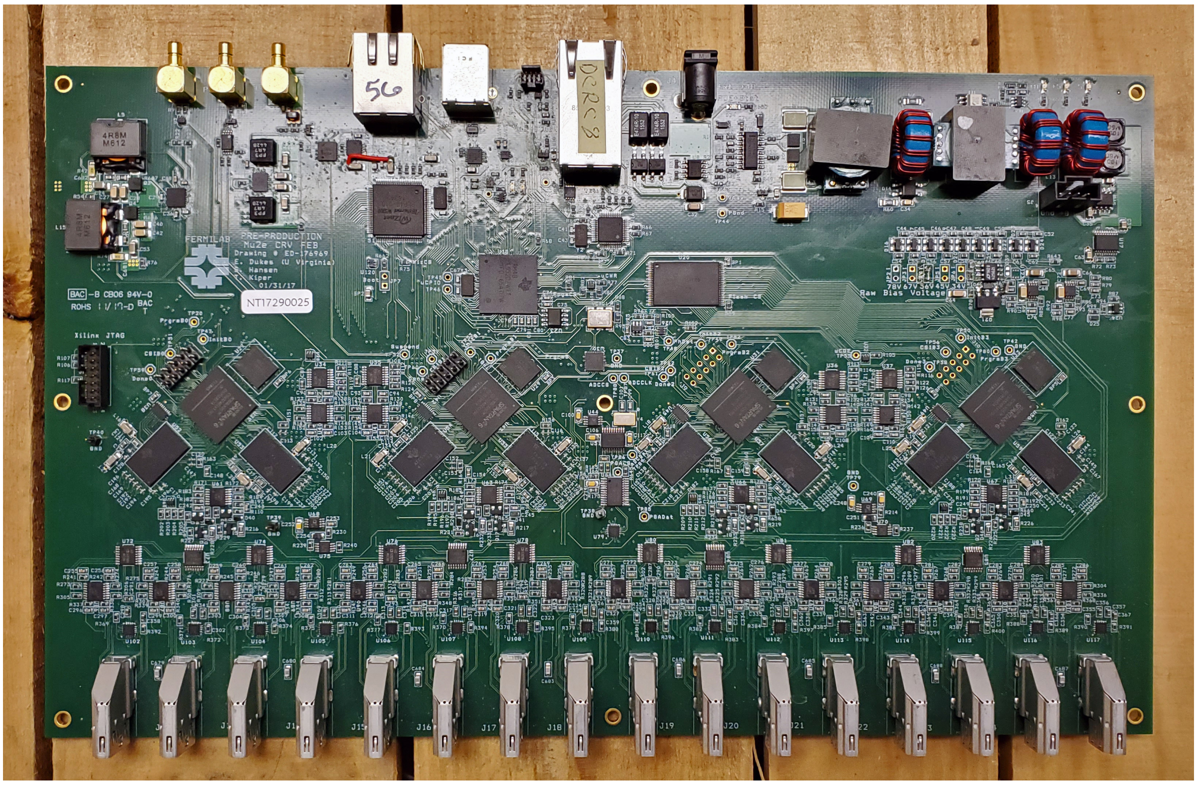

Figure 3.44.: Photograph of a Front End Board (FEB). At the bottom are the 16 HDMI headers used to interface with the CMBs, with voltage trim DACs just above them. Eight octal ultrasound chips feed data into four FPGAs (middle) for a total of 64 channels. Cat6 PoE connections (top) are used for power and data transfer. In the upper-right corner is the on-board bias generator.

A block diagram showing the flow path of the data is presented in Fig. 3.45. Once zero-suppressed, digitized signals are passed through the event-building logic in the FPGA, complete events are stored in a 2 GB LPDDR RAM buffer until it is read out or overwritten. This memory size was selected to record an entire supercycle worth of data. Control and readout of the FEB is managed by a medical-grade Texas Instruments RM48 arm-cortex microcontroller [75], which can self-detect and correct single-bit upsets, with the ability to take advantage of 64 MB of flash ROM to reflash the FPGAs in situ (50 ms), if needed.

Several useful features were implemented in the design of the FEB that are controlled by the FPGAs. Features relevant to the digitization and readout of the SiPM signals

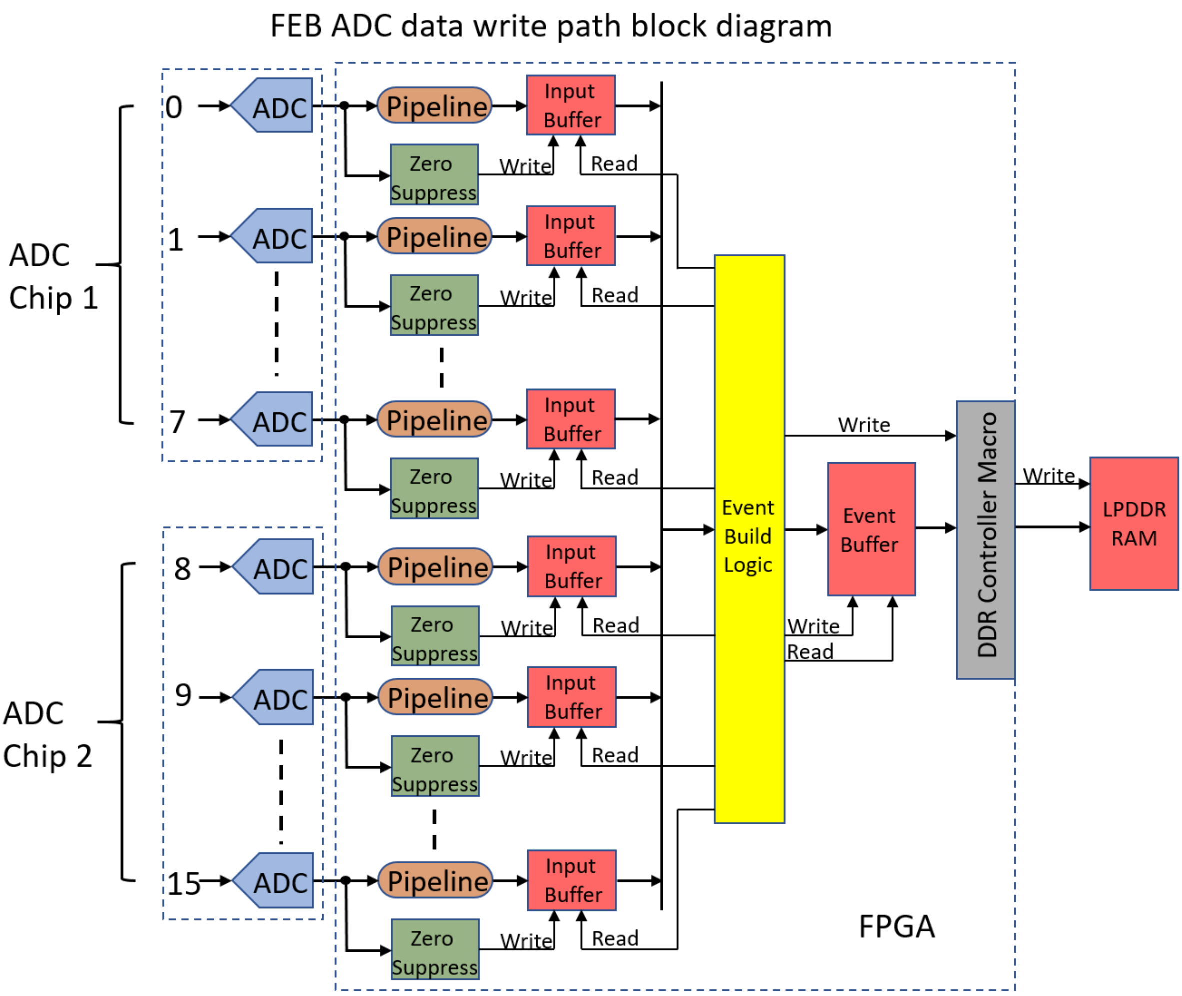

Figure 3.45.: Front End Board block diagram showing the flow path for the ADC data coming from two ultrasound chips into an FPGA and the buffer memory.

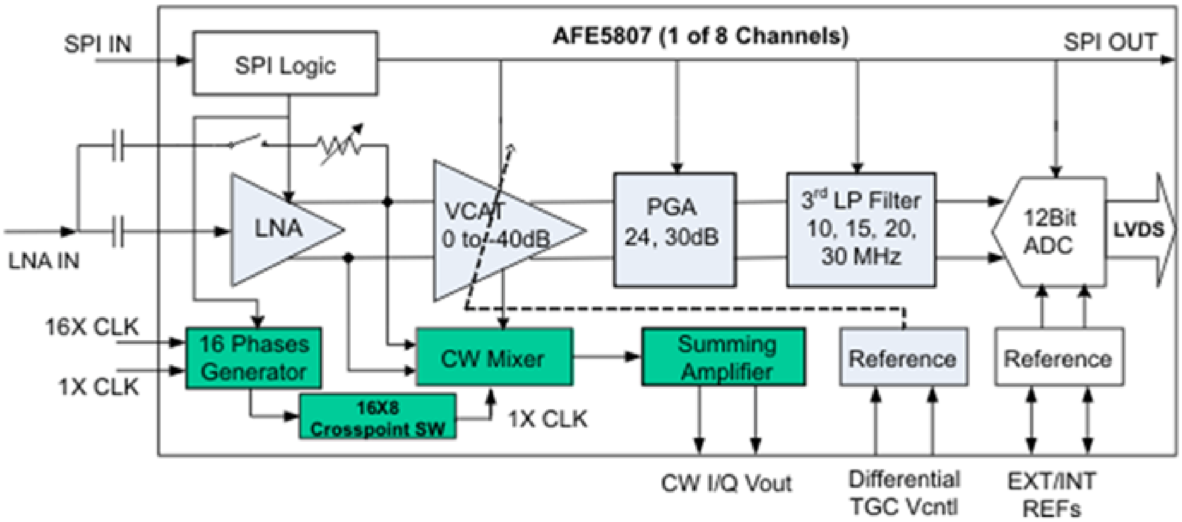

Figure 3.46.: Block diagram of a single digitizer channel of the AFE5807 ultrasound processor used for signal digitization.

include, for example, control over the attenuation and amplification settings in the ultrasound chips, the ability to select the number of samples for zero suppression, and an adjustable sample delay to account for trigger signal propagation time. Event recording is selectable between internally-generated triggers, using an on-board frequency generator, external triggering, through a SMB connector, or FM-encoded signals received over Ethernet. The latter method is used in normal data taking. The gate in which triggers are valid can be internally or externally generated through similar means. Additional settings in the FEB are used to set the flash gate time and LED intensity and duration. To reduce the data bandwidth, a zero-suppression algorithm that eliminates events with no signals above a threshold is employed. The zero suppression algorithm uses correlated dual sampling to handle baseline shifts while selecting pulses with a given ADC increase. Additionally, the FPGAs are capable of generating histograms from ADC data using a peak-finding algorithm. The plot in Fig. 3.43 was generated in this manner.

Quality Control

After fabrication by the vendor, every FEB undergoes several function checks and calibration at Kansas State University. These tests include a general power-on test, including the bias generator, and a self-check of the memory. Calibration of each input channel is performed by adjusting the voltage offset until the measured voltage across the input is 0 V. This ensures the voltage settings for each SiPM is true and accurate. The calibration values are saved to memory.

Radiation Tolerance

Radiation tolerance of the FEB was studied using a 200 MeV proton beam at the Northwestern Medicine proton therapy cyclotron [72]. A powered FEB was exposed to a fluence of 5×10^{10} p/cm^{-2} (1 MeV neutron equivalent, 2.5 kRad in silicon) without any measurable change in behavior or performance. During a 60 minute exposure of 5×10^{8} protons at normal incidence to the FPGA, there were 18 correctable and 2 uncorrectable single event upsets (SEUs) for 4.5×10^{6} configuration bits. The annual expected dose summed over all FEBs in the CRV is 7.54×10^{10} cm^{-2}/yr (1 MeV neutron equivalent). This yields 10,800 correctable and 1080 uncorrectable SEUs for the whole CRV each year.

Magnetic Field Tolerance and Mitigation

The FEBs, in most cases, are mounted on the side modules so that short (1.2 m) HDMI cables can be used. The presence of large fringe fields generated by the solenoids demands that the FEBs be housed in magnetic-shielding enclosures, shown in Fig. 3.47. An FEB was tested up to 300 Gauss with the field directions perpendicular and parallel to the FEB. No effects were observed up to 300 Gauss in the perpendicular direction, however

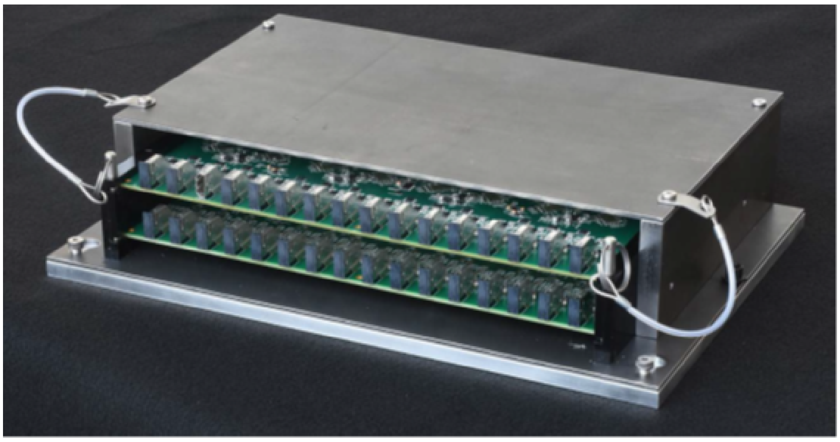

Figure 3.47.: The Front End Board Enclosure (FEBE) provides magnetic shielding for two FEBs. Mounting plates for FEBEs are glued to the side modules.

the FEB ceases to operate in a field strength of 240 ± 10 Gauss parallel to the board [76]. It was decided that the field strength should be kept below 150 Gauss in the both directions. A full simulation of the solenoids was conducted using OPERA [77] and the field evaluated in the regions where the FEBs are mounted [78]. Three types of enclosures were designed: aluminum and thin steel versions, which share the same dimensions, and a thick steel version that is needed to reduce the field strength significantly in certain regions. While all enclosures could be of the thick steel design, such a decision is not cost-effective and the enclosure weight is twice that of the thin-gauge steel design (14.5 kg versus 7.1 kg) making it difficult for personnel to install the enclosures. The drawings for each enclosure type are shown in Appendix J. With an appropriate selection of enclosure type for each region in which FEBs are mounted, the field strength can be reduced to below the set limit. The field strength as a function of position is presented in Ref. [78].

Control and Readout Software for Fabrication Tests and Test Beam Efforts

A program used to interface directly with the FEB for control and readout was developed for various tests. Written in C# and run in Windows, the program has a graphical user interface and a multi-threaded back-end for ease of use and efficiency. The main purpose of the program is to facilitate the recording and acquisition of data from any number of FEBs. Regardless of the FEB trigger settings, self-triggered or externally triggered, the program monitors the spill status of every board and reads the data when the spill ends. Data is received in binary in the format shown in Appendix M. A multi-threaded approach allows data from multiple FEBs to be read while data is written to disk. Settings in the program allow the data to be written to disk in ASCII or binary format. For additional control of the FEB and for debugging purposes, an interactive console was developed that allows the console history to be saved and a file containing FEB parameters, such as gain and SiPM bias, to be read and sent to the FEBs.

Fabrication efforts were made easier by the inclusion of several specialized interfaces for each quality control test. One interface features controls for dicounter source testing and light-leak testing (see Section 5.1), which displays real-time current measurements and the ability to save the measurements to the disk. Another interface was designed specifically for CMB testing and displays test information for the user and saves diagnostic data to a file. A separate interface is used for general debugging of the FEBs: it allows the user to view FEB parameters, set the bias, measure the current of individual channels, and view the CMB temperatures.

3.3.4. Readout Controllers

Acting as a link between the experiment's DAQ and the 316 FEBs of the CRV, 16 rack-mounted Readout Controllers (ROCs, shown in Fig. 3.48) supply timing, trigger, and power to, and receive slow control information and data from up to 24 FEBs through an array of Cat6 PoE connections. Each connection to an FEB has a 100 Mb/s bandwidth and can supply up to 24 W of power. Two 2.5 Gb/s optical fiber transceivers are present, one of which interfaces with the DTC from which it receives trigger and status requests

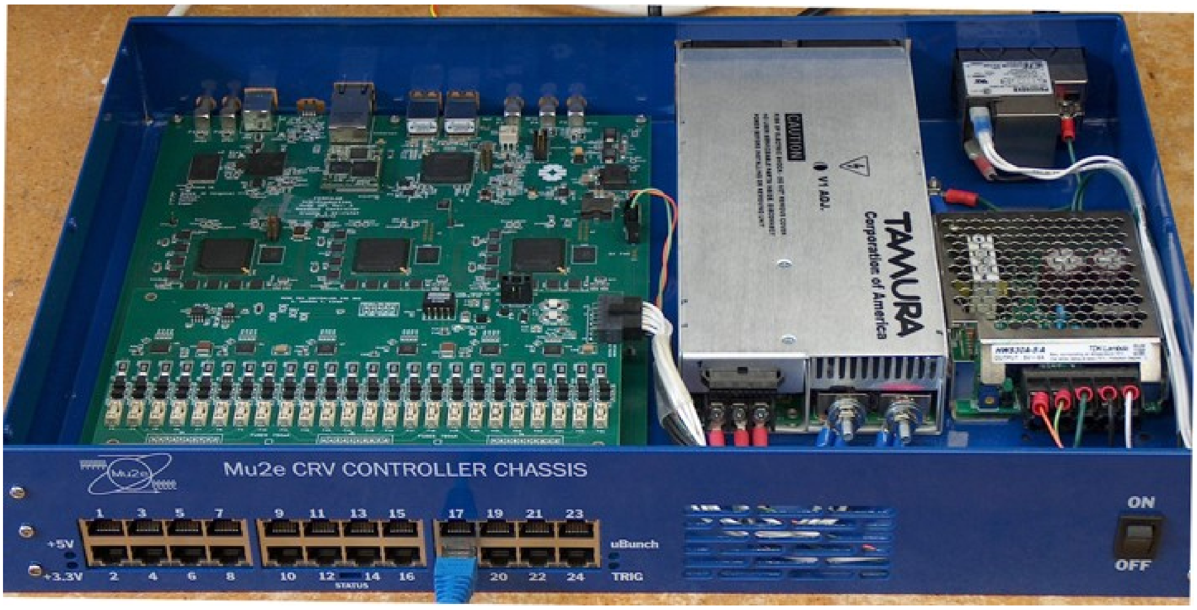

Figure 3.48.: The Readout Controller for the CRV supplies timing, trigger, and power to, and receives slow control and event data from, up to 24 FEBs through an array of Cat6 PoE connections on its front panel.

and sends FEB data and status information. The second optical transceiver is used to daisy chain multiple ROCs together. A 40 MHz timing link from the Encoded System Clock (Fig. 3.24) establishes synchronization of the CRV readout electronics with a clock from the accelerator. The 24 RJ45 ports are divided into three groups of eight, each group serviced by a Xilinx Spatan-6 FPGA that handles event building and temporary storage in a 2 Gb LPDDR. Accumulated events in each of these groups are transferred to a FPGA-microcontroller (Spartan-6 FPGA [74] and Texas Instruments Stellaris microcontroller [79]) pair whose purpose is to handle packetization and transmission of the data over the optical link to a DTC. This FPGA-microcontroller pair also handles the receipt and processing of trigger and status requests, and other controls for the FEBs. The block diagram shown in Fig. 3.49 shows the data path for events read from the FEBs. Every ROC is programmed and tested at Fermilab to check the nominal power consumption and supply, communication interfaces, the microcontroller, FPGAs, and memory.

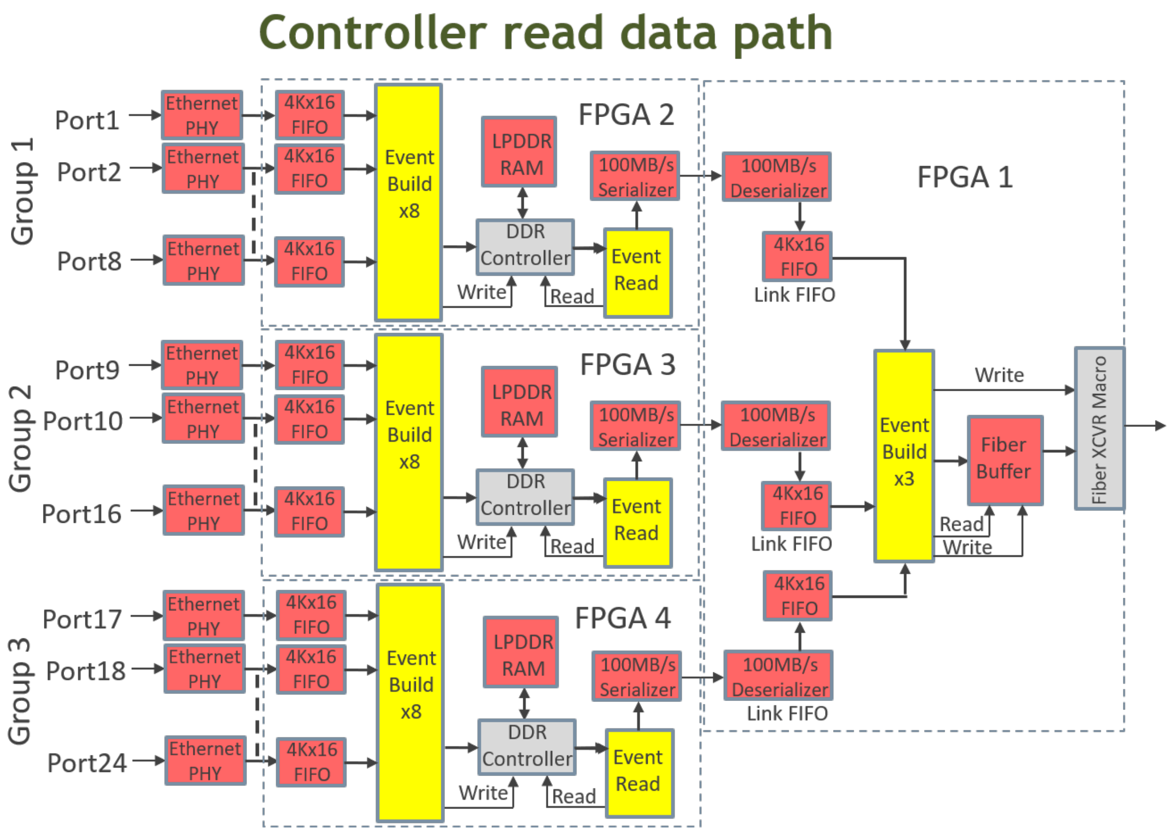

Figure 3.49.: Block diagram showing the data path for the ROC from the FEBs.

Status and Slow Control

The FEBs send and receive fast and slow status and control information to the Readout Controllers. Slow status information is delivered at a rate on the order of 1 Hz and includes information about power supply voltages, temperature, and run configuration. A description of the status block for the FEB is presented in Appendix O. A block of memory space in the ROC is configured to store detailed status information for up to 24 FEBs and the ROC itself. The experiment's DAQ accesses this memory block through the fiber link to read the status information when desired.

In addition to the slow status monitoring, fast status information is sent by the FEBs, which is related to and transmitted with the most recent data. Fast status is available on an event-by-event basis. Control of the CRV's electronics parameters is through settings sent to the ROCs from the DAQ and is distributed to the FEBs. There is no immediate feedback when setting the readout system parameters, but the status blocks are updated to reflect the changes.

3.3.5. Timing

In order to keep coincidence windows as short as possible to reduce dead time (Ch. 4.6), 1 ns timing over the entire detector system is desired. The ROC receives information about the accelerator cycle as well as a 1.695 μs microbunch reference marker. The jitter on the microbunch marker is expected to be 200 ps. The ROC synchronizes to this marker using a phase lock loop (PLL) and multiplies the clock to a convenient frequency using a voltage controlled crystal oscillator (VCXO). The multiplied clock, along with the punched clock encoded accelerator status information, is sent to the FEBs and synchronized again by a PLL. This clock drives the ADCs in the ultrasound chips clocks with sub-nanosecond jitter. Because the clocks for FEBs on either end of a module

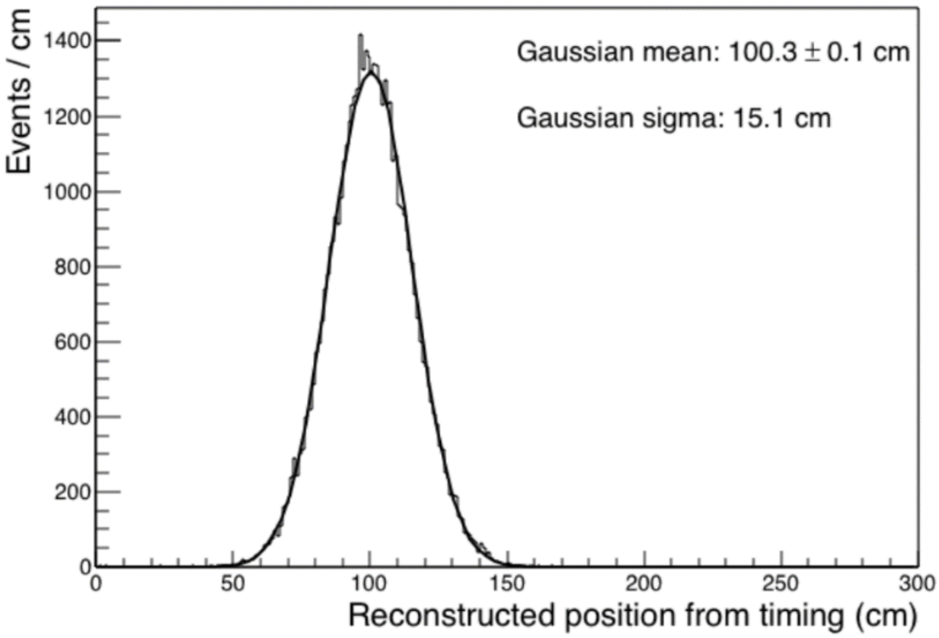

Figure 3.50.: The reconstructed longitudinal position of protons normally incident 100 cm from one end of a counter. The time difference between light arriving at each end of a counter is used to localize hit positions to within 15.1 cm.

are synchronized, longitudinal hit positions can be localized to within 15.1 cm using the difference in arrival time for light at each end of the counter (Fig. 3.50).

While it is expected some propagation delay will arise from temperature variations that change the lengths of interconnecting cables, a loopback measurement and cosmic-ray muons are used to determine and monitor the timing synchronization. Some fraction of cosmic rays will traverse the tracker and calorimeter and allow cross-correlations of the timing to be made.

3.3.6. The Cosmic Ray Muon Veto

A coincidence in time and space for adjacent counters in different layers will be used to indicate the ingress of a cosmic-ray muon into the apparatus. Track stubs are created by using the spatial positions of counters that see a combined signal in both fibers, on one end of a counter, above a set threshold and within coincidence window of 10 ns. The opposite end of the counter is treated independently, in the same manner. A 3/4 layer coincidence is used in the in CRV-L, CRV-R, and in the stopping target and downstream regions of CRV-T. As described in Ch. 4.6, a 4/4 layer coincidence is used in the CRV-U, CRV-D, CRV-TS, and CRV-TS-Ext sectors due to the high background rates in these sectors. A veto time of 170 ns is used for data taken by the Tracker and Calorimeter. This is done in the offline analysis; in other words, no coincidence forming takes place in real time.

3.3.7. Performance

A total of 203,425, 1695 ns long microbunches are delivered during a spill duration of 0.3798 seconds at a duty factor of 0.587. The interspill period, in which 10,202 microbunches are delivered, is 1.0202 seconds long. This cycle of beam delivery and interspill period repeats every 1.400 seconds (supercycle period). Data taking will continue as normal during the interspill period in order to directly measure the cosmic-ray induced background rate. During the spill the average (maximum) hit rate observed by the SiPMs is expected to be 55 KHz (825 KHz), caused by neutron and gamma backgrounds (Ch. 4.6). The rate of cosmic-ray muons over the entire CRV is 14.5 KHz [80]. The system is designed to handle a per-SiPM rate of 1 MHz. It is expected that the dark noise will average about 10 KHz at a hit threshold of 3.5 PE for non-irradiated devices. The maximum data rate out of the FEB is 12.5 MB/s. The average (maximum) expected data rate is 1 MB/SC (2.4 MB/SC)[†] [81]. Unlike the Tracker and Calorimeter, which stream data continuously to the Mu2e DAQ to form the trigger, the CRV is a triggered system. The triggers select microbunches of interest. Simulations show that less than one out of every 100 microbunches satisfy the trigger requirements.

[†] SC is used here as an abbreviation for supercycle, 1.4 s.

Chapter 4.

Meeting the Veto Requirements

The CRV is required to limit the conversion-electron background to no more than 0.2 events (at 90 % CL) over the experiment live time, while producing no more than 10 % experimental dead time, and using no more than 20 % of the total DAQ bandwidth. Experimental dead time is the amount of live time that has been discarded by the CRV due to the detection of cosmic-ray muons. Described in depth in the next sections, the detector's required coverage and overall inefficiency have been estimated through extensive simulation.

4.1. Simulations of the Cosmic Ray Background

A global Monte Carlo simulation was performed that determined the distribution of cosmic-ray muons that produce conversion-like electrons in the apparatus. This was used to determine the areas that must be covered by the detector and a minimum detection efficiency it had to obtain. Targeted simulations focused on regions with unavoidable gaps in coverage, such as the opening for the Transport Solenoid. In both simulations, the response of the entire Mu2e apparatus and propagation of particles was simulated

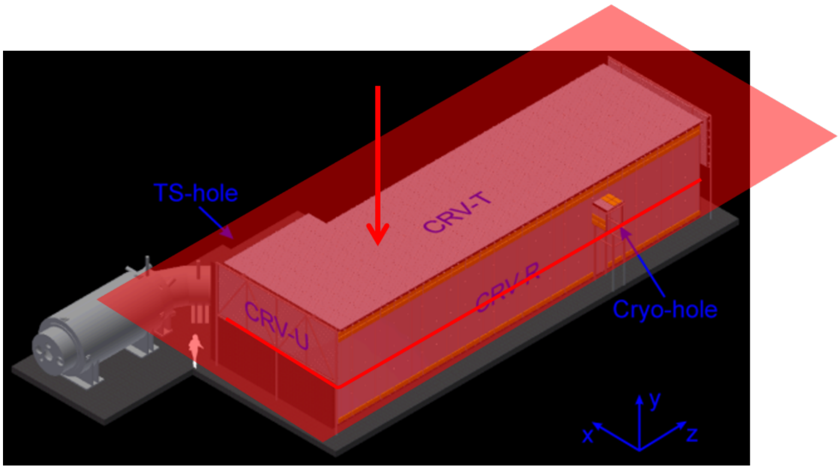

Figure 4.1.: The first stage of the global simulation utilized a horizontal plane level with the center of the tracker.

using GEANT4 [82] within the Fermilab ART Framework [83]. Analysis was performed using ROOT [84].

4.1.1. Global Simulation

A total of 5.00×10^{11} cosmic-ray muon events were generated for the global simulation, which corresponds to a live time of 5.35×10^{6} s [80]. This is 50.5 % of the experiment's anticipated total veto live time (1.06×10^{7} s). In an effort to achieve better statistics, the conversion-like electron momentum signal interval was increased eight times, from 1.25 MeV/c to 10 MeV/c, which yields 4.04 times the experiment's live time with the standard momentum window. To save on computing resources, the simulation was performed in stages.

The first stage utilized the Daya Bay model [85] to generate cosmic-ray muons of energy 0.5 GeV to 5000 GeV on an 800 m^2 horizontal plane (Fig. 4.1) that was level with the center of the Tracker. Cosmic-ray muons from this plane were back-propagated until they reached the surface and then down again, keeping only those with a momentum of at least 45 MeV/c. At the end of the first stage, only 4.4×10^{9} events survive.

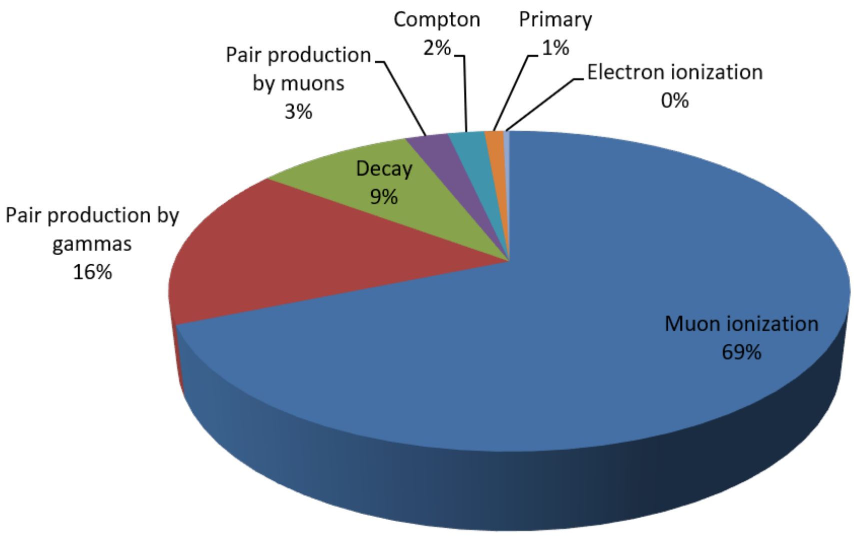

Figure 4.2.: The production processes for conversion-like electrons caused by cosmic-ray muons. The creation of delta-rays (muon ionization) is the primary background causing process.

The second stage propagated the surviving events through the tracker, keeping only those that had a minimum of 15 straw hits (as required by the track-finding algorithm). Of the starting 4.4×10^9 events, only 1.6×10^9 pass this stage.

The third stage involved the digitization of straw hits and track reconstruction with a downstream-going electron hypothesis. Events that had a reconstructed momentum between 50 MeV/c to 200 MeV/c were kept, which reduced the number of events to 5.7×10^5.

The fourth stage applied quality, geometry, and particle ID cuts on the reconstructed tracks, keeping only those consistent with conversion-like electrons. Events that could be reconstructed as upstream-going electrons were removed. At the end of this stage, only 3170 events survived. The primary background generating process was the production of delta rays within the apparatus, shown in Fig. 4.2. Many of the conversion-like backgrounds originate from the stopping target, shown in Fig. 4.3, which is why the CRV is vital for detecting cosmic-ray muons incident on the apparatus.

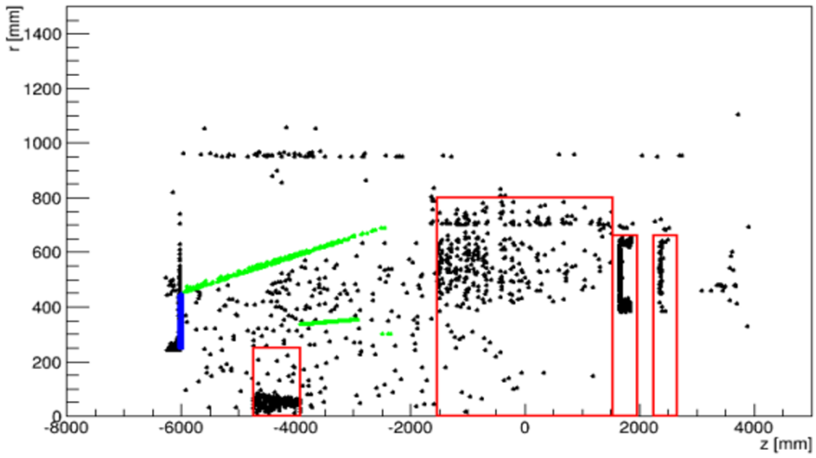

Figure 4.3.: The initial radial versus z positions of electrons caused by cosmic-ray muons. The z-axis is parallel to the beam axis of the DS. The red boxes outline key components of the apparatus (from left to right): the stopping target, the tracker, and the two calorimeter disks. The blue dots indicate electrons that originate from a collimator at the entrance to the DS. The green dots indicate electrons that originate from a proton absorber that surrounds the stopping target.

The positions of the cosmic-ray muons producing conversion-like electrons were recorded at the planes of the CRV modules. The purpose of this was to determine the spatial distribution of muons that result in conversion-like events, shown in Figs. 4.4 – 4.6. The location of each dot represents the position of the cosmic ray at the plane and the red outline shows the nominal shape of the CRV. The lengths of each module were determined from this simulation. For instance, the endcap modules were shortened due to the lack of background-causing cosmic-ray muons near the base of the apparatus in this region.

Of the 3170 events, only 1 event did not intersect the nominal CRV position. As expected, this event is near the Transport Solenoid entrance. To veto such events, the CRV-U modules were lengthened and two additional modules, CRV-TS-Ext, were added. When scaled to the live time of the experiment the total number of conversion-like events is 785. With a desired background level of no more than 0.1 events, the CRV requires an overall detection inefficiency of no more than 1×10^{-4}. This requirement is independent of detector design.

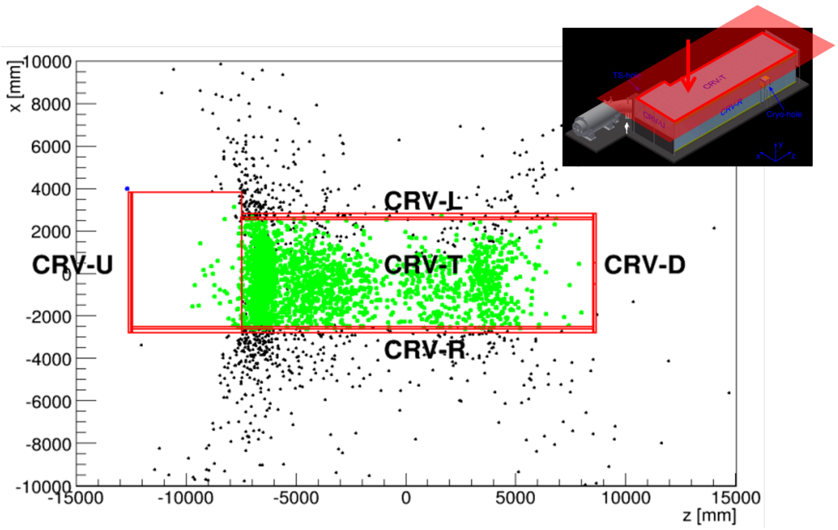

Figure 4.4.: The x-z positions of cosmic-ray muons that result in conversion-like electrons recorded at a plane located at the top sector of the CRV (CRV-T). Green dots are cosmic-ray muons that intersect only the CRV-T sector, blue dots are muons that did not intersect any CRV sector, and black dots are muons not in either of these categories. The red lines outline the nominal top module coverage.

The majority of the background-causing cosmic-ray muons are primarily located around the stopping target region, with some muons coming from the upstream or downstream directions relative to the long axis of the Detector Solenoid. From this, it is critical that the CRV provides coverage that surrounds the Detector Solenoid, especially in the stopping target region.

The required inefficiencies per sector are different, as the number of background causing muons passing through each sector is different, with the percentage of background causing muons in each sector presented in Fig. 4.7.

4.1.2. Targeted Simulations

To better understand the regions where there are unavoidable gaps in coverage, several targeted simulations were carried out with the same parameters and in a similar manner as the global simulation, but with cosmic-rays generated over much smaller areas [80].

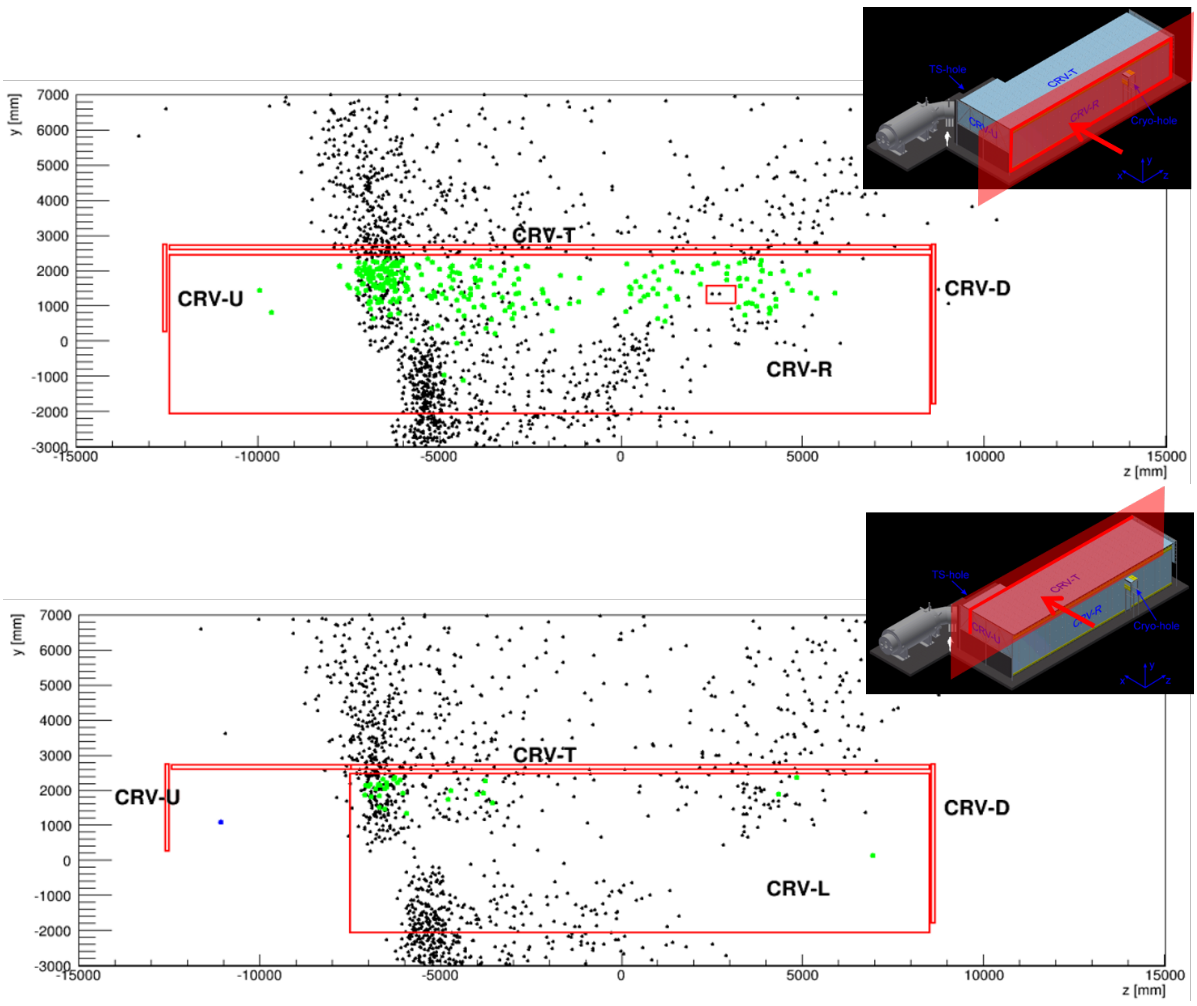

Figure 4.5.: The y-z positions of cosmic-ray muons that result in conversion-like electrons recorded at planes located at the right (top) and left (bottom) sector of the CRV (CRV-R, CRV-L). Green dots are cosmic-ray muons that intersect only the CRV-R/CRV-L sector, blue dots are muons that did not intersect any CRV sector, and black dots are muons not in either of these categories. The red lines outline the nominal coverage provided by CRV-R and CRV-L

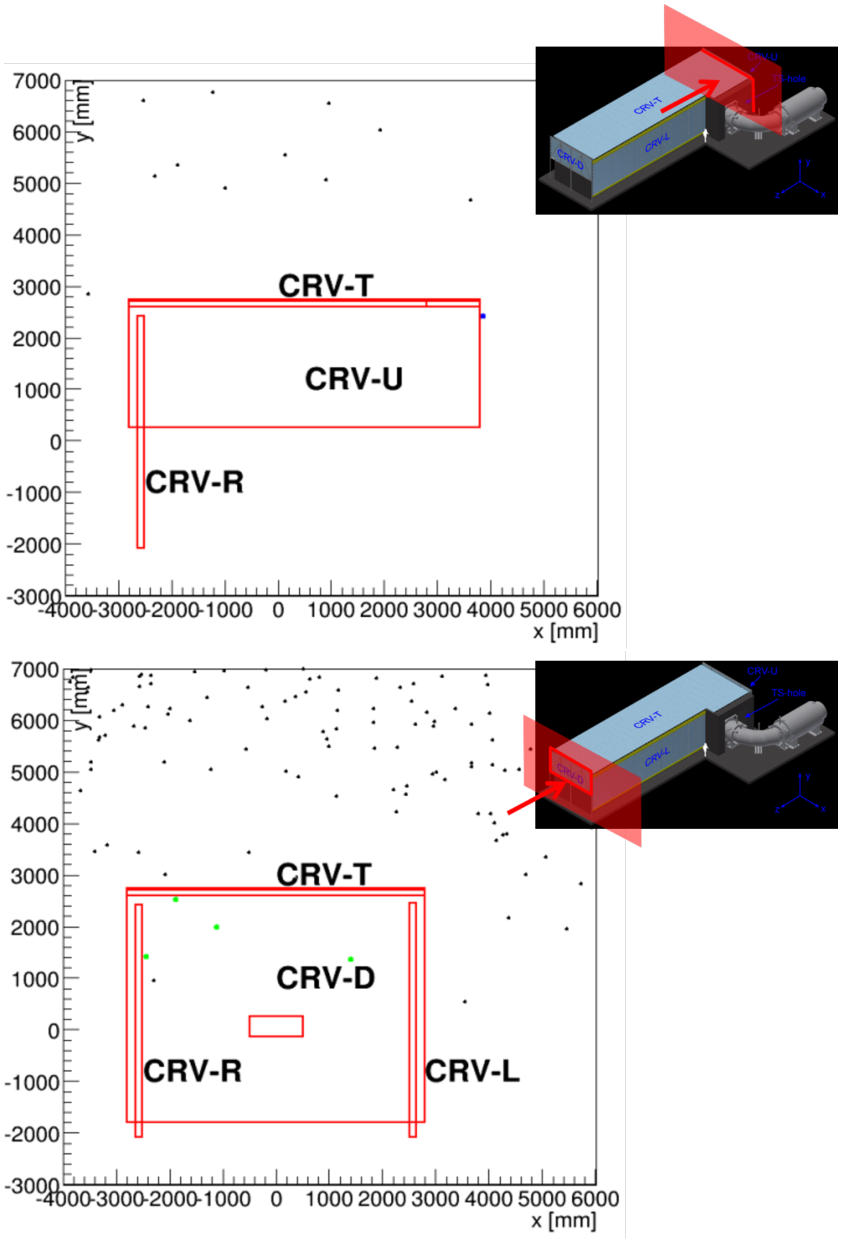

Figure 4.6.: The x-y positions of cosmic-ray muons that result in conversion-like electrons recorded at planes located at the upstream (top) and downstream (bottom) sectors of the CRV (CRV-U, CRV-D). Green dots are cosmic-ray muons that intersect only the CRV-U/CRV-D sector, blue dots are muons that did not intersect any CRV sector, and black dots are muons not in either of these categories. The red lines outline the nominal coverage provided by CRV-U and CRV-D.

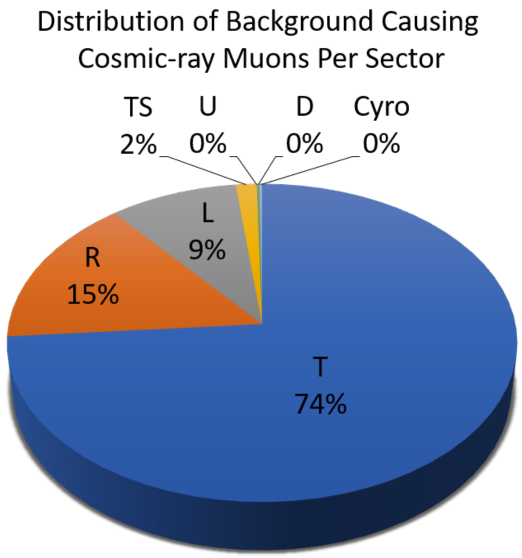

Figure 4.7.: The distribution of background causing cosmic-ray muons per sector.

The first targeted region was the Transport Solenoid entrance. A total of 1×10^{12} muons were produced at a $100\,\mathrm{m}^2$ vertical plane at the TS entrance. This corresponds to a simulated live time of $3.41 \times 10^8\,\mathrm{s}$, which is 32.2 times the total live time of $1.06 \times 10^7\,\mathrm{s}$. Using the same eight-times wider momentum interval, the simulated live time is equivalent to 257 times the total veto live time with the standard momentum interval. Of the total cosmic-ray muons simulated, 15.5×10^4 events resulted in conversion-like events. The distribution of cosmic-ray muon positions at a plane coincident with CRV-L is shown in Fig. 4.8. A total of 39 tracks entered the TS opening and did not intersect any elements of the CRV. Scaled to the anticipated live time of the experiment with the standard signal momentum window, 61 tracks in this region cause conversion-like events, of which 0.15 events do not intersect the CRV. This is an irreducible background for the CRV, although additional shielding has been proposed to reduce their number.

The second targeted region was located at the plane of CRV-U. A total of 9.99×10^{11} cosmic-ray muons were generated. With the same scaled live time as the first targeted simulation, the total number of muons that produced conversion-like events was 318, of

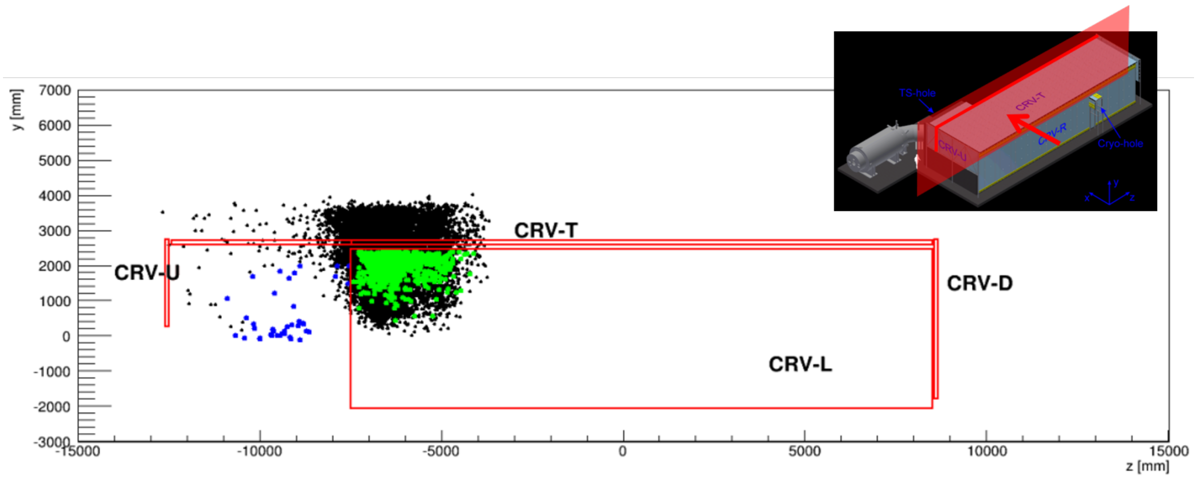

Figure 4.8.: The y-z positions of cosmic-ray muons producing conversion-like electrons at a plane located at the left sector of the CRV (CRV-L) from the first targeted simulation. Green dots are cosmic-ray muons that intersect only the CRV-L sector, blue dots are muons that did not hit any CRV sector, and black dots are muons not in these categories. The red lines outline the nominal coverage of CRV-L.

which 22 did not intersect the CRV. The 22 muons of this targeted study were merely a subset of the tracks seen in the first targeted study as they all went through the TS opening. Scaled to the live time of the experiment with the standard momentum window yields 1.2 total background generating events with only 0.09 that fail to intersect the CRV. As shown in Fig. 4.9, the cosmic-ray muons that missed the CRV entirely were adjacent to CRV-U. As a result of this simulation, the decision was made to extend CRV-U.

The third targeted region was located at the plane of CRV-D. A total of 9.99×10^{11} cosmic-ray muons were generated. With the same scaled live time at the first targeted simulation, the total number of muons that produced conversion-like events was 2042. Of these, there were no events that failed to intersect the CRV. Scaled to the total live time of the experiment with the standard signal momentum window, this corresponds to 7.9 total events. The most prominent feature of this study was that coverage in the downstream region is adequate.

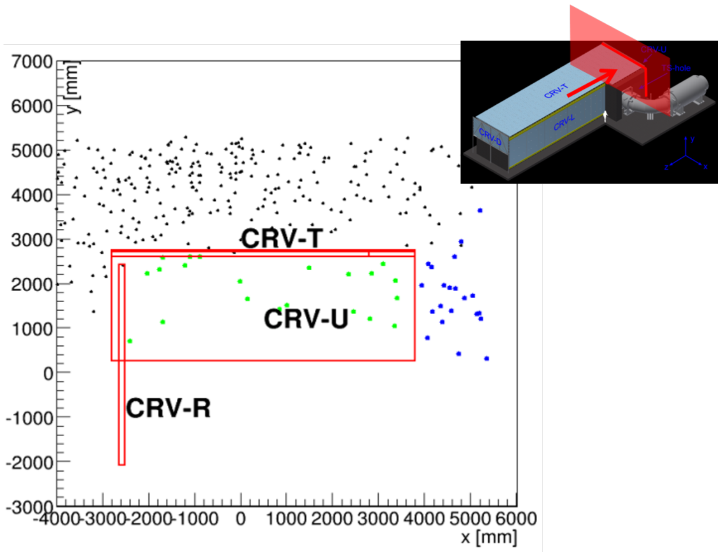

Figure 4.9.: The x-y positions of cosmic-ray muons producing conversion-like electrons at a plane located at the upstream sector of the CRV (CRV-U) from the second targeted simulation. Green dots are cosmic-ray muons that intersect only the CRV-U sector, blue dots are muons that did not hit any CRV sector, and black dots are muons not in these categories. The red lines outline the nominal coverage of CRV-U. From this simulation, it was decided that CRV-U would be extended.

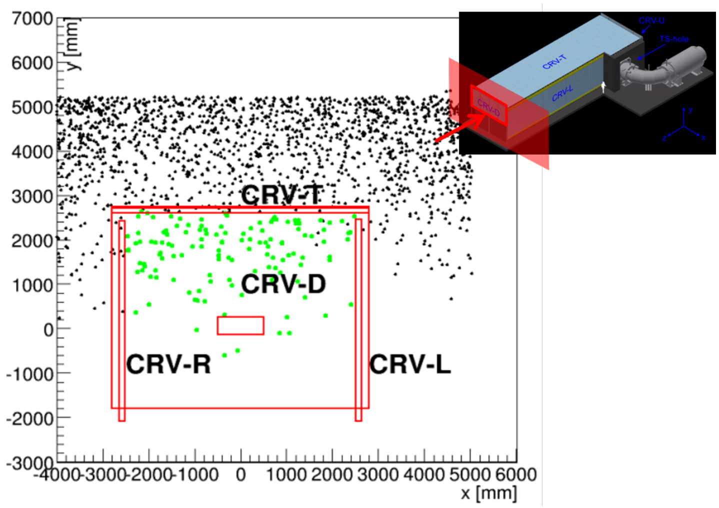

Figure 4.10.: The x-y positions of cosmic-ray muons producing conversion-like electrons at a plane located at the downstream sector of the CRV (CRV-D) from the third targeted simulation. Green dots are cosmic-ray muons that intersect only the CRV-D sector, blue dots are muons that did not hit any CRV sector, and black dots are muons not in these categories. The red lines outline the nominal coverage of CRV-D, which is adequate.

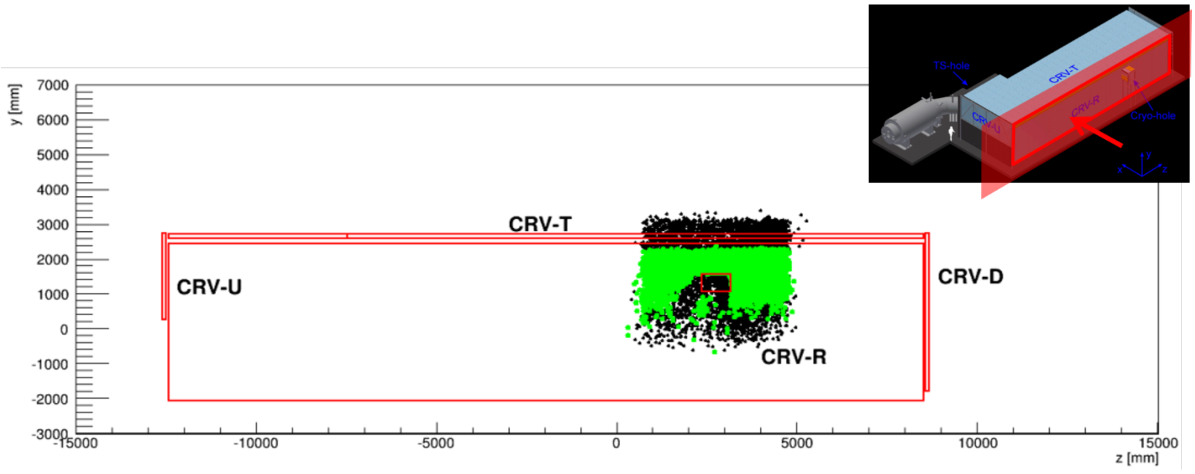

Figure 4.11.: The x-z positions of cosmic-ray muons producing conversion-like electrons at a plane located at a hole in CRV-R, which is for a cryogenic pipe, from the fourth targeted simulation. Green dots are cosmic-ray muons that intersect only the CRV-R sector, blue dots are muons that did not hit any CRV sector, and black dots are muons not in these categories. The red lines outline the nominal coverage of CRV-R.

The fourth targeted region was at a hole in CRV-R for a cryogenic pipe that services the cryostat for the Detector Solenoid. A total of 2×10^{11} events were produced at a $16\,\mathrm{m}^2$ vertical plane coincident with the opening of the hole. The number of events in this simulation was equivalent to 4.26×10^8 seconds, or 40.2 times the experiment's anticipated live time. Using the same expanded signal momentum interval, this was equivalent to 322 times the experiment's live time with the standard momentum window. The number of conversion-like events from this region was 7832, which is equivalent to 24.3 scaled events. There were no events that did not intersect the CRV.

The last of the targeted regions were the regions between the top (CRV-T) and side (CRV-R/L) modules. In both regions, 2.5×10^{10} cosmic-ray muons were generated at long rectangular planes centered on the gap between the modules. On the left (right) side, this corresponds to 22 (17) times the anticipated live time. Shown in Fig. 4.12, it was found that 0.27 and 0.06 scaled events for the left and right modules, respectively, had short or no path lengths through the CRV. The decision was made to set the spacing to 90 mm between CRV-T and CRV-L/R because the gap could not be reduced further due

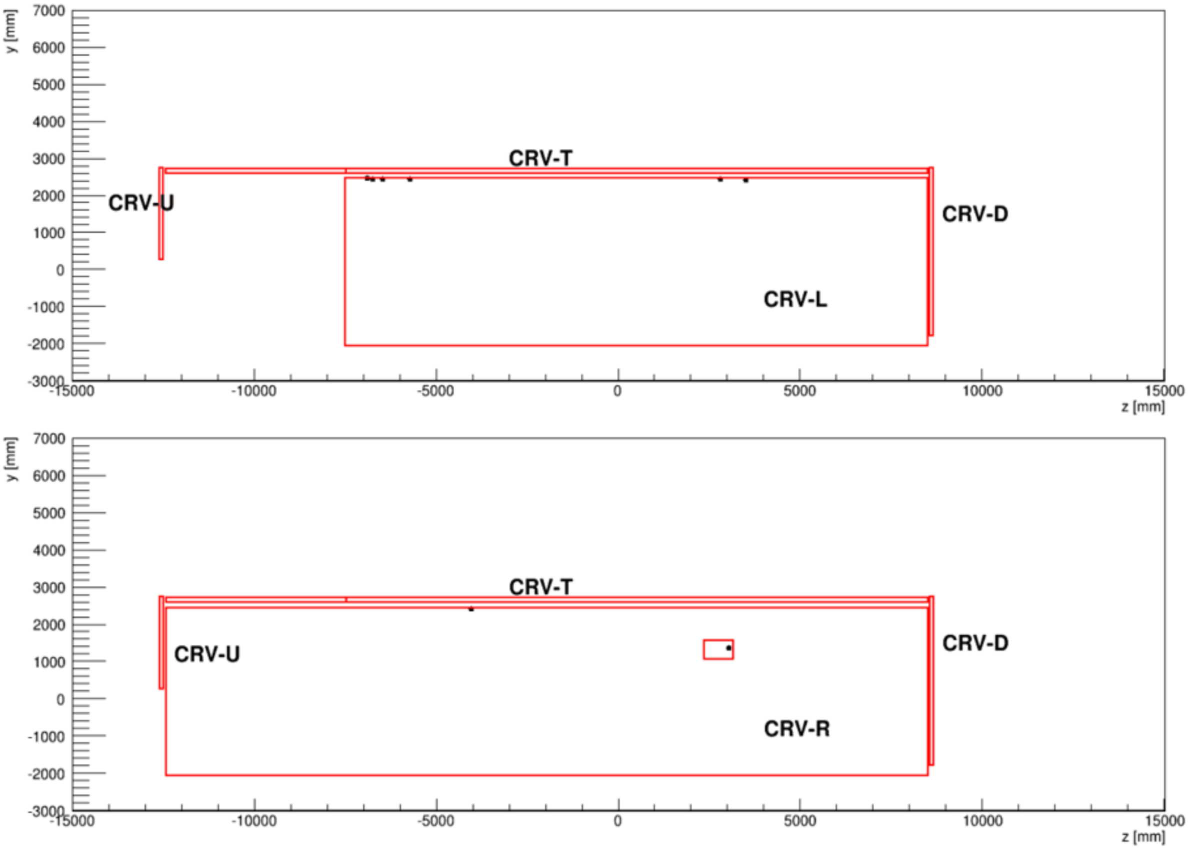

Figure 4.12.: The y-z positions of cosmic-ray muons producing conversion-like electrons at a plane located at a gap between CRV-T and CRV-L (top) and CRV-R (bottom), from the fifth and sixth targeted simulations. The dots indicate cosmic-ray muons that had path lengths too short to be vetoed by the CRV.

to the need for space to be able to service the readout electronics for the side modules. As a result of the simulation CRV-T was increased in length from 5.6 m to 6.0 m to veto cosmic rays that would otherwise pass through the gap.

4.2. Measuring the Detector Performance

The most important property of the CRV that dictates the detection efficiency is the amount of light produced by the passage of charged particles. Making use of Fermilab's Test Beam Facility [59], the light yield for various prototype counters was evaluated. The dicounters were 3 m in length (the longest the facility can accommodate) and assembled in accordance with the described processes (Ch. 5.1). Minor variations in scintillator type and dimensions were tested, as presented in Table 4.1. Each dicounter was read out using two FEBs, one on each end. Data were delivered to a computer through a non-standard Readout Controller, which also provided clock and trigger information to both boards. A 120 GeV proton beam was incident on the counters every 62.5 s for a 4.0 s duration. The dicounters were mounted in an aluminum fixture, shown in Fig. 4.13, and were stacked parallel to the beam direction so that the beam was incident on the same position for each dicounter. Horizontal and vertical positions were controlled using a motion table, allowing the beam to be scanned across the dicounters in both dimensions. Proton track reconstruction was made possible through the use of 1.0 mm pitch multi-wire proportional chambers (MWPCs), with time-to-digital-conversion readout. Two MWPCs were upstream at $z = -3667$ and -906 mm and two downstream at $z = 1935$ and 9672 mm, relative to the upstream-most counter face ($z = 0$ mm). Track candidates were required to have hits in at least three out of four MWPCs, yielding high-quality, straight-line fits ($\chi^2 < 2$) with residuals on the order of 0.5 mm. The measured beam profile was 4 mm FWHM, with tails reaching out to 10 mm. The trigger was defined by a coincidence of three 101.6 mm $\times$ 101.6 mm square scintillator paddles, one upstream of the test stand and two downstream. Upon receipt of a trigger signal, the FEBs digitized a total of 127 samples, 12.6 ns apart (1/79.5 MHz intervals), for a total trace time of 1597 ns. Temperature of the test beam enclosure was recorded via Fermilab's ACNET and the CMB temperatures were recorded for the 2018 and 2020 tests.

Calibration for single photo-electrons was determined using pedestal-subtracted trace data. The pedestal was found by using the most probable ADC value in the pre-signal region, which was the first 75 samples or roughly 1000 ns. Signals were fit with Gumbel distributions [86] and the integral of a signal computed for single and double fired pixels. The photoelectron peaks were fit using a Gaussian distribution, allowing the gain for

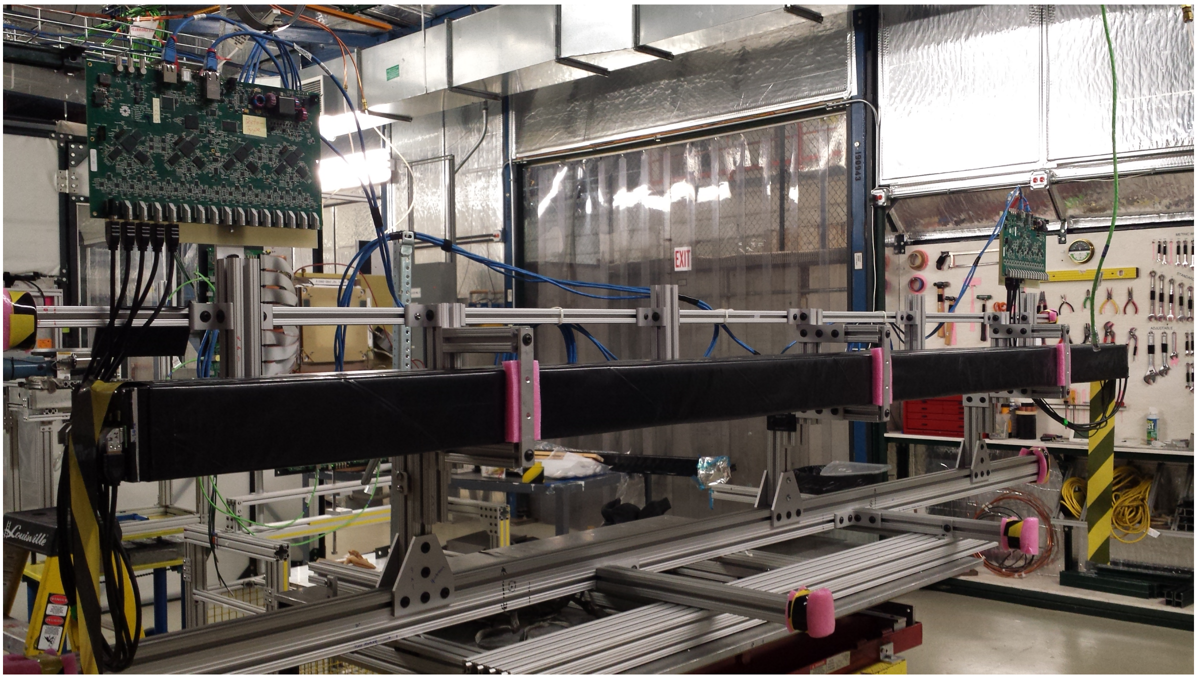

Figure 4.13.: A stack of dicounters, supported by an aluminum fixture on a motion table, evaluated at Fermilab's Test Beam Facility (FTBF). The beam direction is to the left, perpendicular to the counter length. Front End Boards are present on each end for counter readout, synchronized to the same clock and trigger delivered by a Readout Controller.

Table 4.1.: Dicounter production dates, dimensions, and use in various test beam studies.

Year	Dicounters	Extrusion Date	Assembly Date	Single Counter Dimensions	SiPM Type (V_{br}@25°C)	Test Beam Dates Jun 2016	Jun 2017	Nov 2018	Feb 2020
2016	108, 109, 110	April 2016	May 2016	19.74 mm × 49.40 mm	R&D Batch $V_{br}: 52.1V$	x	x	x	x
2017	274, 275, 292	June 2016	April 2017	19.74 mm × 49.40 mm	R&D Batch $V_{br}: 52.1V$		x	x	x
2018	1114, 1275, 1227, 1324	April 2018	June/ July 2018	19.76 mm × 51.34 mm	Pilot Batch $V_{br}: 51.2V$			x	x

the SiPM, in photoelectrons per ADC count, to be determined. Using this calibration method, conversion factors were stable to better than ±1 % between temperature-stable runs (±0.5 °C). The temperature-corrected PE yield as a function of overvoltage was determined through a scan of the overvoltage applied at 25 °C and shown in Fig. 4.14 for the R&D and pilot SiPMs. The temperature dependence of the breakdown voltage was calculated using:

$$V_{br} = V_{br@298\,\mathrm{K}} + ((T - (298\,\mathrm{K})) \times 54\,\mathrm{mV/K}). \tag{4.1}$$

The correction slope of $54\,\mathrm{mV\,K^{-1}}$ is provided by Hamamatsu, the device manufacturer. The breakdown voltage for each device is different and was found by extrapolating the gain versus overvoltage to the voltage at which the gain is zero. The breakdown voltage was found to vary by no more than ±0.1 V, so the same bias voltage of 53.7 V was applied to all the SiPMs. For each run, the average PE yield was found by histogramming the light yield over all events and fitting a combination of Gaussian and Landau distributions, with the mean representing the average PE yield. With more than 50,000 events per run, the statistical uncertainties on PE yield are low, less than 0.1 %, with the observed variations attributed to the uncertainties in the calibration, temperature, and statistical limitations of the analysis method. From the 2017 run, with the beam at a position of 1 m from the readout end centered between the two fibers, the PE yield was measured to be approximately 50.0 ± 0.2 PE on average, shown in Fig. 4.15 [87]. Transverse and longitudinal scans, shown in Fig. 4.16, were used to register the simulations and evaluate the counter response along each dimension.

Some of the counters that were studied in the test beam, excluded from the previously quoted light yield (Fig. 4.15), had fiber channels filled with a liquid silicone-based polymer (SKTN-MED [88]), which has an index of refraction closely matched to the scintillator and is radiation hard [89]. Others had reflectors on the far end for single-ended readout, and

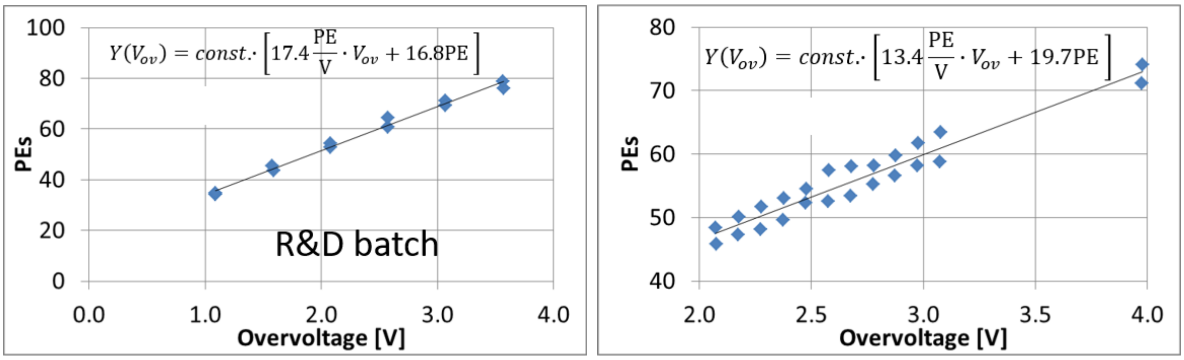

Figure 4.14.: PE yield as a function of overvoltage. SiPMs biased with different overvoltage. Left: R&D SiPM batch. Right: Pilot SiPM batch.

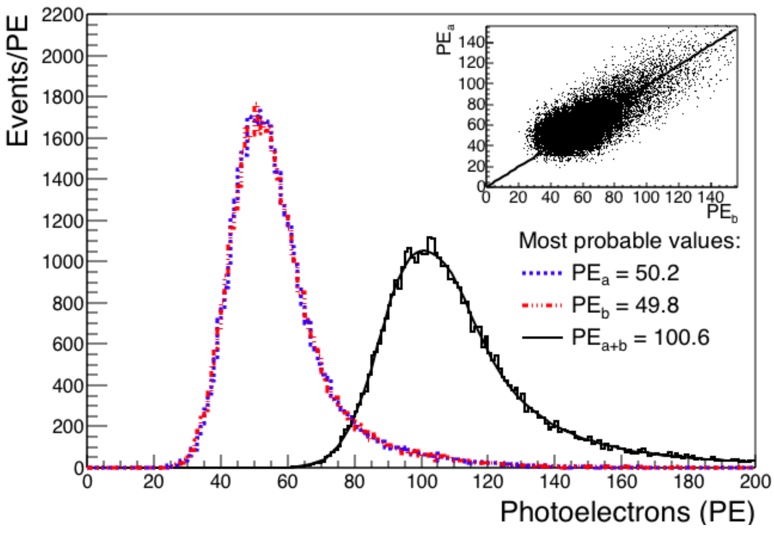

Figure 4.15.: The response of a 2017 counter, in photoelectrons, to the 120 GeV proton beam positioned equidistant between the two fibers at 1 m from the readout end. Dashed and dotted curves are the respective responses for each of the two SiPMs on the same side of the counter. The solid line is the sum of the responses. The fit, a sum of a Gaussian and a Landau function, is shown. The inset shows the correlation between the two channels [87].

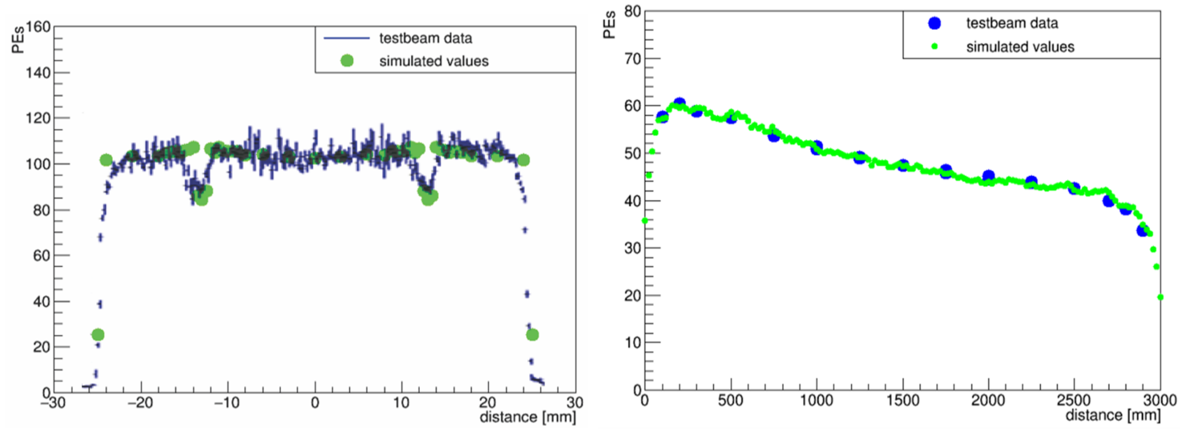

Figure 4.16.: Transverse (left) and longitudinal (right) scans of a dicounter at the 2017 Test Beam compared to simulations.

some had the addition of optical grease between the SiPM and WLS fiber to improve the optical coupling. When compared to unfilled counters, the filled counters demonstrated a 30 % improvement in light yield. Filling the fiber channels is a tedious process, but may serve to be useful for regions of the CRV where a higher light yield is needed. Efforts related to dicounter filling are presented in Ch. 6. For counters with single-ended readout, a VM2000 reflector [48] was placed on the far end. The light yield with a reflector was found to increase by 37 % [87]. Investigation of the efficacy of improving the optical coupling between the SiPM and the WLS fiber using BC-630 silicone optical grease [46] is also presented in Ref. [87] and was found to only improve the light yield by 10 %. The use of a larger diameter fibers for light yield improvement is favored over the use of optical grease.

4.3. Detector Aging

The light yield decline rate originally assumed in Ref. [27] was 3 %, based on measurements of similar extrusions. To better understand what the actual decrease in light yield as a function of time since extrusion was for the CRV (aging), several studies were carried out.

Using test-beam data, the light yield as a function of time since extrusion fabrication was determined. Shown in Fig. 4.17, the temperature corrected PE yield as a function of time (in months) was determined to fall off between 6 % to 10 % per year with an average rate of 8.7 %. The uncertainty in the time for each point is 0.5 months. The solid markers are used to indicate that the test beam detector hall (ACNET) temperatures were used to correct the PE yield, while hollow markers are used to indicate that CMB temperatures were used. For the ACNET adjusted points, the statistical error is the standard deviation of the mean PE yield, with the systematic error being the maximum difference between the PE yield based on CMB temperature (0.7 PEs). For the CMB temperature adjusted points, the statistical uncertainty is the standard deviation of the mean PE yield. The uncertainty in these measurements is likely attributed to changes in the test-beam environment and differences in the scintillator components and preparation. Additional details are presented in Ref. [87].

Non-accelerated aging was studied for a small collection of dicounters that had their light yield measured periodically over the course of several years at UVa. Four 2 m long dicounters were assembled in April 2017 (extruded June 2016). The light yield was determined through measurement of SiPM current in response to a Cs-137 source placed 1 m away from the readout end. Current measured without the source was subtracted from current measured with the source. The result was corrected for aging of the source (2.3 % per year) and SiPM temperature. The normalized current responses for all channels were fit using a double exponential and found to decrease by 8.7 % per year when corrected for the 2.3 % aging of the source (Fig. 4.18) [91]. A decrease of approximately 12 % was observed in the first year. The results of this study are in fair agreement with the Test Beam results. A measurement of the light yield of a LYSO

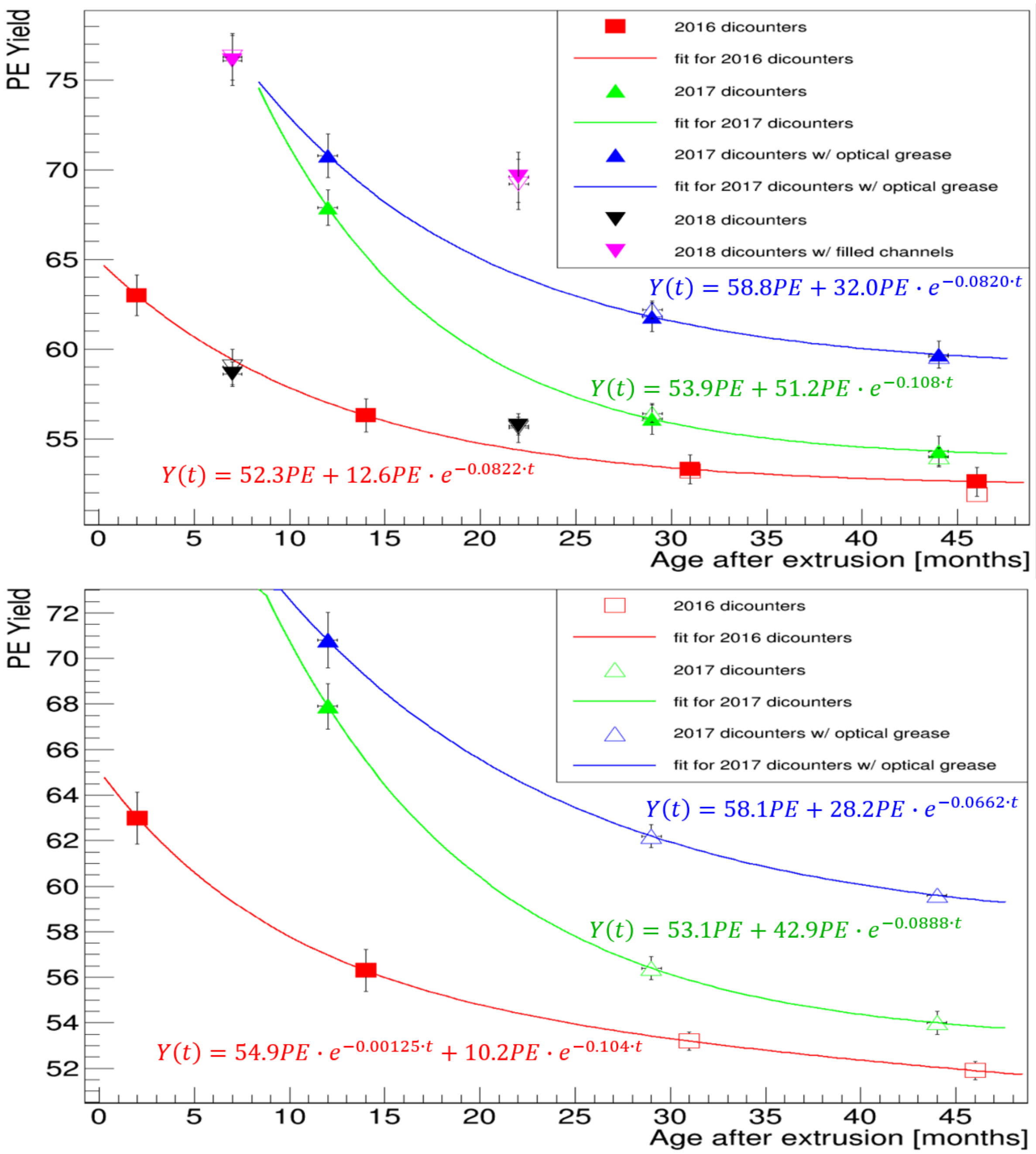

Figure 4.17.: Photoelectron yield as a function of dicounter age in months since extrusion for different dicounter types, listed in Table 4.1. The top plot shows the temperature corrected PE yield (and best fit) using Fermilab's ACNET reported enclosure temperature, where the bottom plot shows temperature corrected PE yield (and best fit) using CMB and ACNET reported temperatures. The solid markers represent ACNET adjusted PE yield and the hollow markers represent CMB adjusted PE yield. [90]

crystal using the same readout shows no aging, indicating that the readout electronics are not the source of the decline.

A total of twelve dicounter and fiber samples were placed into a Proportional-Integrated-Derivate-Controlled convection oven [92], with one additional dicounter and fiber sample kept at room temperature as a reference. The dicounter samples were short 0.3 m pairs of scintillator extrusions without WLS fibers or Fiber Guide Bars. Each month, a dicounter and fiber sample was removed from the oven and tested. A removable jig, containing four fibers and a readout manifold, was used to measure the light yield of each dicounter sample in response to a Cs-137 source through measuring the current of the SiPMs. Attenuation of light through the fiber was determined by excitation of the fiber with a UV LED, measuring the transmittance as a function of distance using the fiber testing apparatus described in Ch. 5.1. The purpose of the oven is to simulate years of aging in a relatively short time span. An aging factor (f_{age}) between a heated sample and reference sample can be computed through use of the Arrhenius equation [93] and taking the ratio of the rate at higher and lower temperatures:

$$f_{age} = e^{\frac{E_a}{R}(\frac{1}{T_{ref}} - \frac{1}{T_{oven}})}, \tag{4.2}$$

where E_a is the activation energy for the scintillator, R is the universal gas constant, T_{ref} is room temperature, and T_{oven} is the oven temperature. The effective aging time,

$$t_{\mathit{eff}} = f_{age} t_{oven}. \tag{4.3}$$

is the amount of time in the oven scaled by the factor computed from Eq. 4.2. Each sample's measurement was normalized to an initially measured response. For scintillator aging, there is a non-constant degradation in performance as a function of time, shown in Fig. 4.19. The aging rate was determined to be 8 % in the first two years (4 % average

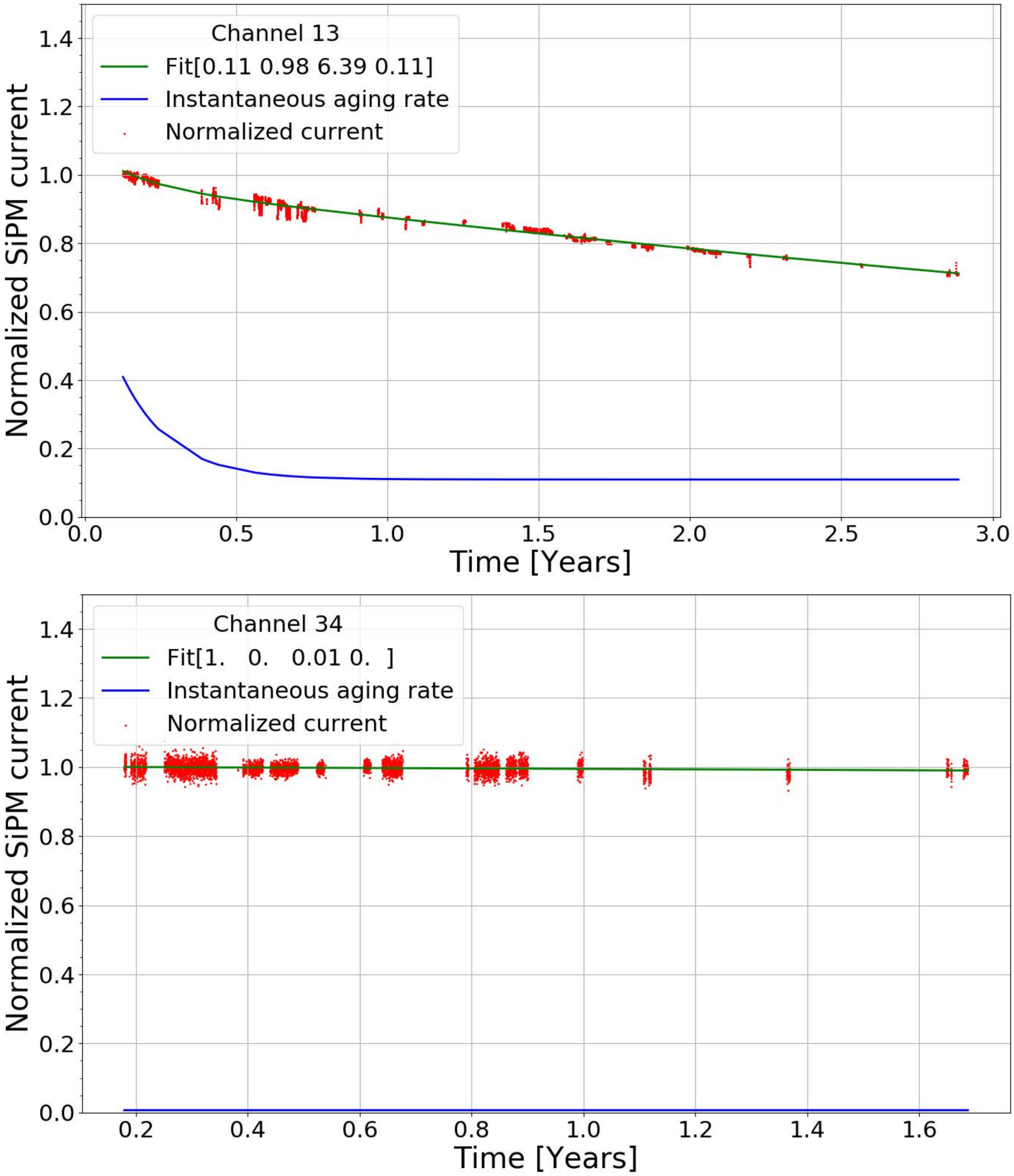

Figure 4.18.: Measurement of the response of several dicounters to a Cs-137 source as a function of time since extrusion. The red dots are the normalized response data. The green curve is a double exponential fit to the data. The blue curve shows the instantaneous aging rate. The top plot shows the typical normalized current response for one channel of a dicounter. The curve shown has a best fit of: $0.11e^{-6.39t} + 0.98e^{-0.11t}$, and includes the aging of the Cs-137 source. The bottom plot shows the normalized current response from a LYSO crystal that was used as a reference.

per year), but only 23 % for the first decade (2.3 % average per year). The fiber aging was determined to be less than 1 %/year (Fig. 4.19). The results of this study are largely inconclusive due to a large uncertainty in the activation energy for the scintillator but also due to possible annealing. The activation energy from a previous study is $E_a = 91\,\mathrm{KJ/mol}$ [94]. Modern publications suggest a range of activation energies for most polymers between 85 KJ/mol to 110 KJ/mol [95, 96]. The activation for this particular scintillator blend is not known. To further compound the issue, the accelerated aging does not explain the fast and slow components observed, which may be attributed to possible annealing that occurs at higher temperatures. In short, the results shown here are for illustrative purposes only and not used when determining the expected aging.

The mechanism(s) that cause dicounter aging is/are currently not known, but similar scintillator aging has been observed in CDF-II scintillator counters [97].

4.4. Meeting the Efficiency Requirement

The required overall inefficiency was established by the global simulation [80] and was independent of the detector design. While it is required that the overall inefficiency of the detector be no more than 1×10^{-4}, sector-based inefficiencies vary, particularly in regions that do not have a large flux of conversion-like producing muons. The actual efficiency for each sector largely depends on detector-specific parameters such as the layer offset in each module and gaps between counters, light yield of the scintillator, the number of dead SiPMs, and parameters of the coincidence-finding algorithm. In an effort to estimate the effects of the parameters on the cosmic-ray induced background, the inefficiencies as a function of layer offset and inter-module gaps, for different expected light yields, was simulated [98]. This allowed the geometry of a CRV module to be optimized to best minimize the inefficiency. After the optimal layer offsets and the effects of inter-module

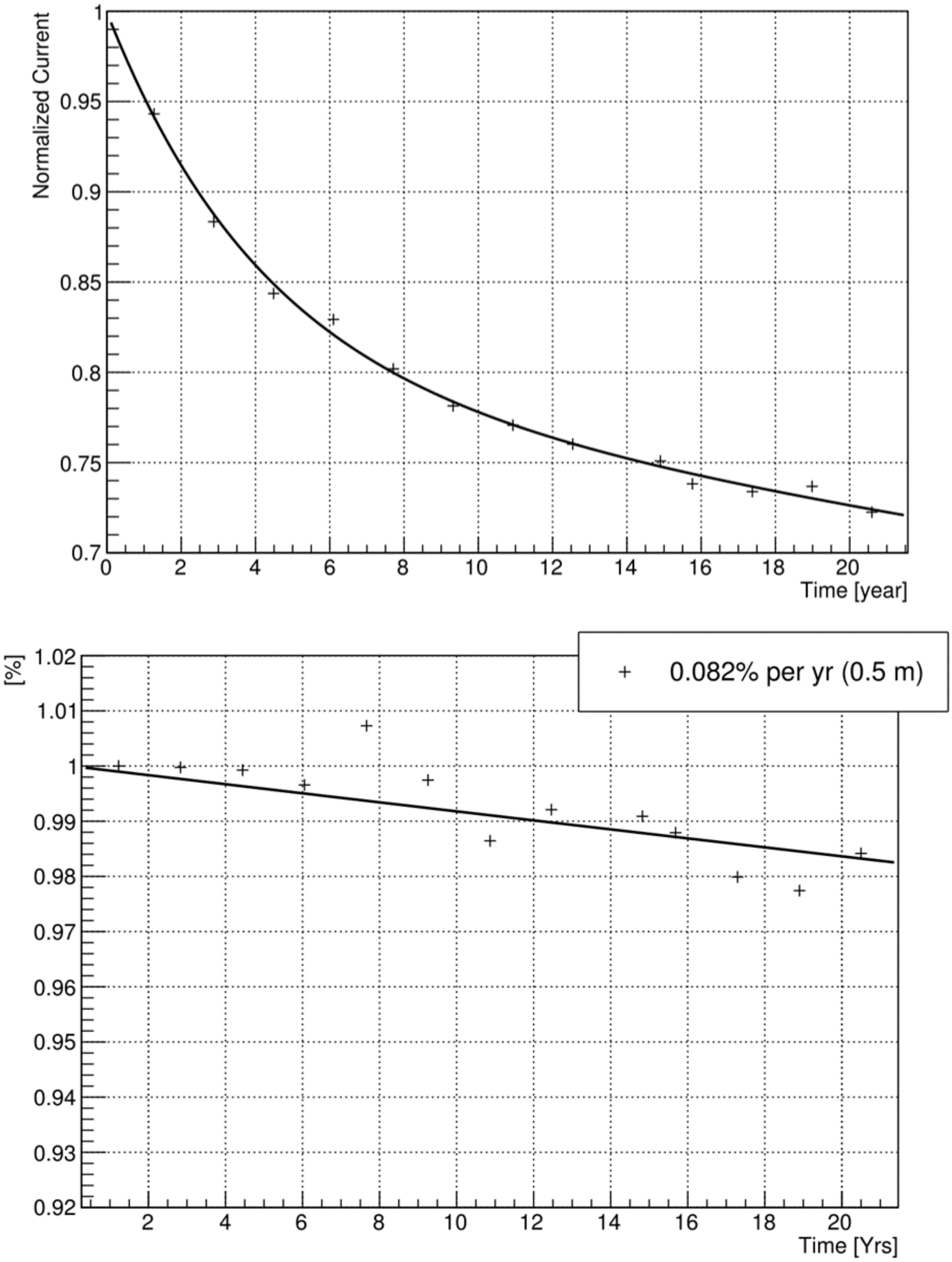

Figure 4.19.: Accelerated aging of scintillator (top) and fiber (bottom). The scintillator aging, fit with a double exponential, indicates a non-constant decay rate. The aging was 8 % in the first two years (4 %/year average), then dropped 23 % after 10 years (2.3 %/year). The fiber aging, fit with a simple exponential, is less than 1 % per year.

gaps were found, the inefficiency as a function of the PE threshold for various light yields was determined. This allows the expected backgrounds to be computed based upon the actual light yields of a module.

4.4.1. Simulating CRV Response and Muon Track Stub Finding

The full CRV response was simulated using muons that were propagated through the CRV extrusions, appropriately simulating the energy deposition and tracking them through the plastic. This simulation took an excessive amount of CPU time, hence lookup tables were generated. The results were compared to test beam data (see Ch. 4.2). Ideally, the PE yield for relevant counter lengths would have been tested in the test beam, but counters longer than 3 m could not be tested in the test beam facility. A comparison of a longitudinal scan of a counter and simulation, using a 120 GeV proton beam normally incident and equidistant between the fibers, is shown in Fig. 4.20. The response of the SiPMs to this light was accurately depicted with the inclusion of cross-talk, dark counts, and sensor saturation (see Ch. 3.3.1). The SiPM response waveforms were digitized in the same manner as the front-end electronics (12.5 ns sampling rate, see Ch. 3.3.3). Finally, a coincidence finding algorithm was applied to identify cosmic-ray muons.

Identification and veto of a cosmic-ray muon is made by a coincidence of hits in adjacent counters, in at least three out of four layers of the CRV. A hit is defined as the number of PEs (see Ch. 3.3) observed in the readout electronics above a set PE threshold (Fig. 4.21). A zero-suppression algorithm is also applied, reducing the data to only hits above the threshold. Each fiber end is handled separately. Hits are required to occur within 10 ns (leading edge) of one another (5 ns within a layer). Localization is determined by computing the two-dimensional slope (in local CRV detector coordinates) between hits in subsequent layers (Fig. 4.21). The slope magnitudes are required to be less than 7.0: this restricts the association of hits to be no more than two extrusions away.

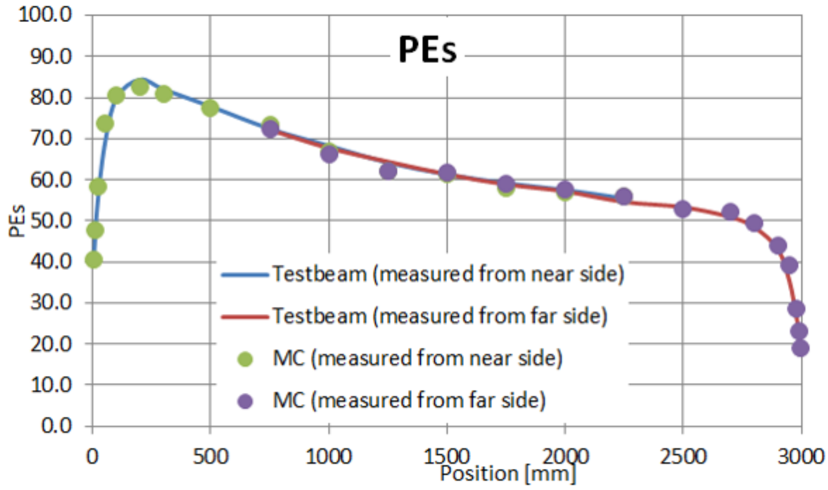

Figure 4.20.: Longitudinal scan of a 3 m dicounter using normally-incident 120 GeV protons, performed in a simulation (green/purple dots) and compared with the actual response as measured in the test beam (blue/red line). The near side is defined as the readout end closest to the beam spot, with the far side being the readout end furthest away.

The inter-layer slope differences are restricted to a magnitude of no more than 2.0, which constrains hit aggregations to straight lines while also accounting for the staggering of extrusions. When a coincidence is formed, a veto time of 170 ns is imposed, starting at the leading edge of the earliest hit in the triplet. It is possible for hits to be associated to more than one triplet, for which the overlapping veto times are merged by disjunction.

4.4.2. Determination of the layer offsets

In an effort to minimize the effects of projective gaps, the inefficiency of each sector of the CRV to incident cosmic-ray muons as a function of layer offset was determined. The muons used were not isotropically generated but were those that resulted in conversion-like backgrounds. Two different PE thresholds were used in coincidence finding. The inefficiencies for the different sectors are shown in Figs. 4.22 – 4.25 [98]. The CRV-U and CRV-D modules do not have any layer offset because, due to their horizontal orientation, their projective gaps point to where very few background-causing muons are. It was

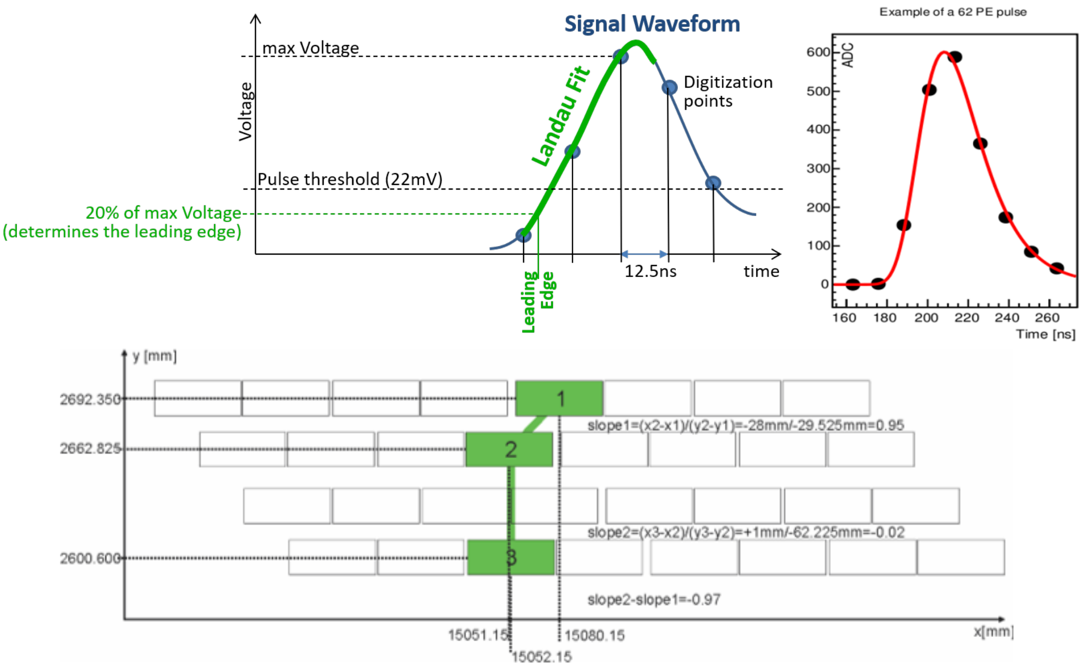

Figure 4.21.: Shown in the upper left, SiPM waveforms are digitized with a sample interval of 12.5 ns. When a waveform exceeds the hit threshold, a Landau fit is used to determine the leading edge. The time of the leading edge is 20 % of the peak value. An example of a real digitized waveform is shown in the upper right. At the bottom: using local CRV coordinates, hits are localized in space to form track stubs by restricting the slopes between adjacent hits.

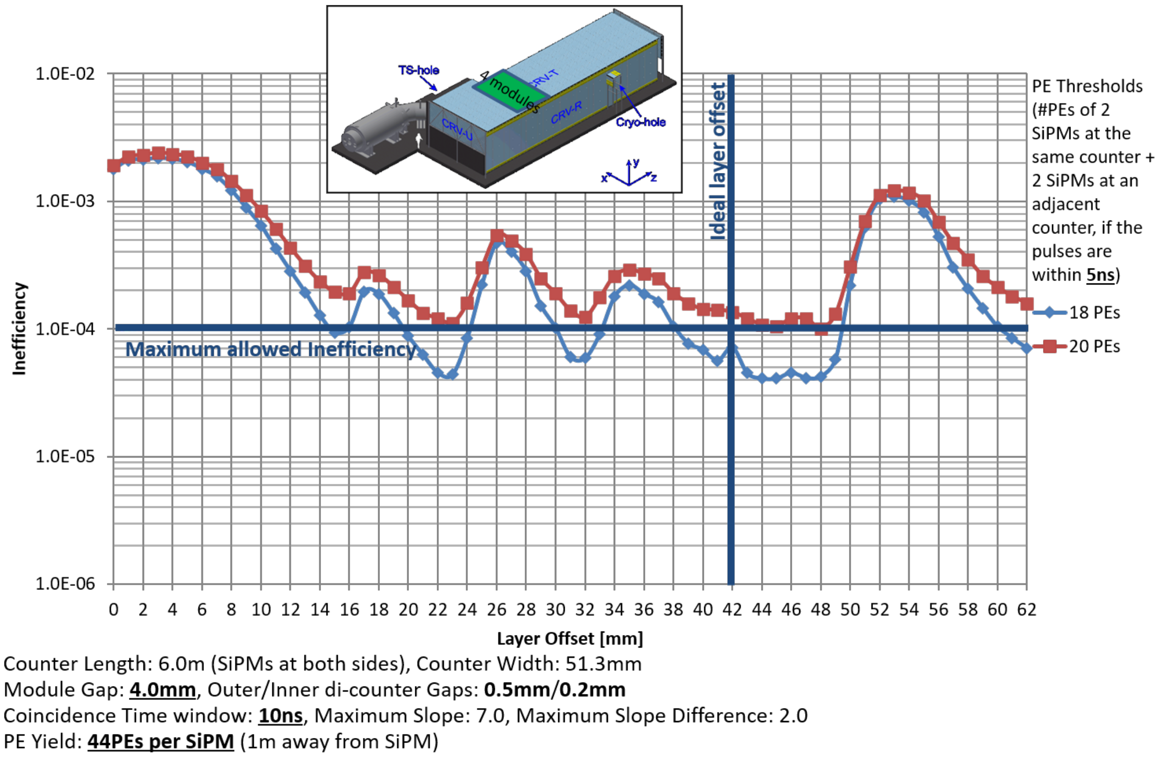

Figure 4.22.: Inefficiency versus layer offset for the top modules (CRV-T) in the stopping target region for two different combined PE thresholds. This region contains the greatest number of background causing cosmic-ray muons.

found that a layer offset of 42 mm was optimal and that it should not vary by more than 3 mm.

Because inter-module gaps can form projective gaps in the coverage, the inefficiency as a function of layer offset for different PE yields and various gap sizes between modules was studied. This is shown for CRV-T modules in Fig. 4.26 [99]. The spacing between modules should be kept below 5 mm, especially for a lower than expected light yield.

4.4.3. Inefficiencies for Different PE Thresholds and Light Yields

The inefficiency as a function of light yield was determined for various coincidence thresholds for each sector the CRV. The results of this were used to estimate the actual efficiencies for each sector (using light yield measurements from cosmic-ray tests, see Ch.

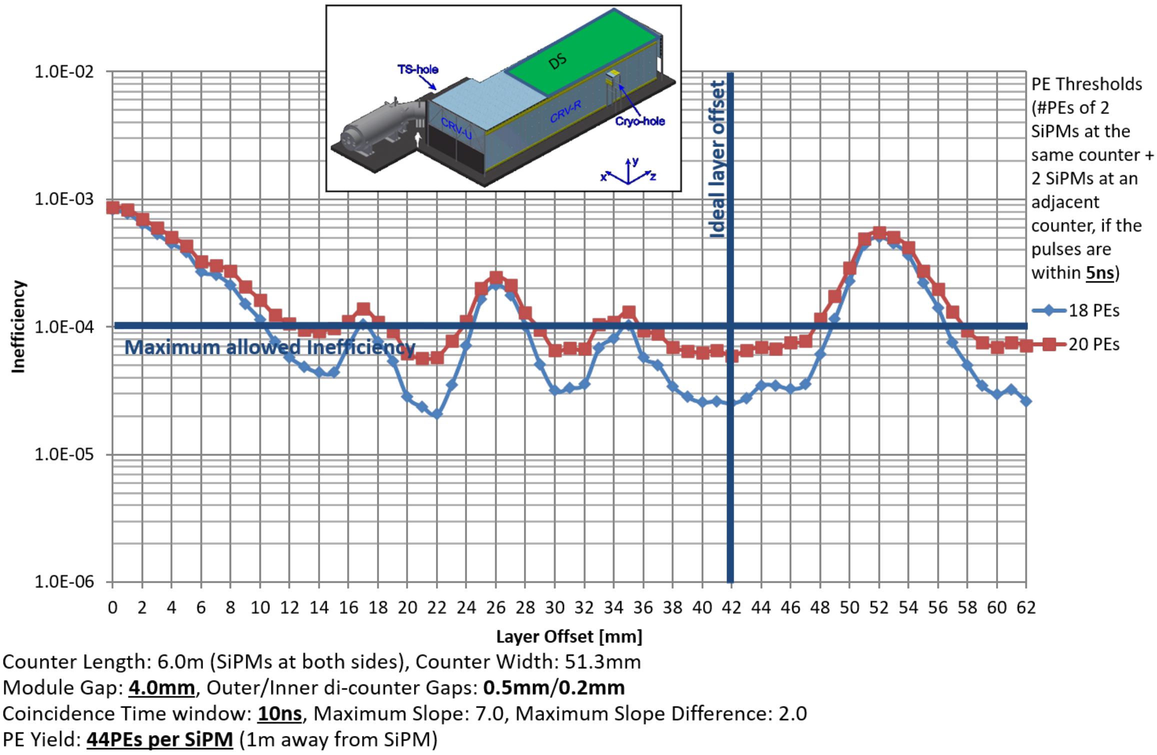

Figure 4.23.: Inefficiency versus layer offset for the top modules (CRV-T) for two different combined PE thresholds. This region contains a large number of background causing cosmic-ray muons.

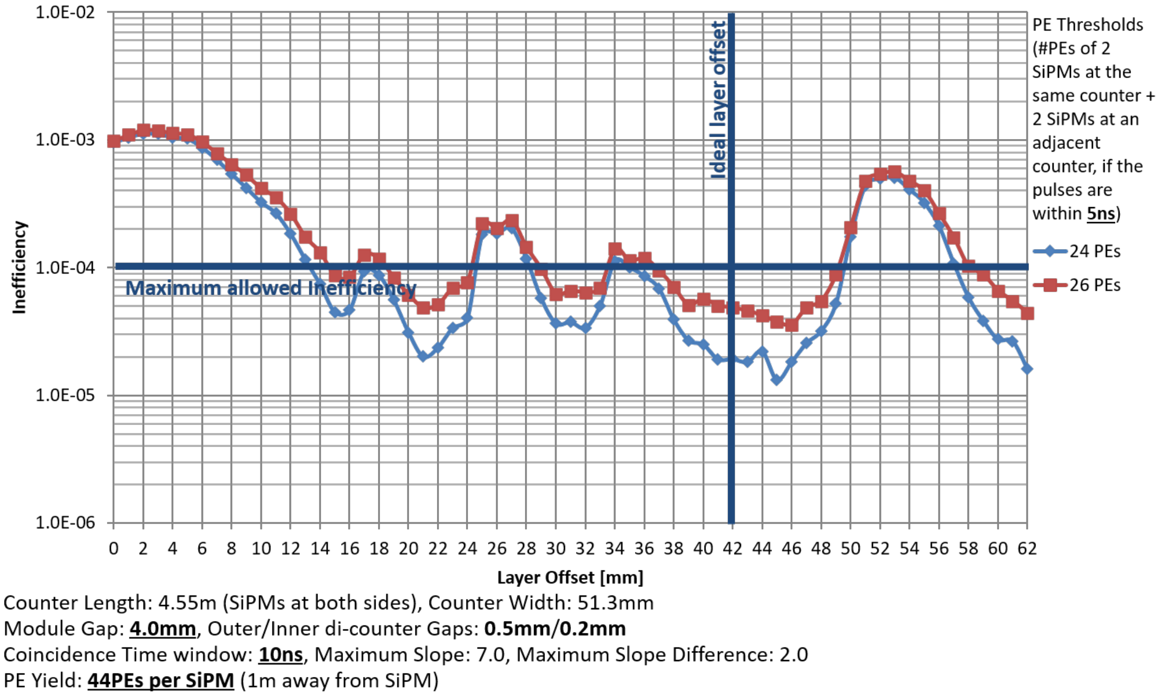

Figure 4.24.: Inefficiency versus layer offset for the right modules (CRV-R) for two different combined PE thresholds.

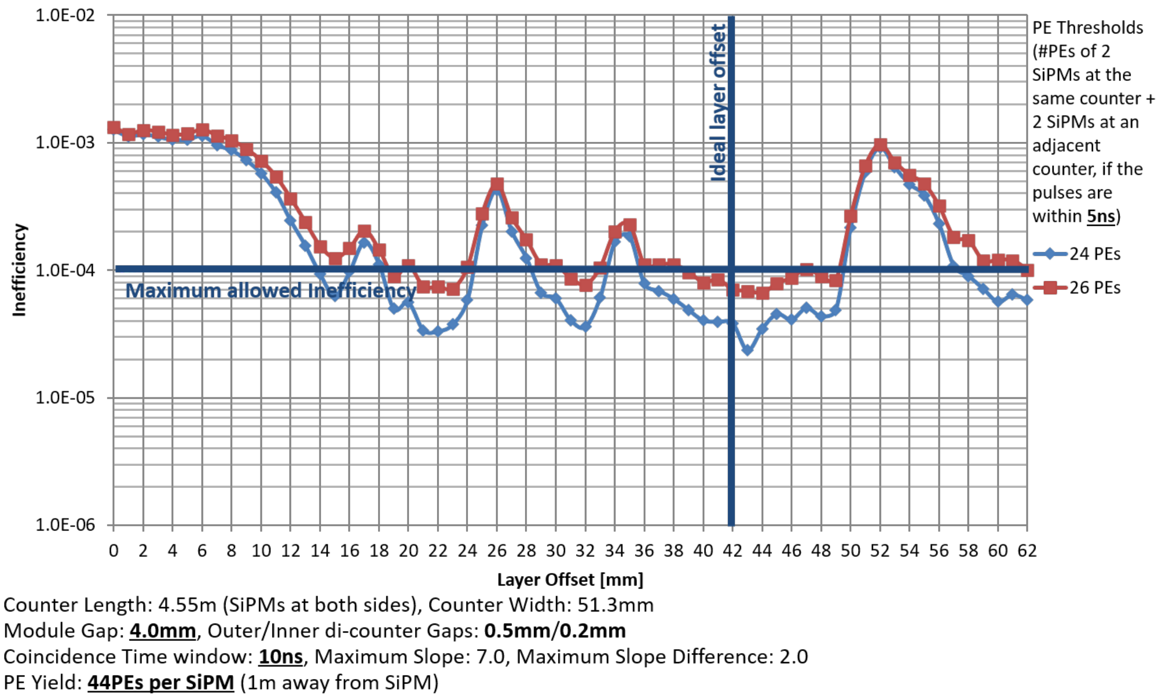

Figure 4.25.: Inefficiency versus layer offset for the left modules (CRV-L) for two different combined PE thresholds.

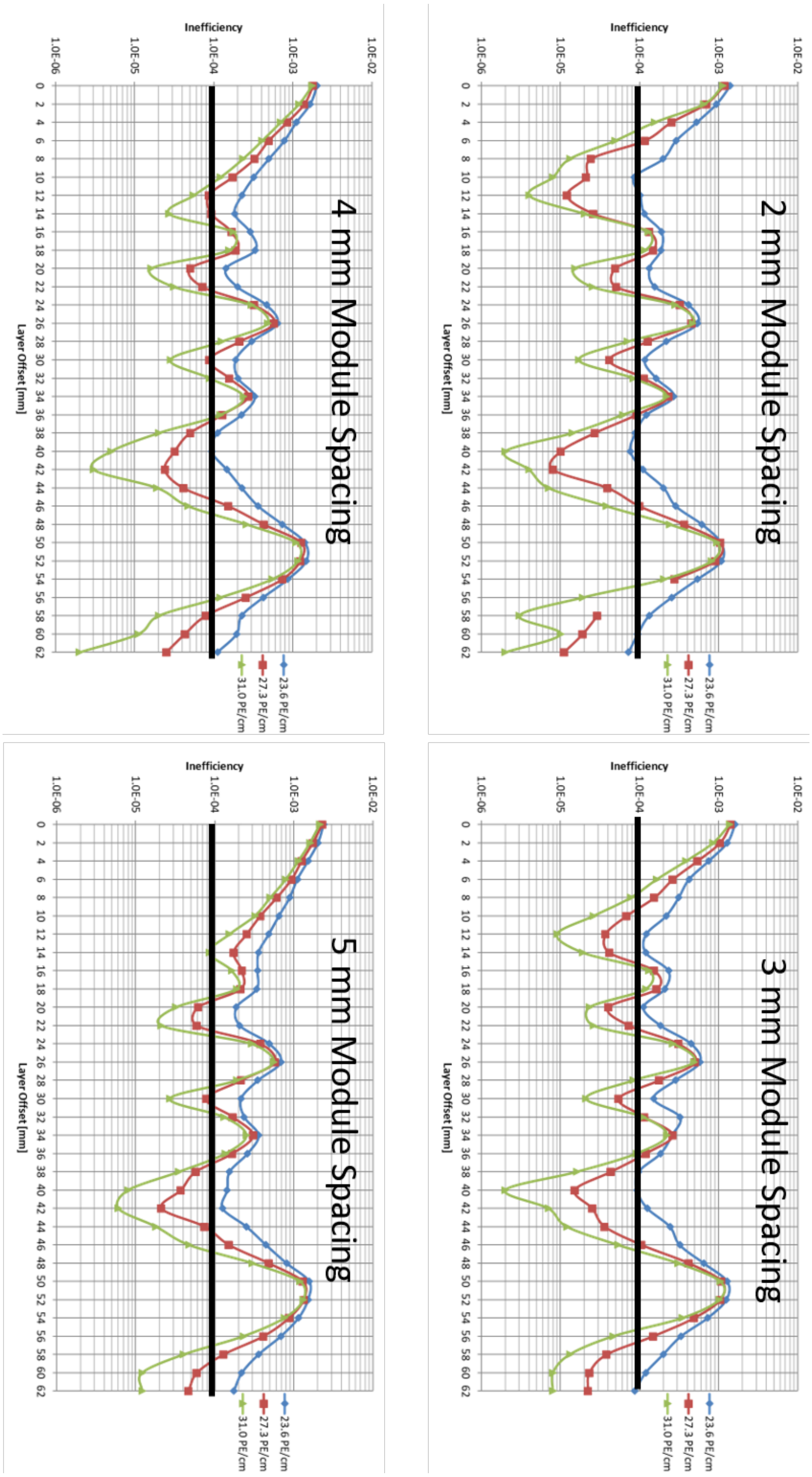

Figure 4.26.: Inefficiency as a function of layer offset for various gap sizes between CRV-T modules. The effect of module gaps becomes more pronounced for small layer offsets, less so for large ones (42 mm ideal gap). The horizontal line represents the maximum allowed inefficiency.

5.3) and determine the anticipated cosmic-ray induced backgrounds. Because the cosmic-ray distribution is different for different sectors, the maximum allowed inefficiencies vary. Top modules were subdivided and studied separately. These modules are responsible for vetoing most of the background-causing cosmic rays with a majority of them passing through the modules in the stopping target region. The muons that were used were not isotropically generated, but those that result in conversion-like backgrounds. The inefficiency curves for each sector are presented in Figs. 4.27 – 4.33 [98].

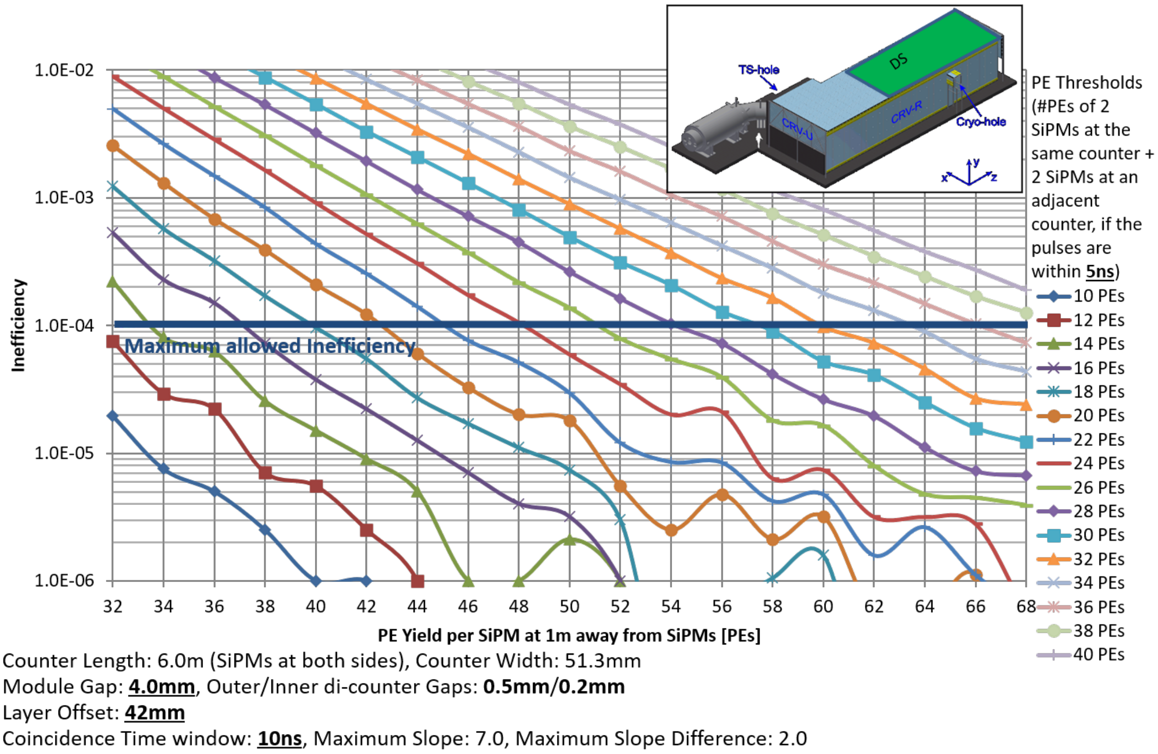

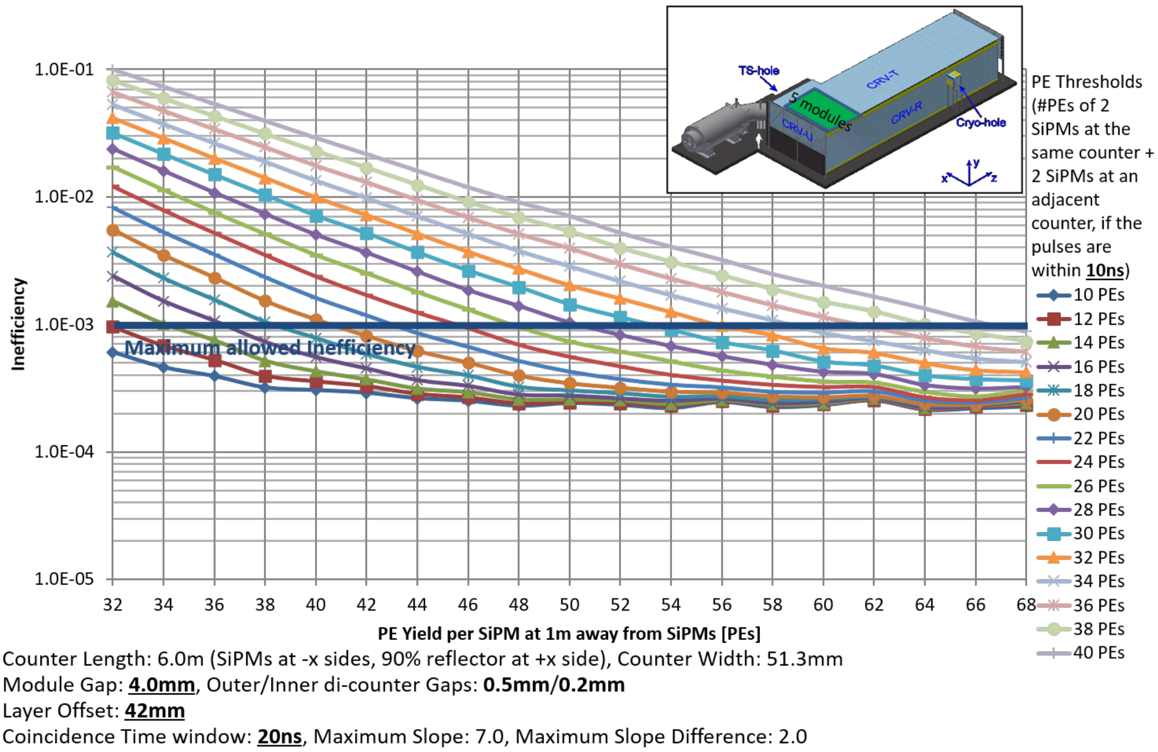

Figure 4.27.: Inefficiency as a function of PE yield for various PE thresholds for two CRV-T subsectors. The five modules upstream (bottom) were studied separately since they are single-ended readout with reflectors on the ends near the TS opening. The blue horizontal line is the nominal target inefficiency for these sectors.

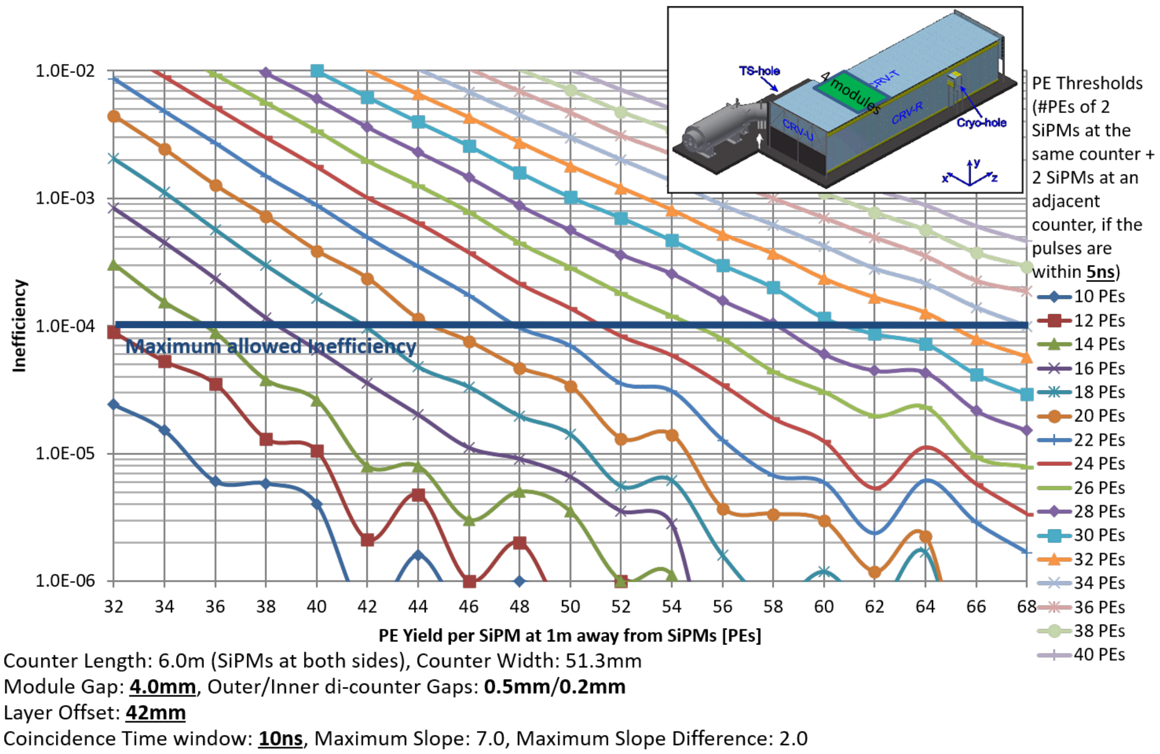

Figure 4.28.: Inefficiency as a function of PE yield for various PE thresholds for CRV-T modules in the stopping target region. These four modules around the stopping target region were studied separately since they are responsible for vetoing most of the background-causing muons. The blue horizontal line is the nominal target inefficiency for this sector.

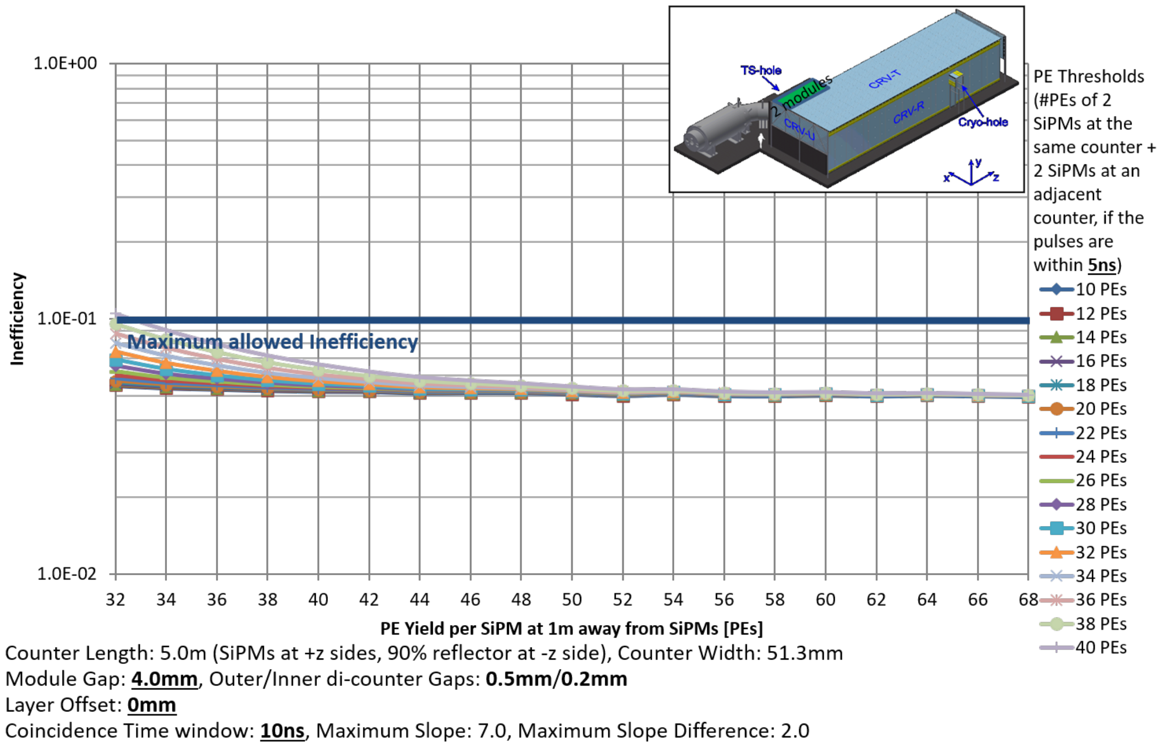

Figure 4.29.: Inefficiency as a function of PE yield for various PE thresholds for CRV-TS-Ext. The blue horizontal line is the nominal target inefficiency for this sector. Due to the lower background causing cosmic-ray muon flux, the maximum allowed inefficiency for this sector is higher.

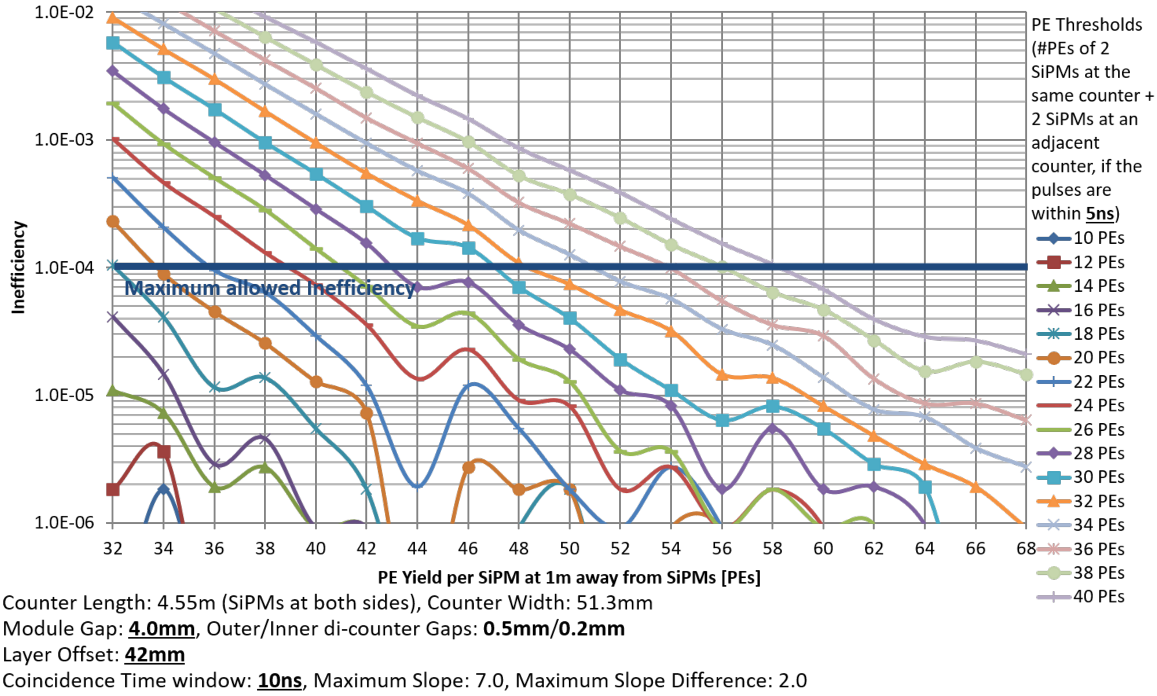

Figure 4.30.: Inefficiency as a function of PE yield for various PE thresholds for CRV-R. The blue horizontal line is the nominal target inefficiency for this sector.

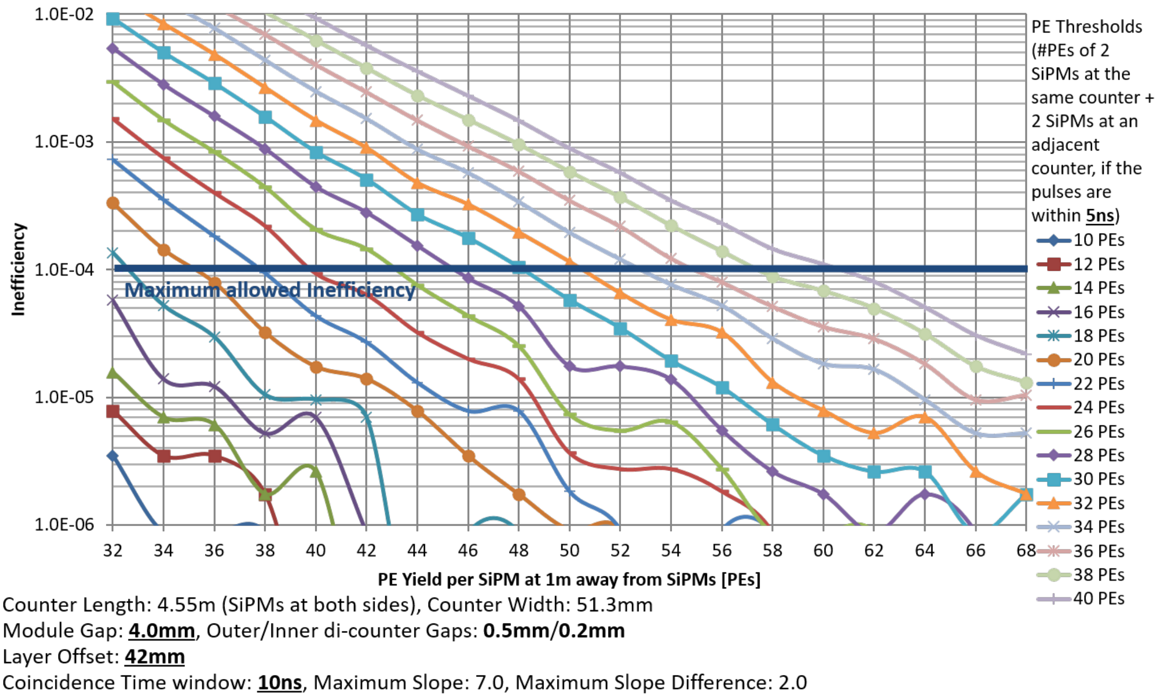

Figure 4.31.: Inefficiency as a function of PE yield for various PE thresholds for CRV-L. The blue horizontal line is the nominal target inefficiency for this sector.

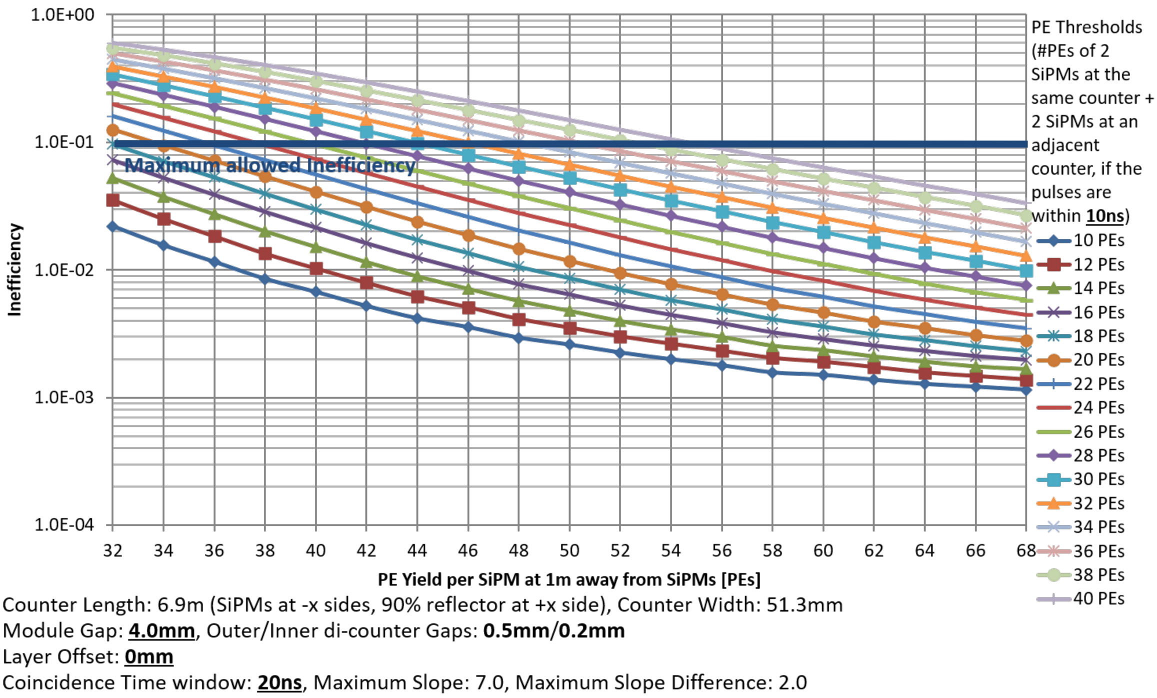

Figure 4.32.: Inefficiency as a function of PE yield for various PE thresholds for CRV-U. The blue horizontal line is the nominal target inefficiency for this sector. Due to the lower background causing cosmic-ray muon flux, the maximum allowed inefficiency for this sector is higher.

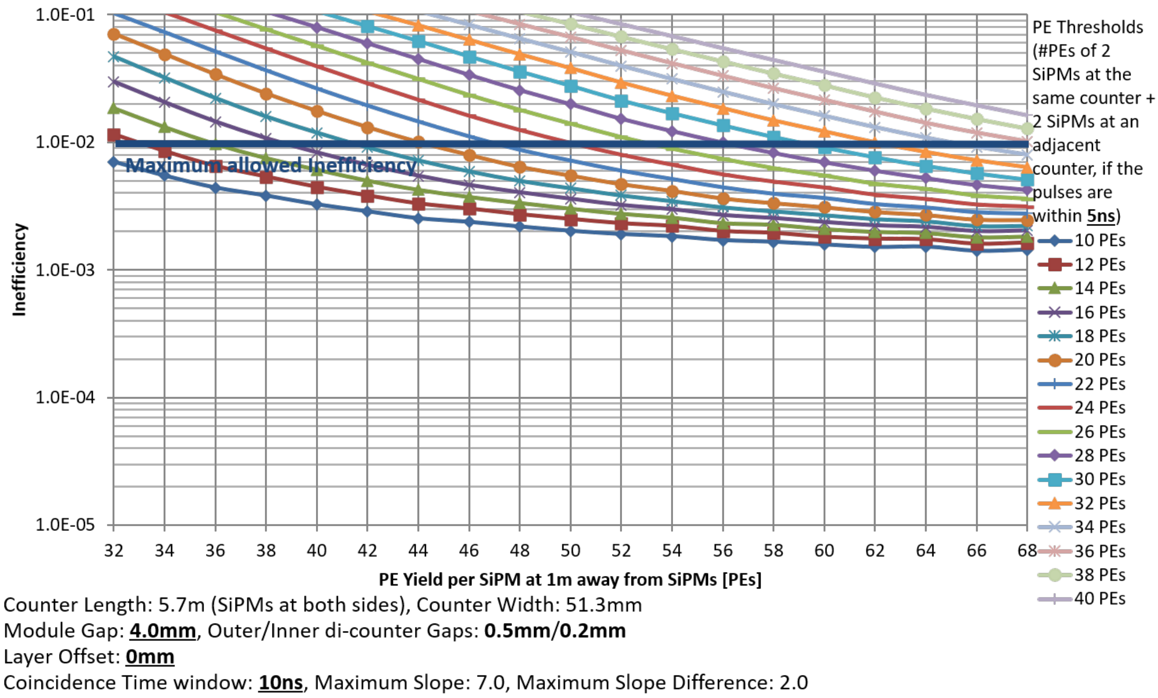

Figure 4.33.: Inefficiency as a function of PE yield for various PE thresholds for CRV-D. The blue horizontal line is the nominal target inefficiency for this sector. Due to the lower background causing cosmic-ray muon flux, the maximum allowed inefficiency for this sector is higher.

4.5. Anticipated Cosmic Ray Induced Background

Using the estimated module inefficiencies and anticipated light yields, as measured from actual module production cosmic-ray data (see Ch. 5.2), the anticipated background for a three year run (of 3.6×10^{20} protons on target), beginning in year 2024 is 0.03 events using a 0 % safety factor on PE yield and an aging rate of 8.7 %. Including the un-vetoed background that enters through the TS opening, the expected background is 0.13 events. Backgrounds from the TS opening and neutrals only depend on the live time. To keep the deadtime to less than 10 % (see Ch. 4.6), a 4/4 layer coincidence is used in the CRV-U, CRV-TS, CRV-TS-Ext, and CRV-D sectors. All other sectors use a 3/4 layer coincidence. The assumed dead time is 4.5 %. A zero-suppression threshold of 5.5 PE is used. The expected background with the breakdown by sector is shown in Table 4.2.

A background of 0.13 events is expected using a 30 % safety factor on the PE yield (reduction in light yield) and an aging rate of 6.5 %[†]. Including the un-vetoed background that enters through the TS opening, the expected background is 0.23 events. The expected background and breakdown by sector is shown in Table 4.3. The run plan of the Mu2e experiment is evolving, so a more up-to-date background estimate is presented in Ref. [100].

4.6. Rates and Deadtime

The production of the muon beam used to search for muon-to-electron conversion is not without side effects: neutrons and other particles produced from the both the proton beam interacting with the production target and surrounding materials and the secondary beam interacting with collimators and apparatus materials, create hits in the CRV and

[†]Recent aging measurements, yet to be confirmed, indicate a lower aging rate.

Table 4.2.: The anticipated non-vetoed background per year for a three year run starting 2024. No safety factor on the PE yield (overall decrease in light) and an aging rate of 8.7 % is assumed. To keep deadtime below 10 % a 4/4 layer coincidence is used in the CRV-U, CRV-TS, CRV-TS-Ext, and CRV-D sectors. All other sectors use a 3/4 layer coincidence requirement. The deadtime was assumed to be 4.5 %, yielding a 95.5 % detector live time. The light yield at the start of the run takes into account the aging the occurred from initial manufacture (2018) to first use. A 90 % experimental running efficiency was assumed. The gross live time is the fraction of time Mu2e will be recording data. The modules classes range from 1 to 3, where class 1 modules receive the most muons and class 3 modules receive the least muons.

Non-vetoed Background vs Year				**2024**			**2025**			**2026**		
				1	3	Beam type	1	3	Beam type	1	3	Beam type
	1.00E+07	Reference live s			52	Weeks		52	Weeks		52	Weeks
	70%	Gross live time			90%	Efficiency		90%	Efficiency		90%	Efficiency
	95.5%	Detector live time			8.40E+12	p/supercycle		8.40E+12	p/supercycle		8.40E+12	p/supercycle
					1.400	Supercycle		1.400	Supercycle		1.400	Supercycle
	POT	Live veto s			6.00E+12	Protons/s		6.00E+12	Protons/s		6.00E+12	Protons/s
Run 1	3.60E+20	9.61E+06			2.00E+07	Run time (s)		2.00E+07	Run time (s)		2.00E+07	Run time (s)
					3.20E+06	Veto time (s)		3.20E+06	Veto time (s)		3.20E+06	Veto time (s)
	8.7%	Aging/year			1.000	POT/nominal		1.000	POT/nominal		1.000	POT/nominal
	0%	PE safety factor			1.20E+20	POT		1.20E+20	POT		1.20E+20	POT
	53	Year 0 PE Yield	**1**									

Sector	Module Class	Layer Coinc Rqmt	PE boost	Unscaled Bkgnd	Total non-vetoed Bkgnd	PE thr.	Scaled Bkgnd	Ineff.	Non Vetoed Bkgnd	PE thr.	Scaled Bkgnd	Ineff.	Non Vetoed Bkgnd	PE thr.	Scaled Bkgnd	Ineff.	Non Vetoed Bkgnd
							31	PE yield			29	PE yield			26	PE yield	
TS-U	3	4/4	1.00	0.5	0.00	8	0.1	0.00147	0.000	8	0.1	0.00195	0.000	8	0.1	0.00283	0.000
TS-D	3	3/4	1.00	2.6	0.00	8	0.8	0.00001	0.000	8	0.8	0.00001	0.000	8	0.8	0.00003	0.000
T-U	1	3/4	1.00	100.0	0.00	8	32.0	0.00001	0.000	8	32.0	0.00002	0.001	8	32.0	0.00005	0.002
	2		1.00	0.0	0.00	8	0.0	0.00001	0.000	8	0.0	0.00002	0.000	8	0.0	0.00005	0.000
	3		1.00	3.9	0.00	8	1.3	0.00001	0.000	8	1.3	0.00002	0.000	8	1.3	0.00005	0.000
T-D	1	3/4	1.00	126.6	0.00	8	40.6	0.00001	0.000	8	40.6	0.00002	0.001	8	40.6	0.00006	0.002
	2		1.00	96.2	0.00	8	30.8	0.00001	0.000	8	30.8	0.00002	0.001	8	30.8	0.00006	0.002
	3		1.00	10.6	0.00	8	3.4	0.00001	0.000	8	3.4	0.00002	0.000	8	3.4	0.00006	0.000
T-Ext	3	4/4	1.00	0.1	0.01	8	0.0	0.05043	0.002	8	0.0	0.05081	0.002	8	0.0	0.05110	0.002
L	1	3/4	1.00	100.0	0.00	8	32.0	0.00001	0.000	8	32.0	0.00001	0.000	8	32.0	0.00001	0.000
	2		1.00	30.2	0.00	8	9.7	0.00001	0.000	8	9.7	0.00001	0.000	8	9.7	0.00001	0.000
	3		1.00	26.3	0.00	8	8.4	0.00001	0.000	8	8.4	0.00001	0.000	8	8.4	0.00001	0.000
R	1	3/4	1.00	27.5	0.00	8	8.8	0.00001	0.000	8	8.8	0.00001	0.000	8	8.8	0.00001	0.000
	2		1.00	36.5	0.00	8	11.7	0.00001	0.000	8	11.7	0.00001	0.000	8	11.7	0.00001	0.000
	3		1.00	30.8	0.00	8	9.9	0.00001	0.000	8	9.9	0.00001	0.000	8	9.9	0.00001	0.000
U	3	4/4	1.00	0.1	0.00	8	0.0	0.02095	0.000	8	0.0	0.03218	0.001	8	0.0	0.04841	0.001
D	3	4/4	1.00	0.5	0.00	8	0.1	0.00384	0.001	8	0.1	0.00557	0.001	8	0.1	0.00859	0.001
Cryo	3	3/4	1.00	1.2	0.00	8	0.4	0.00100	0.000	8	0.4	0.00100	0.000	8	0.4	0.00100	0.000
TS hole				0.09	0.09		0.0	1.0000	0.029		0.0	1.0000	0.029		0.0	1.0000	0.029
Neutrals				0.02	0.02		0.0	1.0000	0.005		0.0	1.0000	0.005		0.0	1.0000	0.005
			Total:	593.7			190.2		0.006		189.8		0.008		189.8		0.013
				Total					0.040				0.042				0.046
Total (no TS hole/neutrals):				**0.03**	**0.03**												
Total (w TS hole+neutrals):				**0.13**	**0.13**												

Table 4.3.: The anticipated non-vetoed background per year for a three year run starting 2024. A safety factor of 30 % is applied to the PE yield (overall decrease in light) and an aging rate of 6.5 % is assumed. To keep deadtime below 10 % a 4/4 layer coincidence is used in the CRV-U, CRV-TS, CRV-TS-Ext, and CRV-D sectors. All other sectors use a 3/4 layer coincidence requirement. The deadtime was assumed to be 4.5 %, yielding a 95.5 % detector live time. The light yield at the start of the run takes into account the aging the occurred from initial manufacture (2018) to first use. A 90 % experimental running efficiency was assumed. The gross live time is the fraction of time Mu2e will be recording data. The modules classes range from 1 to 3, where class 1 modules receive the most muons and class 3 modules receive the least muons.

Non-vetoed Background vs Year

1.00E+07	Reference live s	
70%	Gross live time	
95.5%	Detector live time	
	POT	Live veto s
Run 1	3.60E+20	9.61E+06
6.5%	Aging/year	
30%	PE safety factor	
52	Year 0 PE Yield	1

	2024	2025	2026
Beam type	1 3	1 3	1 3
Weeks	52	52	52
Efficiency	90%	90%	90%
p/supercycle	8.40E+12	8.40E+12	8.40E+12
Supercycle	1.400	1.400	1.400
Protons/s	6.00E+12	6.00E+12	6.00E+12
Run time (s)	2.00E+07	2.00E+07	2.00E+07
Veto time (s)	3.20E+06	3.20E+06	3.20E+06
POT/nominal	1.000	1.000	1.000
POT	1.20E+20	1.20E+20	1.20E+20
PE yield	24	23	21

Sector	Module Class	Layer Coinc Rqmt	PE boost	Unscaled Bkgnd	Total non-vetoed Bkgnd	2024 PE thr.	2024 Scaled Bkgnd	2024 Ineff.	2024 Non Vetoed Bkgnd	2025 PE thr.	2025 Scaled Bkgnd	2025 Ineff.	2025 Non Vetoed Bkgnd	2026 PE thr.	2026 Scaled Bkgnd	2026 Ineff.	2026 Non Vetoed Bkgnd
TS-U	3	4/4	1.00	0.5	0.00	8	0.1	0.00408	0.001	8	0.1	0.00593	0.001	8	0.1	0.00864	0.001
TS-D	3	3/4	1.00	2.6	0.00	8	0.8	0.00006	0.000	8	0.8	0.00011	0.000	8	0.8	0.00018	0.000
T-U	1	3/4	1.00	100.0	0.03	8	32.0	0.00011	0.004	8	32.0	0.00023	0.007	8	32.0	0.00046	0.015
	2		1.00	0.0	0.00	8	0.0	0.00011	0.000	8	0.0	0.00023	0.000	8	0.0	0.00046	0.000
	3		1.00	3.9	0.00	8	1.3	0.00011	0.000	8	1.3	0.00023	0.000	8	1.3	0.00046	0.001
T-D	1	3/4	1.00	126.6	0.04	8	40.6	0.00014	0.006	8	40.6	0.00027	0.011	8	40.6	0.00050	0.020
	2		1.00	96.2	0.03	8	30.8	0.00014	0.004	8	30.8	0.00027	0.008	8	30.8	0.00050	0.015
	3		1.00	10.6	0.00	8	3.4	0.00014	0.000	8	3.4	0.00027	0.001	8	3.4	0.00050	0.002
T-Ext	3	4/4	1.00	0.1	0.01	8	0.0	0.05162	0.002	8	0.0	0.05211	0.002	8	0.0	0.05258	0.002
L	1	3/4	1.00	100.0	0.00	8	32.0	0.00001	0.000	8	32.0	0.00001	0.000	8	32.0	0.00003	0.001
	2		1.00	30.2	0.00	8	9.7	0.00001	0.000	8	9.7	0.00001	0.000	8	9.7	0.00003	0.000
	3		1.00	26.3	0.00	8	8.4	0.00001	0.000	8	8.4	0.00001	0.000	8	8.4	0.00003	0.000
R	1	3/4	1.00	27.5	0.00	8	8.8	0.00001	0.000	8	8.8	0.00002	0.000	8	8.8	0.00003	0.000
	2		1.00	36.5	0.00	8	11.7	0.00001	0.000	8	11.7	0.00002	0.000	8	11.7	0.00003	0.000
	3		1.00	30.8	0.00	8	9.9	0.00001	0.000	8	9.9	0.00002	0.000	8	9.9	0.00003	0.000
U	3	4/4	1.00	0.1	0.01	8	0.0	0.06901	0.002	8	0.0	0.09162	0.002	8	0.0	0.11863	0.003
D	3	4/4	1.00	0.5	0.01	8	0.1	0.01298	0.002	8	0.1	0.01858	0.003	8	0.1	0.02645	0.004
Cryo	3	3/4	1.00	1.2	0.00	8	0.4	0.00100	0.000	8	0.4	0.00100	0.000	8	0.4	0.00100	0.000
TS hole				0.09	0.09		0.0	1.0000	0.029		0.0	1.0000	0.029		0.0	1.0000	0.029
Neutrals				0.02	0.02		0.0	1.0000	0.005		0.0	1.0000	0.005		0.0	1.0000	0.005
			Total:	593.7			190.2		0.022		189.8		0.038		189.8		0.066
				Total					0.056				0.072				0.100
Total (no TS hole/neutrals):				**0.13**	**0.13**												
Total (w TS hole+neutrals):				**0.23**	**0.23**												

can cause additional dead time for the experiment. The majority of particles that cause hits in the CRV are electrons and positrons, produced from gamma rays. These gamma rays are largely produced from captured neutrons. Hits in the CRV are also caused by neutrons colliding with hydrogen nuclei, which recoil and deposit energy in the counters. The sources of neutrons are shown in Fig. 4.34. From a simulation of the 8 GeV proton beam incident on the production target, it is expected that the dead time as a result from accidental coincidences is approximately 4.5 % [101]; less than the 10 % requirement [102]. The deadtime contributions of the CRV-TS and CRV-U sectors are greatly reduced by implementation of a 4/4 layer coincidence requirement (Fig. 4.35). A 4/4 layer coincidence is also used in the CRV-D sector due to large accidental coincidences caused by background sources. The neutron fluences at the end of the anticipated three-year run are shown in Fig. 4.36. The hit rates, shown in Fig. 4.37 per SiPM, are 55 KHz on average at a 5.5 PE threshold (zero-suppression) [101], well below the maximum rate (1 MHz) allowed by the electronics.

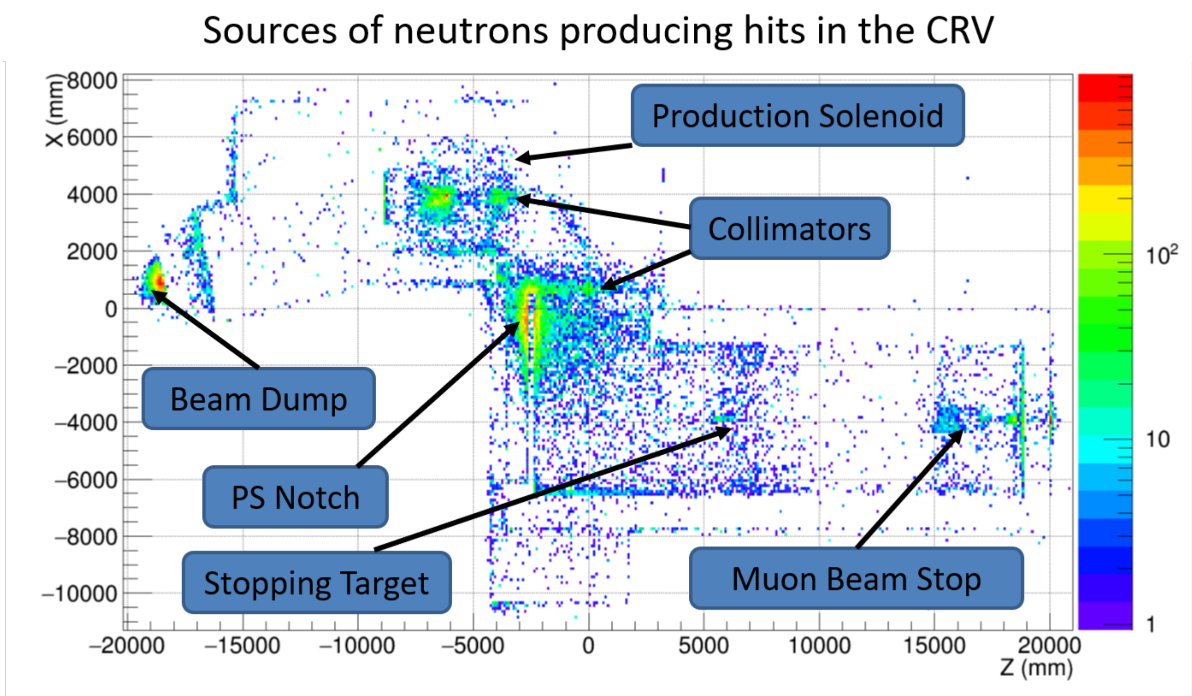

Figure 4.34.: The sources of neutrons producing hits in the CRV, starting from 8 GeV protons incident on the production target. Neutrons collide with hydrogen nuclei that recoil and deposit energy in the counters, or are captured and result in gamma rays that pair-produce. The sources are identified in the figure. Shielding is used to minimize the impact of neutrons and gammas from these sources.

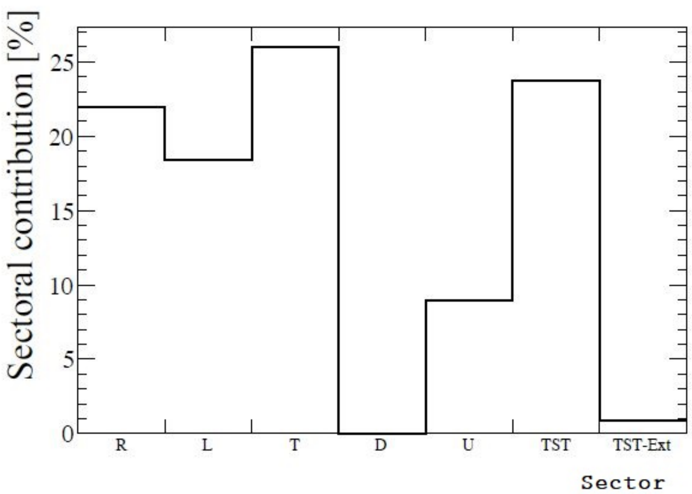

Figure 4.35.: The contributions of each sector to the deadtime estimate of 4.5 %.

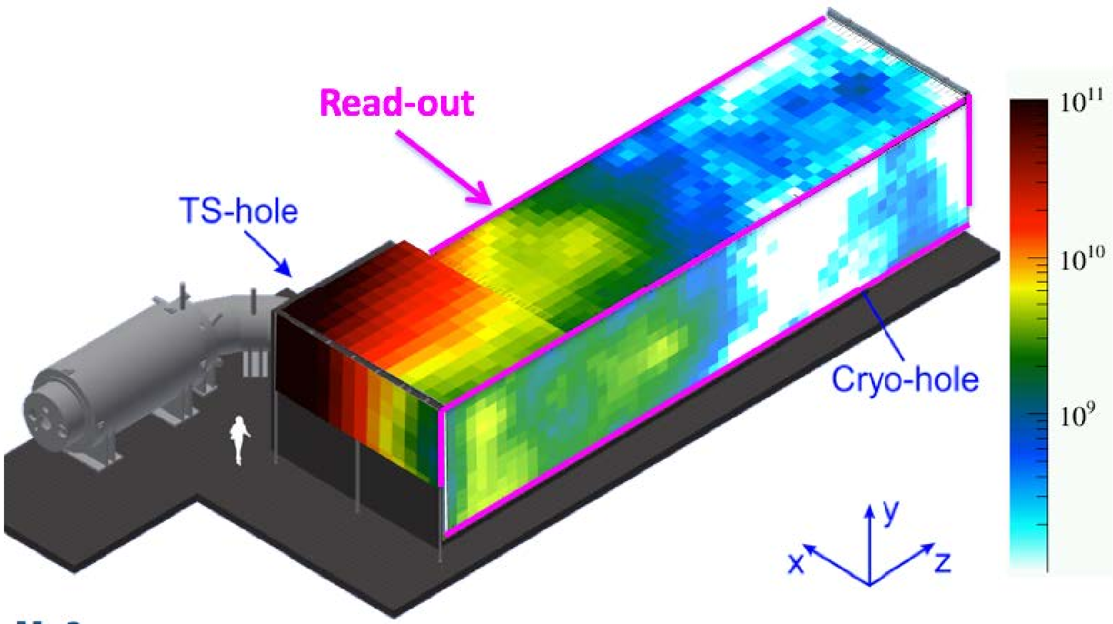

Figure 4.36.: The expected neutron fluences (1 MeV equivalent) across the CRV at the end of the anticipated three-year run period. The readout electronics for each sector are highlighted in pink.

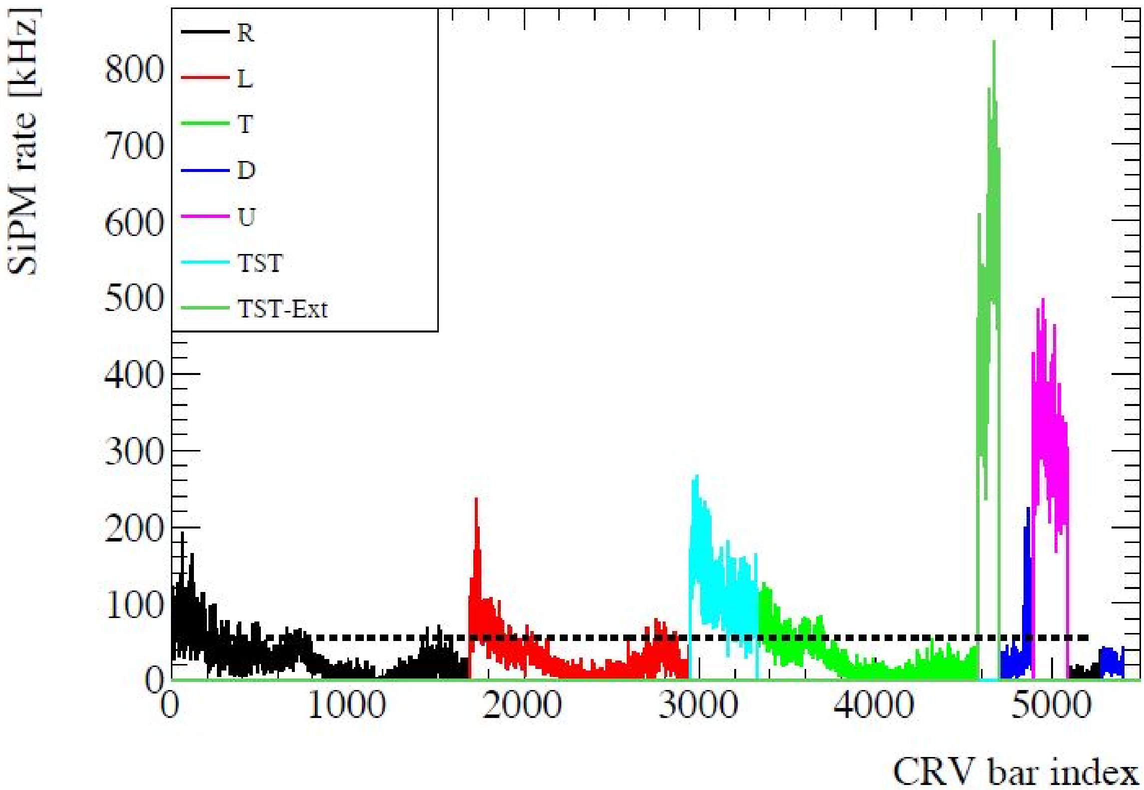

Figure 4.37.: Expected hit rates for SiPMs, shown by counter number. Each color represents a different sector of the CRV. The average hit rate is 55 KHz above a 5.5 PE threshold, shown by the black dashed line. The two tallest peaks in the right side of the plot, from left to right, correspond to SiPMs in the CRV-TS-Ext and CRV-U regions, respectively. The maximum rate allowed by the electronics is 1 MHz.

Chapter 5.

Cosmic Ray Veto Fabrication

Fabrication of the CRV takes place in the Module Factory located in the High Energy Physics building at the University of Virginia. Several areas of the building have been allocated for use by technicians, students, and faculty to participate in the assembly of the CRV. Most of the fabrication takes place in the High Bay room, which is a roughly 3000 ft^2 hall serviced by a high bay door leading to a loading dock and a 3 ton, polar-coordinate crane. Crates of scintillator extrusions are received from the Fermilab/NICADD extrusion facility. These are stored in their shipping crates in the building, an adjacent outbuilding, a UVa-owned storage facility, and a commercial storage facility, all climate controlled. Fiber used for fabrication is stored in a climate controlled room of the High Bay room.

Numerous safety documents and standard operating procedures were written to ensure personnel safety and appropriate fabrication standards. The list of documents is presented in Ref. [103]. Module Factory safety was reviewed by Fermilab and UVa industrial hygienists on two occasions. During module assembly, the large amounts of epoxy used generates volatile fumes. Measurement of volatile vapor levels in the Module Factory atmosphere during epoxy use were found to be below the threshold for mandatory respirator use. Because exposure to epoxy fumes could cause respiratory harm over

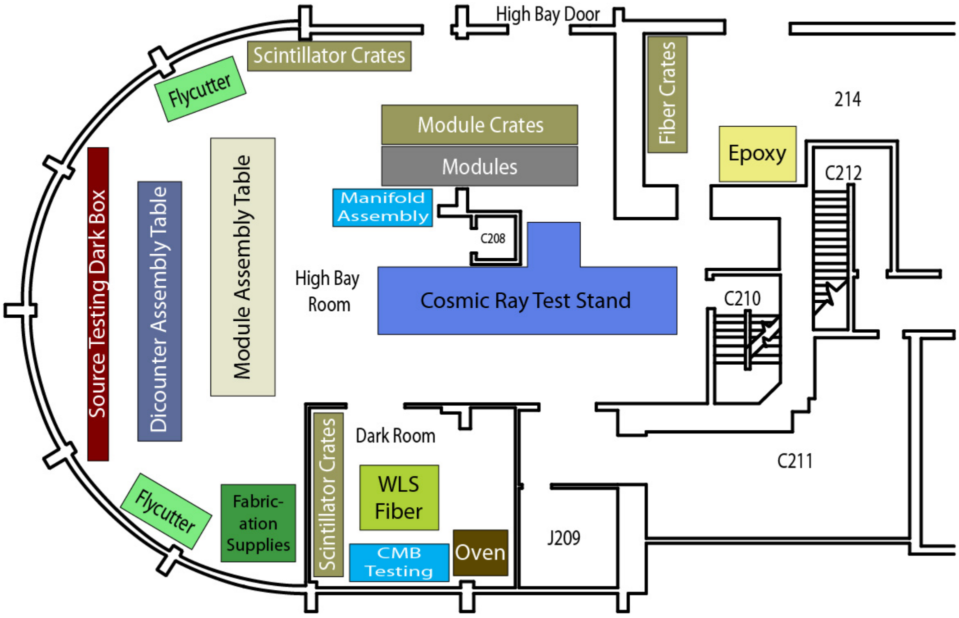

Figure 5.1.: Floor plan of the High Bay room of the Module Factory in the High Energy Physics building at UVa. A 3 ton crane covers the semi-circular portion of the High Bay room. The loading dock is located at the top. The dark room is where CMB and fiber testing takes place, in addition to the storage of some scintillator extrusions and WLS fiber. Fabrication supplies are located near the assembly tables. Epoxy used in module assembly is stored in an adjacent room.

time and could lead to sensitization and asthma, it is required that all personnel wear respirators during module assembly. Safety at the Module Factory is in compliance with OSHA regulations and University policy under the direction of the University's Environmental Health and Safety department.

5.1. Dicounter Assembly

The basis for every CRV module is the dicounter whose fabrication and quality control processes are listed in Ref. [104]. As outlined in the mechanical design of the dicounter, two scintillator extrusions are used to create a dicounter. Pairs of extrusions are cut to length using a chop saw fixture that has an adjustable stop for fine tuning the length and squareness of the cut (Fig. 5.2) [105]. A single long edge of each counter is scored using Scotch-Brite [106] and cleaned using isopropanol, which prepares the surface for bonding. The counters are placed into a vertical fixture and 3M DP420 [43] epoxy is used to bond the pairs together. The ends of each counter in a pair are made flush with one another. The fixture, shown in Fig. 5.3, applies pressure to up to four pairs of extrusions to ensure an adequate bond as the epoxy cures. While the pairs are bonding, wavelength-shifting fibers are inserted into each hole of a counter. Approximately 50 mm to 100 mm of fiber protrudes from either end of the extrusion, which facilitates the mounting of Fiber Guide Bars (FGBs, Fig. 5.4) [107]. The FGB is bonded to the counter pair using fast-curing 3M DP100 [44] epoxy held into place with #4-20 3/8" Plastite screws [45]. The screws do not have any measurable effect on the light yield. The WLS fibers are glued into the FGBs using DP100 epoxy. After the epoxy has cured, excess fiber is cut off using a nichrome-wire hot knife (Fig. 5.5) [108]. This method of trimming prevents cracking and damage to the fiber. Polishing of each fiber face is performed using one of three re-purposed NOvA flycutters, typically one at each end, shown in Fig. 5.6. The diamond-tipped flycutters employ a SICK IVC-3D smart camera [109], and several motion tables, to scan and adjust to variations in the position of the FGB, to provide consistent, repeatable flycuts [108]. The flycutter performs two rough cuts each 0.5 mm deep, and a final polish 0.1 mm deep. The cutter head speed is nominally 3500 RPMs. The quality of the flycutting is checked with two procedures: fiber faces are photographed and visually inspected and flycutting quality is analyzed using a surface roughness tester (Ch. 5.1.3).

5.1.1. Scintillator Fabrication and Quality Control

The scintillator extrusions were fabricated at the Fermilab-NICADD extrusion facility [53]. A total of 31.3 km of scintillator was extruded over the span of 5 months, starting in January 2018. Several adjustments to the extrusion die and sizer were made to tune

Figure 5.2.: Left: A custom-made chop saw fixture used for cutting scintillator extrusions to the proper length. Right: An adjustable stop is used to fine tune the length of the counters, with separate adjustments for squareness, so all extrusions lengths are within $\pm 0.5\,\mathrm{mm}$.

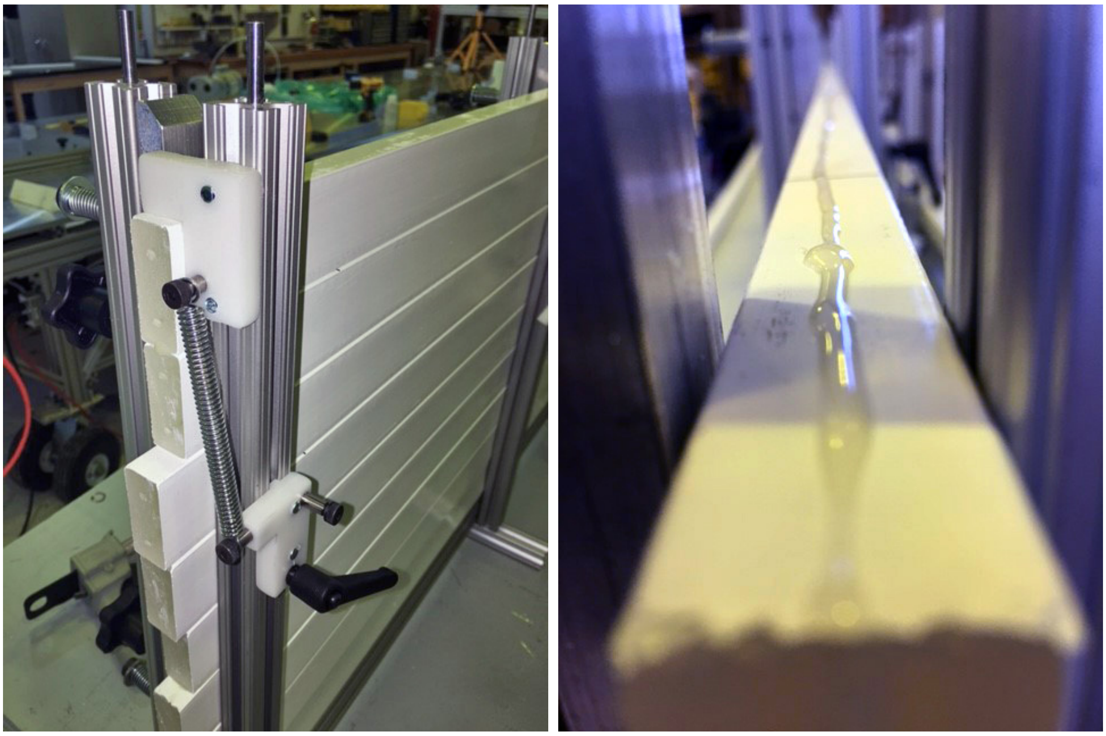

Figure 5.3.: A vertical fixture (left) is used to glue pairs of scintillator extrusions together. The fixture applies spring pressure to the stack of scintillator to ensure an adequate bond is made between extrusions. Shown on the right is a bead of epoxy on one short side of an extrusion.

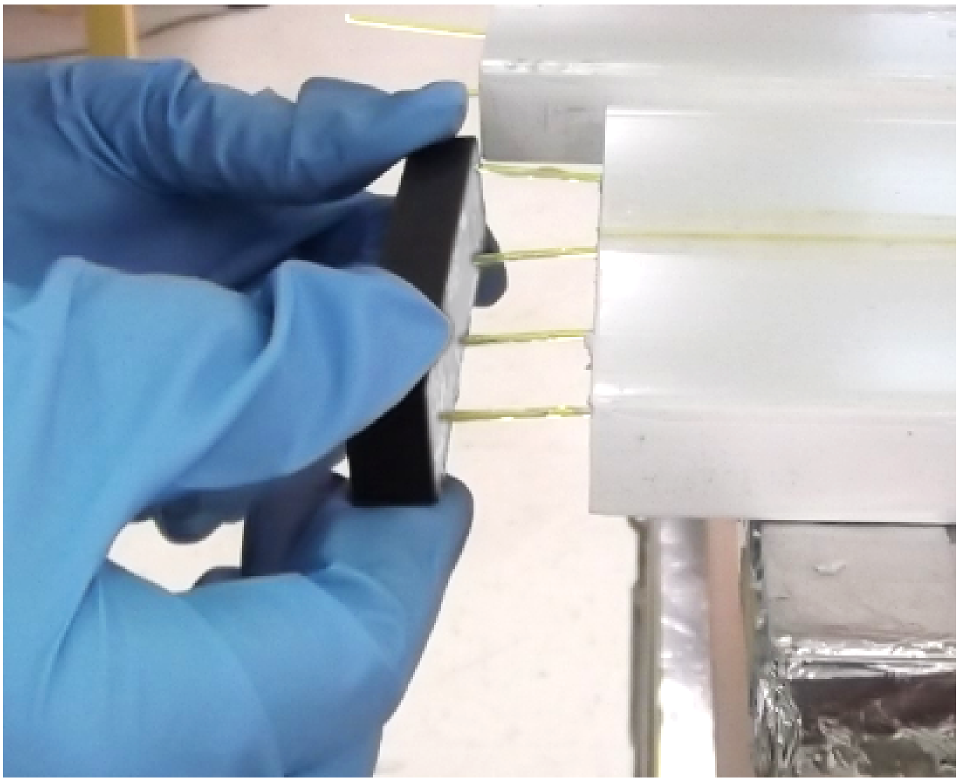

Figure 5.4.: Several inches of fiber protrude from the end of each extrusion pair that facilitates the installation of the Fiber Guide Bar.

Figure 5.5.: A nichrome-wire hot knife is used to trim the excess WLS fiber after being glued into the FGB. This method prevents cracking when removing excess fiber.

Figure 5.6.: Shown on the left is one of three flycutters used for polishing dicounter ends. Controlled by a computer, a laser camera identifies and adjusts the diamond-tipped flycutter to polish the faces of the WLS fibers embedded in the FGB. On the right is a view inside of the machine showing the flycutter head and laser camera, on the left, polishing a dicounter.

the extrusion profile. It was important to meet the target counter width with minimal variation for two reasons: a width of 51.3 mm allows all modules to fit within various physical constraints without the need to build special half-width modules, and minimal width variation is necessary to prevent excessive gaps between dicounters or over-sized dicounters that would extend beyond the module aluminum. To form the fiber channels, nitrogen was injected into the molten plastic during extrusion. The titanium dioxide coating was also co-extruded.

After every 10th extrusion, a short 14 cm section of scintillator was evaluated for size, shape, and light yield [110]. The height and width of the section were measured using calipers and recorded, shown in Fig. 5.7. The profile of the scintillator throughout the extrusion process was consistent. A conical gauge was used to measure the hole size. Periodically the mechanical drawing, which includes tolerances, was superimposed onto an image of the profile of the sample, yielding confirmation that the holes were properly sized and located and the extrusion is within manufacturing tolerances. An example of this qualitative check is presented in Fig. 5.8.

To evaluate light-yield consistency, a 1.2 mm WLS fiber, 1 m in length with a mirrored end, was inserted into one of the holes of the sample and the response to a Cs-137 source, placed 10 cm above the sample, was measured by a photomultiplier tube [110]. The number of counts measured during a one-minute interval was recorded. A reference sample was also measured as a control. The light yield as a function of time is shown in Fig. 5.9, normalized to the control sample. It was discovered during the manufacturing run that use of a new polystyrene batch resulted in a decrease in light yield of around 13 %. The reason for this decrease is not known. Further, an issue regarding the vacuum used in the extrusion process was identified and corrected. The higher light yield extrusions are used in sectors where higher efficiencies are needed.

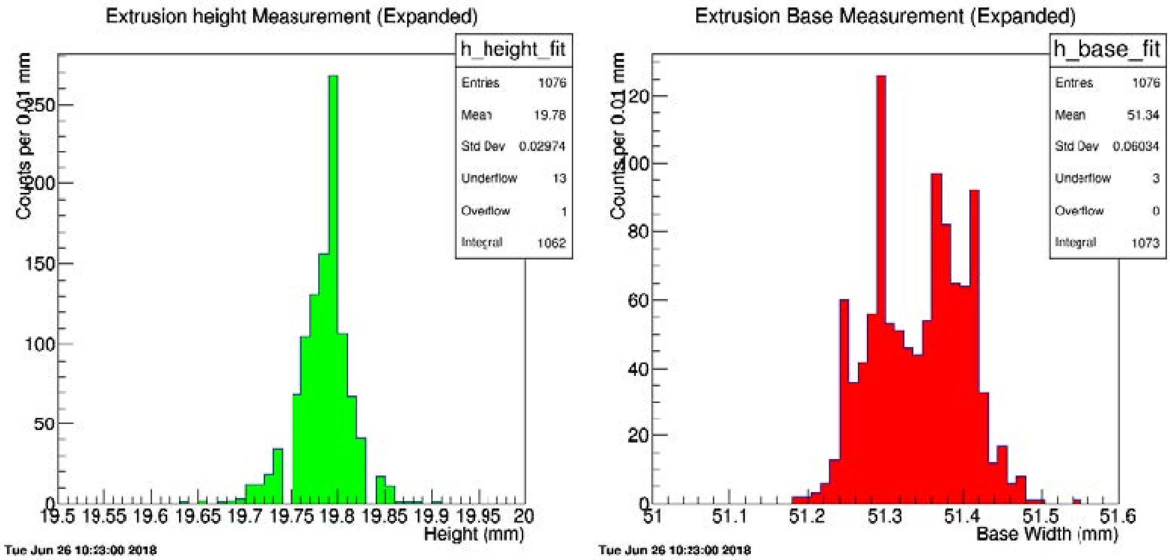

Figure 5.7.: Left: Distribution of the heights of all scintillator samples. The nominal height was 20 mm. Right: Distribution of the widths of all scintillator samples. The target width was 51.3 mm, with a minimum (maximum) allowed width of 51.2 mm (51.5 mm).

At the Module Factory, the widths and lengths of every counter and dicounter are measured. The width of each counter and dicounter are measured at the middle and at each end using calipers and are found to be very consistent and agree with the measurements taken at the extrusion facility. The width measurements of a sample of 1530 counters and 1250 dicounters are shown in Fig. 5.10. The epoxy thickness between two counters is approximately 0.01 mm (Fig. 5.10). Strict control on the widths of the extrusions and assembled dicounters is important in ensuring dicounters are not too wide, which would result in the dicounters within a layer exceeding the width of the aluminum in a module. Too narrow a width would result in inter-dicounter gaps that are excessive and reduces the detection efficiency of a module.

The deviation in length of every counter from a reference extrusion of the desired length (golden) is measured using a special jig shown in Fig. 5.11. The extrusion is placed against a fixed stop and a dial indicator measures the deviation from the target length. The deviation of 4700 counters from their target length is shown in Fig. 5.12.

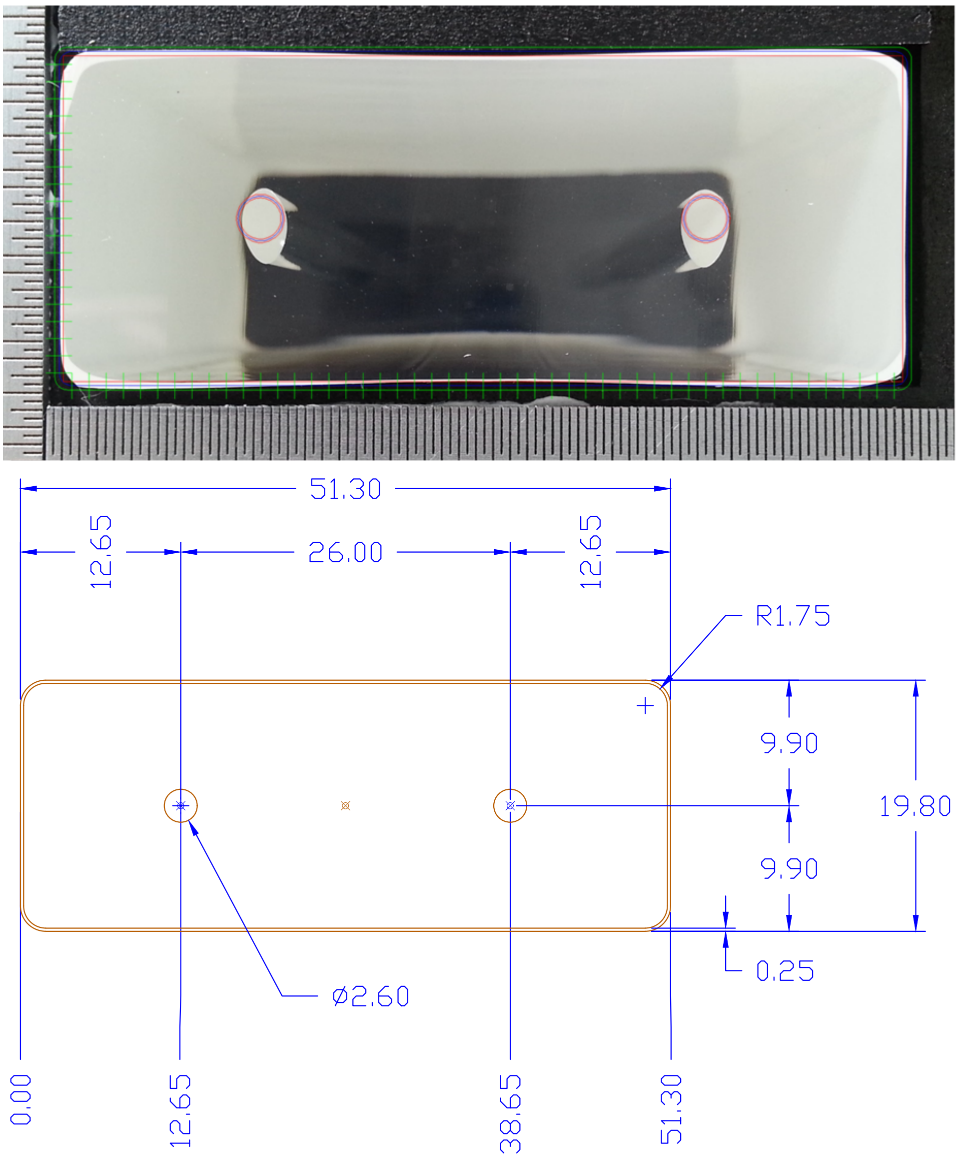

Figure 5.8.: Photograph of the profile of a scintillator sample (top) with the drawing (bottom) and tolerances superimposed.

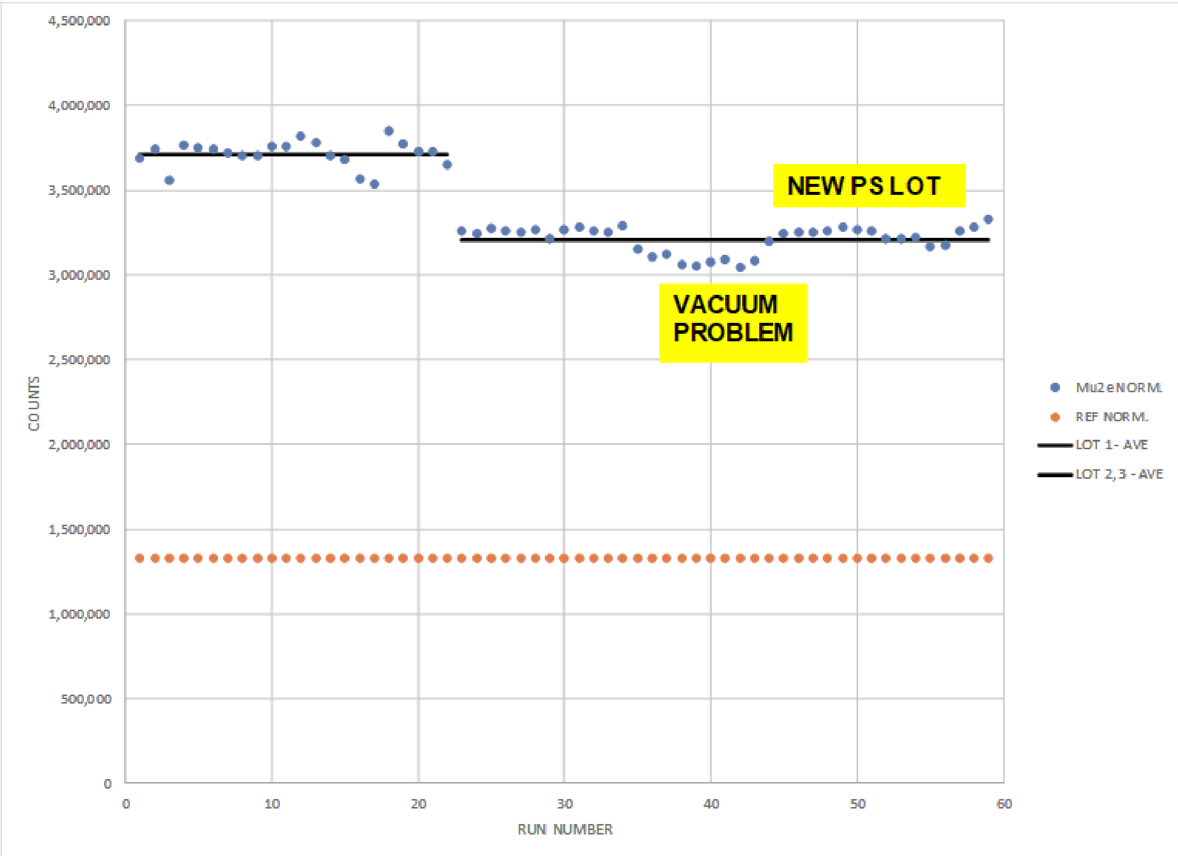

Figure 5.9.: The light yield, measured in counts using a PMT, in response to a Cs-137 source for each scintillator sample as a function of extrusion number (blue dots). The orange dots represent the response of a reference sample to the Cs-137 source to which all of the measurements have been normalized. After a new polystyrene (PS) batch was used, the light yield noticeably decreased by roughly 13 %. An issue with the vacuum used in production also lowered the light yield [111].

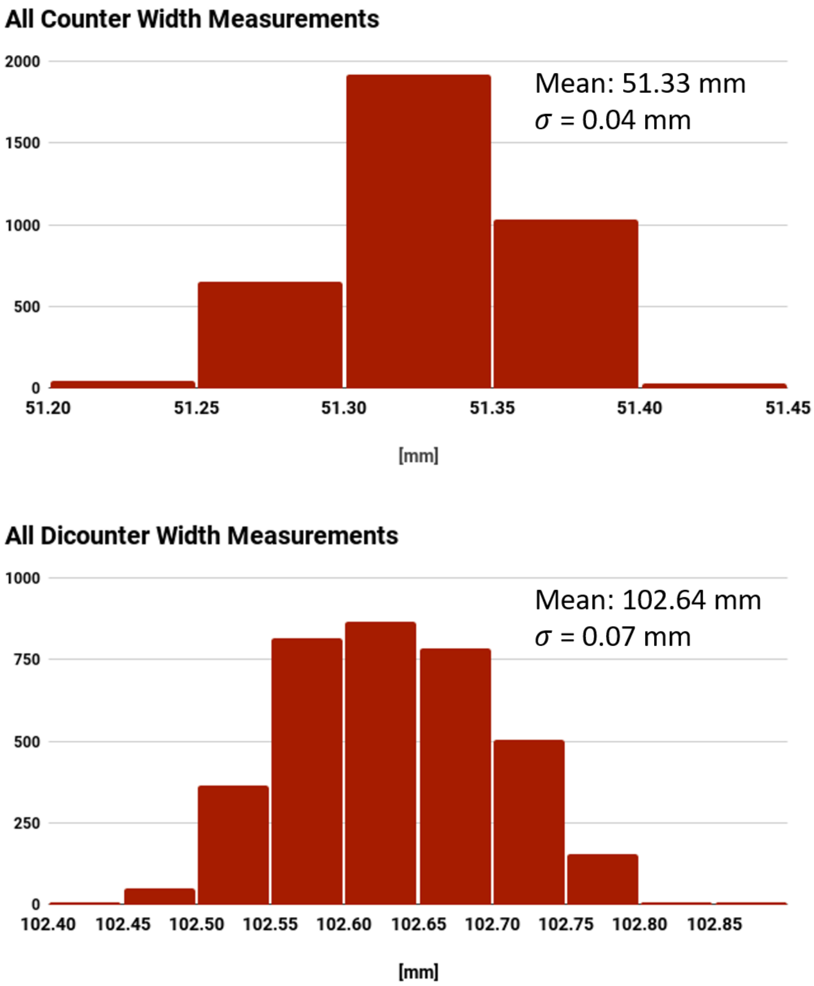

Figure 5.10.: Counter and dicounter widths measured at the Module Factory. Top: 1530 counter (single extrusion) widths; the designed counter width is 51.3 mm. Bottom: 1250 dicounter widths; nominal dicounter widths are expected to be 102.6 mm.

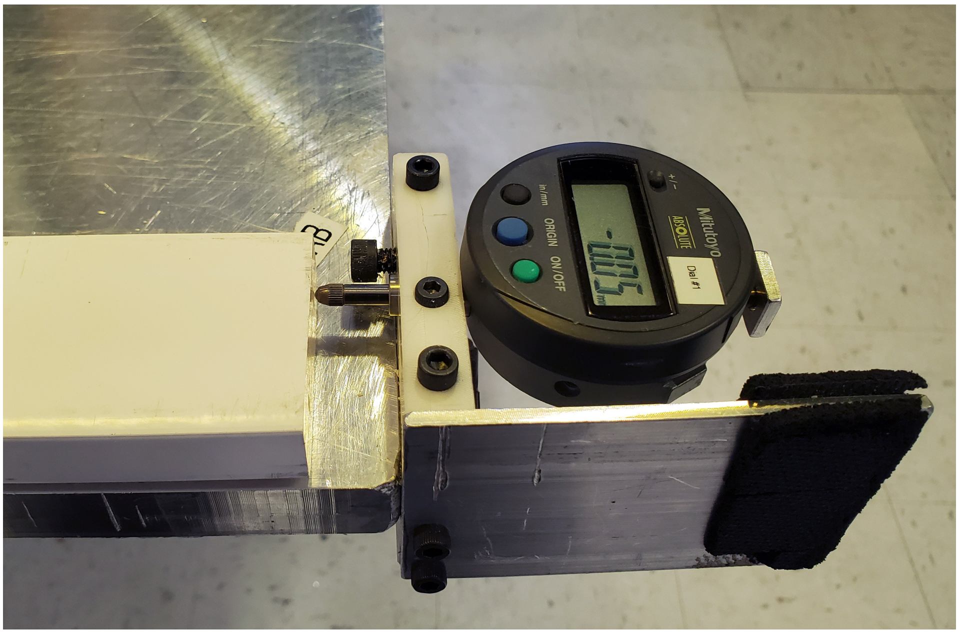

Figure 5.11.: Placing the extrusions against a stop, a dial indicator measures the length relative to the target length.

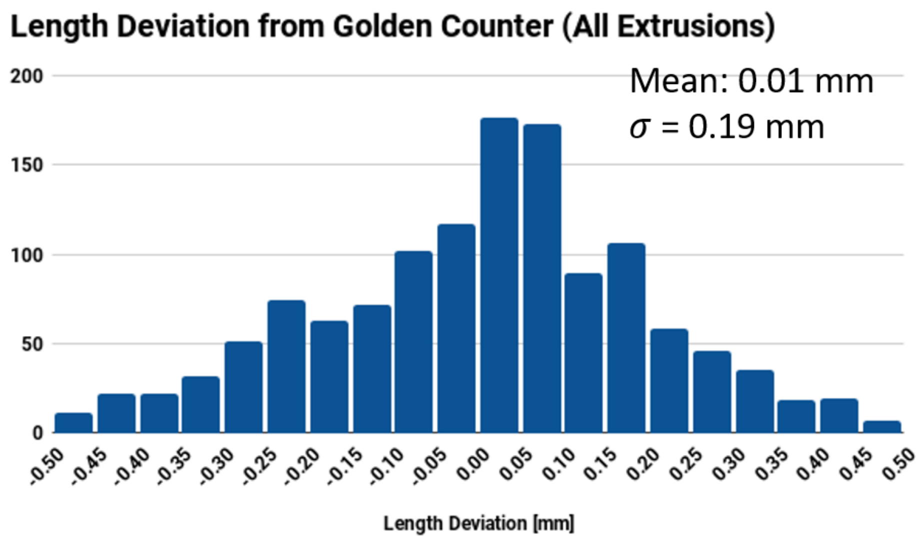

Figure 5.12.: The counter lengths are measured relative to a reference (golden) counter of the target length. No counter outside of ± 0.5 mm is accepted. Outliers were cut shorter or recycled into shorter counters.

Counters are required to be within ± 0.5 mm of the specified length. Those longer than the specification are re-cut and counters that are too short are recycled into shorter dicounters or scrapped altogether.

5.1.2. Fiber Quality Control

The WLS fiber, 60 km total, was delivered to UVa on cardboard spools, with 0.58 km of fiber per spool. A fiber scanner, shown in Fig 5.13, was fabricated that measures the light yield as a function of distance from the light source at various wavelengths in order to evaluate the quality of fiber used in the CRV [60]. Light yield was determined by exciting the fiber using a 405 nm LED [112] and measuring the absolute light yield at the end of the fiber using a Hamamatsu S1227-1010BR photodiode [113]. Also present at the end of the fiber was an Ocean Optics STS-VIS spectrophotometer [114] for measuring the spectral light yield. Up to 25 m of fiber, with a diameter up to 2 mm, can be tested. The production fiber was required to have at least 80 % of the light yield of the pre-production fiber samples (6 km of fiber). The manufacturer provided additional quality measurements with the following acceptance criteria:

1. Fiber diameter average is 1.400 ± 0.006 mm, with diameter RMS less than 0.037 mm.
2. The number of 9 % surface defects is less than 15 km^{-1}.
3. The fiber eccentricity $(D_{max} - D_{min})/(D_{max} + D_{min})$ is less than 1.0 %.
4. The attenuation length is greater than 3.6 m, with a variation (RMS/AVG) less than 15 %.
5. Light yield variation (RMS/AVG) is less than 15 %.

The first 25 m of every spool was tested, yielding a total test length of 2.6 km or 4.3 % of all the fiber. A 1 km spool of pre-production fiber was tested in prototype dicounters at the Fermilab Test Beam Facility and found to be satisfactory [87], thus serving as a reference to which the production fiber was compared. The result from the spectrometer scan, showing the measured light intensity for various wavelengths at several distances from the excitation point and the computed attenuation length, is shown in Fig. 5.14

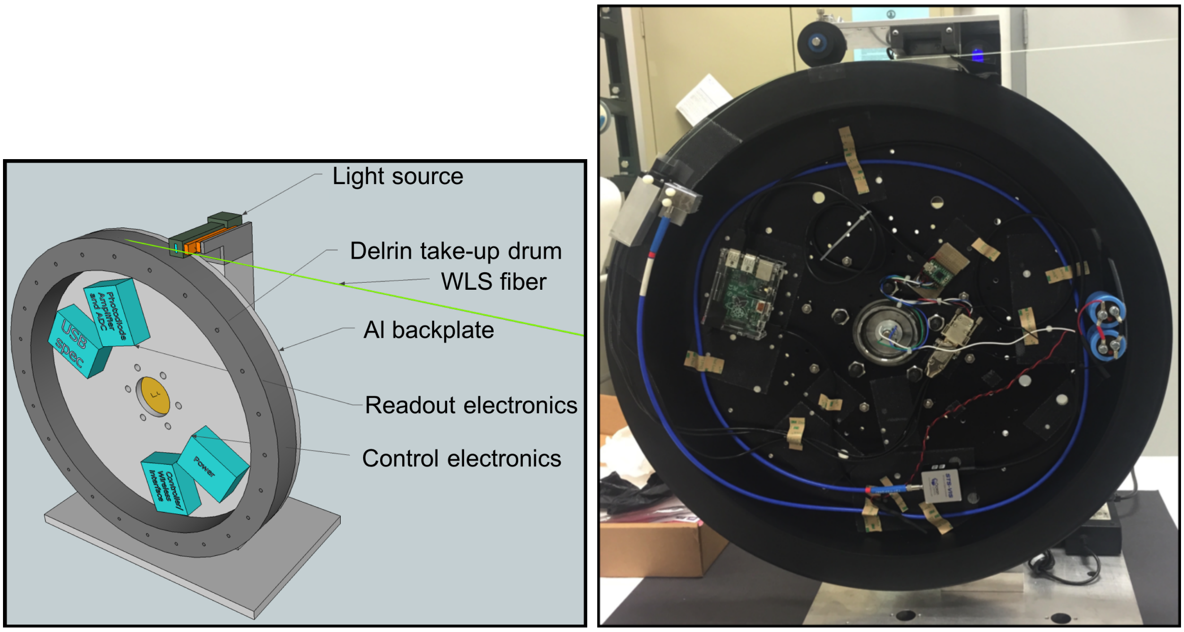

Figure 5.13.: Left: A schematic of the fiber tester and its various components. Right: An image of the fiber tester.

[60]. The light yield as a function of distance from the excitation point, as measured by the photodiode, is shown in Fig. 5.15 for all 104 spools. On average, the production fiber performed 7 % better than the reference, shown in Fig. 5.16, which gives the light yield as a function of distance from the excitation point, normalized to the reference spool, for all 104 spools. Only one fiber spool failed this test and was promptly replaced by the vendor.

The light yield as a function of distance from the excitation point is best fit using a single exponential ($f(x) = Ae^{-x/\lambda}$) in the range of 0.5 m to 3 m (3 m to 25 m) to extract the short (long) attenuation lengths λ_S (λ_L) [60]. The average short (long) attenuation length was found to be 5.8 ± 0.7 m (10.0 ± 0.1 m), which was greater than the attenuation length of the reference fiber, 5.2 ± 0.1 m (8.3 ± 0.1 m). Shown in Fig. 5.17, which also includes the reference fiber, both attenuation lengths were largely consistent between spools and better than the measured value quoted by the vendor (4.23 ± 0.15 m @ 1 m to 3 m). The fiber diameter for each fiber spool was measured with calipers and found

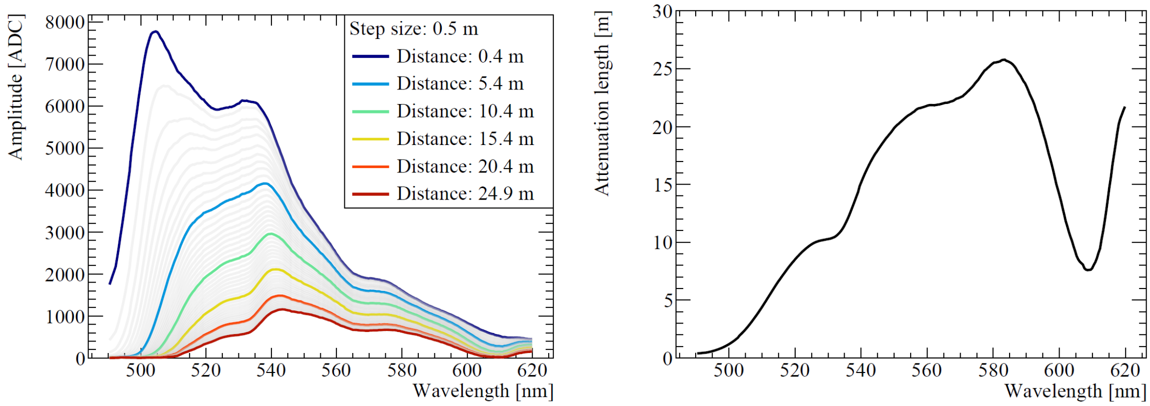

Figure 5.14.: Left: Measured intensity at the end of a fiber spool as a function of wavelength at various distances from the excitation point. Right: The attenuation length as a function of wavelength [60].

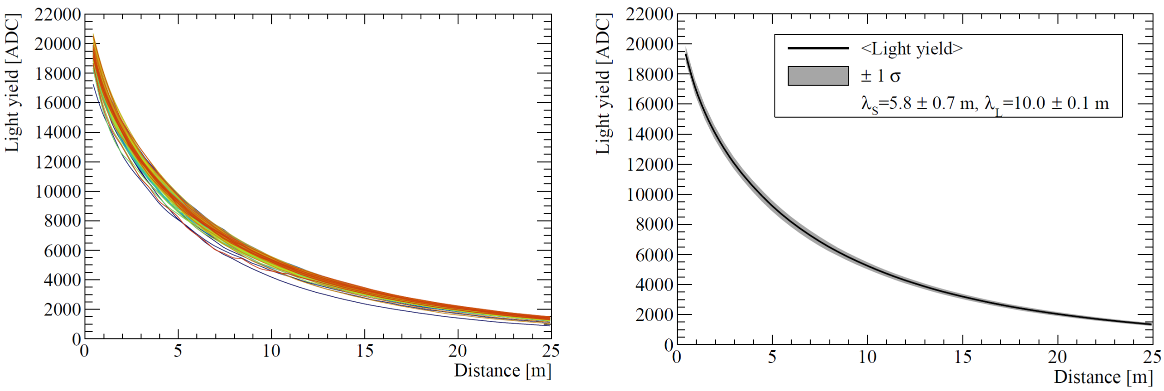

Figure 5.15.: Light yield as a function of distance for all 104 production spools (left) and the average (right). The average short (λ_S, 0.5 m to 3 m) and long (λ_L, 3 m to 25 m) attenuation lengths are shown in the legend in the right plot.

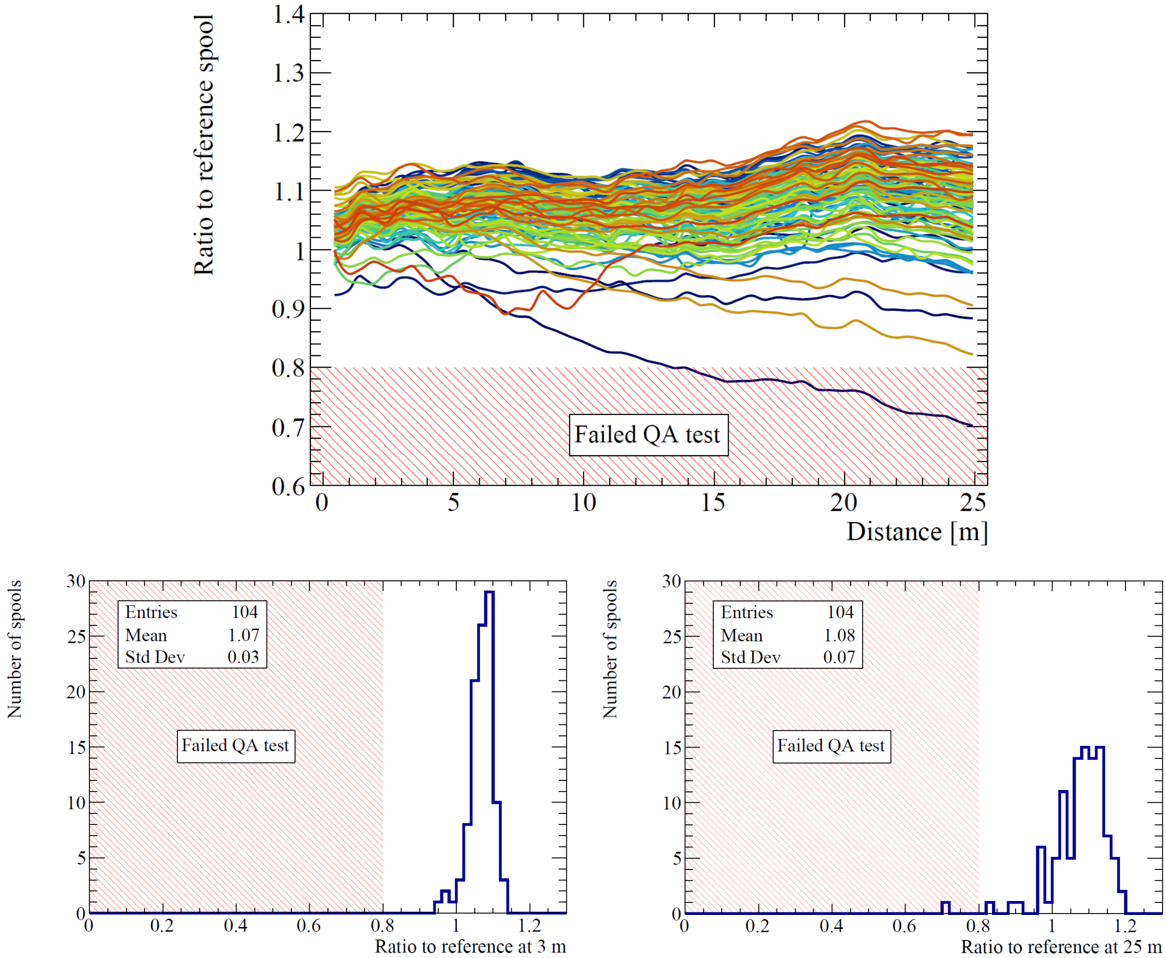

Figure 5.16.: Light yield as a function of distance from the excitation point for all 104 production spools of fiber, normalzied to the reference fiber. It was required that all spools perform at least 80 % or better than the reference fiber. One spool failed and was replaced. The bottom two histograms show the relative light yield of all spools at 3 m (left) and 25 m (right).

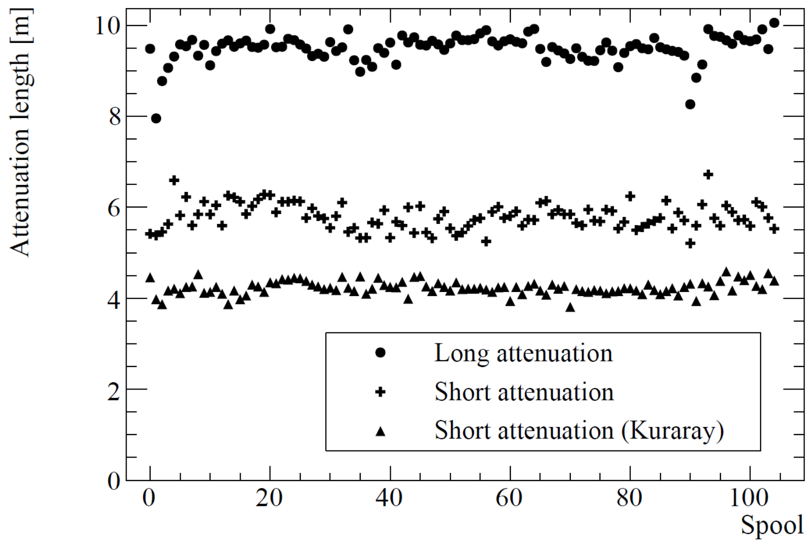

Figure 5.17.: Short (0.5 m to 3 m) and long (3 m to 25 m) attenuation length for each spool. Included is the short attenuation length as measured by the vendor, Kuraray, in the region of 1 m to 3 m. The reference fiber is included, which is the first point in the plot.

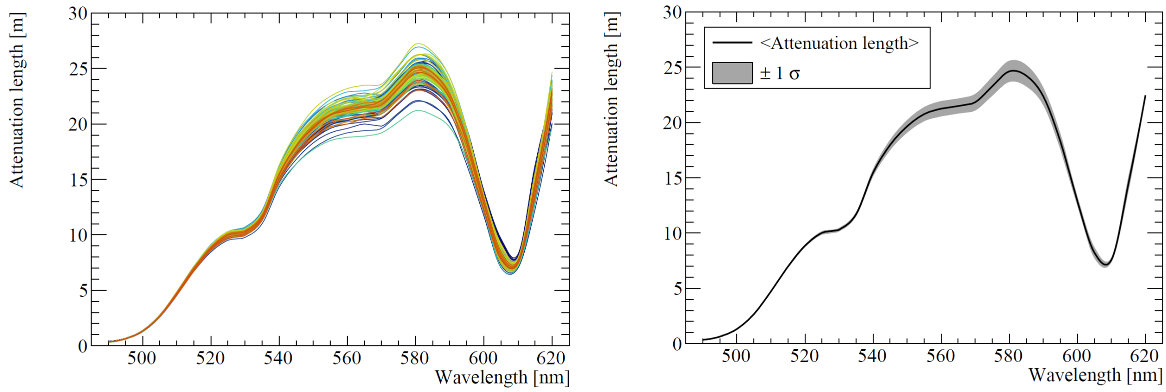

Figure 5.18.: Attenuation length as a function of wavelength for all production fiber spools (left), averaged on the right.

to be within specification (1.39 ± 0.01 mm). The attenuation length as a function of wavelength for all the spools is shown in Fig. 5.18.

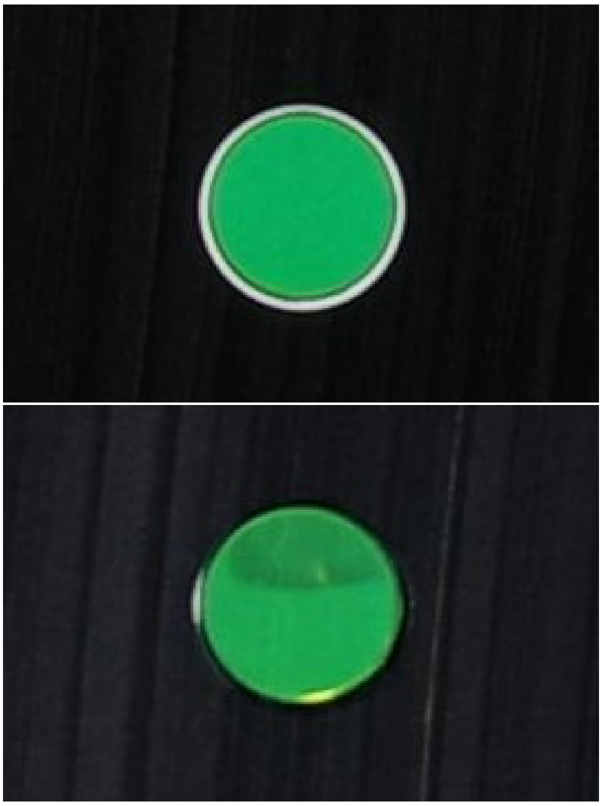

Figure 5.19.: Top: an image of an undamaged fiber. The epoxy that holds the fiber in place in the Fiber Guide Bar is visible as the light ring surrounding the fiber. The darker ring surrounding the bright green fiber core is the cladding. Bottom: a damanged fiber that has a crack just below the surface, resulting in the darker portion visible at the top of the fiber face.

5.1.3. Dicounter Quality Control

Using a Pentax K-1 36.2 MP DSLR camera with a 110 mm f/28 macro lens, a visual inspection of the fiber faces is performed by a human [115]. A Python program automatically crops, displays for the operator, and saves the image of each fiber face. A typical abnormality is visible when a crack develops just below the face of the fiber, usually as a result of flycutting. A visual comparison between an acceptable and unacceptable fiber is shown in Fig. 5.19. Typically cracks in a fiber are eliminated by re-flycutting, however dicounters that have cracks deeper in the fiber that are unable to be repaired in this manner are recycled.

A Mitutoyo Surftest SJ-210 series surface roughness tester [116], shown in Fig. 5.20, is used to provide a quantifiable measurement as to the quality of the flycut. Surface roughness, R_z, is defined as the average vertical distance between the highest peak and lowest troughs over several sampling lengths. The sampling length used is 0.1 mm and three samples are obtained. The surface roughness of the FGBs for a sample of 1250 dicounters, measured in accordance with ISO 4287/4288, was found to be $3.23 \pm 1.01\,\mu$m (Fig. 5.21). There is no appreciable degradation in flycut quality over time (Fig. 5.22).

After confirmation that there are no defects after flycutting, the dicounter ends receive sleeves for mounting the manifolds. The fibers are then evaluated for light transmission; a test designed to determine the presence of damage to the fiber that was not visible using the camera [117]. A custom device, shown in Fig. 5.23, which has two testing heads that attach to opposite ends of the dicounter, uses an LED and a PIN-diode to measure light transmission through each fiber. A comparison for each fiber is made to the mean response of all tested fibers: those with a transmission of less than 90 % are flagged as defective. The normalized response of a sample of 694 counters, of 2.37, 3.20, 4.55 and 6.00 m lengths, is shown in Fig. 5.24. The spread is only 1.7 %. A single bad counter is barely visible in this histogram, with a response of 87 % of the mean.

The light yield of each counter is measured using a radioactive source [118]. The dicounter is placed into a 7 m long dark box and located on top is a movable 1.0 mCi Cs-137 source. Measurements are made 1 m from each readout end (separately). The same manifolds and SiPMs are used for each dicounter. The current is measured for each of the eight SiPMs, with and without the source. It is compared to a 2.3 m reference dicounter (referred to as the golden dicounter), which is measured at the same time in the same manner. This method identifies inadequate dicounter light yield or issues with the transmission of light through the fiber.

Figure 5.20.: The surface roughness testing apparatus. A dicounter is placed into the jig at the top and the surface roughness is measured by a Mitutoyo Surftest SJ-210 (bottom).

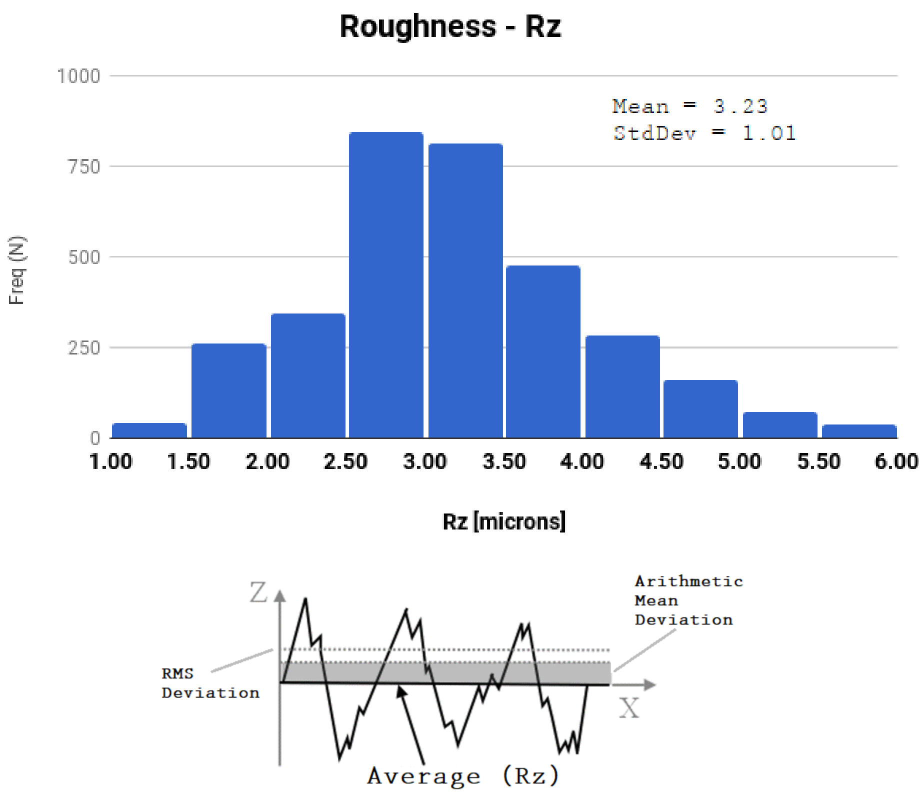

Figure 5.21.: Top: the surface roughness of the FGB after flycutting for 1250 dicounters. Bottom: the roughness is the average of the vertical distance between highest peak and lowest trough over a sampling length.

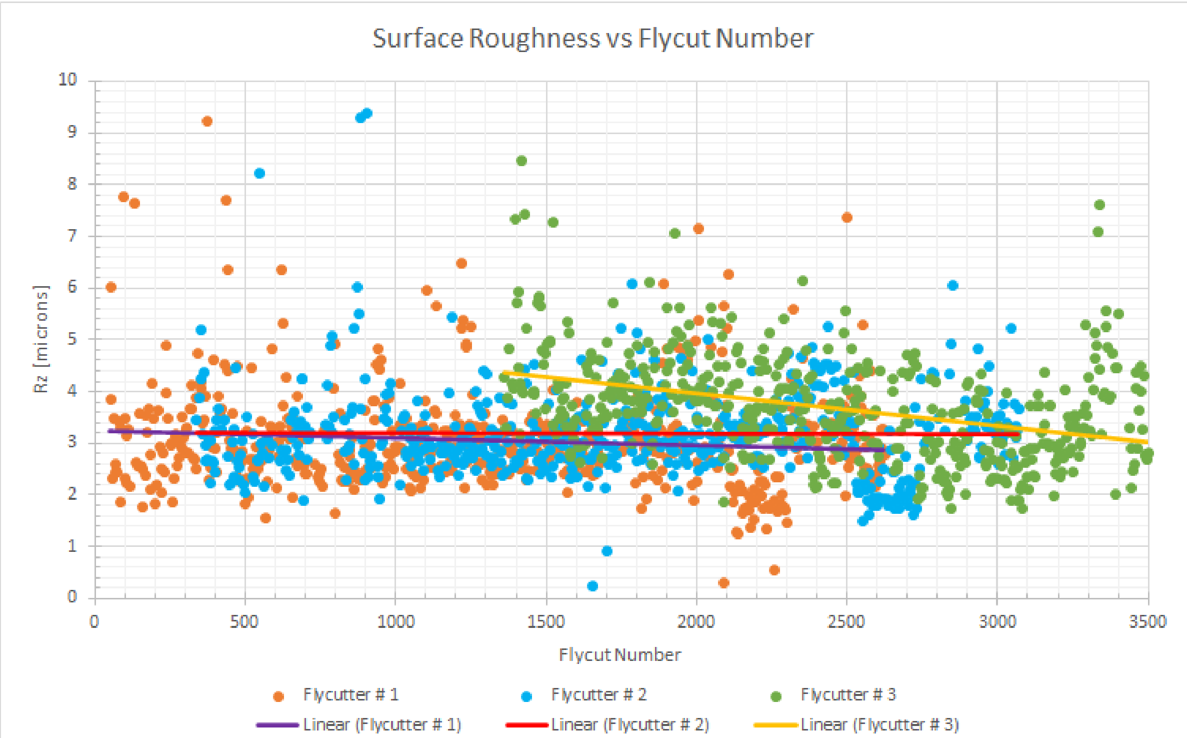

Figure 5.22.: The surface roughness of the FGB for 1250 dicounters versus flycut number for each of the three flycutters that are used in the Module Factory. The surface roughness has remained constant or better over time.

Figure 5.23.: Fiber Tester Apparatus. The control box (top) interfaces with a computer and the two tester heads (middle) that have the LEDs and PIN diodes (bottom) used to measure the transmission of light through the fibers.

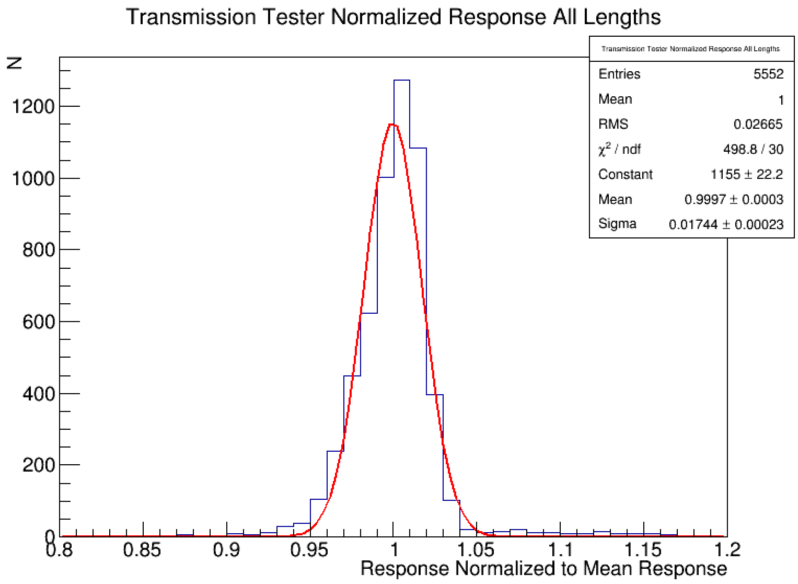

Figure 5.24.: Normalized light transmission for 694 dicounters with lengths from 2.37 m to 6 m. The response (transmission) of each fiber was normalized to the mean response for all fibers. The spread is 1.7 %. Any counters falling below 90 % of the mean are flagged as defective.

While SiPMs are temperature sensitive devices, the corrections are negligible due to the room's climate control that is typically stable to within ±0.5 degrees. During the times when the loading dock is used and the high-bay door is open, that is not the case. At the same time the light yield of a dicounter is measured, the light yield of a $2\,\mathrm{mm} \times 2\,\mathrm{mm} \times 20\,\mathrm{mm}$ LYSO crystal is also measured. Due to its minimal aging and a low light yield dependence on temperature ($-0.28\,\%/°\mathrm{C}$), it serves as an additional normalization for the temperature dependence of the SiPMs and the aging of the cesium source (2.3 %/year).

The normalized response of 1270 dicounters to the Cs-137 source, which includes lengths of 2.3, 3.2, 4.55 and 6 m, is presented in Fig. 5.25. Typically, 95 % of the counters have a light yield within 12 % of the mean. No correction was made for the length of the dicounter, which results in a slightly larger spread in the far-end light yield. No dicounters have been flagged for abnormal response at the far end. Dicounters that have

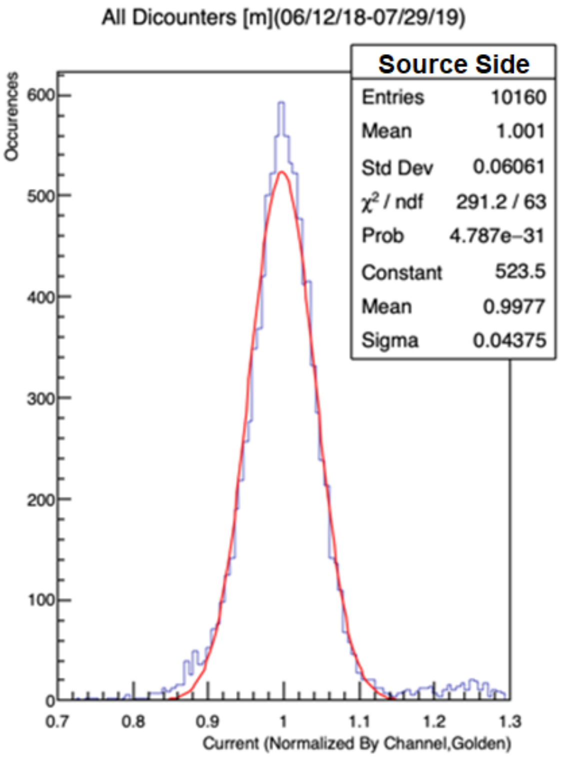

Figure 5.25.: The SiPM response of 1270 dicounters, 2.3, 3.2, 4.55 and 6 m in length, to a Cs-137 source placed 1 m from the readout end, normalized to the the response of a 2.3 m reference counter measured in the same manner. Left: Normalized response from the readout end closest to the source. Right: Normalized response from the readout end furthest from the source.

a light yield that is 20 % or lower than the golden dicounter are discarded; less than 1 % of dicounters are rejected based on this criteria.

5.2. Module Assembly

Previously described in the mechanical design section, a module consists of 32 dicounters, a total of four layers, with eight dicounters per layer. Between each layer is a 9.525 mm thick aluminum absorber. Modules are assembled in accordance with Ref. [119], with the process outlined in this section. Each module is assigned a serial number, which started at 101 and increases monotonically for each assembled module.

The bonding surfaces of the aluminum sheets are first measured upon arrival to ensure they meet specifications. Prior to use they are scrutinized for defects and scored in preparation for epoxy. Aluminum dust from scoring, and other contaminants, are removed by wiping the surfaces clean with isopropanol.

The module assembly table is leveled in accordance with a leveling procedure described in Ref. [120]. Module table flatness is typically within 1.5 mm. The positions of the module components, the dicounters and aluminum, are dictated by cleats installed on the module assembly table (Fig. 5.26).

Dicounters are prepared for module assembly by the application of aluminum tape around the FGB-scintillator interface, as well as the sides of the outermost dicounters in each layer, to prevent light leaks (Fig. 5.27). The bonding surfaces of the dicounters are scored using Scotch-Brite [106] and cleaned of contaminants using isopropanol. A dry-stack is performed and plastic shims, if needed, are placed between dicounters in each layer to evenly space the dicounters across the full width of the module. Typically four 0.51 mm shims are used.

All epoxy used in the module assembly process is Devcon HP-250 [61], applied using electronically actuated dispensing guns with manufacturer recommended mixing tubes. Adhesive strength was found to be sufficient in holding the module together according to the studies presented in Ref. [63]. Module assembly begins by bonding a layer of dicounters to the strongback using epoxy. A bead of black Geocel-3300 RTV [51] is applied to dicounter edges that are on the outer perimeter of the module, and between dicounters at each end, to eliminate light leaks (Fig. 5.28). Using a vacuum lifter [121], an aluminum absorber sheet is bonded to the dicounter layer, which has RTV is applied to all edges. Successive layers are bonded in the same manner. The last layer of dicounters has a 3.175 mm thick aluminum cover sheet bonded to it.

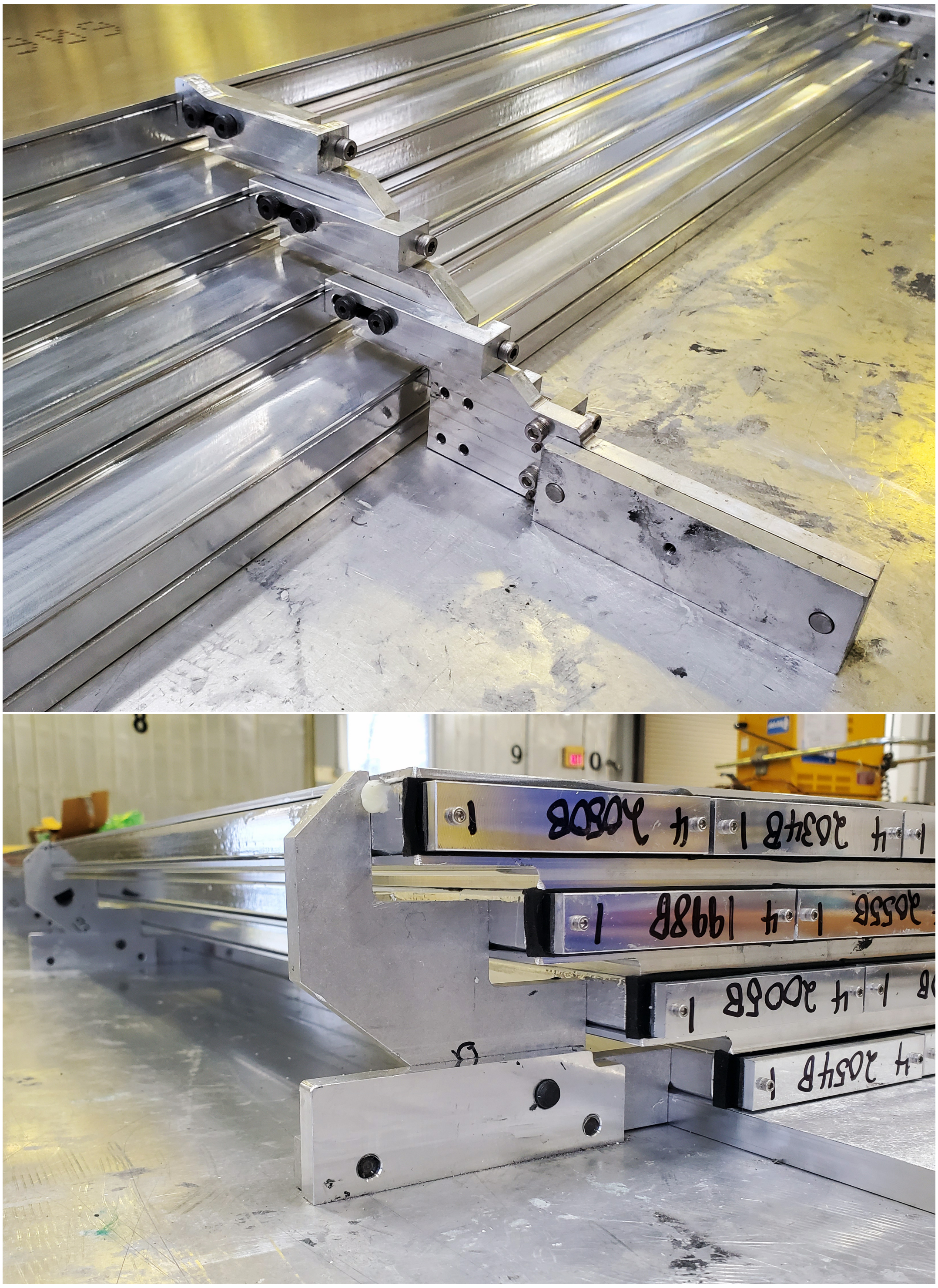

Figure 5.26.: Mounted to the table used for module assembly are cleats that dictate the offset between layers. Shown above are the cleats used for the top and side modules where each scintillator layer is offset by 42 mm. An adjustable cleat (top) forces the dicounters and absorbers against the fixed cleat (bottom) and eliminates gaps between dicounters and constrains the profile of the module to specification.

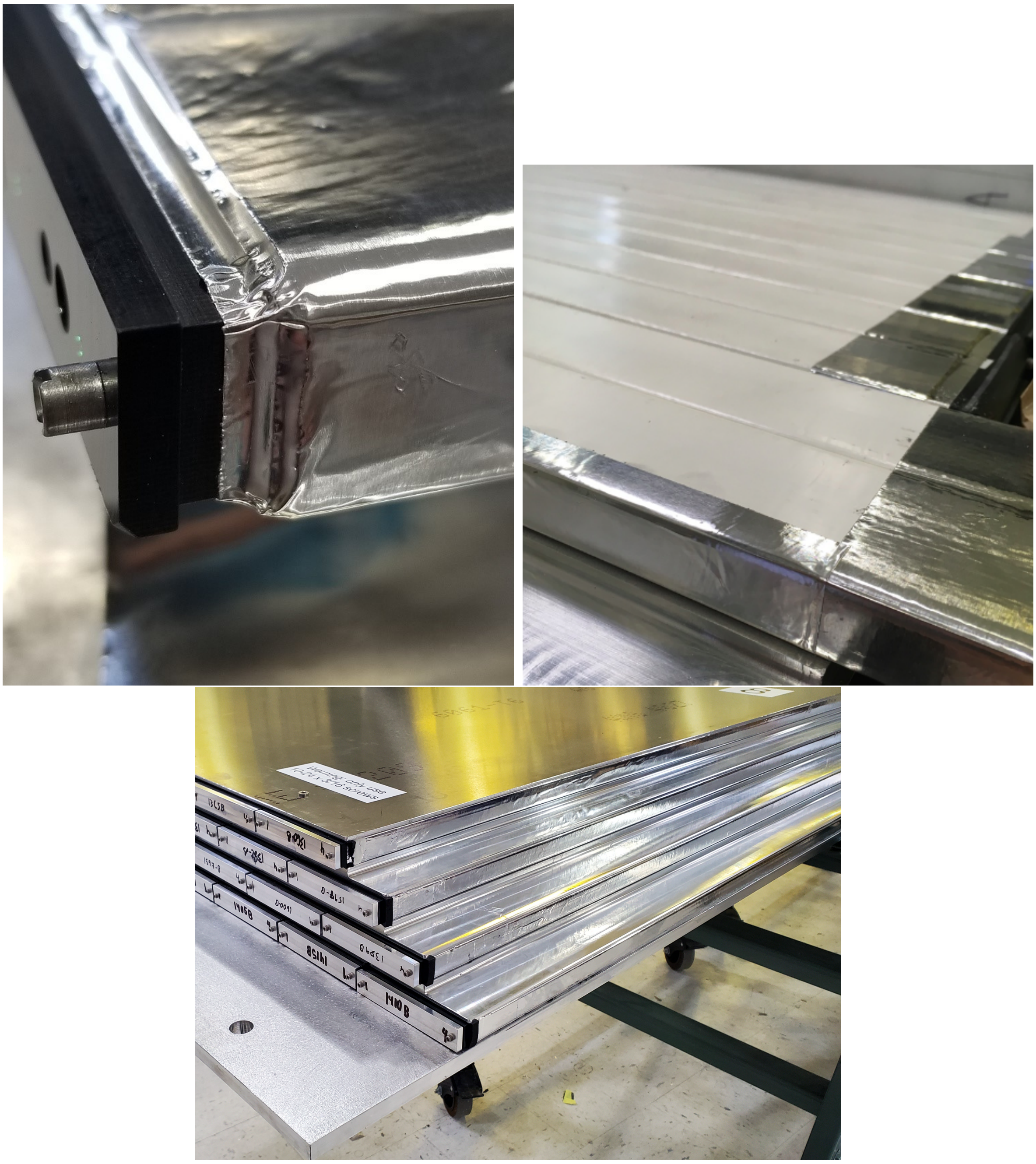

Figure 5.27.: Top left: Aluminum tape applied to the dicounter ends in preparation for module assembly. Top right: Dicounters that are at the outer edges of the modules receive an additional strip of tape along the side. Bottom: the dicounters that are at the edge of a module have tape along their length. The purpose of the tape is to block light from entering the dicounters.

Figure 5.28.: Geocel 3300 [51] black RTV is applied to the outer edges of the module and between dicounters at each end of a module.

Once all the layers are epoxied together, a process that takes about 2 hours on average, the entire assembly is placed under vacuum for 24 hours while the epoxy cures (Fig. 5.29). A plastic sheet is placed over the module to prevent excess epoxy and RTV from contaminating a layer of felt and the vacuum bag, which are reused. The felt acts as a breather fabric that forms an air passage in the vacuum envelope. Vacuum bagging is necessary to ensure adequate adhesion between all interfaces and to press out any warpage in the aluminum. The vacuum is generated using a rotary-vane roughing pump, with an oil trap on the vacuum side to prevent oil contamination of the module, in parallel with a diaphragm pump for redundancy. A back-up generator is available for use in the event of power-outage. A time-lapse video of the assembly of a module is shown in Ref. [122].

After the epoxy is cured, the module is measured for flatness and epoxy and the RTV press-out is removed. Low-friction fiberglass Teflon PTFE coated tape [62] is applied to the long edges for protection (Fig. 5.30). The modules are outfitted with manifolds and undergo light-leak testing using flood lights, shown in Fig. 5.31. Light leaks are found by measuring the current of the SiPMs in the absence of ambient light (dark current) and with flood lights. An increase of 10 % or more is classified as a leak. Areas that allow light into the module are sealed with RTV. Once the module is light-tight, it undergoes extensive testing in the Cosmic Ray Test Stand.

5.2.1. Aluminum Quality Control

Although the aluminum vendor, Pierce Aluminum [123], makes a series of dimensional measurements we specified, the aluminum sheets, upon arrival, are checked by Module Factory personnel for conformity to specifications through a number of measurements. Features, such as the terraced edges, are checked for proper dimensions using calipers and thickness using a Dakota PVX ultrasonic thickness gauge [124] in accordance with Ref.

Figure 5.29.: A module under vacuum, a process necessary to ensure adequate adhesion between all the interfaces of a module and to press out any warpage in the aluminum.

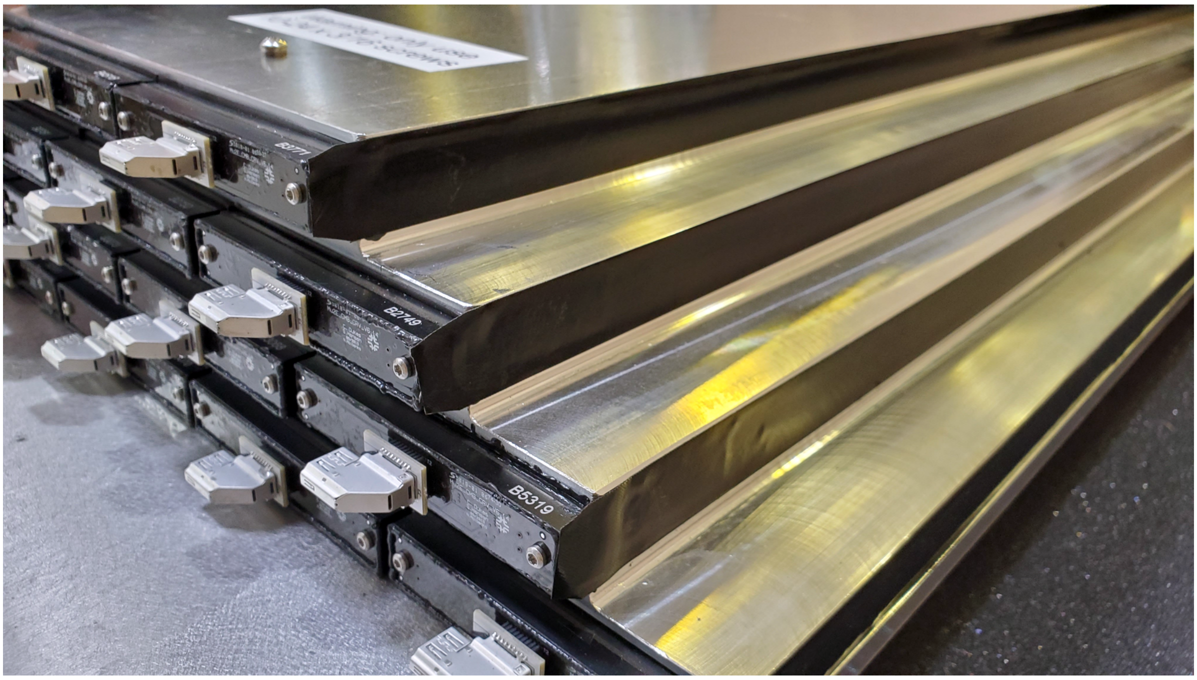

Figure 5.30.: Low-friction fiberglass Teflon PTFE coated tape is applied to the long edges of every module for protection.

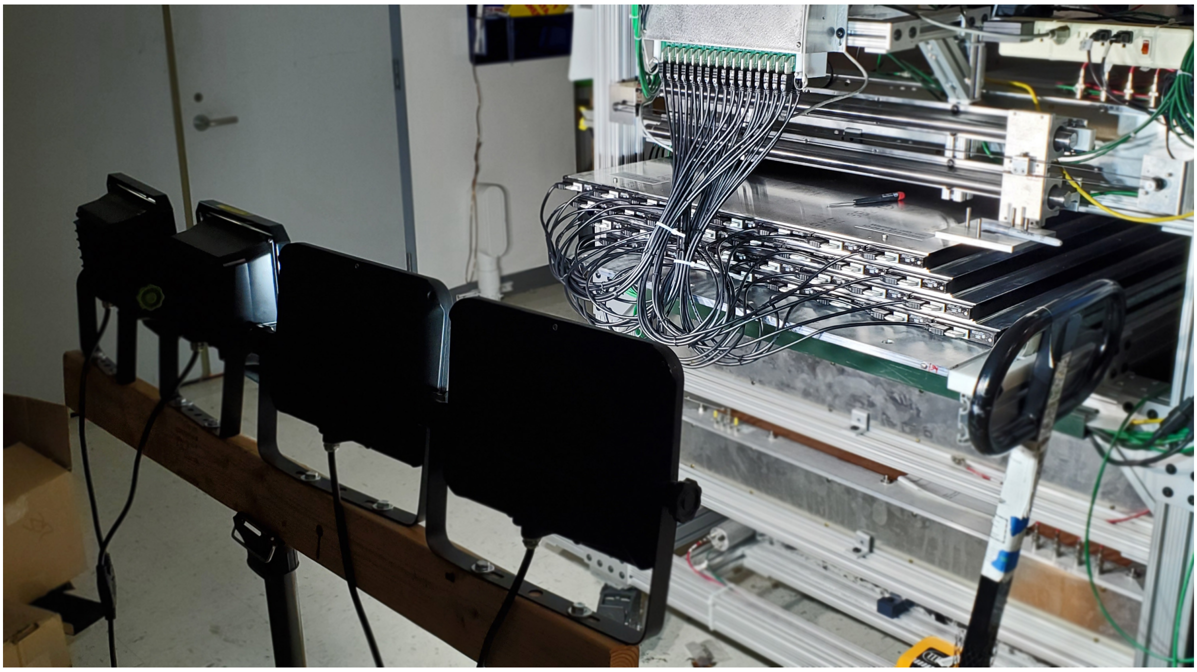

Figure 5.31.: Light tight testing is performed using a series of flood lights by measuring current changes in the SiPMs.

[125]. See Appendix I for a complete list of measurements. Of the 38 modules produced so far, every aluminum sheet has met the specifications within the set tolerances.

5.2.2. Module Shipping

Completed modules are first shipped to and stored at a local freight carrier, Reo Logistics [126]. After staging up to 12 crates of modules, they are loaded onto a Conestoga-type trailer and shipped to Fermilab's Wideband building. A crate design with three different length configurations was developed [127] and a set of eight crates (5.1 m long) were assembled by Basic Crating & Packaging [128]. When placed into a crate, modules are padded with foam and wrapped in a plastic sheet along with two bags of desiccant (1.13 kg total). The modules are fastened to the crate using mounting points on the strongback (Fig. 5.32). Crates are returned from Fermilab to the Module Factory and reused. Drawings of the crates are shown in Appendix S.

A custom logging unit, assembled using off the shelf components from Adafruit [129], records location, temperature, humidity, and acceleration experienced during transit. The collected data is visualized using Google Earth [130] (Fig. 5.33), which allows easy identification of how much acceleration is experienced by the module and where it was located (e.g., on the road, at a rest area, or at a loading dock).

At Wideband, the modules are unpacked and inspected for damage, undergo light-leak testing, and are evaluated for mechanical interface with other modules.

Figure 5.32.: A module loaded into a shipping crate. The ends of the module are fixed to the crate, taking advantage of mounting points on the strongback. Foam padding is placed above and below the module.

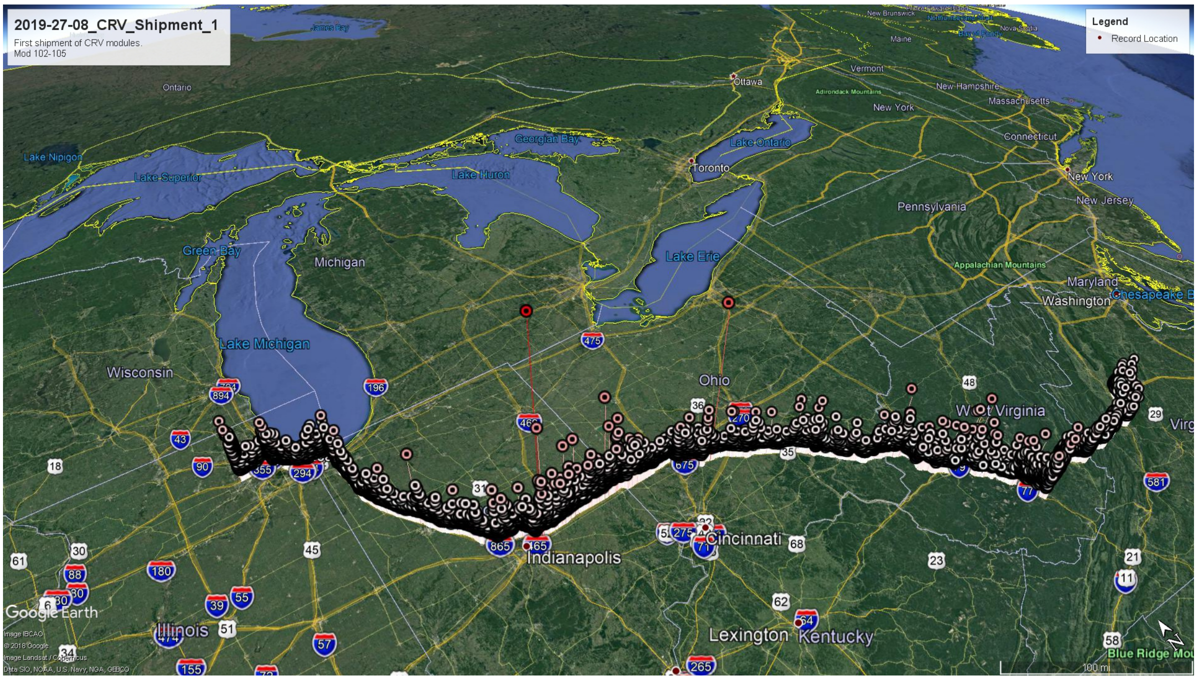

Figure 5.33.: The acceleration experienced by the first module shipment to Fermilab. The height, color, and location of the marker indicate the magnitude of the acceleration and location it was experienced (the maximum shown here was 10 G).

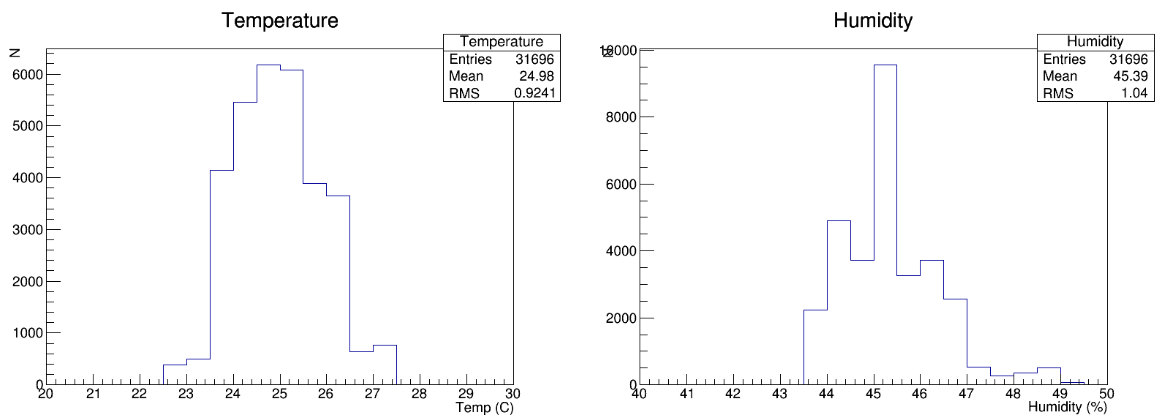

Figure 5.34.: The temperature (left) and humidity (right) measured during shipment of the first four fabricated modules.

5.3. Module Performance

5.3.1. Cosmic Ray Test Stand

Modules are evaluated for light yield and per-layer detection efficiency in the Cosmic Ray Test Stand (CRTS). The CRTS is a scintillator-triggered test stand that uses cathode strip chambers (CSCs) to provide tracking information for use in module quality control. The decision to use CSCs was made due to an availability of spare parts to assemble the chambers. Because having an adequate light yield is paramount for the CRV to meet its efficiency requirement, this is the most valuable test of each module prior to being shipped to Fermilab. The apparatus, shown with a module under test, is presented in Fig. 5.35. The frame of the CRTS was assembled from commercially available T-slot aluminum extrusions [131]. Due to space limitations in the module factory, the entire assembly was required to be self-contained and mobile, and so was fitted with rubber casters. Located on the test stand and as several movable entities, roller tables are used to support and move modules through the test stand (Fig. 5.36).

Contained in a rack on the CRTS are several electrical systems. Shown in Fig. 5.37, a Tripp-Lite SmartPro 2U uninterruptable power supply [132] provides power to all electrical components on the test stand. Power strips provide power for two DAQ computers (one for the CSCs and one for the module FEBs), a NIM crate, and the four FEBs required to read out a module. An Agilent 5761A 1080 W power supply [133] and NOvA power distribution box [57] provide power for the readout electronics of the CSCs. A NIM crate contains the trigger logic and high voltage for the CSCs and the photomultiplier tubes that read out the scintillator paddles. An additional transformer provides low voltage power for fans used to cool the readout electronics, which are contained within Faraday cages.

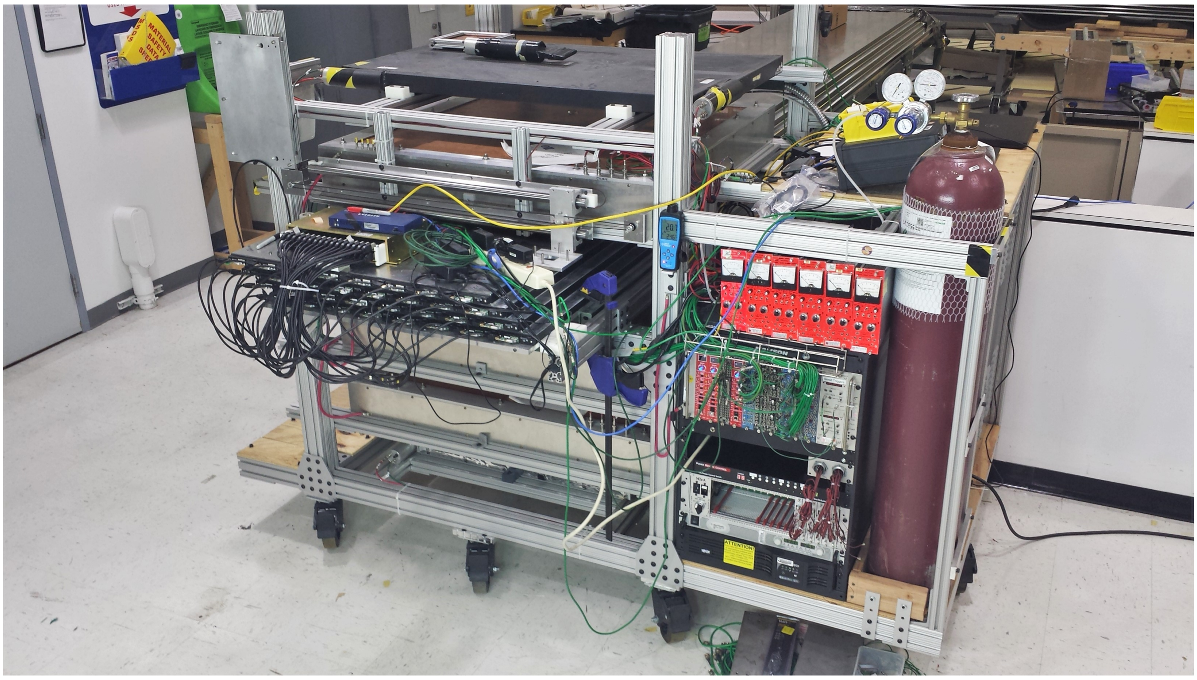

Figure 5.35.: Image of the entire Cosmic Ray Test Stand, shown with a module under test.

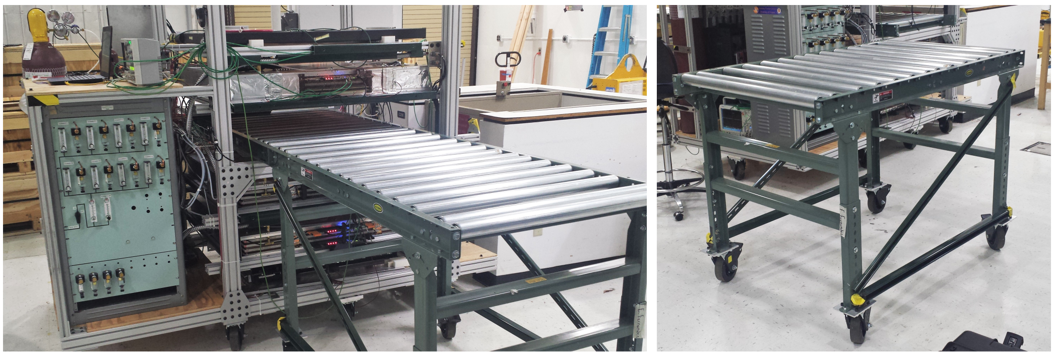

Figure 5.36.: The CRTS is fitted with a roller table (left) to allow modules to be fed into the test stand. Stand-alone roller tables (right) can mate with the test stand and are used to move modules through the test stand.

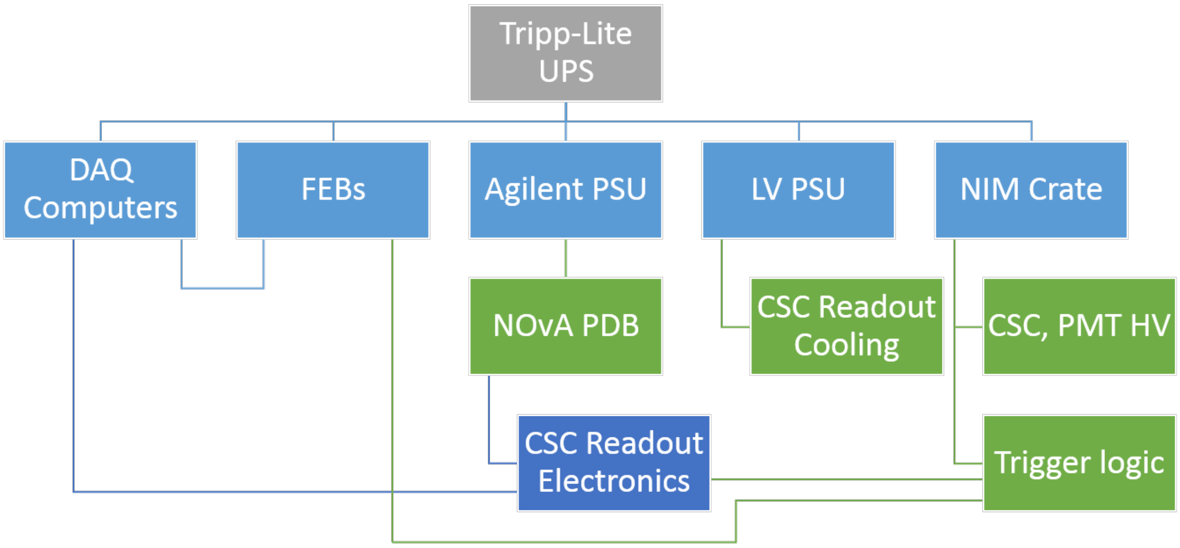

Figure 5.37.: Schematic of the electrical components and their connections within the CRTS.

Cathode strip chambers for use in particle tracking offer a number of beneficial features: reliable and low maintenance operation, high detection efficiency, and good position resolution. They operate on the principle of a strong electric field accelerating electrons that are liberated from the gas volume during the traversal of a charged particle, resulting in an electron avalanche at an anode wire. Charge accumulation at the wire induces charge on the adjacent cathode strips. A precision measurement of the charge induced on each strip provides particle position information. Figure 5.38 shows an example of the charge measured on a series of strips as a result of a particle passing through the detector. The green distribution on the anode wire represents the charge from the electron avalanche, while the vertical bars represent the charge measured on each strip due to induction by the wire. The cathode strip chambers in the CRTS use an 80 % Argon, 20 % CO_2 gas mixture [134], which provides the necessary electron lifetime and quenching of emitted light, respectively. This gas is supplied by a K-type cylinder

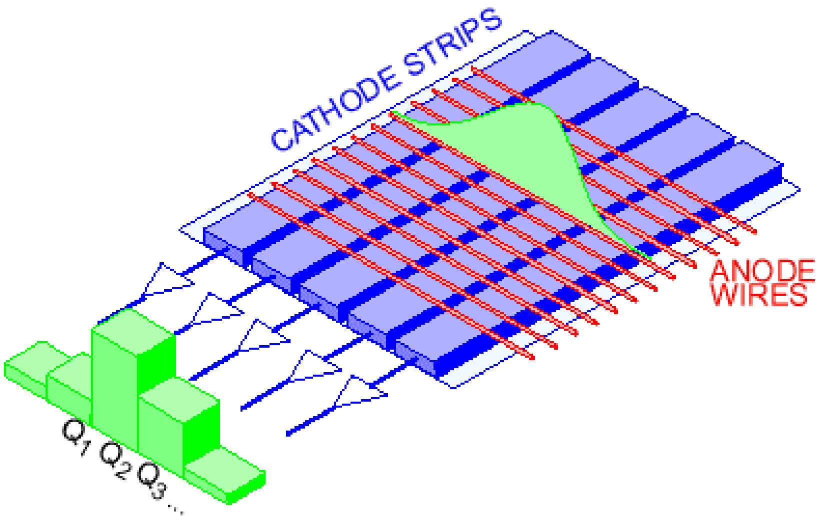

Figure 5.38.: Example of the typical distribution of charges seen in a cathode strip chamber due to the ionization of gas from a passing charged particle. The green distribution on the anode wire is the induced charge distribution due to electron avalanche at the wire. The vertical green bars at the end of each strip represent the charge measured on each strip [135].

attached to the CRTS and a gas distribution rack built specifically for the chambers. The rack contains a low-pressure regulator, three flow meters, and three mineral-oil bubblers, one for each chamber. A schematic of the gas system is presented in Fig. 5.39.

A total of four chambers were assembled and tested at Fermilab [136]. Three chambers are in the CRTS, another chamber is located at Brookhaven National Lab. Only two of the three chambers on the test stand are used. The specifications for the CSCs are listed in Table 5.1. Each chamber has a 0.894 m $\times$ 0.894 m active area. The active area is spanned by 299 gold-plated 50 μm diameter tungsten anode wires spaced 3 mm apart, with a total of two gold-plated 200 μm diameter copper-beryllium edge wires. There are a total of four anode wire planes and all wires run in the same direction, parallel to high-voltage connectors. On both sides of each wire plane are a set of 64 copper cathode strips, 13.46 mm wide with a 13.96 mm pitch, running parallel and perpendicular to the wires to form an X-Y plane (Fig. 5.41). There are a total of four X planes and four Y planes. The wires run parallel to the Y planes. Each cathode strip panel is a

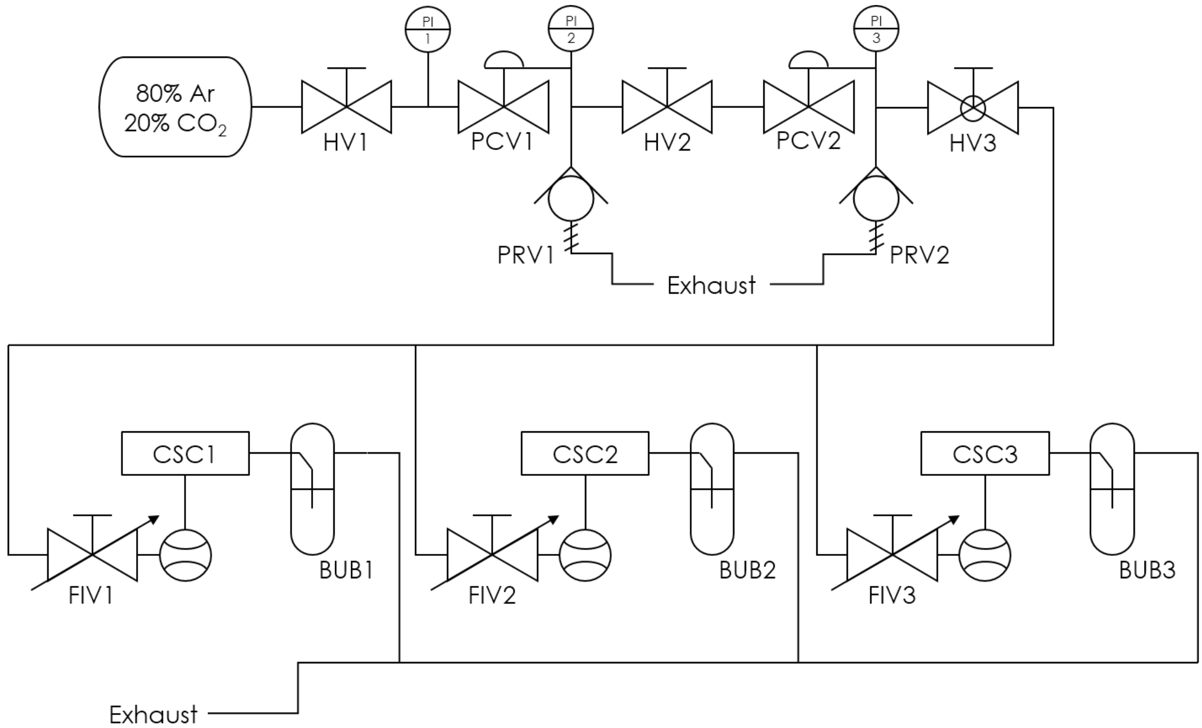

Figure 5.39.: Schematic of the gas system that services the cathode strip chambers of the CRTS. HV1 is a manual valve on the cylinder. PI1 is a high-pressure gauge before the pressure regulator PCV1, which regulates the pressure to 6.9×10^4 Pa (10 PSI). PI2 is a gauge that shows this regulated pressure. PRV1 is a pressure relief valve set to open at 7.0×10^4 Pa. HV2 is a manual valve between PCV1 and a downstream secondary regulator PCV2, which regulates the pressure to 3.4×10^4 Pa (5 PSI), displayed by gauge PI3. PRV2 is a second pressure relief valve that is set to open at 4.1×10^4 Pa (6 PSI). HV3 is a quarter-turn manual valve that is used to isolate the chambers from the regulated pressure. The flow indicator valves (FIV1–FIV3) are used to adjust the gas flow through each chamber, set at 50 cc/min. The bubblers (BUB1–BUB3) indicate gas flow and prevent back-flow of ambient air into the chambers.

Table 5.1.: Cathode strip chamber specifications.

Panel type	Polycarbonate honeycomb with copper-clad FR-4 laminates
Panel thickness	15.9 mm
Number of panels	5
Number of cathode planes	8
Number of cathode strips	64 /plane
Cathode width	13.46 mm
Cathode pitch	13.96 mm
Gap between cathodes	9.52 mm
Number of anode planes	4
Number of anode wires	299 + 2 edge wires
Wire pitch	3.175 mm
Anode wires	50 μm diameter gold-plated tungsten
Edge wires	200 μm diameter gold-plated copper beryllium
Active area	894 mm × 894 mm
Gas mixture	80 % Argon, 20 % CO_2

15.9 mm thick polycarbonate honeycomb laminated with copper-clad FR-4. The anode wires are at a positive high voltage and the cathode strips are at ground. The spacing between each panel is 9.52 mm, which yields 4.76 mm of clearance between the wires and strips. The gas mixture flows through this region. The cross section of a chamber is shown in Figs. 5.40 and 5.41. The chambers are hermetically sealed but have a leak rate of 5 cc/min. The flow rate of gas through each chamber is 50 cc/min, which provided sufficient gas for gain and quenching (spark prevention).

Described in Ref. [136] and shown in Fig. 5.42, the chamber efficiency was measured as a function of high voltage using signals from the anode wire planes. This was used to set the operating voltage for each plane.

Readout of the chambers is done by custom-made boards that feature a VMM3 ASIC designed for use in the ATLAS New Small Wheel upgrade [137]. Each board (Fig. 5.43) has 64 charge-sensitive input channels and is connected a single 129 pin header (Fig. 5.44)

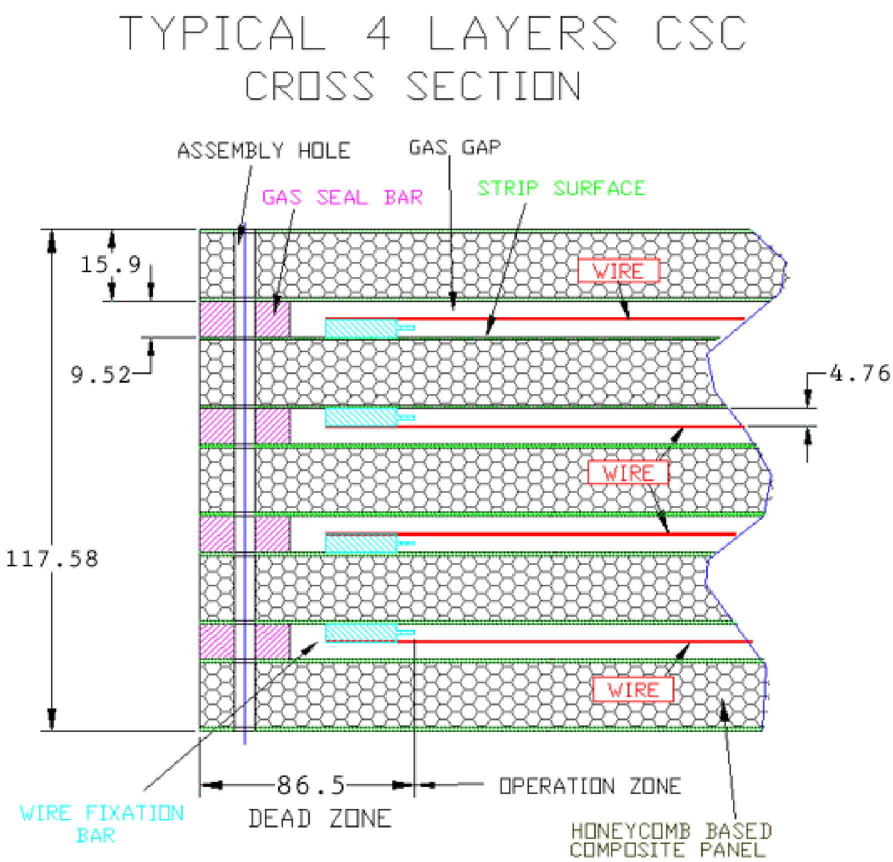

Figure 5.40.: Cross section of a cathode strip chamber. Five honeycomb panels make up four planes for particle tracking. Located midway between panels in the gas volume, the spacing defined by plastic bars that provide support and sealing of each layer, sit the anode wires. Each wire is tensioned across a fixation bar. Located on the inner surfaces of each panel, on both sides of the wires, are the cathode strips.

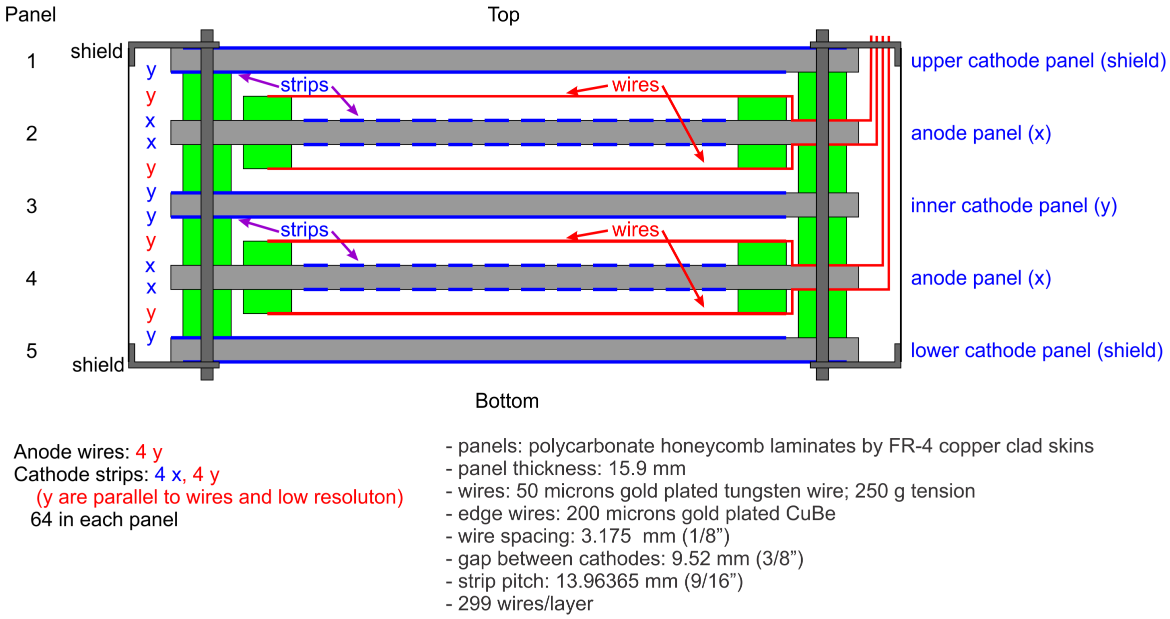

Figure 5.41.: Arrangement of cathode strips and anode wires within each cathode strip chamber.

used to read out a cathode strip plane (64 channels of strip/ground connection pairs and one additional ground pin). Power to the boards is delivered through a barrel jack with on-board 42 V to 3.3 V DC-DC converters. An Agilent power supply [133] provides up to 100 A at 6 V. A collection of LEMO connectors provides cathode strip analog output, cathode strip digital output, and trigger input. The charge gain is variable from 0.5 mV/fC to 16 mV/fC and the time resolution is 1 ns. Each channel has a four-deep digital FIFO buffer for storing hits, defined as integrated charge above a set threshold, and their associated time stamps relative to the board clock in units of TDC (1 ns/TDC). Data readout was initiated by an external signal received from the test-stand trigger logic. The time stamp of the trigger relative to the board clock was also read out. Due to the slow trigger rate (30 Hz) and higher noise rates in the chambers, the FIFO buffers were always full. Shown in Fig. 5.45 is the time difference, in units of TDC, between the hit time and the trigger time. A cut is placed on the time difference, from −10 TDC to 0 TDC, and all hits within this window are accepted.

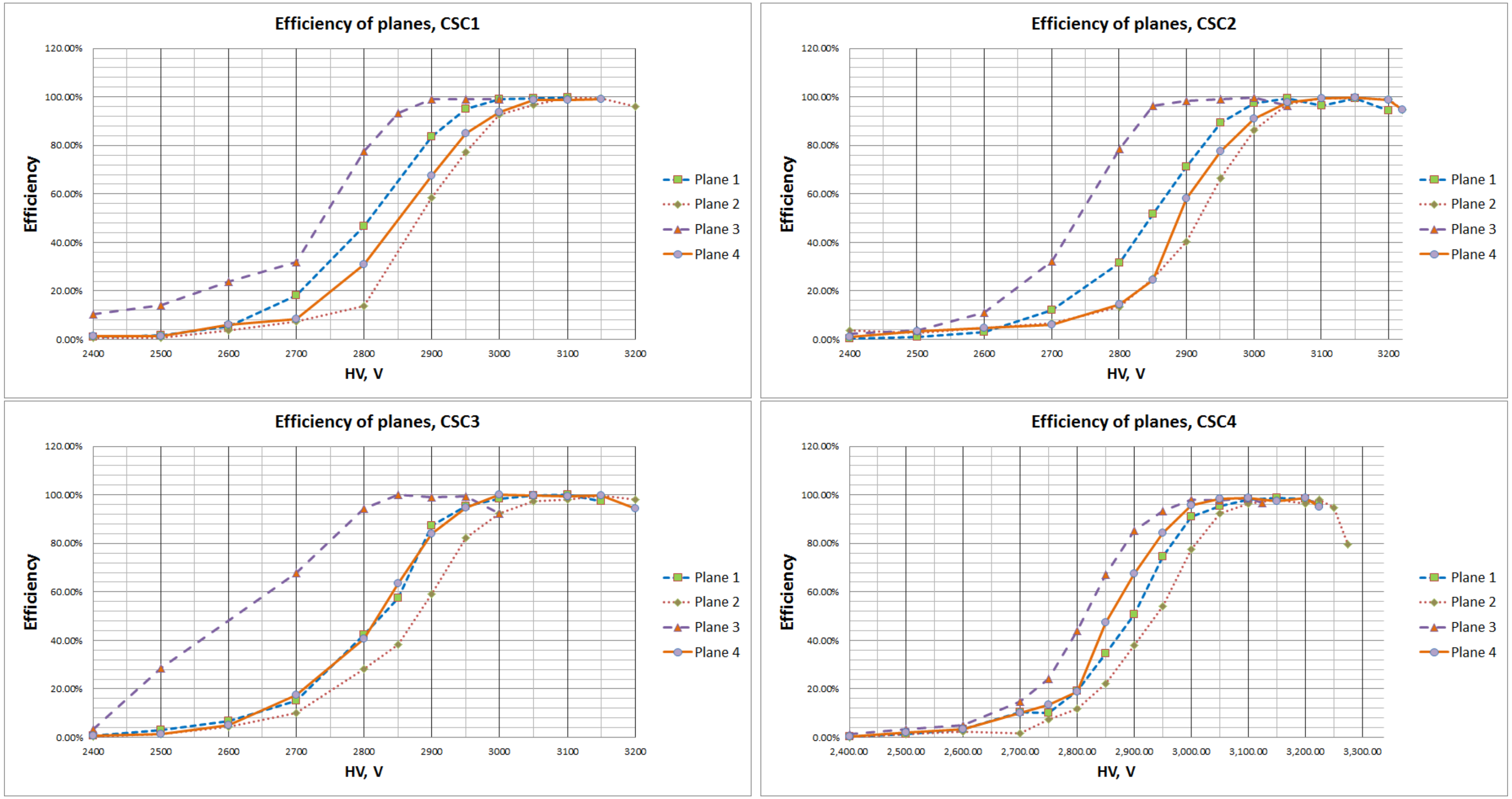

Figure 5.42.: Efficiencies plotted as a function of voltage for each anode plane of each cathode strip chamber. The process for determining chamber efficiencies is presented in Ref. [136]. This was used to set the operating voltage for each plane of every chamber.

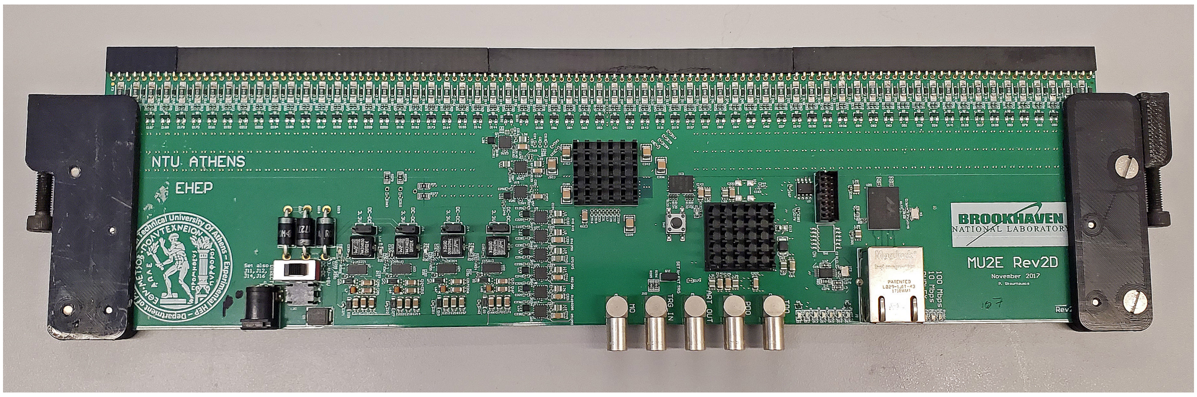

Figure 5.43.: A photograph of a custom-made board, which employs a VMM3 ASIC [137], used to read out the cathode strips of the CSCs in the CRTS. Along the top edge is a 129 pin header that interfaces with the CSCs. Data is transferred via a Cat6 Ethernet connection. The board is triggered via a LEMO connector. Power is supplied through a barrel-jack. On the left and right side of the board is the mounting hardware.

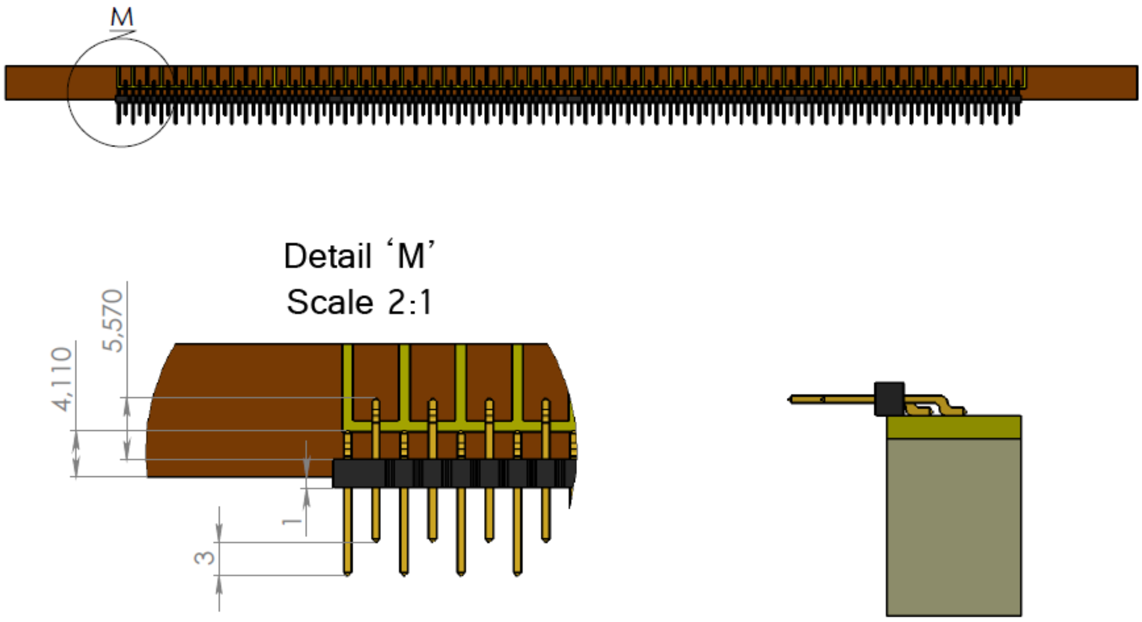

Figure 5.44.: The 129-pin header used for readout of a single cathode strip plane. There are 64 strip/ground pairs plus an additional ground pin.

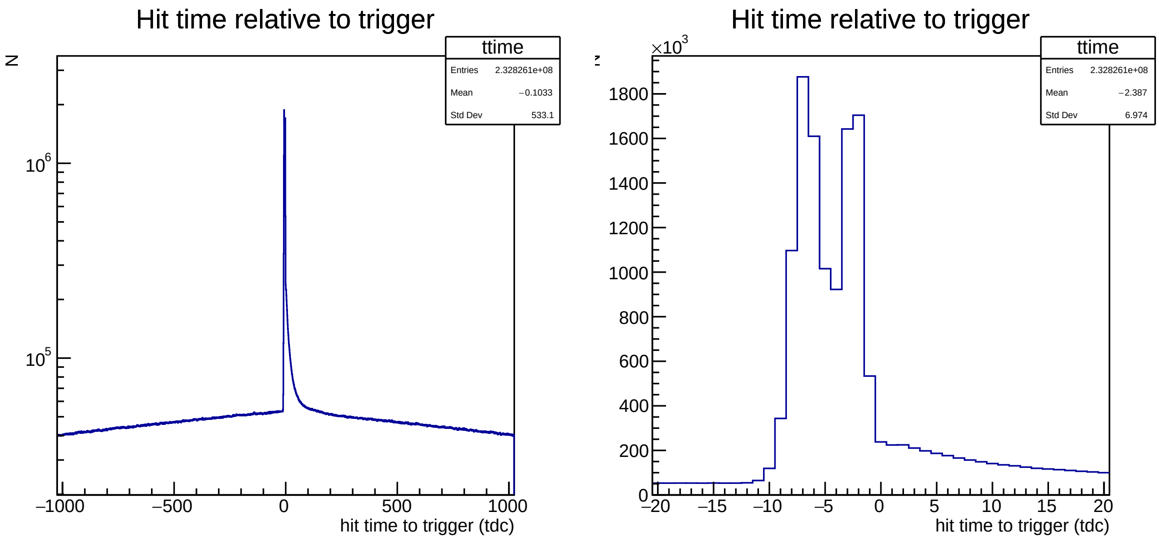

Figure 5.45.: Frequency of hit times relative to the trigger time, in units of TDC (1 ns/TDC), for all planes of two chambers in single run of 700,000 triggers. The time difference is the hit time minus the trigger time. The plot on the right is a magnified view of the plot on the left. The peaks are the hits associated with the trigger signal. A cut on the time difference, from −10 TDC to 0 TDC, kept only hits associated with the trigger. The double peak visible in the plot on the right are the of the time-of-flight differences between the upper and lower chamber.

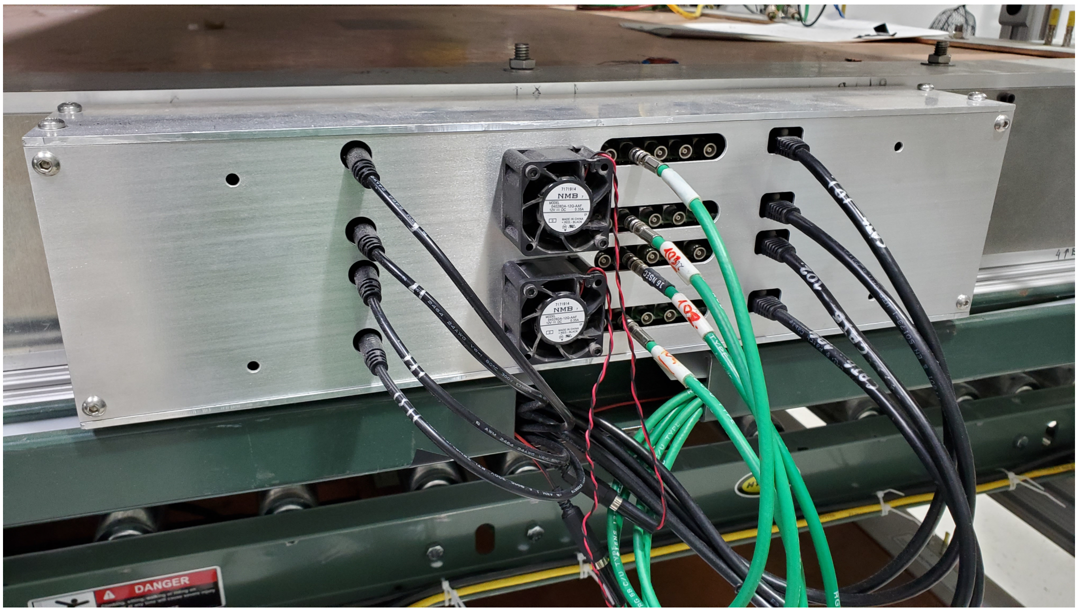

Figure 5.46.: Photograph of a Faraday cage that isolates the CSC digitizer boards from RF noise. Connections for DC power (left), trigger (middle), and DAQ (right) are also shown here. Brush-less fans provide cooling.

Connection to each board for data acquisition is made over Ethernet, through a 24-port switch, to a Unix DAQ computer. Special mounting hardware was designed and 3D-printed, shown in Fig. 5.43, that allows installation and removal of the digitizer boards without damage to the chamber. To reduce the effects of RF noise picked up by the chambers, Faraday cages were designed and installed around the boards, shown in Fig. 5.46. All sides of the chambers are shielded. Brush-less fans provided cooling for the boards.

Readout of both the CSC digitizer boards and the module FEBs is initiated by triggers generated from coincidences between scintillator counters at the top and bottom of the test stand, shown in Fig. 5.47. The top counter is 1260 mm × 752 mm × 51 mm and the bottom counter is 865 mm × 865 mm × 51 mm. Shown in Fig. 5.48, each counter has two WLS bars on two edges, read out by Hamamatsu R2154-02 photomultiplier tubes (PMTs) [138]. Drawings of the scintillator counters are shown in Appendix P. Signals from the PMTs that are above a 100 mV threshold are converted to 60 ns long NIM-logic

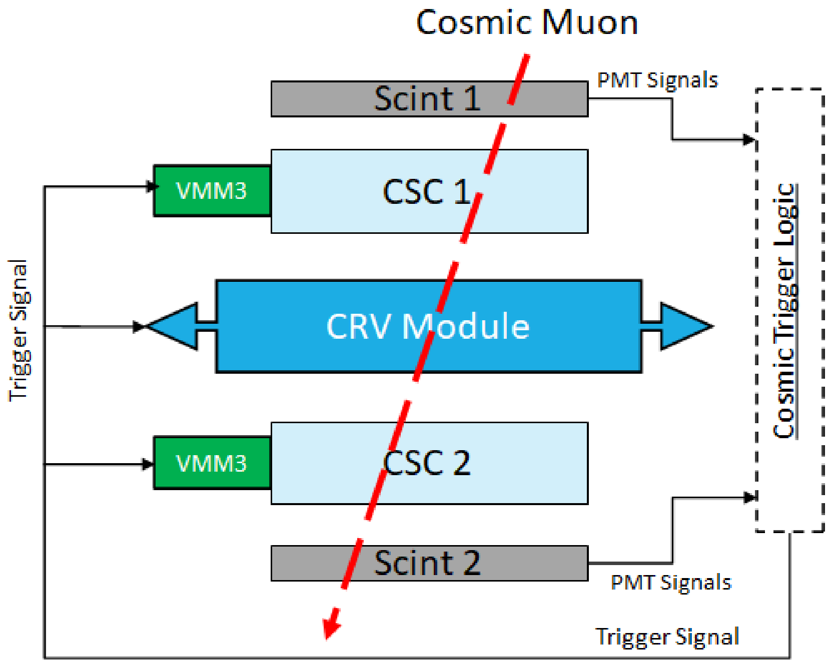

Figure 5.47.: Schematic showing the location of the scintillator counters that trigger readout of the cathode strip chambers and CRV module Front End Boards in the Cosmic Ray Test Stand.

level signals through the use of a LeCroy 623 discriminator [139]. For track purity, a four-fold coincidence is formed between the top and bottom counters using a Phillips 755 coincidence module [140]. The output is a 100 ns wide pulse. Due to the time required to read out hits in the CSC digitizer boards, a 1.0 ms trigger hold-off is introduced by a Phillips 794 gate generator [141]. In addition to the trigger hold-off, triggers are only enabled during the first 7 seconds of a 10 second long spill gate. The remaining 3 seconds are used for reading out the module FEBs. Converted to the appropriate logic level and distributed using Phillips 726 translator [142] and LeCroy 429A logic-fan in/out modules [143], the triggers are delivered to the CSC digitizer boards and CRV FEBs. A schematic of the trigger logic is shown in Fig. 5.49.

The operating voltages of the photomultiplier tubes used to read out the scintillator counters were found by taking the ratio of the number of four-fold coincidences to the number of three-fold coincidences, omitting the PMT in question. The number of

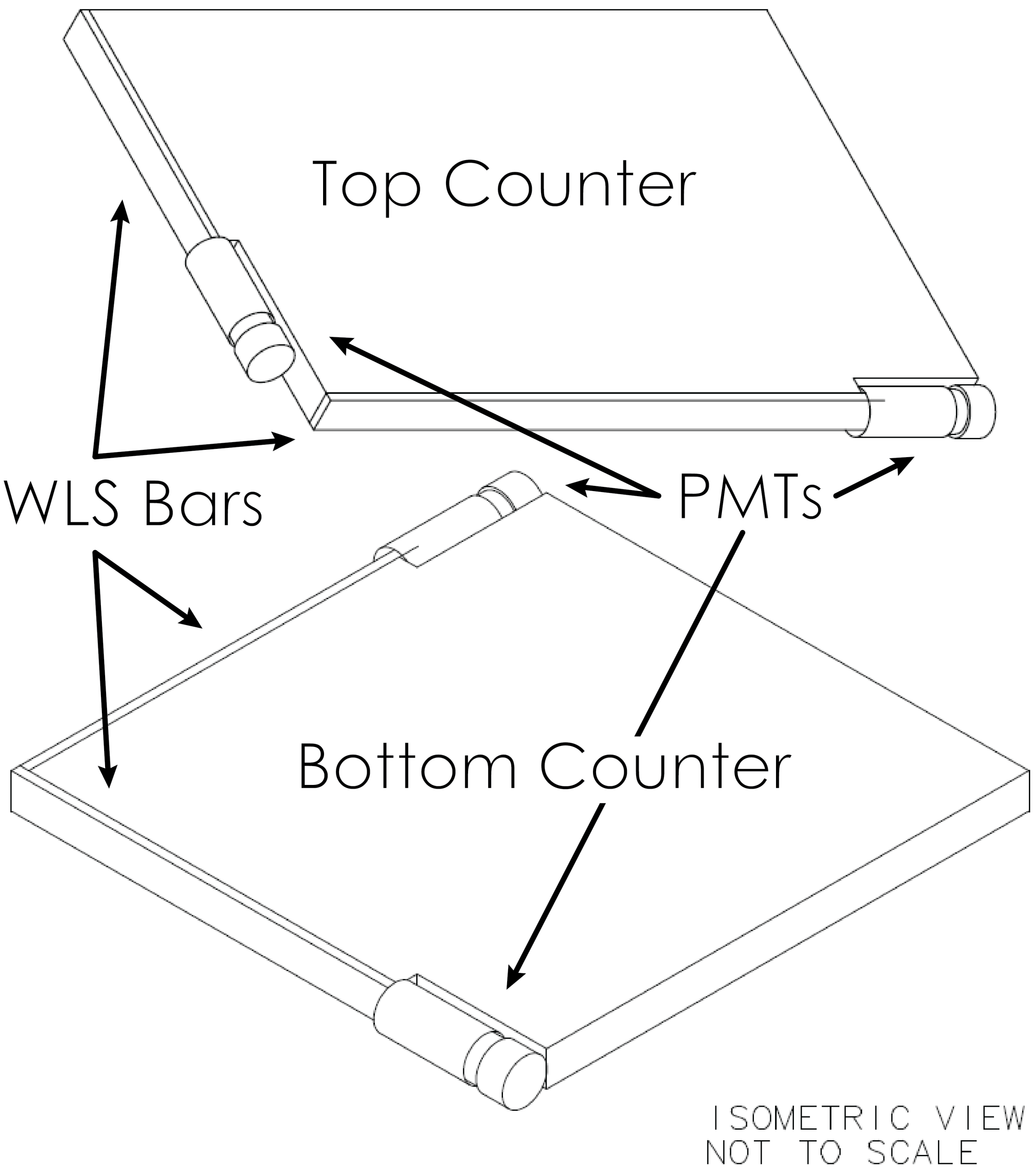

Figure 5.48.: The scintillator counters used for triggering in the CRTS. There are two edges with WLS bars that are read out by Hamamatsu R2154-02 photomultiplier tubes [138].

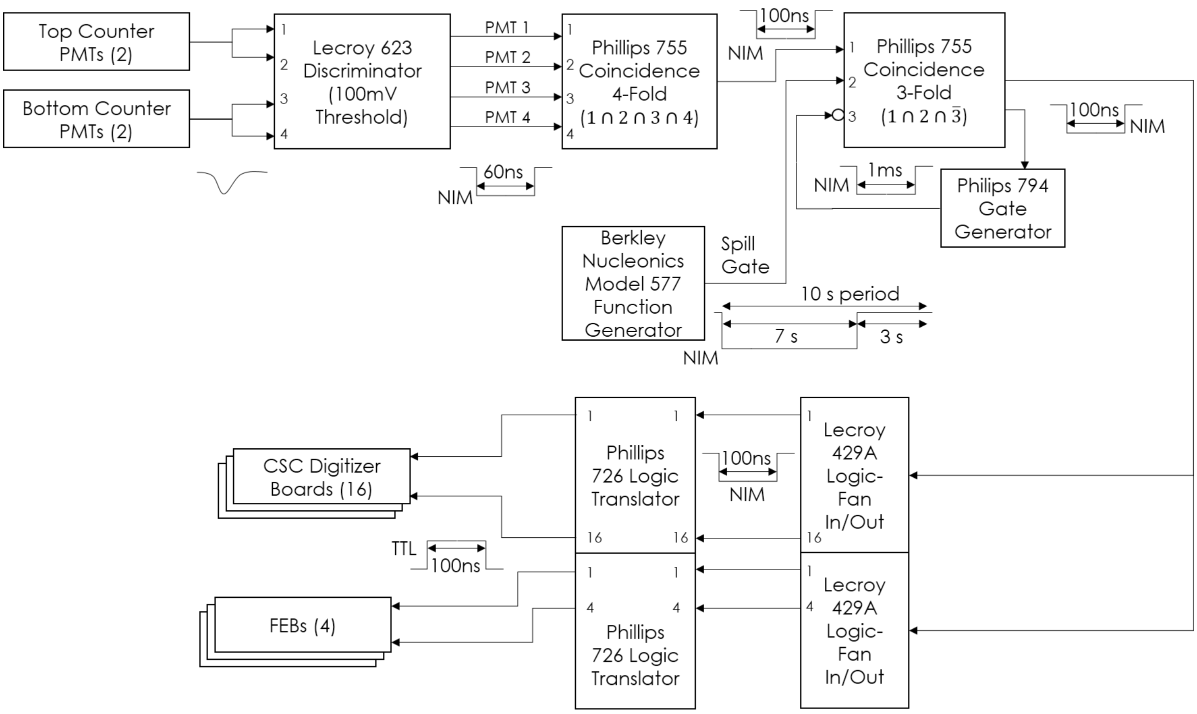

Figure 5.49.: Schematic of the trigger logic used in the Cosmic Ray Test Stand.

coincidences was recorded over a 100 second period at different voltages. The plateaus and operating voltages are presented in Ref. [144]. All PMTs have efficiencies greater than 98 % at their operating voltages.

Using a Berkeley Nucleonics Model 577 pulse generator [145], a 10 second spill gate is generated for the module FEBs and the CSC digitzer boards. During the first 7 seconds of the gate triggers are enabled. During the remaining 3 seconds of the gate triggering is disabled so data from the FEBs can be transferred to the FEB DAQ computer. Data from the CSC digitizer boards are received continuously during the spill gate by the CSC DAQ computer. Because each trigger is shared by both systems, events are synchronized by trigger number.

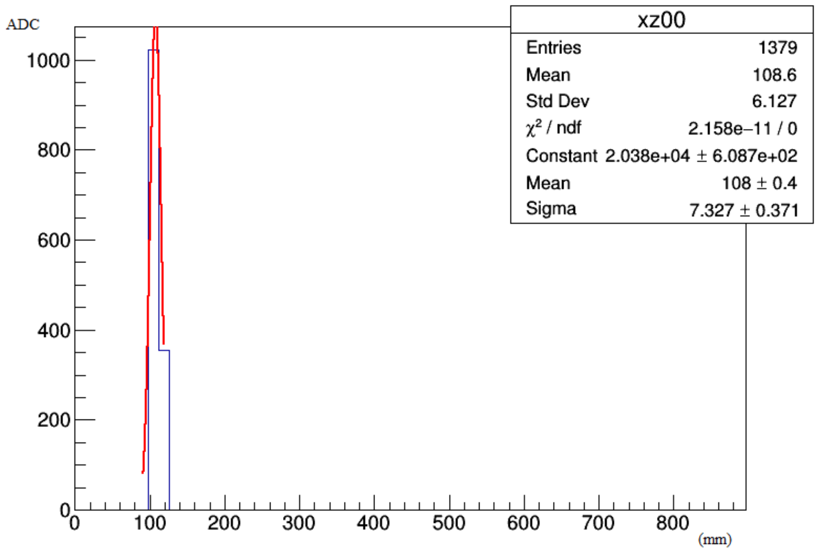

Figure 5.50.: An example of a Gaussian fit for two strips with measured charge for a single cathode strip chamber plane.

5.3.2. Module Light Yield

Cosmic-ray muon tracks are reconstructed from the CSC data. Only two chambers are used for tracking: one above and one below the module. Particle positions in each plane are determined by fitting a Gaussian to the measured charge. The choice of a Gaussian fit is consistent with the actual distribution of charge as described in Ref. [146]. Spurious noise is infrequent and has a low measured charge, so only the strip reporting the highest charge and its neighboring strips are used in the fit. An example is shown in Fig. 5.50 where the track position in plane was determined by fitting a Gaussian to the two strips that had charge above threshold. For tracking, it is required that there be at least one X and one Y hit per chamber. A straight line fit is made using all positions, and cuts are placed on the quality of the fit ($\chi^2 < 2$). Residuals are on the order of 2.6 mm (Fig. 5.51 and Appendix Q.1), and the position resolution is around 0.5 mm (Fig. 5.52).

Modules are evaluated in the test stand centered at 1 m from each readout end. Due to the geometry of the test stand, shown in Fig. 5.53, this means that response

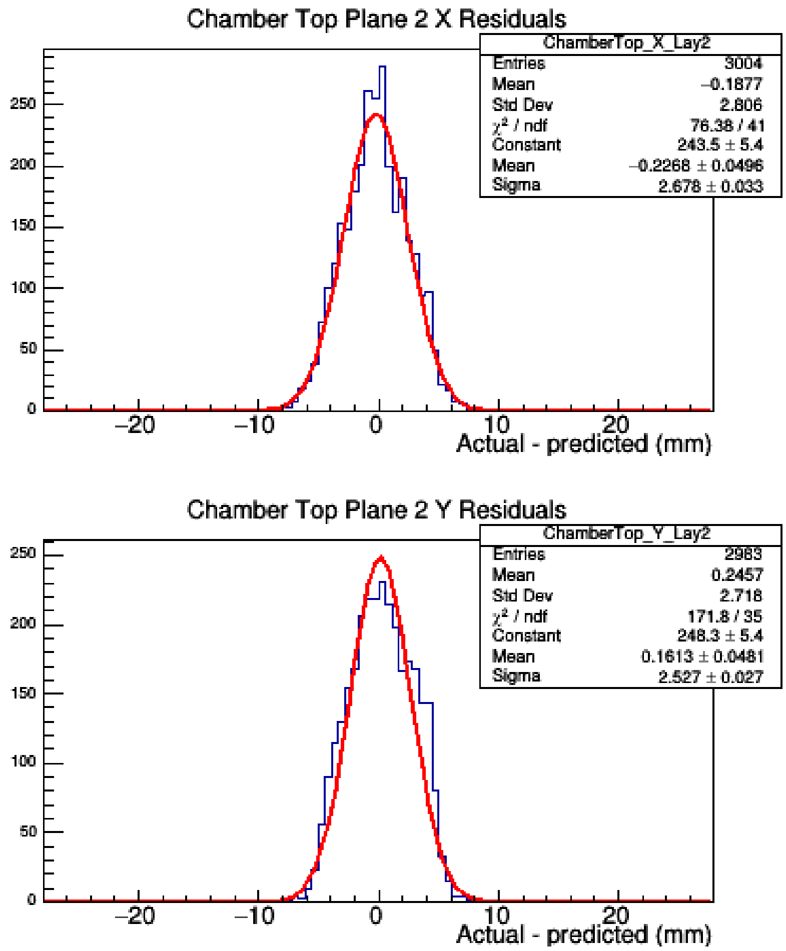

Figure 5.51.: The residuals for the third X plane (top) and third Y plane (bottom) of CSC 1. The red line is a Gaussian fit to the distribution. The residuals are computed as the actual hit position minus the predicted hit position using a trajectory from other planes.

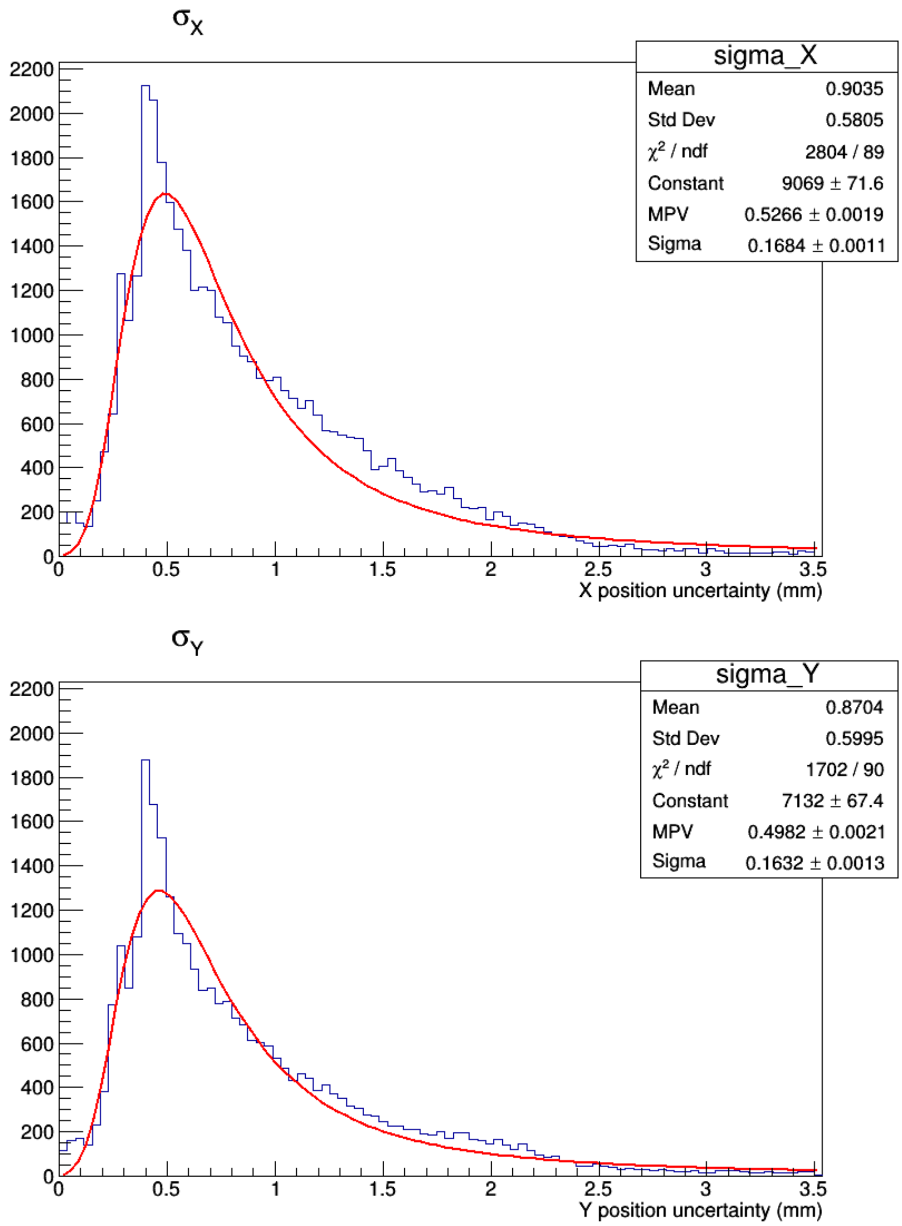

Figure 5.52.: The uncertainty on the track position at the module being tested in the X dimension (top) and Y dimension (bottom). The red lines are a Landau fit to the distributions.

from approximately 0.6 m to 1.4 m from the readout end is recorded. Calibration for single photoelectrons is determined using pedestal-subtracted noise data. The pedestal is found by using the most probable ADC value in the pre-signal region, which is the first 75 samples or roughly 1000 ns. The pedestal does not include contributions from photoelectrons. First and second photoelectron signals versus time are fit using a Gumbel distribution [86] and the integral is computed. The distribution of integral values, in units of ADC $*$ ns, shows peaks associated with the first and second photoelectrons and are fit using a Gaussian distribution. The means of the Gaussian fits represent the expected integral value for each photoelectron number. Linear regression is used to determine the relationship between the integral values and the number of photoelectrons.

For events that have valid tracks (around 40 %) the light yield per centimeter path-length is computed in the scintillator by summing the total photoelectrons for counters that were hit along the track and dividing it by the path length through the counter. The path length is found by using the reconstructed track from the CSCs for the counter of interest. Only tracks near the center of the counter are used, which eliminates short path lengths due to tracks grazing the edges of the counter as well as the effects of track position uncertainties. The path length computed using track information from the CSCs is shown in Fig. 5.55. An example showing a cosmic-ray muon passing through a module and generating light in several counters is presented in Fig. 5.56. The light yields per centimeter of path length per SiPM for five of the first modules produced are presented in Fig. 5.57. Modules 101 to 105 are single-ended readout (reflectors on the opposite end) CRV-TS modules (6 m long). Module 107 is a CRV-L-Endcap module (3.2 m long). The mean path-length light yield at 1.0 ± 0.4 m from the readout end was 25 ± 2 PE/cm per SiPM.

A major problem with the readout electronics for the CSCs prevented any more than sporadic use in module light yield measurements: the digitizer boards, individually, reset

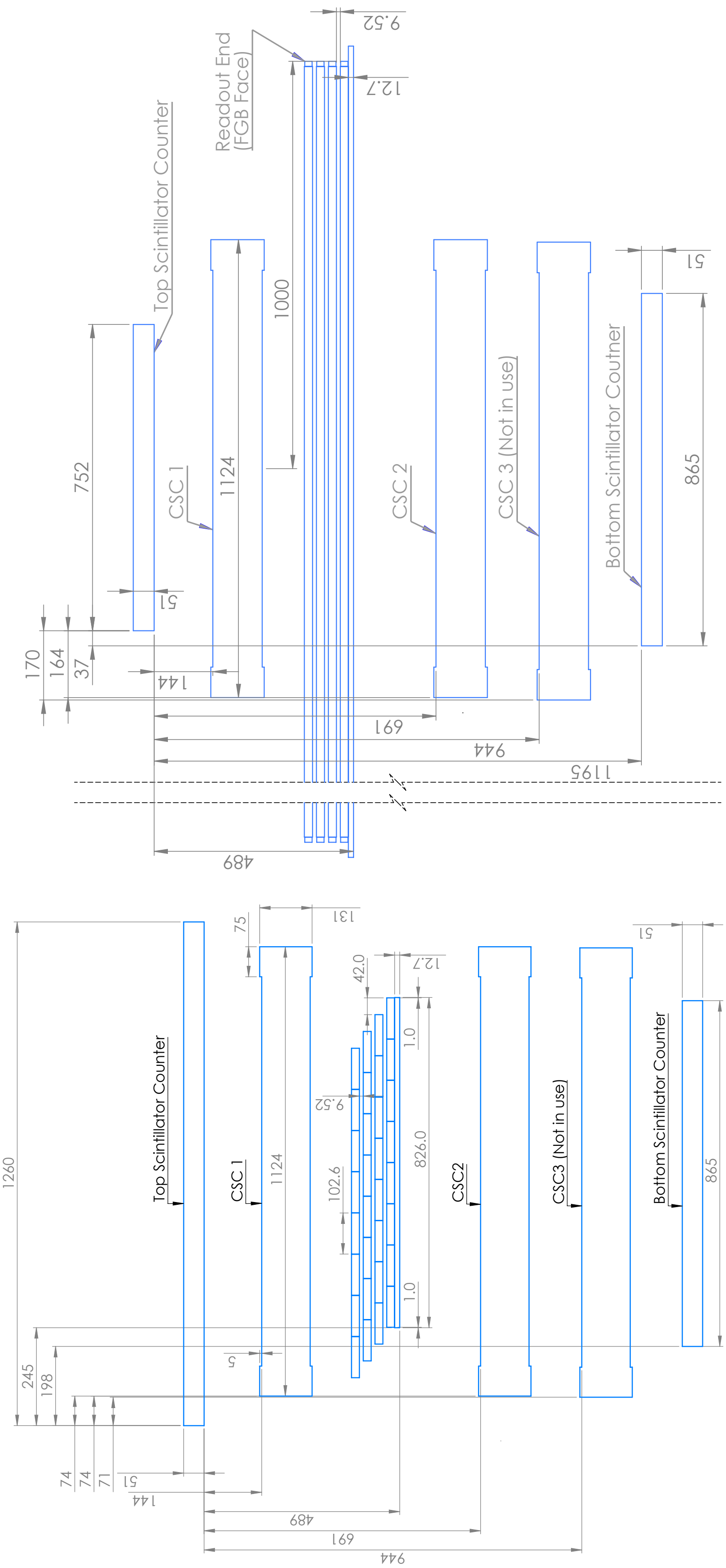

Figure 5.53.: The geometry of the Cosmic Ray Test Stand, along with the profile of a CRV-T module. Left is the end view; right is the side view. All units are in millimeters.

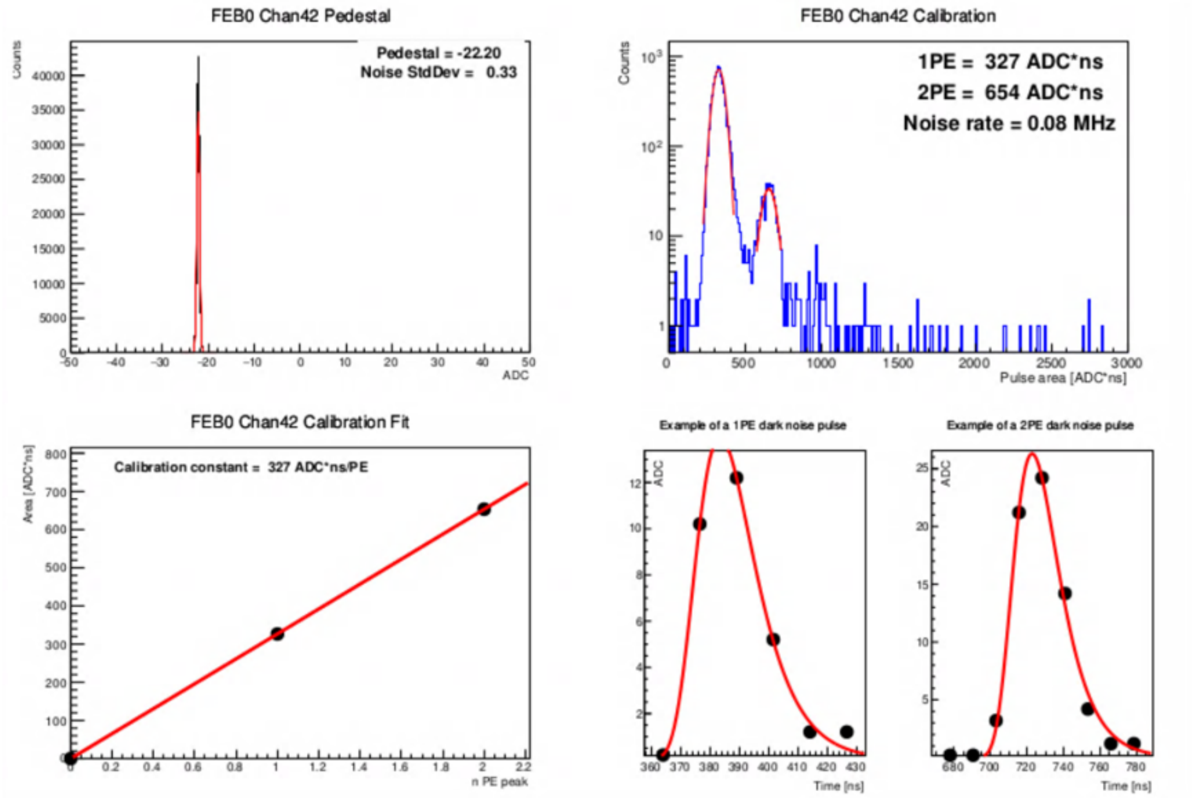

Figure 5.54.: Determining the the PE yield for a given SiPM. The upper left plot shows the pedestal samples from the pre-signal region. A Gaussian fit is shown in red with the mean representing the pedestal value. The negative pedestal value is due to settings in the FEB. The upper right shows the integrals computed from fits to pedestal-subtracted pre-signal pulses. A Gaussian fit is made to each peak that yields the mean integral value for each photoelectron. These values are plotted in the lower left and fit with a straight line that gives the expected integral per photoelectron ($\mathrm{ADC} * \mathrm{ns}/\mathrm{PE}$). The lower right plots show two pulses, a single PE (left) and double PE (right), from the pre-signal region that are fit with a Gumbel function, shown in red.

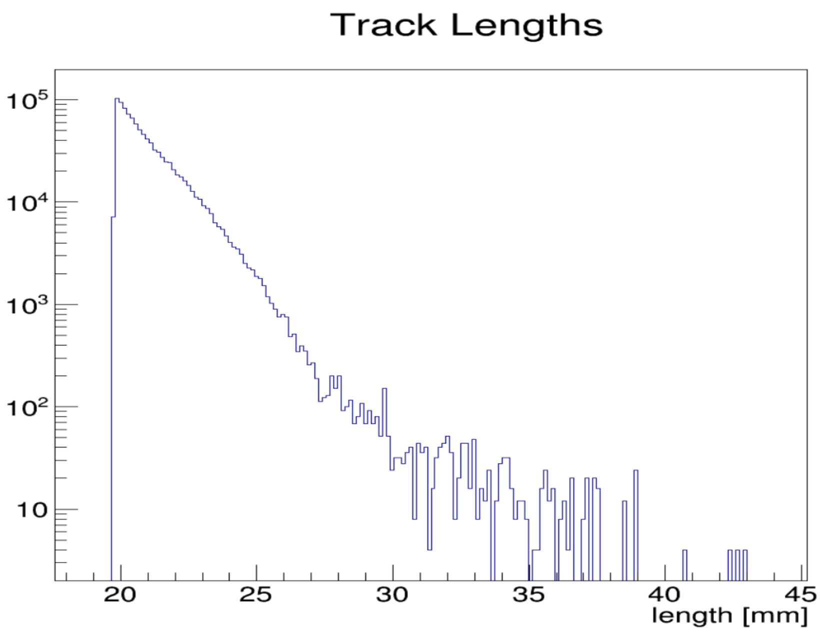

Figure 5.55.: The path length through the counters computed using tracking information from the CSCs.

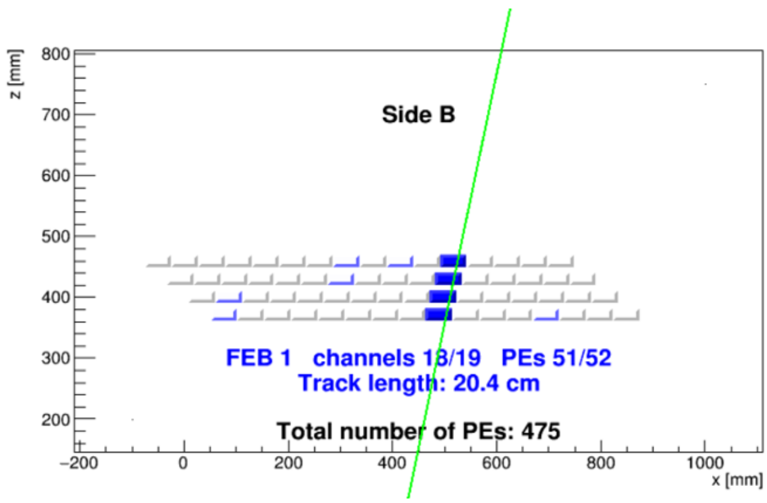

Figure 5.56.: An example event display of a cosmic-ray muon passing through a module. The green line is the track reconstructed by the cathode strip chambers and the blue rectangles highlight the counters that saw a high number of photoelectrons.

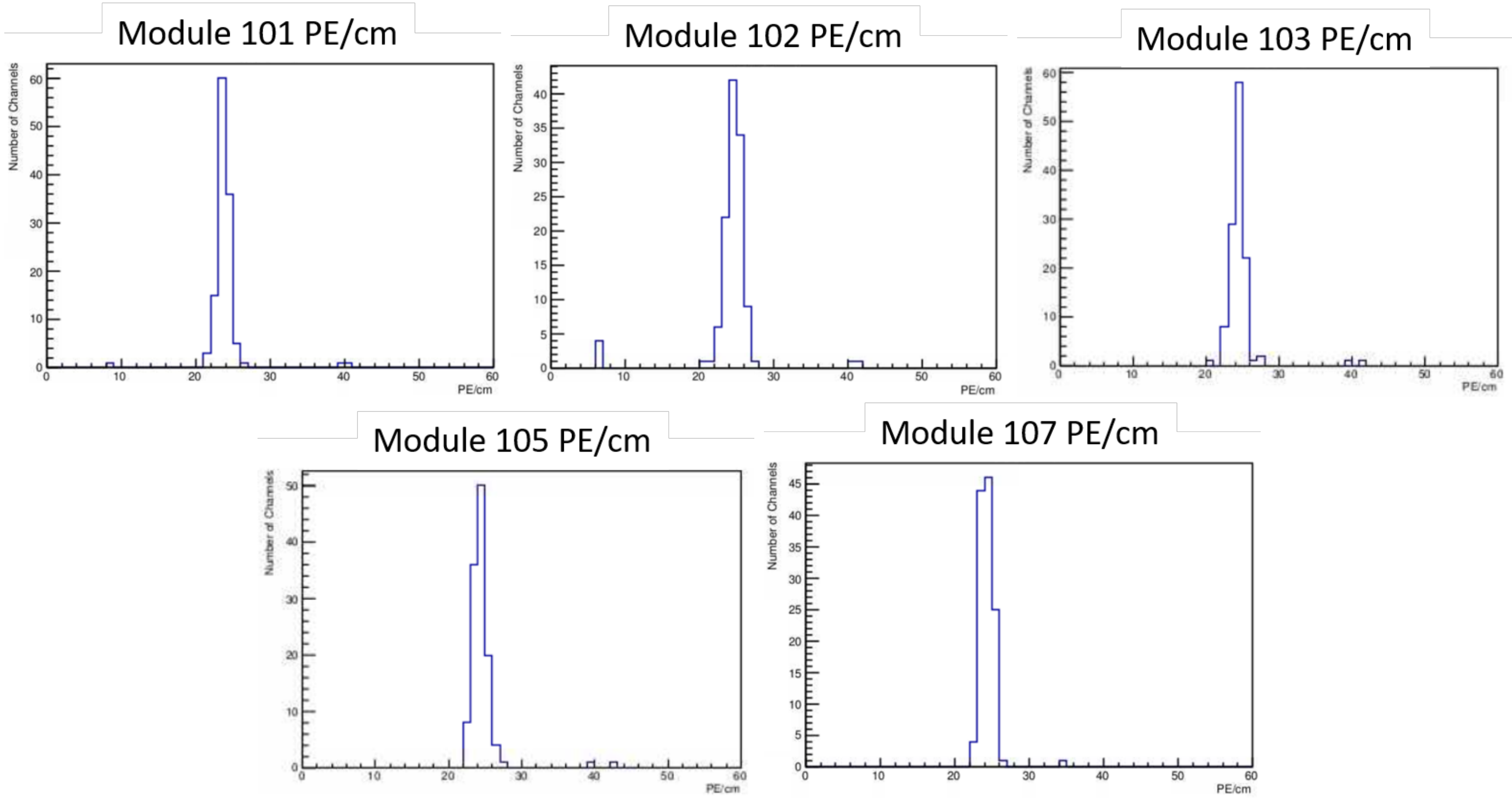

Figure 5.57.: The light yield per centimeter per SiPM for four single-ended readout CRV-TS modules (Module 101 to 105) evaluated at $1.0 \pm 0.4\,\mathrm{m}$ from the readout end and one CRV-L-Endcap module (Module 107). The average path-length light yield was found to be $25 \pm 2\,\mathrm{PE/cm}$. Outliers are due to bad FEB channels.

at random times during operation. Upon reset, the boards stop digitizing CSC signals and, as a result, the tracking efficiency steadily decreases from over 80 % at the start of a run to 0 % after only a few hours of operation. This problem has not been resolved despite extensive collaboration with the board designers and the consensus is the problem is an inherent flaw in the board or ASIC.

Most of the remaining modules only utilize the scintillator trigger in order to measure their light yields. The calibration method is the same as previously described. The number of photoelectrons is recorded for every SiPM and the resulting distribution fit with a Gaussian/Landau distribution (example: Fig. 5.58). All of the SiPMs for each end of a module have their mean values placed into a histogram to obtain a plot such as the one shown in the right of Fig. 5.59. If a channel is found to have a low value, the manifold to which it belongs is replaced. The average path length through a counter is close to 2 cm, so the path-length light yield can be estimated from the PE yield measured using only the scintillator trigger. The path-length light yield per SiPM and PE yield per SiPM without computing the path length for module 101 are shown in Fig. 5.59.

For the first 33 modules, the bias voltage for the SiPMs was set to a nominal 53.7 V. This bias voltage was selected based on the mean breakdown voltage for the pilot batch of SiPMs (51.2 V for 200 SiPMs) and adding 2.5 V for the desired operating voltage. The breakdown voltage of each device was not known at the time. For the 34th module (module 134), and all subsequent modules, the bias voltage for each device was set to 2.5 V over the measured breakdown voltage. This change resulted in a similar PDE across all the devices, which gives a better estimate of the light yield. The changes in light yield measurements were minimal, as shown in Fig. 5.60. The light yield per SiPM for 38 modules are shown in Appendix R. The average light yield for all the SiPMs of a module for 46 modules is presented in Fig. 5.61. The decrease in light yield around module 114 is due to the lower light yield scintillator mentioned in Ch. 5.1.1.

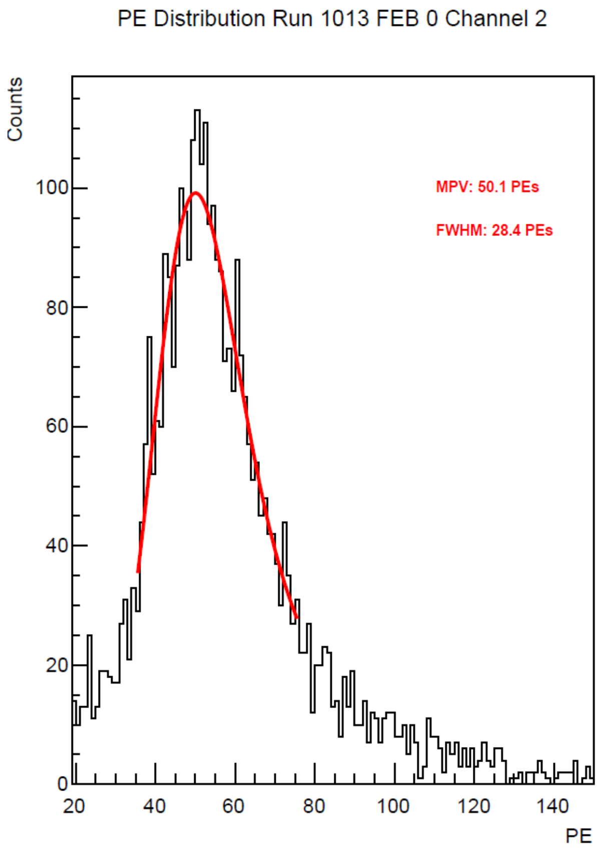

Figure 5.58.: The PE yield at 1.0 ± 0.4 m for a particular SiPM of module 101. The bulk of the distribution is fit with a Gaussian/Landau distribution, shown in red, yielding the most probable number of photoelectrons generated by a passing cosmic-ray muon.

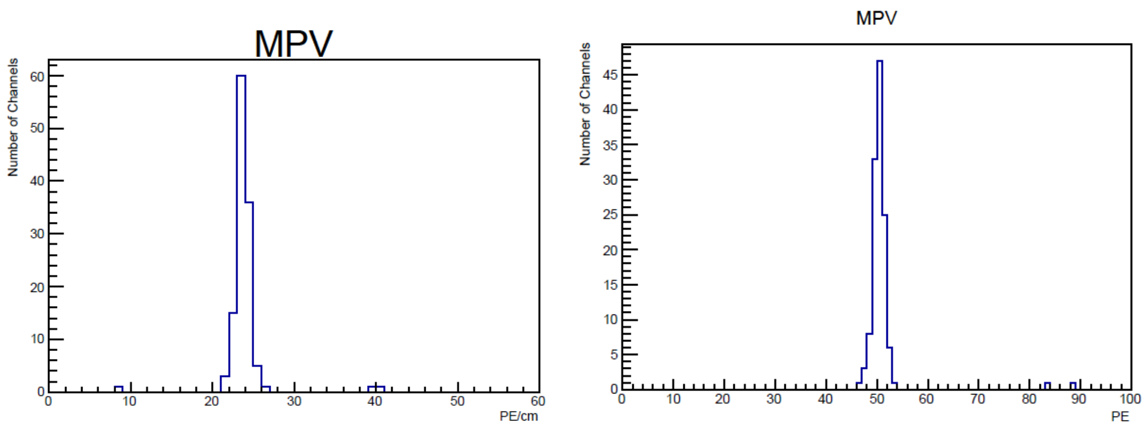

Figure 5.59.: The path-length light yield (PE/cm) per SiPM (left) and the measured PE yield for all SiPMs (right) in module 101, at 1.0 ± 0.4 m from the readout end.

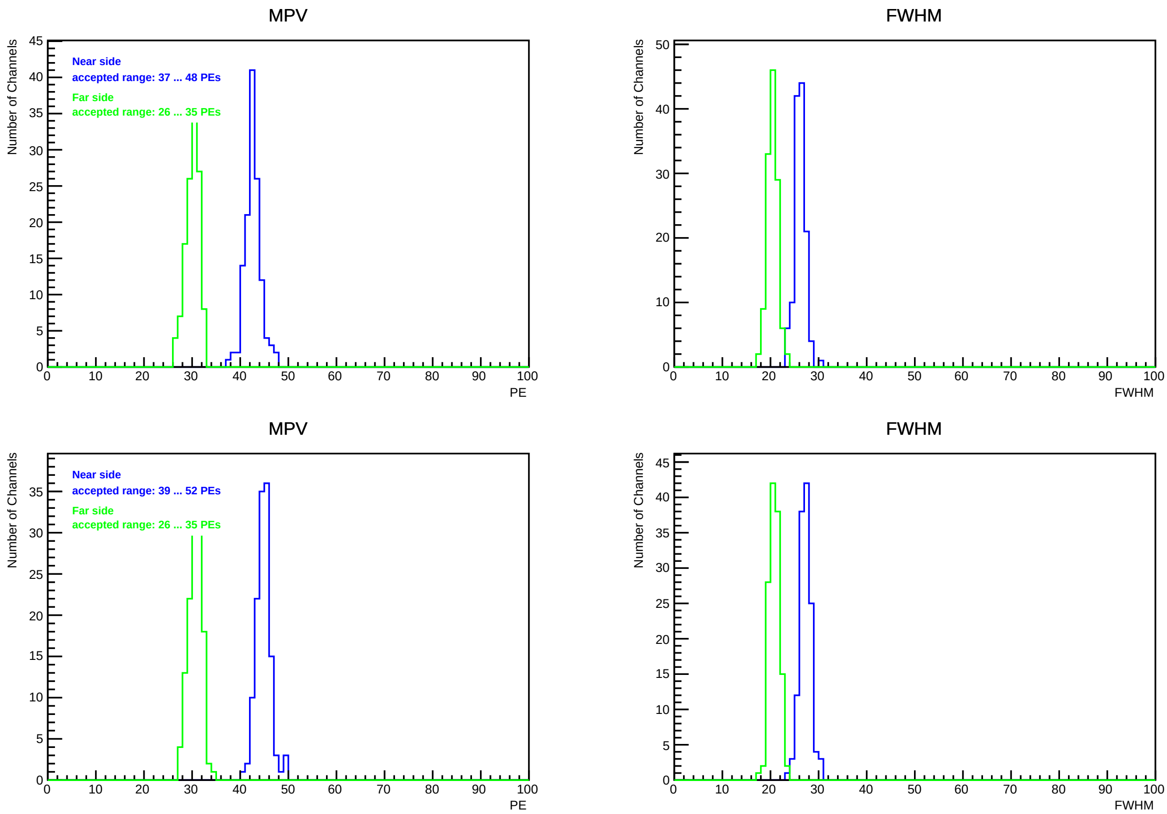

Figure 5.60.: The PE yields for module 134 with the SiPMs at a nominal bias voltage of 53.7 V (top) and a bias voltage of 2.5 V over their measured breakdown voltages (bottom), at 1.0 ± 0.4 m from the readout end. The most probable PE value (left) and FWHM (right) are shown. The PE yield for the readout end closest (furthest) to the test region is shown in blue (green). The impact of this change on the measured light yield is minimal, but results in a better measurement due to a similar PDE across all devices.

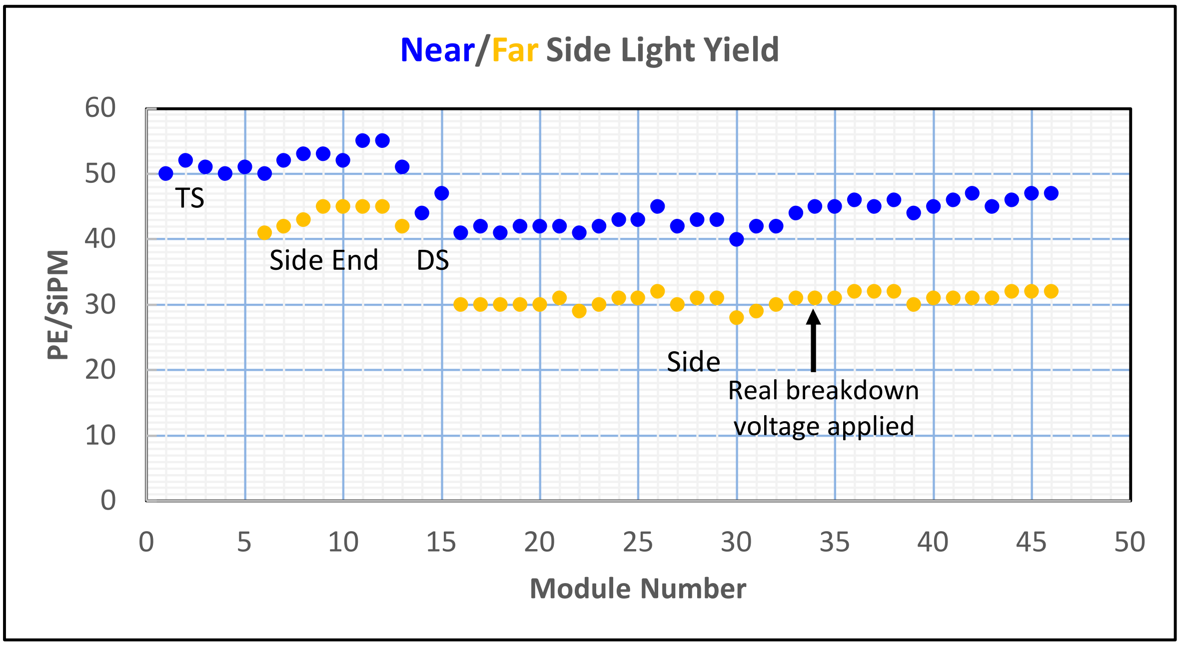

Figure 5.61.: Average light yield per SiPM of all SiPMs for 46 modules for the nearest (blue) and furthest (yellow) readout ends. The modules that do not have a far side measurements have single-ended readout. The decrease in light yield around module 114 is due to the lower light yield scintillator mentioned in Ch. 5.1.1.

5.3.3. Module Efficiency

Average module efficiencies are determined from the average single-layer efficiencies calculated in the follow way. Hits that are equal to or less than 5 PEs are ignored to simulate the FEB's zero suppression. A threshold of 20 PEs (14 PEs) for the summed response of both SiPMs in the same (neighboring) counter is used to define hits. The neighboring counter is only used for muons that partially hit adjacent counters. Hits located in the green region of Fig. 5.62, are used in the formation of a track stub. No CSC tracking data are used. To avoid edge effects, a track stub is only considered valid if at least three layers have hits in the blue region of Fig. 5.62. The single-layer efficiencies, for each module end separately, are then computed as the number of hits in each layer divided by the total number of valid track stubs. Shown in Fig. 5.63, to meet a desired track stub inefficiency of better than 10^{-4}, the single layer inefficiency must be no more

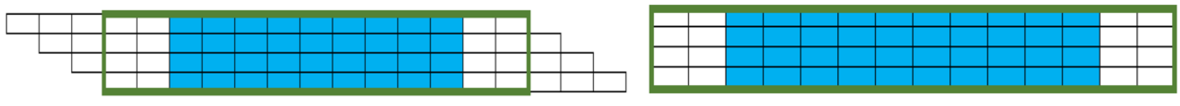

Figure 5.62.: Zones used for the calculation of overall module efficiency from per-layer efficiencies. Only hits within the green regions were used in efficiency calculations. To avoid edge effects, an event used for efficiency calculation is only considered usable if there are hits in at least three layers in the blue region. The module profile on the left does not accurately depict the 42 mm offset between layers, but is drawn in this manner out of convenience.

than 4×10^{-3}. Single layer inefficiencies at a threshold of 20 PE, shown in Fig. 5.64, are expected to be 0.2 %. The average module efficiency for a 3/4-layer requirement is calculated using a binomial expansion from single-layer efficiencies:

$$\epsilon_{3/4} = \epsilon_1\epsilon_2\epsilon_3 + \epsilon_1\epsilon_2\epsilon_4 + \epsilon_1\epsilon_3\epsilon_4 + \epsilon_2\epsilon_3\epsilon_4 - 3\epsilon_1\epsilon_2\epsilon_3\epsilon_4, \tag{5.1}$$

where ϵ_i is the efficiency of the ith layer. Average module inefficiencies at both the 20 and 14 PE thresholds were found to be better than 1×10^{-4}, shown in Fig. 5.65. Module assembly and testing is ongoing, and the modules tested so far all meet requirements.

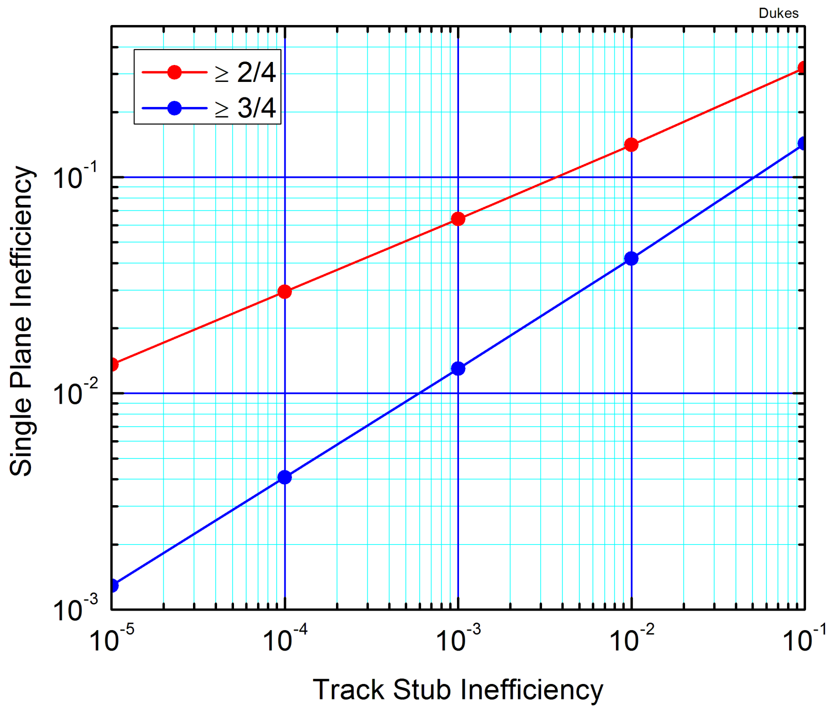

Figure 5.63.: The required single layer inefficiency as a function of track stub inefficiency for 2/4 and 3/4 layer coincidences.

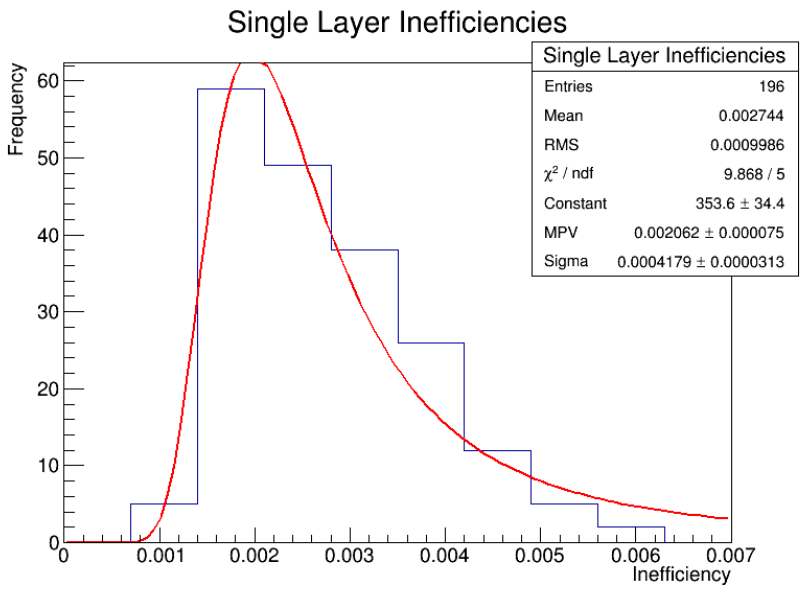

Figure 5.64.: Single module layer inefficiencies of the first 28 modules, for each readout end, with hit thresholds of 20 PE. Not every module is read out on both ends. The red line is a Landau fit with a most probable layer inefficiency of 0.2 %.

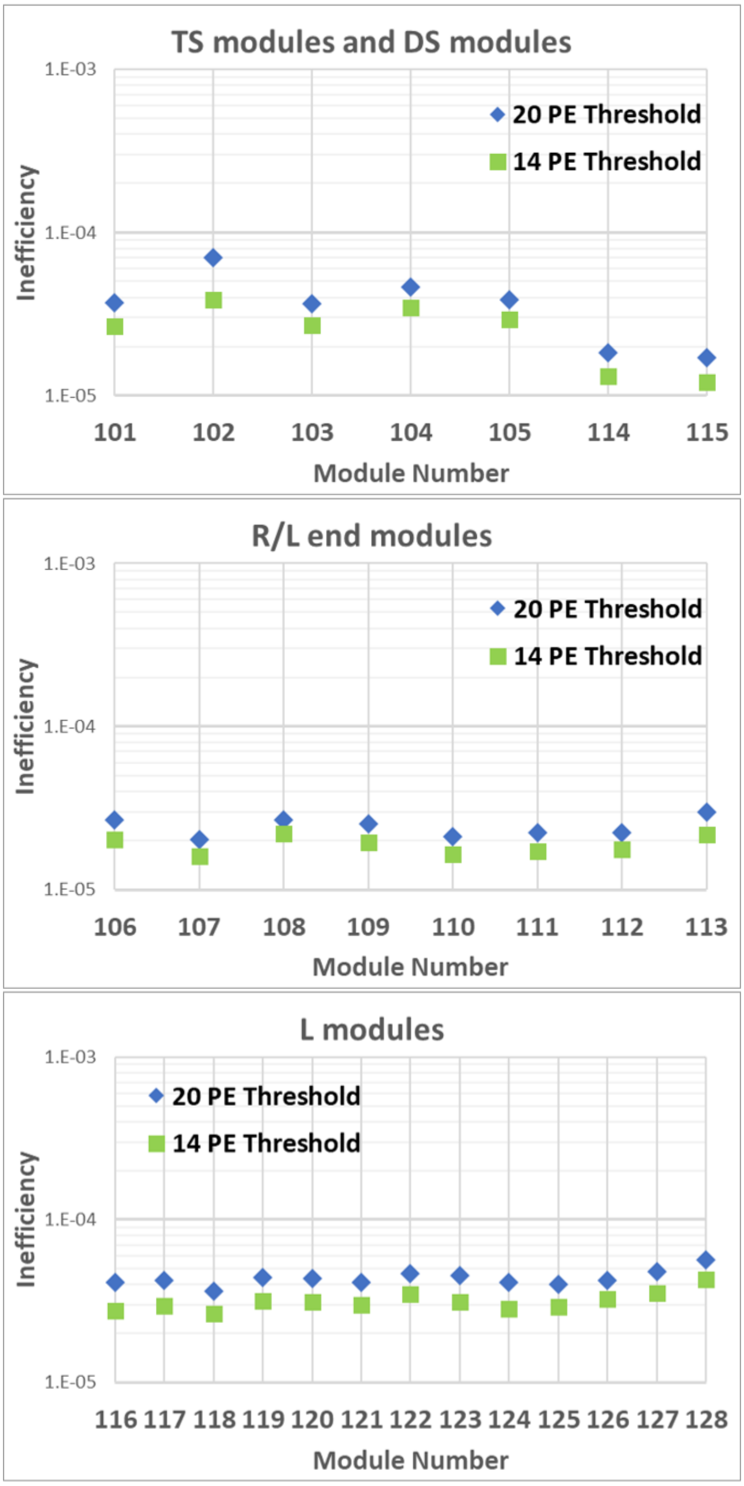

Figure 5.65.: Module inefficiencies calculated by finding per-layer efficiencies with hit thresholds of 20 and 14 PE for modules evaluated in the Cosmic Ray Test Stand. Top: Transport Solenoid (TS) and Downstream (DS) module inefficiencies. The higher inefficiency in the first five modules is attributed to being single-ended readout modules. Middle: Right (R) and Left (L) endcap module inefficiencies. Bottom: Left (L) module inefficiencies (excluding endcap).

Chapter 6.

Increasing the Light Yield

In an effort to improve the light yield in response to greater than anticipated aging coupled to a delayed run start, the process and effects of filling dicounters with silicone-based liquid polymers were explored. The two fluids that were considered are SKTN-MED siloxane [88] and XIAMETER^{TM} PMX-200 polydimethylsiloxane [147]. Due to the closely matched index of refraction of these fluids (n =1.40) to the scintillator and WLS fiber, the optical coupling is improved, which increases the light yield. Additionally, it was observed that these fluids greatly reduce aging. Filling dicounters is not without potential downsides: it takes additional time to fill dicounters and fluid leaks are undesired and may damage the SiPMs.

6.1. Filling Time, Sealing, and Prototype Filling Apparatus

The purpose of this study was to evaluate the feasibility of filling for mass production. One feature of siloxane fluids is their availability in different viscosities. To understand

Table 6.1.: Time to fill a 4.5 m long dicounter with PMX-200 of different viscosities at room temperature and 13.7×10^3 Pa (2 PSI) of fill pressure.

Viscosity (cSt)	Fill Time (s)	Ratio to 10 cSt Fill Time
10	40	1
100	358	$\sim$9
1000	3900	$\sim$98

how to balance fluid viscosity with filling time, several 4.5 m long counters were filled with PMX-200 with viscosities[†] ranging from 10 cSt to 1000 cSt and the fill time was recorded. Fill holes were 4.76 mm in diameter, drilled 2.5 cm from each counter end, to the depth of the fiber channel. The holes were drilled prior to the installation of the fibers. The DP100 epoxy that was used to attach the FGB was applied around each fiber channel to prevent leaks. Dicounters were filled level. All tests were carried out at room temperature with a constant fill pressure of 13.7×10^3 Pa (2 PSI). The results are presented in Table 6.1.

For each order of magnitude increase in viscosity it took approximately one order of magnitude more time to fill the counter. To minimize manufacturing time, it is necessary to keep the viscosity as low as possible. A disadvantage in using a low-viscosity filler is the flow rate for a leaking dicounter is much higher than that of one using a high-viscosity filler.

One can decrease the fill time of a more viscous fluid by increasing the fill pressure. Using dicounters of varying lengths from a few centimeters to 4.5 m, the fill time for 1000 cSt PMX-200 as a function of dicounter length for two different pressures is plotted in Fig. 6.1. The maximum tested fill pressure that a dicounter safely withstood was 241.3×10^3 Pa (35 PSI). The fill pressure utilized in mass production will likely be restricted by the pressure rating of the filling apparatus.

[†]Water at 20 °C has a viscosity of 1 cSt.

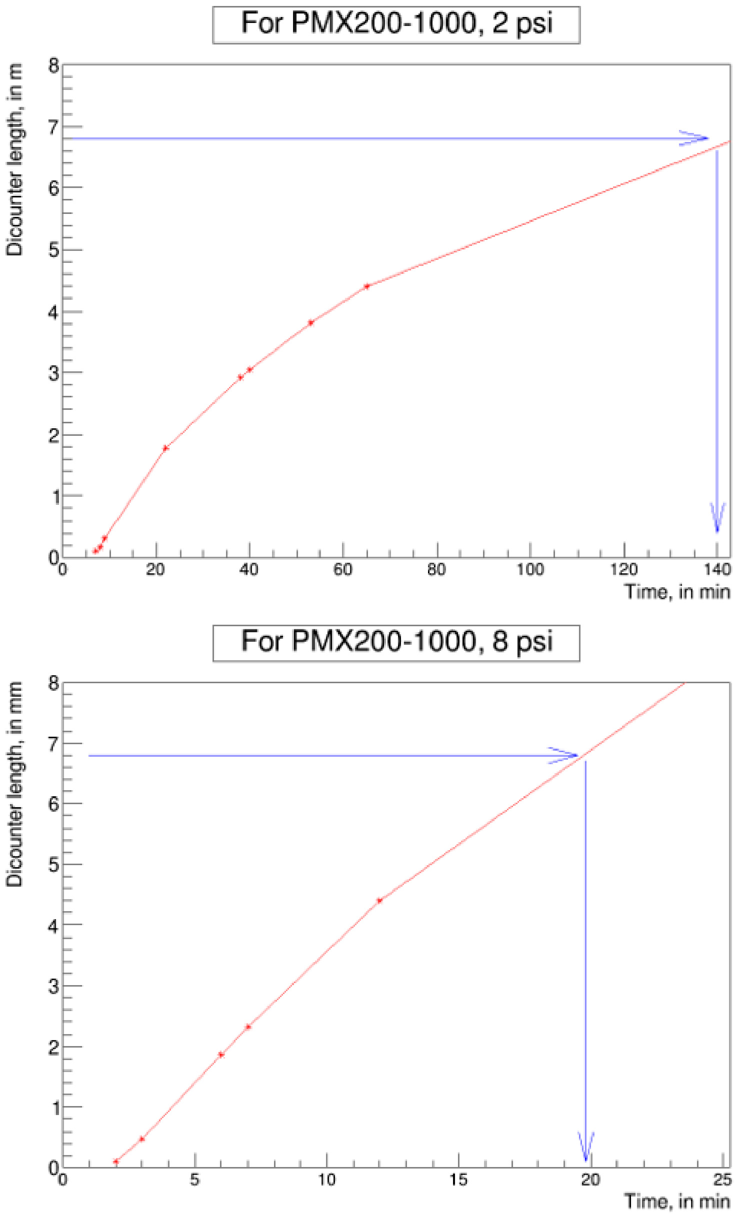

Figure 6.1.: Dicounter length versus fill time at fill pressures of 13.7×10^3 Pa (2 PSI) (left) and 55.2×10^3 Pa (8 PSI) (right). The fluid used was 1000 cSt PMX-200. The blue lines indicate the fill time for a 6.8 m-long dicounter. The maximum tested fill pressure a dicounter safely withstood was 241.3×10^3 Pa (35 PSI).

Sealing of filled dicounters was found to be most effective using a chemically-similar (polysiloxane), solvent-less RTV silicone that is commercially available as an automotive windshield and glass sealant. Several mixtures of varying ratios of PMX-200 and Permatex®-81730 [148] were evaluated for curing. All mixtures were left open in air to cure at room temperature. The ratios of PMX-200 to sealant that were evaluated were 1:1, 2:1, 3:1, and 4:1. It was found that after 24 hours of cure time ratios above 2:1 were uncured, viscous fluids [149]. Excess PMX-200 was removed from the fill holes using a syringe before application of the sealant. The sealant was injected into the hole and mixed with a small wooden dowel. A total of 10 filled dicounters, which equates to 80 fill holes, were sealed using the windshield sealant and exhibited no leaks after one year. Sealing of dicounters was also attempted using other methods, but were found to be ineffective or too time consuming. It was concluded that the commercially available sealant is ideal for effectively sealing filled dicounters.

Since it was demonstrated that dicounters could be filled with a radiation hard fluid (see Ch. 6.3) that greatly improves light yield, a prototype filling apparatus was designed and built. The apparatus was designed to fill up to eight dicounters simultaneously, with little supervision required during filling. For a 4.5 m long counter, the fill time with 1000 cSt PMX-200 was approximately 10 minutes at 96.5×10^3 Pa (14 PSI). The apparatus is comprised of three main components, a pressurized fluid reservoir (Fig. 6.2), a filling manifold (Fig. 6.3), and an exhaust manifold (Fig. 6.4). A check valve in the reservoir prevents air from being injected into the dicounters should the reservoir empty during filling. Compressed air is delivered through a regulator that ensures a constant filling pressure. Valves on the reservoir are used to isolate dicounters from the reservoir pressure for connection/disconnection of filling manifolds. The filling and exhaust manifolds are designed to clamp onto the dicounter using thumbscrews, forming an adequate seal to the filling holes through the use of rubber O-rings. The exhaust manifold contains a check valve for each fiber channel, which prevents additional fluid

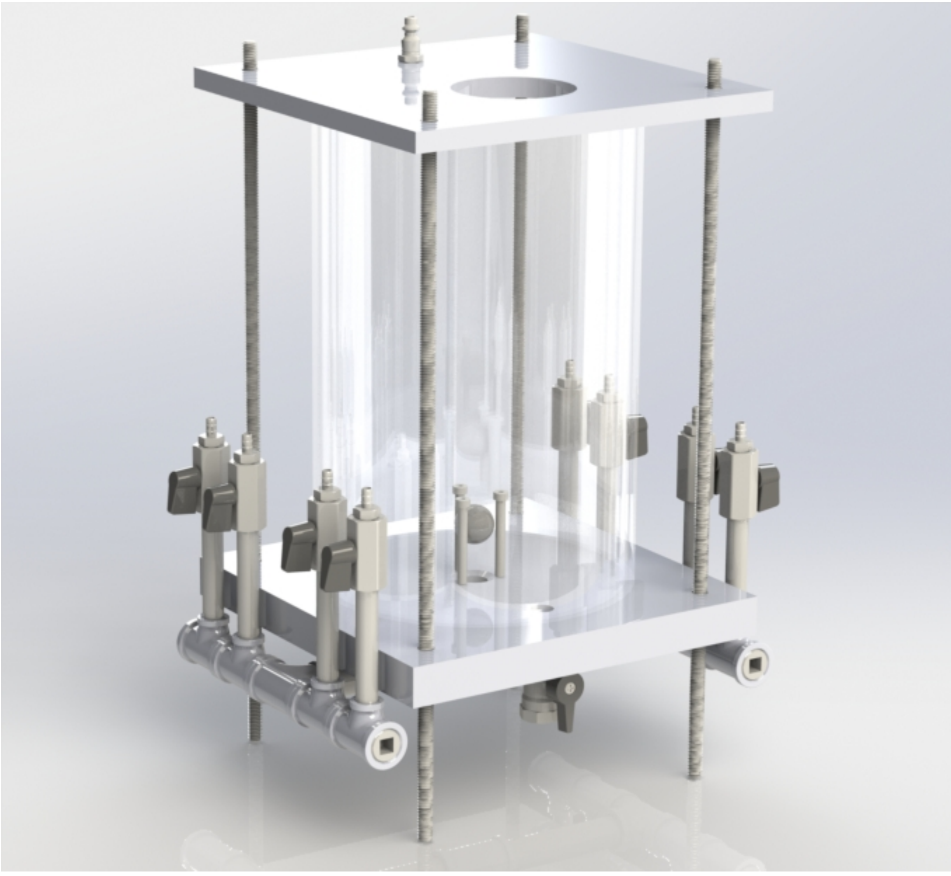

Figure 6.2.: Rendering of the prototype Dicounter Filler Reservoir. The reservoir holds the siloxane fluid. A check valve in the center of the reservoir prevents dicounters from being filled with air should the reservoir empty during filling. Up to eight dicounters can be filled simultaneously. Compressed air provide the pressure for filling.

from flowing through that channel and eliminating waste once that channel is filled. The assembled prototype is shown filling a short dicounter in Fig. 6.5.

6.2. Light Yield Improvement

Using the same Cs-137 source and dicounter testing apparatus described in Ch. 5.1.3, the improvement in light yield between an unfilled dicounter and dicounter filled with SKTN-MED siloxane fluid was determined. Using a 4.5 m long dicounter, the SiPM current response to the source at several distances from the readout end was measured

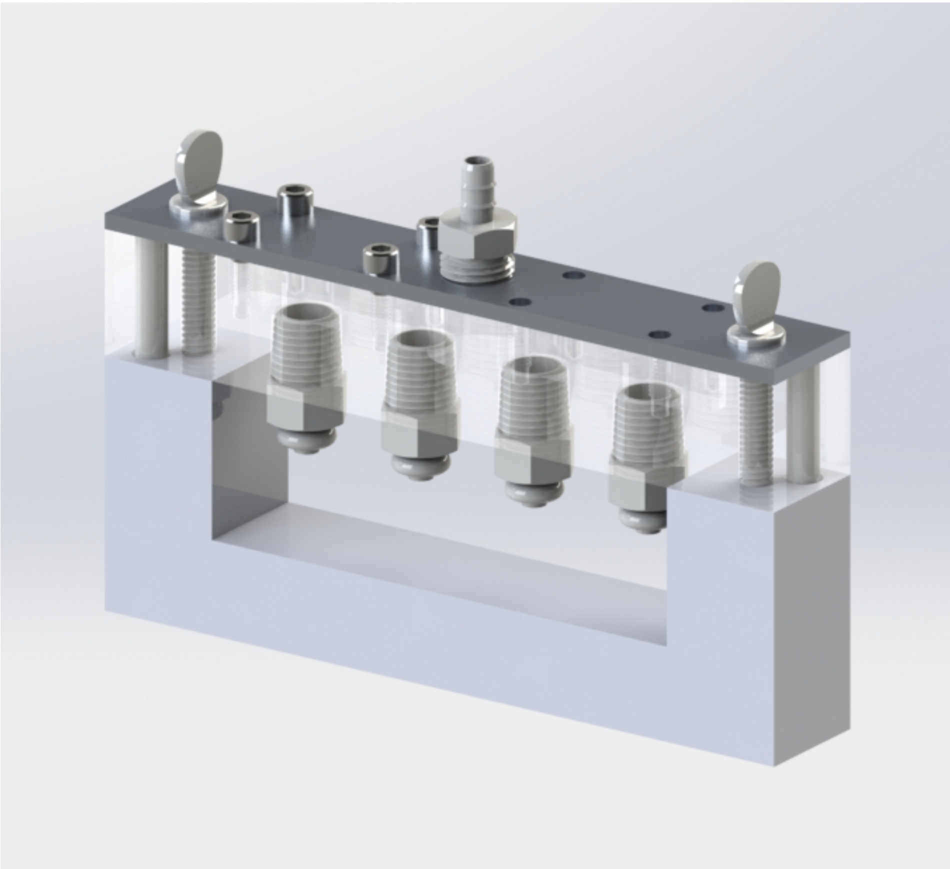

Figure 6.3.: Rendering of the prototype Dicounter Filler Manifold. Fluid entering the manifold is distributed to each of the four fiber channels. Sealing of each fill hole is made by o-rings on the filling nozzles. Clamping pressure, through the use of thumbscrews, allows the manifold to be easily installed or removed from the end of a dicounter. The dicounter is not shown.

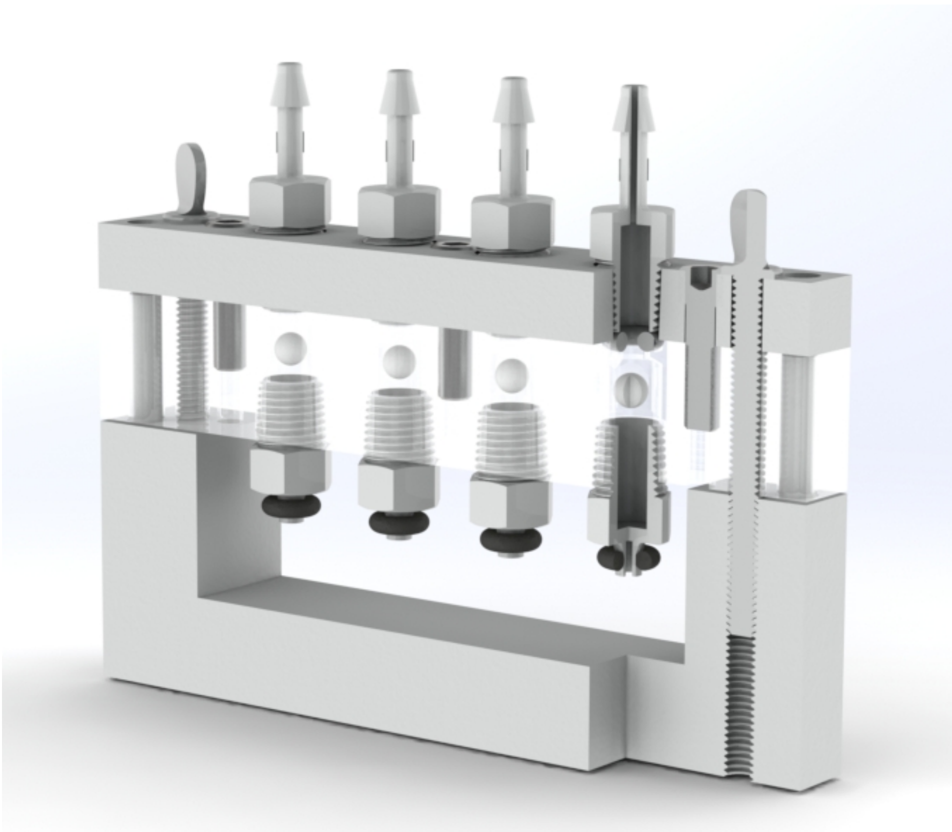

Figure 6.4.: Rendering of the prototype Dicounter Filler Exhaust manifold. A check valve in each filling channel seals the channel off when it is completely filled, preventing fluid waste. Clamping pressure, through the use of thumbscrews, allows the manifold to be easily installed or removed from the end of a dicounter. The dicounter is not shown.

Figure 6.5.: Completed prototype of the Dicounter Filler apparatus. Pictured is a short dicounter being filled by the apparatus. A regulator on the reservoir allows for the filling pressure to be adjusted. The tubes from the exhaust manifold were placed into water to observe the fluid flow by the presence of bubbles.

before and after filling. Located 2.5 cm from each readout end, each fiber channel had a small hole (4.6 mm) that was used for fluid injection. The holes were drilled prior to the installation of the fibers. Filling of each dicounter was accomplished through the use of a specially designed pneumatic filler, separate from the one described in the previous section and shown in Fig. 6.6, that forced the viscous fluid (SKTN-MED Grade D) through each fiber hole at a constant pressure. After filling, excess fluid from each hole was removed using a syringe. The hole was then sealed with DP-100 epoxy injected into the hole. All dicounters were filled level.

The ratio of the SiPM current response before and after filling is plotted as a function of distance from the readout end, shown in Fig. 6.7, yielding an average improvement in the light yield of about 30 % for SKTN-MED [150]. The same study was repeated using a more readily-available fluid: XIAMETER™ PMX-200 polydimethylsiloxane

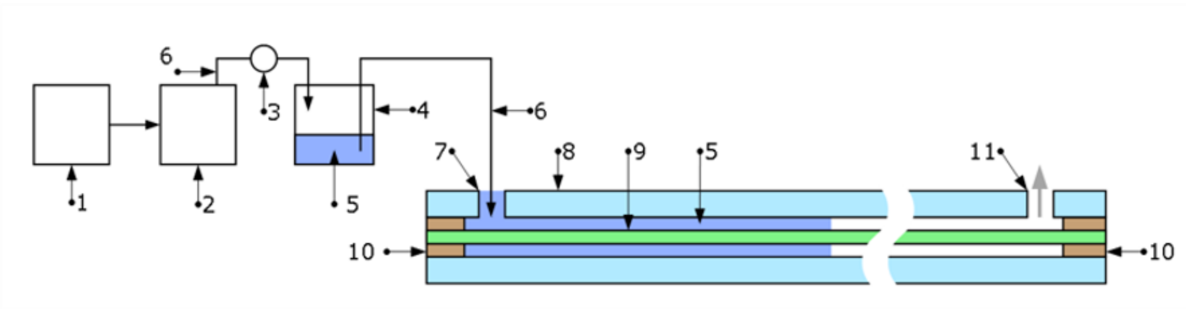

Figure 6.6.: Setup to pump the high-viscosity silicone-based fluid into the co-extruded hole of the scintillator bar (not to scale). Shown is the dry-type compressor (1); digital liquid dispenser SL101N (2); manometer (3); special vessel with siloxane fluid (4); siloxane fluid (5); PVC tubing (6); inlet for filling (7); scintillator bar (8); WLS fiber (9); DP-100 epoxy plug (10); and exhaust outlet for air (11).

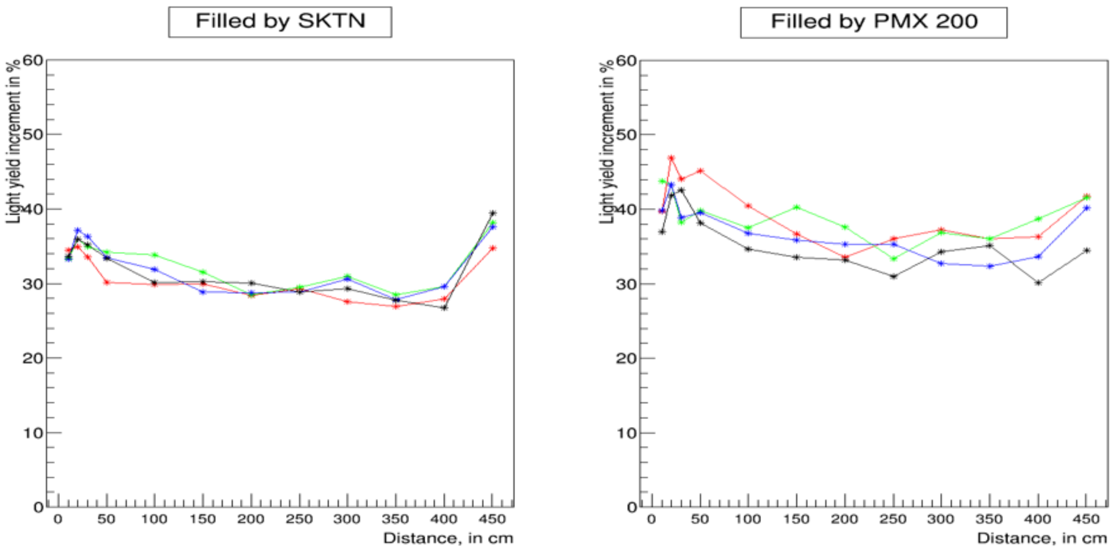

Figure 6.7.: The light yield improvement (%) for each channel at various distances from the readout end for two 4.5 m dicounters filled with siloxane fluid compared to unfilled dicounters. Each line represents a fiber channel in the dicounter tested. Left: dicounter filled with SKTN-MED Grade D. Right: dicounter filled with PMX-200 1000 cSt.

[147], 1000 cSt viscosity. The improvement in light yield was slightly better, also shown in Fig. 6.7 [150].

Due to the limited availability of SKTN-MED in the United States, the comparable and commercially available PMX-200 is the ideal choice for dicounter filling. The light yield study was repeated with several viscosities of PMX-200 ranging from 10 cSt to

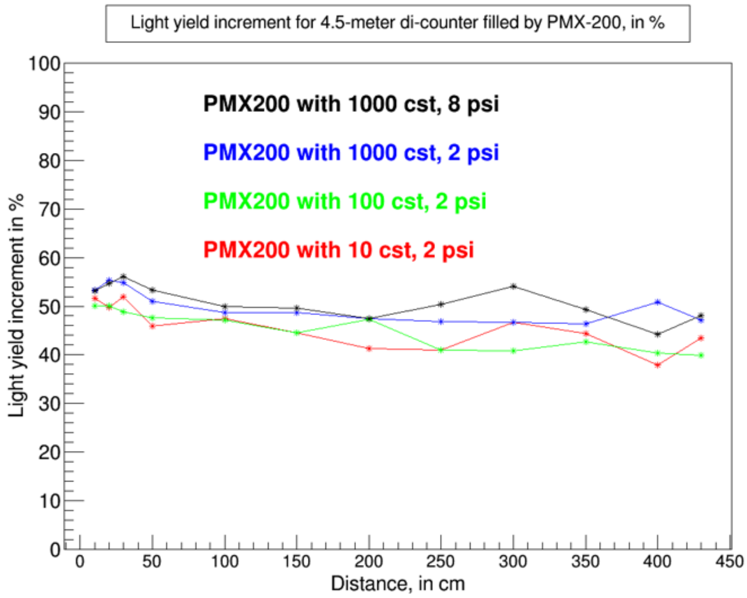

Figure 6.8.: The light yield increase in a 4.5 m long dicounter for different viscosity PMX-200 fillers. The time since fabrication for this dicounter was 1 year.

1000 cSt. Shown in Fig. 6.8, there was no discernible difference in light yield for different viscosity fillers [151].

It was observed that counters that were filled further from their fabrication date had greater improvements in light yield. The dicounter used in Fig. 6.8 was filled 1 year after fabrication and exhibited an average light yield improvement of 48 % (30 cm to 200 cm). In Fig. 6.9, the light yield for two dicounters, one filled 2 months after fabrication and one 3 years after fabrication, exhibited a 41 % and 54 % average light yield improvement (30 cm to 200 cm), respectively. The reason why older dicounters show greater light yield improvement after filling is currently not known, but it is suspected that the fluid fills small cracks around the fiber channels that develop over time due to internal stresses in the scintillator (Fig. 6.10).

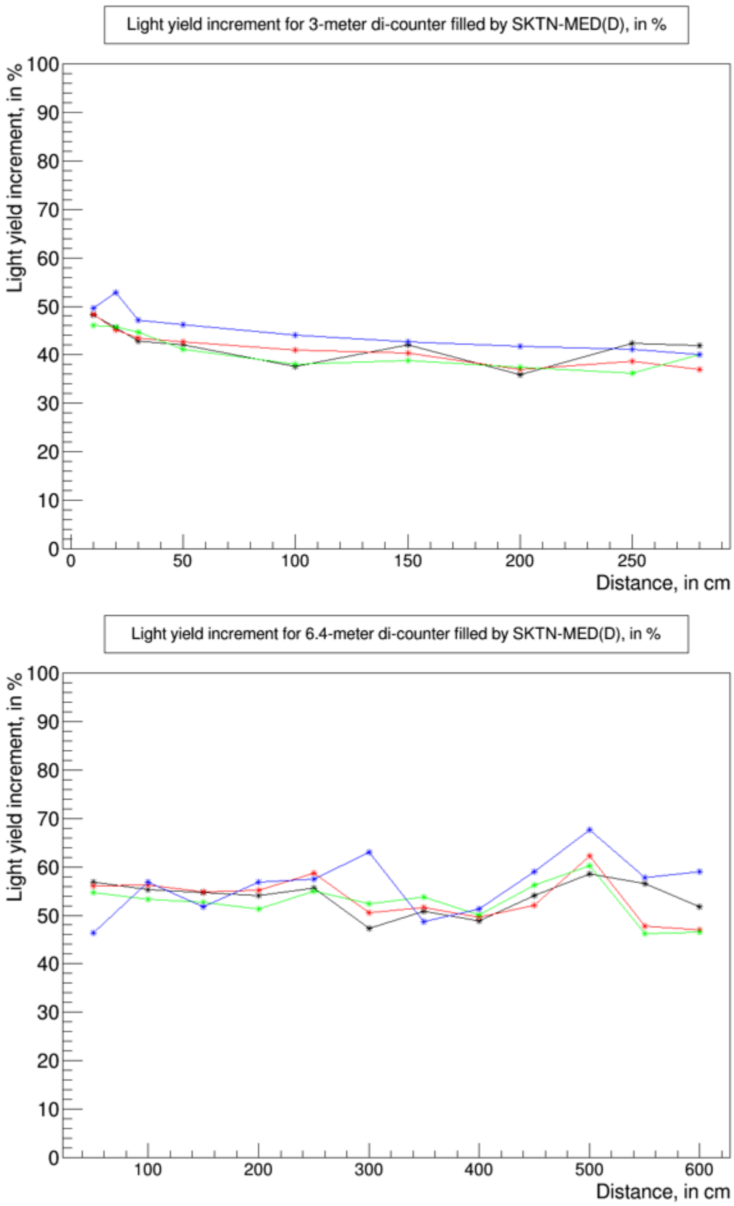

Figure 6.9.: The light yield increase for a 2 month old, 3 m long dicounter (top) and a 3 year old, 6.4 m long dicounter (bottom). Each color represents one of the four fiber channels. The average light yield increase over a comparable region (30 cm to 200 cm) is 41 % for the 3 m long dicounter and 54 % for the 6.4 m long dicounter.

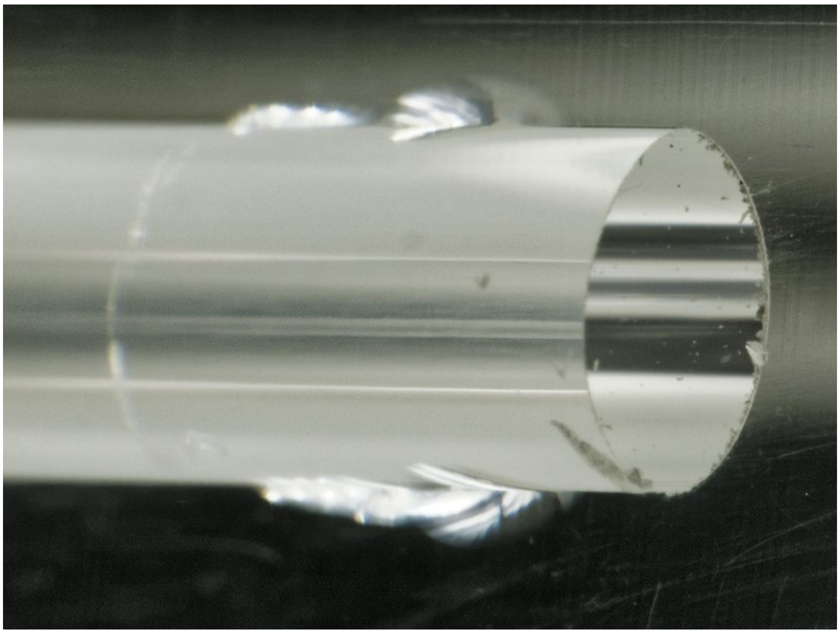

Figure 6.10.: Small cracks around a fiber channel.

6.3. Radiation Tolerance

Like the other components of the CRV, the radiation tolerance of the silicone-based fluid used for dicounter filling must be understood. Samples of polymerized and un-polymerized SKTN-MED siloxane fluid [88], of two different viscosities, and BC-600 [46], for comparison, were irradiated at the IBR-2M reactor irradiation facility in Dubna, Russia [152]. There were eight, 25 mm × 30 mm × 4 mm (3 mL) polymerized samples: four SKTN-MED Grade D and four BC-600. There were twelve non-polymerized 50 mL samples: four SKTN-MED Grade D viscosity, four SKTN-MED Grade E viscosity, and the remaining four were BC-600 (800 cSt). Groups of samples were irradiated, in the same time span, to neutron fluences (E >1 MeV) of 1.2×10^{14}, 3.8×10^{14} and $16.0 \times 10^{14}\,\mathrm{n/cm^2}$. The spectral transmittance of each sample was evaluated using a Shimadzu SolidSpec-3700DUV spectrophotometer [153] before and after irradiation. It was found that polymerized SKTN-MED only suffered a slight decrease (<3 %) in transmittance in the 400 nm to 500 nm region at the maximum radiation dose, and the non-polymerized samples (regardless of viscosity) exhibited even better radiation hardness, shown in Figs. 6.11 and 6.12 [89]. One caveat is that the non-polymerized samples at the highest radiation dose could not be evaluated in the same way as the other liquid samples as the high dose polymerized them. The BC-600 polymerized samples exhibited very poor radiation hardness, while the non-polymerized samples performed better, but still worse than SKTN-MED, also shown in Figs. 6.11 and 6.12 [89]. It can be concluded that liquid SKTN-MED is a viable filler material due to its radiation tolerance at levels exceeding the maximum expected fluence of $10^{11}\,\mathrm{n/cm^2}$ in Mu2e.

6.4. Filling Conclusions

While filling dicounters is shown to improve the light yield by as much as 50 % for aged counters (30 % for newly manufactured), the decision was made to not fill the dicounters of the CRV. The additional manufacturing time and labor, material cost, and potential for leaks, was not approved by project management. However, dicounter filling is being considered for critical regions of the CRV in a future, upgraded Mu2e, called Mu2e-II [154].

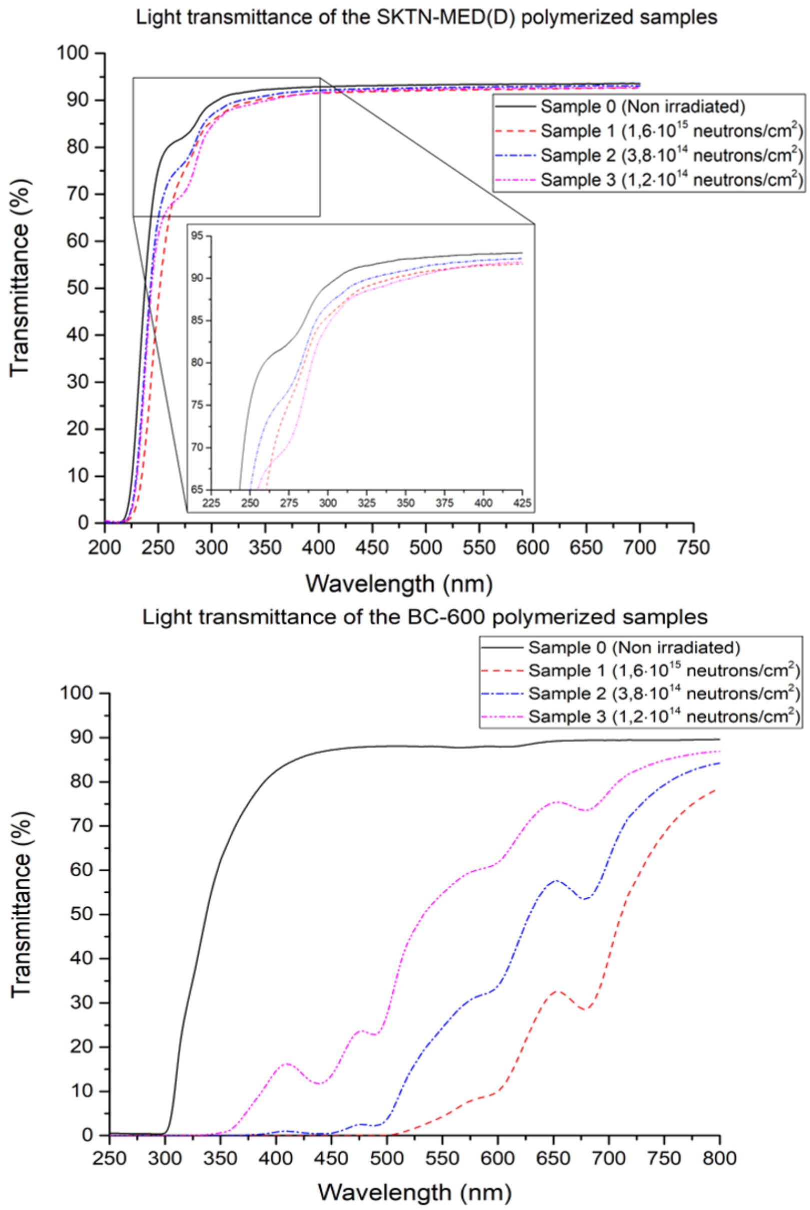

Figure 6.11.: Transmittance of irradiated and non-irradiated, polymerized SKTN-MED and BC-600. Top: Transmittance for polymerized SKTN-MED Grade D viscosity. Bottom: Transmittance for polymerized BC-600.

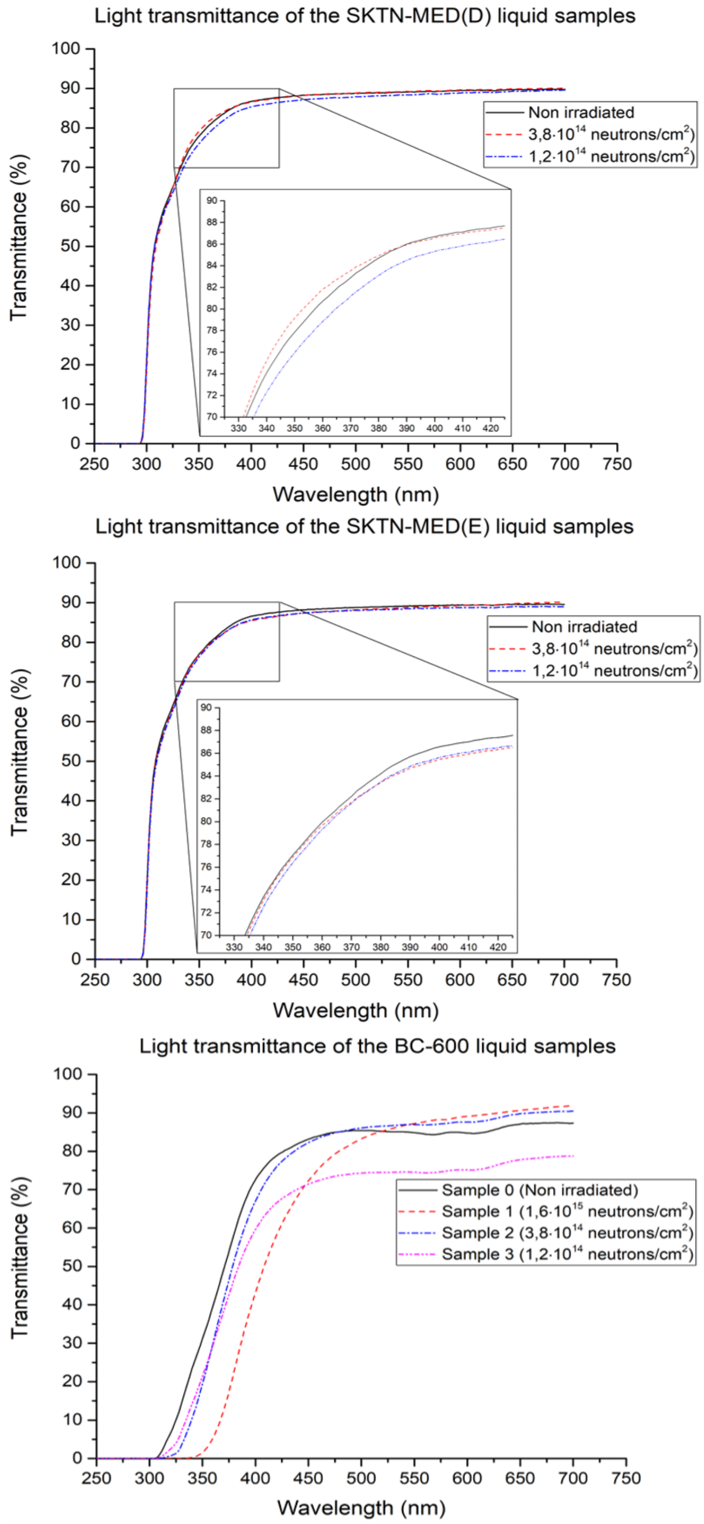

Figure 6.12.: Transmittance of irradiated and non-irradiated, non-polymerized SKTN-MED and BC-600. Top (middle): Transmittance for non-polymerized, liquid SKTN-MED Grade D (E) viscosity. Bottom: Transmittance for non-polymerized, liquid BC-600. Note: liquid SKTN-MED irradiated to $1.6 \times 10^{15}\,\text{n/cm}^2$ was unable to be evaluated due to becoming polymerized by radiation.

Chapter 7.

Applications of the Design Beyond Mu2e

The scintillator detector design of the CRV has been adopted for use, or is being considered for use, in several experiments due to its simplicity, compact readout, and ease of manufacture, while still boasting a high light yield. Currently, the Light Dark Matter eXperiment, and Exploring the Great Pyramid (EGP) and Chichen Itza projects, and Mu2e-II intend to make use of derivatives of the CRV design.

7.1. Light Dark Matter eXperiment

The Light Dark Matter eXperiment (LDMX) is designed to search for dark matter particles in the MeV to GeV region through a missing-momentum measurement from dark bremsstrahlung in an electron beam at the Standford Linear Accelerator Center (SLAC) [155]. The experiment intends to employ a high-efficiency hadronic veto calorimeter to detect neutral hadrons and other minimum-ionizing particles. Design of the calorimeter makes use of scintillator-based sampling between steel absorbers, a design that is a direct

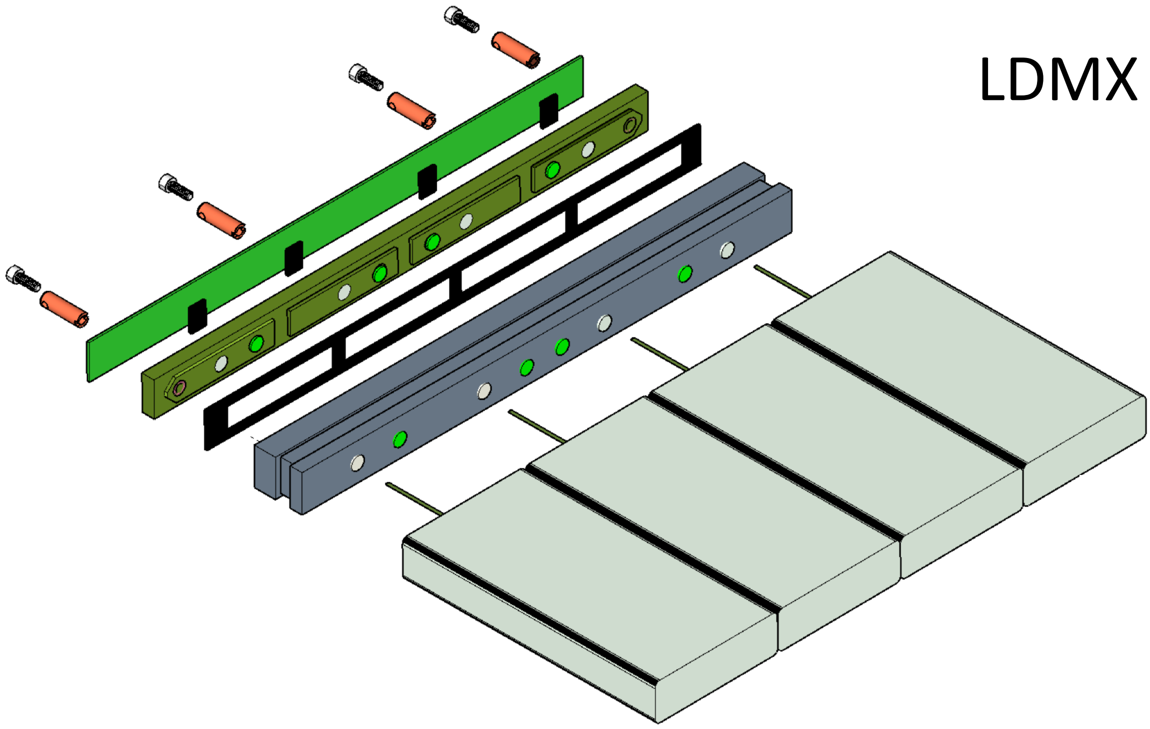

Figure 7.1.: A rendering of the LDMX quadcounter, drived from the dicounter design of the CRV. The profile of each extrusion is 20 mm × 50 mm and has a single WLS fiber. A longer version of a FGB is attached to each group of four extrusions and the fibers are read out by a longer version of the CMB.

derivative of the CRV [155] [156]. The design is similar to that of the CRV, except an extrusion profile of 20 mm × 50 mm with a single WLS fiber per extrusion is used. Four extrusions are bonded together to form a quadcounter [155]. A rendering of the proposed quadcounter design and calorimeter is presented in Figs. 7.1 and 7.2.

7.2. Exploring the Great Pyramid and Chichén Itzá Projects and Mu2e-II

In an effort to noninvasively study the interior of the Great Pyramid of Khufu, the EGP project proposes the use of the same technology of the CRV to conduct muon tomography

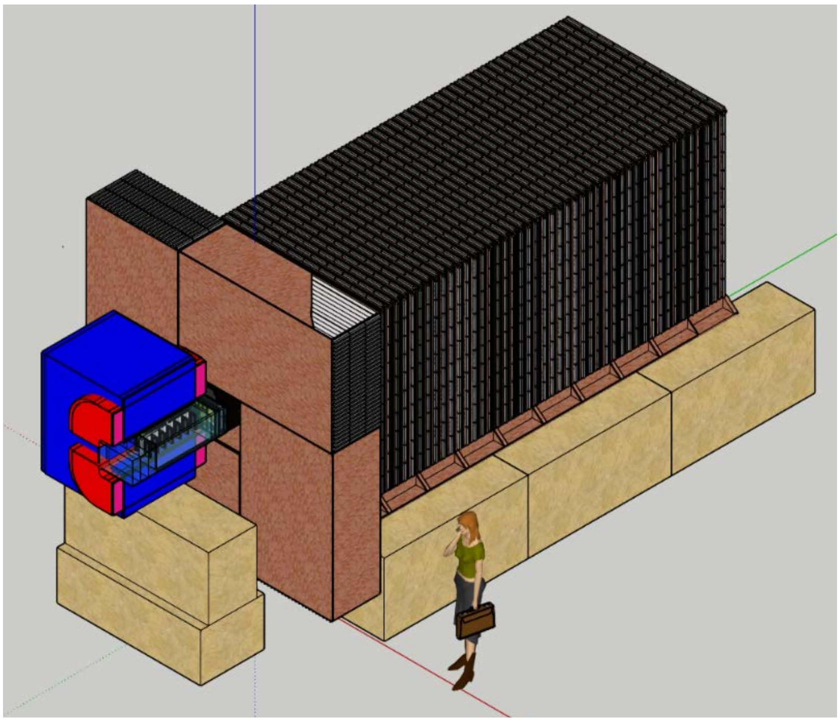

Figure 7.2.: A rendering of the LDMX detector showing the hadronic veto calorimeter at the rear. The calorimeter design is derived from the CRV.

[157]. The design of the device would employ triangular scintillator extrusions with a single WLS fiber per extrusion, bonded into quadcounters similar to LDMX. The use of triangular extrusions is for a desired 1 mm position resolution. The detectors would be placed into shipping containers outside of the pyramid. This same design is proposed for use in exploring the structure of the Temple of Kukulcán at Chichén Itzá [158]. A similar triangular counter design is being considered for use in Mu2e-II [154].

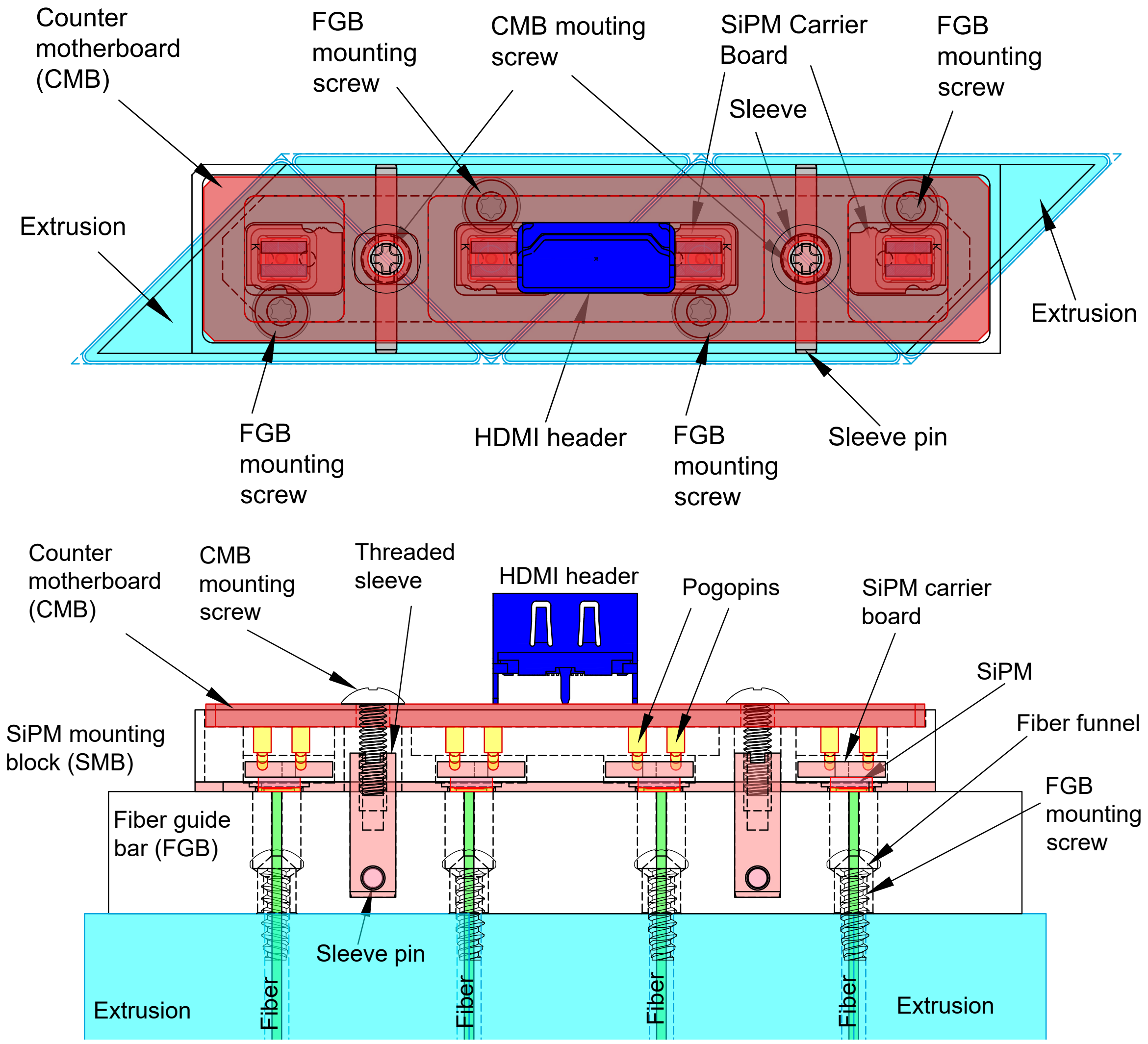

Figure 7.3.: A rendering of the top (top) and side (bottom) x-ray view of the quadcounter proposed for use in the EGP project. The extrusions have a triangular profile with a single WLS fiber for a desired 1 mm position resolution.

References

[1]G. Aad, T. Abajyan, B. Abbott, J. Abdallah, S. Abdel Khalek, A. Abdelalim, O. Abdinov, R. Aben, B. Abi, M. Abolins, and et al., "Observation of a new particle in the search for the Standard Model Higgs boson with the ATLAS detector at the LHC", Physics Letters B **716**, 1–29 (2012).

[2]S. Chatrchyan, V. Khachatryan, A. Sirunyan, A. Tumasyan, W. Adam, E. Aguilo, T. Bergauer, M. Dragicevic, J. Ero, C. Fabjan, and et al., "Observation of a new boson at a mass of 125 GeV with the CMS experiment at the LHC", Physics Letters B **716**, 30–61 (2012).

[3]F. Capozzi, E. Lisi, A. Marrone, D. Montanino, and A. Palazzo, "Neutrino masses and mixings: Status of known and unknown 3 ν parameters", Nuclear Physics B **908**, 218–234 (2016).

[4]F. del Aguila, L. Ametller, J. I. Illana, J. Santiago, P. Talavera, and R. Vega-Morales, "The full lepton flavor of the littlest Higgs model with T-parity", Journal of High Energy Physics **2019** (2019) `10.1007/jhep07(2019)154`.

[5]O. Vives, "Supersymmetry breaking and the SUSY flavour problem", Nuclear Physics B - Proceedings Supplements **117**, 717–719 (2003).

[6]W. Altmannshofer, A. J. Buras, S. Gori, P. Paradisi, and D. M. Straub, "Anatomy and phenomenology of FCNC and CPV effects in SUSY theories", Nuclear Physics B **830**, 17–94 (2010).

[7]A. de Gouvea and P. Vogel, "Lepton flavor and number conservation, and physics beyond the standard model", Progress in Particle and Nuclear Physics **71**, Fundamental Symmetries in the Era of the LHC, 75–92 (2013).

[8]L. Calibbi, D. Chowdhury, A. Masiero, K. M. Patel, and S. K. Vempati, "Status of supersymmetric type-I seesaw in SO(10) inspired models", Journal of High Energy Physics **2012** (2012) `10.1007/jhep11(2012)040`.

[9]J. M. Arnold, B. Fornal, and M. B. Wise, "Phenomenology of scalar leptoquarks", Physical Review D **88** (2013) `10.1103/physrevd.88.035009`.

[10]J. Hubisz, P. Meade, A. Noble, and M. Perelstein, "Electroweak precision constraints on the littlest Higgs model with T parity", Journal of High Energy Physics **2006**, 135–135 (2006).

[11]M. Blanke, A. J. Buras, B. Duling, S. Recksiegel, and C. Tarantino, *FCNC Processes in the Littlest Higgs Model with T-Parity: an Update*, 2009, arXiv:`0906.5454 [hep-ph]`.

[12]C.-H. Lee, P. S. B. Dev, and R. N. Mohapatra, "Natural TeV-scale left-right seesaw mechanism for neutrinos and experimental tests", Physical Review D **88** (2013) 10.1103/physrevd.88.093010.

[13]J. Adam and et al., "New Constraint on the Existence of the $\mu^+ \to e^+\gamma$ Decay", Phys. Rev. Lett. **110**, 801–806 (2013).

[14]Bertl, Wilhelm H. and others, "A Search for muon to electron conversion in muonic gold", Eur. Phys. J. C **47**, 337–346 (2006).

[15]R. Harnik, J. Kopp, and J. Zupan, "Flavor violating Higgs decays", Journal of High Energy Physics **2013** (2013) 10.1007/jhep03(2013)026.

[16]D. Measday, "The nuclear physics of muon capture", Physics Reports **354**, 243–409 (2001).

[17]T. Suzuki, D. F. Measday, and J. Roalsvig, "Total Nuclear Capture Rates for Negative Muons", Phys. Rev. C **35**, 2212 (1987).

[18]A. Czarnecki, X. Garcia i Tormo, and W. J. Marciano, "Muon decay in orbit: Spectrum of high-energy electrons", Physical Review D **84** (2011) {10.1103/physrevd.84.013006}.

[19]R. Szafron and A. Czarnecki, "High-energy electrons from the muon decay in orbit: Radiative corrections", Physics Letters B **753**, 61–64 (2016).

[20]P. Christillin, M. Rosa-Clot, and S. Servadio, "Radiative muon capture in medium-heavy nuclei", Nuclear Physics A **345**, 331–366 (1980).

[21]D. S. Ayers and et al., "Measurements of the lifetimes of positive and negative pions", Phys. Rev. D **3**, 1051–1063 (1971).

[22]R. Bernstein and P. S. Cooper, "Charged lepton flavor violation: An experimenter's guide", Physics Reports **532**, 27–64 (2013).

[23]Bertl, Wilhelm H. and others, "Search for the Decay $\mu^+ \to e^+e^+e^-$", Nucl. Phys. B **260**, 1–31 (1985).

[24]A. M. Baldini, E. Baracchini, C. Bemporad, F. Berg, M. Biasotti, G. Boca, P. W. Cattaneo, G. Cavoto, F. Cei, M. Chiappini, and et al., "The design of the MEG II experiment", The European Physical Journal C **78** (2018) 10.1140/epjc/s10052-018-5845-6.

[25]K. Arndt and et al., *Technical design of the phase I Mu3e experiment*, 2021, arXiv:2009.11690 [physics.ins-det].

[26]N. Teshima, *Status of the DeeMe Experiment, an Experimental Search for μ-e Conversion at J-PARC MLF*, 2019, arXiv:1911.07143 [physics.ins-det].

[27]L. Bartoszek and et al., *Mu2e Technical Design Report*, Technical Design Report (Fermi National Accelerator Laboratory, 2015), eprint: 1501.05241 (physics.ins-det).

[28]R. Abramishvili and et al., "COMET Phase-I Technical Design Report", PTEP **2020**, 033C01 (2020), arXiv:1812.09018 [physics.ins-det].

[29]J. Miller and S. Krave, *Requirements and Specifications for WBS 5.05 - Muon Stopping Target*, Mu2e DocDB Internal Technical Report 1437 (Fermi National Accelerator Laboratory, 2019).

[30]J. Miller and R. Bernstein, *Requirements and Specifications for WBS 5.06 - Muon Stopping Target Monitor*, Mu2e DocDB Internal Technical Report 1438 (Fermi National Accelerator Laboratory, 2016).

[31]J. Miller, *Requirements Document: Anti-Proton Window*, Mu2e DocDB Internal Technical Report 941 (Fermi National Accelerator Laboratory, 2010).

[32]R. Bernstein and A. Mukherjee, *Requirement Documents for Mu2e Tracker*, Mu2e DocDB Internal Technical Report 743 (Fermi National Accelerator Laboratory, 2014).

[33]A. Mukherjee, *CD-3c Review: Mu2e Tracker*, Mu2e DocDB Internal Technical Report 7463 (Fermi National Accelerator Laboratory, 2016).

[34]R. Bernstein, D. Hitlin, and S. Miscetti, *Calorimeter Requirements Document*, Mu2e DocDB Internal Technical Report 864 (Fermi National Accelerator Laboratory, 2016).

[35]DuPont, *Tyvek*, (2021) `https://www.dupont.com/brands/tyvek.html`.

[36]A. Gaponenko, *Summary of Backgrounds for CD3*, Mu2e DocDB Internal Technical Report 7464 (Fermi National Accelerator Laboratory, 2017).

[37]J. A. Bistirlich, K. M. Crowe, A. S. L. Parsons, P. Skarek, and P. Truol, "Photon Spectra from Radiative Absorption of Pions in Nuclei", Phys. Rev. C **5**, 1867–1883 (1972).

[38]D. W. Joseph, "Electron Pair Creation in $\pi + p$ capture reactions from rest", Il Nuovo Cimento **16**, 997–1013 (1960).

[39]H. Rood and H. Tolhoek, "The theory of muon capture by complex nuclei: (III). Radiative muon capture", Nuclear Physics **70**, 658–692 (1965).

[40]H. PRIMAKOFF, "Theory of Muon Capture", Rev. Mod. Phys. **31**, 802–822 (1959).

[41]P. C. Bergbusch and et al., "Radiative muon capture on O, Al, Si, Ti, Zr, and Ag", Phys. Rev. C **59**, 2853–2864 (1999).

[42]D. S. Armstrong and et al., "Radiative muon capture on Al, Si, Ca, Mo, Sn, and Pb", Phys. Rev. C **46**, 1094–1107 (1992).

[43]3M, *3M Scotch-Weld Epoxy Adhesive DP420NS*, (2021) `https://www.3m.com/3M/en%5C_US/company-us/all-3m-products/~/3M-Scotch-Weld-Epoxy-Adhesive-DP420NS/?N=5002385+3293241657%5C&preselect=8710676+8710815+8711736+8712276+8736167+3288748190+3289594041+3289594216+3294059247%5C&rt=rud`.

[44]3M, *3M Scotch-Weld Epoxy Adhesive DP100*, (2021) `https://www.3m.com/3M/en%5C_US/company-us/all-3m-products/~/3M-Scotch-Weld-Epoxy-Adhesive-DP100/?N=5002385+3293242434%5C&rt=rud`.

[45]Research Engineering and Manufacturing Inc., *Plastite Trilobular Stainless Steel Torx Plus Rounded Head #4-20 3/8" Thread-forming Screws*, (2021) `https://www.mcmaster.com/96001A206/`.

[46]Saint-Gobain, *Detector Assembly Materials*, (2021) https://www.crystals.saint-gobain.com/sites/imdf.crystals.com/files/documents/detector-assembly-materials_69673.pdf.

[47]Y. Oksuzian and P. Farris, *Light yield improvement from painting fiber guide bars*, Mu2e DocDB Internal Technical Report 18405 (Fermi National Accelerator Laboratory, June 2018).

[48]3M, *3M Specular Film FS2000MA / Radiant Mirror Film VM2000*, (2021) https://multimedia.3m.com/mws/media/9824490/3mtm-specular-film-df2000ma-technical-data-sheet.pdf.

[49]C.H. Krammes and Company, Inc., *C.H. Krammes and Co. CNC Machining*, (2021) http://www.krammes.com/.

[50]Fermi National Accelerator Laboratory, *Alignment and Metrology Department, Particle Physics Division*, (2021) https://ppd.fnal.gov/align/align.html.

[51]Geocel, *Geocel 3300 Professional Grade Polyurethane Sealant Black GC68103*, (2021) https://www.geocelusa.com/product/3300-professional-grade-polyurethane-sealant/.

[52]Trinseo, *Dow STYRON 665 W Polystyrene*, (2021) https://www.trinseo.com/Products/Plastics/Products/Polystyrene/STYRON.

[53]D. Beznosko, A. Bross, A. Dyshkant, A. Pla-Dalmau, and V. Rykalin, "FNAL-NICADD extruded scintillator", (2005).

[54]D. Michael, P. Adamson, T. Alexopoulos, W. Allison, G. Alner, K. Anderson, C. Andreopoulos, M. Andrews, R. Andrews, C. Arroyo, and et al., "The magnetized steel and scintillator calorimeters of the MINOS experiment", Nuclear Instruments and Methods in Physics Research Section A: Accelerators, Spectrometers, Detectors and Associated Equipment **596**, 190–28 (2008).

[55]L. Aliaga and et al., "Design, calibration, and performance of the MINERvA detector", Nuclear Instruments and Methods in Physics Research Section A: Accelerators, Spectrometers, Detectors and Associated Equipment **743**, 130–159 (2014).

[56]Kuraray Co., LTD, *Plastic Scintilling Fibers*, (2018) http://kuraraypsf.jp/psf/.

[57]D. S. Ayres and et al., "The NOvA Technical Design Report", (2007) 10.2172/935497.

[58]Kuraray Co., LTD, *Wavelength Shifting Fibers*, (2018) http://kuraraypsf.jp/psf/ws.html.

[59]Fermi National Accelerator Laboratory, *Fermilab Test Beam Facility*, (2021) https://ftbf.fnal.gov/.

[60]E. Dukes, P. Farris, R. Group, T. Lam, Y. Oksuzian, and D. Shooltz, "Performance of wavelength-shifting fibers for the Mu2e cosmic ray veto detector", Journal of Instrumentation **13**, 12028–12028 (2018).

[61]ITW Performance Polymers, *Devcon HP 250 Epoxy*, (2021) https://tinyurl.com/DevconHP250.

[62]McMaster-Carr, *Antistatic Low-Friction Fiberglass Tape Coated with Teflon PTFE*, (2021) https://www.mcmaster.com/fastening-tape/antistatic-low-friction-fiberglass-tape-coated-with-teflon-ptfe/.

[63]J. Serrano, "Design and Analysis of CRV components in the Fermilab Mu2e Experiment", 12527, Master's Thesis (Northern Illinois University, Mu2e Document Database, Aug. 2017), pp. 15–90, 119 pp.

[64]V. Zutshi, *Mu2e CRV: Photodetectors*, Mu2e DocDB Internal Technical Report 30529 (Fermi National Accelerator Laboratory, Oct. 2019).

[65]Hamamatsu Photonics K.K., *Hamamatsu S13360-2050VE Silicon Photomultiplier*, (2018) https://www.hamamatsu.com/eu/en/product/type/S13360-2050VE/index.html.

[66]E. Garutti and Y. Musienko, "Radiation damage of SiPMs", Nucl. Instrum. Meth. A **926**, 69–84 (2019), arXiv:1809.06361 [physics.ins-det].

[67]V. Zutshi and et al., *SiPM QA/QC*, Mu2e DocDB Internal Technical Document 6759 (Fermi National Accelerator Laboratory, Aug. 2015).

[68]G. Lindstrom, "Radiation damage in silicon detectors", Nucl. Instrum. Meth. A **512**, edited by P. Holl, G. Lutz, F. Schopper, L. Struder, S. Masciocchi, C. Fiorini, A. Longoni, and M. Sampietro, 30–43 (2003).

[69]Northwestern Medicine, *Northwestern Medicine Proton Center*, (2021) https://www.protoncenter.nm.org.

[70]G. Blazey, J. Colston, A. Dyshkant, K. Francis, J. Kalnins, S. Uzunyan, V. Zutshi, S. Hansen, P. Rubinov, E. Dukes, and et al., "Radiation tests of Hamamatsu multi-pixel photon counters", Nuclear Instruments and Methods in Physics Research Section A: Accelerators, Spectrometers, Detectors and Associated Equipment **927**, 463–470 (2019).

[71]Tektronix, *Tektronix PSPL2600C Pulse Generator*, (2018) https://www.tek.com/datasheet/pspl2600c-pulse-generator-datasheet.

[72]L. Xia, *Mu2e CRV: Electronics*, Mu2e DocDB Internal Technical Report 30124 (Fermi National Accelerator Laboratory, Dec. 2019).

[73]Texas Instruments, *AFE5807 8-Channel analog front end with passive CW mixer for ultrasound*, (2018) https://www.ti.com/product/AFE5807.

[74]Xilinx, *XC6SLX16-3CSG324I Spartan-6LX Field Programmable Gate Arrays*, (2021) https://www.xilinx.com/products/silicon-devices/fpga/spartan-6.html.

[75]Texas Instruments, *RM48L952 16/32-Bit RISC Flash Microcontroller*, (2021) https://www.ti.com/product/RM48L952.

[76]S. Hansen, "Verbal Discussion of FEB Magnetic Field Tolerance Study", 2018.

[77]Dassault Systemes, *OPERA Electromagnetic and Electromechanical FEA Software Suite*, (2019) https://www.3ds.com/products-services/simulia/products/opera/.

[78]H. Glass, *CRV FEB Magnetic Shielding Effectiveness for Enclosure Design Model V4*, Mu2e DocDB Internal Technical Report 18792 (Fermi National Accelerator Laboratory, July 2018).

[79]Texas Instruments, *LM3S5B91 Stellaris Microcontroller*, (2021) `https://www.ti.com/en/download/shared/product-brief-LM3S5B91.pdf`.

[80]R. Ehrlich, *Memo CRV Simulations*, Mu2e DocDB Internal Technical Document 3059 (Fermi National Accelerator Laboratory, Oct. 2018).

[81]L. Xia, *Mu2e CRV: Electronics*, Mu2e DocDB Internal Technical Report 21225 (Fermi National Accelerator Laboratory, Oct. 2018).

[82]S. Agostinelli and et al., "Geant4?a simulation toolkit", Nuclear Instruments and Methods in Physics Research Section A: Accelerators, Spectrometers, Detectors and Associated Equipment **506**, 250–303 (2003).

[83]C. Green, J. Kowalkowski, M. Paterno, M. Fischler, L. Garren, and Q. Lu, "The Art Framework", J. Phys. Conf. Ser. **396**, edited by M. Ernst, D. Dullmann, O. Rind, and T. Wong, 022020 (2012).

[84]R. Brun and F. Rademakers, "ROOT: An object oriented data analysis framework", Nucl. Instrum. Meth. A **389**, edited by M. Werlen and D. Perret-Gallix, 81–86 (1997).

[85]Y. Abe, C. Aberle, J. C. dos Anjos, J. C. Barriere, M. Bergevin, A. Bernstein, T. J. C. Bezerra, L. Bezrukhov, E. Blucher, N. S. Bowden, and et al., "Direct measurement of backgrounds using reactor-off data in Double Chooz", Physical Review D **87** (2013) `10.1103/physrevd.87.011102`.

[86]Wikipedia, *Gumbel Distribution*, (2021) `https://en.wikipedia.org/wiki/Gumbel_distribution`.

[87]A. Artikov, V. Baranov, G. C. Blazey, N. Chen, D. Chokheli, Y. Davydov, E. C. Dukes, A. Dychkant, R. Ehrlich, K. Francis, and et al., "Photoelectron yields of scintillation counters with embedded wavelength-shifting fibers read out with silicon photomultipliers", Nuclear Instruments and Methods in Physics Research Section A: Accelerators, Spectrometers, Detectors and Associated Equipment **890**, 84–95 (2018).

[88]SUREL LLC, *SKTN-MED Low Molecular Weight Siloxanes*, (2021) `http://www.surel.ru/silicone/77/`.

[89]I. Vasilyev and et al., *Radiation hardness study of the synthetic rubber filler for the CRV system of the Mu2e experiment*, Mu2e DocDB Internal Technical Report 11291 (Fermi National Accelerator Laboratory, June 2017).

[90]R. Ehrlich and et al., *Test beam CRV counter aging studies*, Mu2e DocDB Internal Technical Report 32055 (Fermi National Accelerator Laboratory, Mar. 2020).

[91]S. Boi and et al., *Natural aging of CRV counters*, Mu2e DocDB Internal Technical Report 23749 (Fermi National Accelerator Laboratory, Apr. 2020).

[92]Quincy Lab, *31-350ERS DIGITAL BENCH OVEN*, (2018) `https://quincylab.com/digital-bench-oven`.

[93]Wikipedia, *Arrhenius Equation*, (2021) https://en.wikipedia.org/wiki/Arrhenius_equation.

[94]R. Spencer and R. Dillon, “The viscous flow of molten polystyrene”, Journal of Colloid Science **3**, 163–180 (1948).

[95]S. Bourbigot, J. W. Gilman, and C. A. Wilkie, “Kinetic analysis of the thermal degradation of polystyrene-montmorillonite nanocomposite”, Polymer Degradation and Stability **84**, 483–492 (2004).

[96]J. D. Peterson, S. Vyazovkin, and C. A. Wight, “Kinetics of the Thermal and Thermo-Oxidative Degradation of Polystyrene, Polyethylene and Poly(propylene)”, Macromolecular Chemistry and Physics **202**, 775–784 (2001), eprint: https://onlinelibrary.wiley.com/doi/pdf/10.1002/1521-3935\%2820010301\%29202\%3A6\%3C775\%3A\%3AAID-MACP775\%3E3.0.CO\%3B2-G.

[97]A. Artikov, D. Chokheli, G. Pauletta, and A. Simonenko, “The loss of light yield with time in the CDF II scintillation counters”, Nuclear Instruments and Methods in Physics Research Section A: Accelerators, Spectrometers, Detectors and Associated Equipment **672**, 46–51 (2012).

[98]R. Ehrlich, *CRV Sector Inefficiencies*, Mu2e DocDB Internal Technical Document 17468 (Fermi National Accelerator Laboratory, Oct. 2018).

[99]R. Ehrlich, *CRV Inefficiencies of Top Modules*, Mu2e DocDB Internal Technical Document 7993 (Fermi National Accelerator Laboratory, Sept. 2016).

[100]E. Dukes, R. Ehrlich, S. Boi, and Y. Oksuzian, *The Cosmic Ray Background Estimate in a Staged Mu2e*, Mu2e DocDB Internal Technical Report 28266 (Fermi National Accelerator Laboratory, Mar. 2020).

[101]Y. Oksuzian, *CRV Deadtime and Rates*, Mu2e DocDB Internal Technical Document 8627 (Fermi National Accelerator Laboratory, Sept. 2018).

[102]E. Dukes, *Mu2e Cosmic Ray Veto Requirements*, Mu2e DocDB Internal Technical Document 944 (Fermi National Accelerator Laboratory, 2016).

[103]C. Group and et al., *Quality Assurance and Safety Program for the Cosmic Ray Veto Module Factory*, Mu2e DocDB Internal Technical Document 4150 (Fermi National Accelerator Laboratory, 2017).

[104]C. Group and et al., *Dicounter Assembly Procedures for CRV Module Fabrication @ UVA*, Mu2e DocDB Internal Technical Document 6581 (Fermi National Accelerator Laboratory, 2017).

[105]C. Group and et al., *Dicounter Vertical Saw Procedures for CRV Module Fabrication @ UVA*, Mu2e DocDB Internal Technical Document 6582 (Fermi National Accelerator Laboratory, 2017).

[106]3M, *Scotch-Brite Production Hand Pad 8447 VFN*, (2021) https://www.3m.com/3M/en%5C_US/company-us/all-3m-products/~/Scotch-Brite-Production-Hand-Pad-8447/?N=5002385+3293193882%5C&preselect=8692962+8710644+8710812+8710964%5C&rt=rud.

[107] C. Group and et al., *Fiber Guide Bar Assembly Procedures for CRV Module Fabrication @ UVA*, Mu2e DocDB Internal Technical Document 6583 (Fermi National Accelerator Laboratory, 2017).

[108] C. Group and et al., *Hot Knife and Flycutting Procedures for CRV Module Fabrication @ UVA*, Mu2e DocDB Internal Technical Document 6584 (Fermi National Accelerator Laboratory, 2017).

[109] SICK AG, *SICK IVC-3D Machine Vision Smart Camera*, (2021) https://www.sick.com/ag/en/machine-vision/3d-machine-vision/ivc-3d/c/g125453.

[110] A. Pla-Dalmau, *QA/QC procedures for the CRV scintillator strips*, Mu2e DocDB Internal Technical Document 5170 (Fermi National Accelerator Laboratory, Feb. 2015).

[111] A. Pla-Dalmau, *Scintillator Extrusion Production*, Mu2e DocDB Internal Technical Document 18861 (Fermi National Accelerator Laboratory, July 2018).

[112] CREE, *CREE XLamp 3 Model 3XL7090RY-L00-D5-14*, (2018) https://www.cree.com/led-components/.

[113] Hamamatsu Photonics K.K., *Hamamatsu S1227-1010BR Photodiode*, (2018) https://www.hamamatsu.com/us/en/product/alpha/P/4103/S1227-1010BR/index.html.

[114] Ocean Optics, *Ocean Optics STS-VIS spectrophotometer*, (2018) https://oceanoptics.com/product/sts-vis-microspectrometer/.

[115] C. Group and et al., *Imaging for Flycutter QC Procedures for CRV Module Fabrication @ UVA*, Mu2e DocDB Internal Technical Document 6585 (Fermi National Accelerator Laboratory, 2017).

[116] Mitutoyo, *Mitutoyo Surftest SJ-210 Surface Roughness Tester*, (2021) https://ecatalog.mitutoyo.com/Surftest-SJ-210-Series-178-Portable-Surface-Roughness-Tester-C1794.aspx.

[117] C. Group and et al., *Fiber Transmission Tester QC Procedures for CRV Module Fabrication @ UVA*, Mu2e DocDB Internal Technical Document 6586 (Fermi National Accelerator Laboratory, 2017).

[118] C. Group and et al., *Radioactive Source SOP for CRV Module Fabrication at UVA*, Mu2e DocDB Internal Technical Document 7970 (Fermi National Accelerator Laboratory, 2020).

[119] C. Group and et al., *Module Assembly Procedures for CRV Module Fabrication @ UVA*, Mu2e DocDB Internal Technical Document 6587 (Fermi National Accelerator Laboratory, 2020).

[120] C. Group and et al., *CRV Module Table Leveling Procedure for CRV Module Fabrication @ UVA*, Mu2e DocDB Internal Technical Document 12971 (Fermi National Accelerator Laboratory, 2016).

[121] C. Group and et al., *Vacuum Lifter Documentation for the CRV Factory at UVa*, Mu2e DocDB Internal Technical Document 5898 (Fermi National Accelerator Laboratory, 2015).

[122]Y. Oksuzian and et al., *Module Assembly*, (2019) https://www.youtube.com/watch?v=7hDuHsjgUlY.

[123]Pierce Aluminum, *Pierce Aluminum*, (2021) https://piercealuminum.com/.

[124]Dakota Ultrasonics, *Dakota PVX*, (2021) https://dakotaultrasonics.com/product/precision/pvx/.

[125]E. Dukes, *CRV Module Aluminum Measurement Points*, Mu2e DocDB Internal Technical Document 24112 (Fermi National Accelerator Laboratory, Apr. 2019).

[126]REO Logistics Inc., *REO Logstics freight forwarding and supply chain solutions*, (2021) http://www.reologistics.com/.

[127]E. Fernandez and et al., *CAD Design CRV Module Crate*, Mu2e DocDB Internal Technical Report 6560 (Fermi National Accelerator Laboratory, Jan. 2020).

[128]Basic Crating and Packaging Inc., *Basic Crating and Packaging Inc.* (2021) https://www.basiccrating.com/.

[129]Adafruit Industries, *Adalogger Featherwing*, (2018) https://www.adafruit.com/.

[130]Google LLC, *Google Earth*, (2018) https://www.google.com/earth/.

[131]80/20 Inc., *T-Slot Aluminum Building System*, (2021) https://8020.net.

[132]Tripp Lite, *Tripp-Lite SmartPro 2U Uninterruptable Power Supply*, (2019) https://tinyurl.com/TrippLiteSmartPro2UUPS.

[133]Keysight Technologies, *N5700 Series ATE System Power Supplies*, (2019) https://www.keysight.com/us/en/products/dc-power-supplies/ate-system-power-supply/n5700-series-ate-system-power-supplies-750w-1500w.html.

[134]Praxair, *Balance Argon, Carbon Dioxide 20 percent, Certified Grade*, (2019) https://stgb2bpunchout.praxairdirect.com/webapp/wcs/stores/servlet/Product2%5C_12751%5C_10051%5C_19001%5C_-1.

[135]*Atlas Muon Spectrometer Technical Design Report*, tech. rep. CERN-LHCC-97-22 (CERN, Geneva, 1997).

[136]S. Boi, D. Chokheli, and et al., *Cathode Strip Chambers: Specifications*, Mu2e DocDB Internal Technical Report 13613 (Fermi National Accelerator Laboratory, Oct. 2017).

[137]G. Iakovidis, *VMM3, an ASIC for Micropattern Detectors*, tech. rep. ATL-MUON-PROC-2018-003 (CERN, Geneva, Mar. 2018).

[138]Hamamatsu Photonics K.K., *Hamamatsu R2154-02 Photomultiplier Tube*, (2021) https://www.hamamatsu.com/us/en/product/type/R2154-02/index.html.

[139]Fermilab, *Lecroy 623 Octal Discriminator*, (2018) https://prep.fnal.gov/catalog/hardware%5C_info/lecroy/nim/623.html.

[140]Fermilab, *Philips 755 Quad 4-Fold Logic Unit*, (2018) https://prep.fnal.gov/catalog/hardware%5C_info/phillips%5C_scientific/755.html.

[141]Fermilab, *Philips 794 Quad Gate/Delay Generator*, (2018) https://prep.fnal.gov/catalog/hardware%5C_info/phillips%5C_scientific/794.html.

[142]Fermilab, *Philips 726 Logic Level Translator*, (2018) https://prep.fnal.gov/catalog/hardware%5C_info/phillips%5C_scientific/726.html.

[143]Fermilab, *Lecroy 429A Logic Fan-in/out*, (2018) https://prep.fnal.gov/catalog/hardware%5C_info/lecroy/nim/429a.html.

[144]S. Boi and D. Chokheli, *Cathode Strip Chambers: Scintillation Counter Properties*, Mu2e DocDB Internal Technical Report 14289 (Fermi National Accelerator Laboratory, Nov. 2017).

[145]Berkeley Nucleonics Corp, *Berkeley Nucleonics Model 577 0.001Hz to 20MHz Digital Delay/Pulse Generator*, (2018) https://www.berkeleynucleonics.com/model-577.

[146]J. Gordon and E. Mathieson, "Cathode Charge Distributions In Multiwire Chambers. 1: Measurement and Theory", Nucl. Instrum. Meth. A **227**, 267–276 (1984).

[147]Dow, Inc., *XIAMETER PMX-200 Polydimethylsiloxane 1000 cSt viscosity*, (2020) https://www.dow.com/en-us/pdp.xiameter-pmx-200-silicone-fluid-1000-cst.01013246z.html.

[148]Permatex, *Flowable Silicone Windshield and Glass Sealer 81730*, (2018) https://www.permatex.com/products/adhesives-sealants/sealants/permatex-flowable-silicone-windshield-glass-sealer/?locale=en%5C_us.

[149]S. Boi and et al., *Dicounter Filling Study*, Mu2e DocDB Internal Technical Report 23194 (Fermi National Accelerator Laboratory, Dec. 2018).

[150]S. Boi and et al., *About filling CRV dicounters with synthetic silicone resin for mass production*, Mu2e DocDB Internal Technical Report 17078 (Fermi National Accelerator Laboratory, May 2018).

[151]D. Chokheli and et al., *About filling CRV strips with synthetic silicon resin SKTN-MED*, Mu2e DocDB Internal Technical Report 16712 (Fermi National Accelerator Laboratory, Mar. 2018).

[152]M. Bulvain, A. Cheplakov, S. Kulikov, V. Kukhtin, E. Shabalin, and A. Vergoglyadov, "The irradiation facility at the IBR-2M reactor in Dubna", in 14th ICATPP Conference on Astroparticle, Particle, Space Physics and Detectors for Physics Applications (2014), pp. 583–587.

[153]SHIMADZU, *SoliSpec-3700iDUV UV-VIS-NIR Spectrophotometer*, (2021) https://www.shimadzu.com/an/products/molecular-spectroscopy/uv-vis/uv-vis-nir-spectroscopy/solidspec-3700i3700iduv/index.html.

[154]Y. Oksuzian and et al., *CRV at Mu2e-II: Overview*, Mu2e DocDB Internal Technical Report 36360 (Fermi National Accelerator Laboratory, Dec. 2020).

[155]T. Akesson and et al., *Light Dark Matter eXperiment (LDMX)*, 2018, arXiv:1808.05219 [hep-ex].

[156]T. Akesson and et al., *A High Efficiency Photon Veto for the Light Dark Matter eXperiment*, 2019, arXiv:1912.05535 [physics.ins-det].

[157]K. Morishmia and et al., "Discovery of a big void in Khufu's Pyramid by observation of cosmic-ray muons", Nature **552**, 386–390 (2017).

[158]N. S. Foundation, *RUI: Collaboration for Studies of Cosmic Ray Muon Radiation and its Application to Archaeometry, Award Notice*, 2020.

Appendix A.

Dicounter Drawings

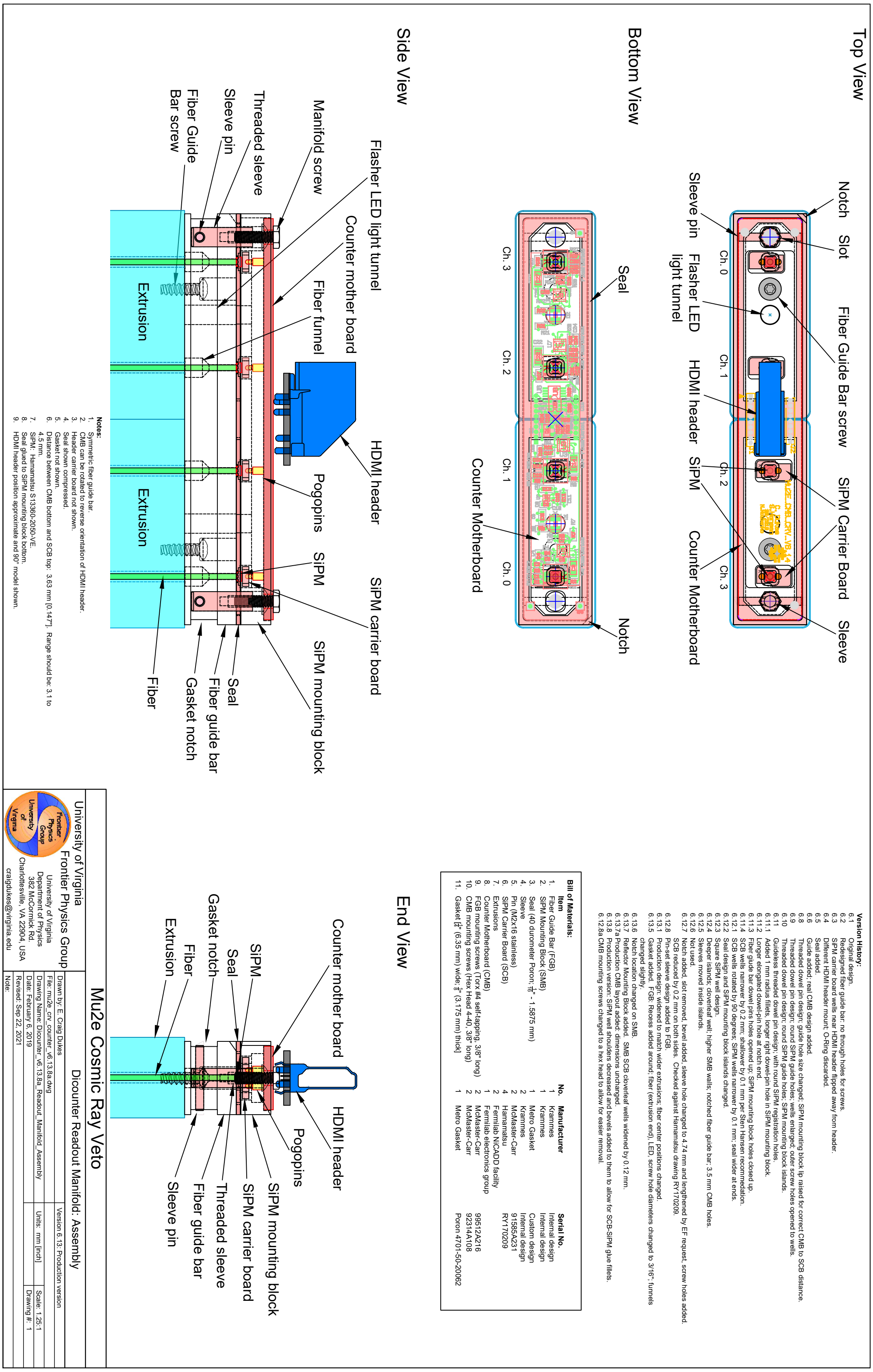

Figure A.1.: Drawing of the Readout Manifold Assembly.

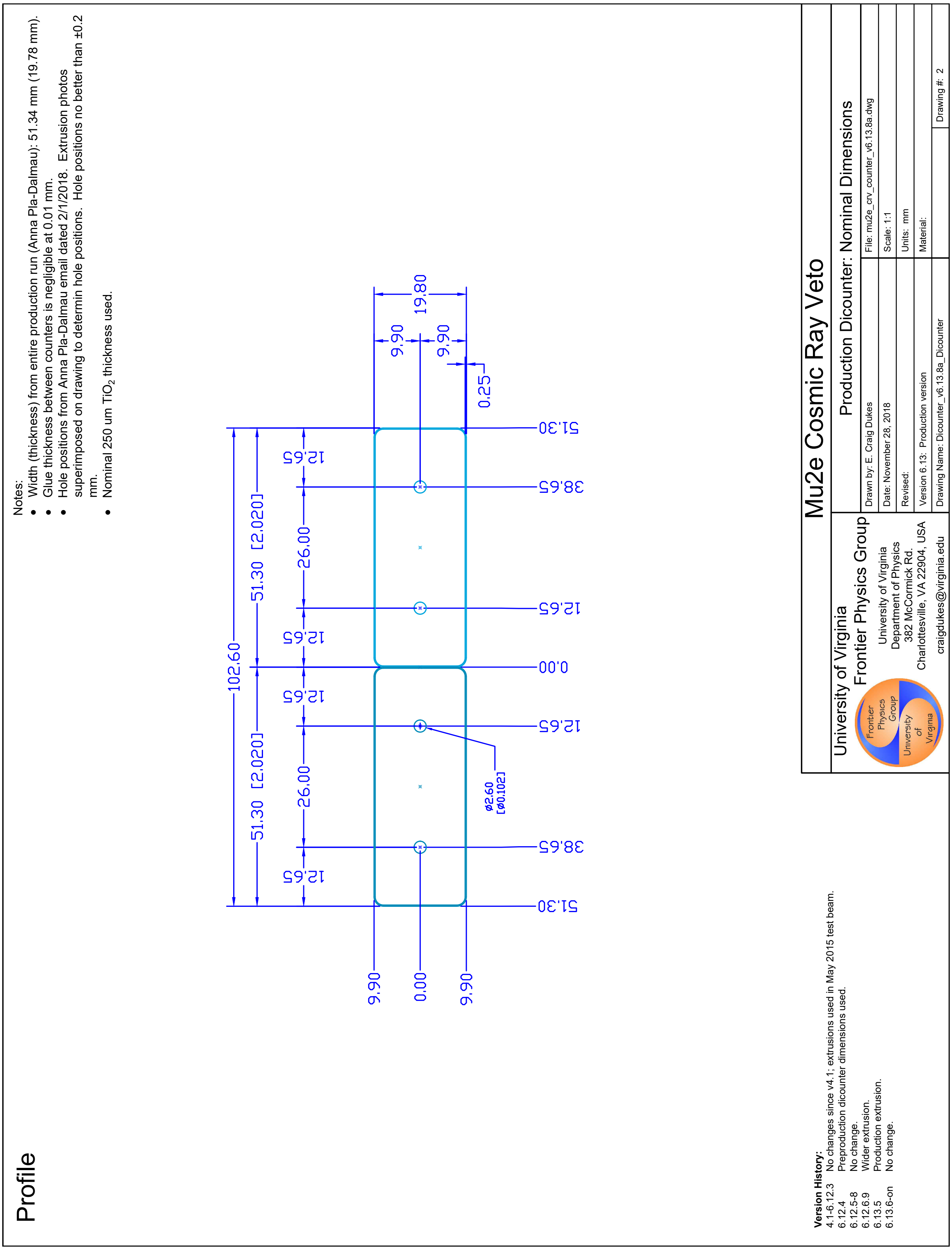

Figure A.2.: Nominal dimensions of a production dicounter.

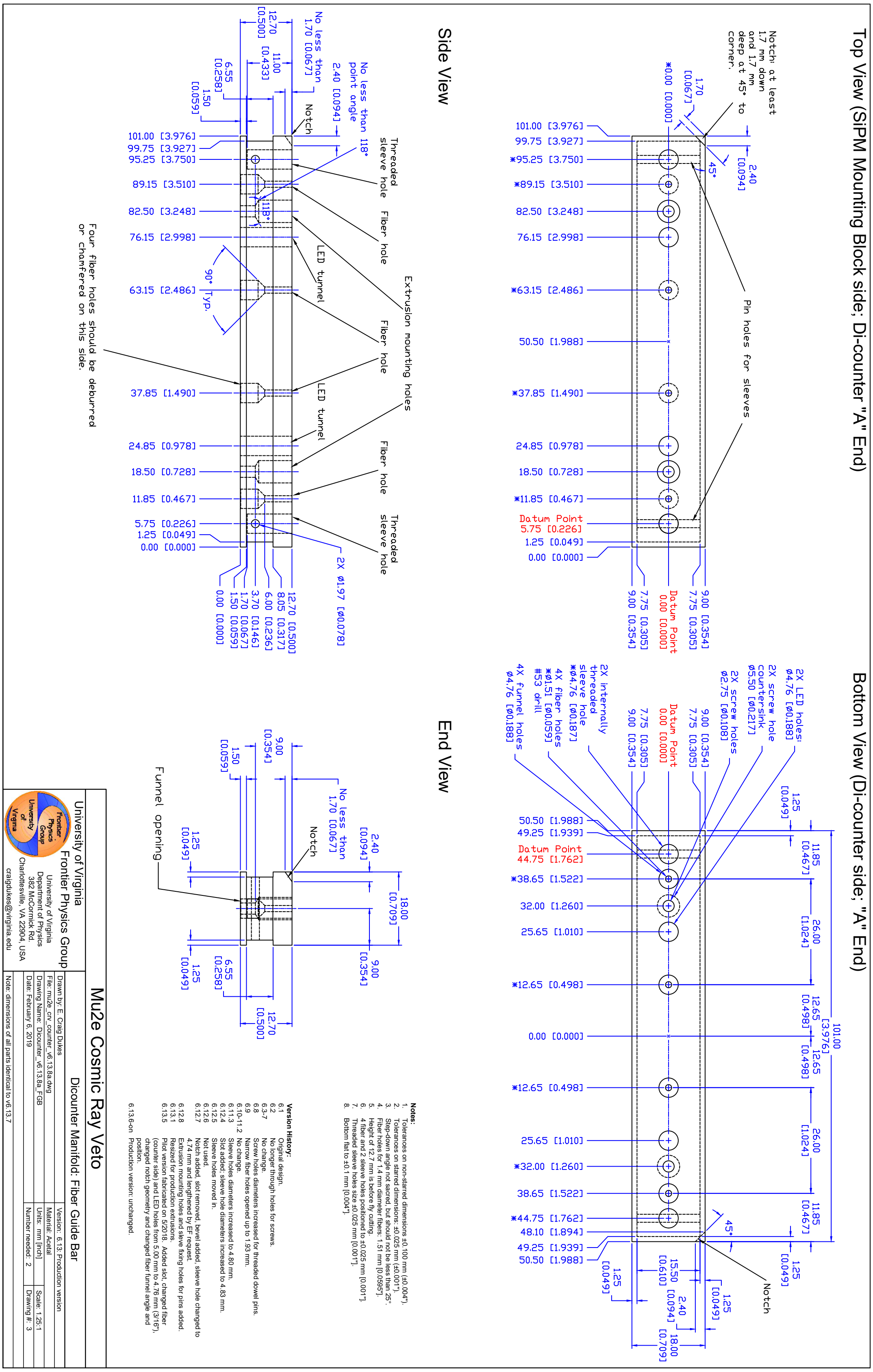

Figure A.3.: Drawing of the Fiber Guide Bar (FGB).

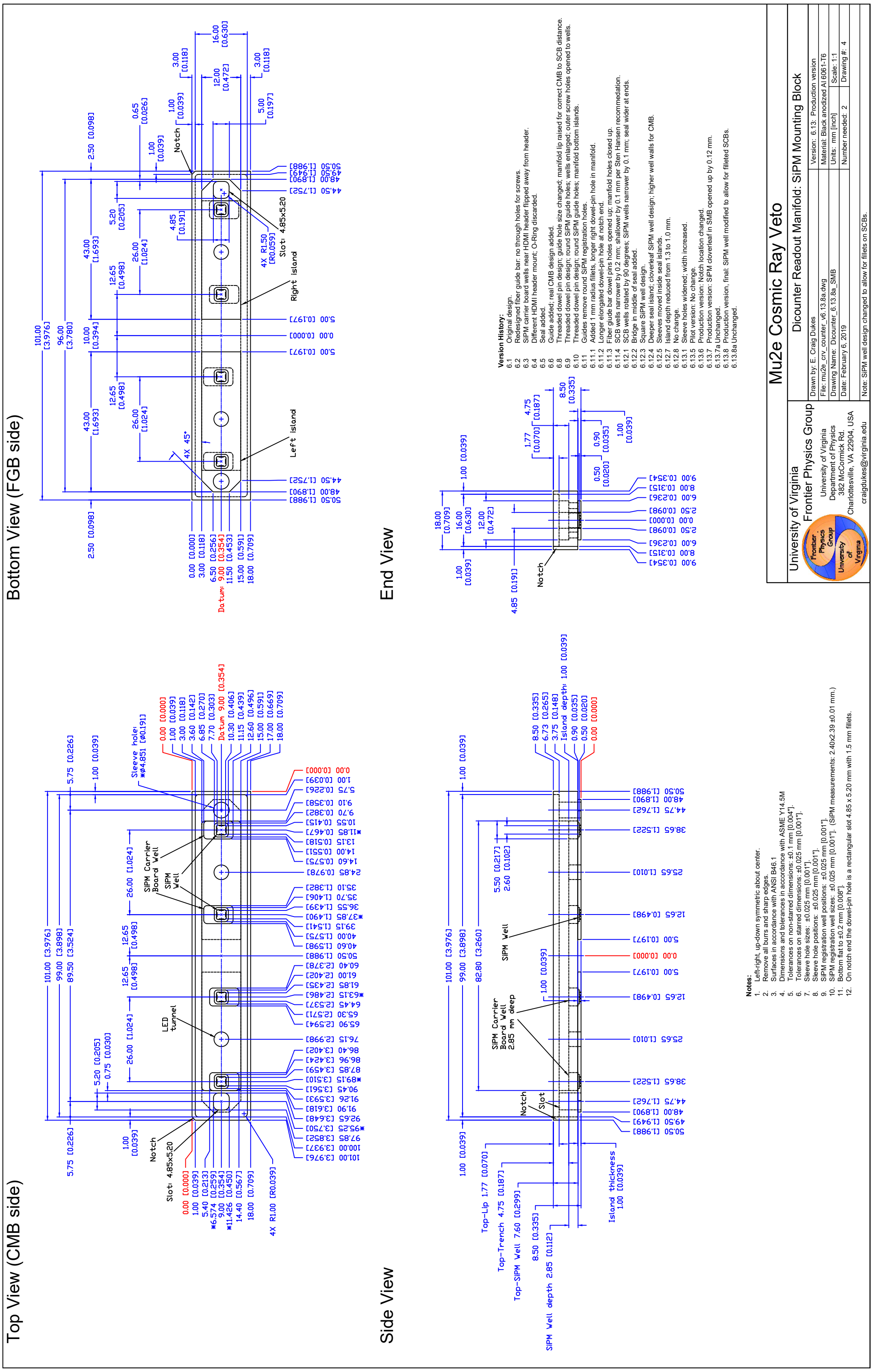

Figure A.4.: Drawing of the SiPM Mounting Block (SMB).

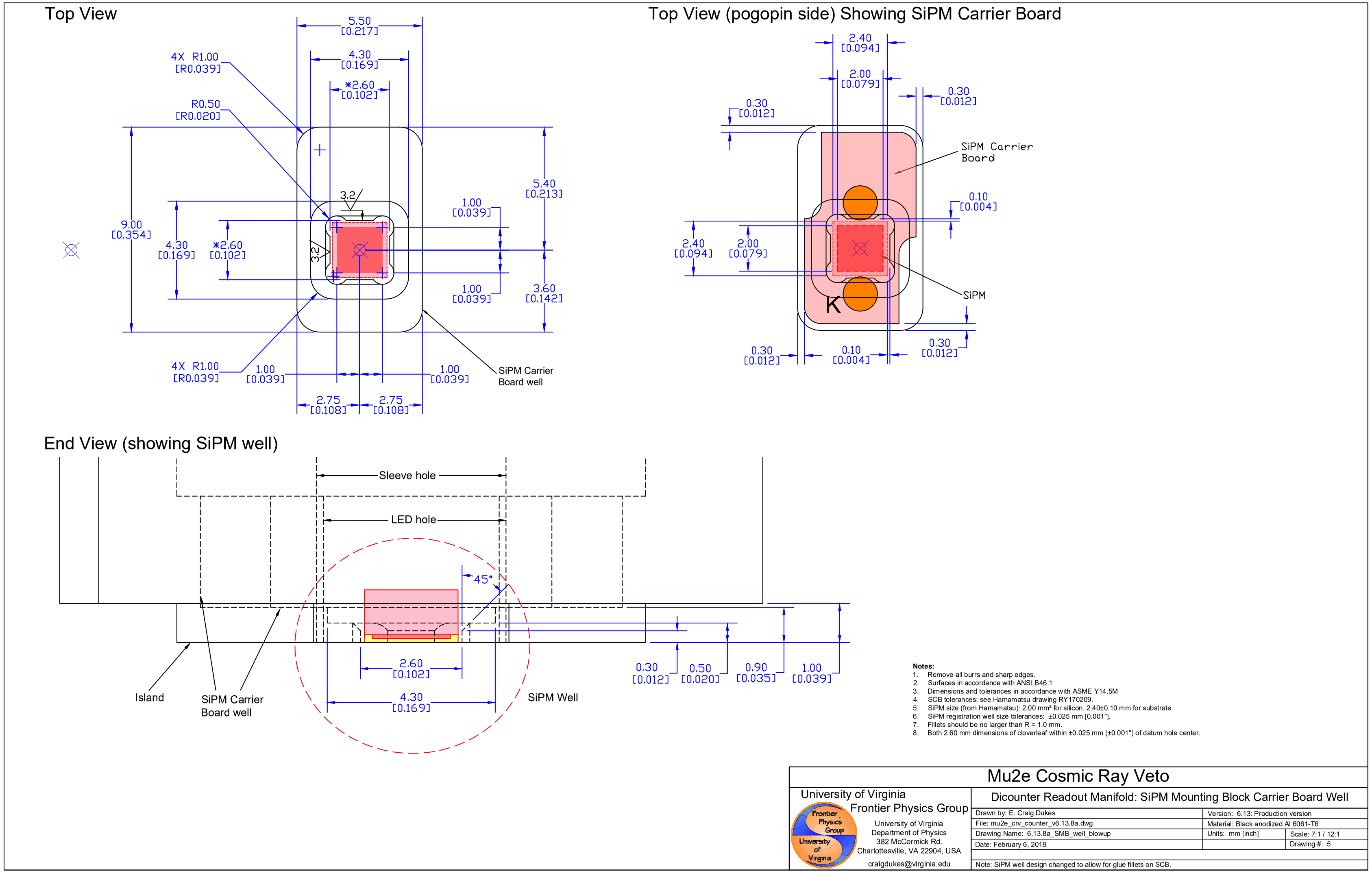

Figure A.5.: Drawing of the carrier board well of the SMB. Shows the SiPM Carrier Board (SCB) in the well.

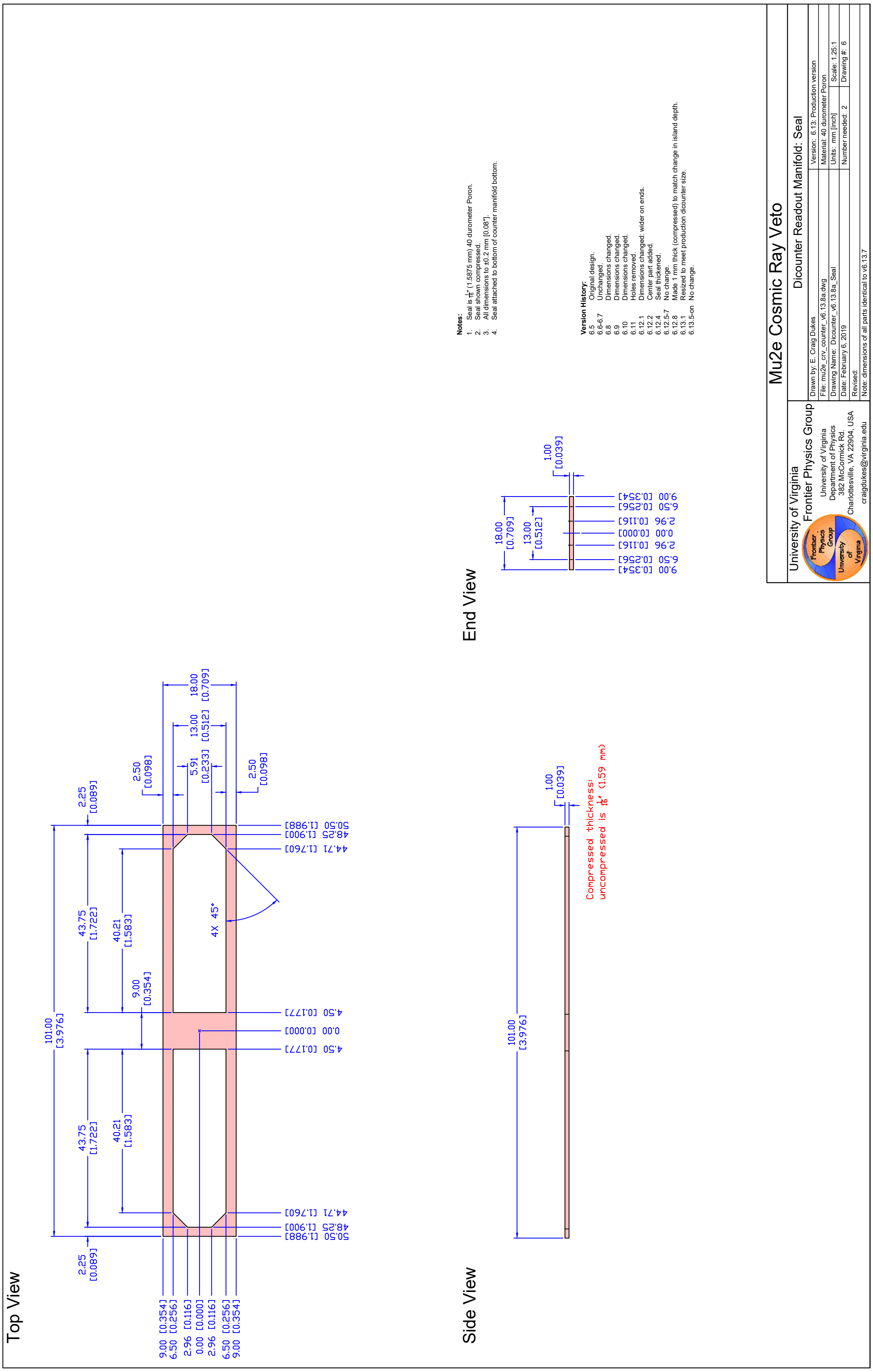

Figure A.6.: Drawing of the manifold assembly seal that sits between the SMB and FGB.

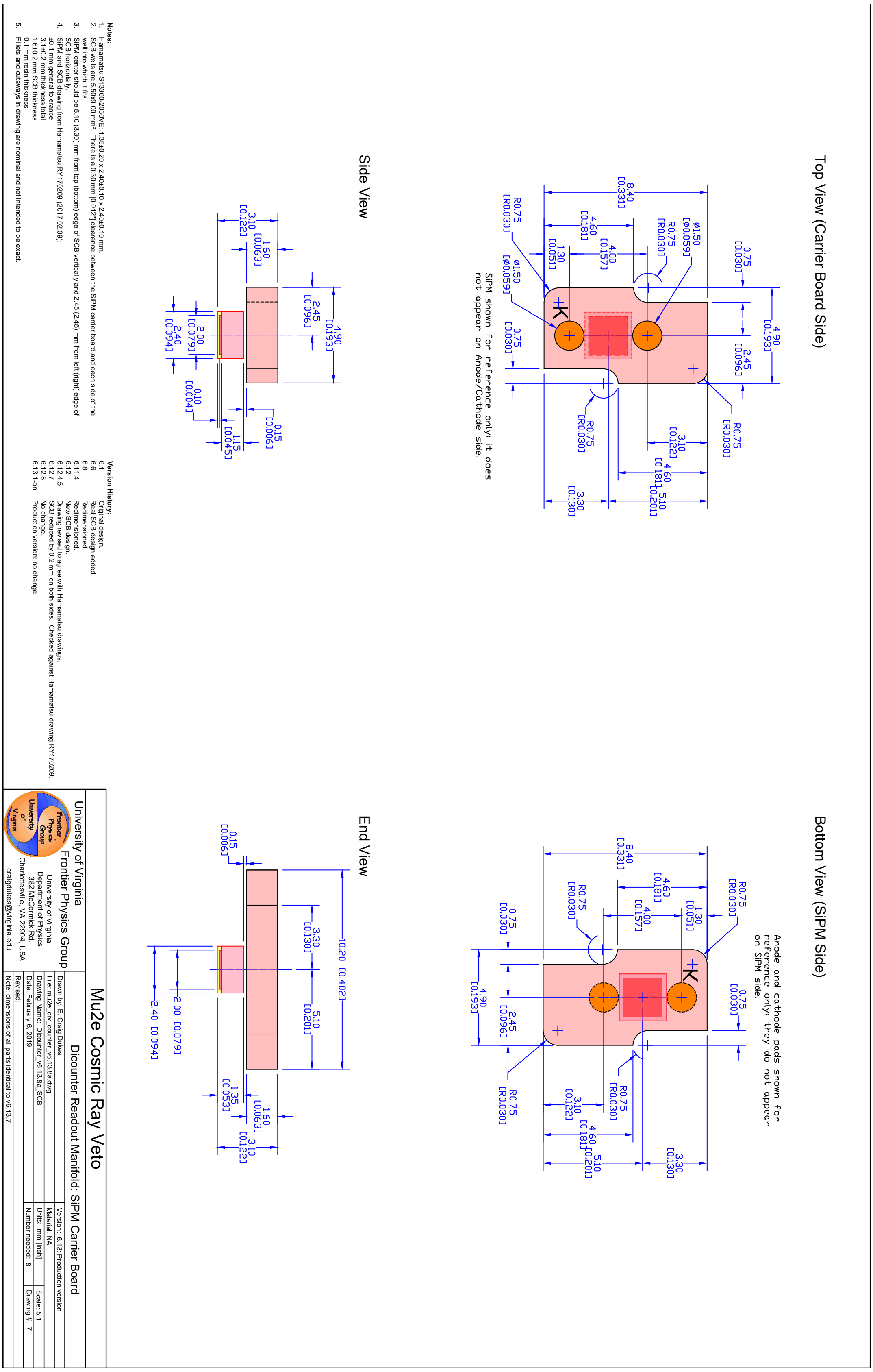

Figure A.7.: Drawing of the SiPM Carrier Board (SCB).

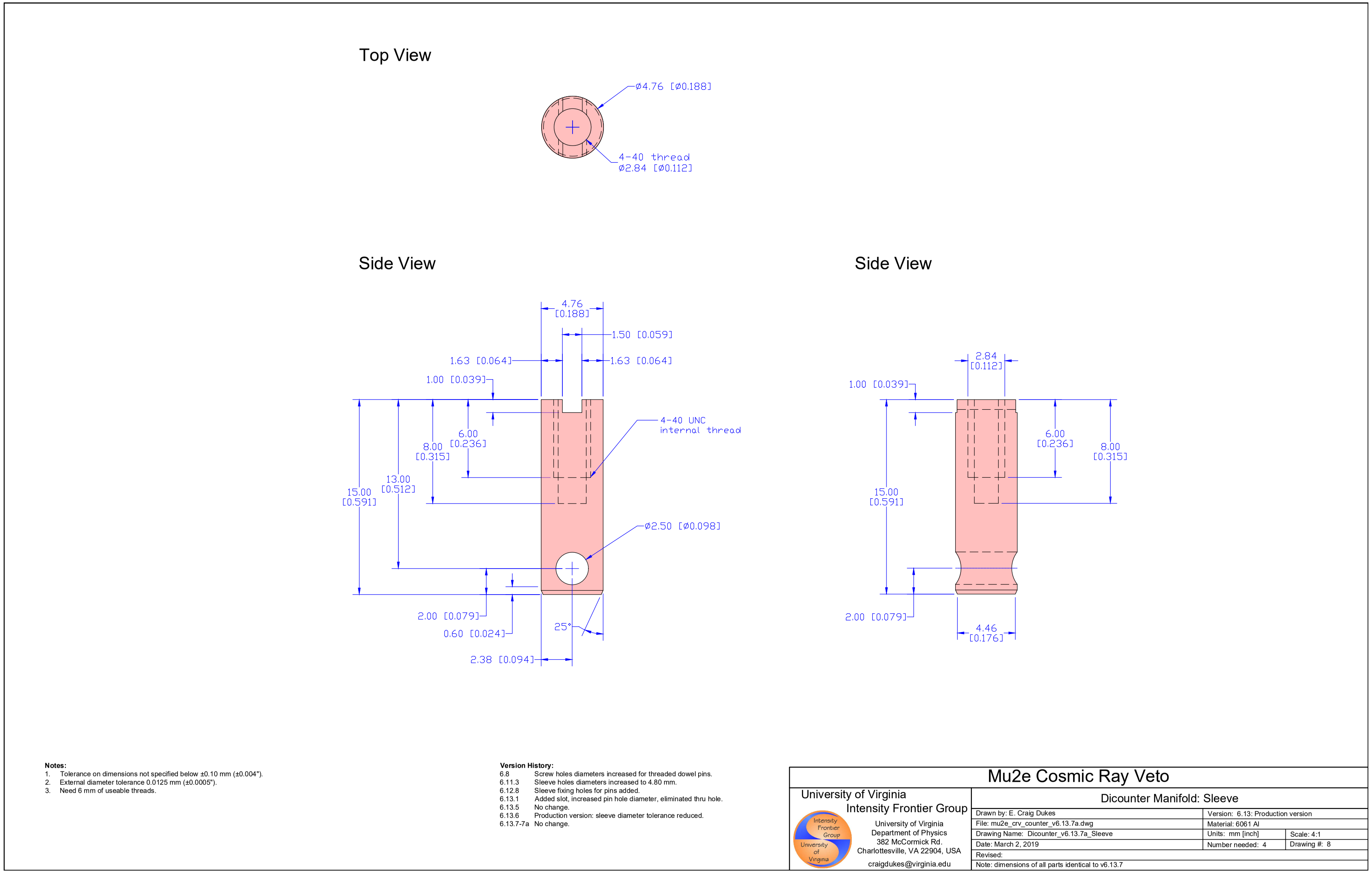

Figure A.8.: Drawing of the sleeve used for mounting readout manifolds. The sleeve is fixed in the FGB.

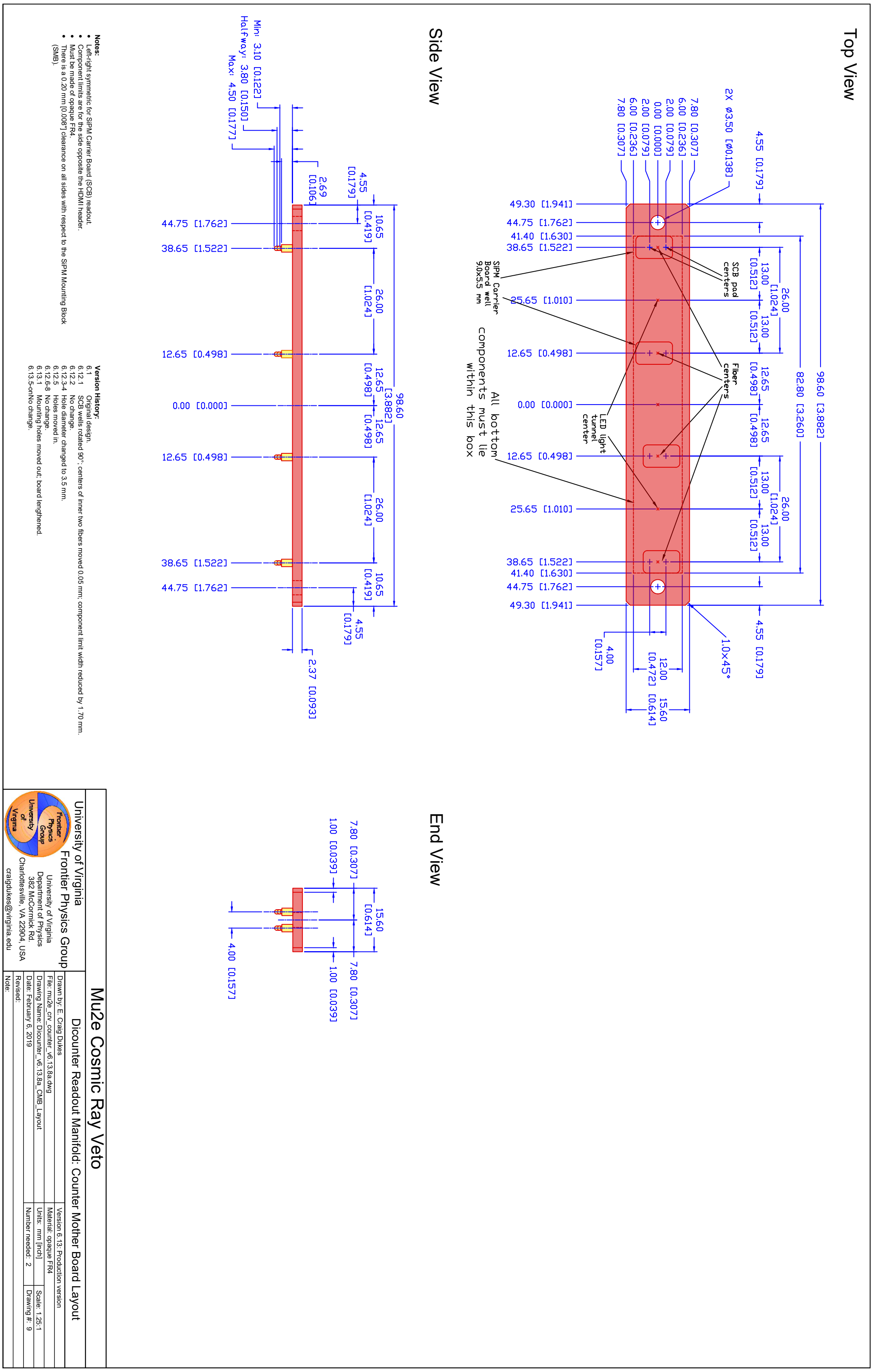

Figure A.9.: Drawing of the Counter Mother Board (CMB) layout.

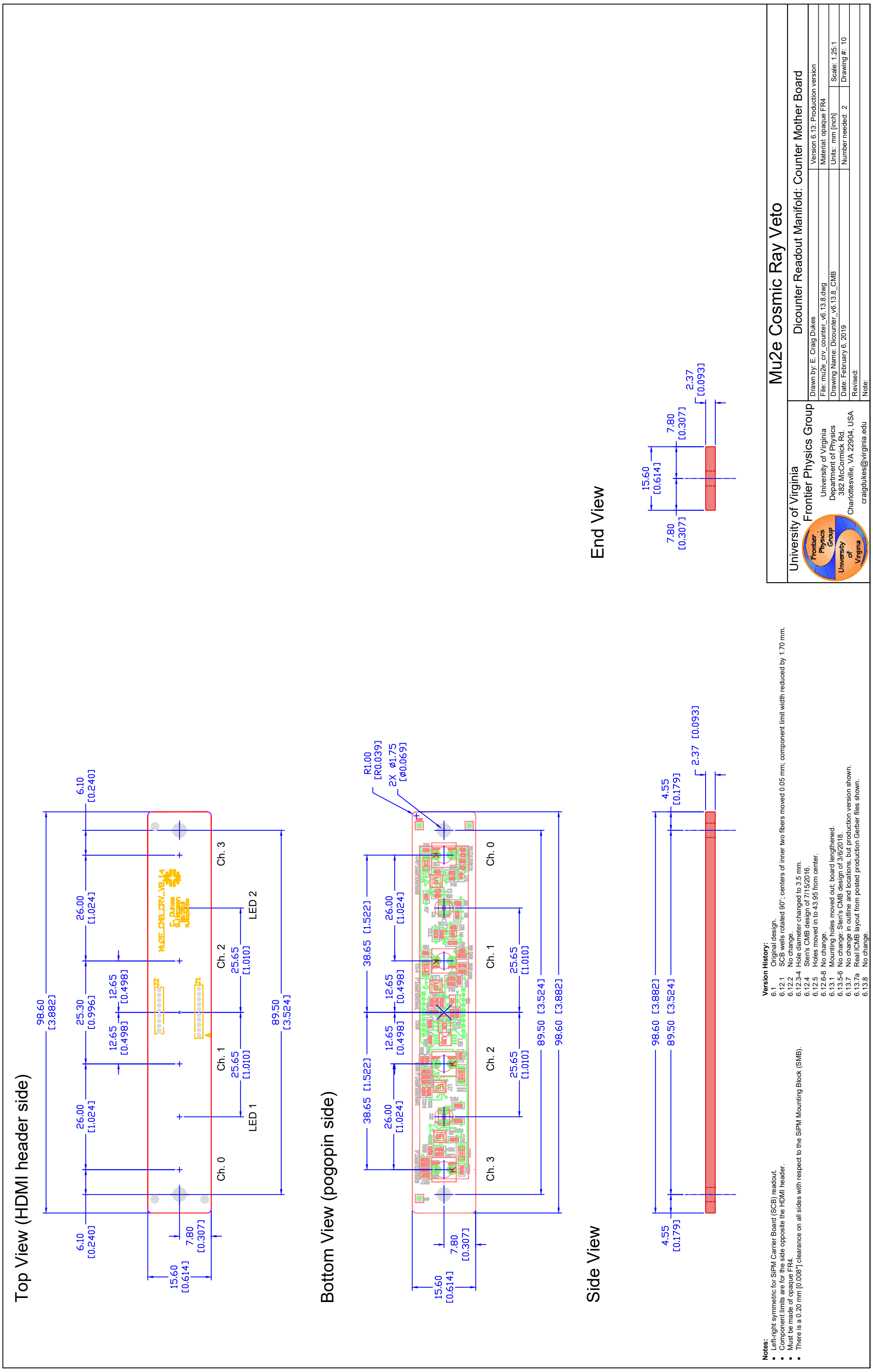

Figure A.10.: Drawing of the Counter Mother Board (CMB).

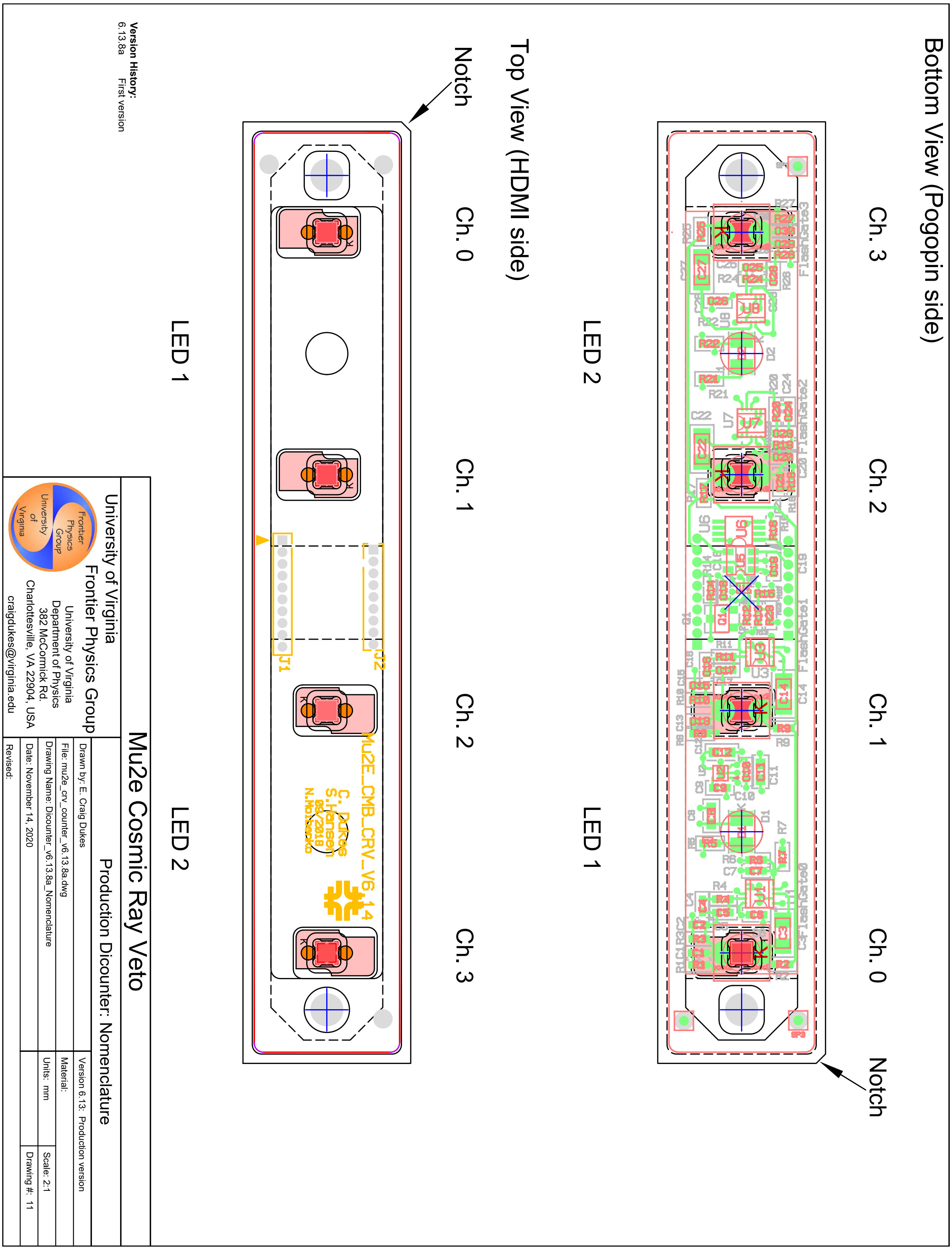

Figure A.11.: Production Dicounter Nomenclature.

Appendix B.

Top (CRV-T/TS) Module

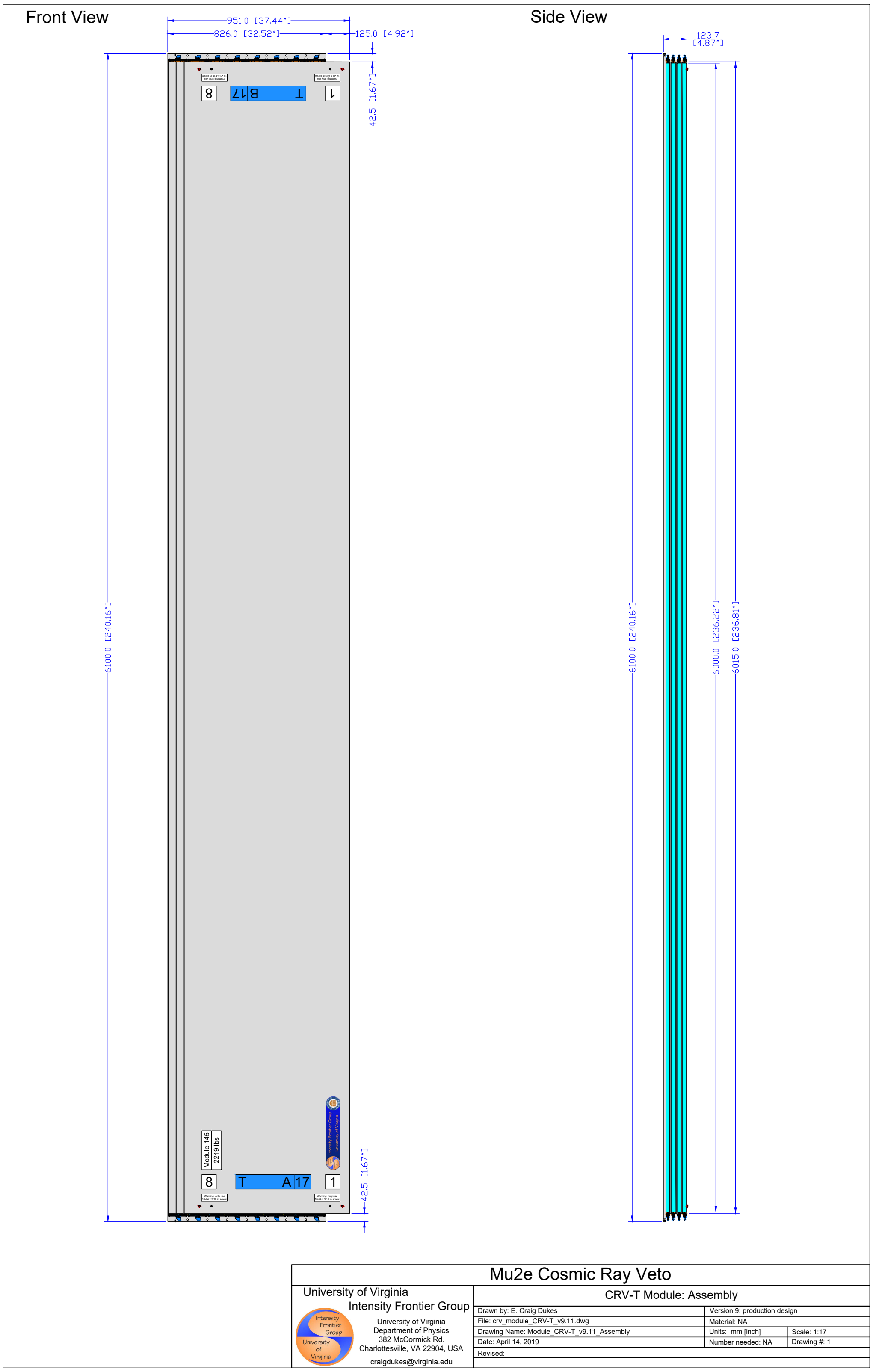

Figure B.1.: Drawing of a Top (CRV-T/TS) module.

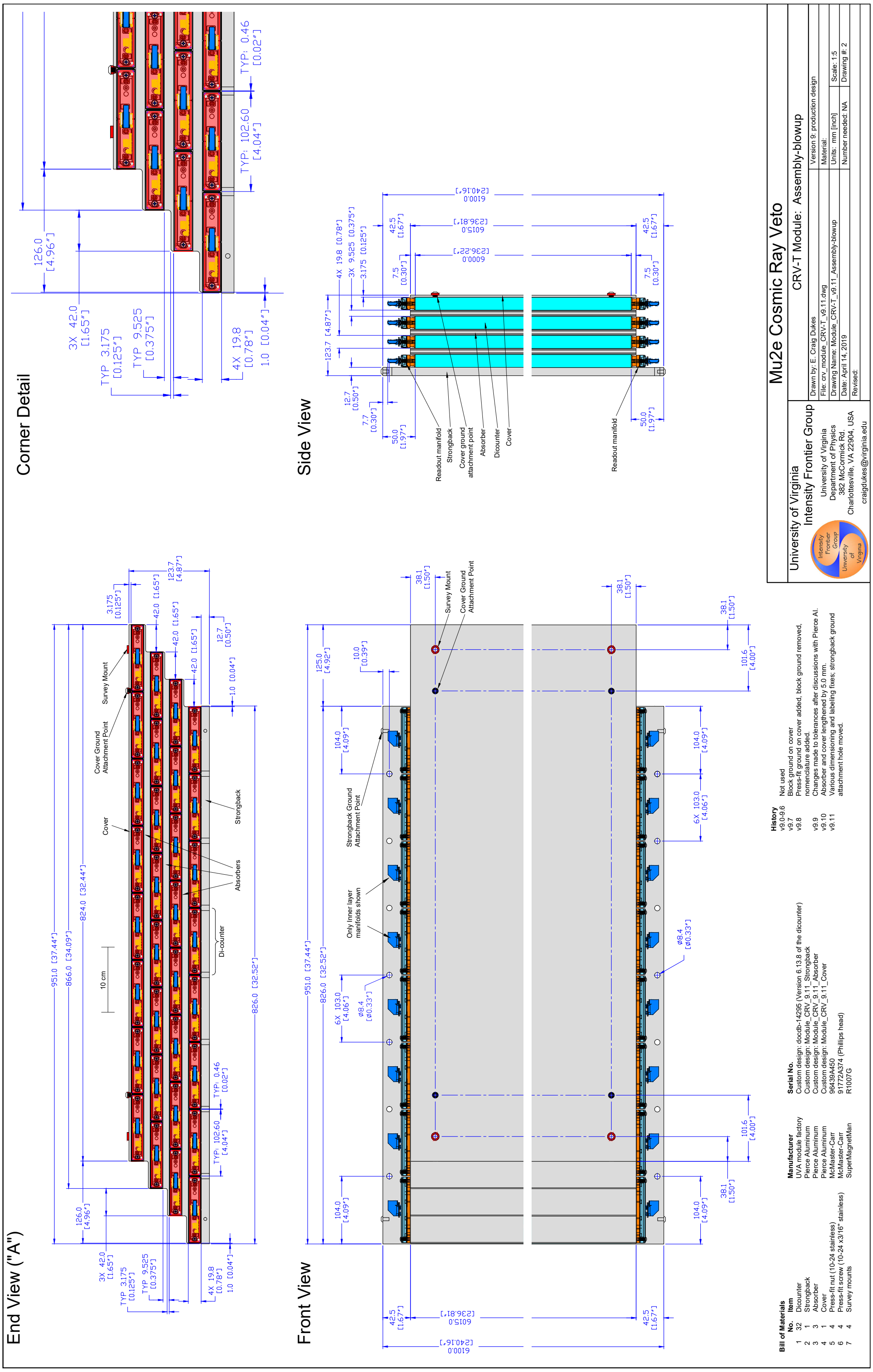

Figure B.2.: Drawing of a Top (CRV-T/TS) module.

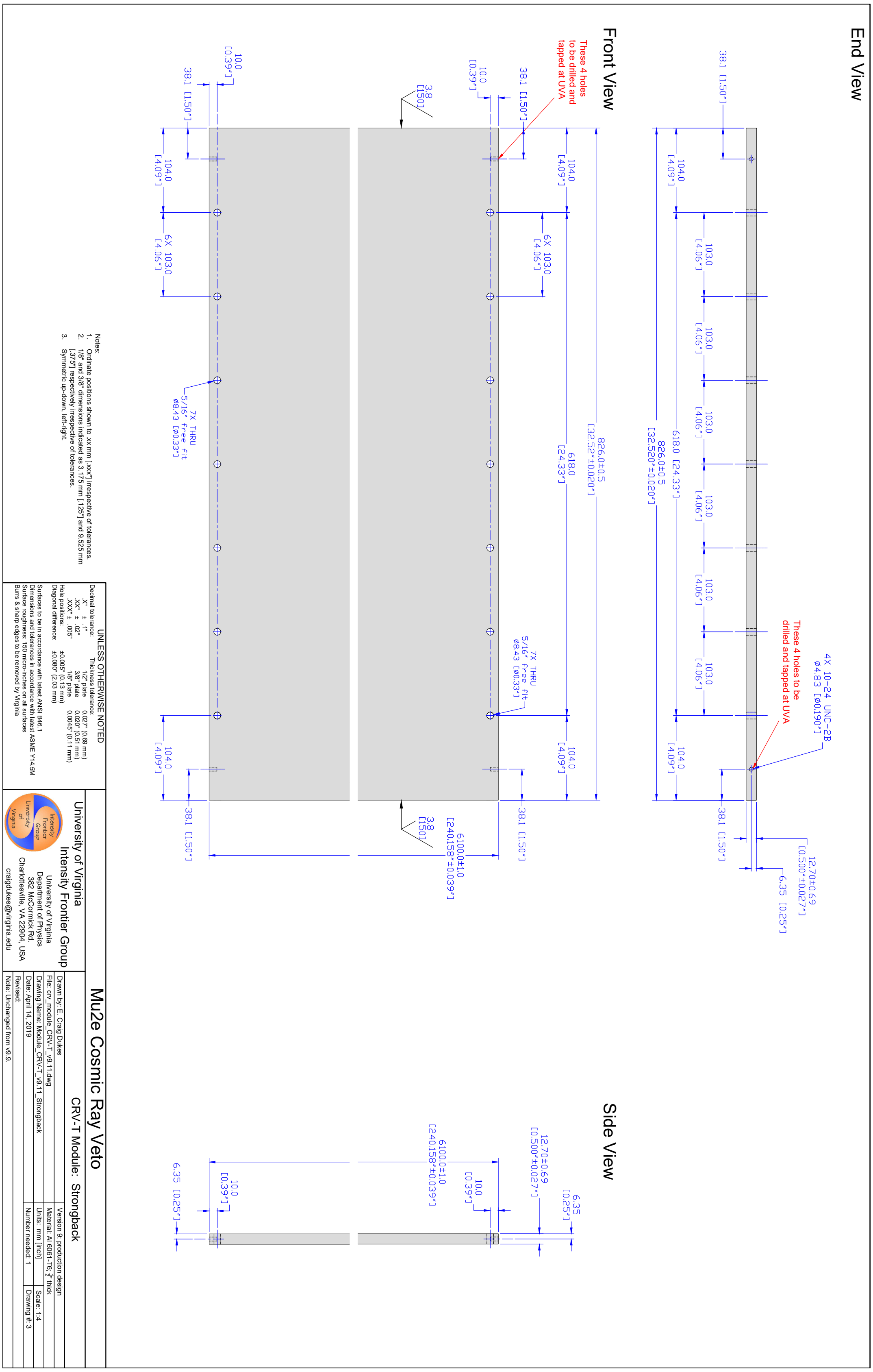

Figure B.3.: Drawing of a Top (CRV-T/TS) module.

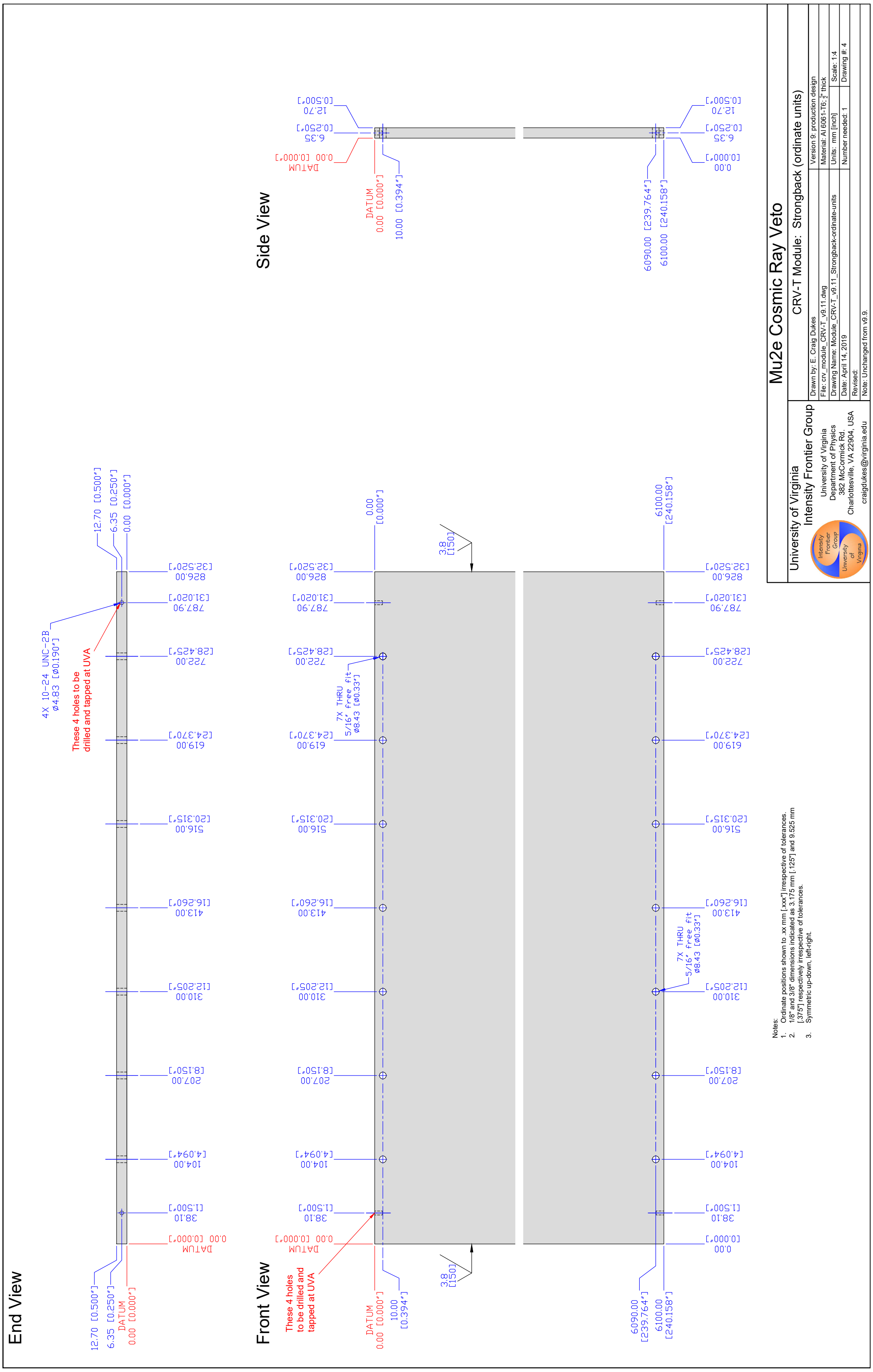

Figure B.4.: Drawing of a Top (CRV-T/TS) module.

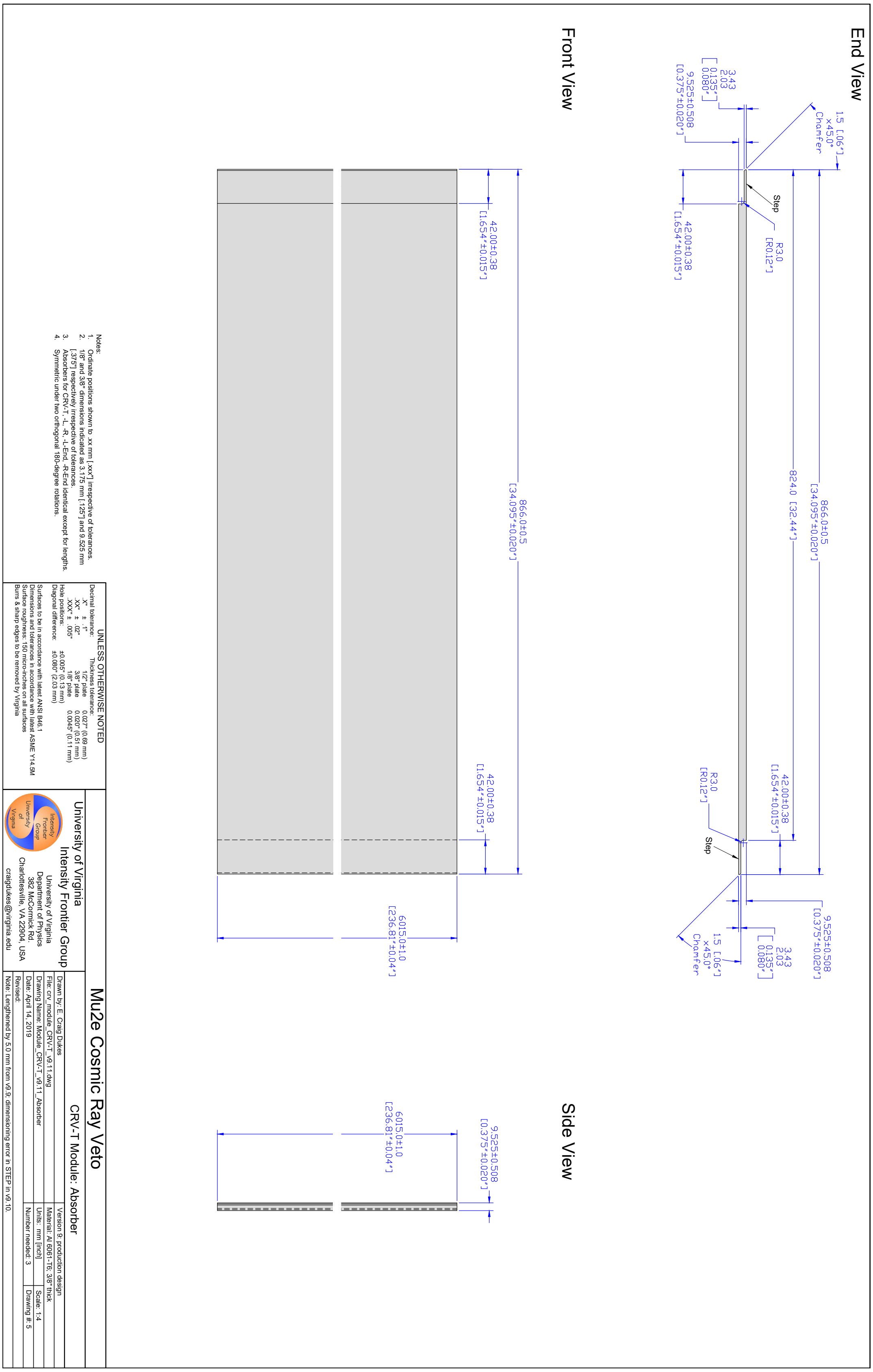

Figure B.5.: Drawing of a Top (CRV-T/TS) module.

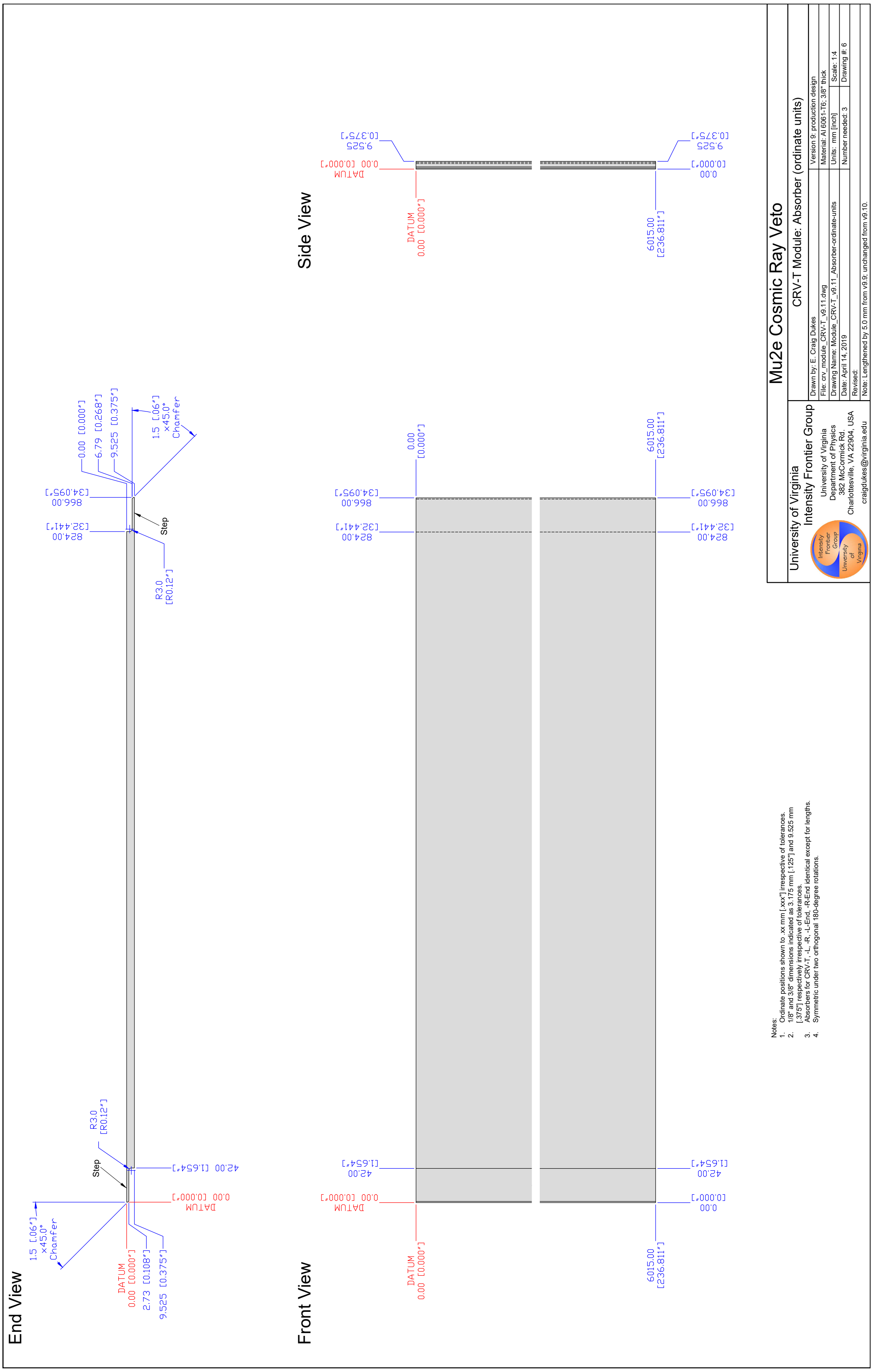

Figure B.6.: Drawing of a Top (CRV-T/TS) module.

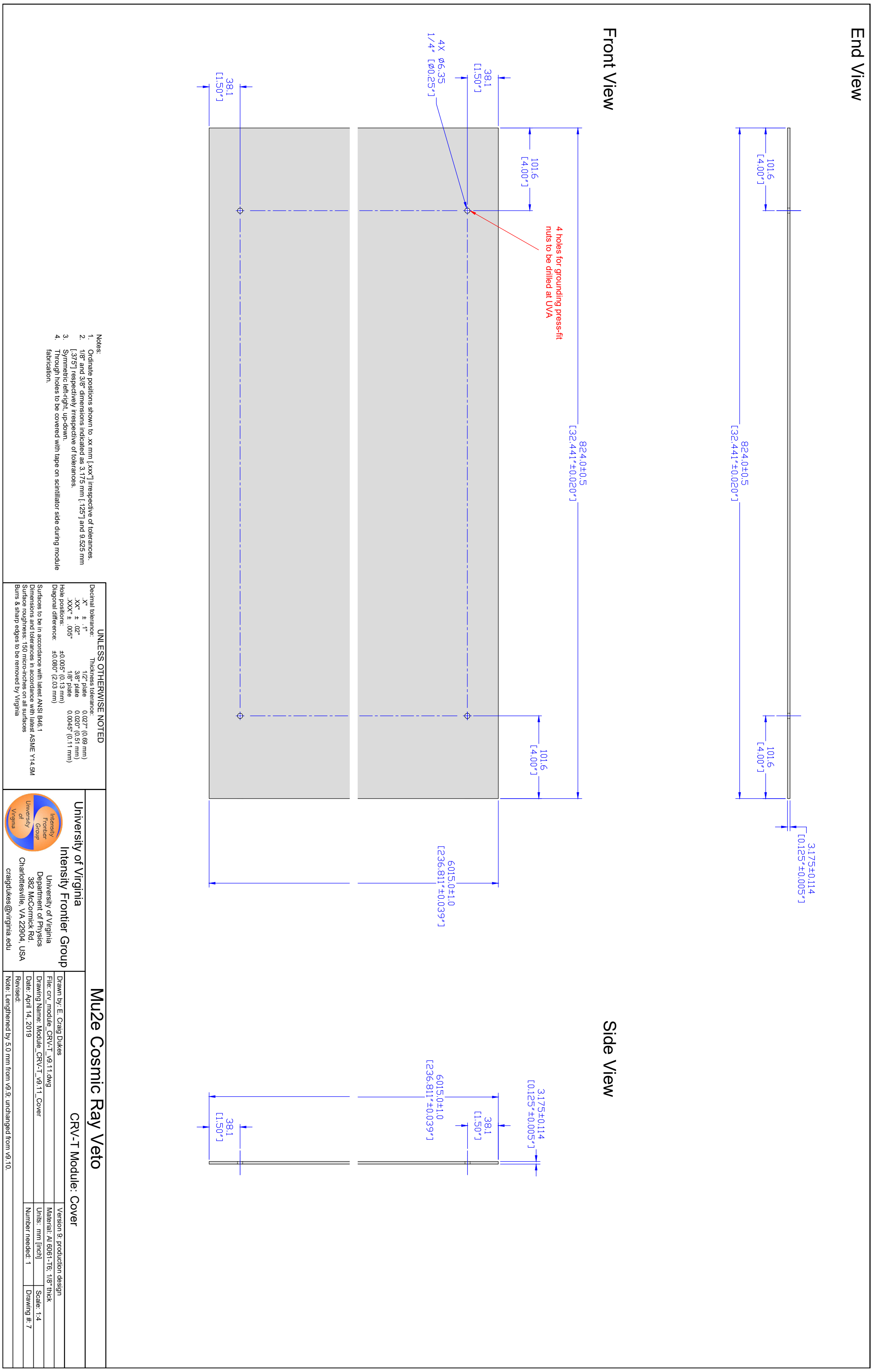

Figure B.7.: Drawing of a Top (CRV-T/TS) module.

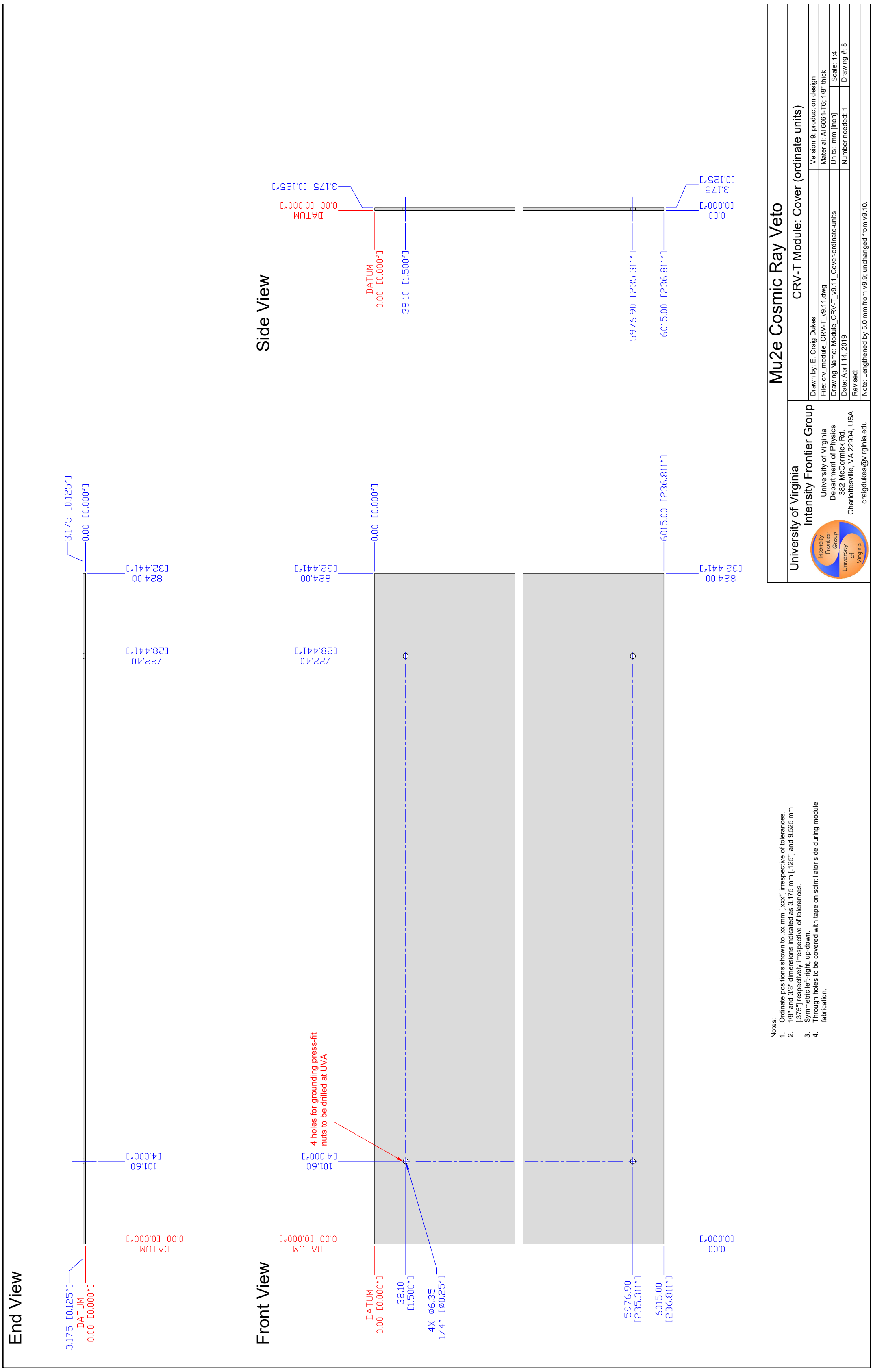

Figure B.8.: Drawing of a Top (CRV-T/TS) module.

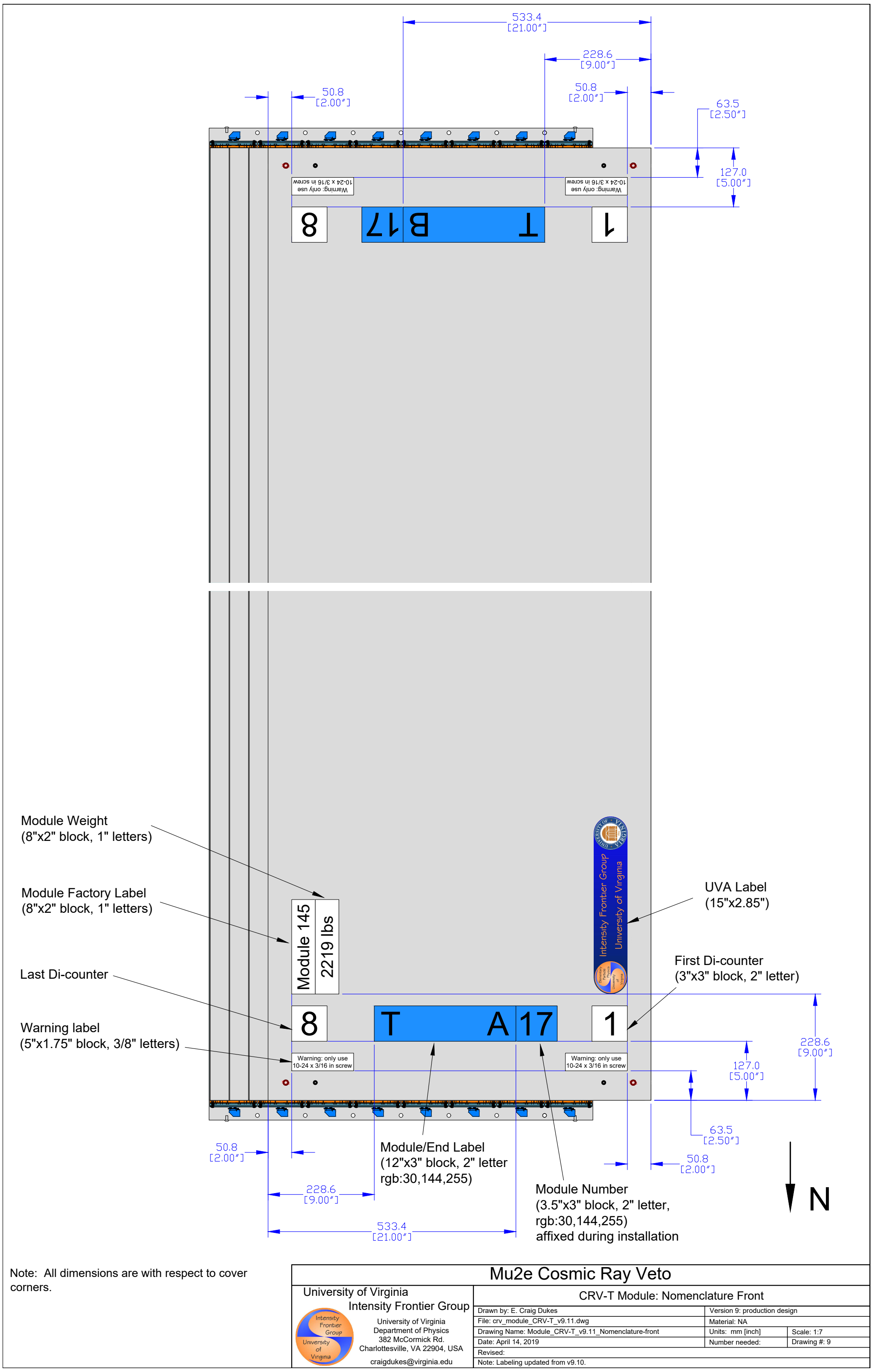

Figure B.9.: Drawing of a Top (CRV-T/TS) module.

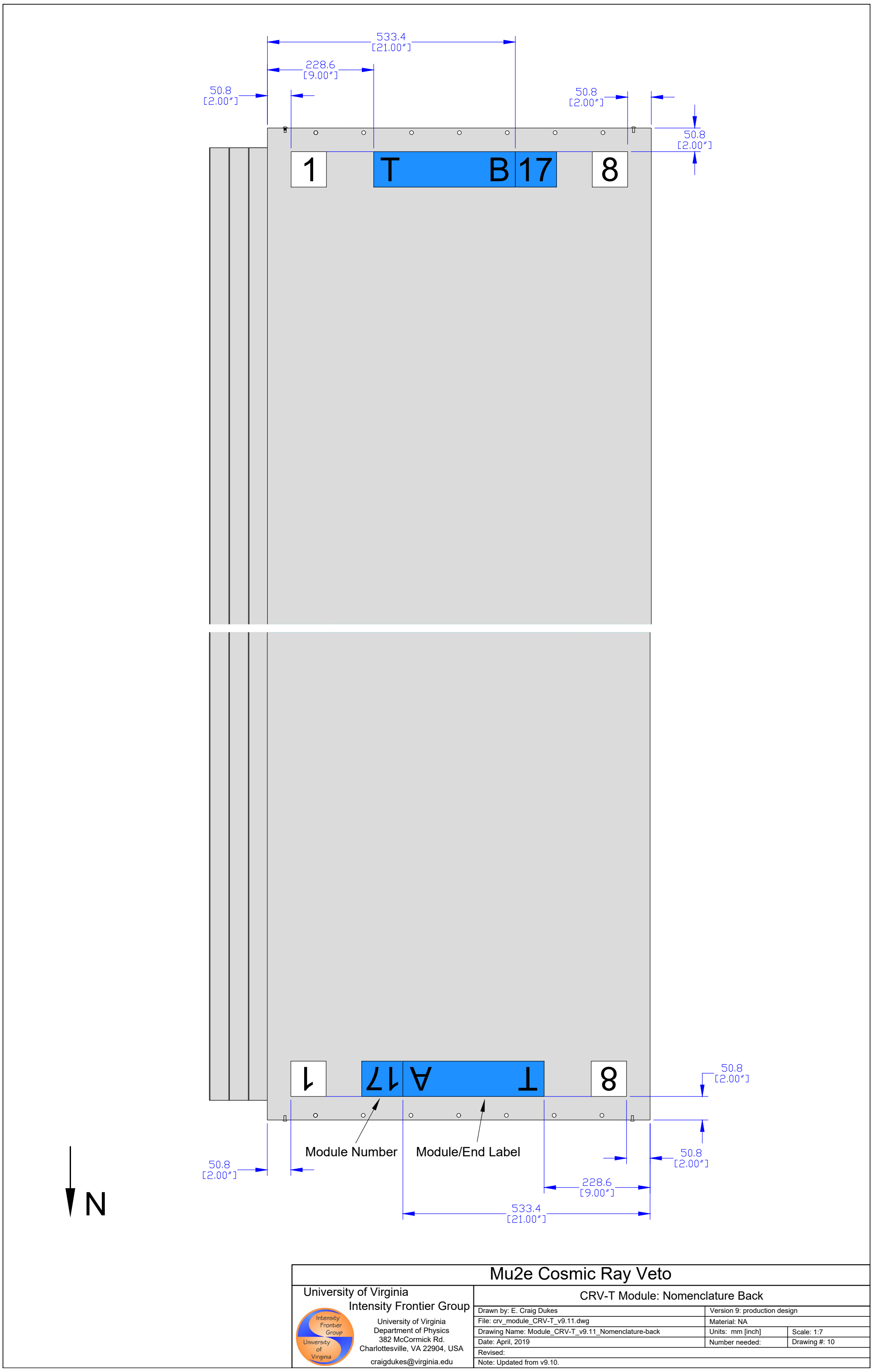

Figure B.10.: Drawing of a Top (CRV-T/TS) module.

Appendix C.

Top Extension (CRV-TS-Ext) Module

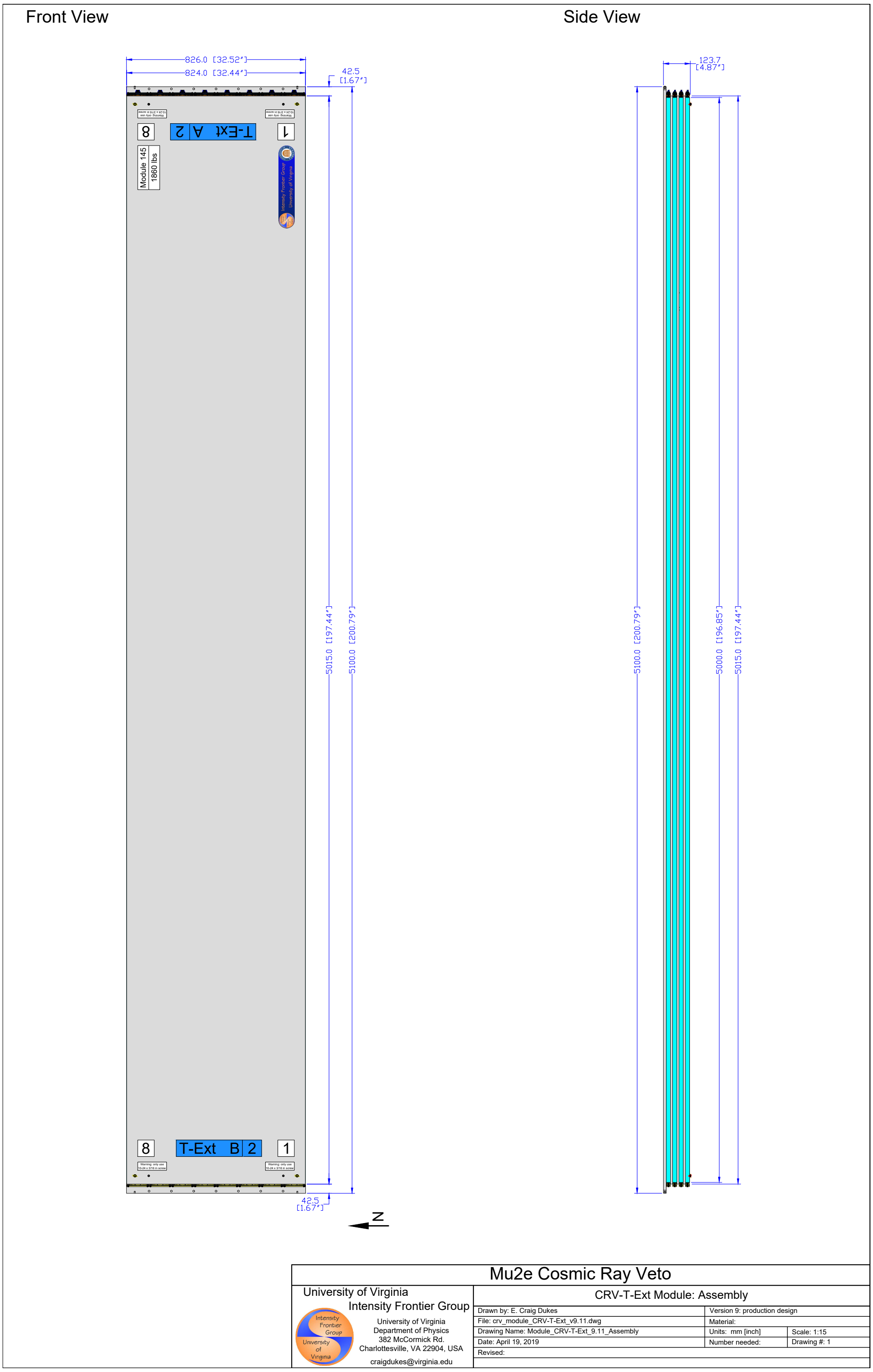

Figure C.1.: Drawing of a Top Extension (CRV-TS-Ext) module.

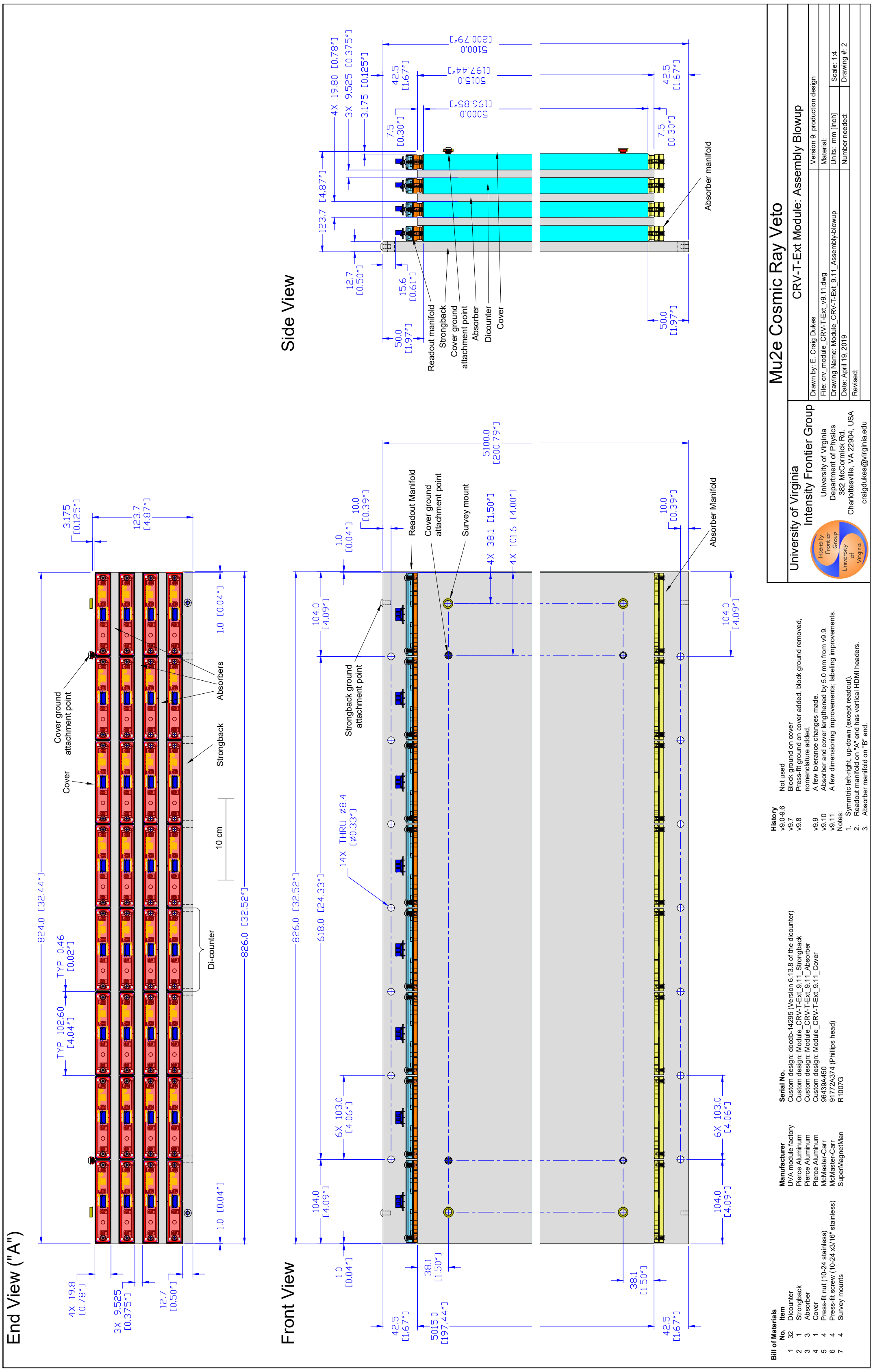

Figure C.2.: Drawing of a Top Extension (CRV-TS-Ext) module.

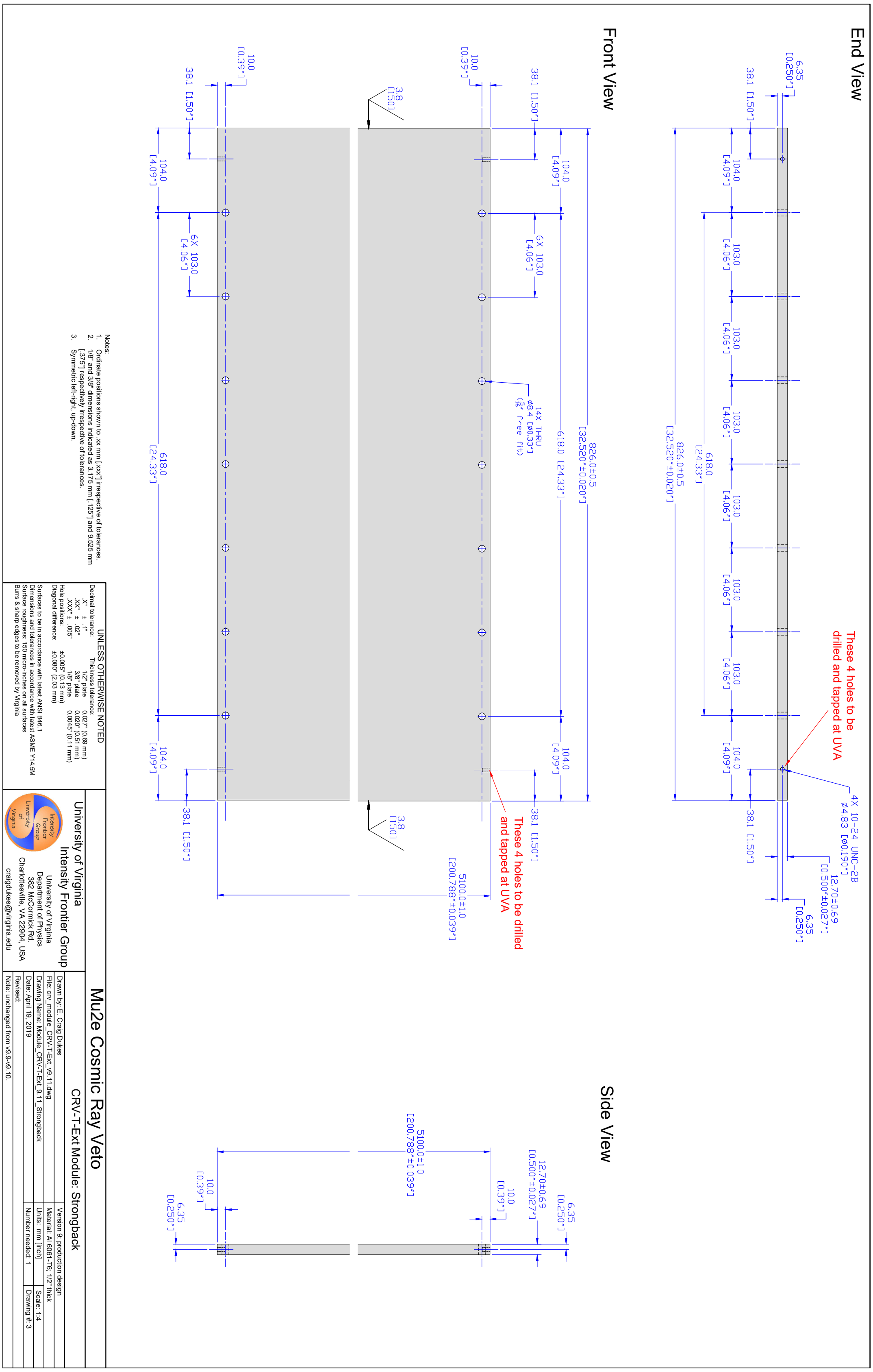

Figure C.3.: Drawing of a Top Extension (CRV-TS-Ext) module.

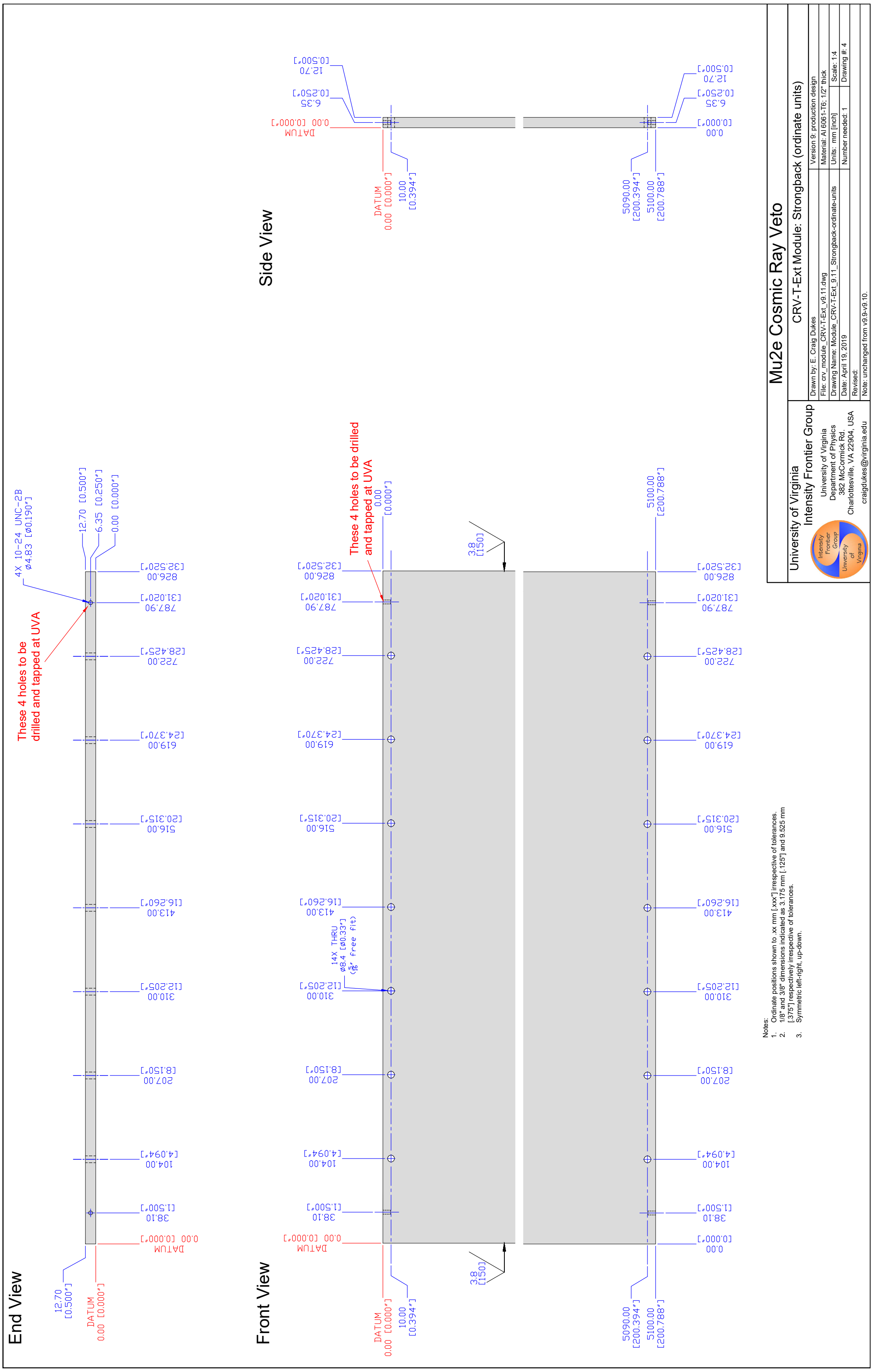

Figure C.4.: Drawing of a Top Extension (CRV-TS-Ext) module.

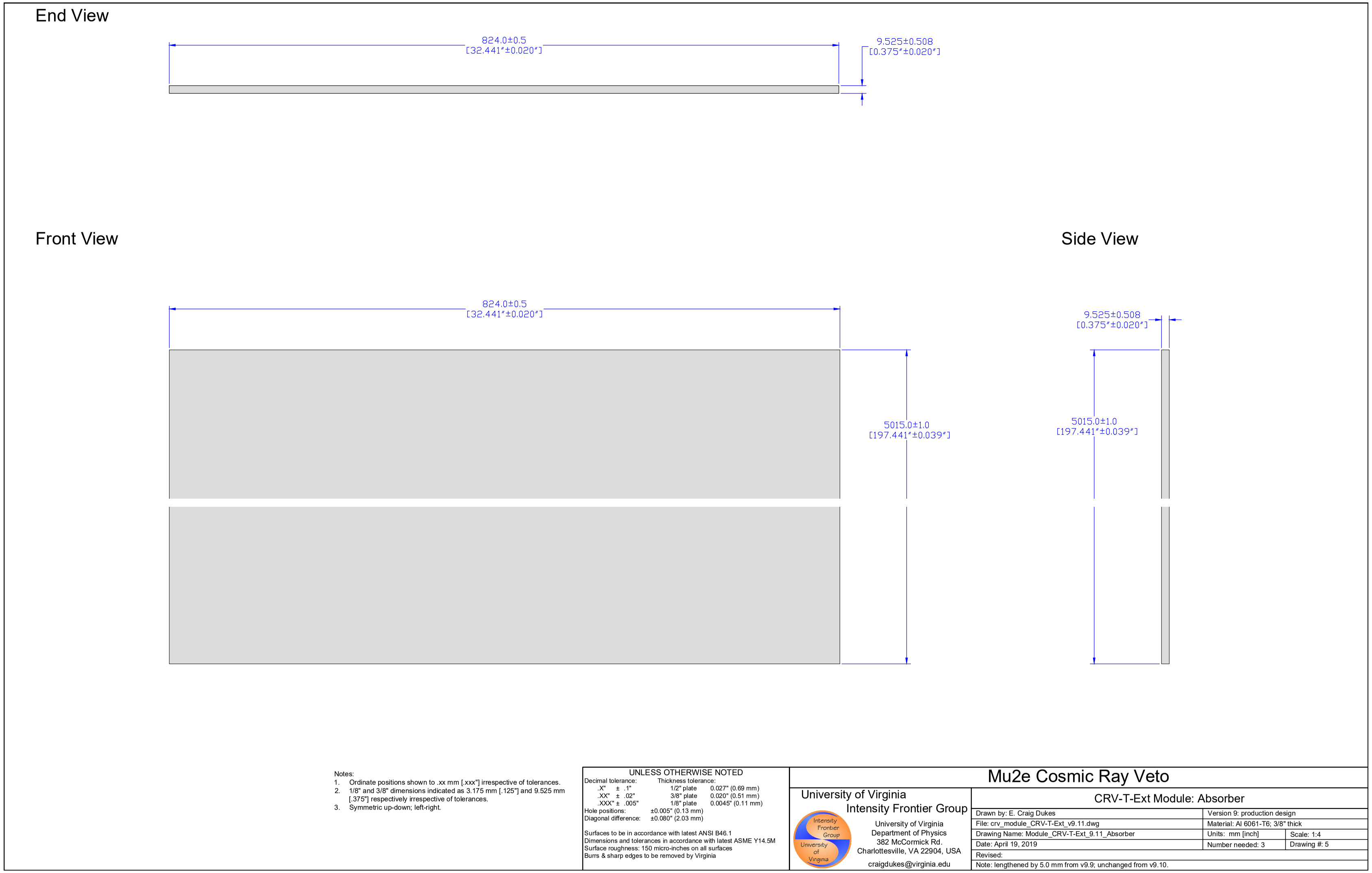

Figure C.5.: Drawing of a Top Extension (CRV-TS-Ext) module.

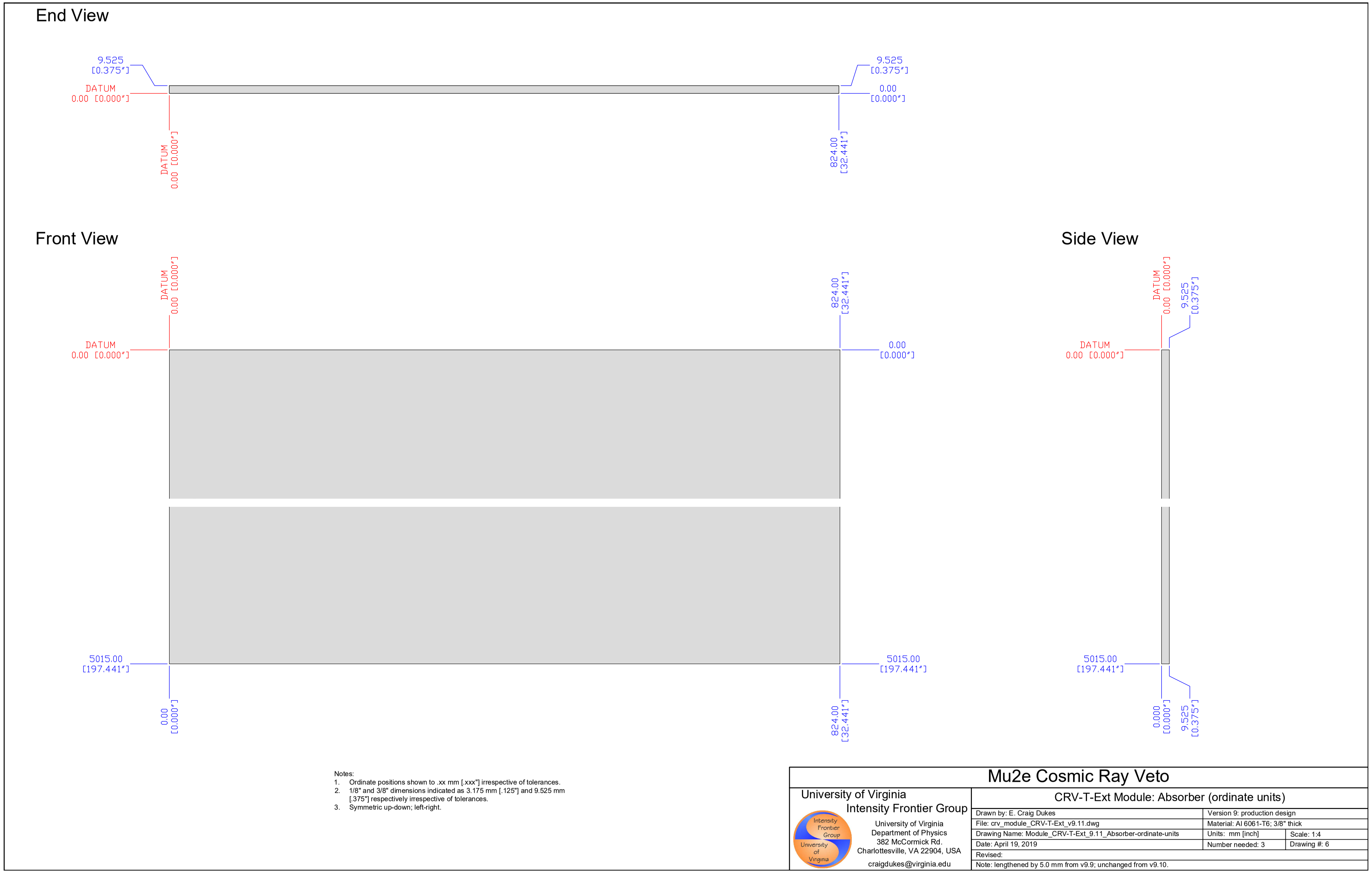

Figure C.6.: Drawing of a Top Extension (CRV-TS-Ext) module.

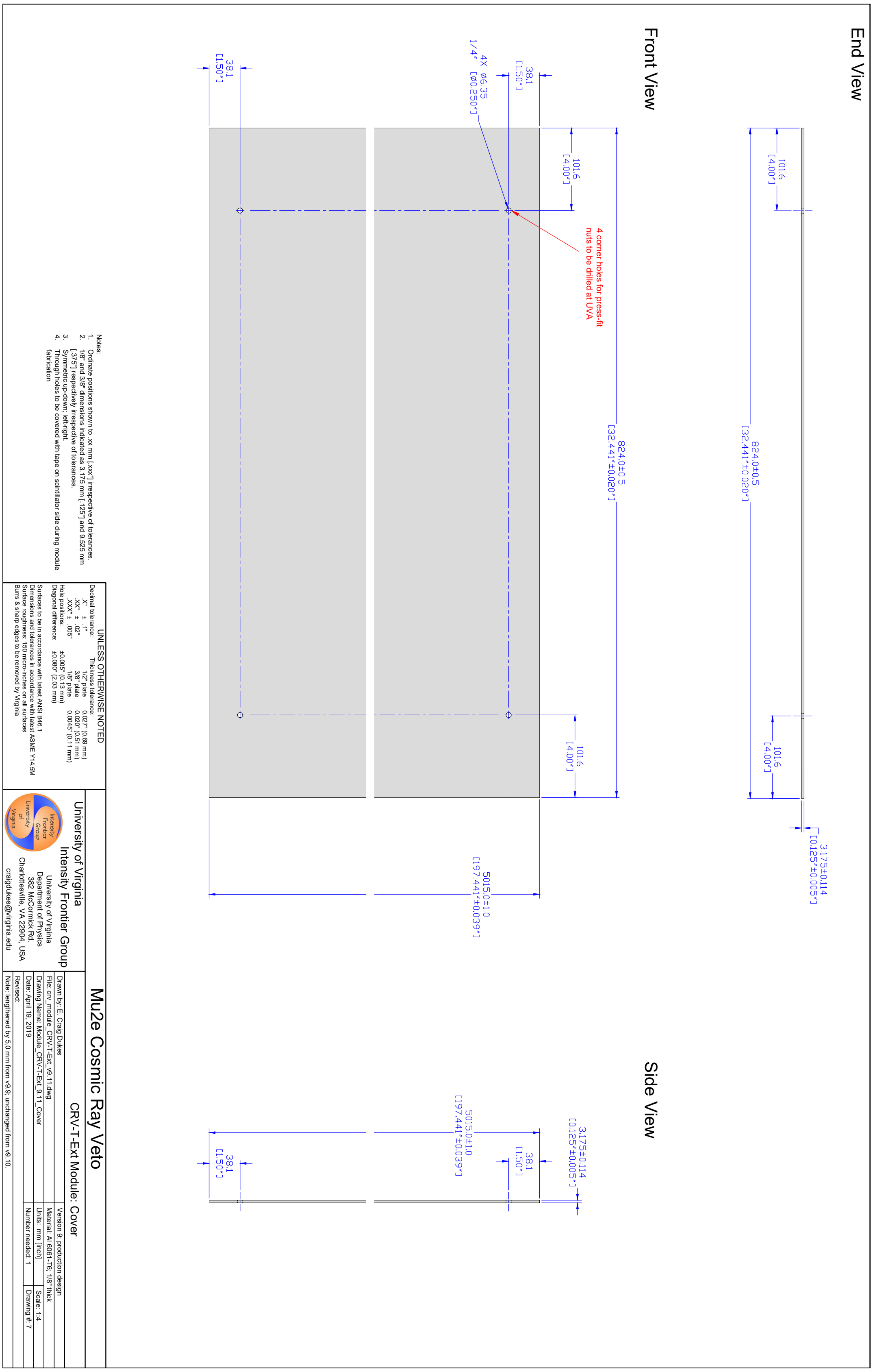

Figure C.7.: Drawing of a Top Extension (CRV-TS-Ext) module.

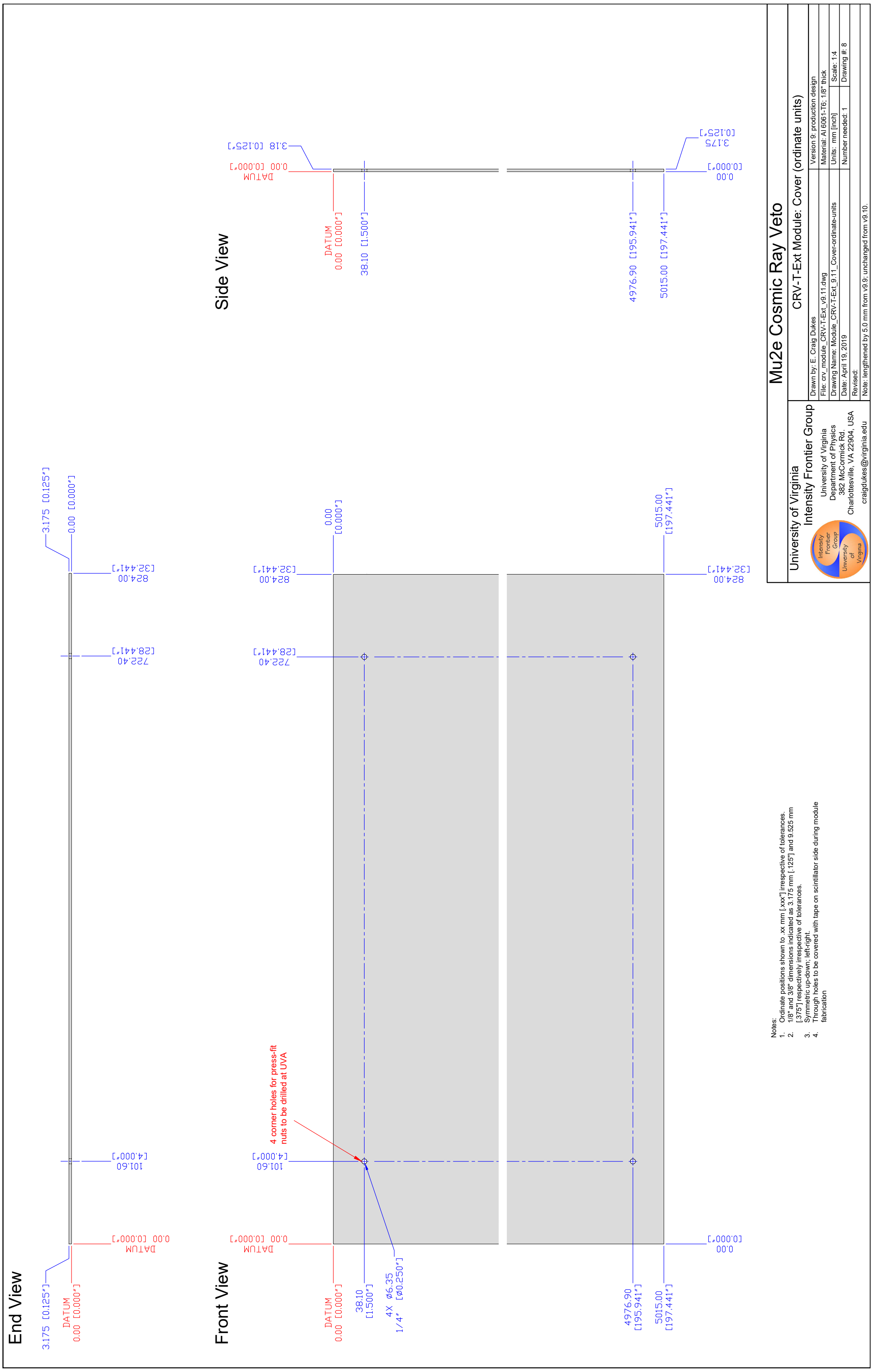

Figure C.8.: Drawing of a Top Extension (CRV-TS-Ext) module.

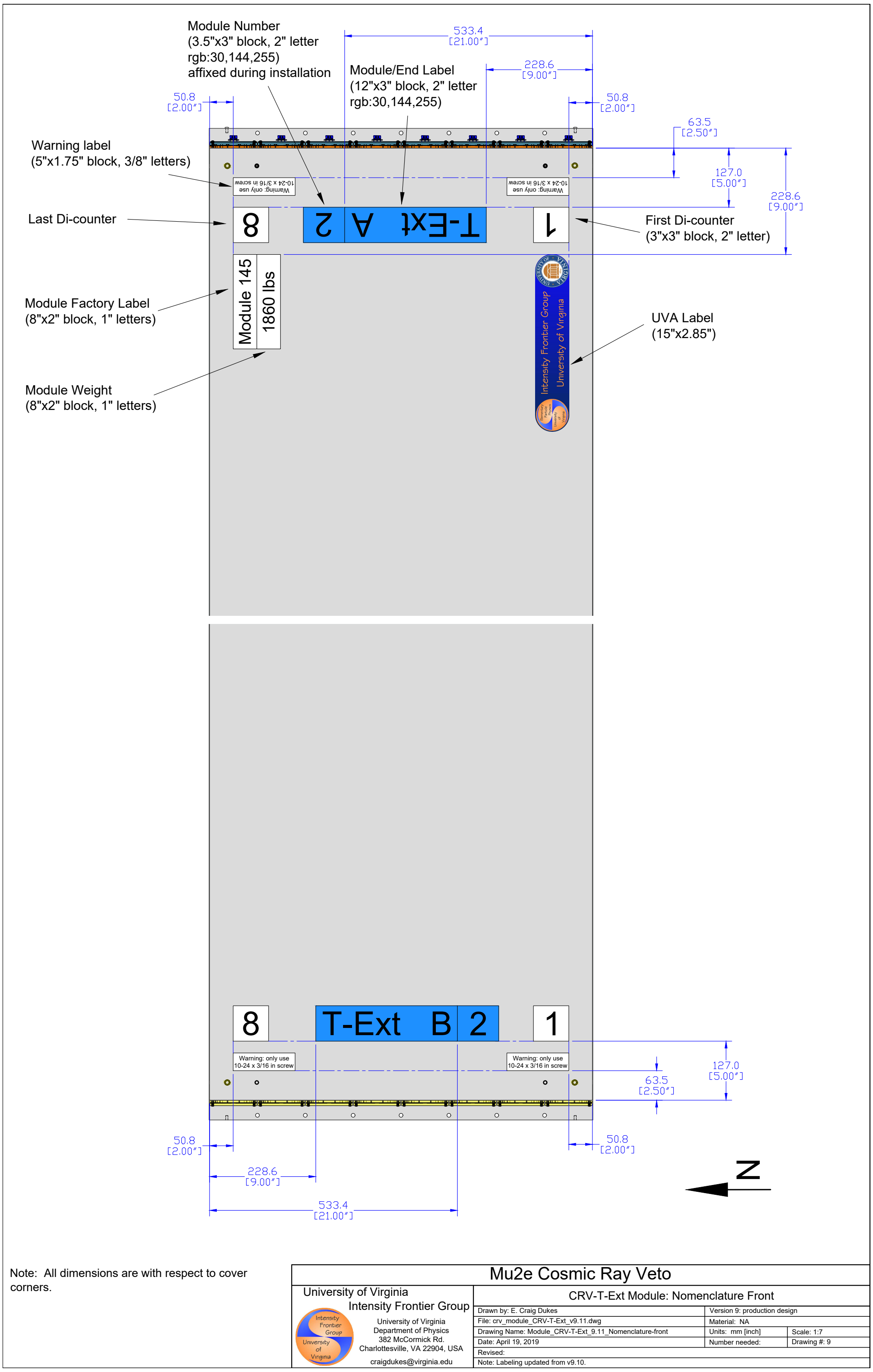

Figure C.9.: Drawing of a Top Extension (CRV-TS-Ext) module.

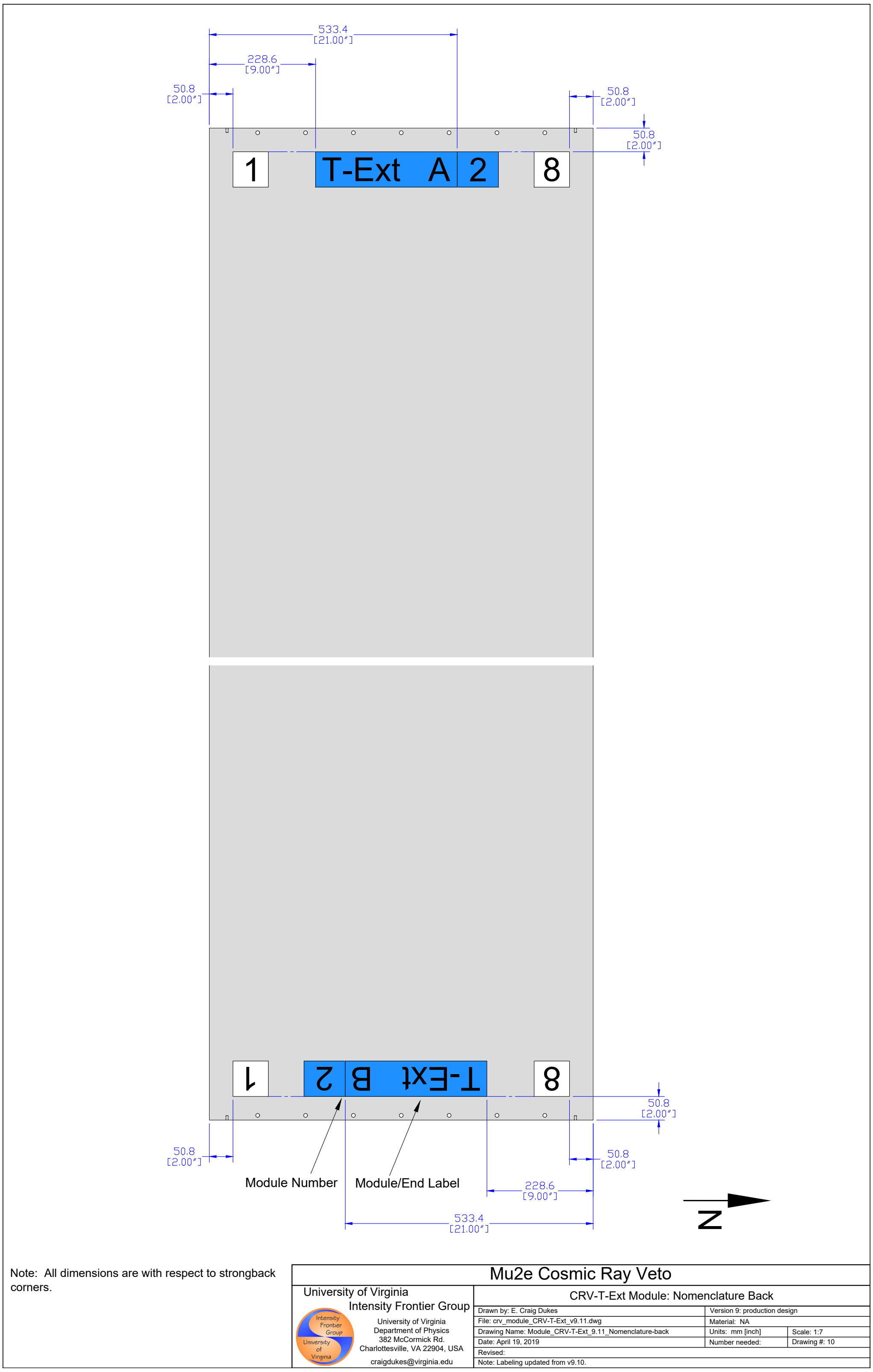

Figure C.10.: Drawing of a Top Extension (CRV-TS-Ext) module.

Appendix D.

Left/Right (CRV-L/R) Module

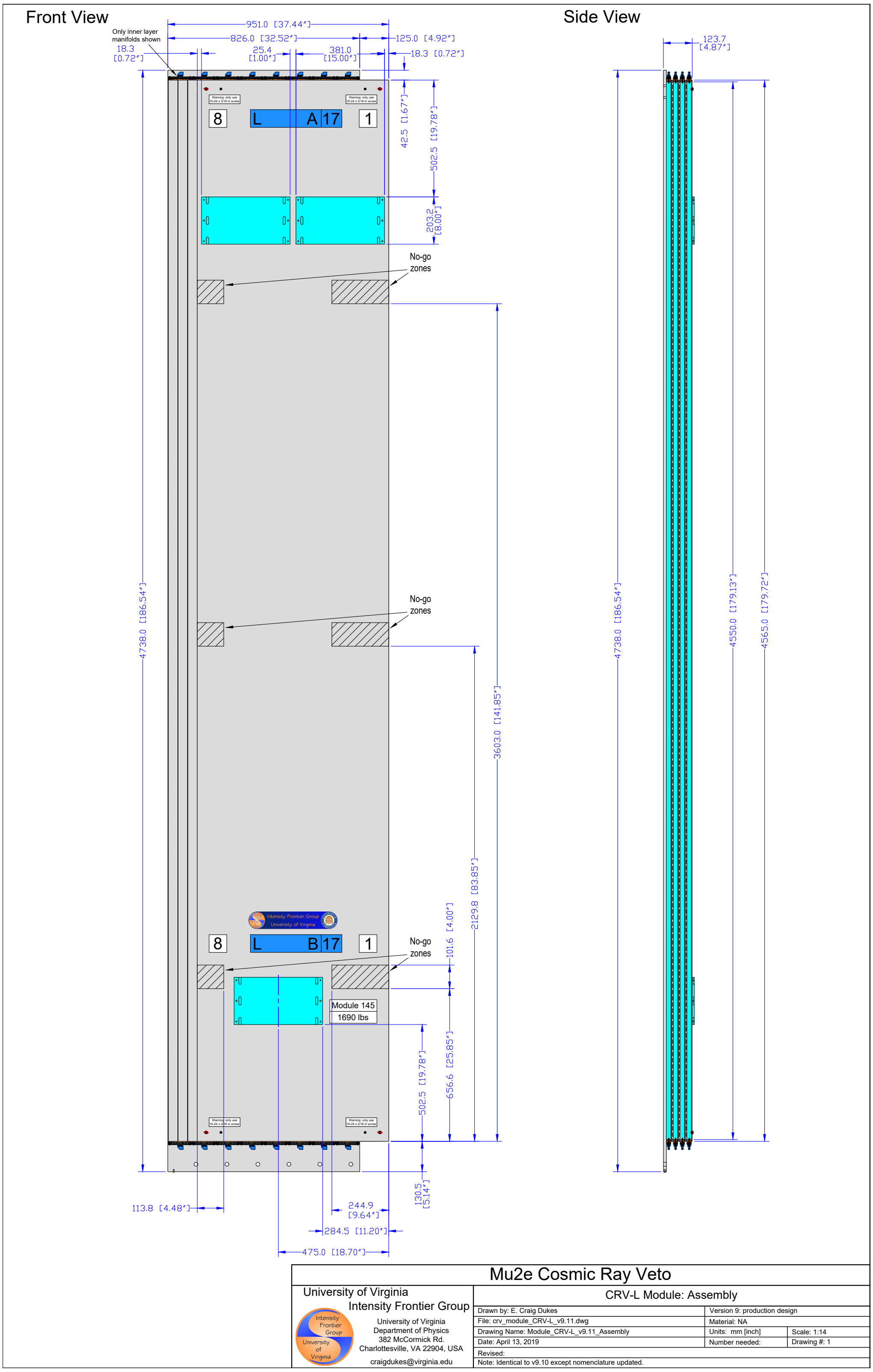

Figure D.1.: Drawing of a Left (CRV-L) module. CRV-R is a mirror image.

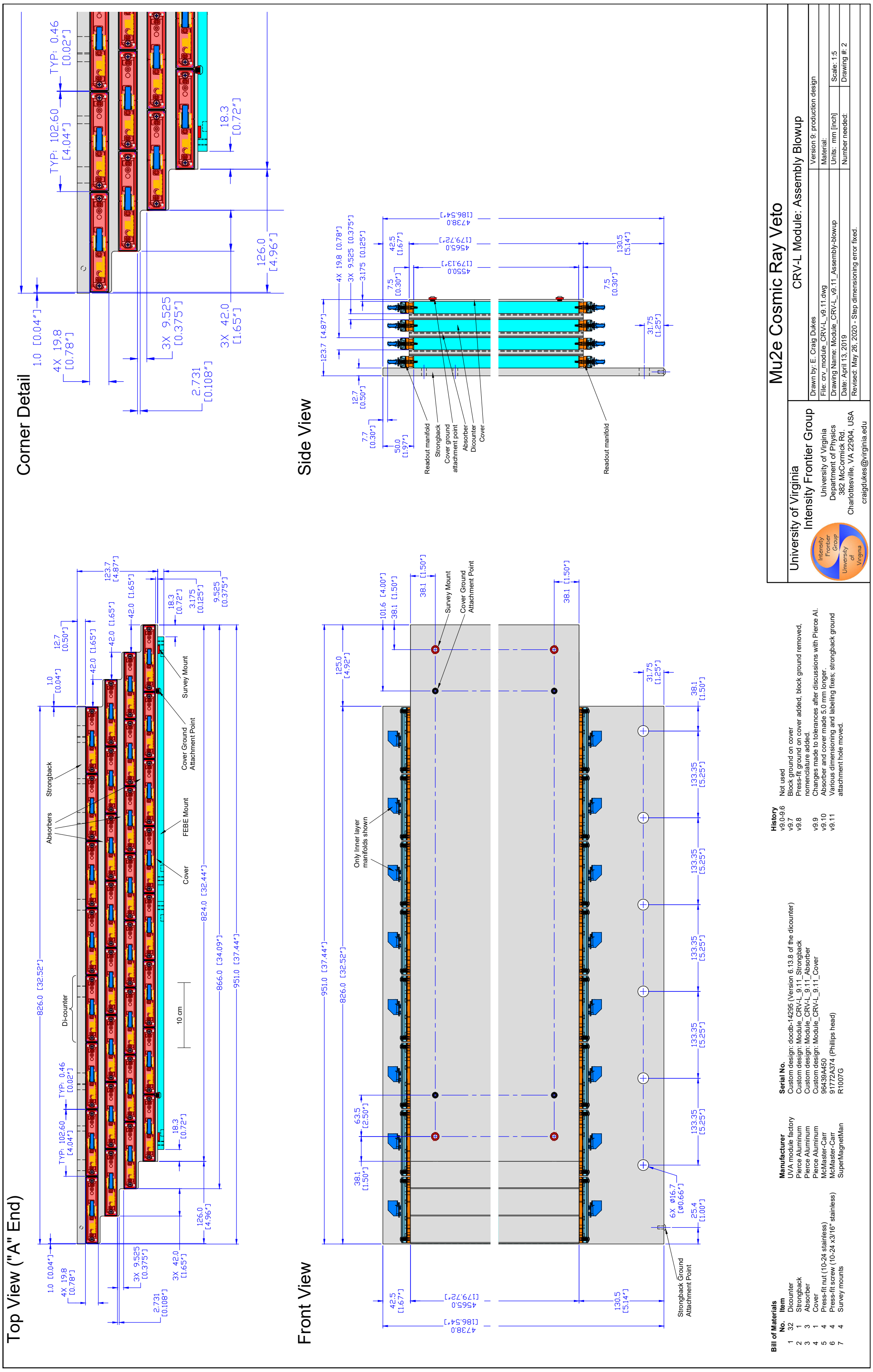

Figure D.2.: Drawing of a Left (CRV-L) module. CRV-R is a mirror image.

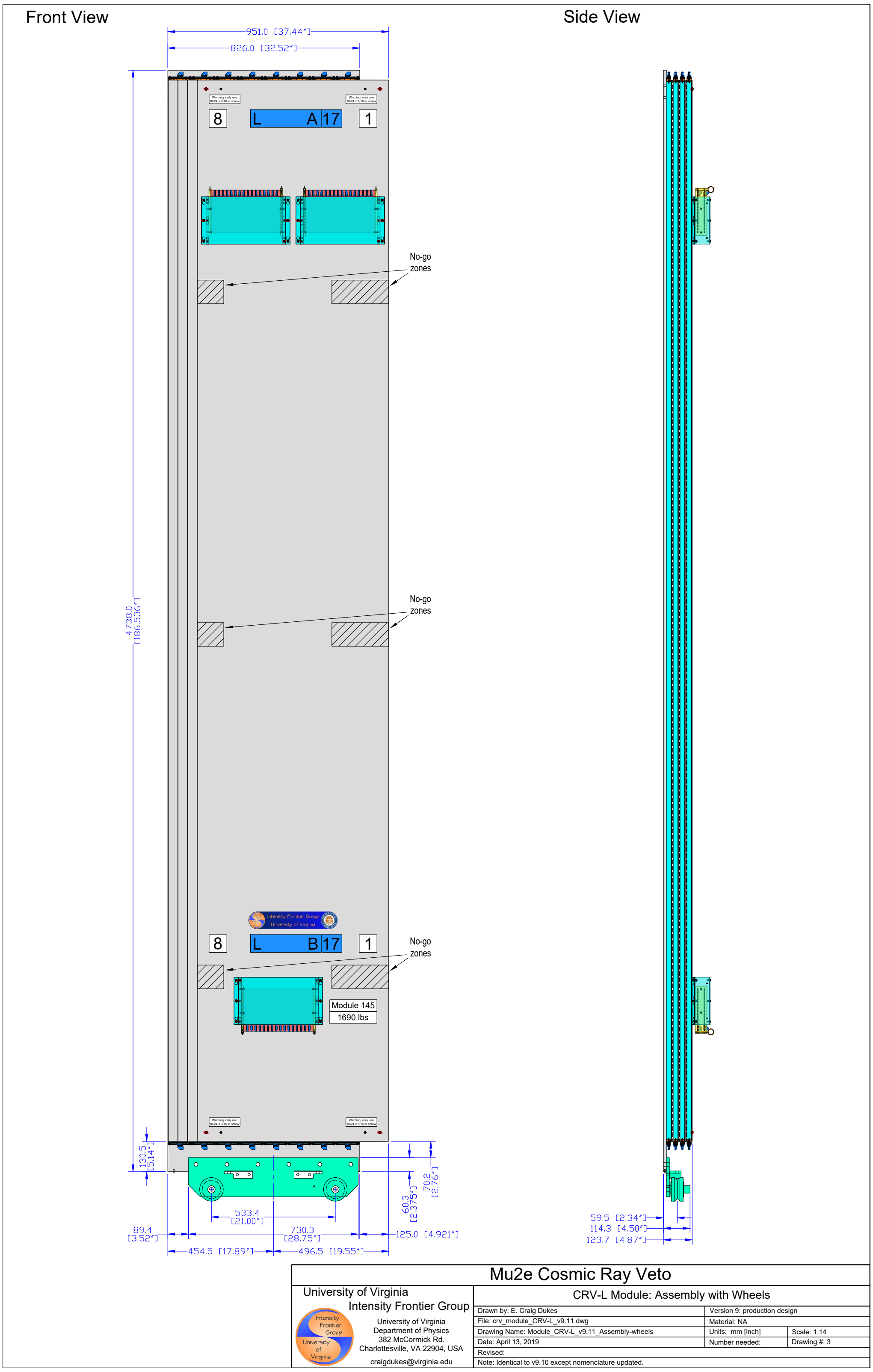

Figure D.3.: Drawing of a Left (CRV-L) module. CRV-R is a mirror image.

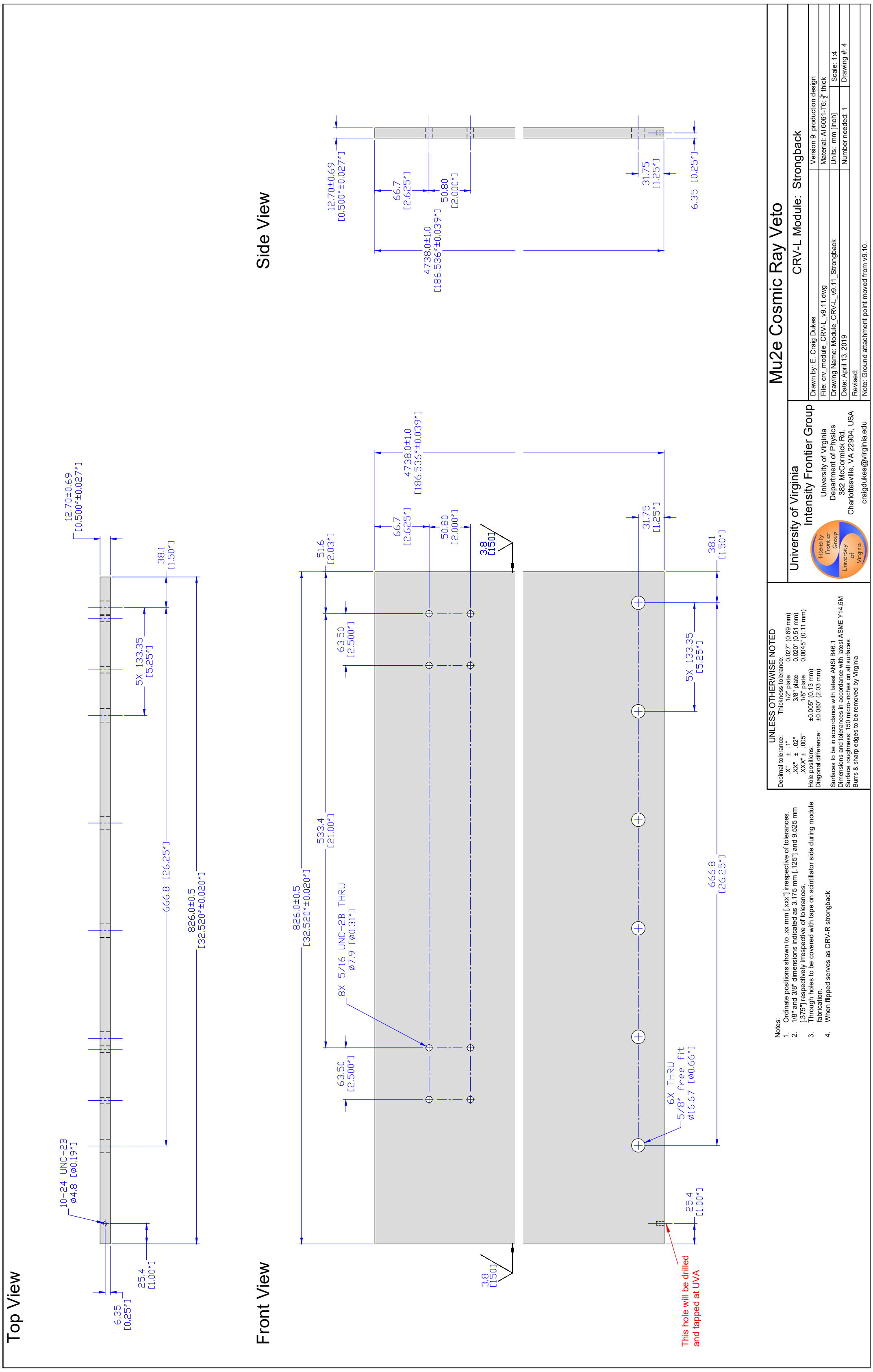

Figure D.4.: Drawing of a Left (CRV-L) module. CRV-R is a mirror image.

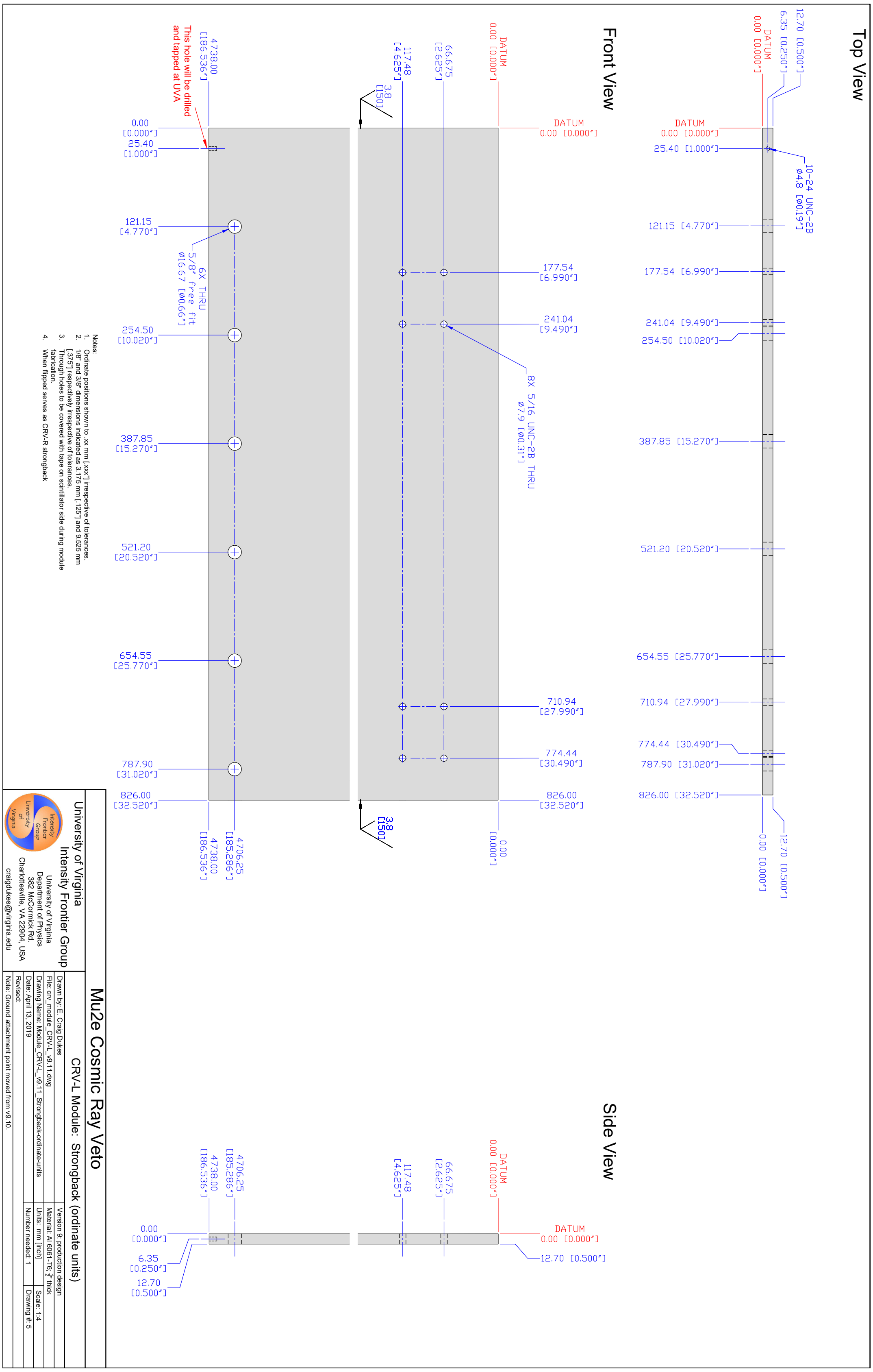

Figure D.5.: Drawing of a Left (CRV-L) module. CRV-R is a mirror image.

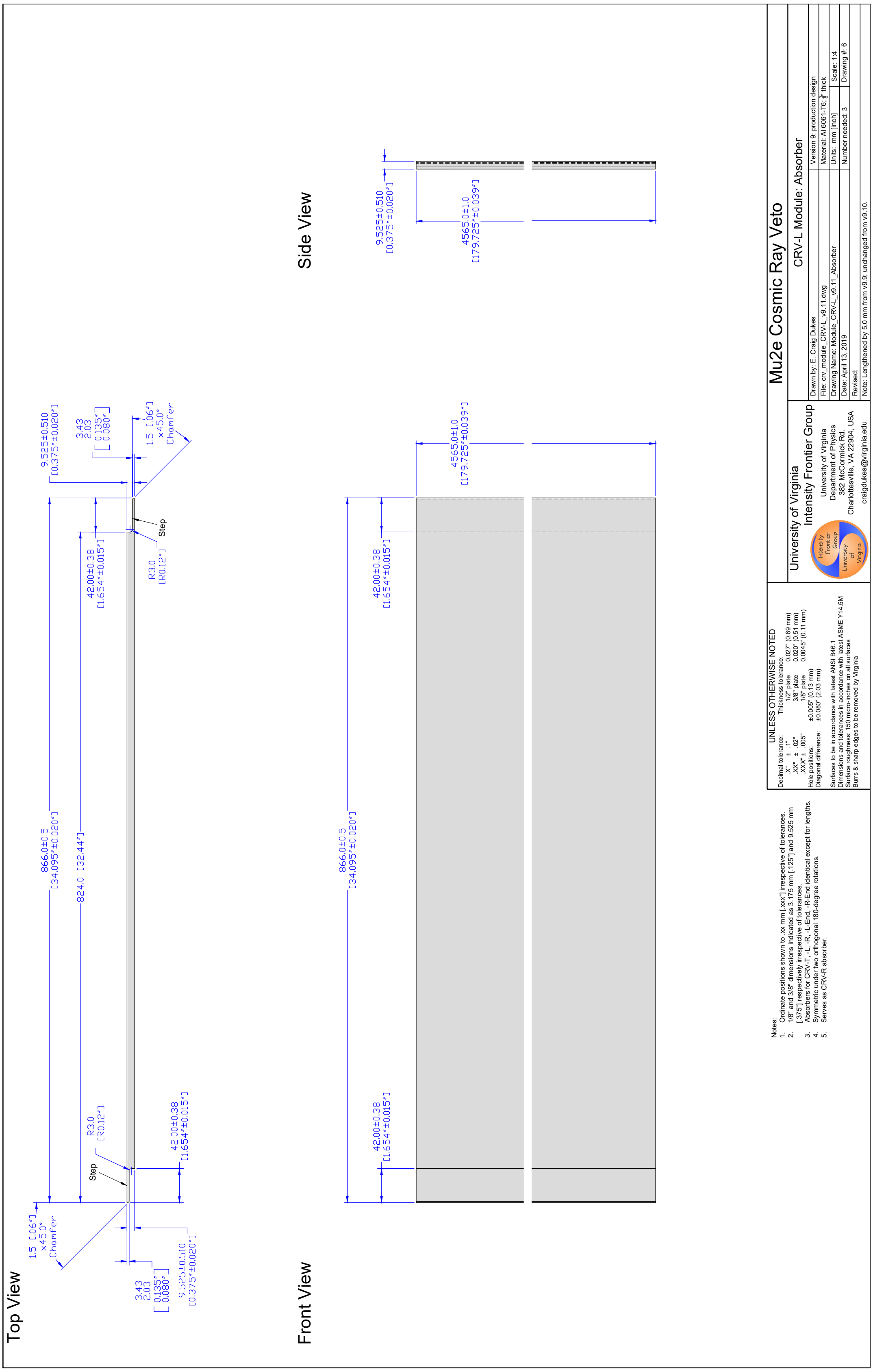

Figure D.6.: Drawing of a Left (CRV-L) module. CRV-R is a mirror image.

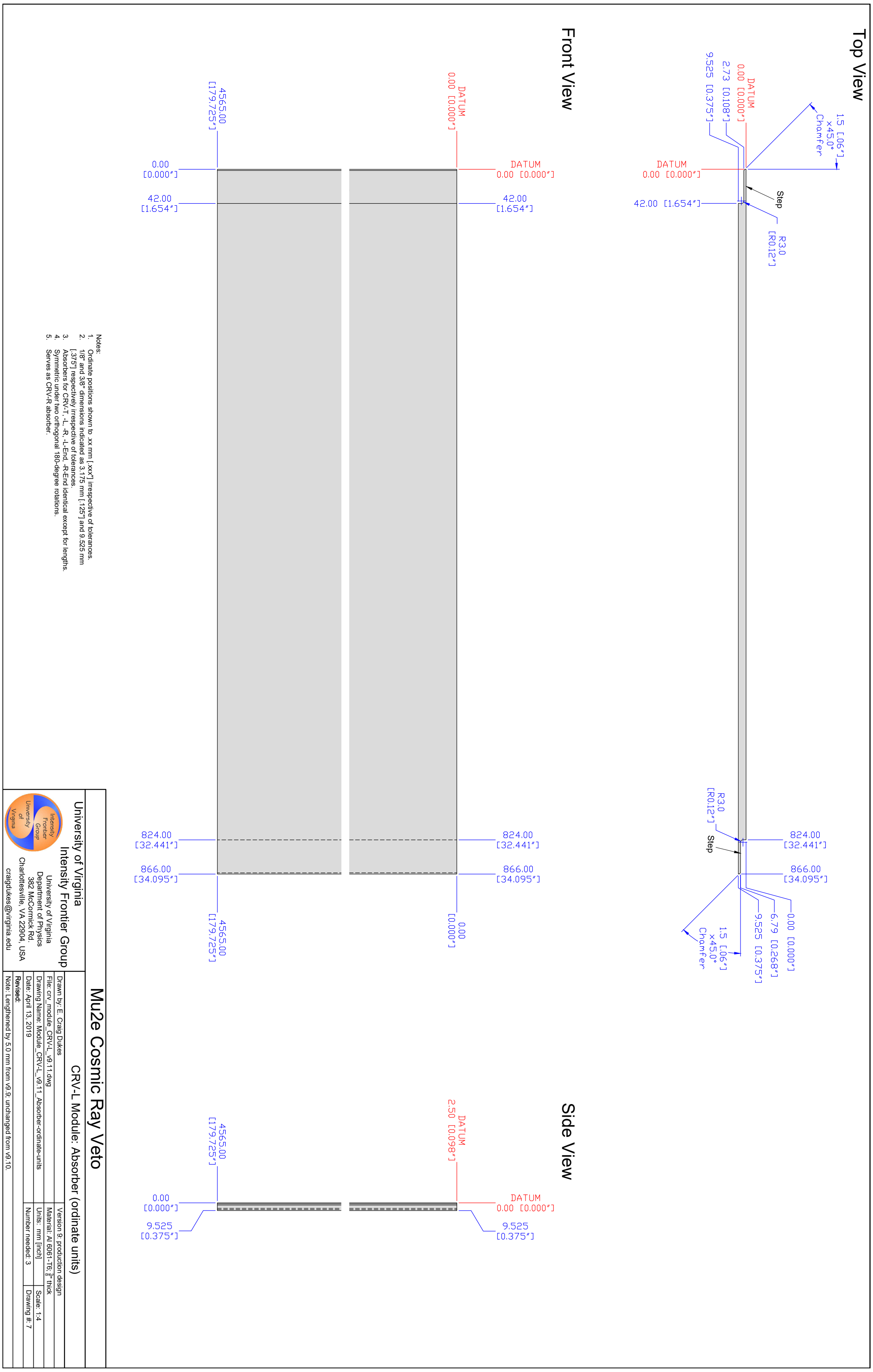

Figure D.7.: Drawing of a Left (CRV-L) module. CRV-R is a mirror image.

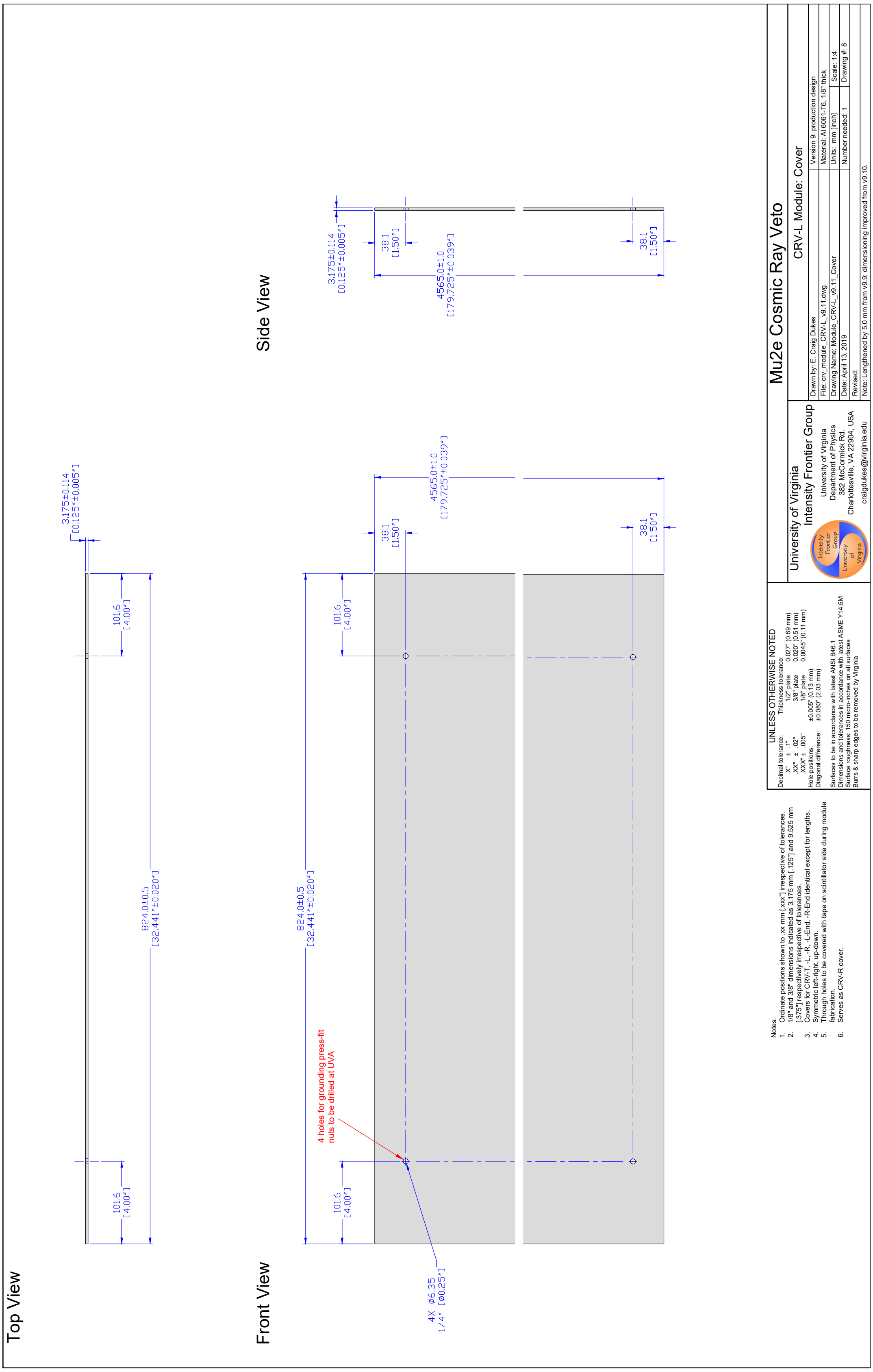

Figure D.8.: Drawing of a Left (CRV-L) module. CRV-R is a mirror image.

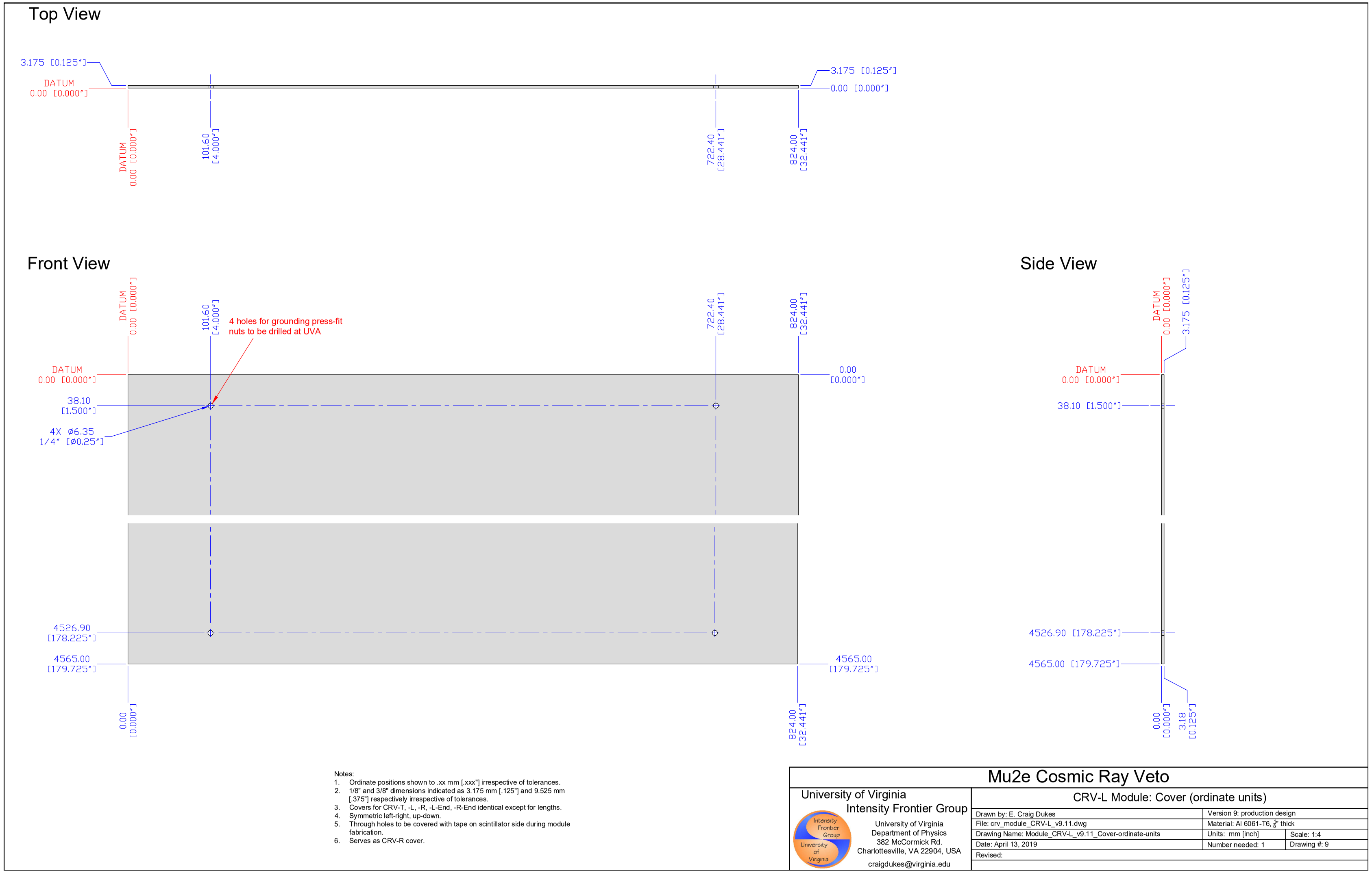

Figure D.9.: Drawing of a Left (CRV-L) module. CRV-R is a mirror image.

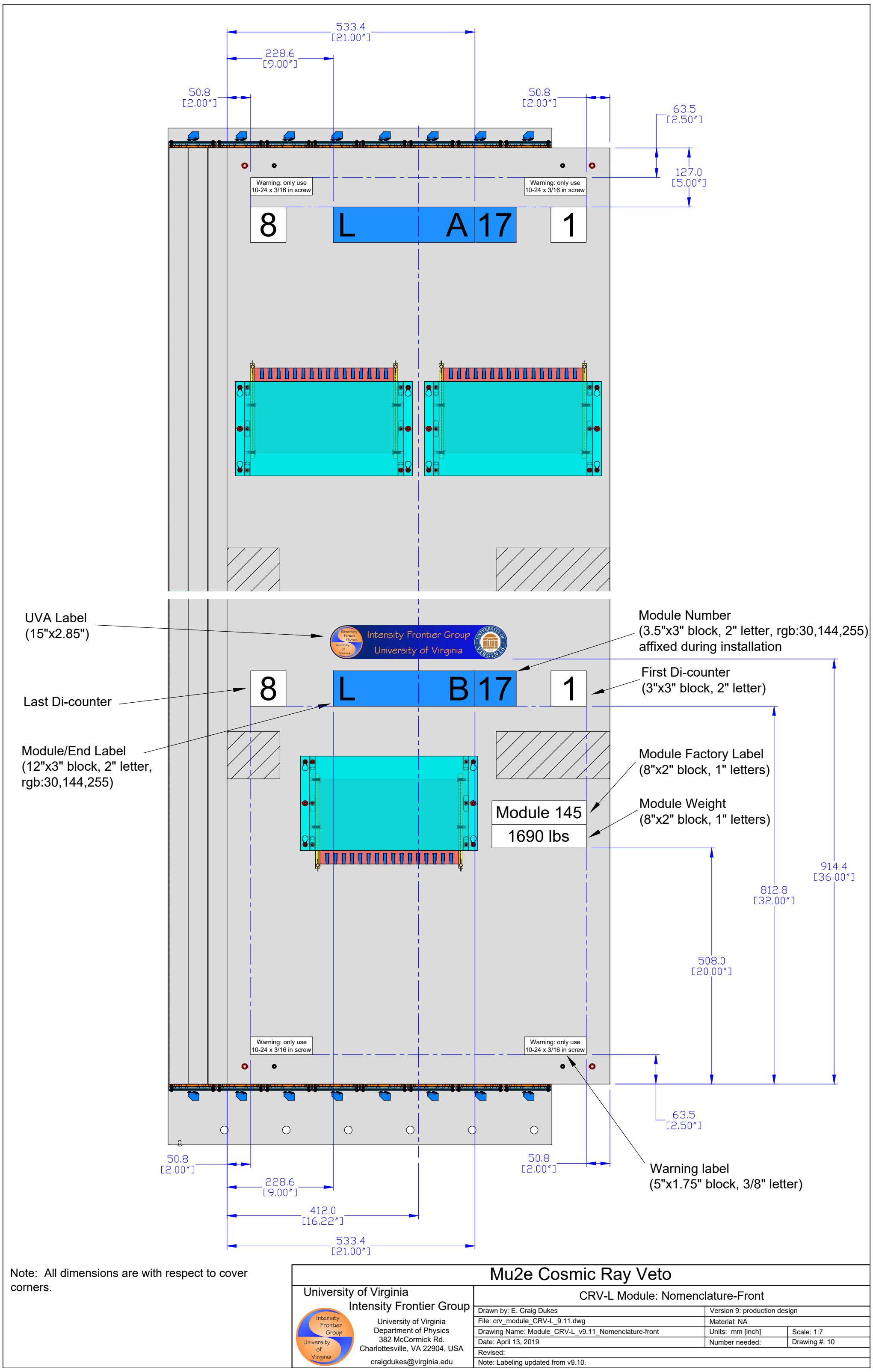

Figure D.10.: Drawing of a Left (CRV-L) module. CRV-R is a mirror image.

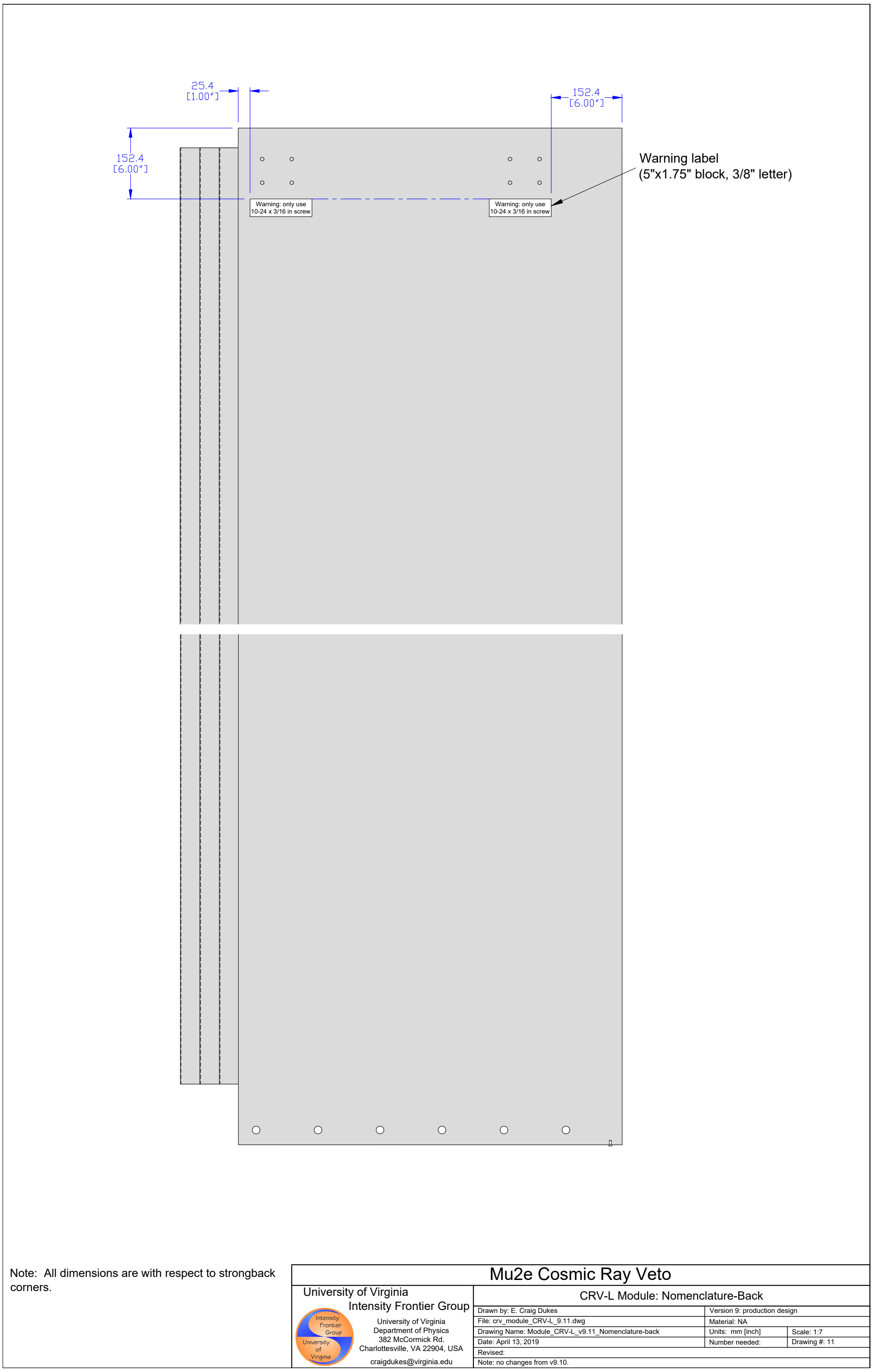

Figure D.11.: Drawing of a Left (CRV-L) module. CRV-R is a mirror image.

Appendix E.

Left/Right Endcap (CRV-L/R-Endcap) Module

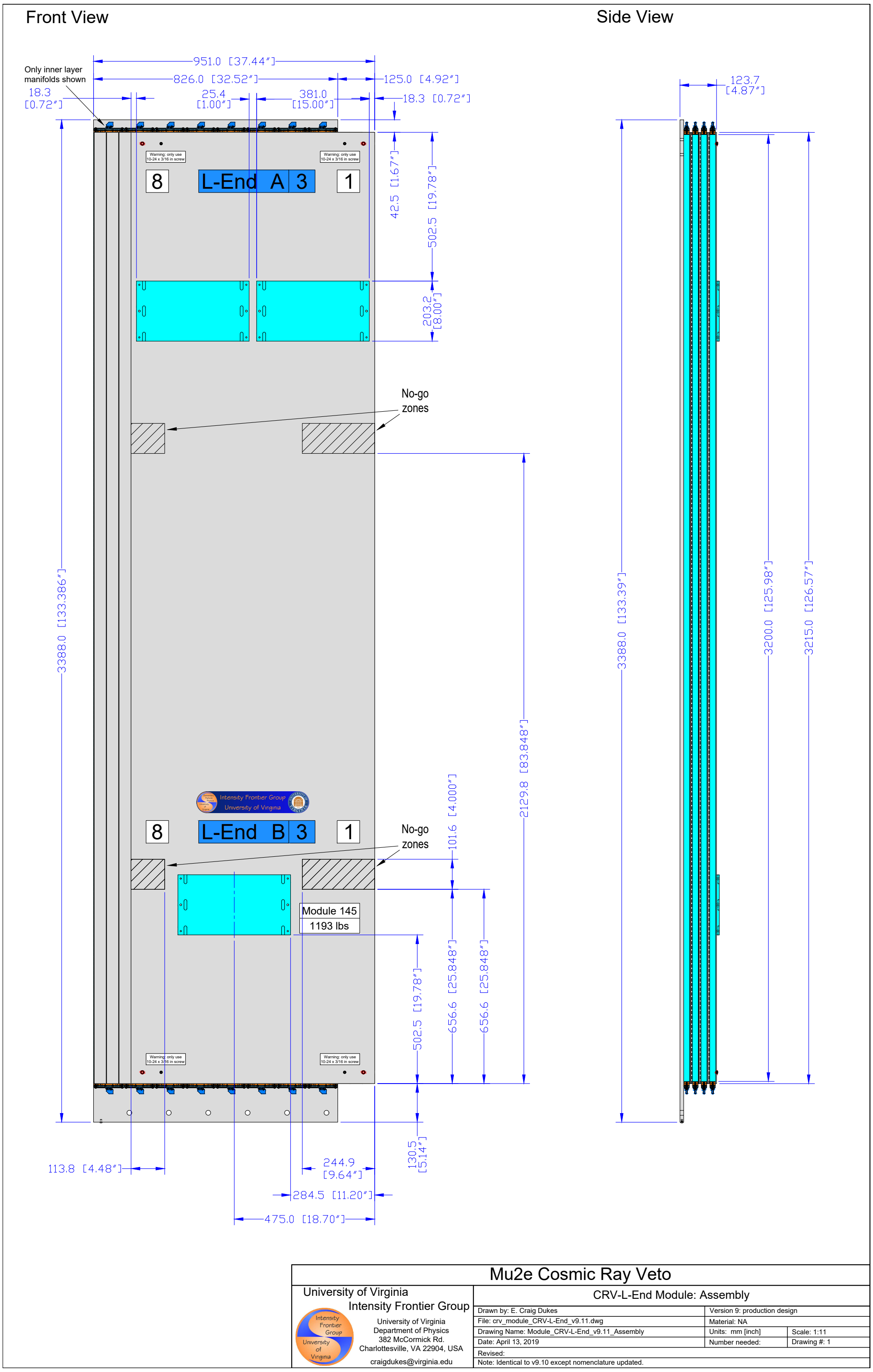

Figure E.1.: Drawing of a Left Endcap (CRV-L-Endcap) module. CRV-R-Endcap is a mirror image.

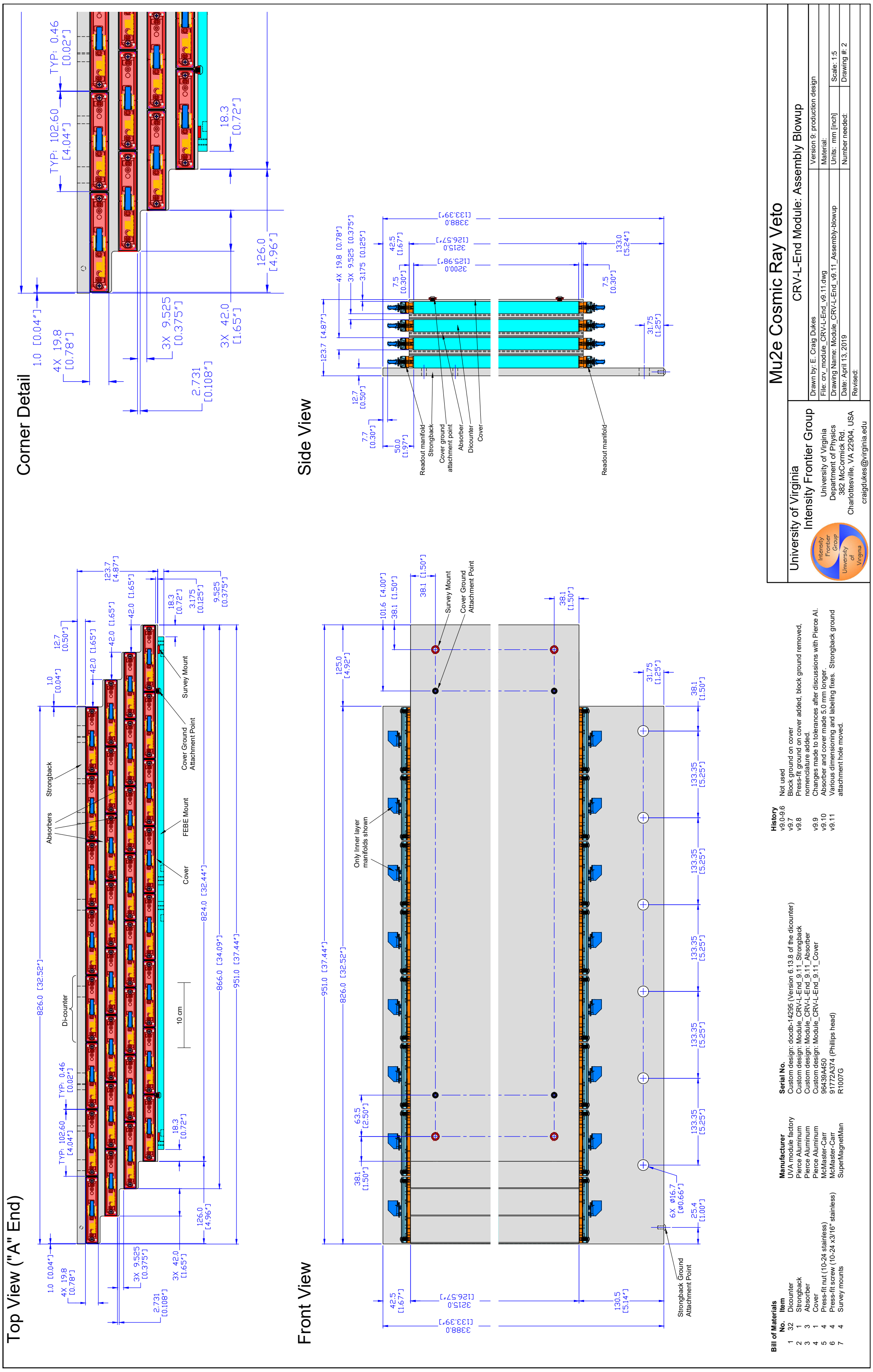

Figure E.2.: Drawing of a Left Endcap (CRV-L-Endcap) module. CRV-R-Endcap is a mirror image.

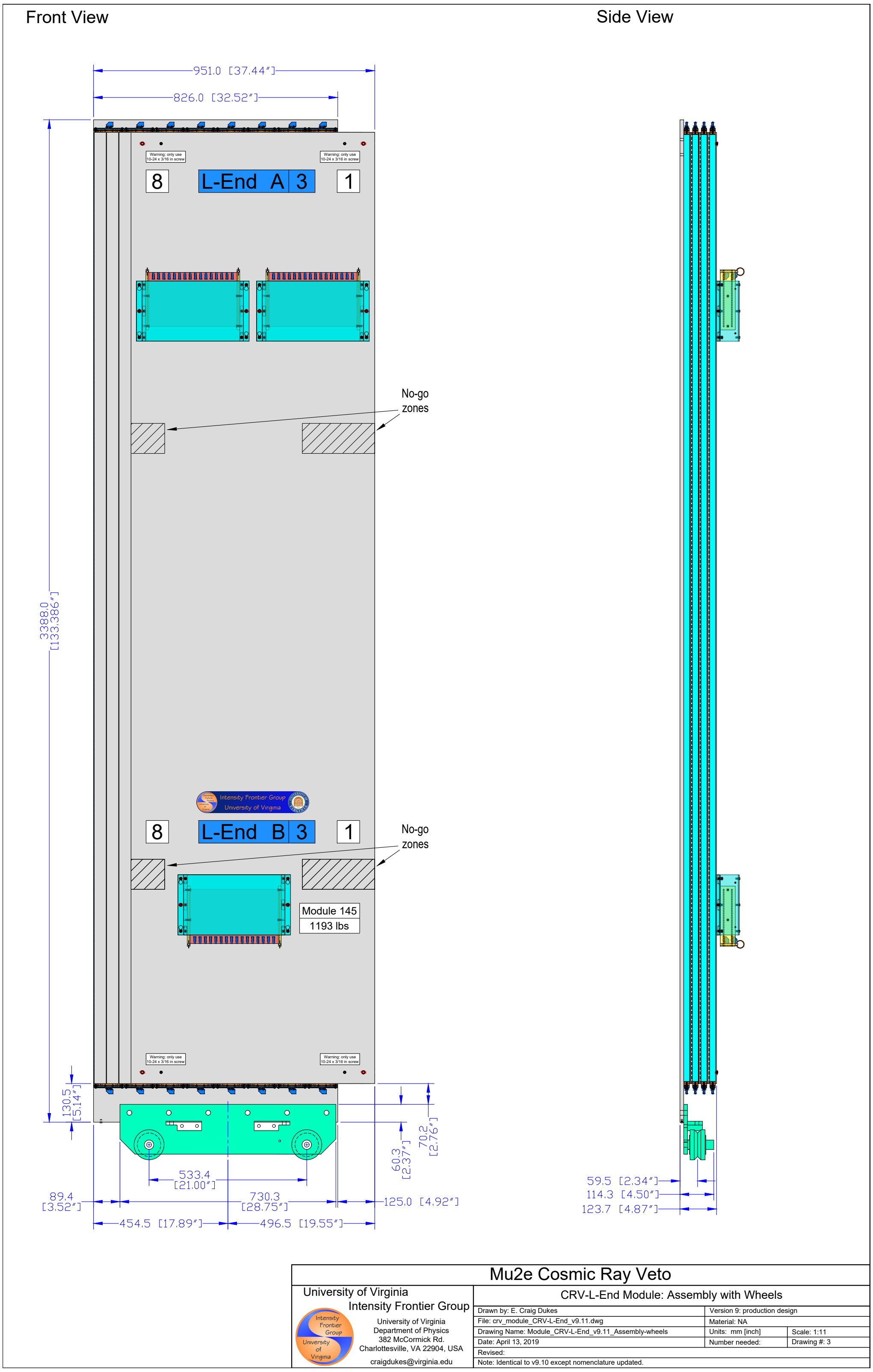

Figure E.3.: Drawing of a Left Endcap (CRV-L-Endcap) module. CRV-R-Endcap is a mirror image.

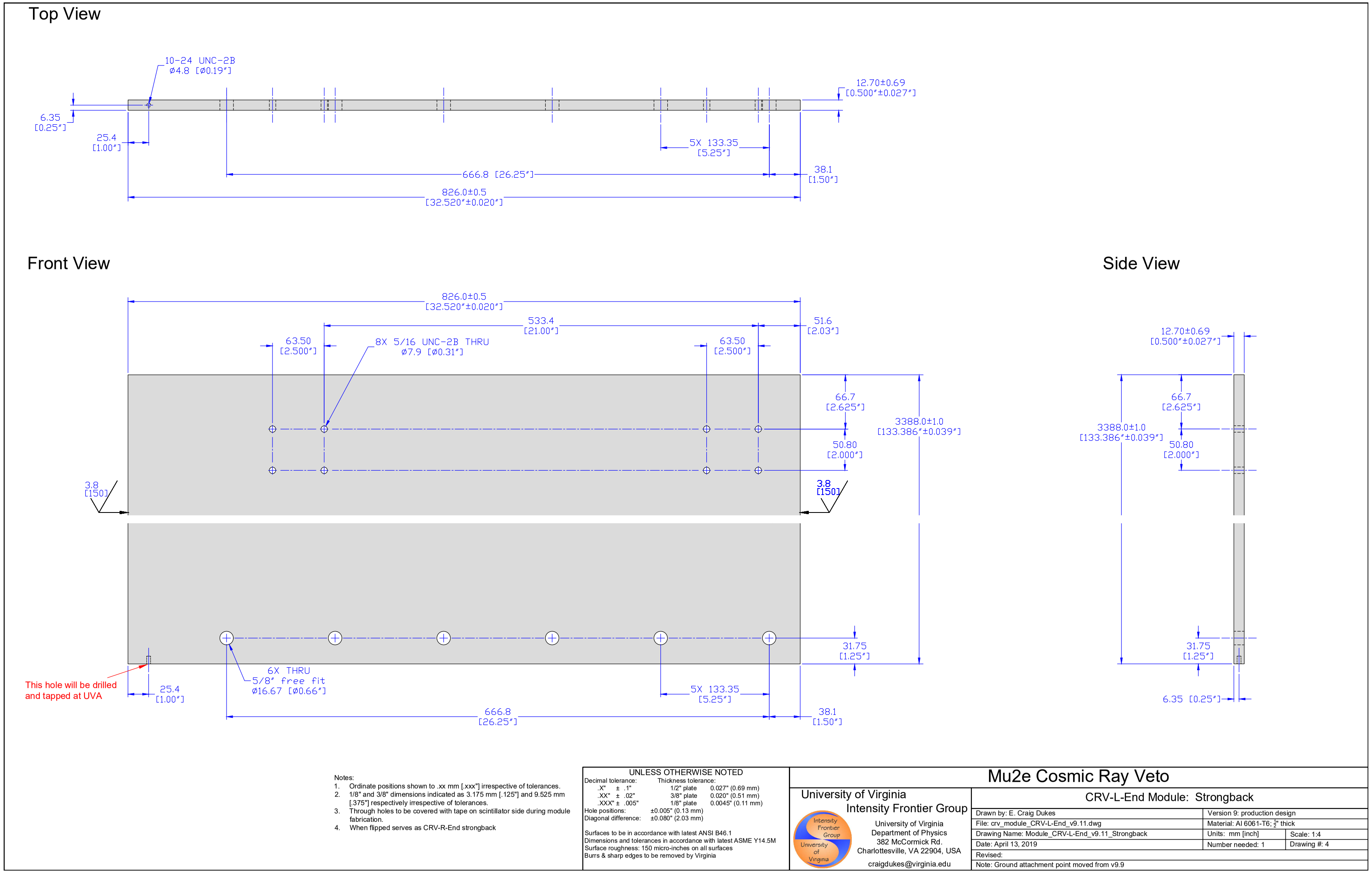

Figure E.4.: Drawing of a Left Endcap (CRV-L-Endcap) module. CRV-R-Endcap is a mirror image.

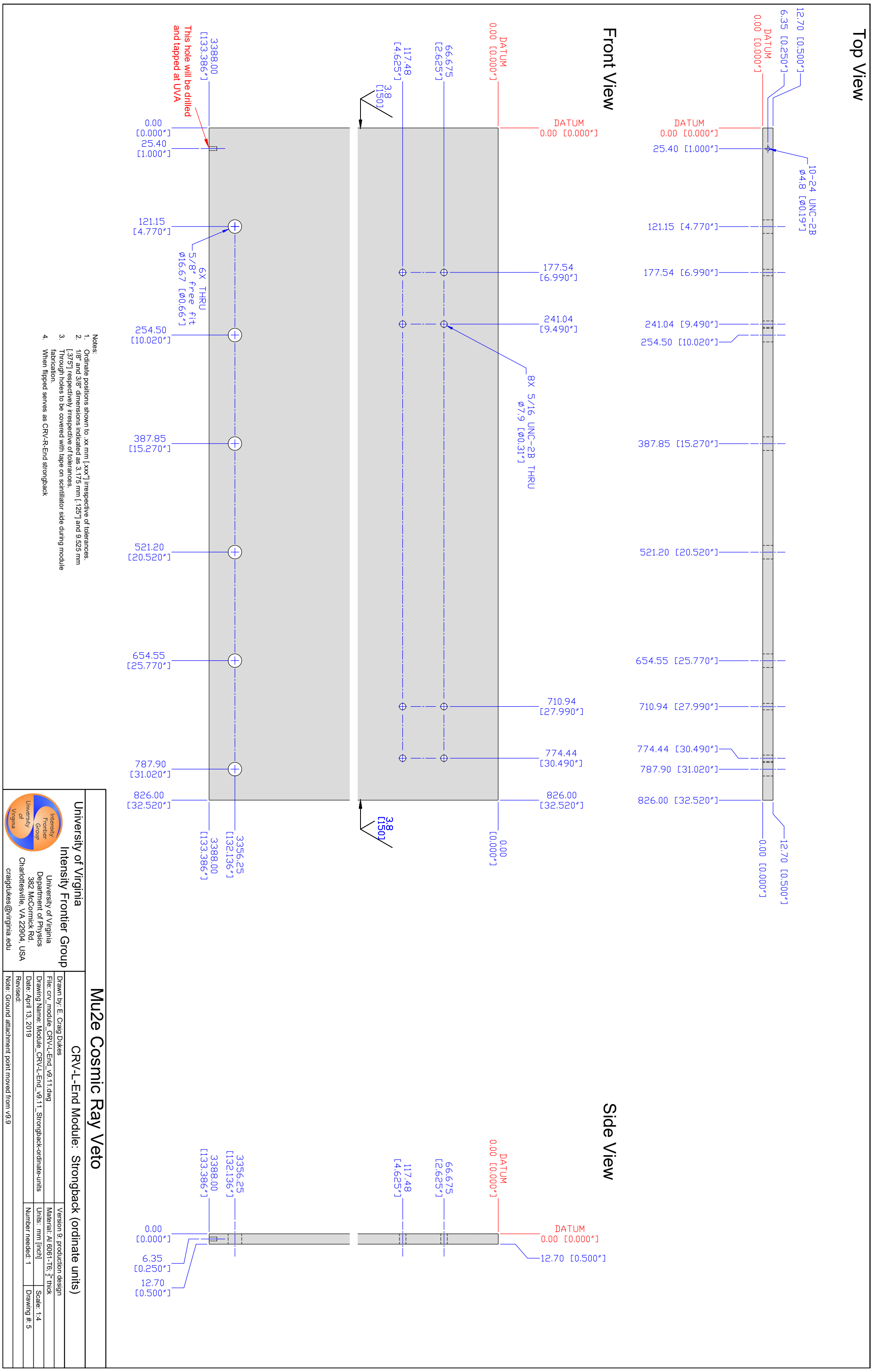

Figure E.5.: Drawing of a Left Endcap (CRV-L-Endcap) module. CRV-R-Endcap is a mirror image.

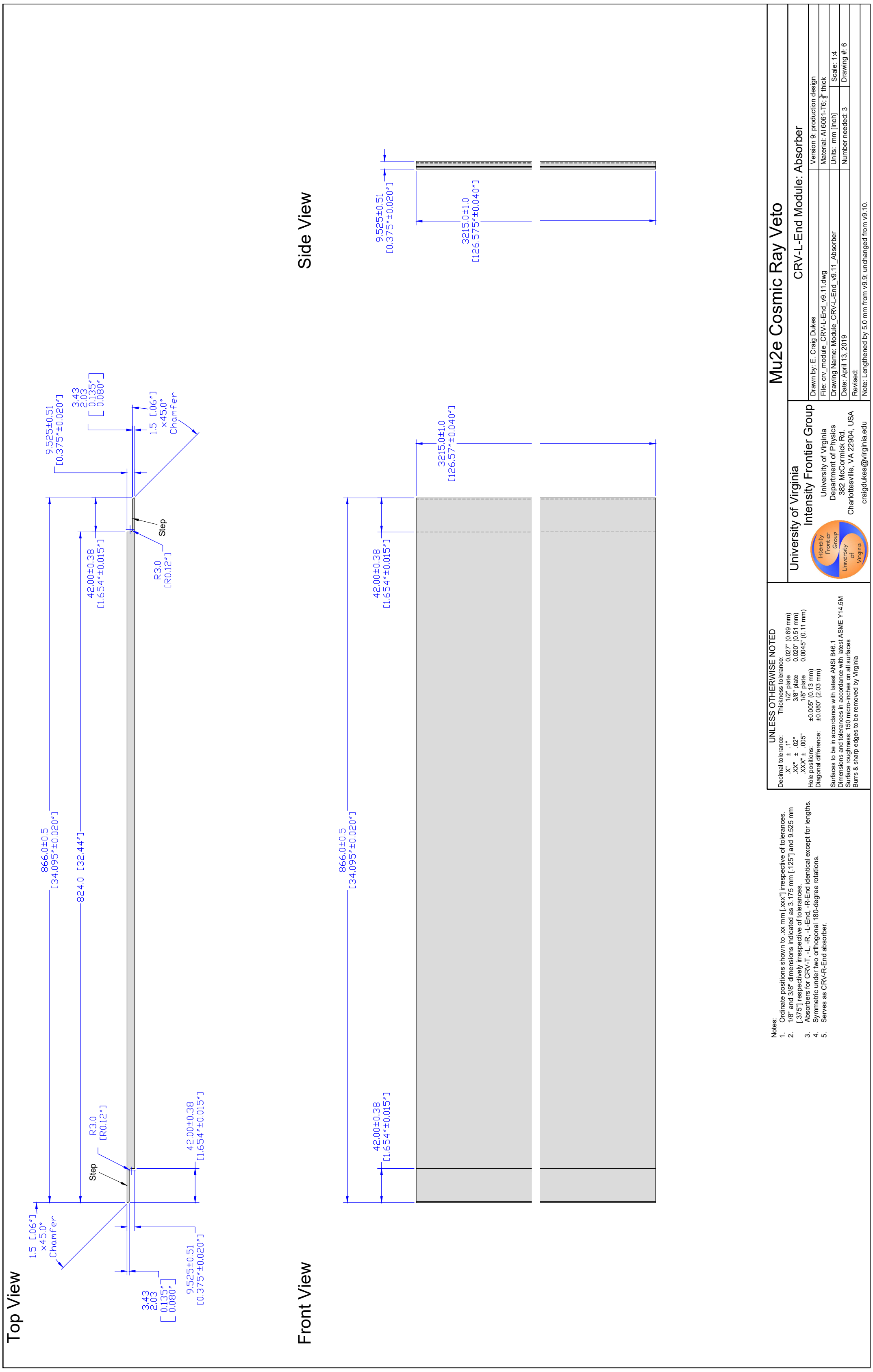

Figure E.6.: Drawing of a Left Endcap (CRV-L-Endcap) module. CRV-R-Endcap is a mirror image.

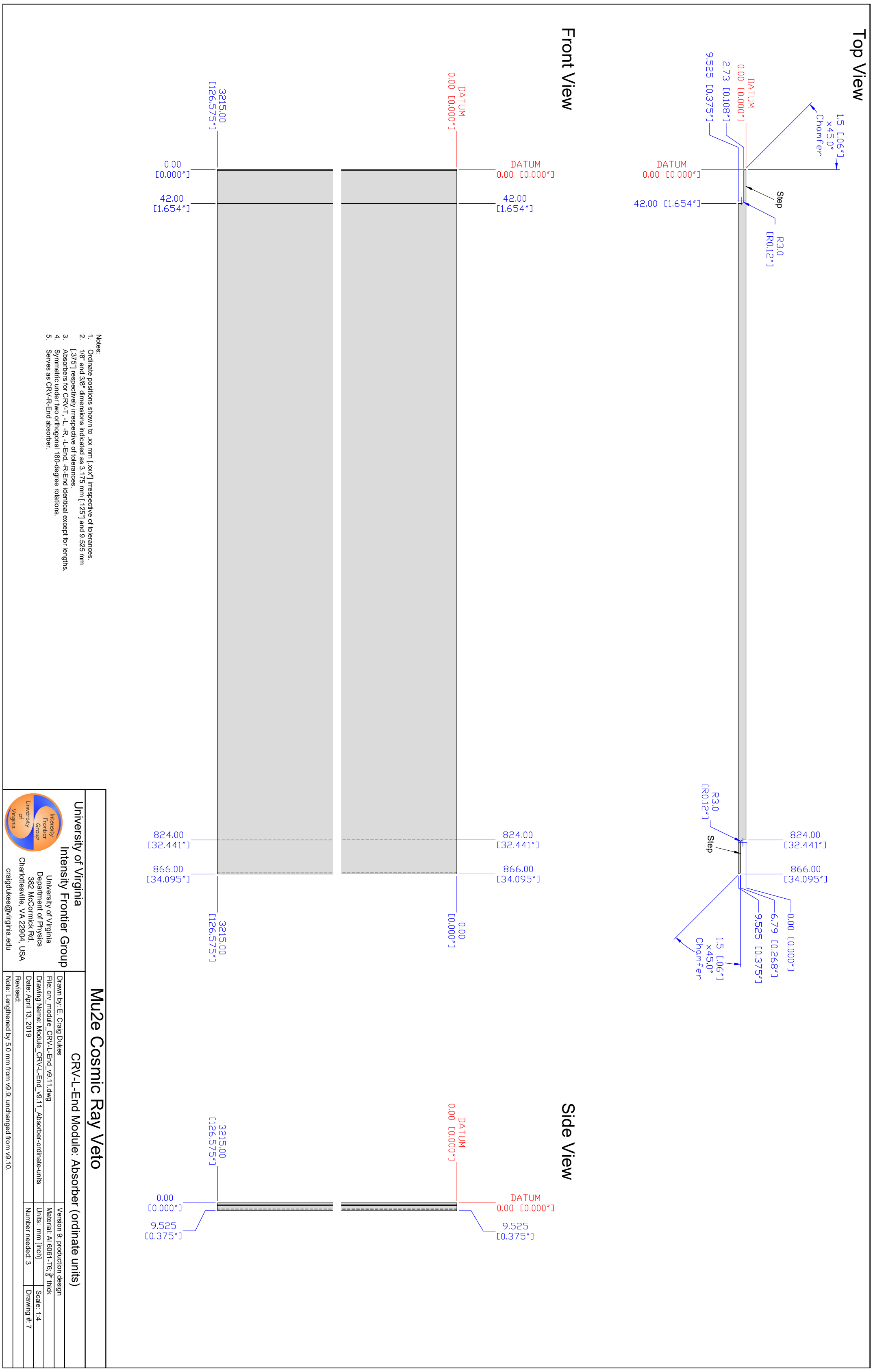

Figure E.7.: Drawing of a Left Endcap (CRV-L-Endcap) module. CRV-R-Endcap is a mirror image.

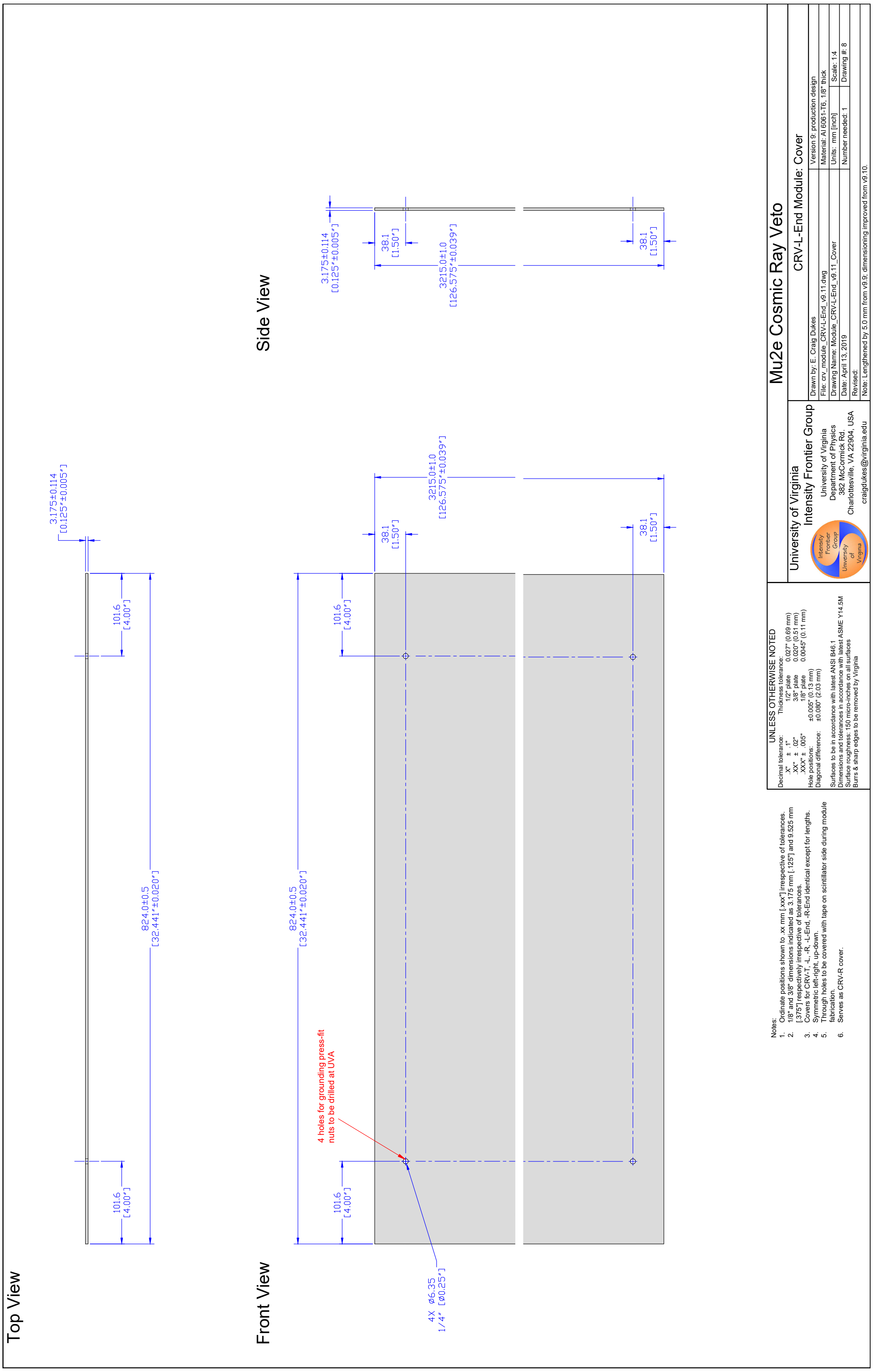

Figure E.8.: Drawing of a Left Endcap (CRV-L-Endcap) module. CRV-R-Endcap is a mirror image.

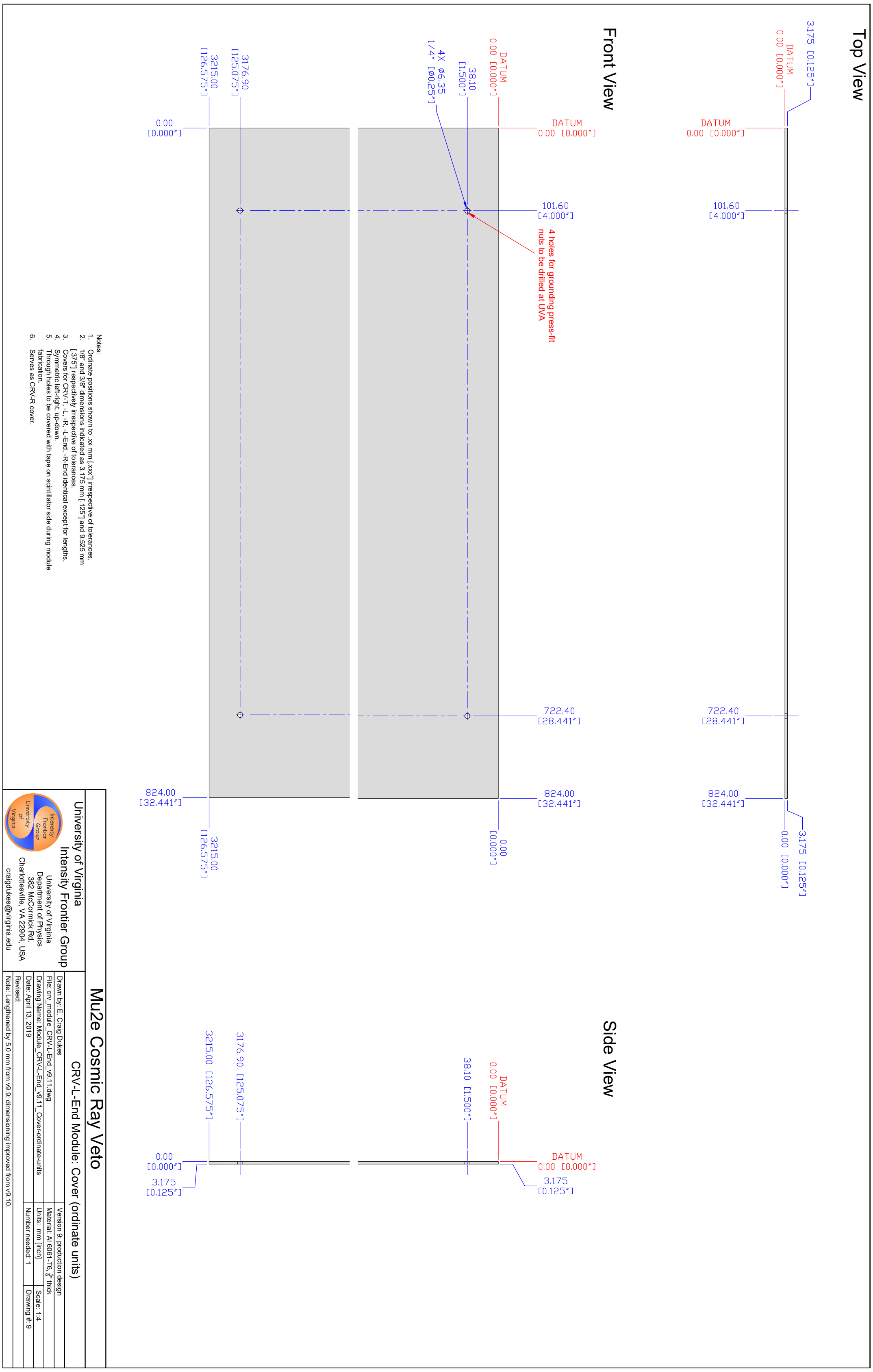

Figure E.9.: Drawing of a Left Endcap (CRV-L-Endcap) module. CRV-R-Endcap is a mirror image.

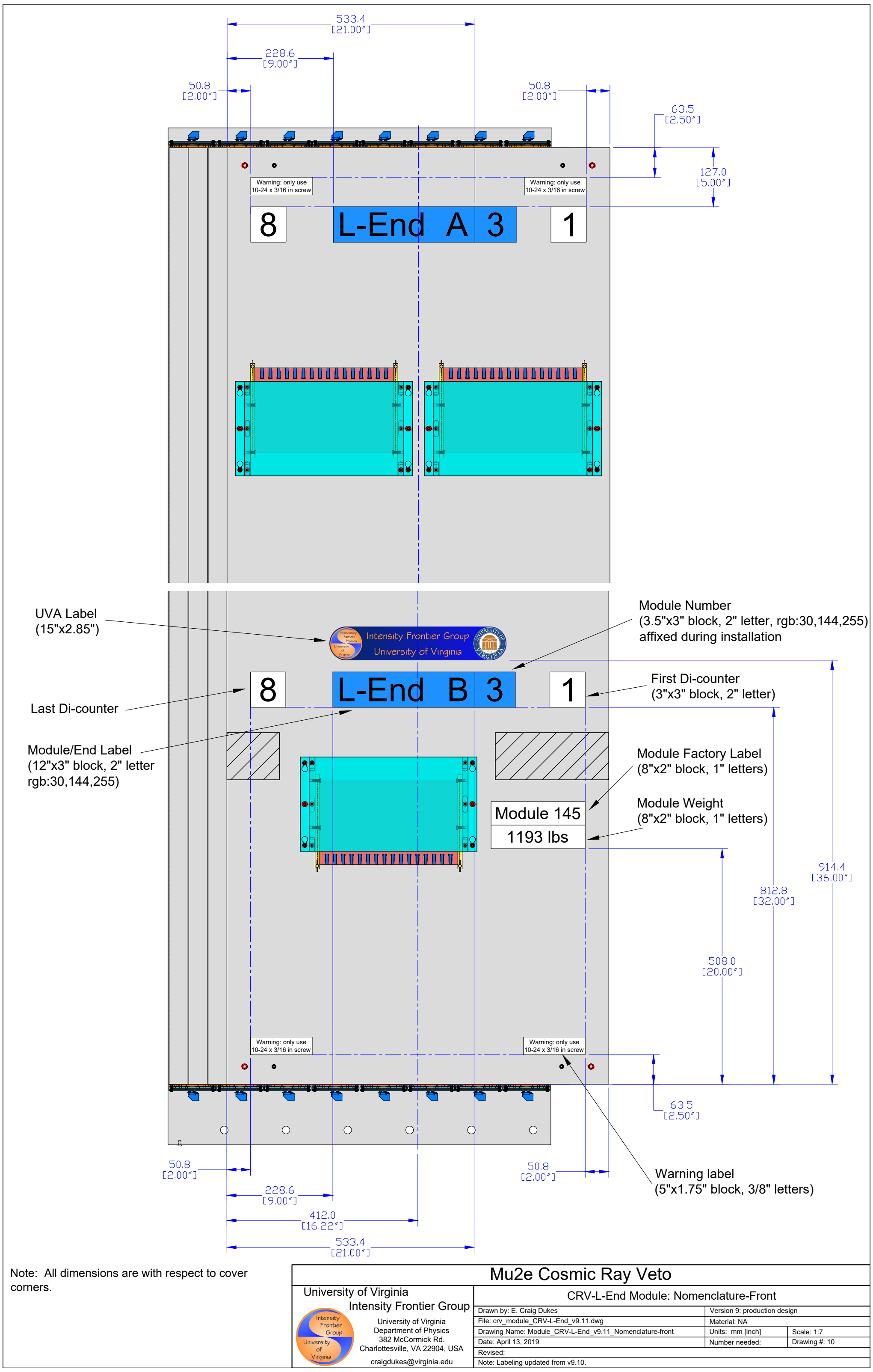

Figure E.10.: Drawing of a Left Endcap (CRV-L-Endcap) module. CRV-R-Endcap is a mirror image.

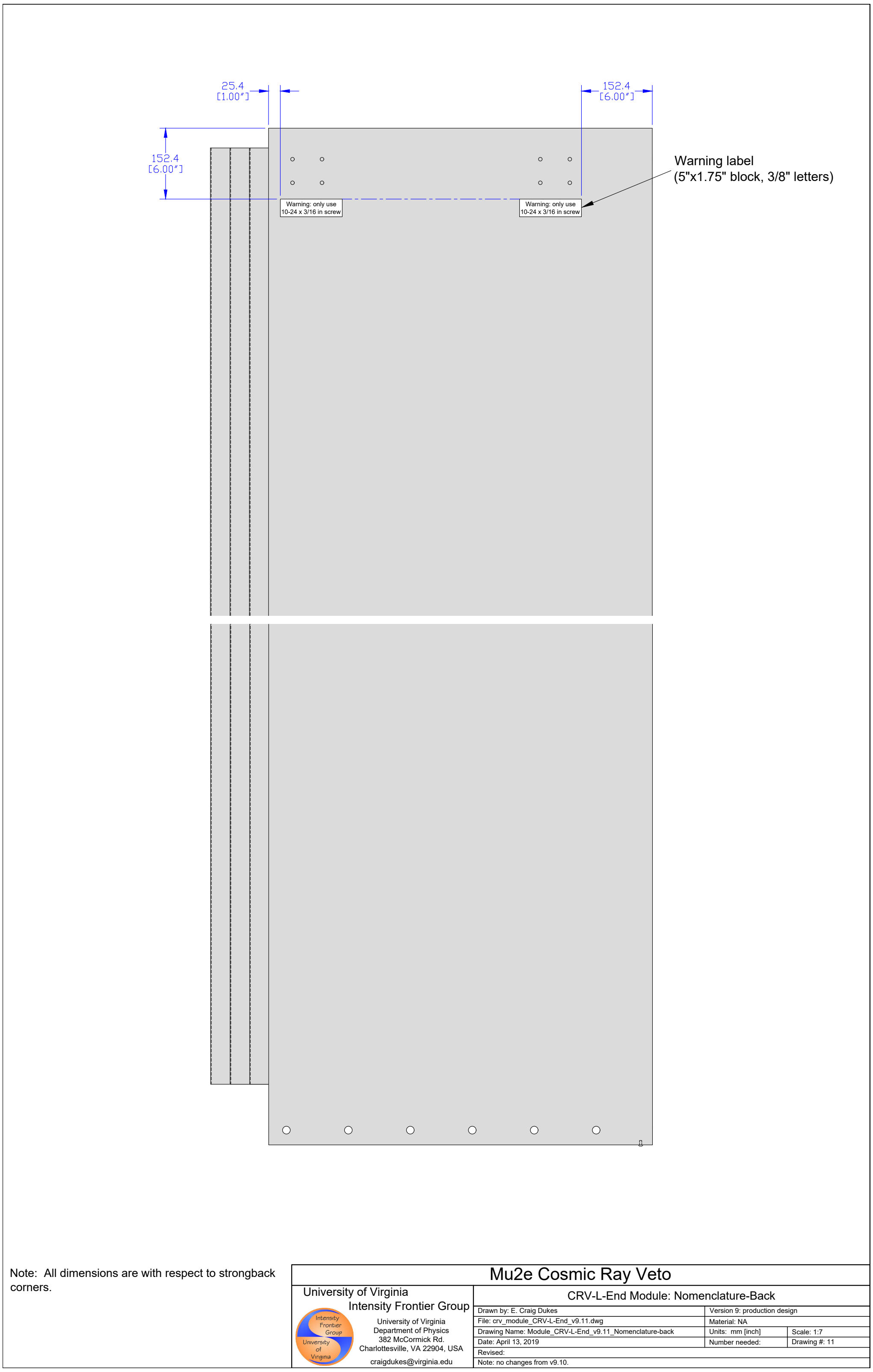

Figure E.11.: Drawing of a Left Endcap (CRV-L-Endcap) module. CRV-R-Endcap is a mirror image.

Appendix F.

Upstream (CRV-U) Module

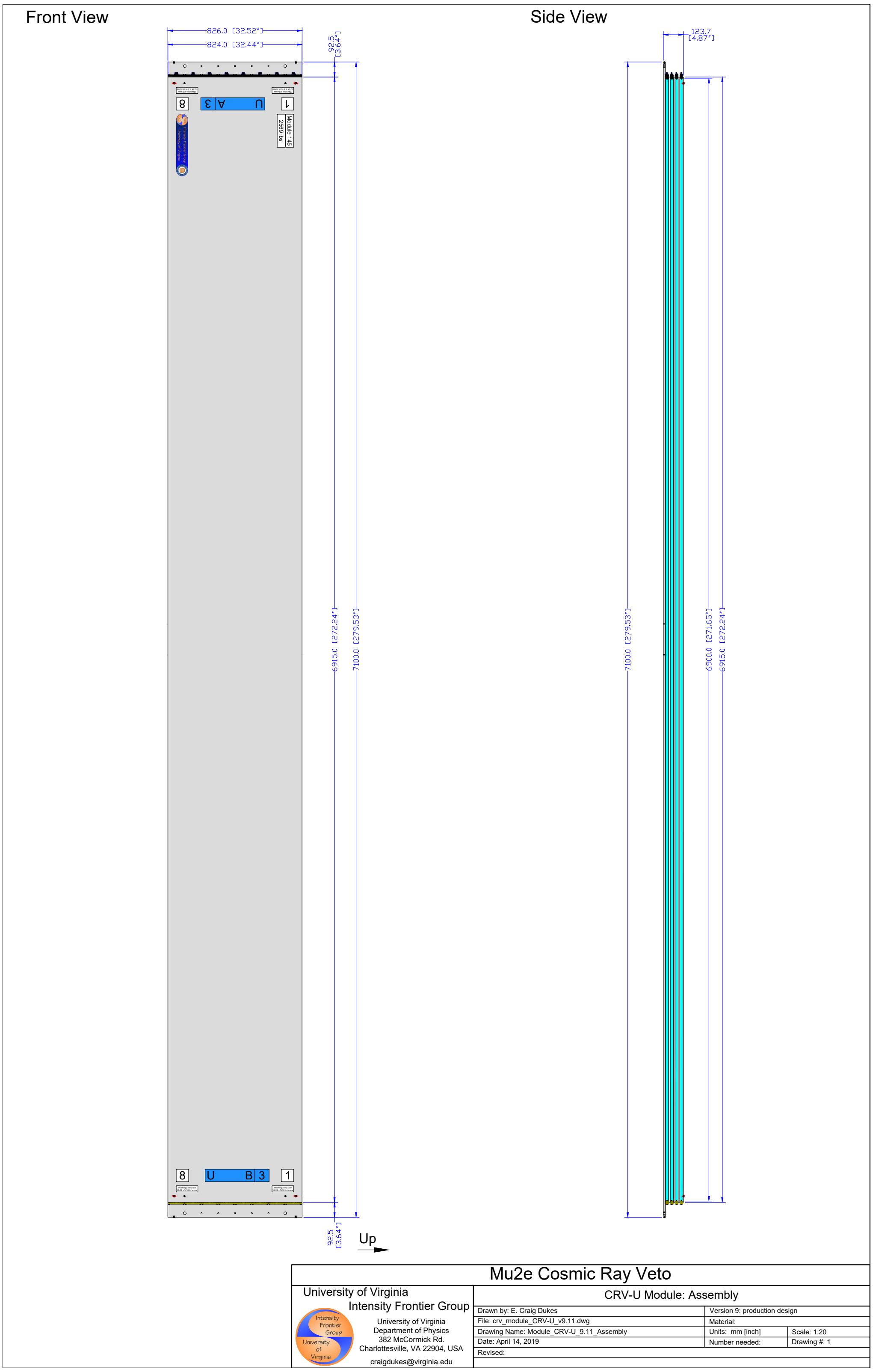

Figure F.1.: Drawing of a Upstream (CRV-U) module.

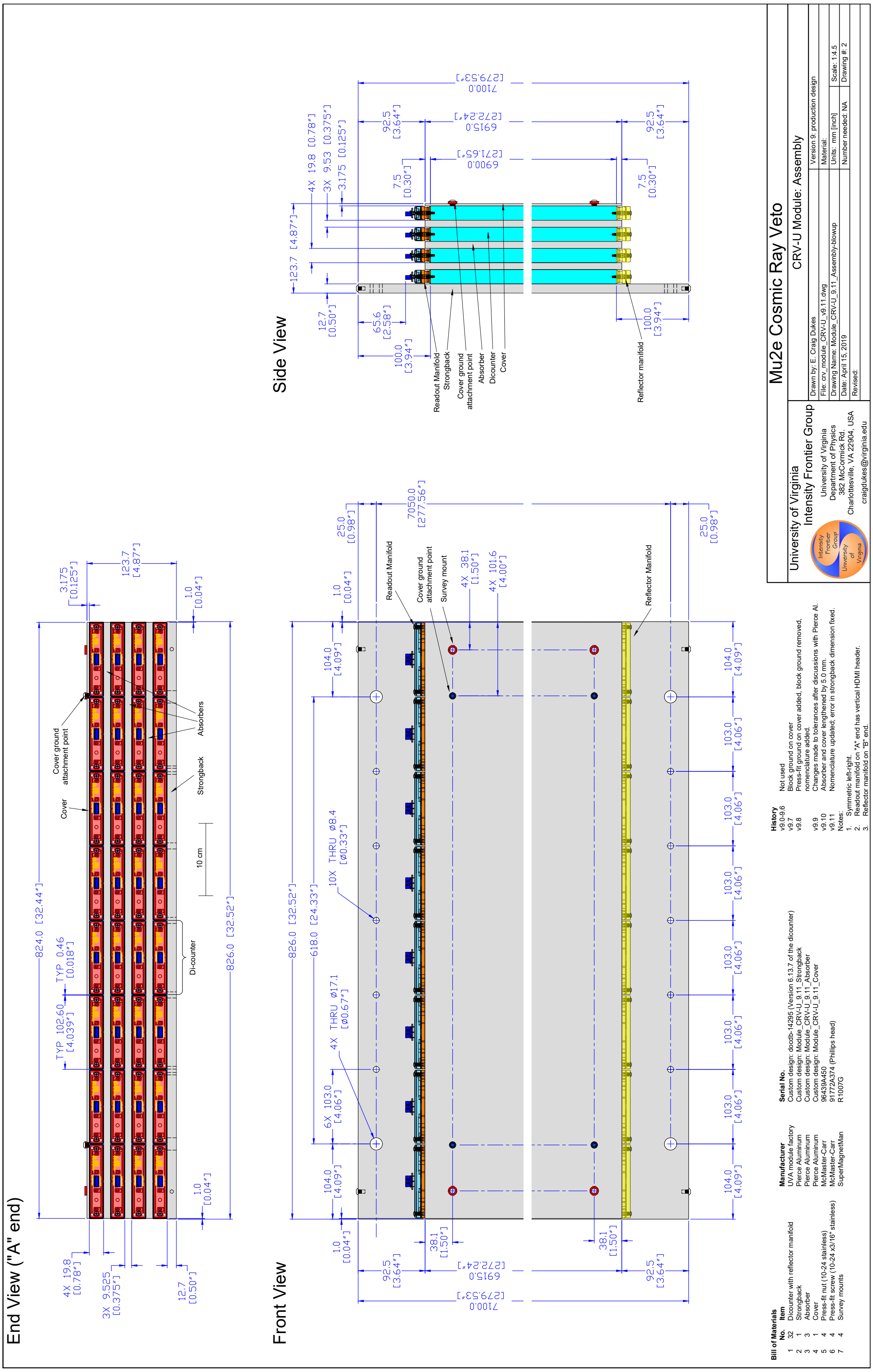

Figure F.2.: Drawing of a Upstream (CRV-U) module.

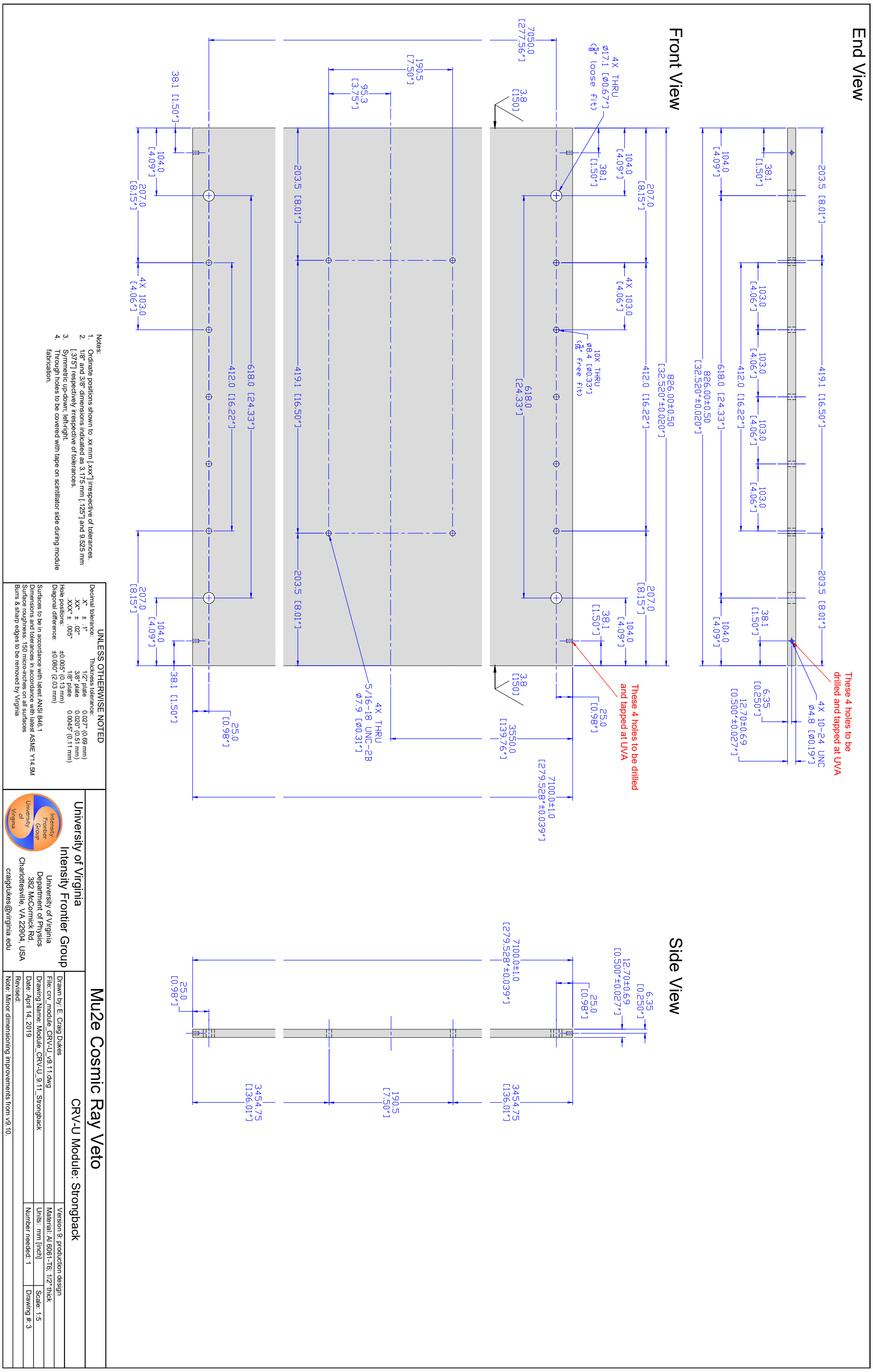

Figure F.3.: Drawing of a Upstream (CRV-U) module.

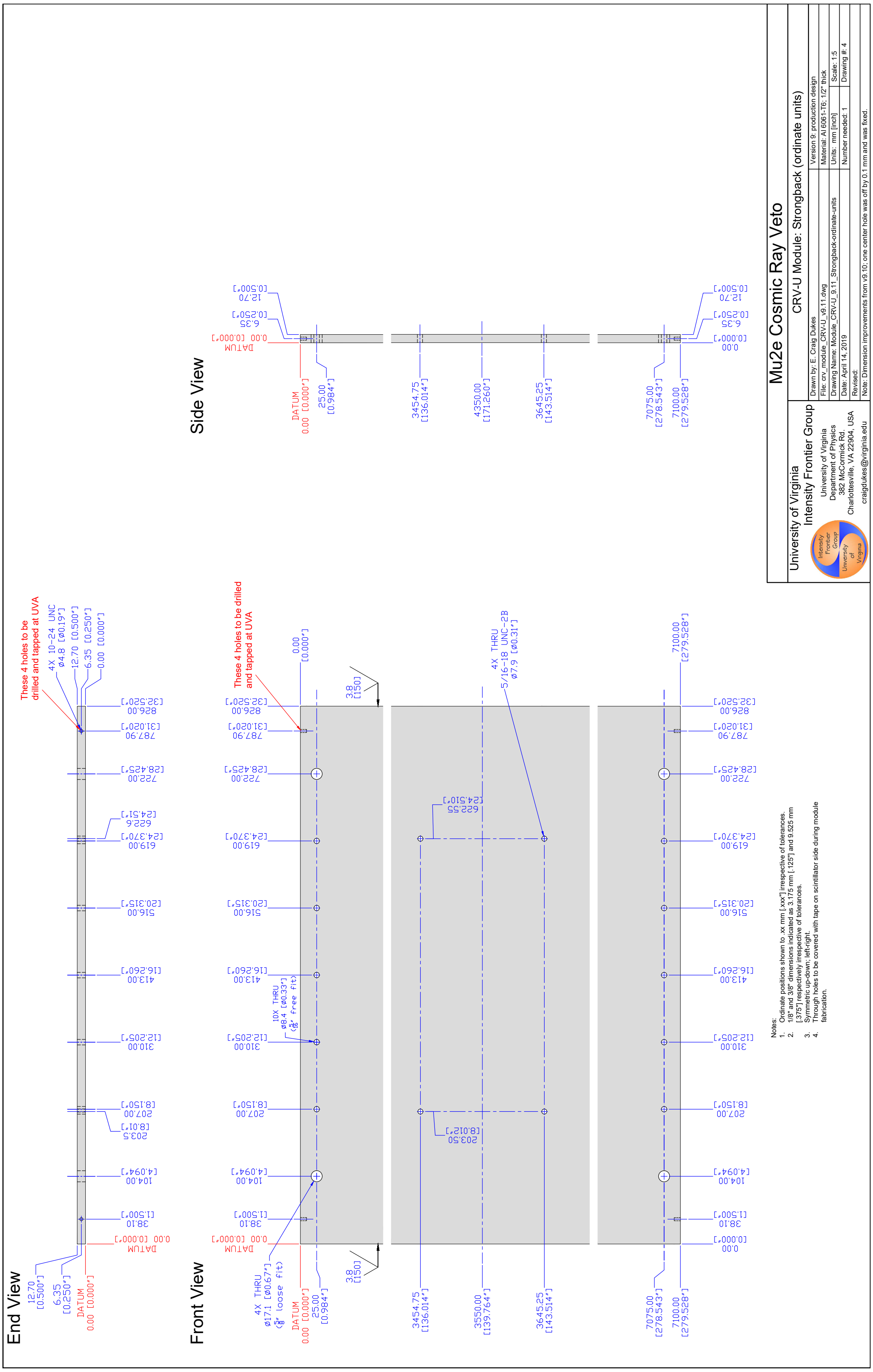

Figure F.4.: Drawing of a Upstream (CRV-U) module.

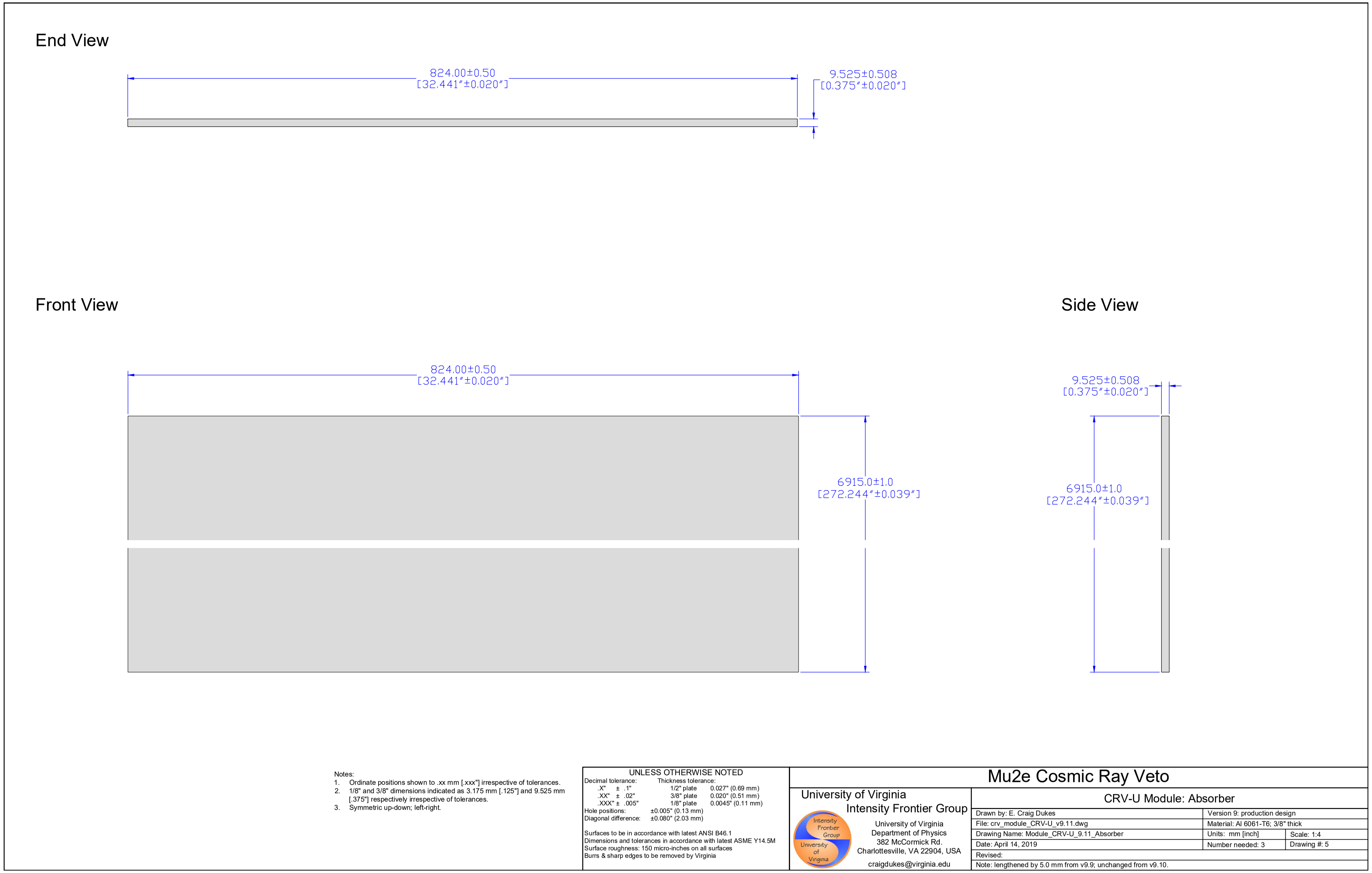

Figure F.5.: Drawing of a Upstream (CRV-U) module.

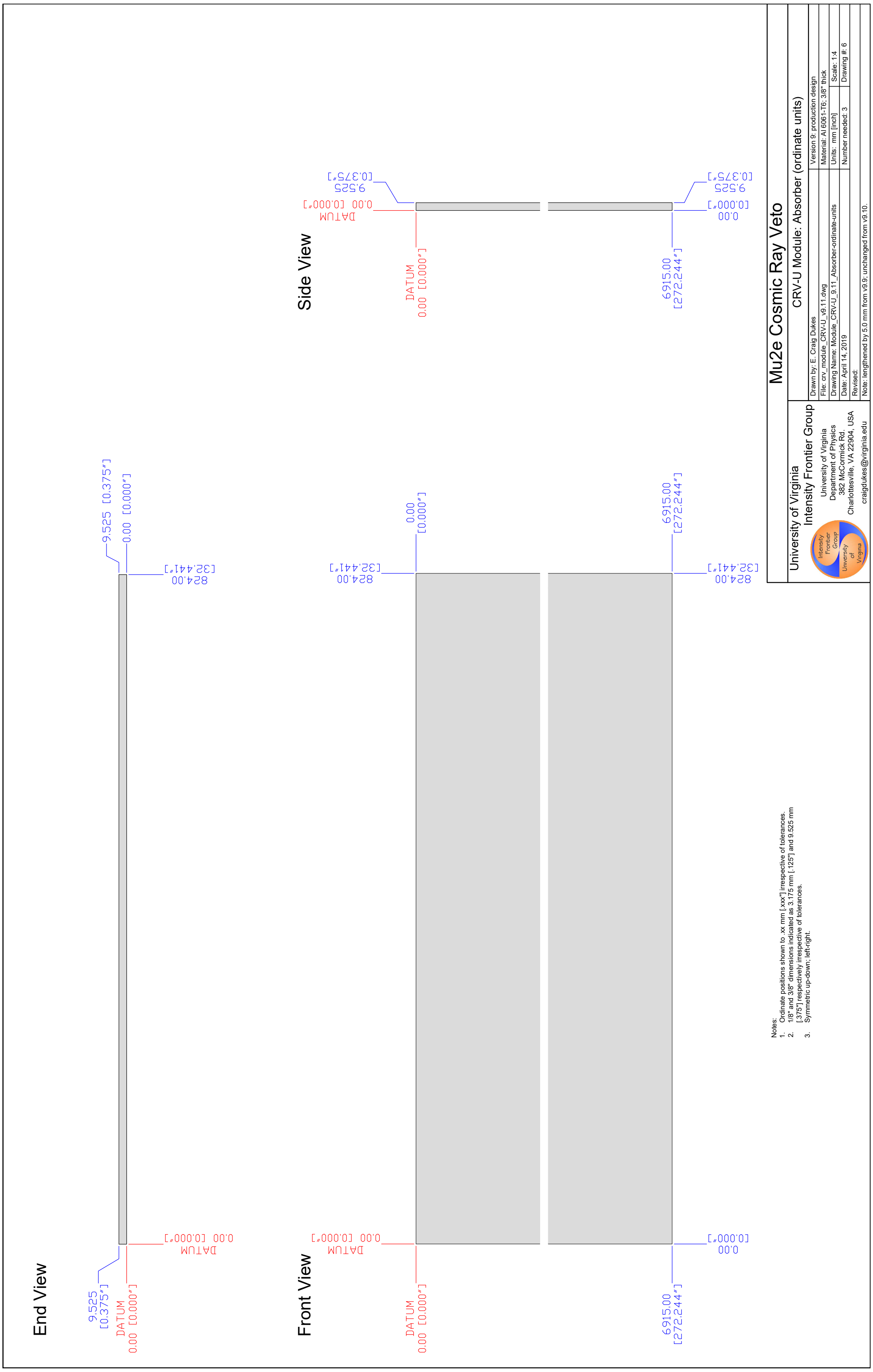

Figure F.6.: Drawing of a Upstream (CRV-U) module.

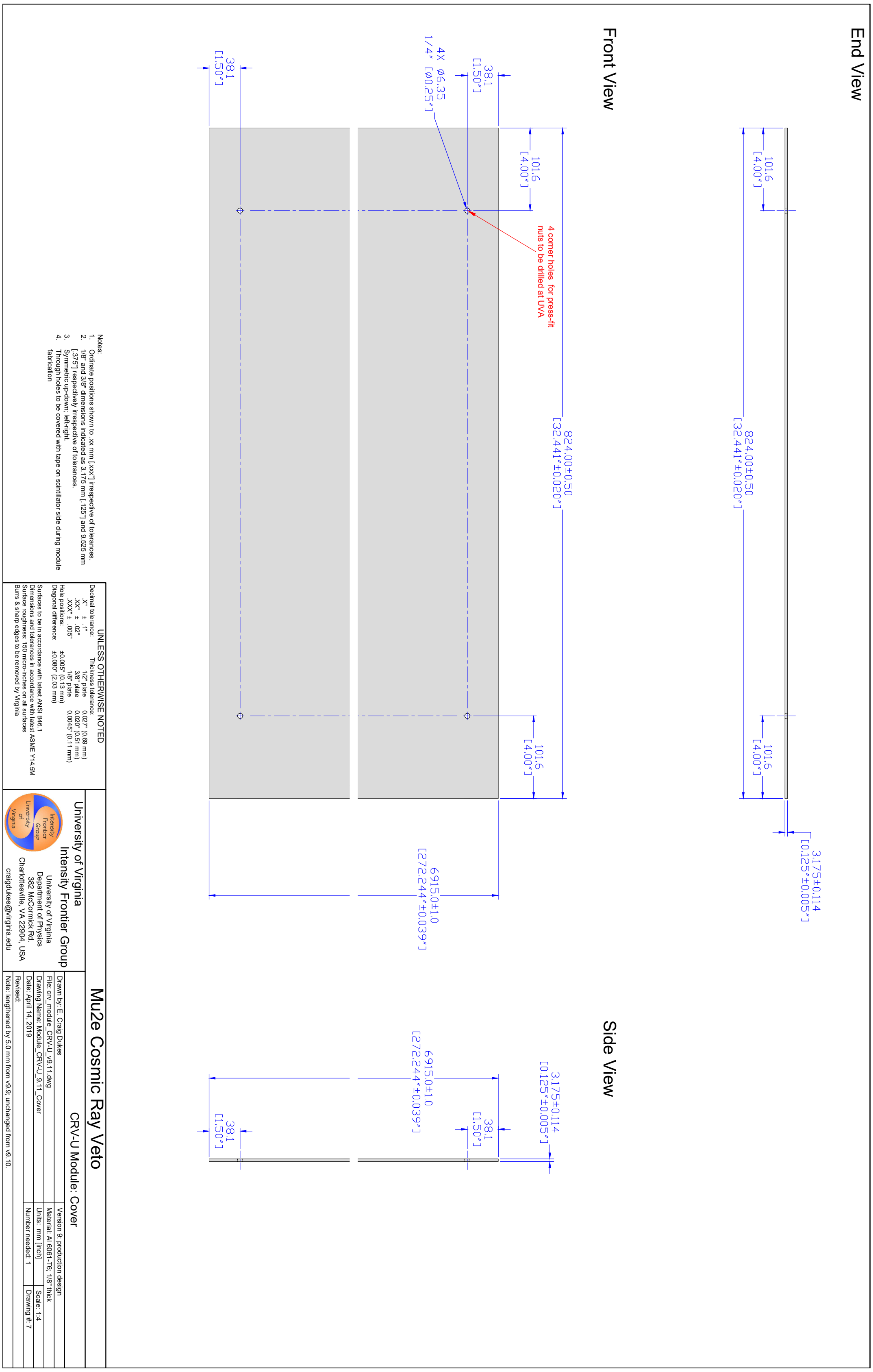

Figure F.7.: Drawing of a Upstream (CRV-U) module.

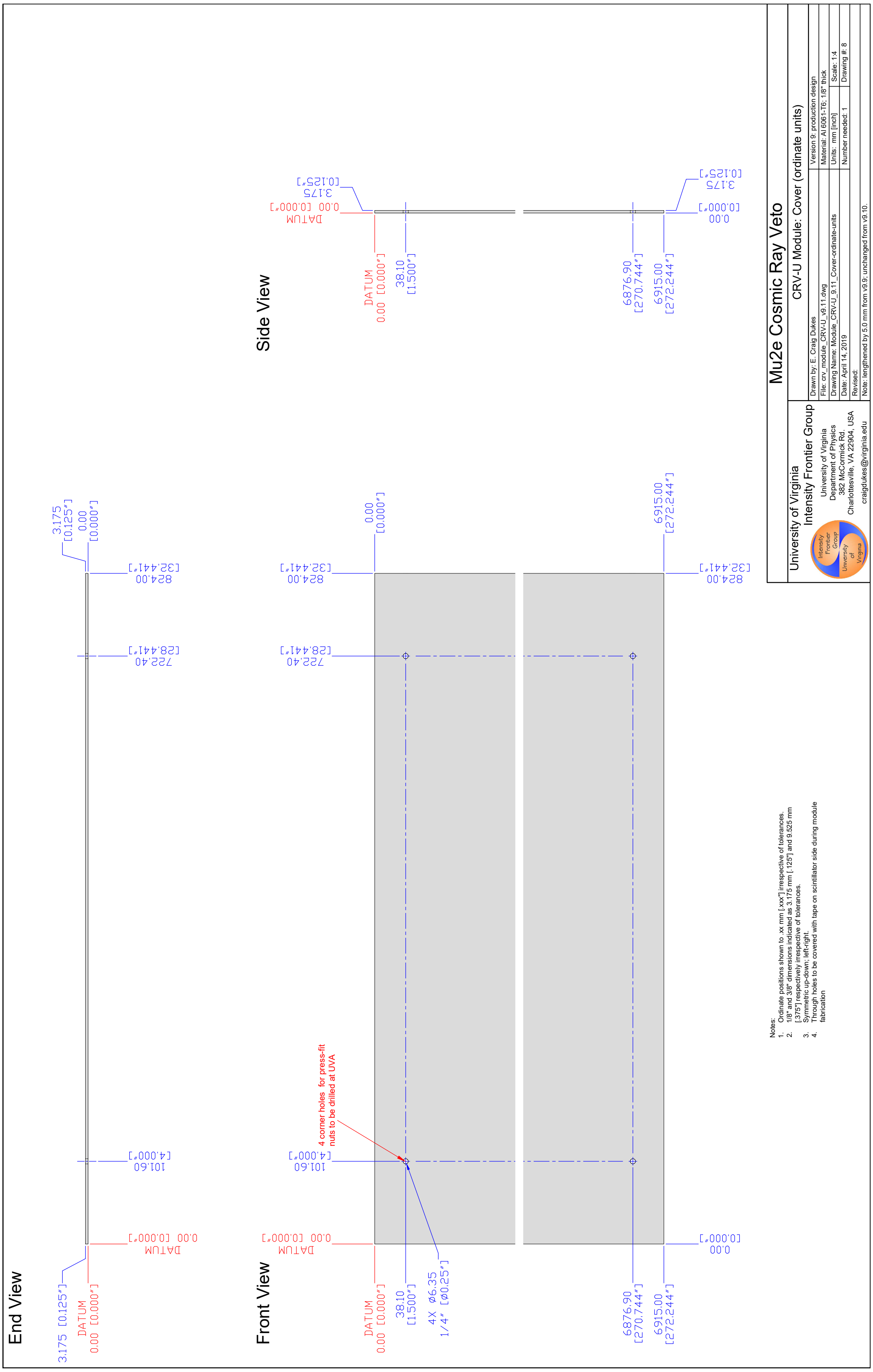

Figure F.8.: Drawing of a Upstream (CRV-U) module.

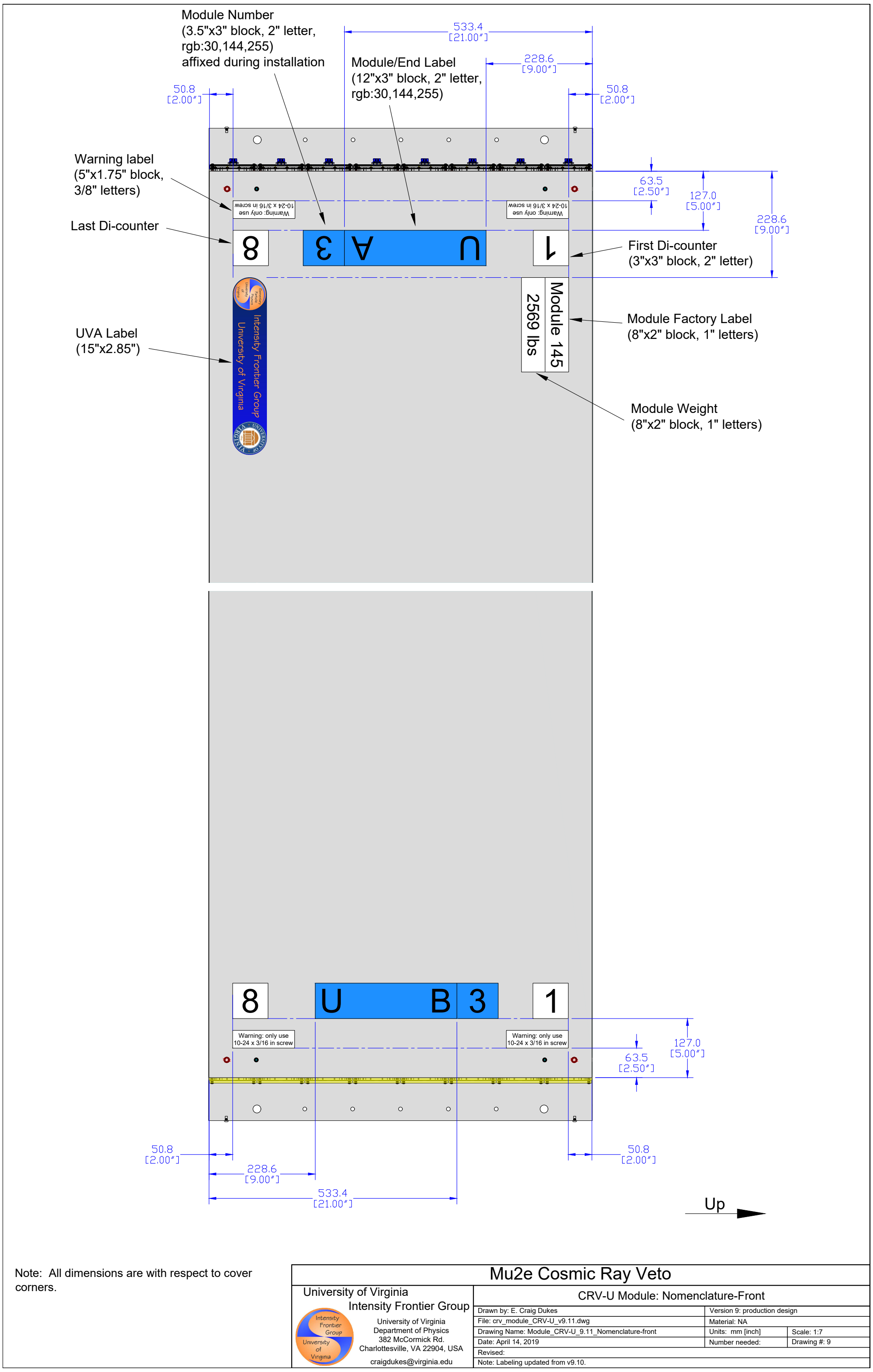

Figure F.9.: Drawing of a Upstream (CRV-U) module.

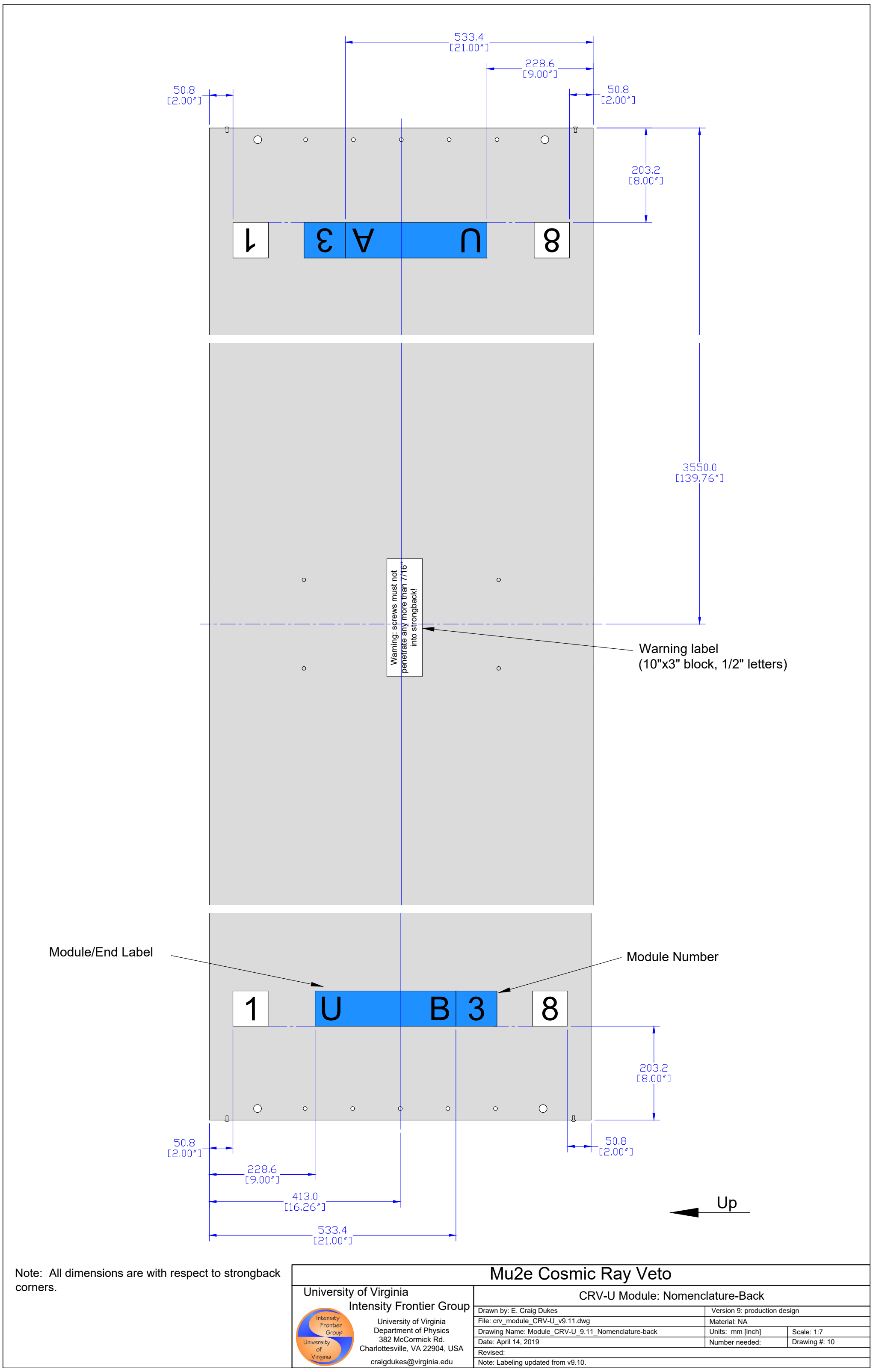

Figure F.10.: Drawing of a Upstream (CRV-U) module.

Appendix G.

Downstream Short (CRV-DS) Module

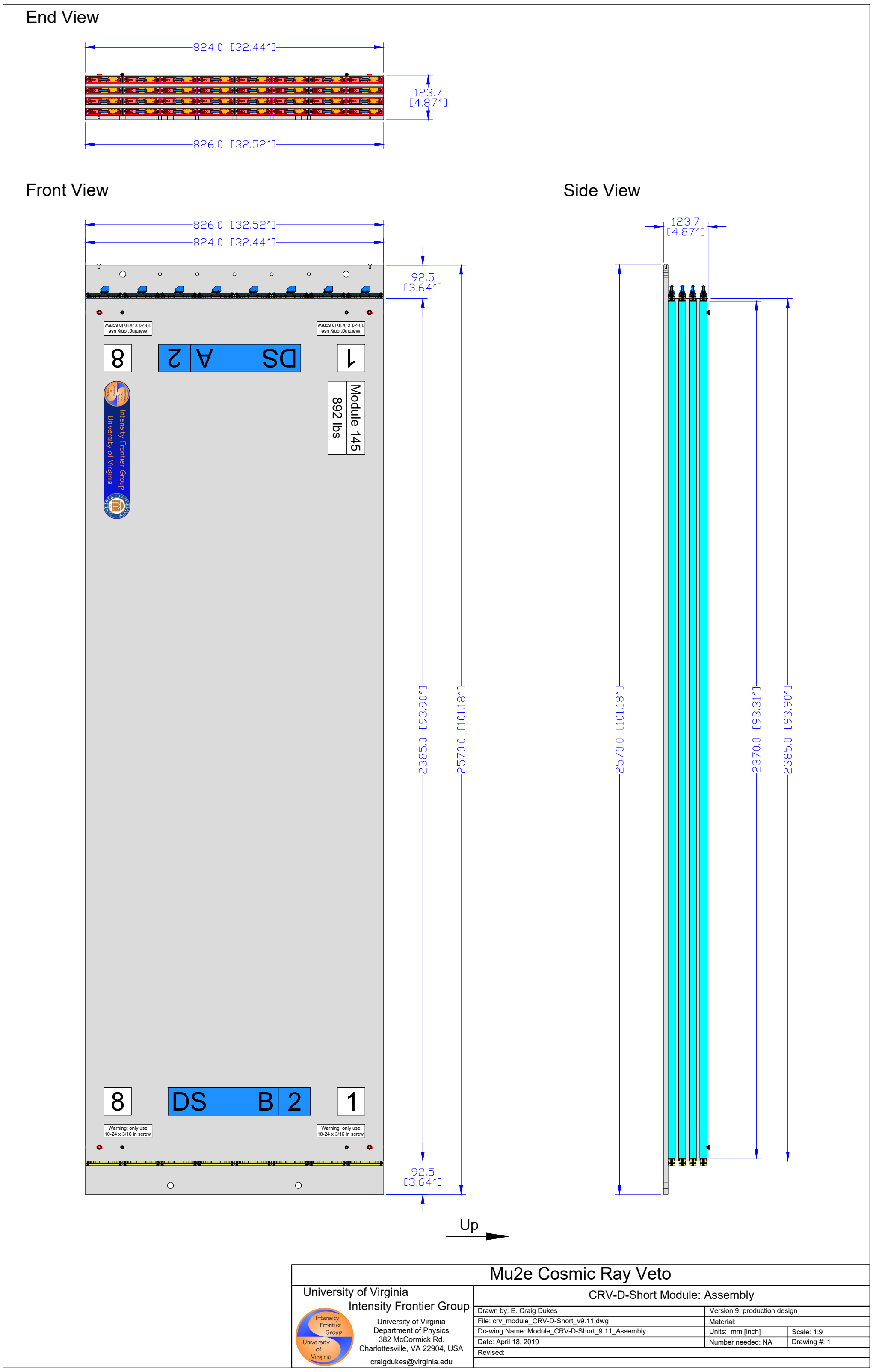

Figure G.1.: Drawing of a Downstream Short (CRV-DS) module.

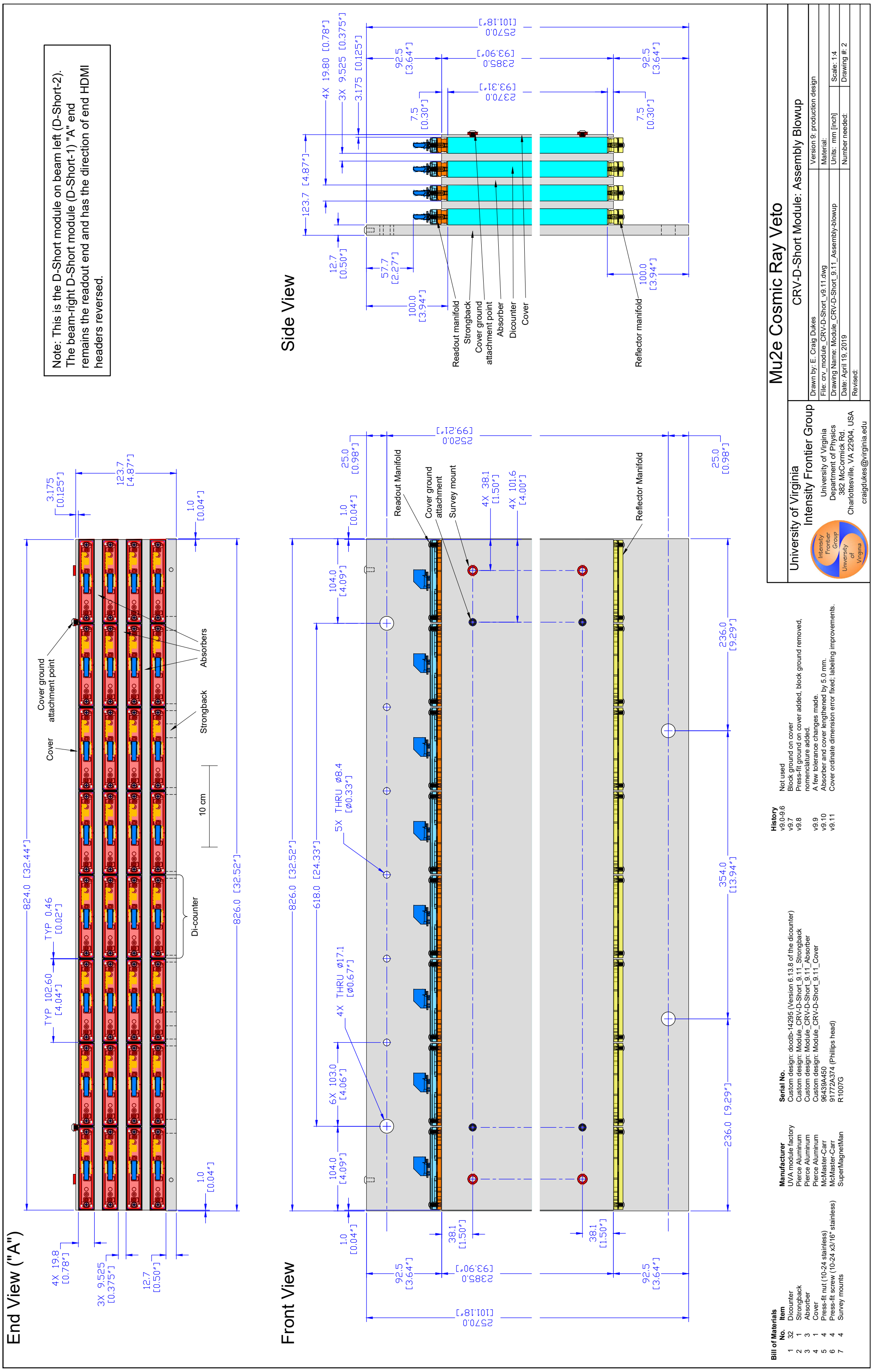

Figure G.2.: Drawing of a Downstream Short (CRV-DS) module.

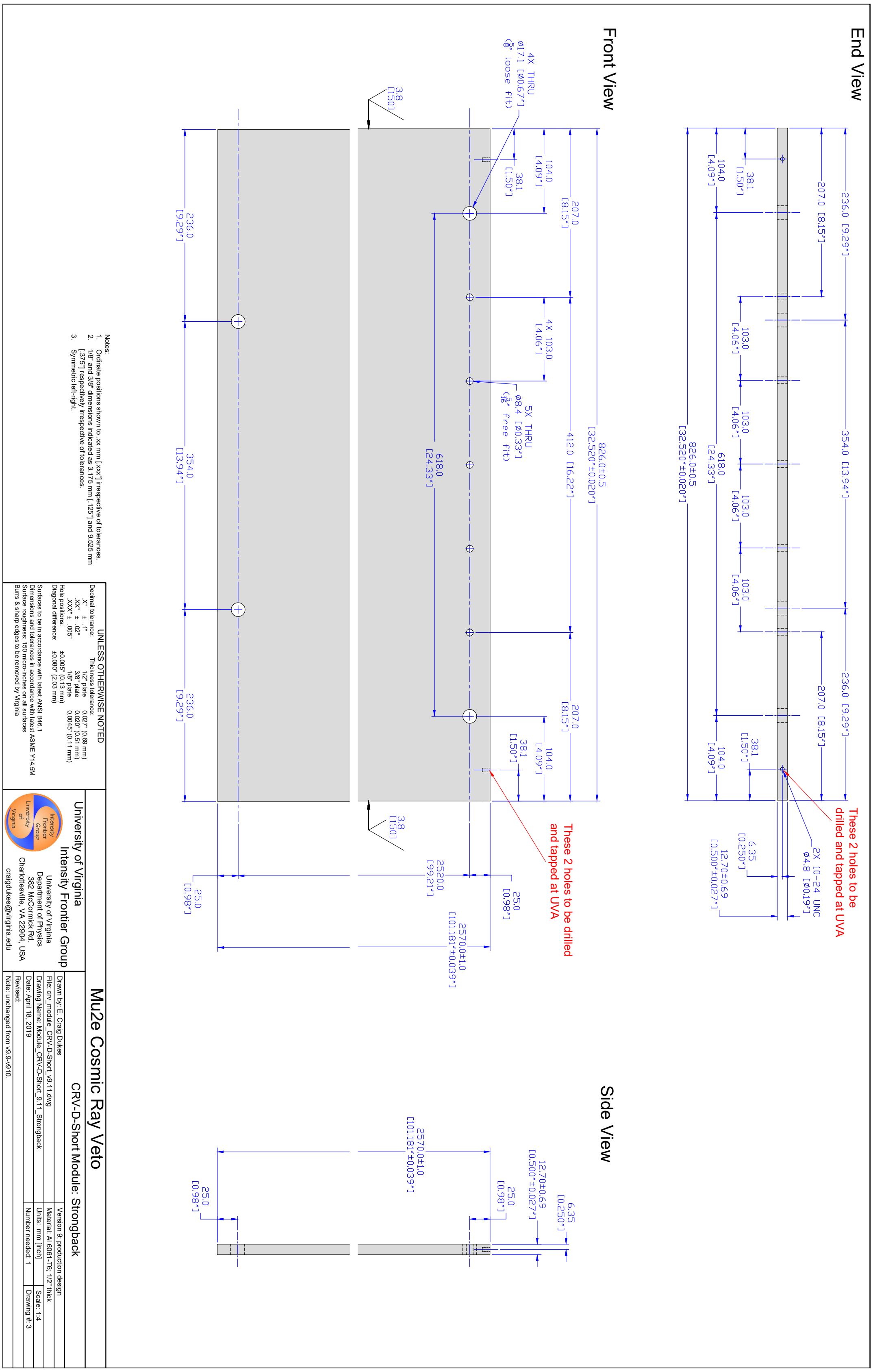

Figure G.3.: Drawing of a Downstream Short (CRV-DS) module.

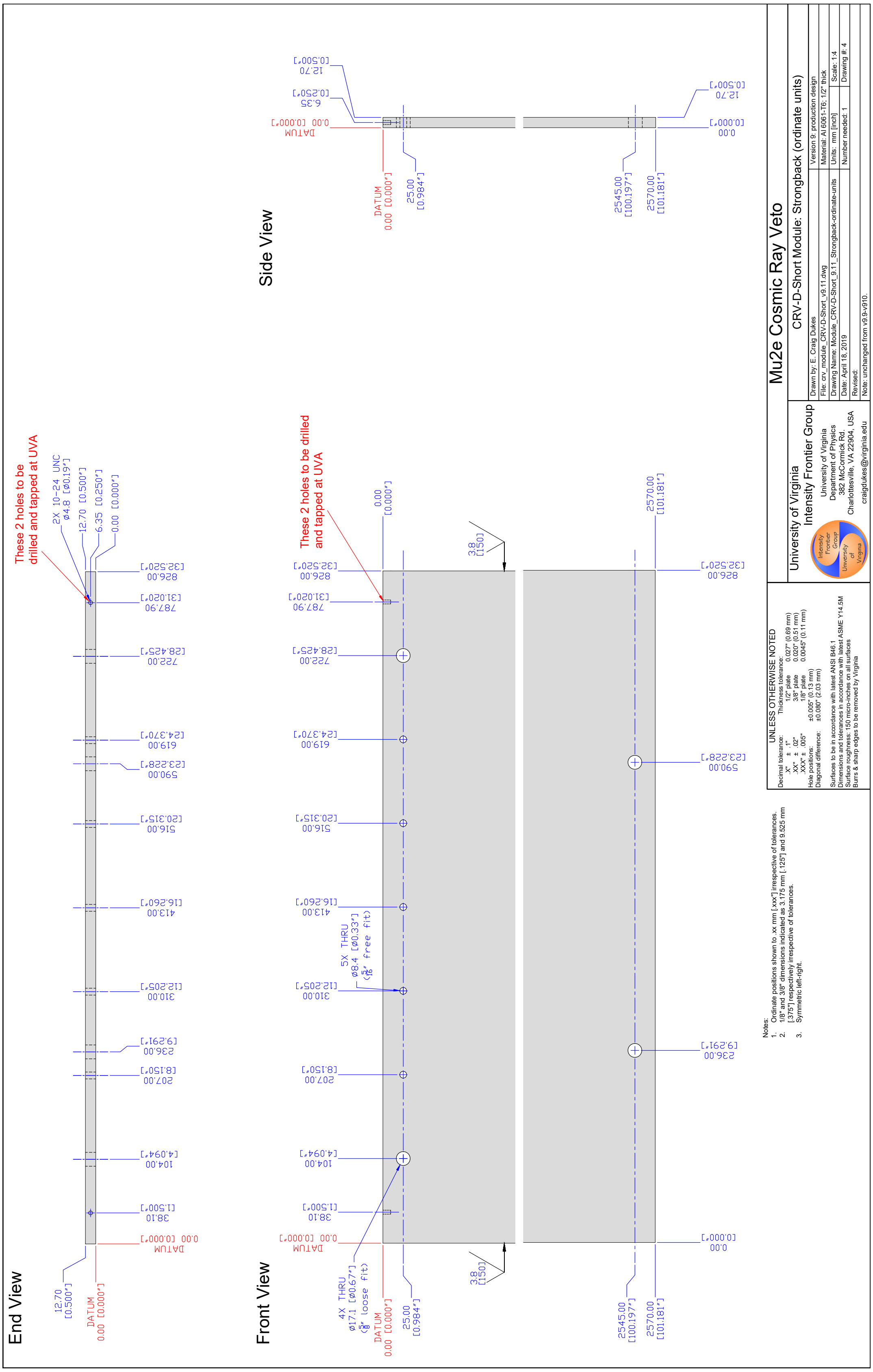

Figure G.4.: Drawing of a Downstream Short (CRV-DS) module.

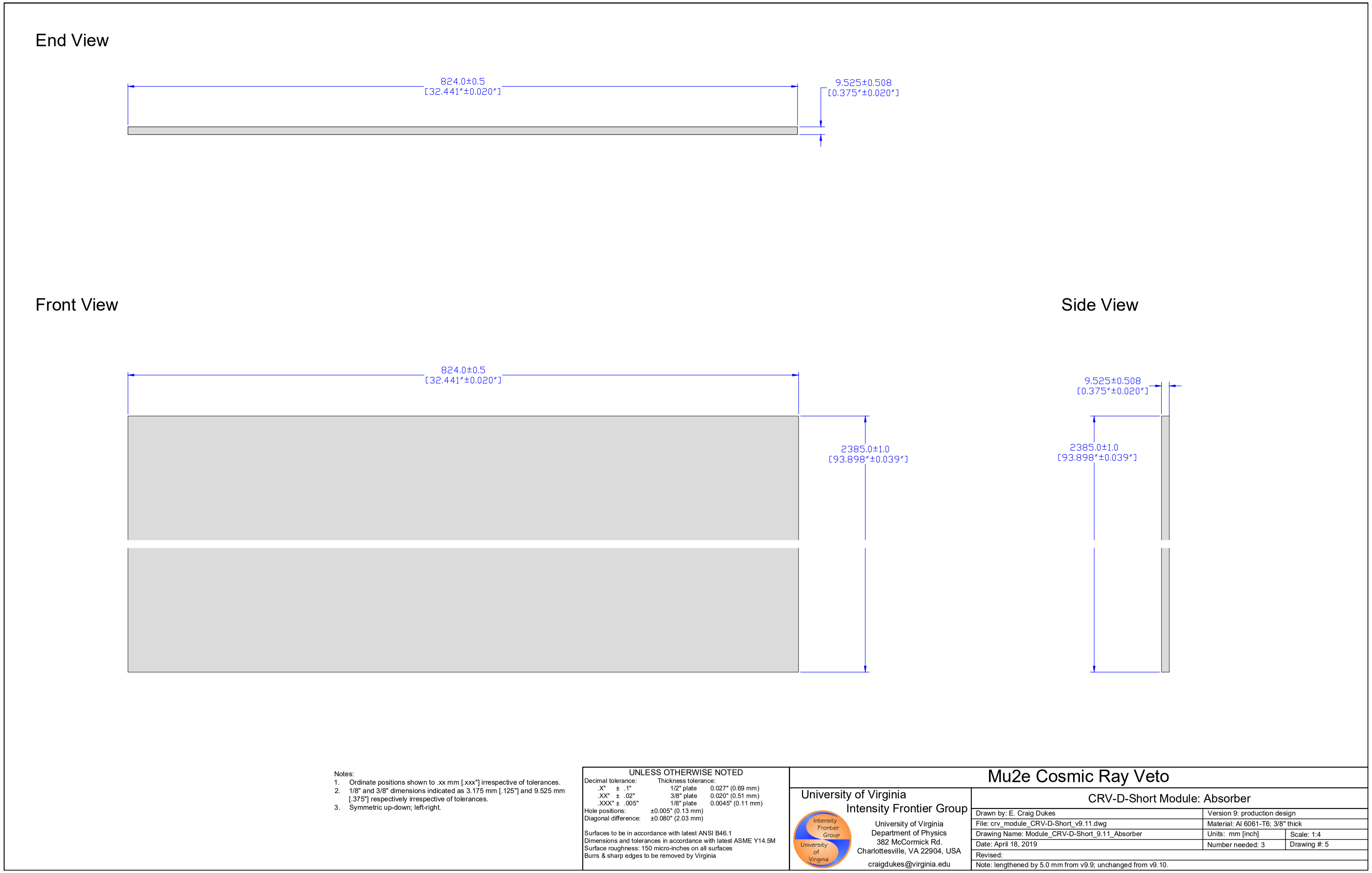

Figure G.5.: Drawing of a Downstream Short (CRV-DS) module.

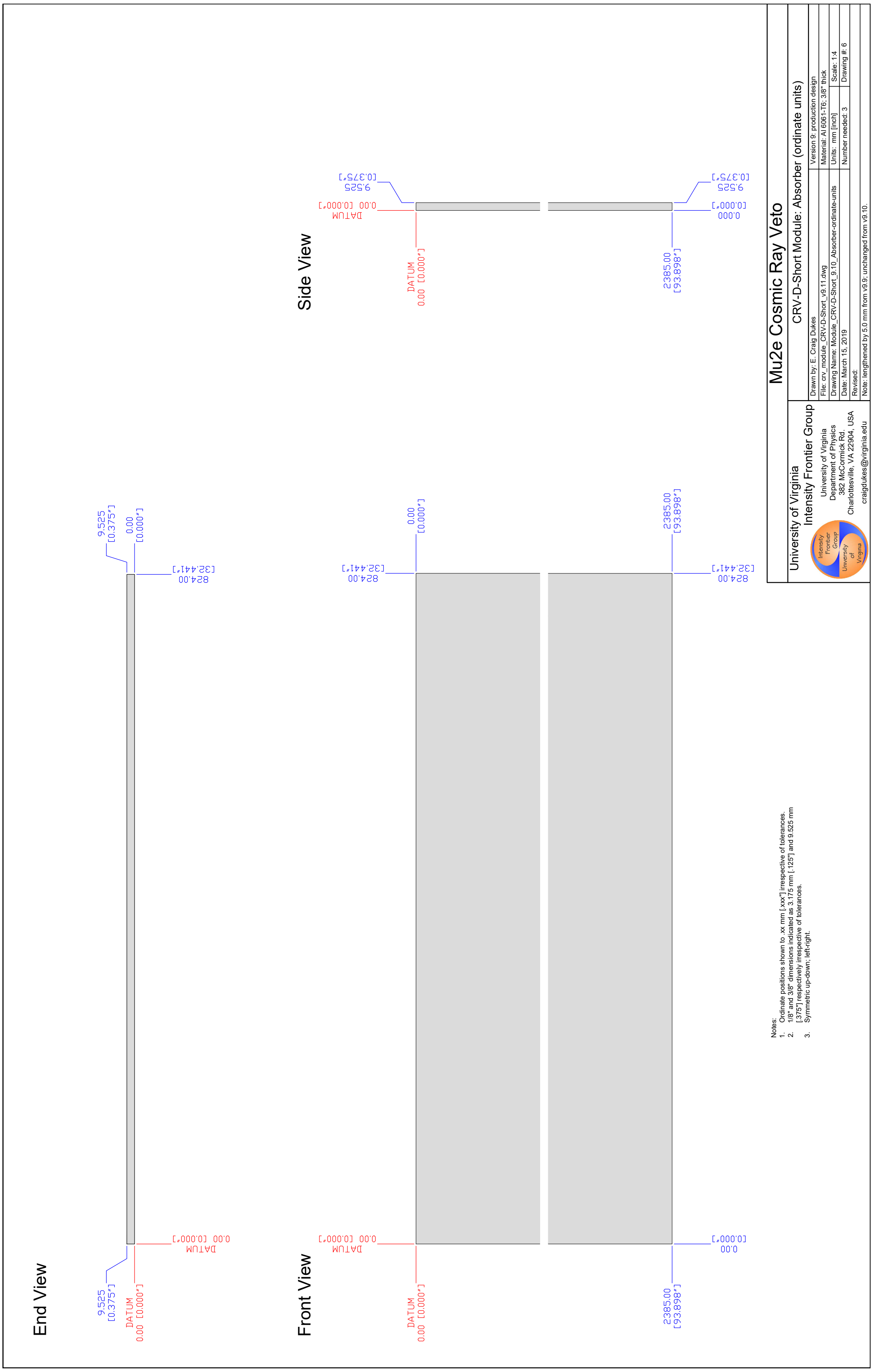

Figure G.6.: Drawing of a Downstream Short (CRV-DS) module.

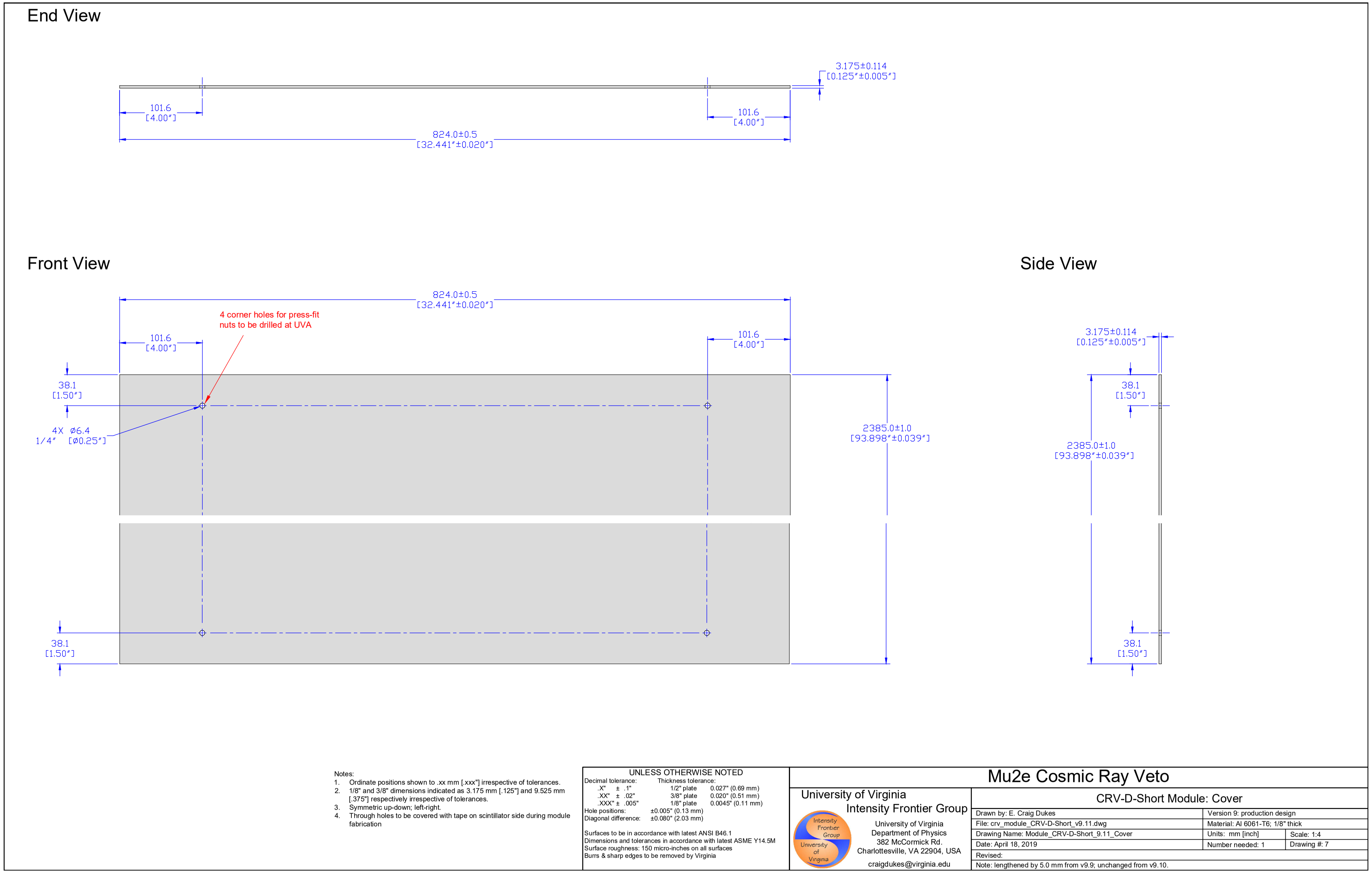

Figure G.7.: Drawing of a Downstream Short (CRV-DS) module.

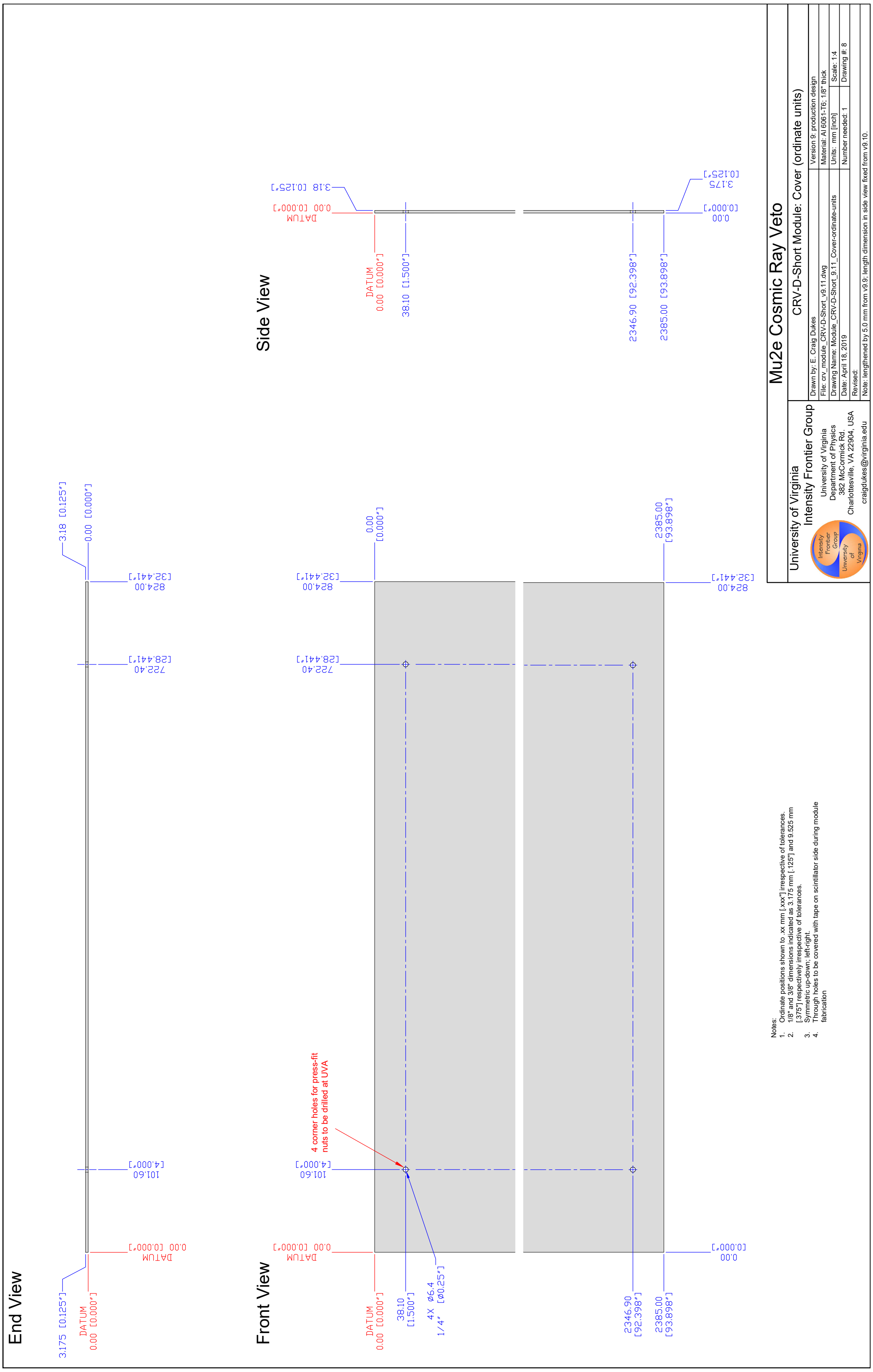

Figure G.8.: Drawing of a Downstream Short (CRV-DS) module.

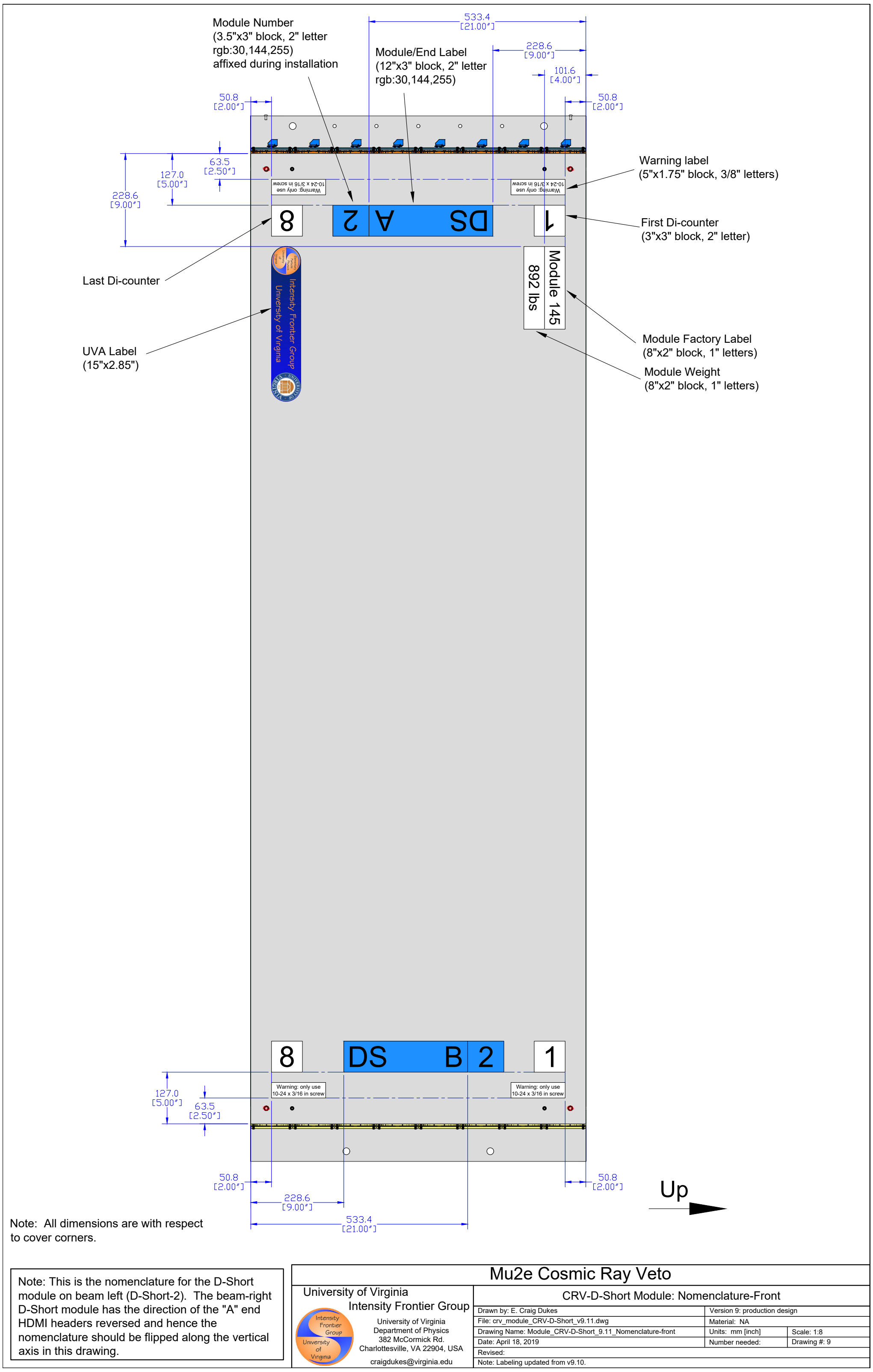

Figure G.9.: Drawing of a Downstream Short (CRV-DS) module.

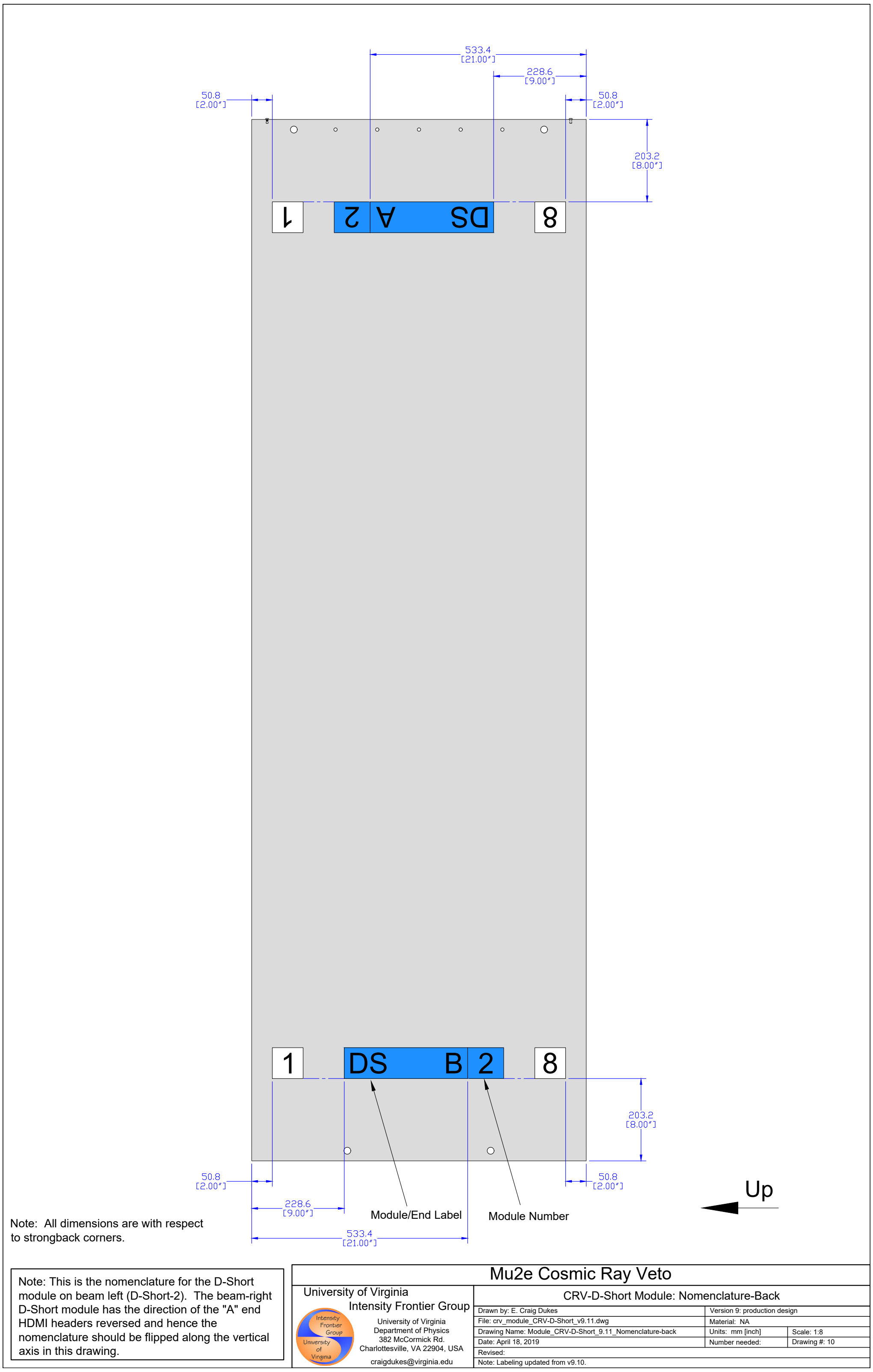

Figure G.10.: Drawing of a Downstream Short (CRV-DS) module.

Appendix H.

Downstream (CRV-D) Module

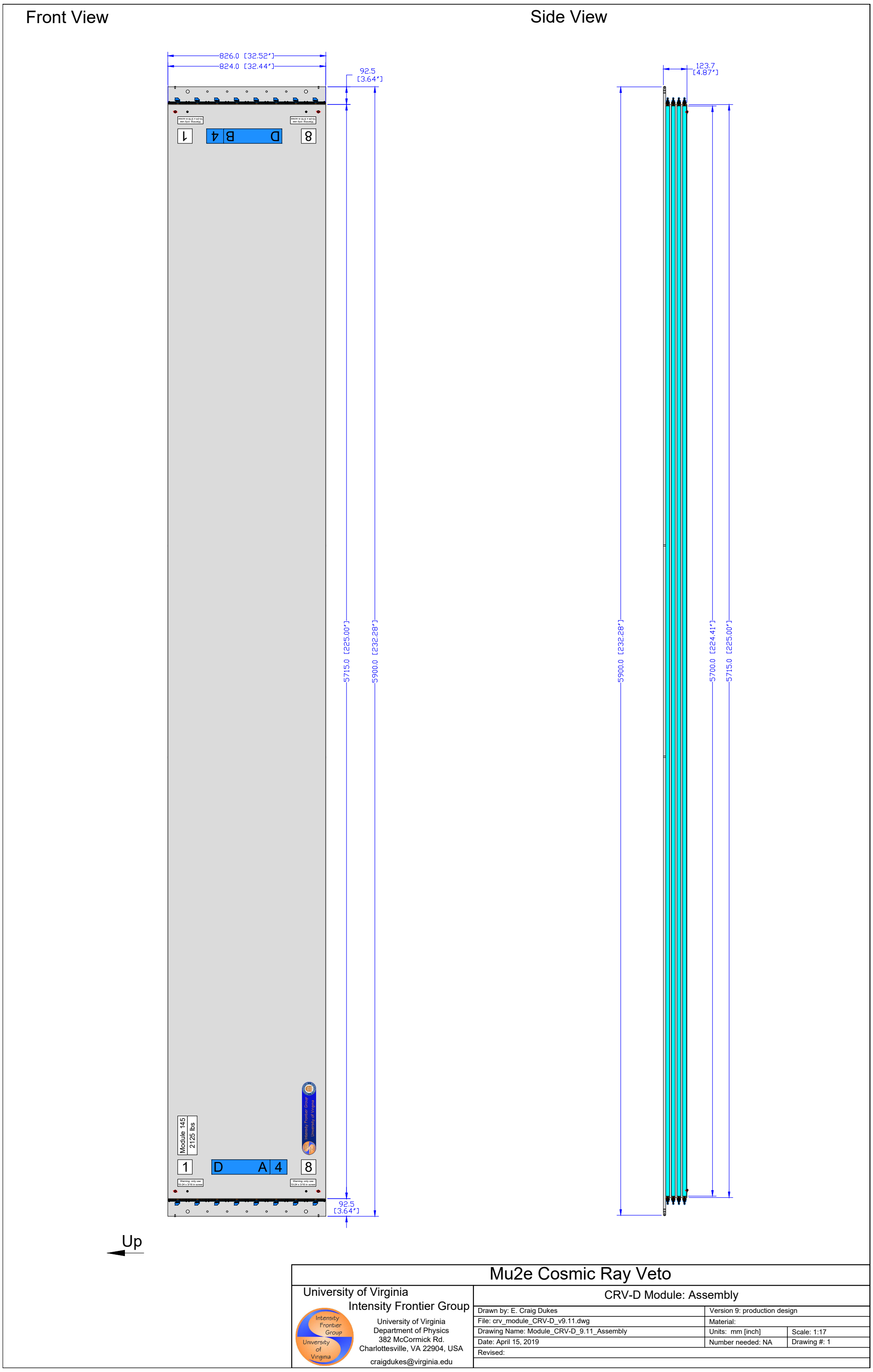

Figure H.1.: Drawing of a Downstream Long (CRV-DL) module.

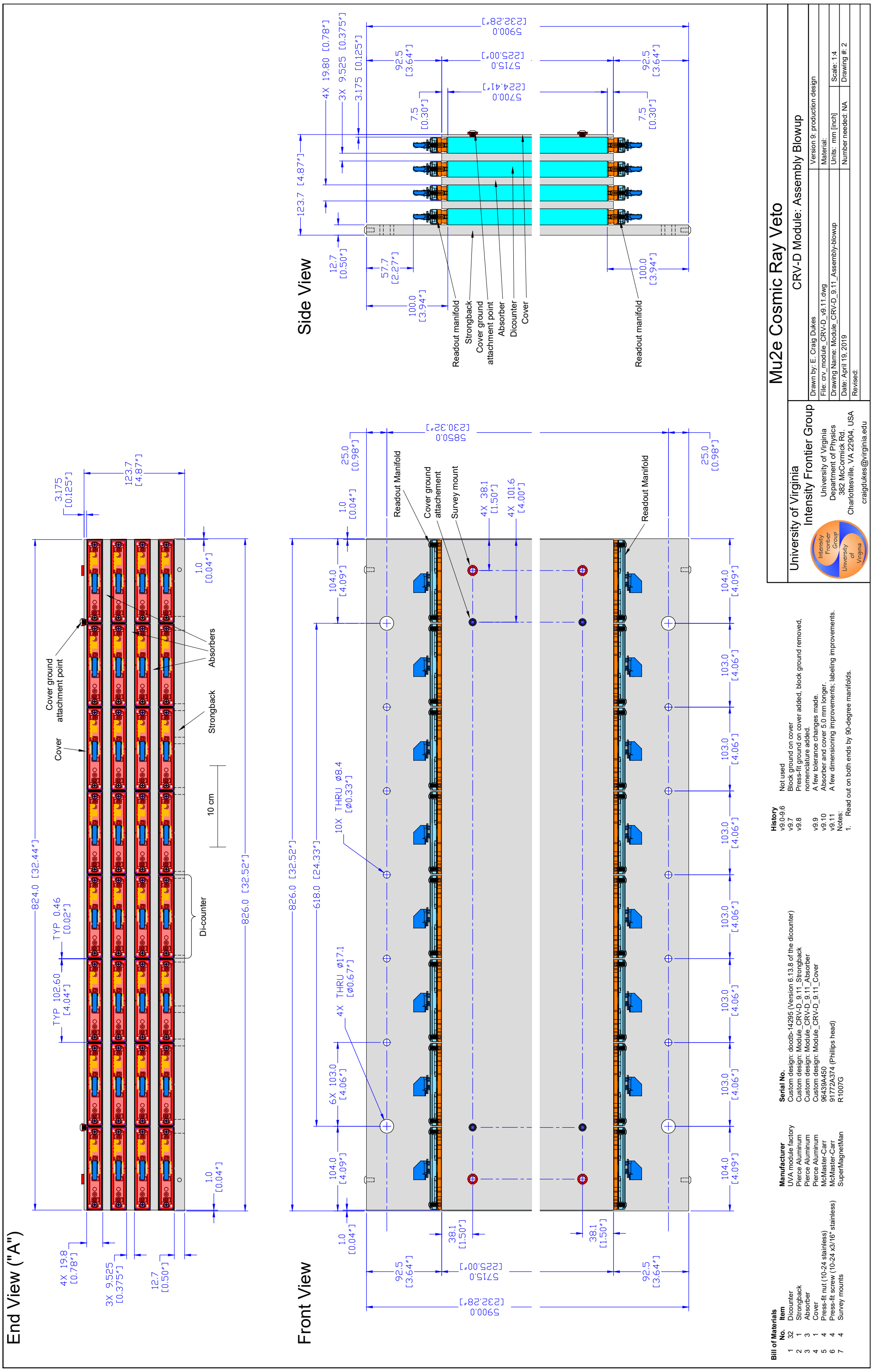

Figure H.2.: Drawing of a Downstream Long (CRV-DL) module.

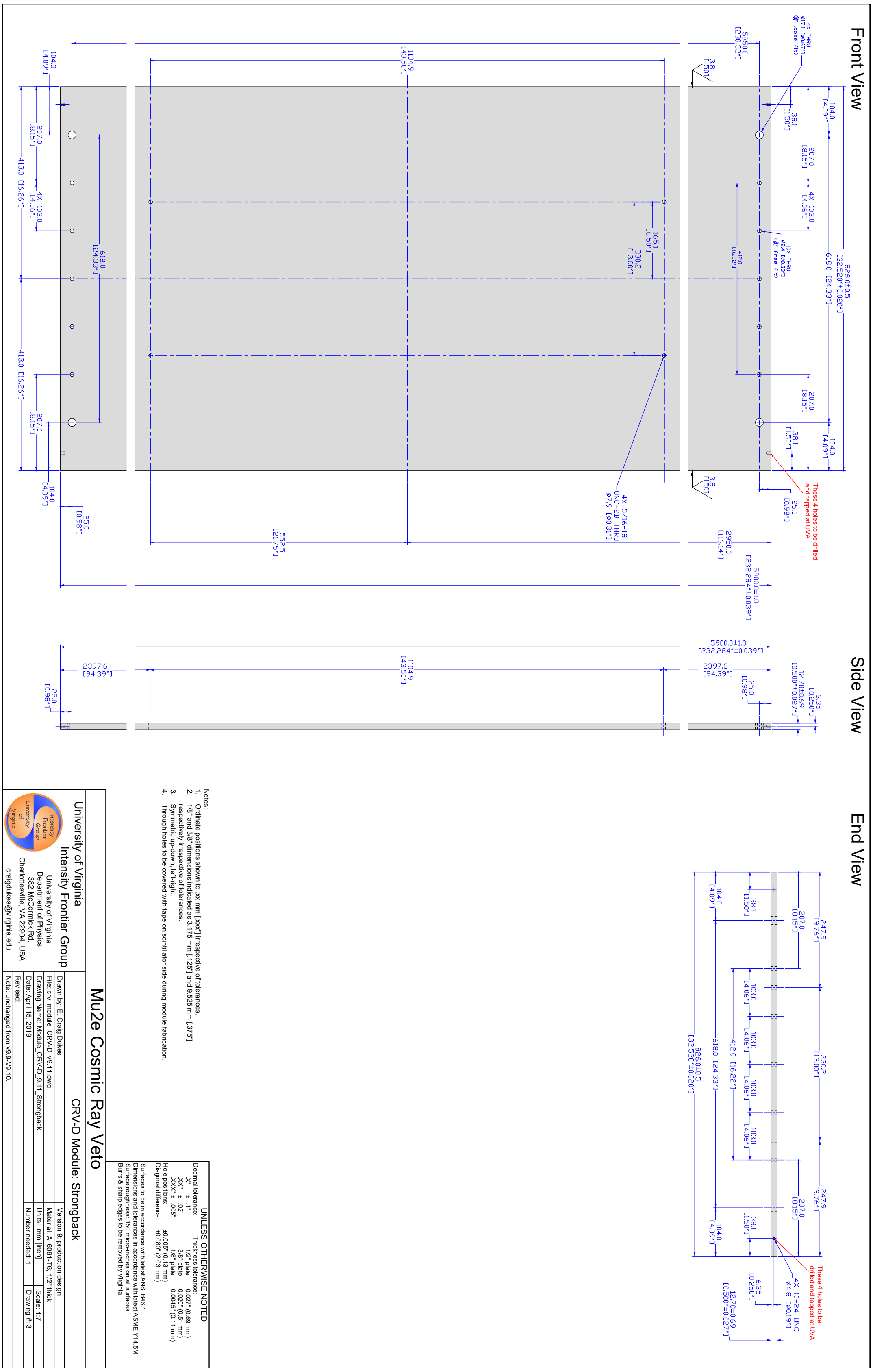

Figure H.3.: Drawing of a Downstream Long (CRV-DL) module.

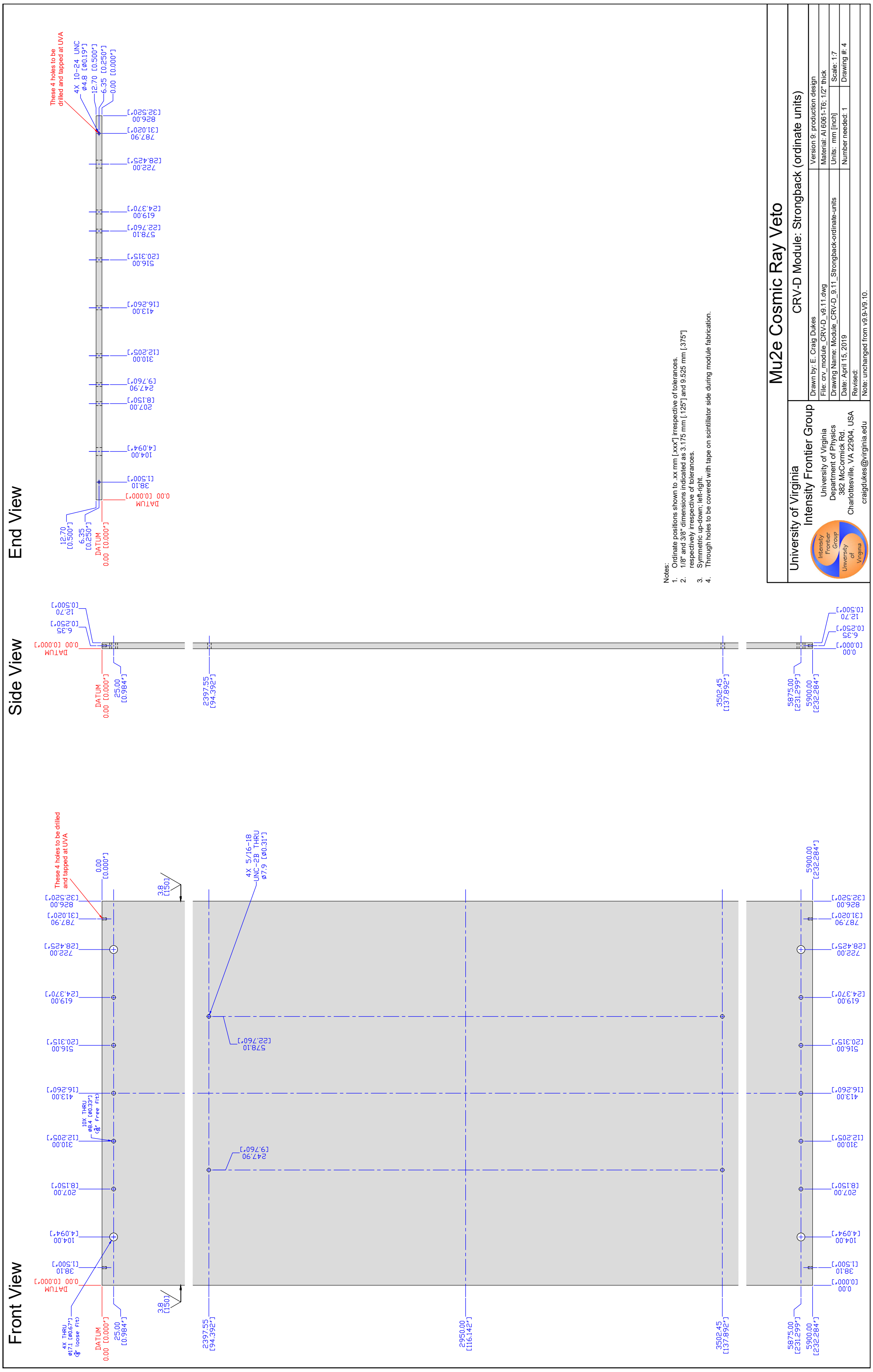

Figure H.4.: Drawing of a Downstream Long (CRV-DL) module.

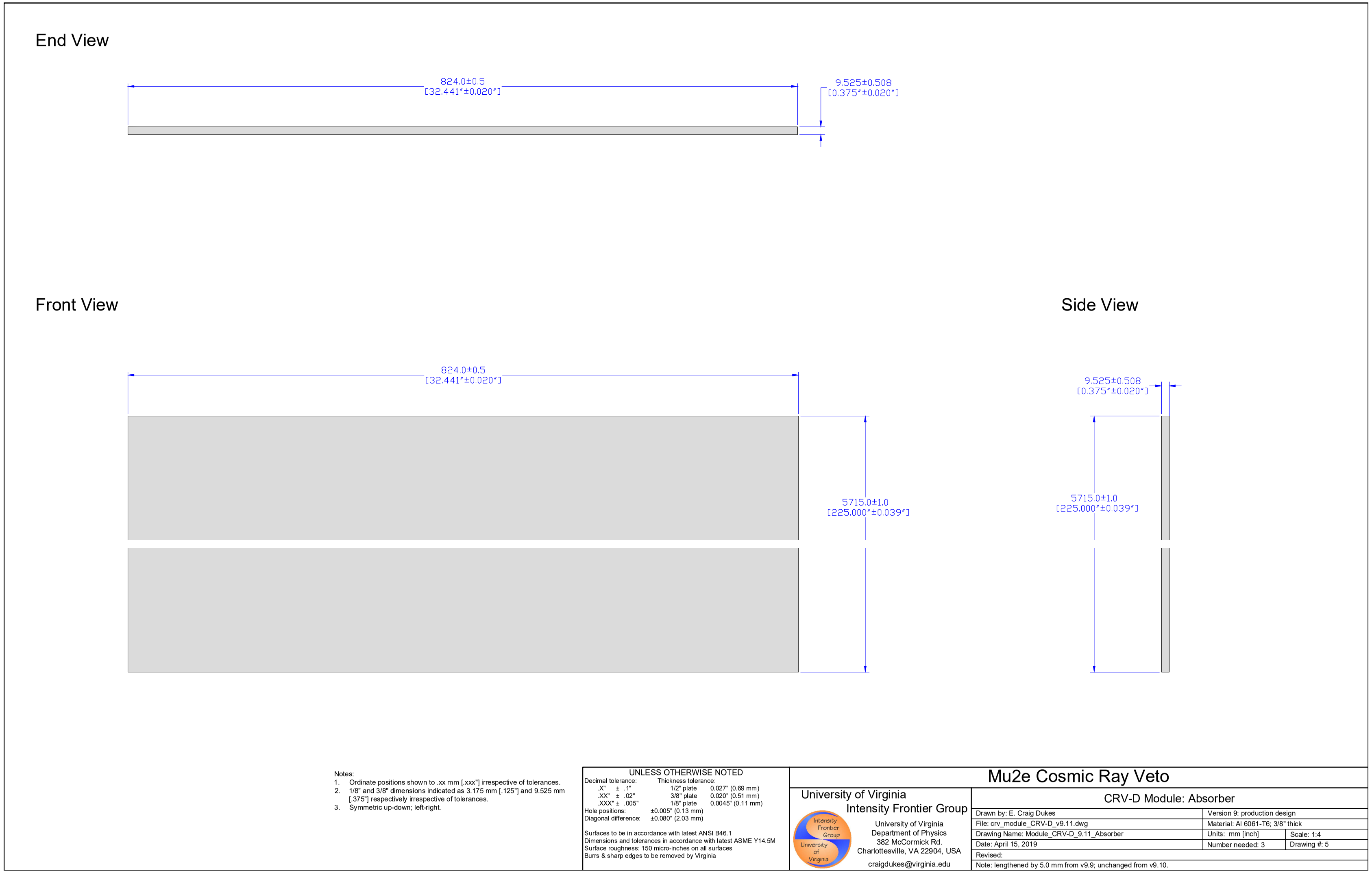

Figure H.5.: Drawing of a Downstream Long (CRV-DL) module.

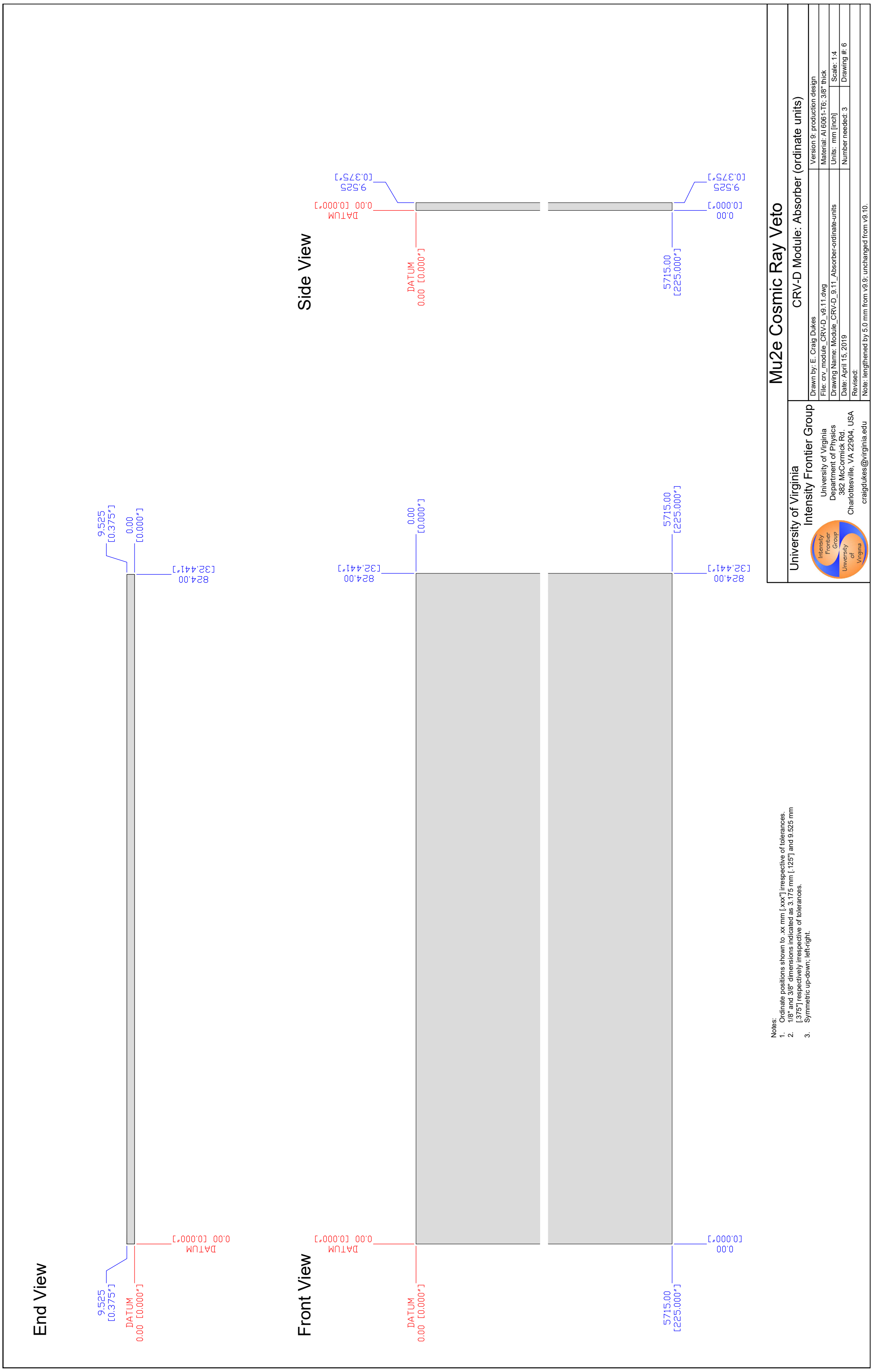

Figure H.6.: Drawing of a Downstream Long (CRV-DL) module.

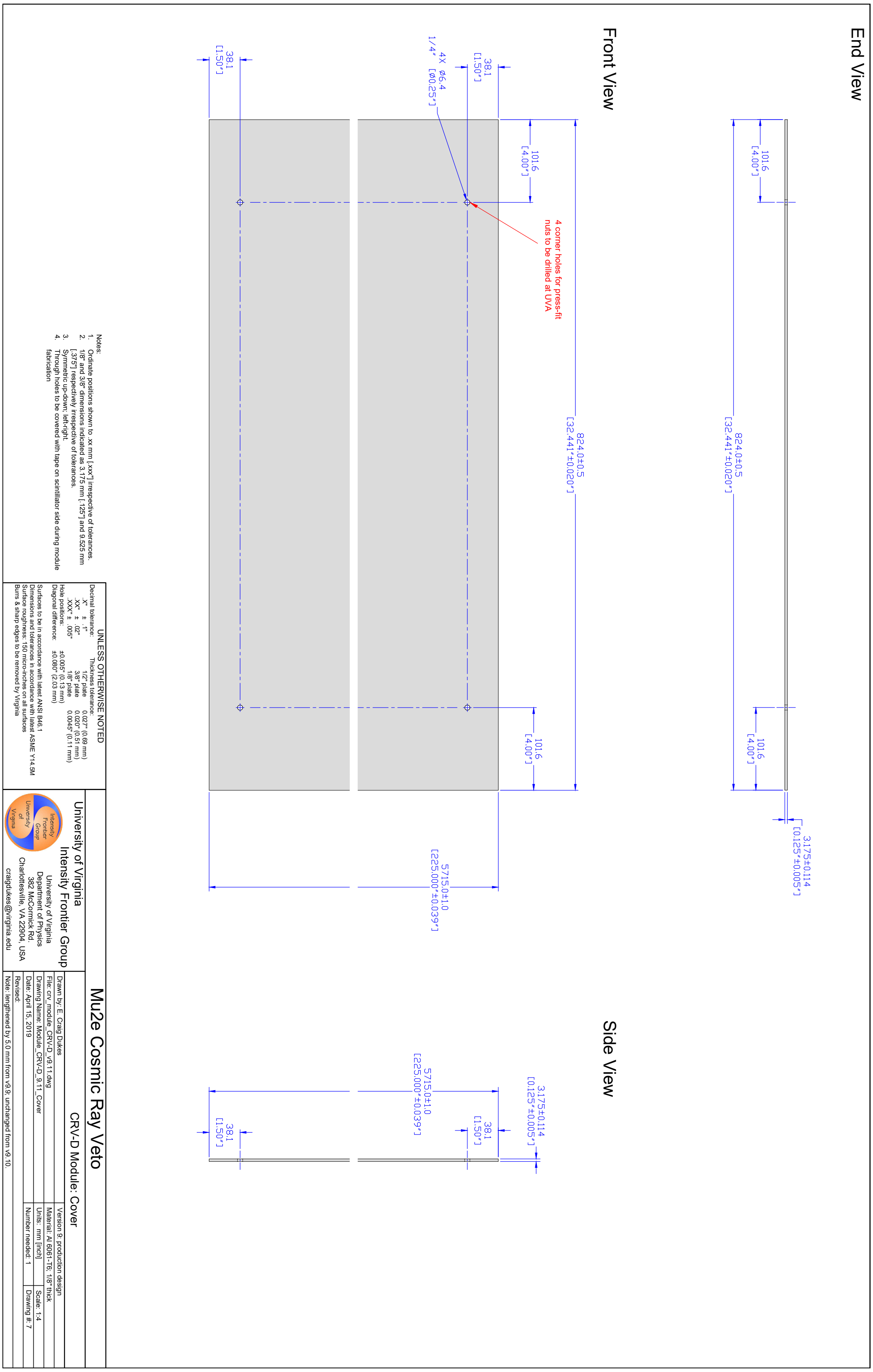

Figure H.7.: Drawing of a Downstream (CRV-D) module.

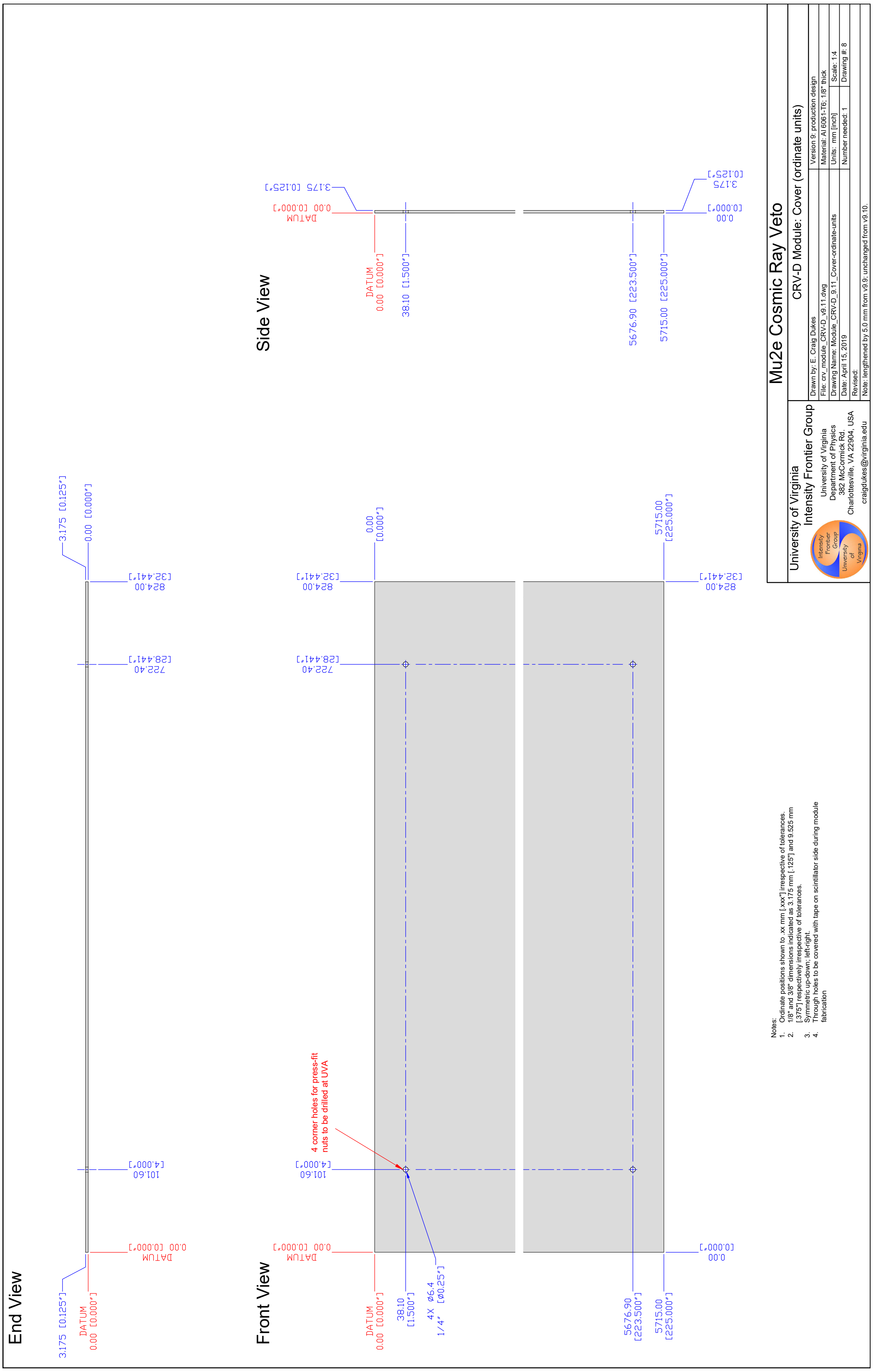

Figure H.8.: Drawing of a Downstream Long (CRV-DL) module.

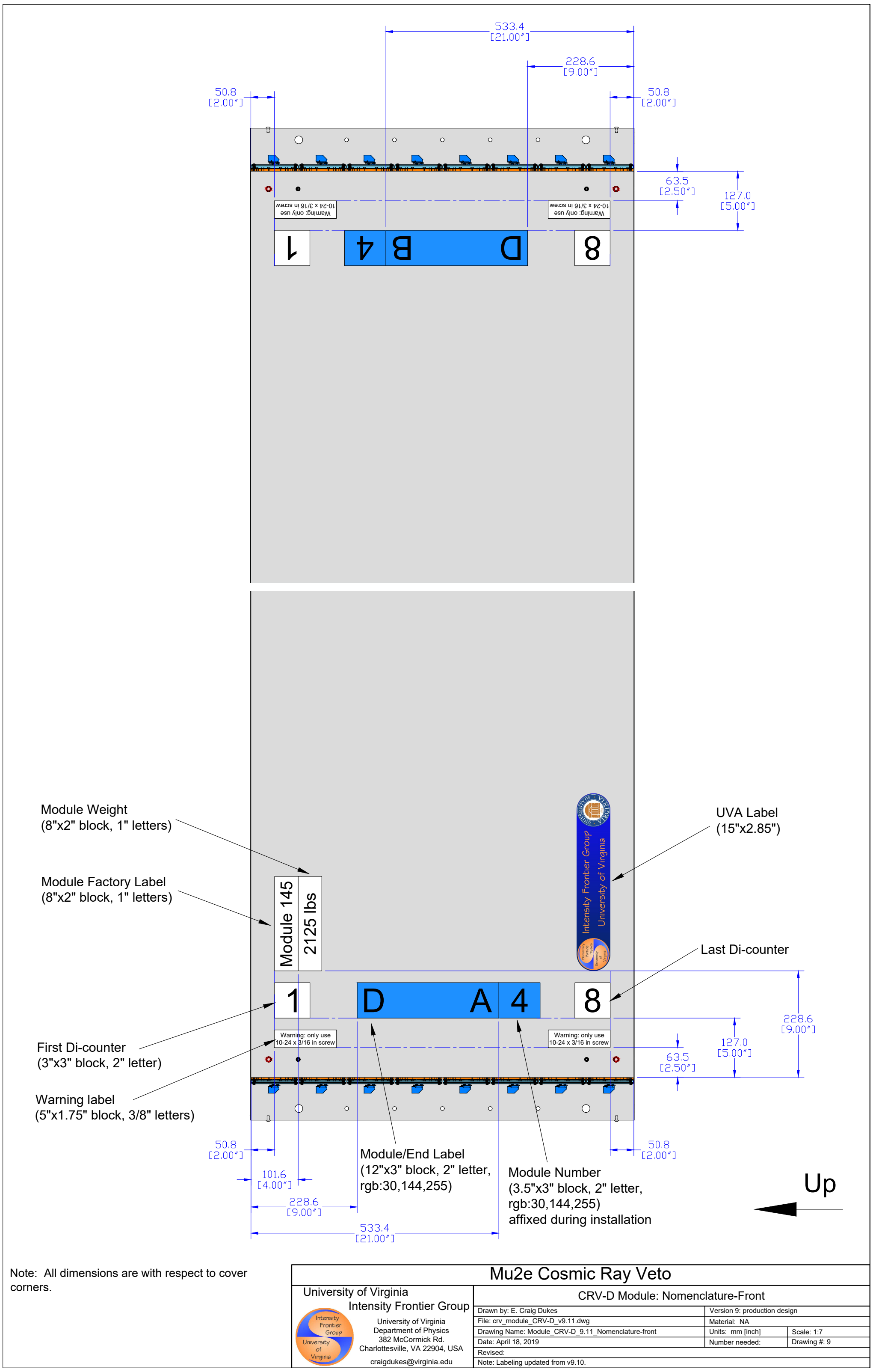

Figure H.9.: Drawing of a Downstream Long (CRV-DL) module.

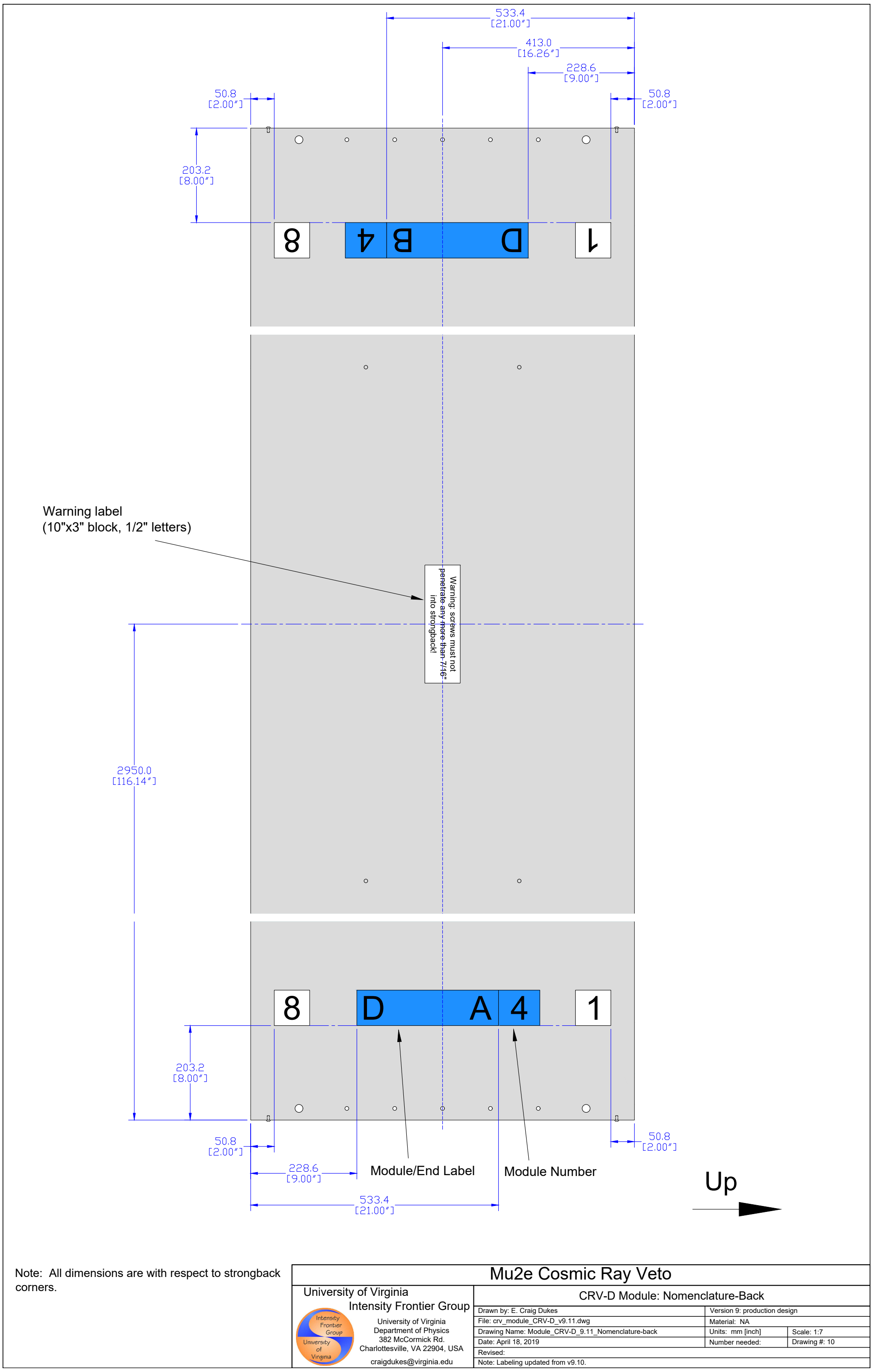

Figure H.10.: Drawing of a Downstream Long (CRV-DL) module.

Appendix I.

Aluminum QC Measurements

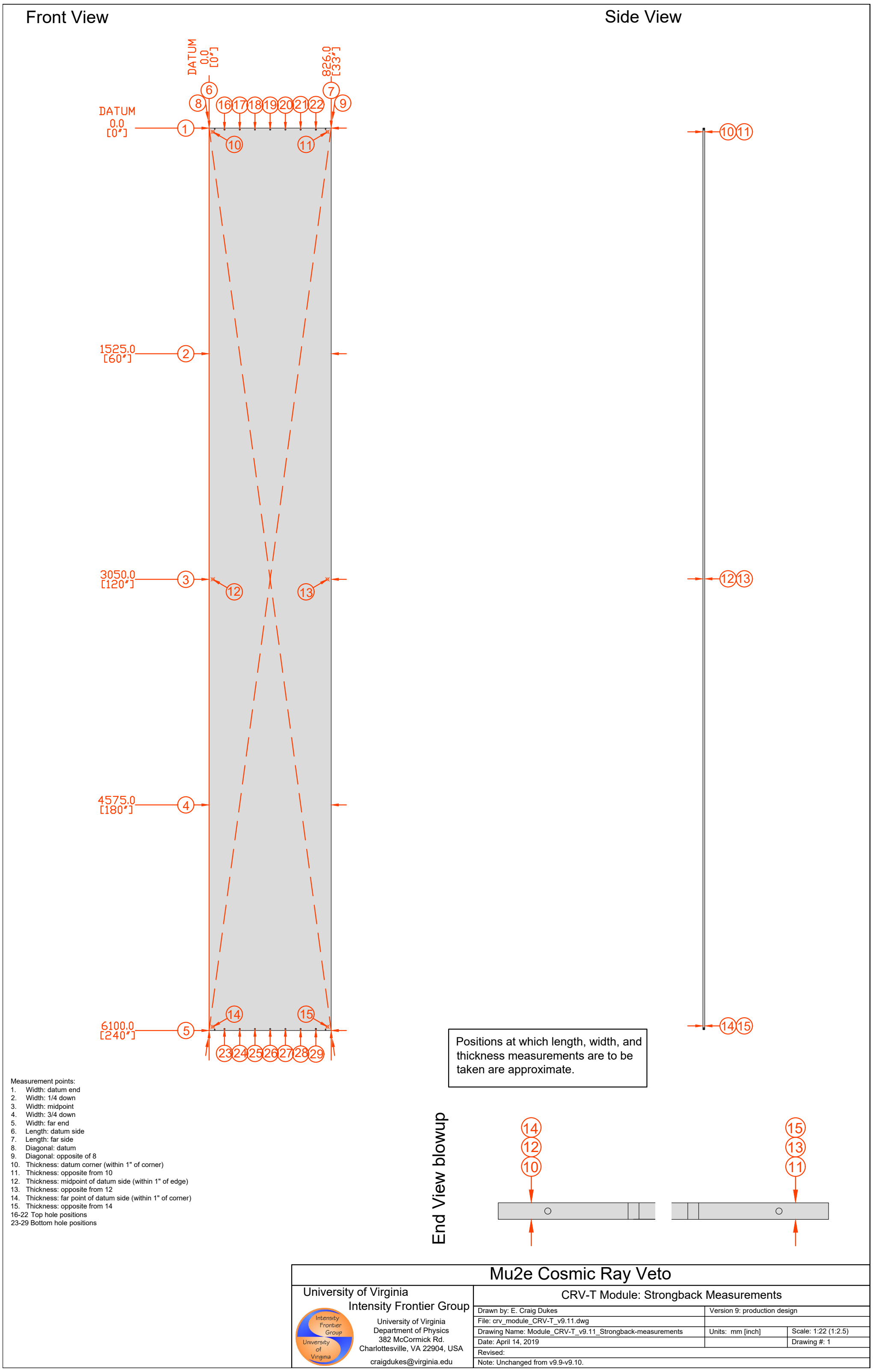

Figure I.1.: Top (CRV-T/TS) Module Strongback QC Measurements.

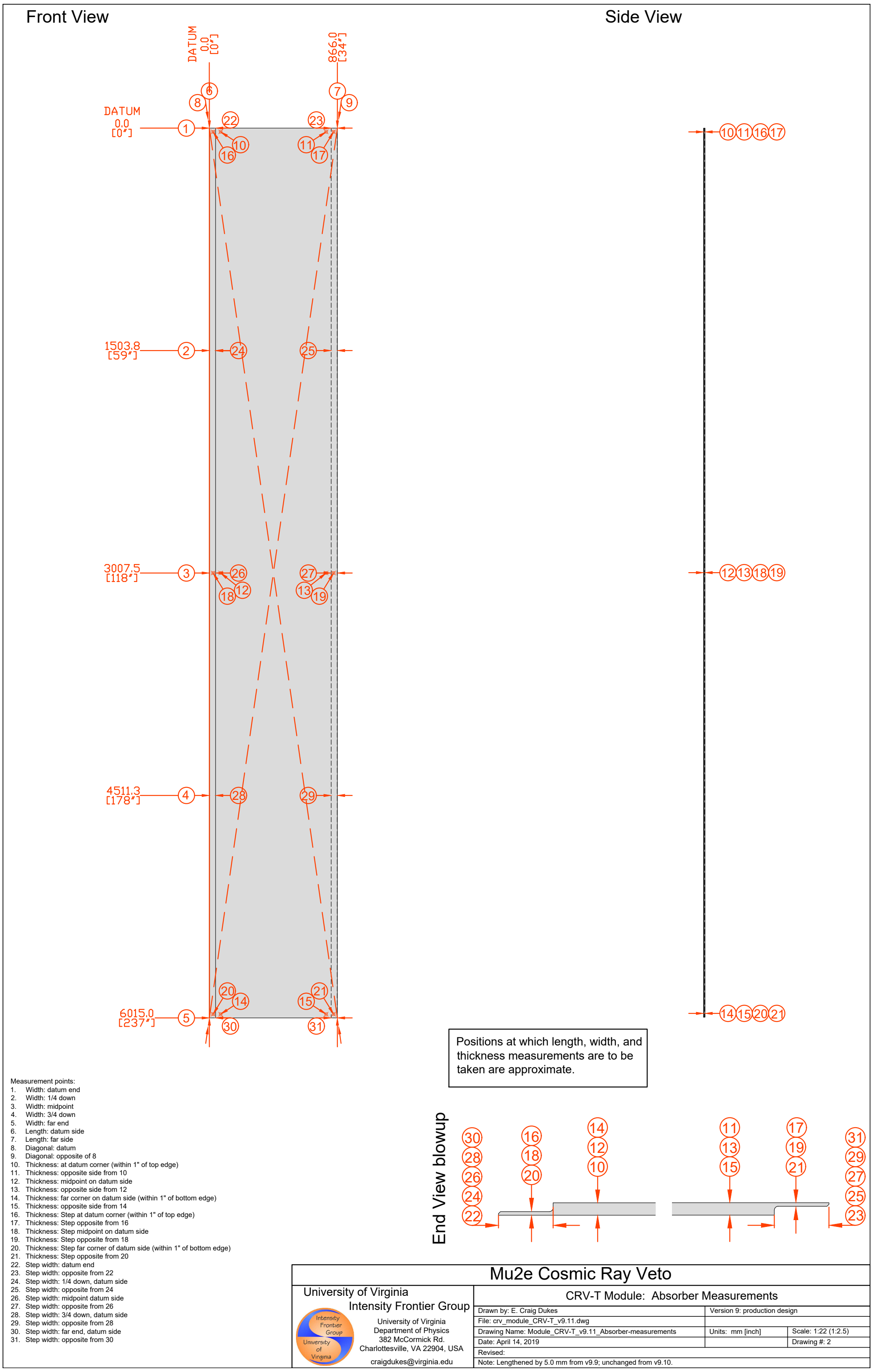

Figure I.2.: Top (CRV-T/TS) Module Absorber QC Measurements.

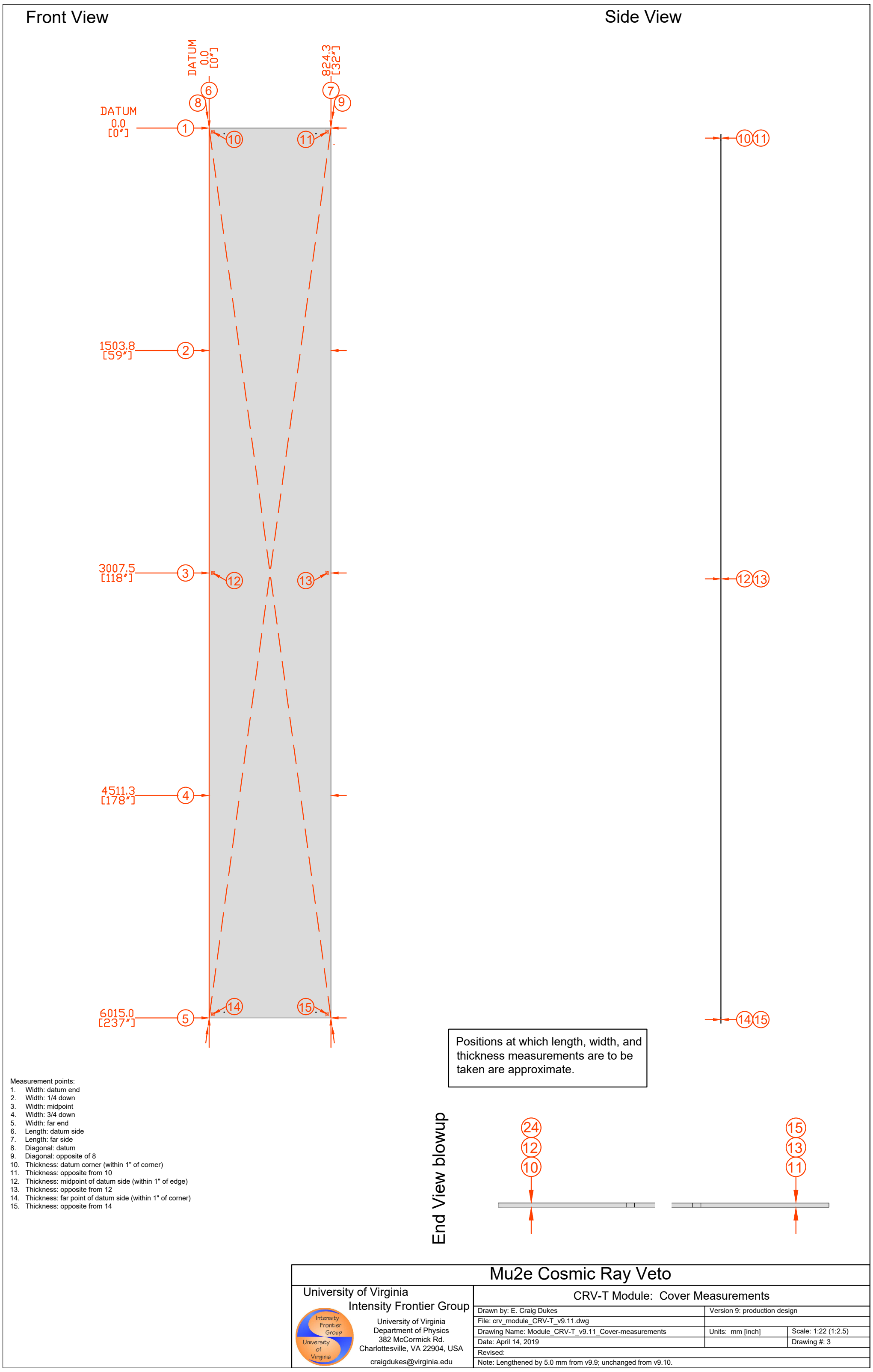

Figure I.3.: Top (CRV-T/TS) Module Cover QC Measurements.

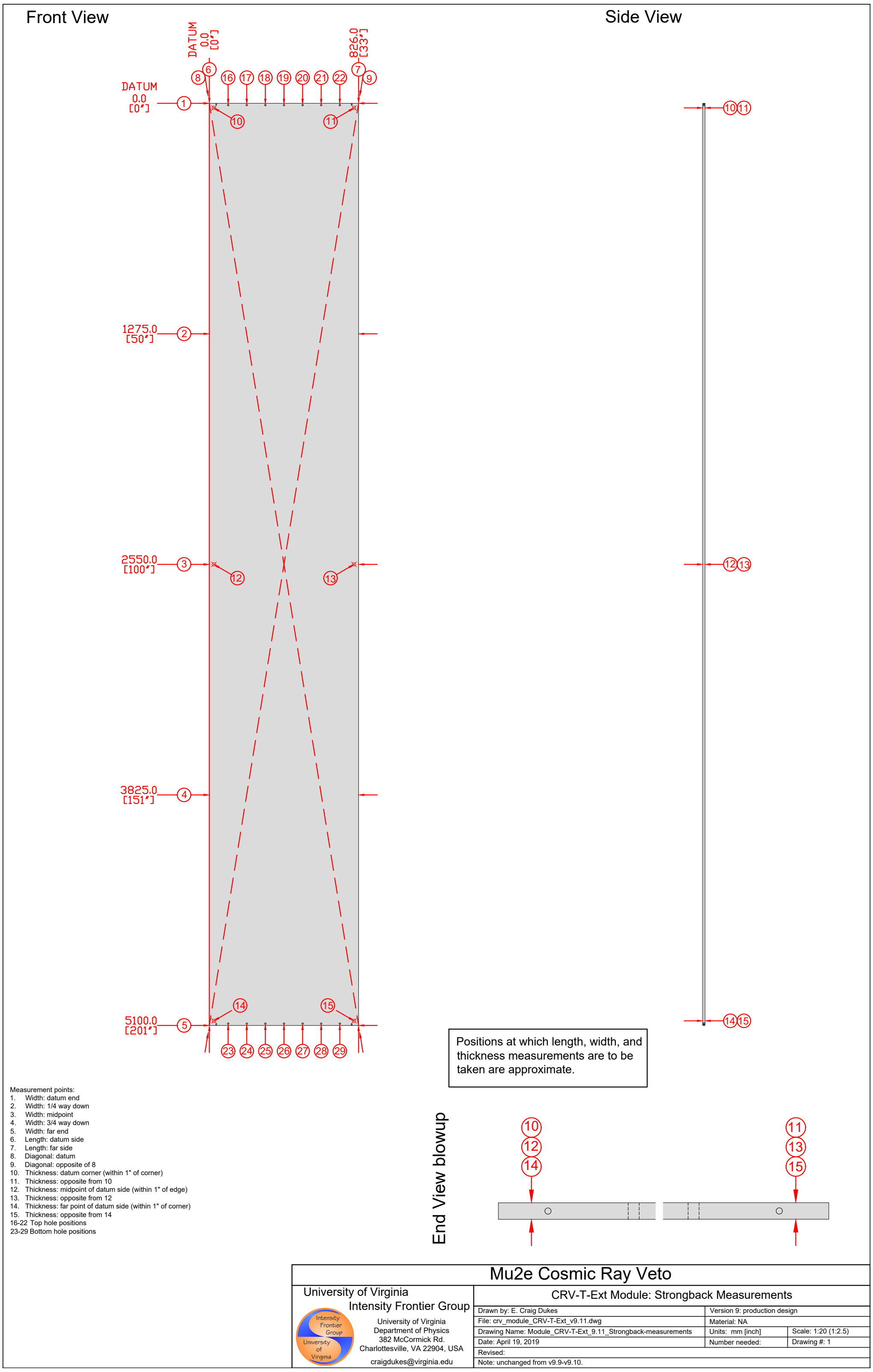

Figure I.4.: Top Extension (CRV-TS-Ext) Module Strongback QC Measurements.

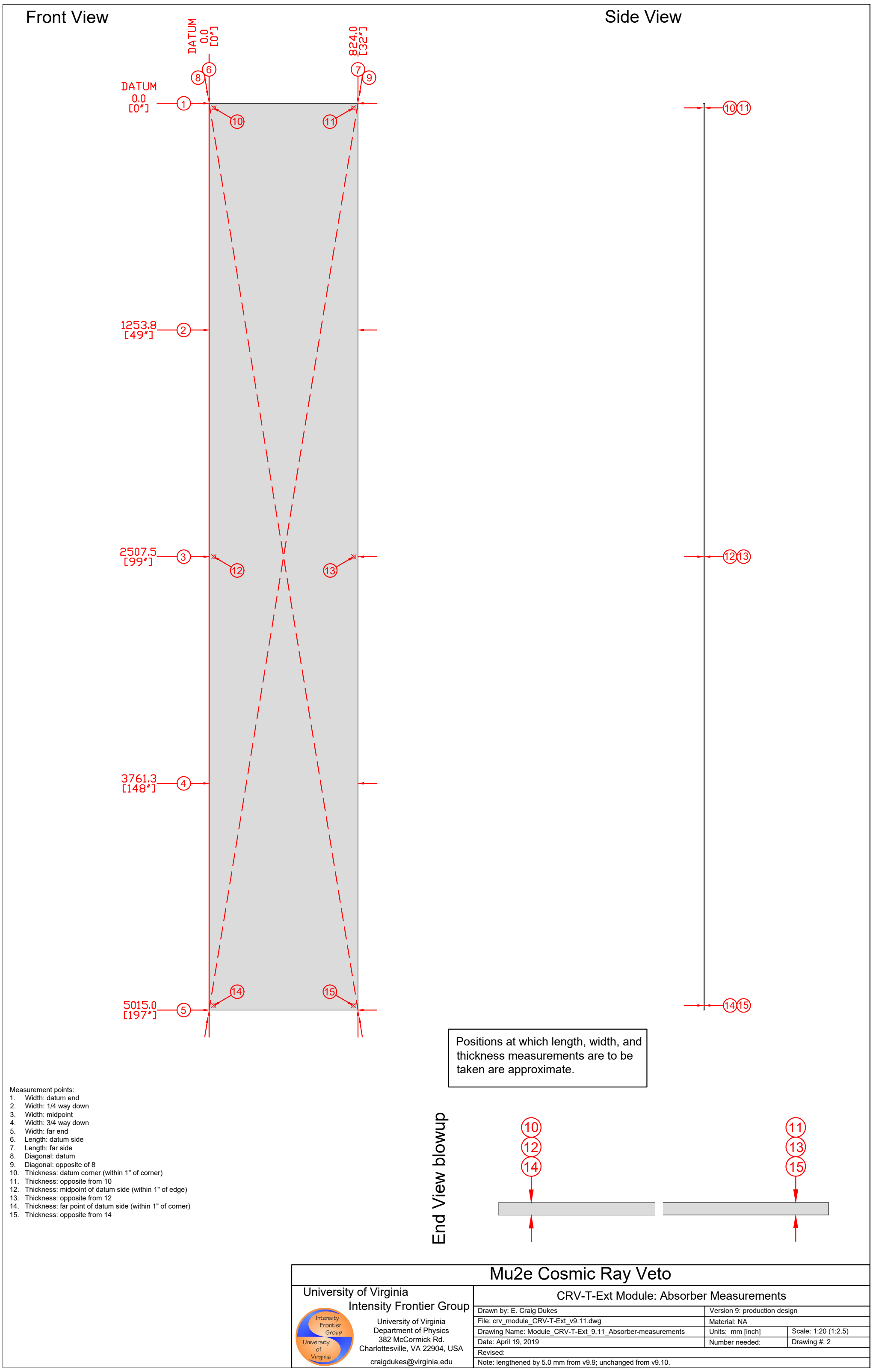

Figure I.5.: Top Extension (CRV-TS-Ext) Module Absorber QC Measurements.

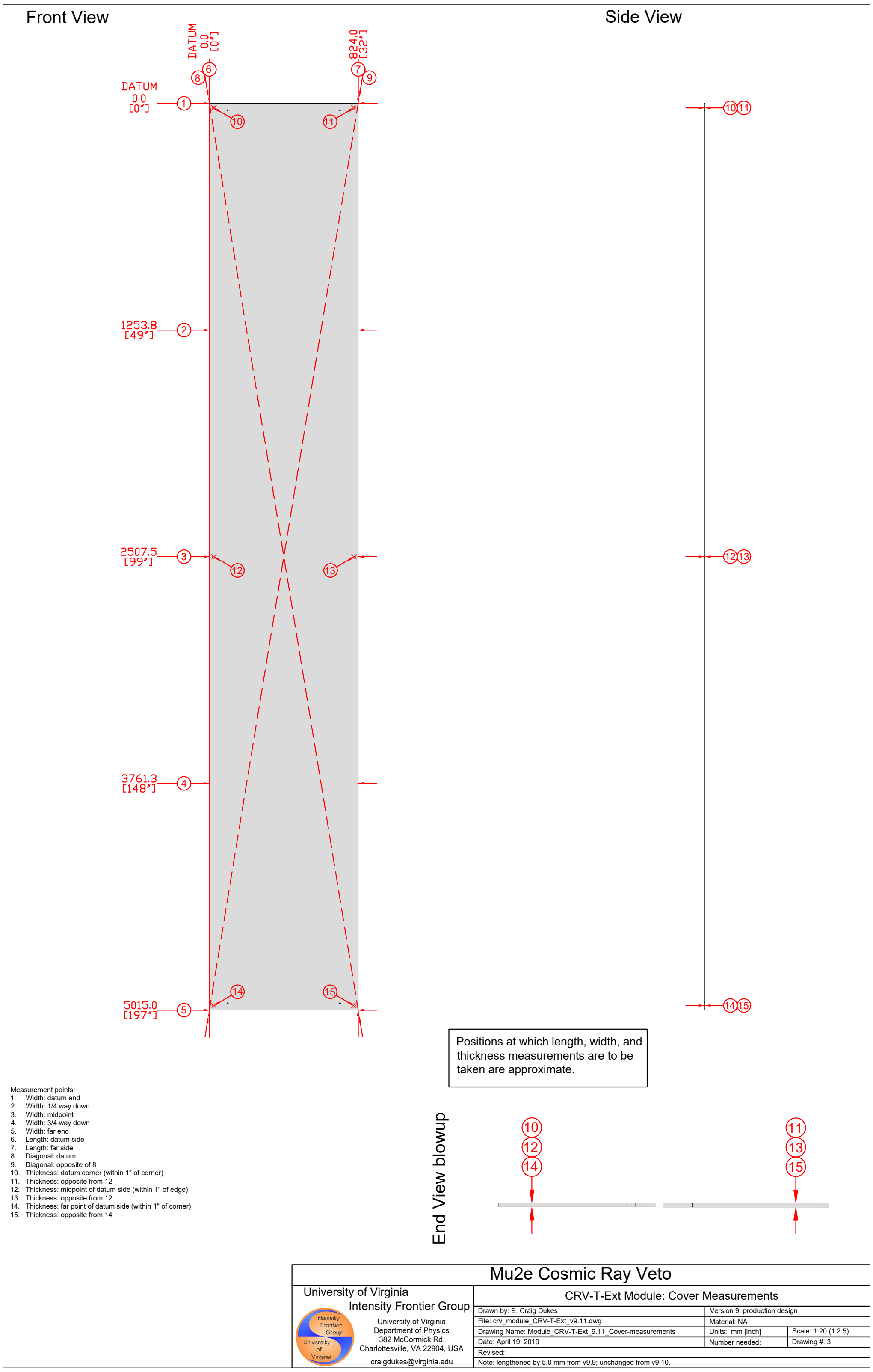

Figure I.6.: Top Extension (CRV-TS-Ext) Module Cover QC Measurements.

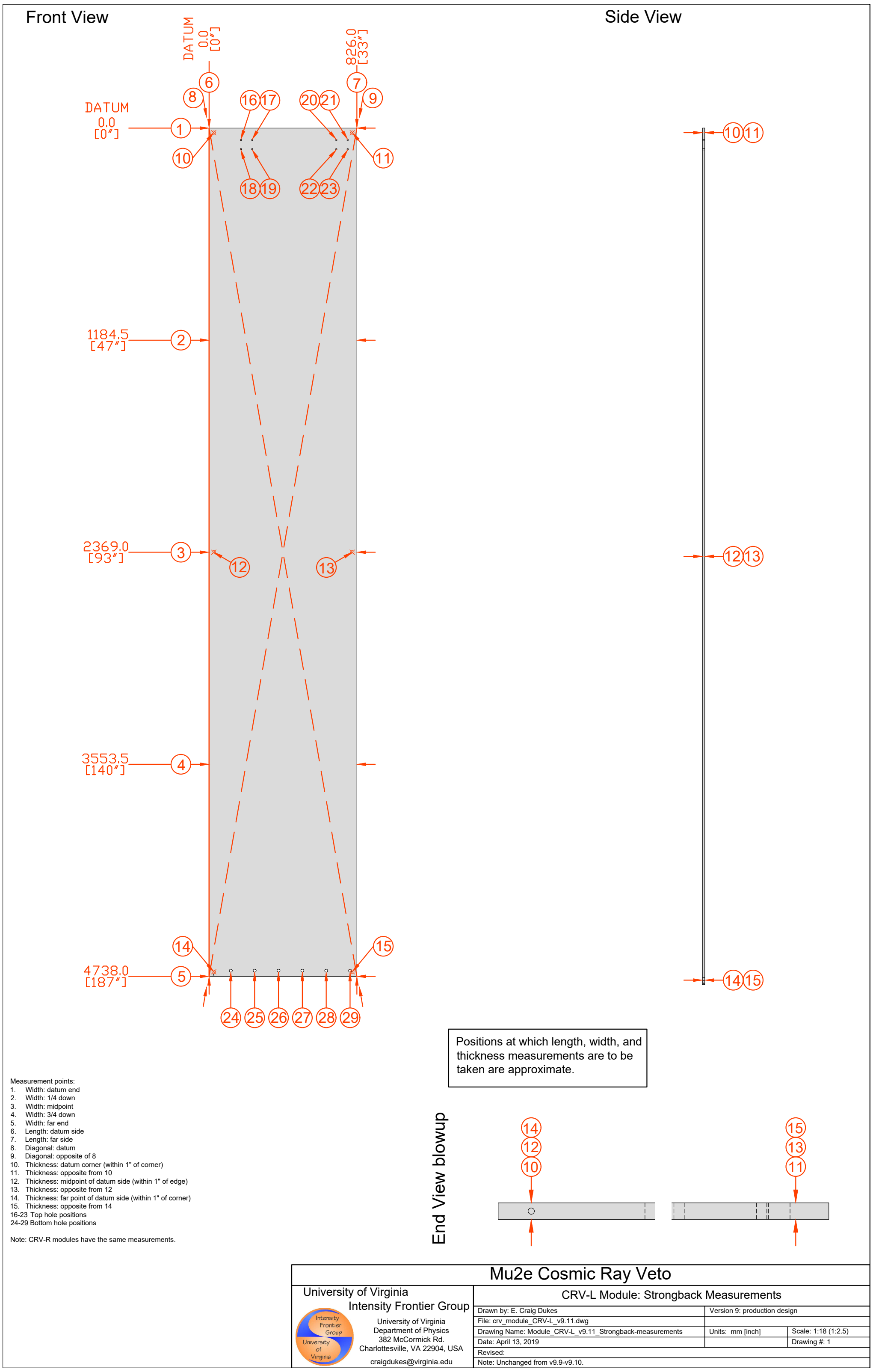

Figure I.7.: Left/Right (CRV-L/R) Module Strongback QC Measurements.

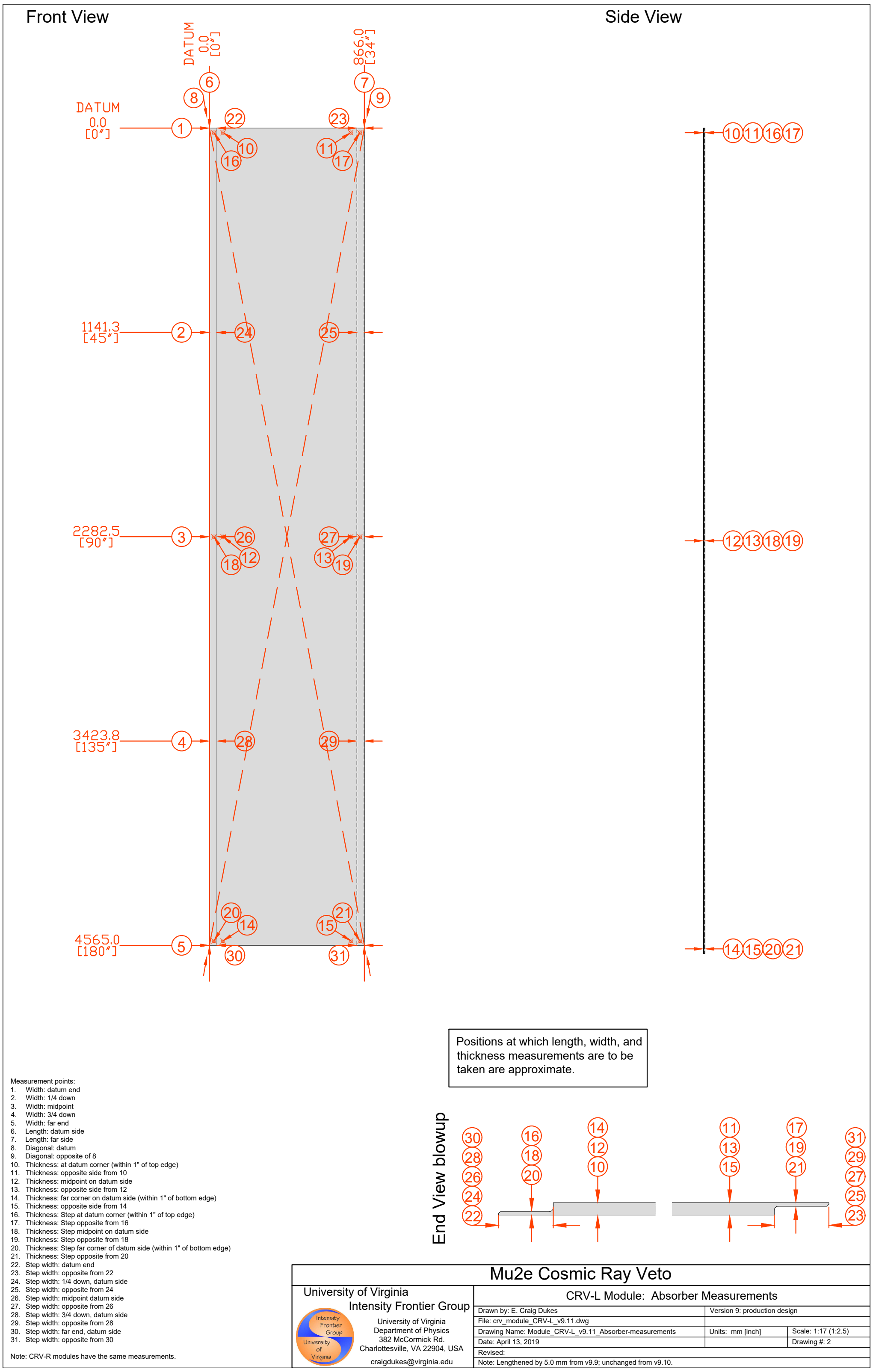

Figure I.8.: Left/Right (CRV-L/R) Module Absorber QC Measurements.

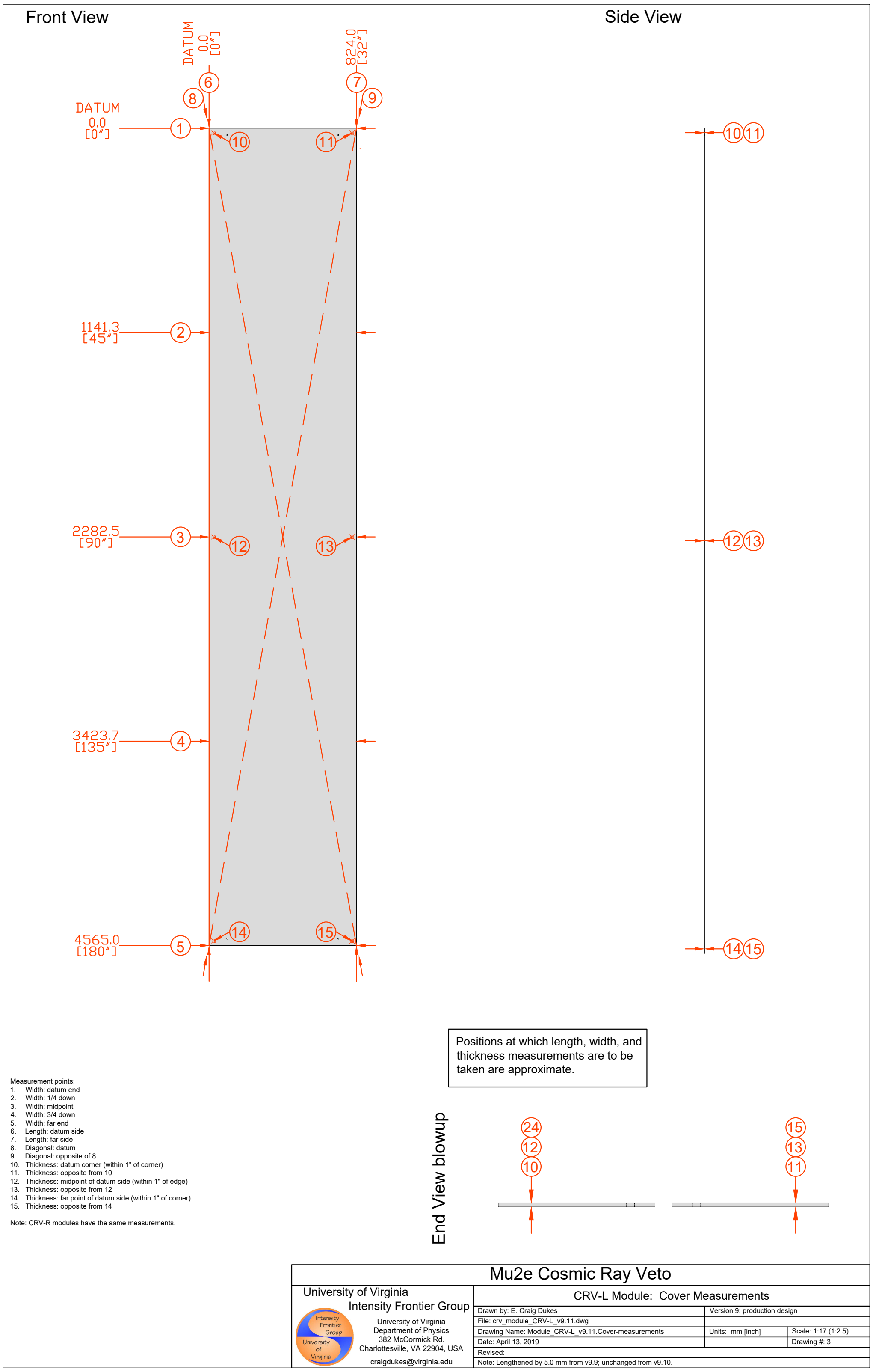

Figure I.9.: Left/Right (CRV-L/R) Module Cover QC Measurements.

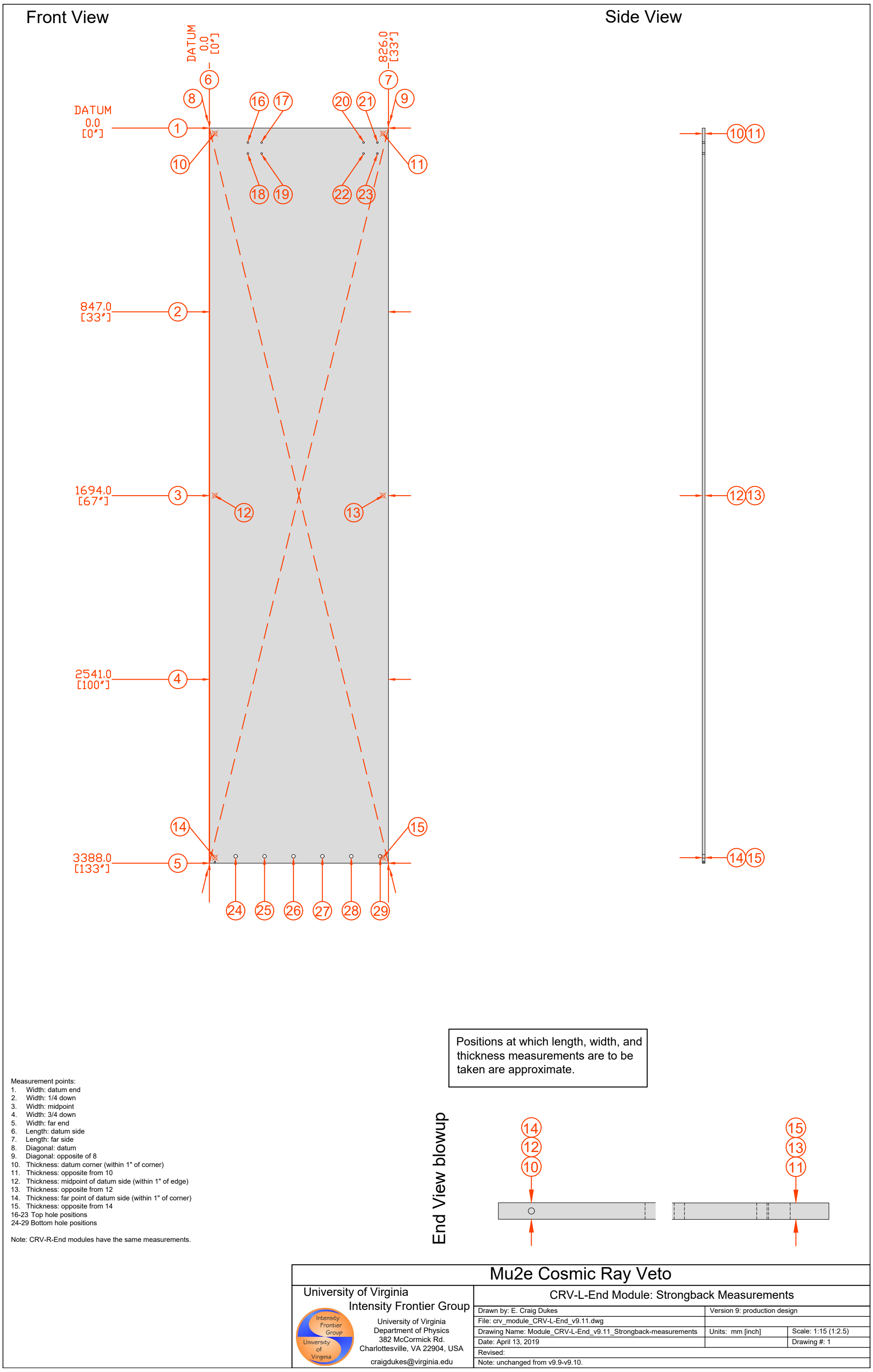

Figure I.10.: Left/Right Endcap (CRV-LE/RE) Module Strongback QC Measurements.

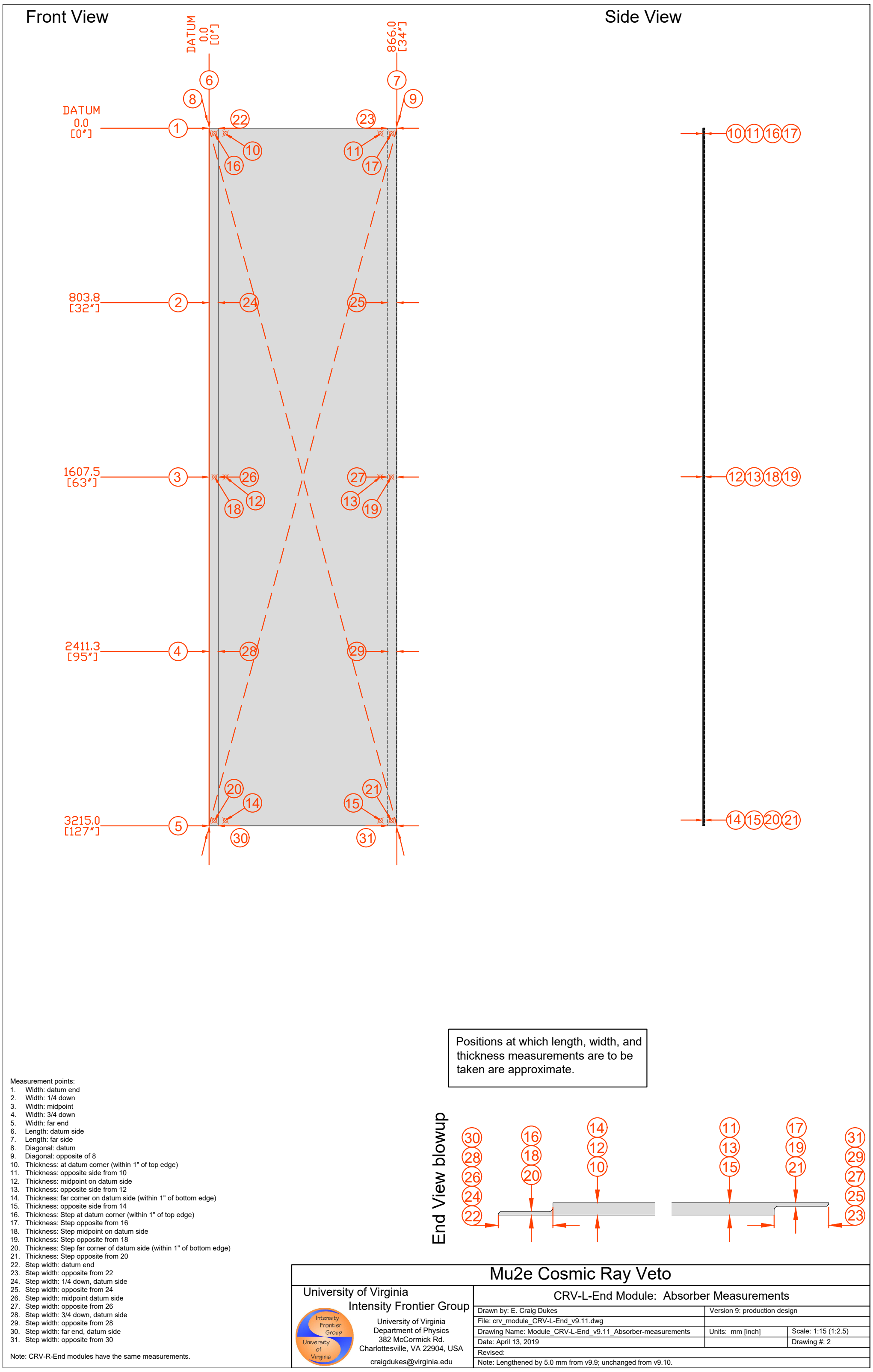

Figure I.11.: Left/Right Endcap (CRV-LE/RE) Module Absorber QC Measurements.

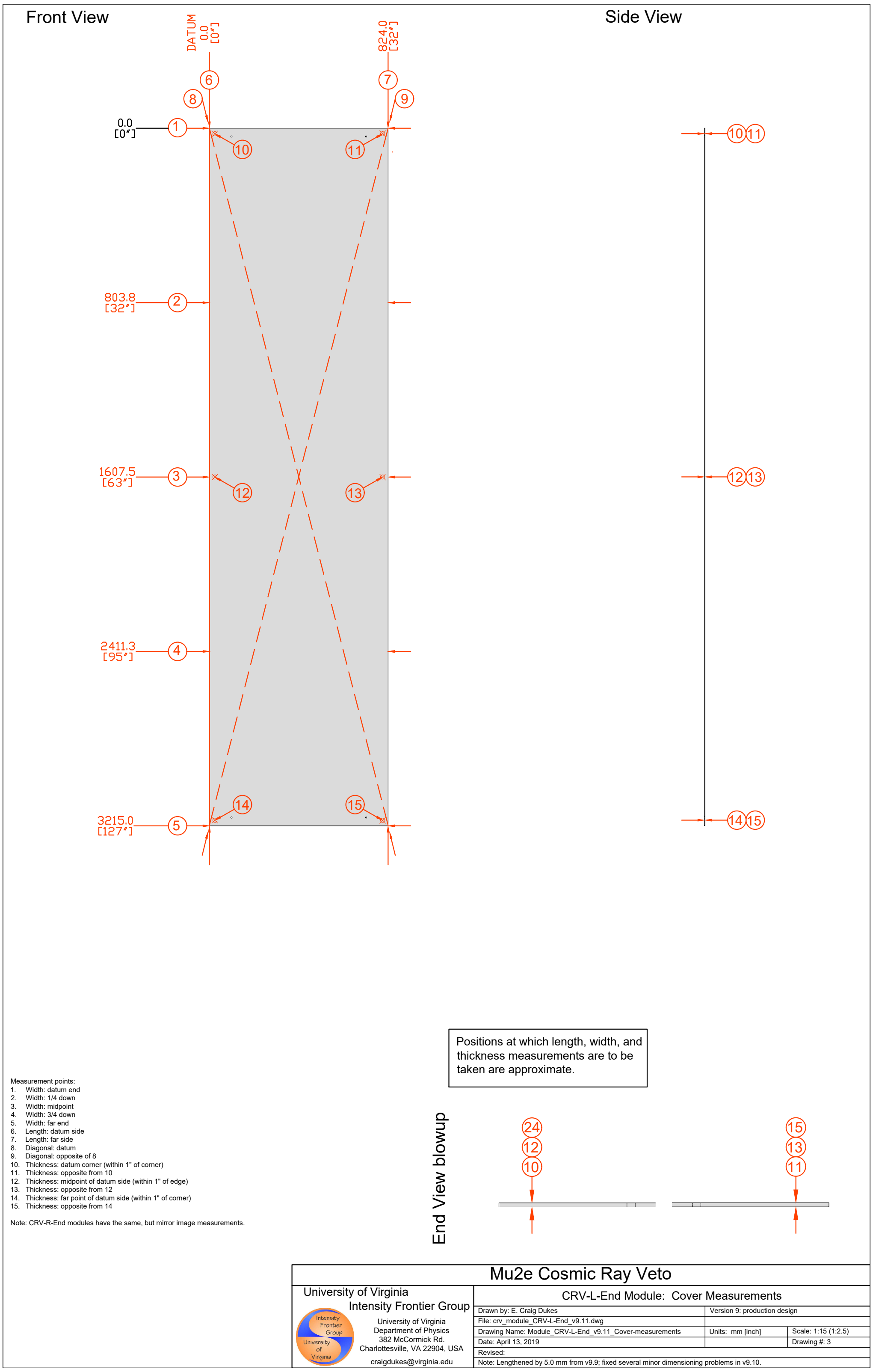

Figure I.12.: Left/Right Endcap (CRV-LE/RE) Module Cover QC Measurements.

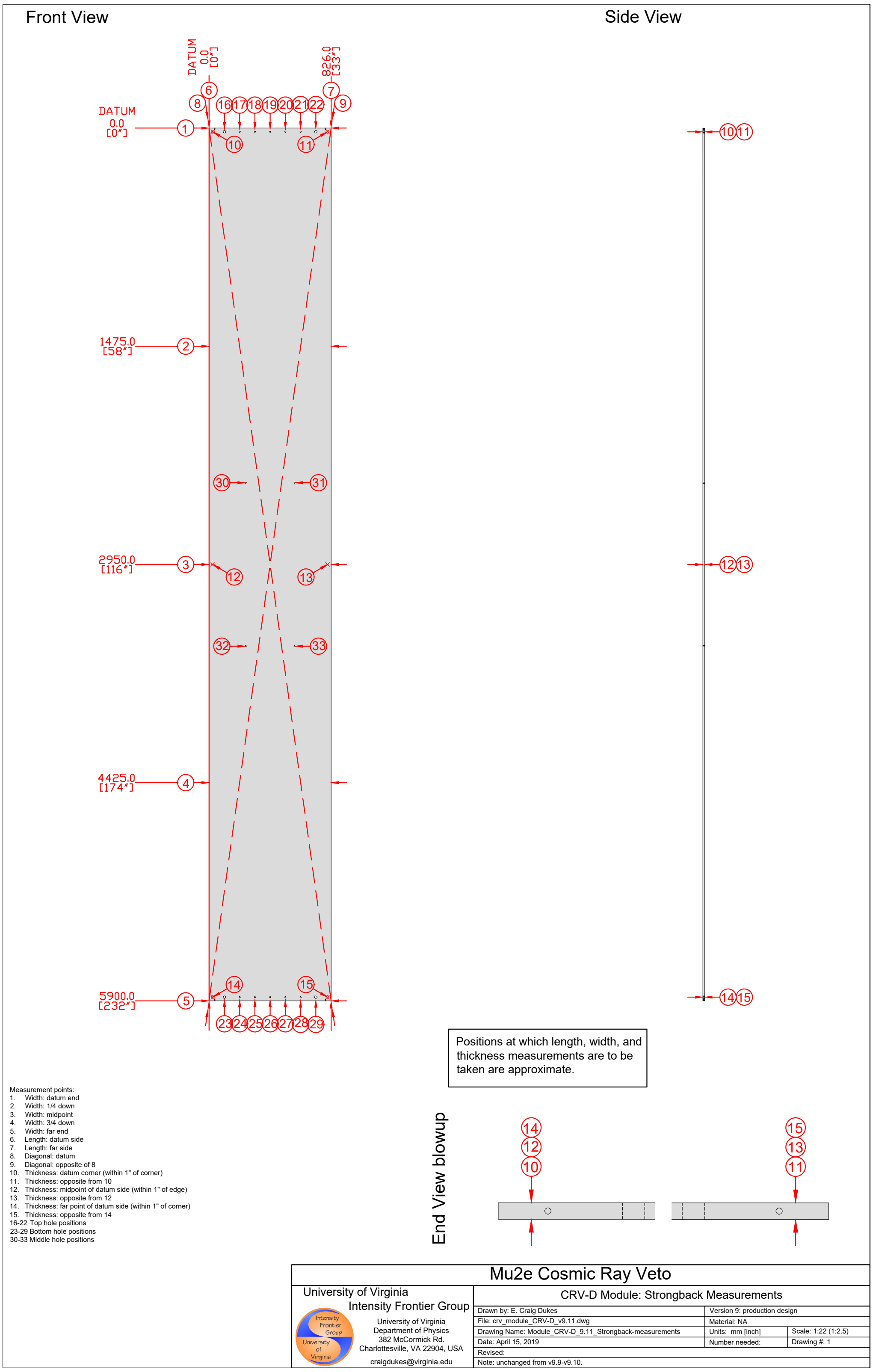

Figure I.13.: Downstream (CRV-D) Module Strongback QC Measurements.

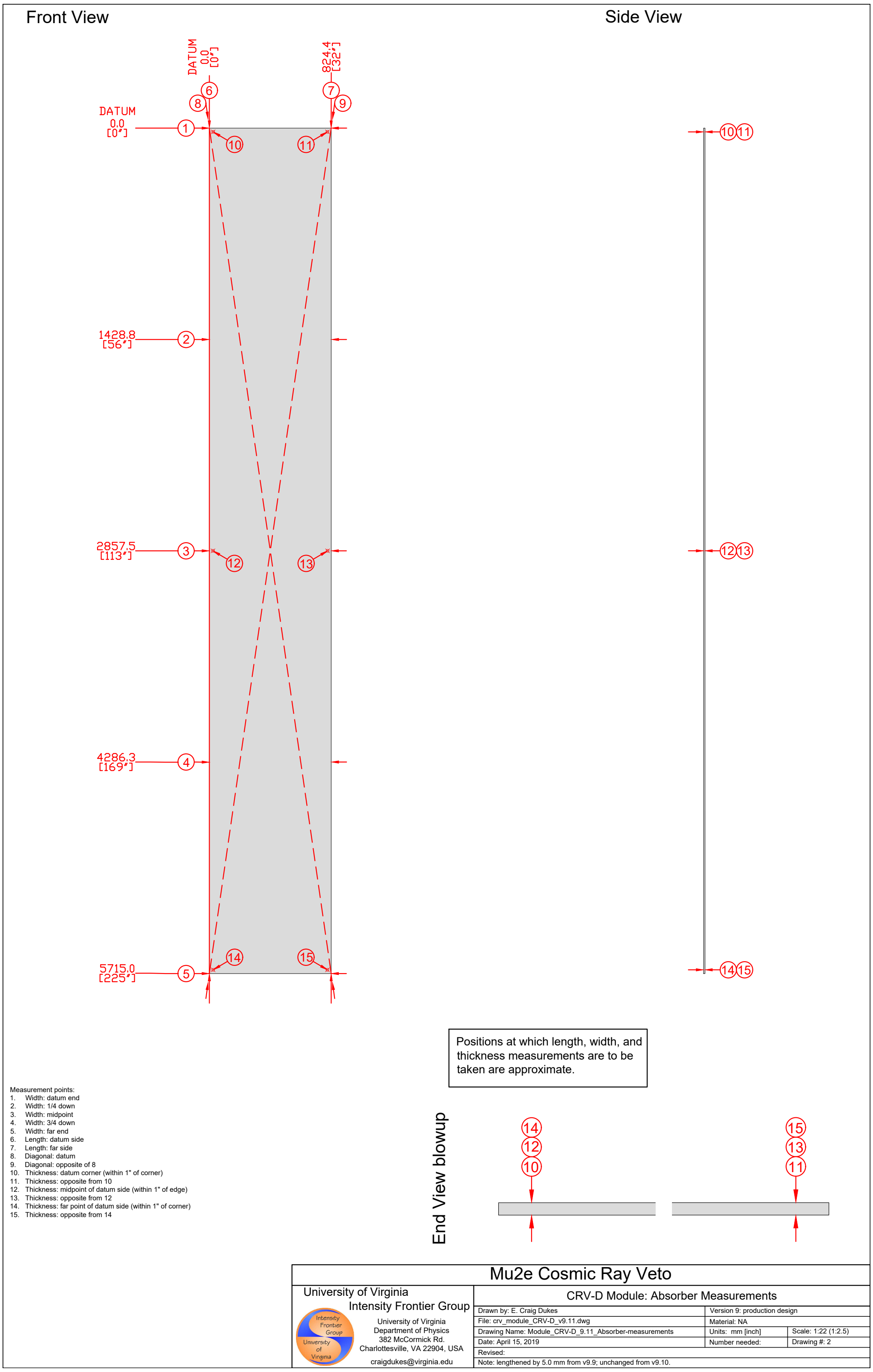

Figure I.14.: Downstream (CRV-D) Module Absorber QC Measurements.

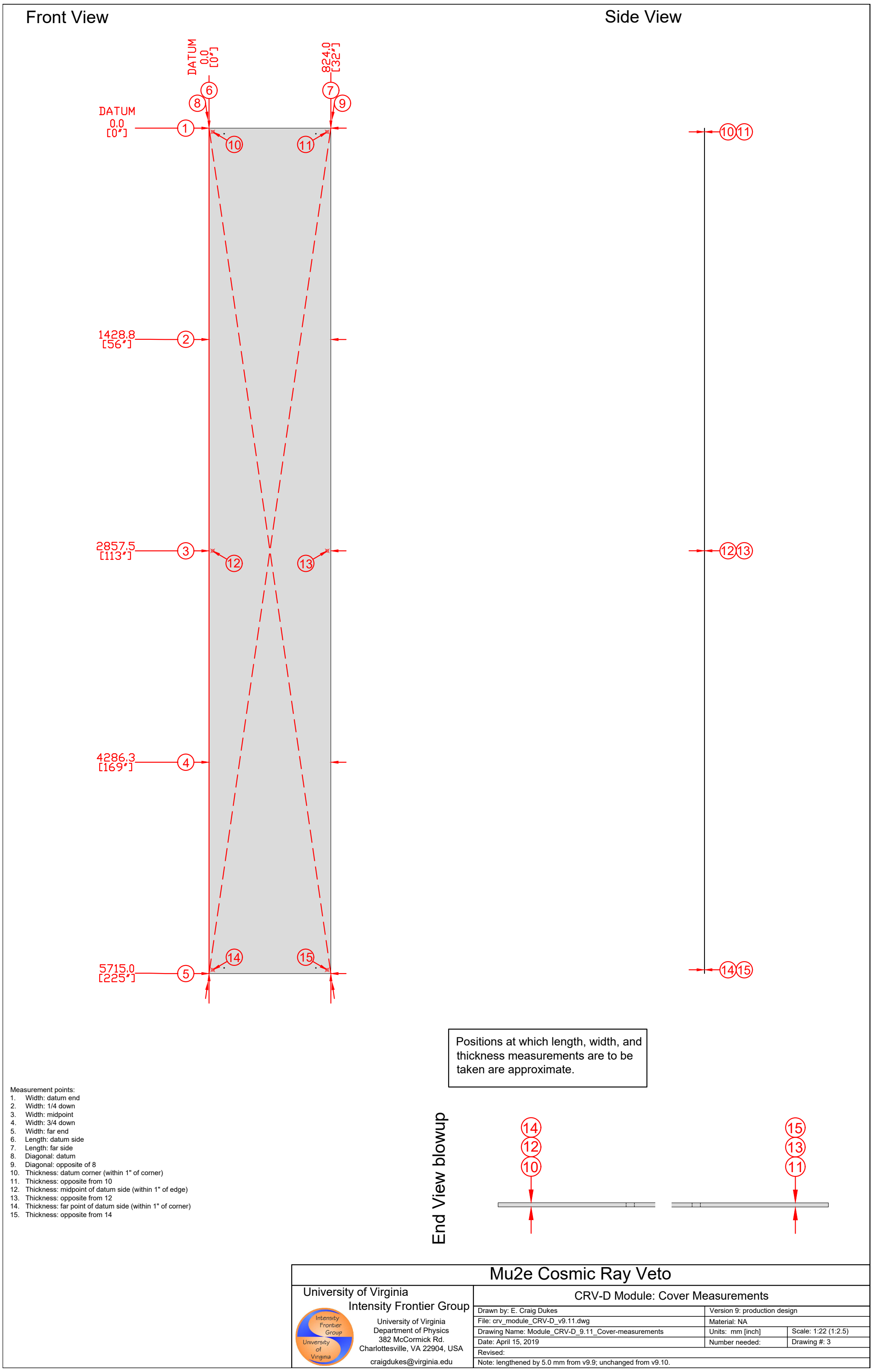

Figure I.15.: Downstream (CRV-D) Module Cover QC Measurements.

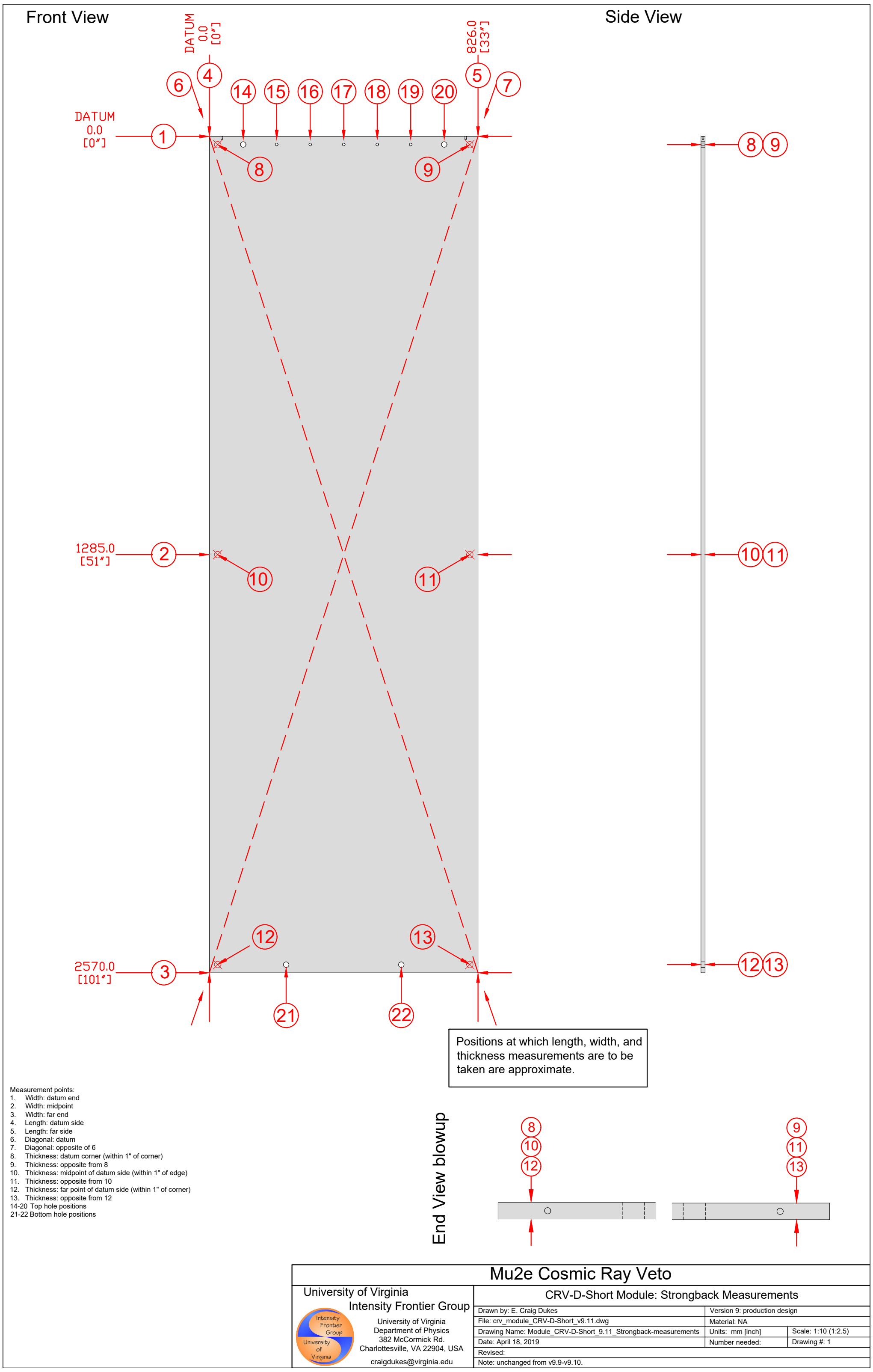

Figure I.16.: Downstream Short (CRV-DS) Module Strongback QC Measurements.

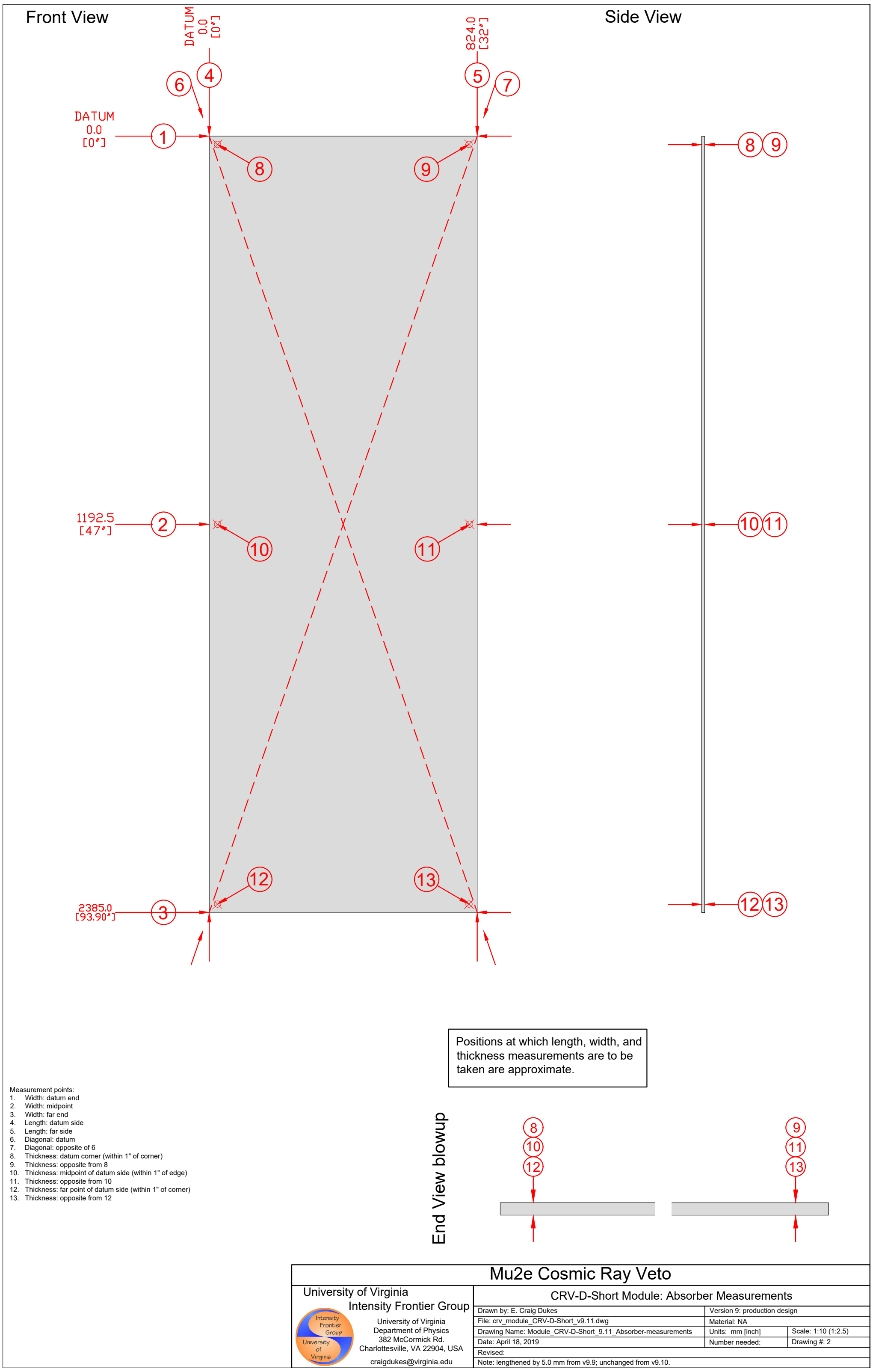

Figure I.17.: Downstream Short (CRV-DS) Module Absorber QC Measurements.

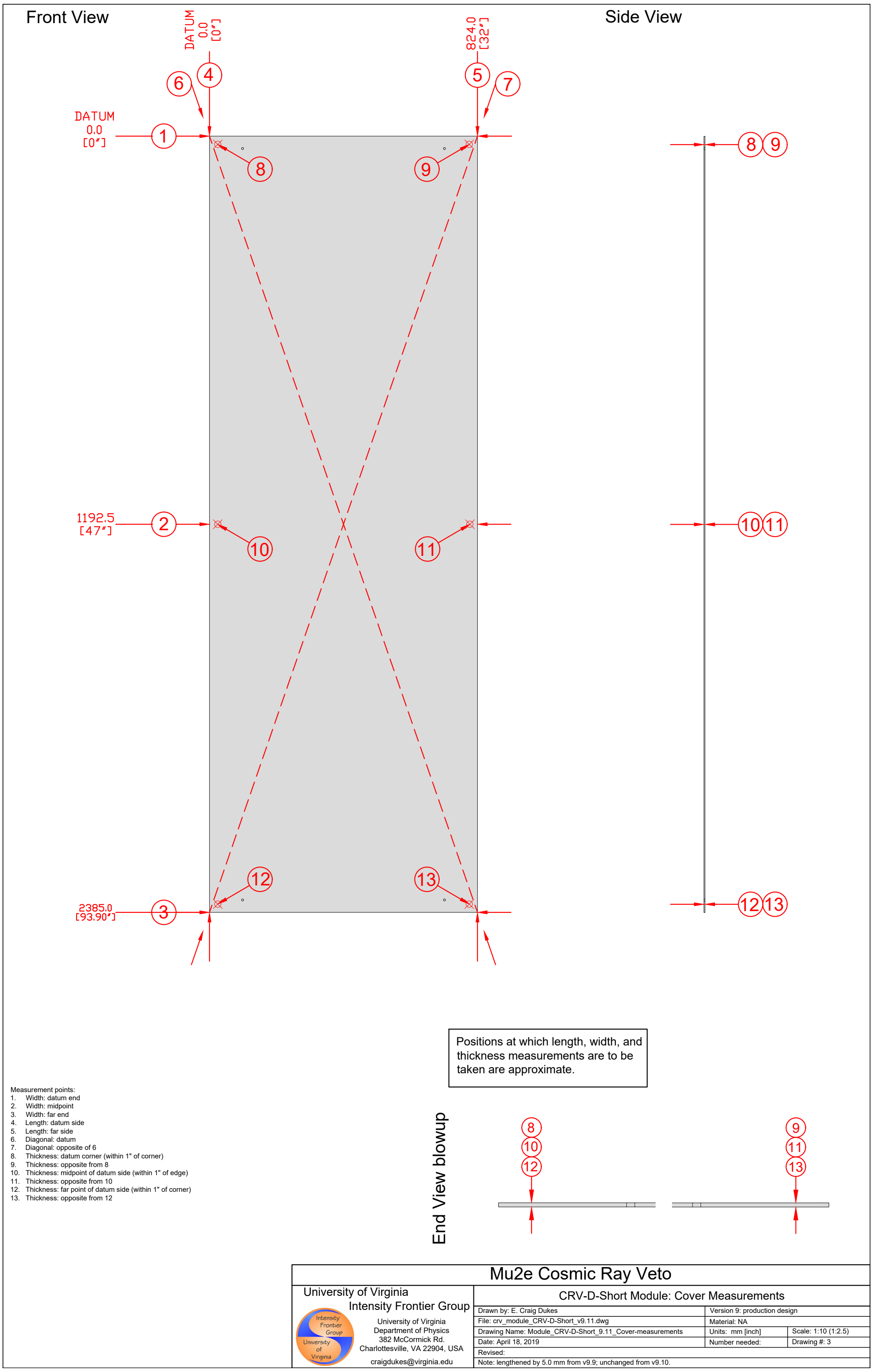

Figure I.18.: Downstream Short (CRV-DS) Module Cover QC Measurements.

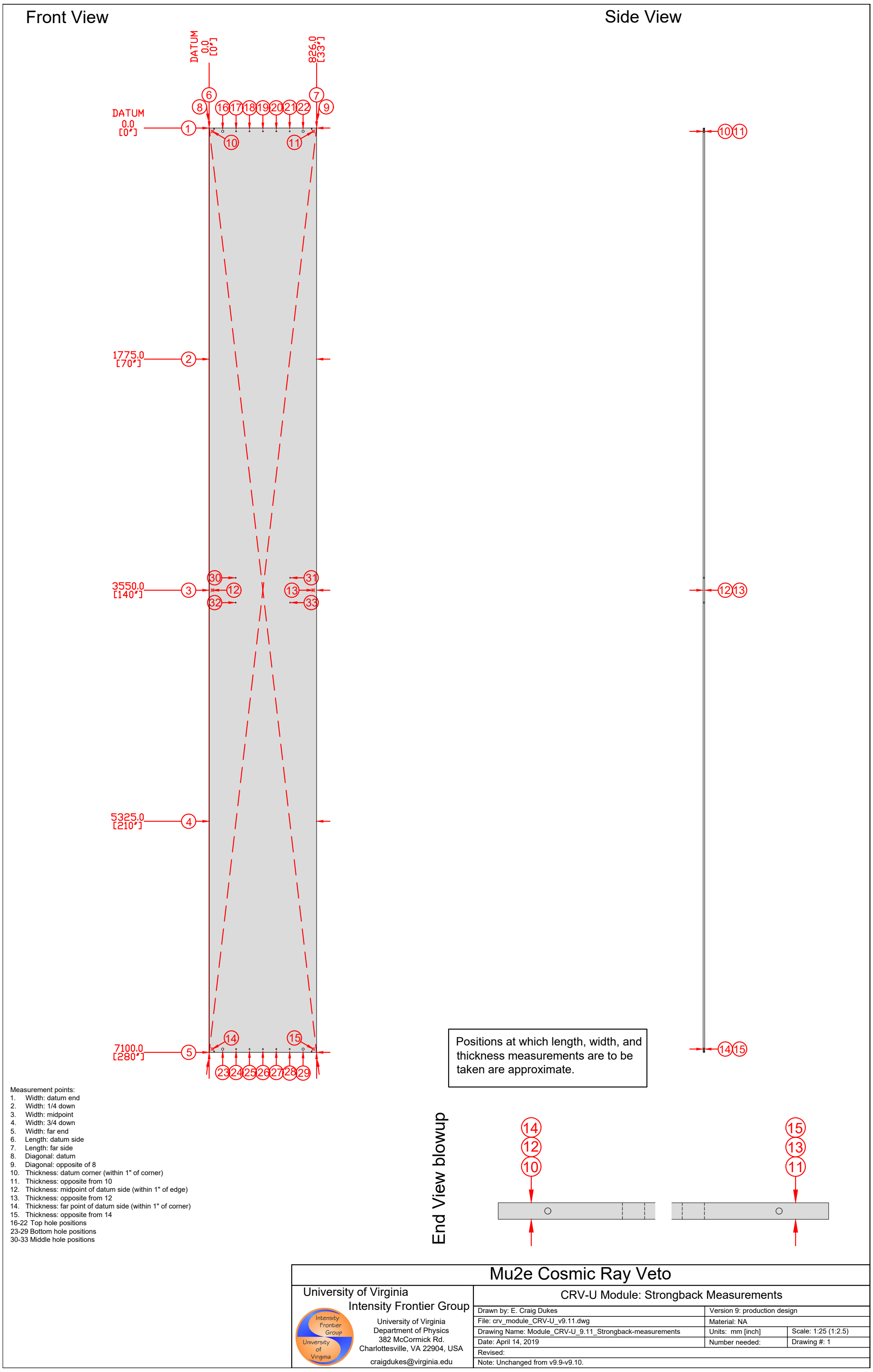

Figure I.19.: Upstream (CRV-U) Module Strongback QC Measurements.

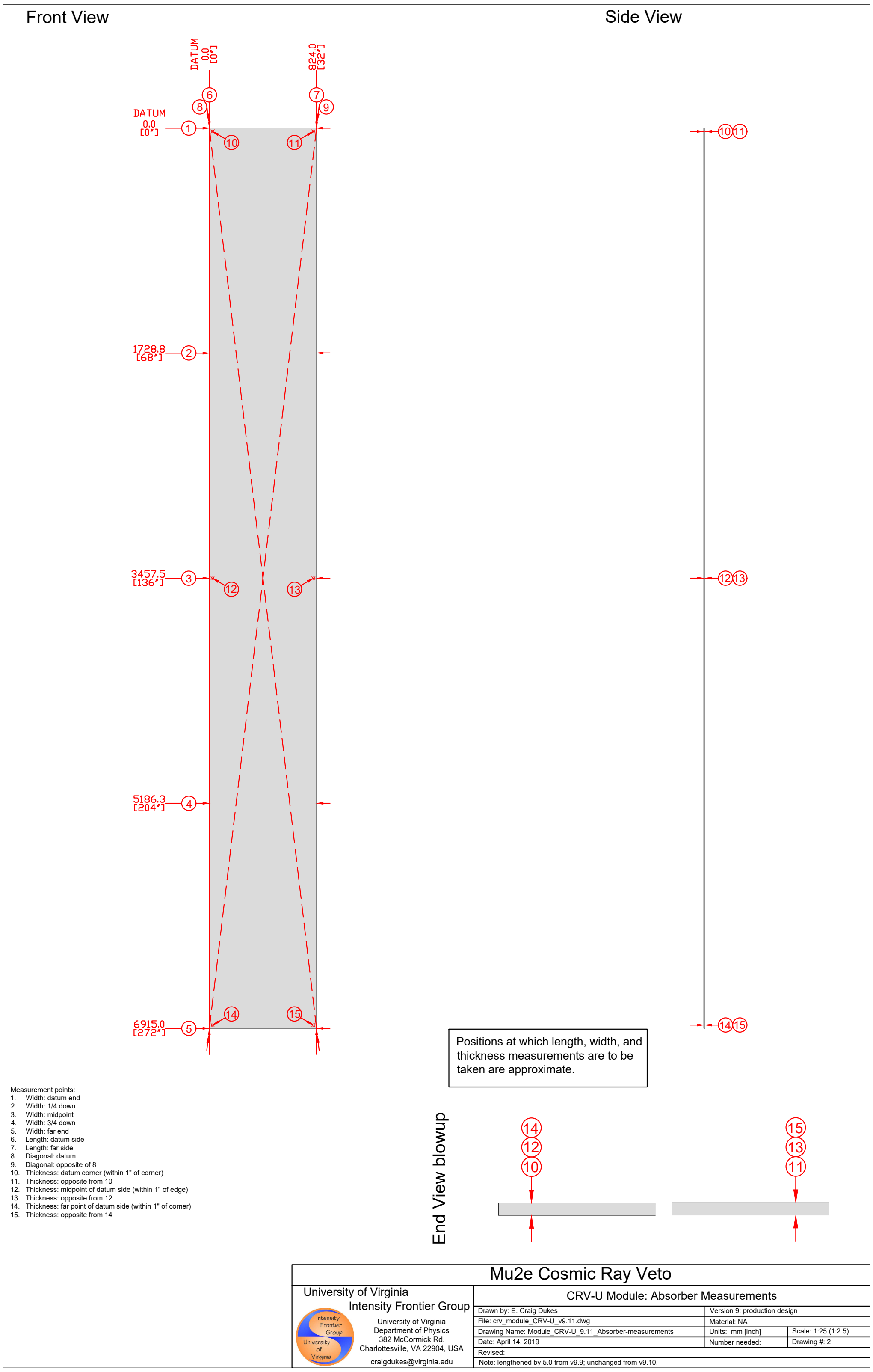

Figure I.20.: Upstream (CRV-U) Module Absorber QC Measurements.

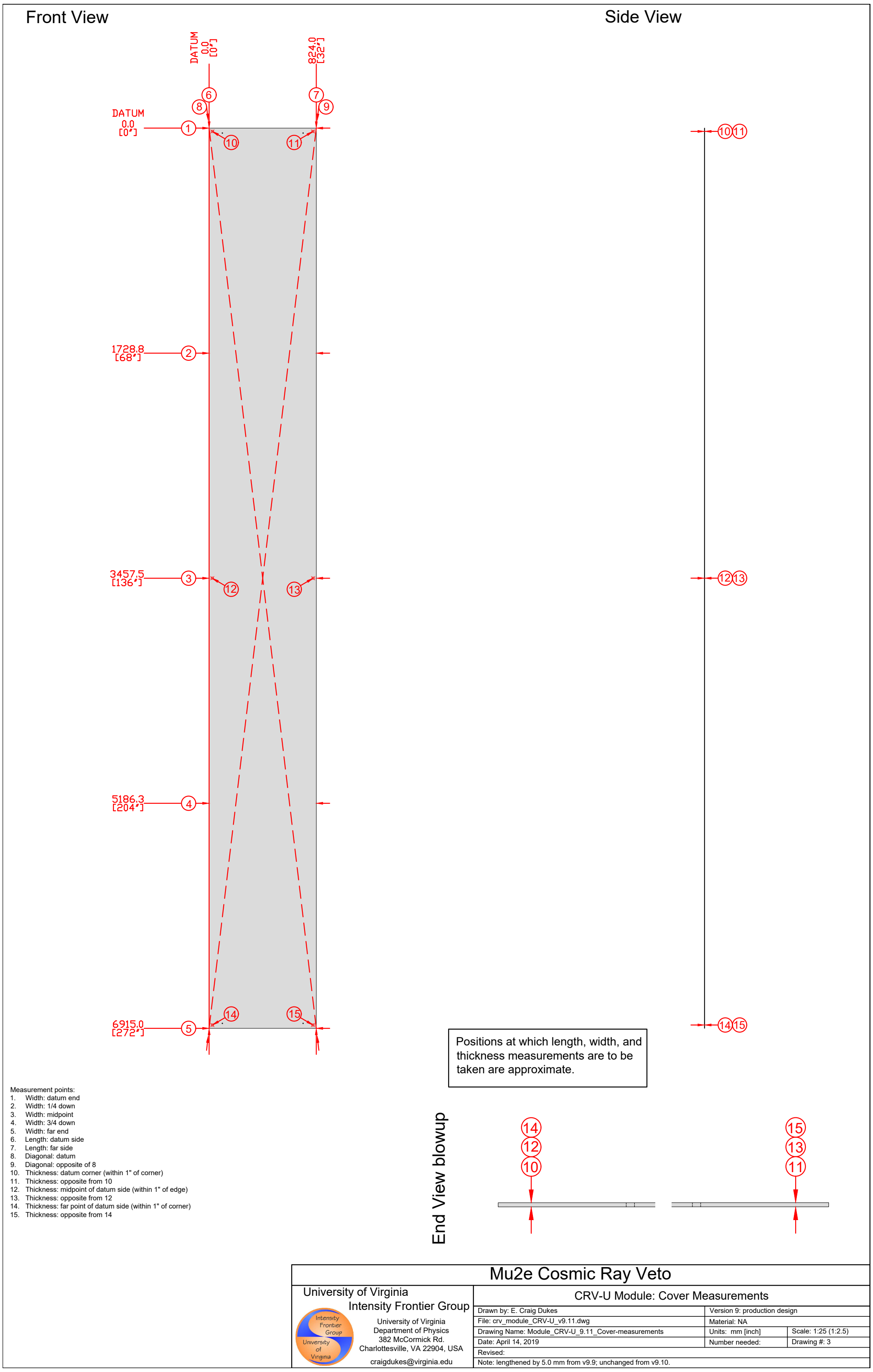

Figure I.21.: Upstream (CRV-U) Module Cover QC Measurements.

Appendix J.

FEB Enclosure

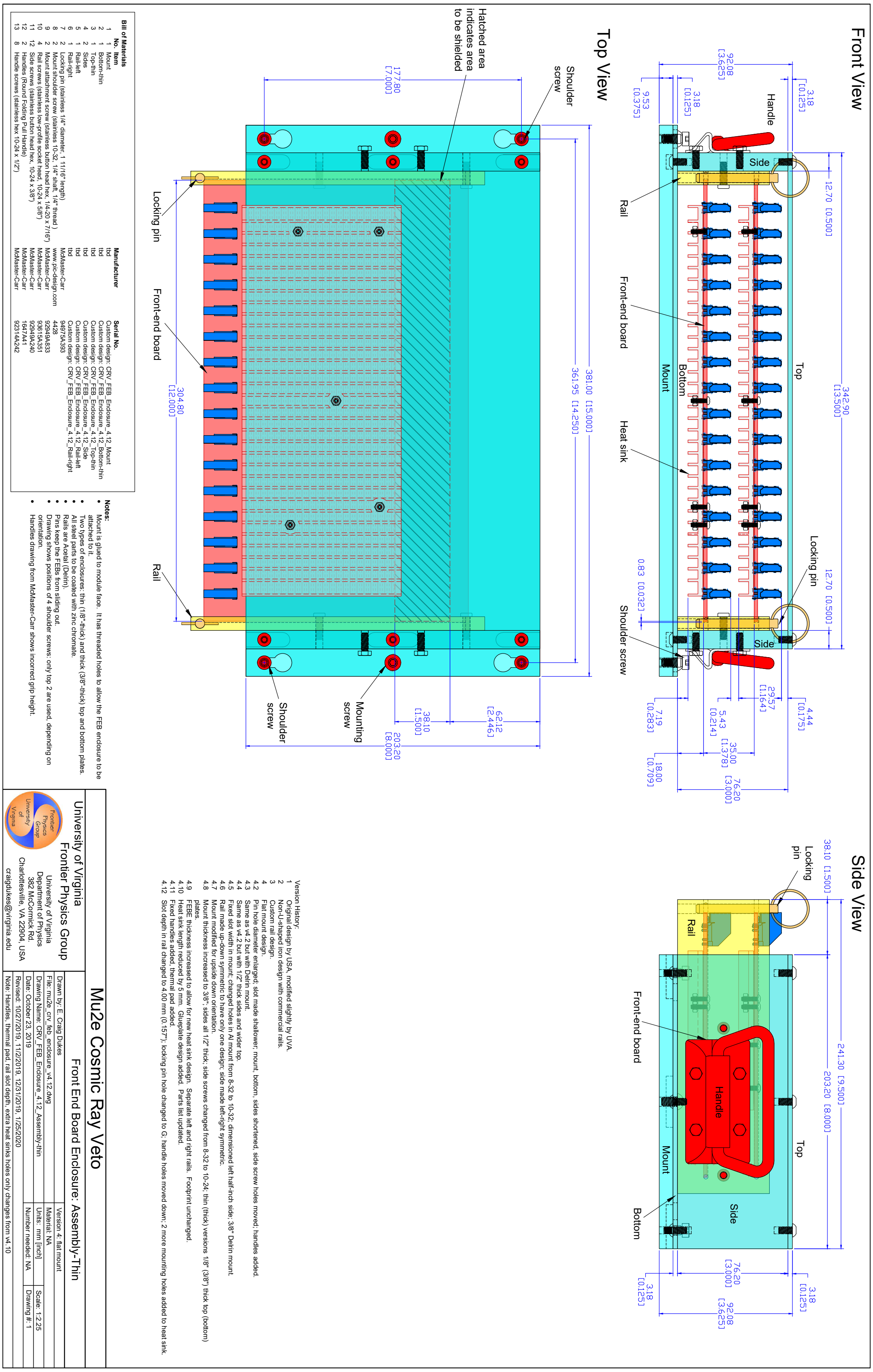

Figure J.1.: Drawing of the thin FEB Enclosure assembly.

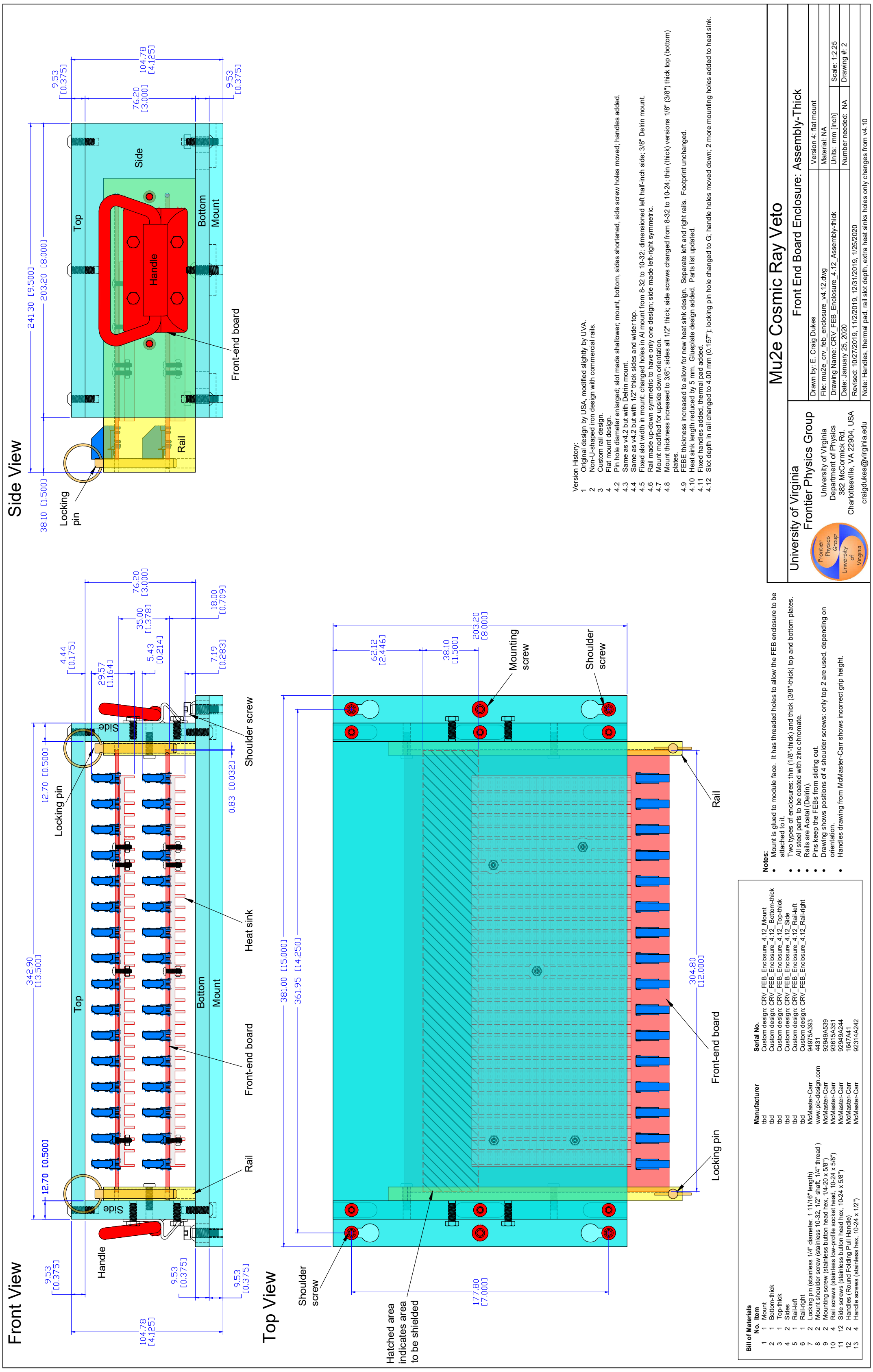

Figure J.2.: Drawing of the thick FEB Enclosure assembly.

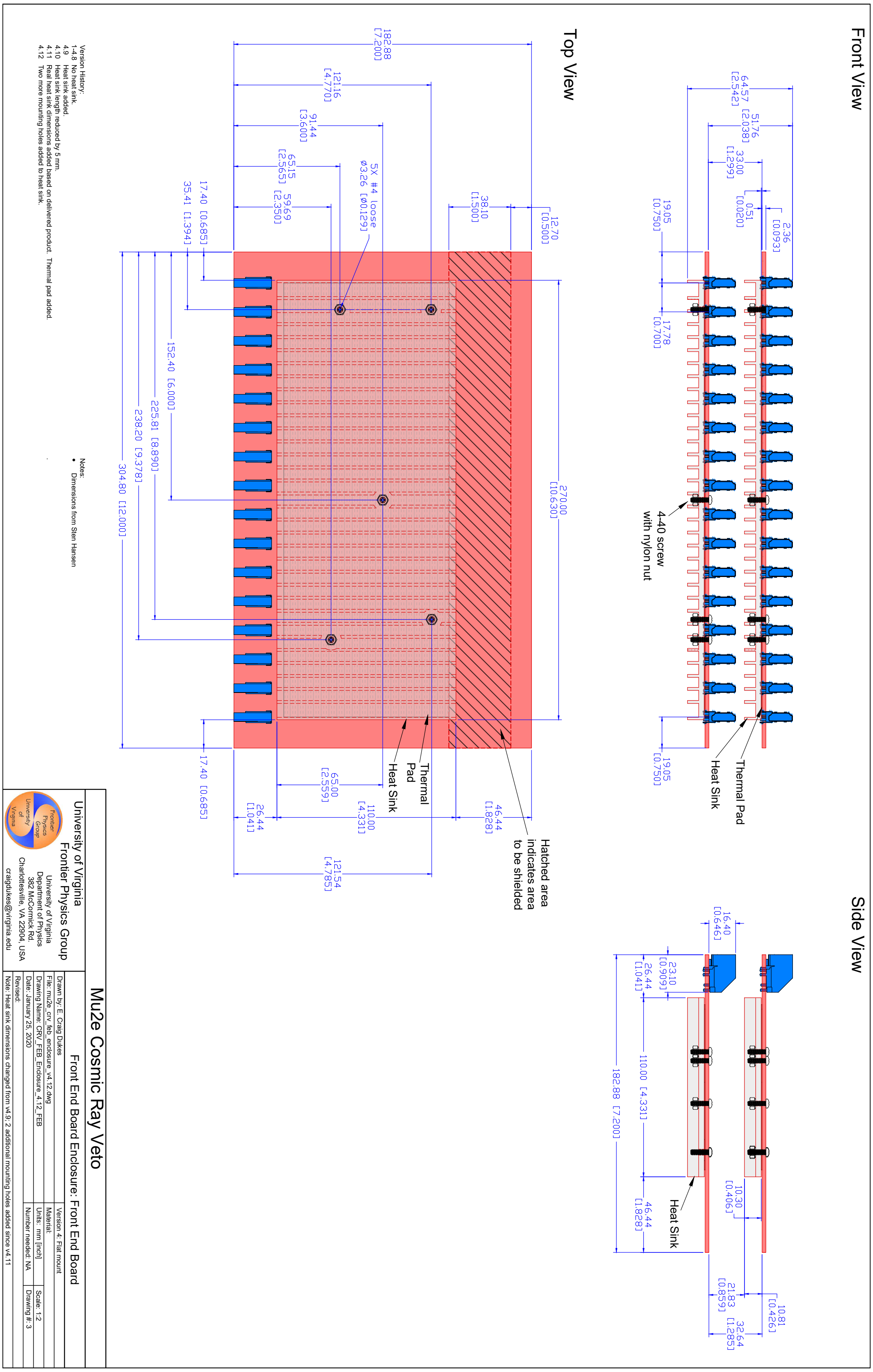

Figure J.3.: Drawing of Front End Board.

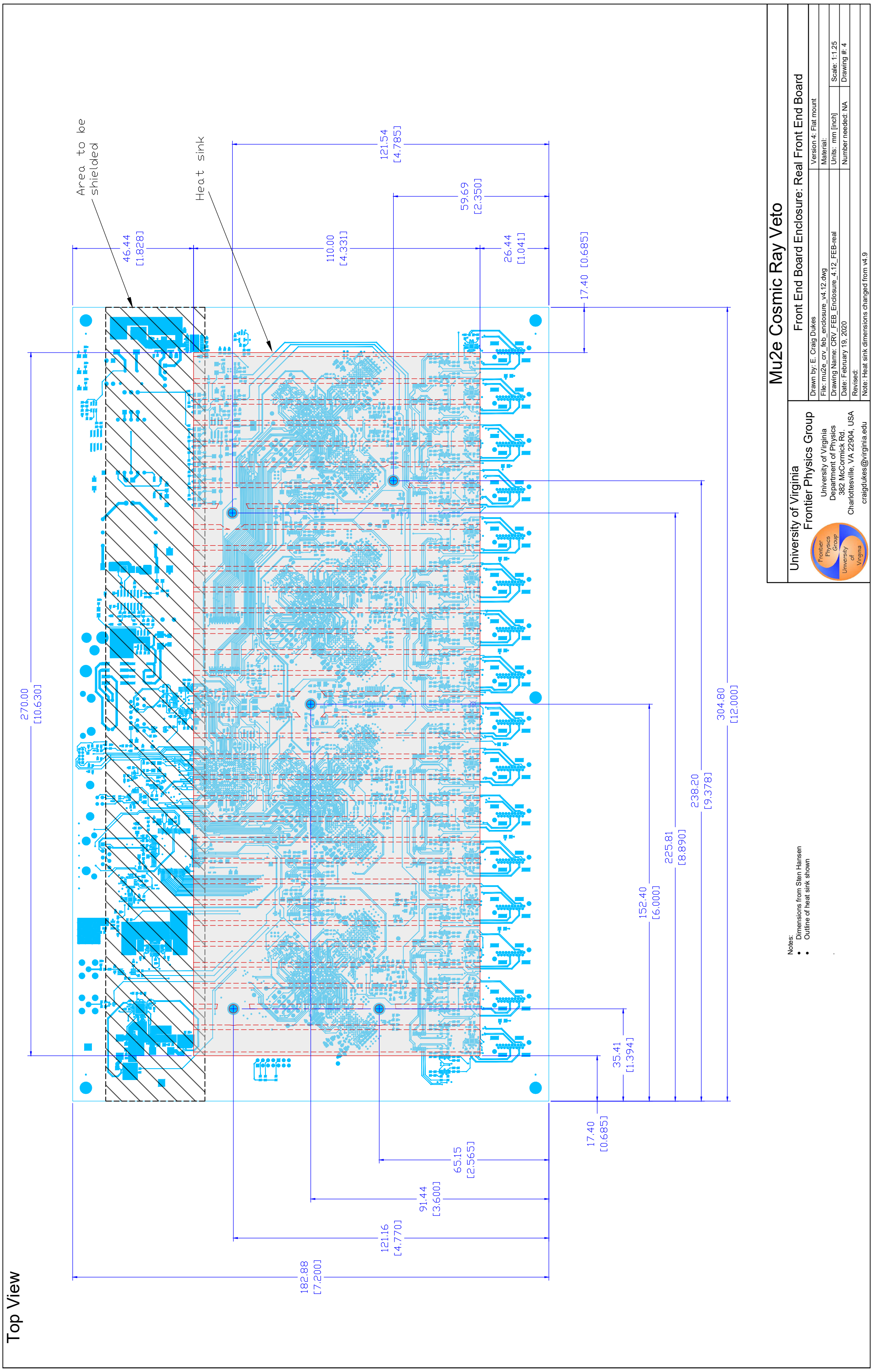

Figure J.4.: Drawing of Front End Board with traces.

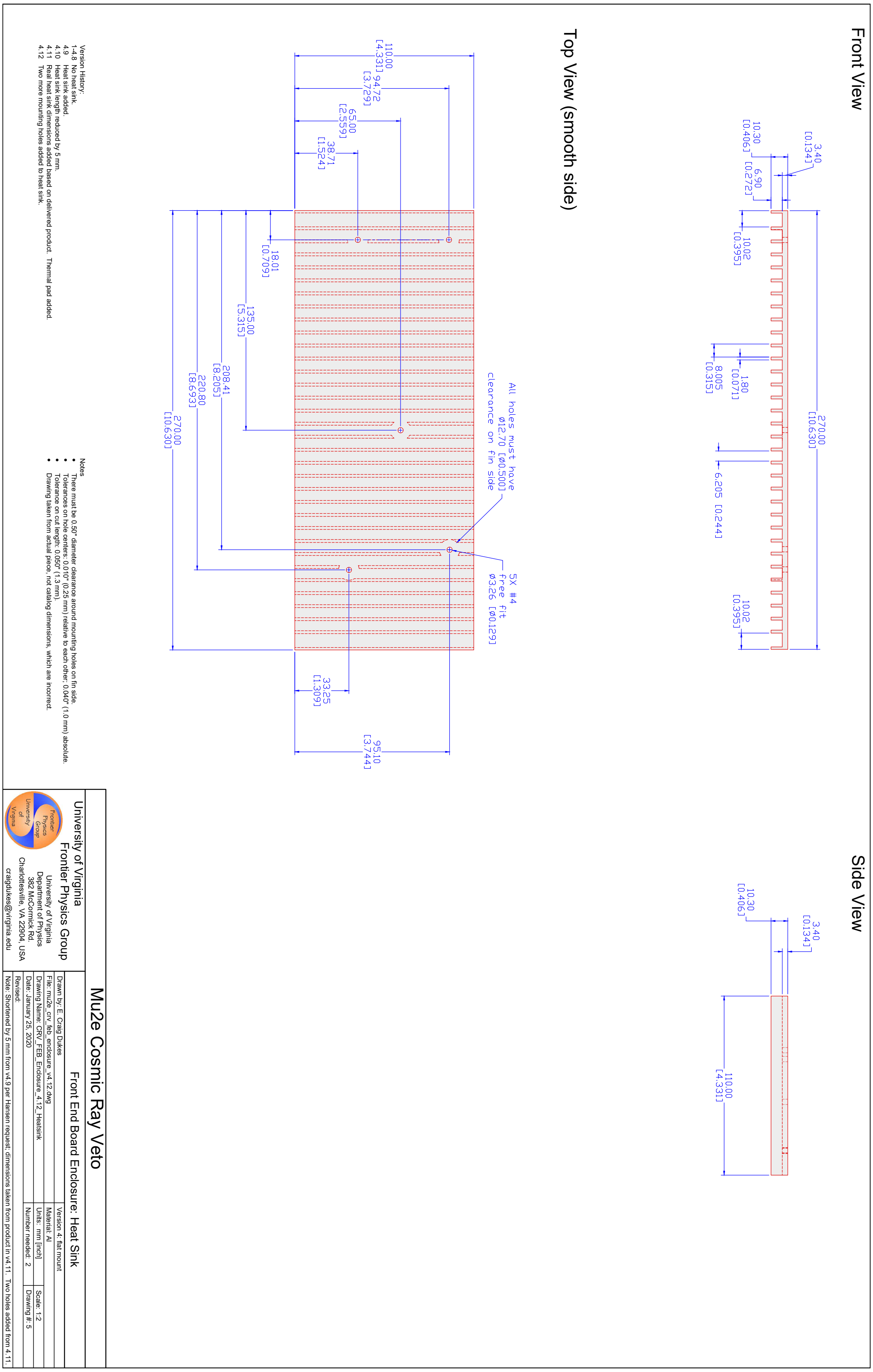

Figure J.5.: Drawing of the FEB heat sink.

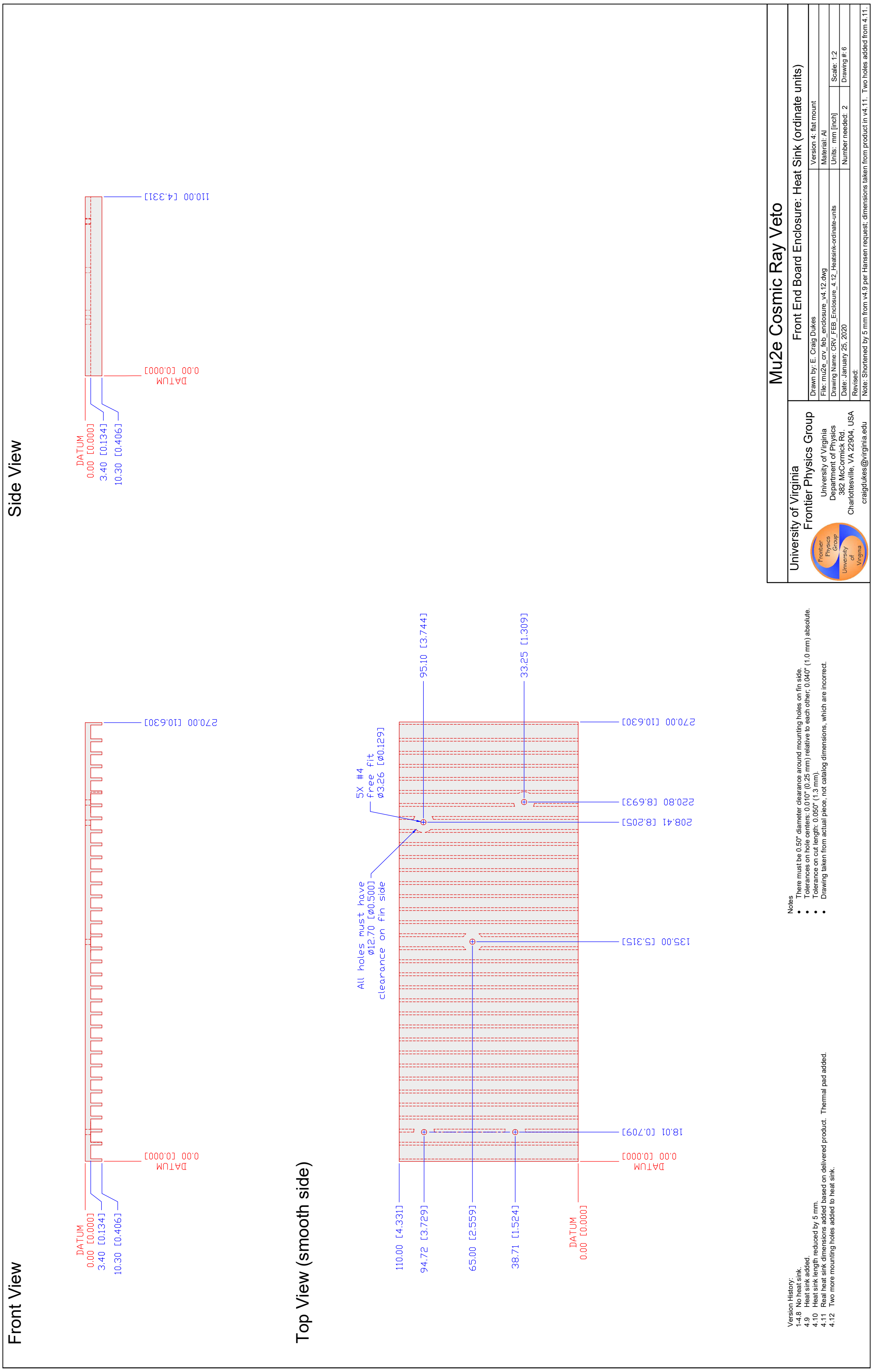

Figure J.6.: Drawing of FEB heat sink.

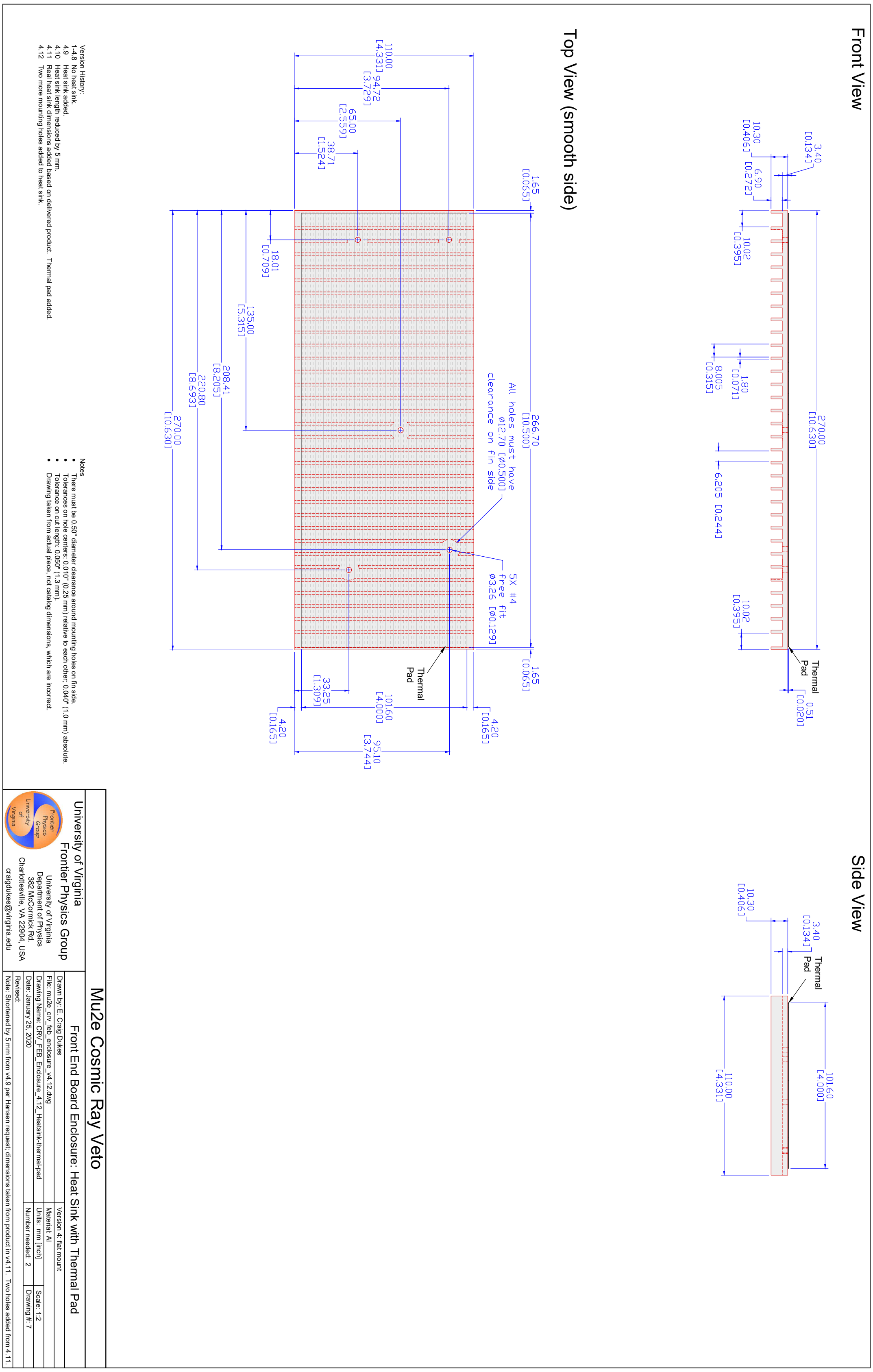

Figure J.7.: Drawing of FEB heat sink and thermal pad.

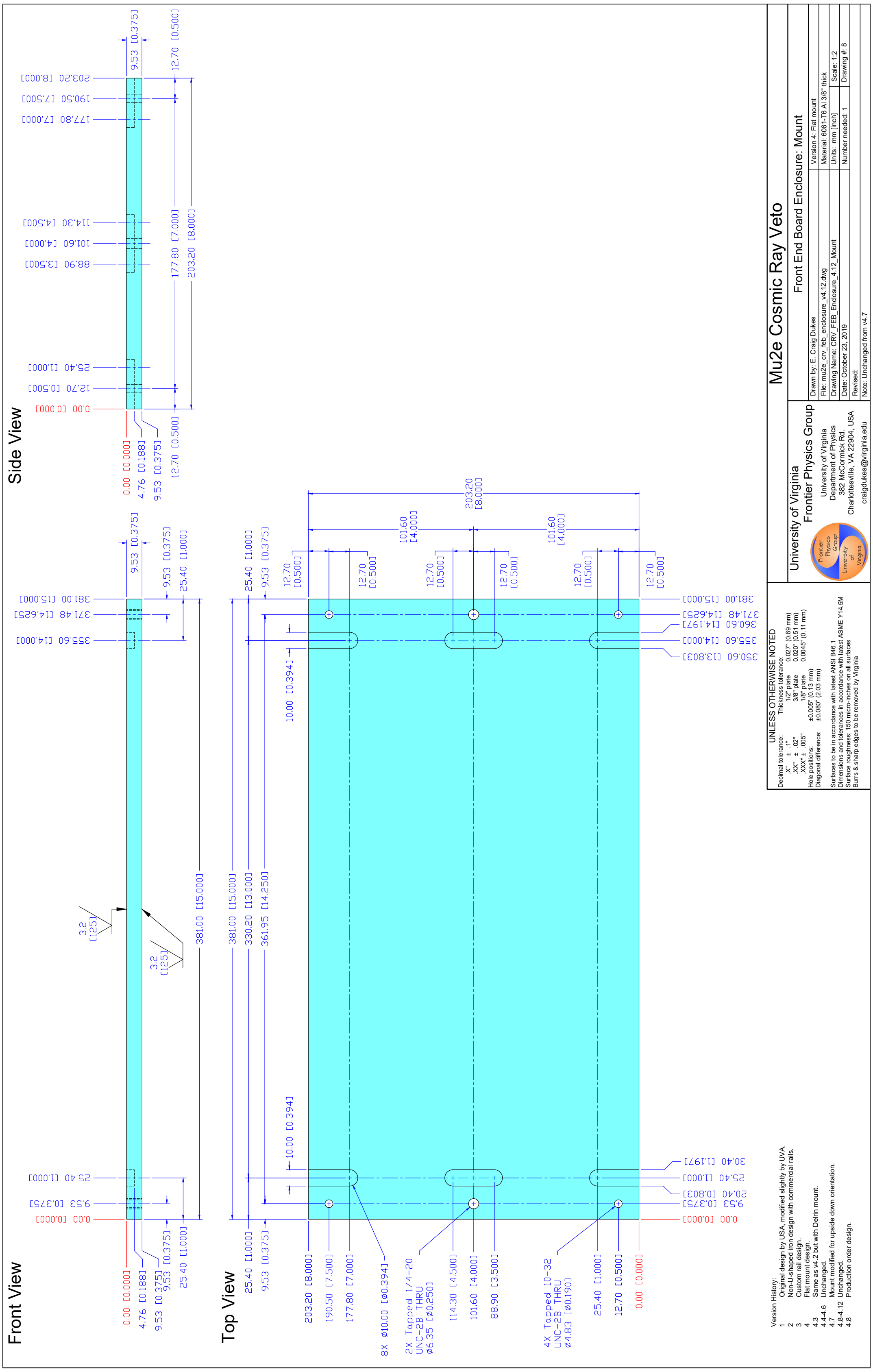

Figure J.8.: Drawing of FEBE mounting plate.

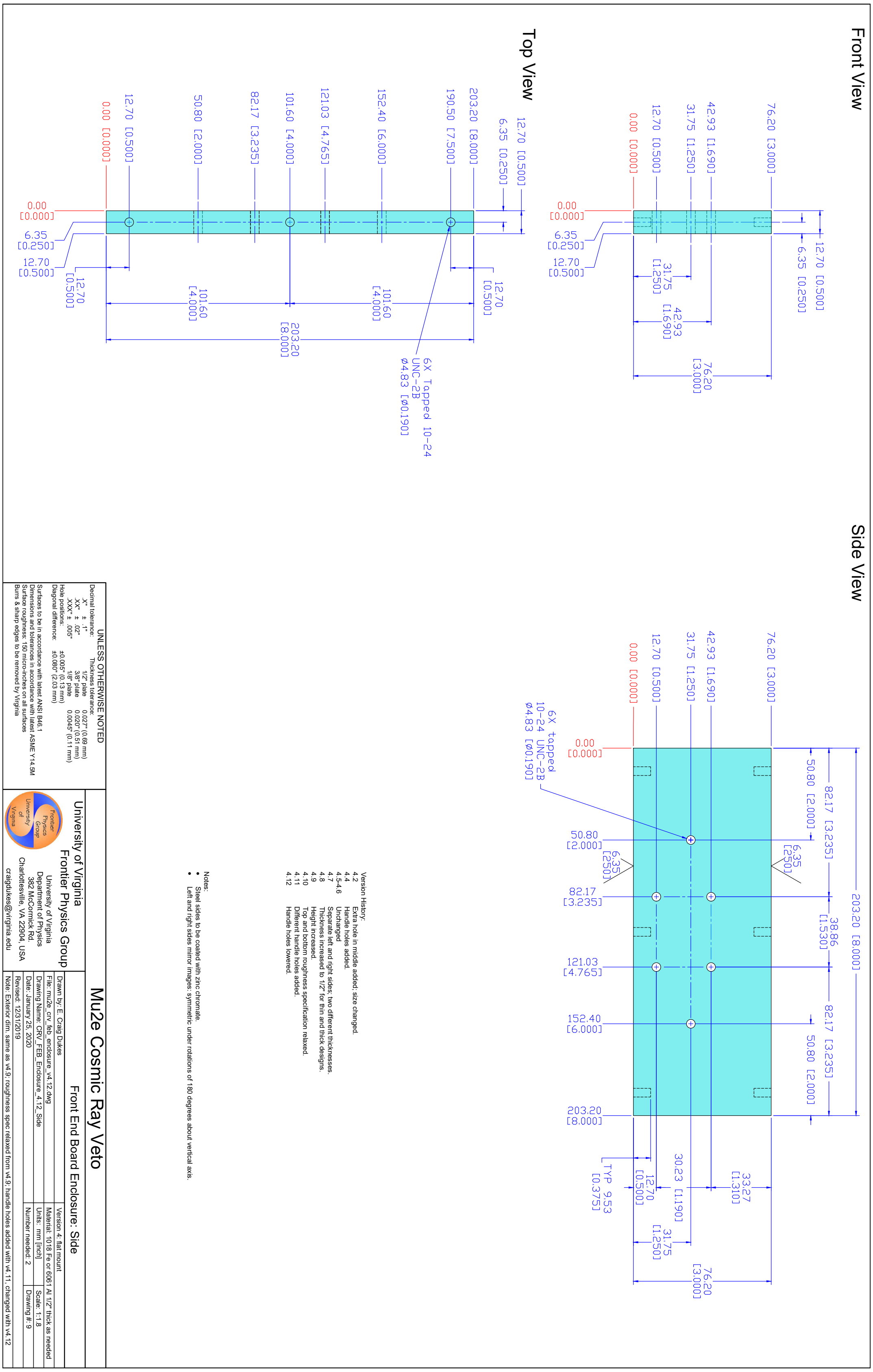

Figure J.9.: Drawing of FEBE side plate.

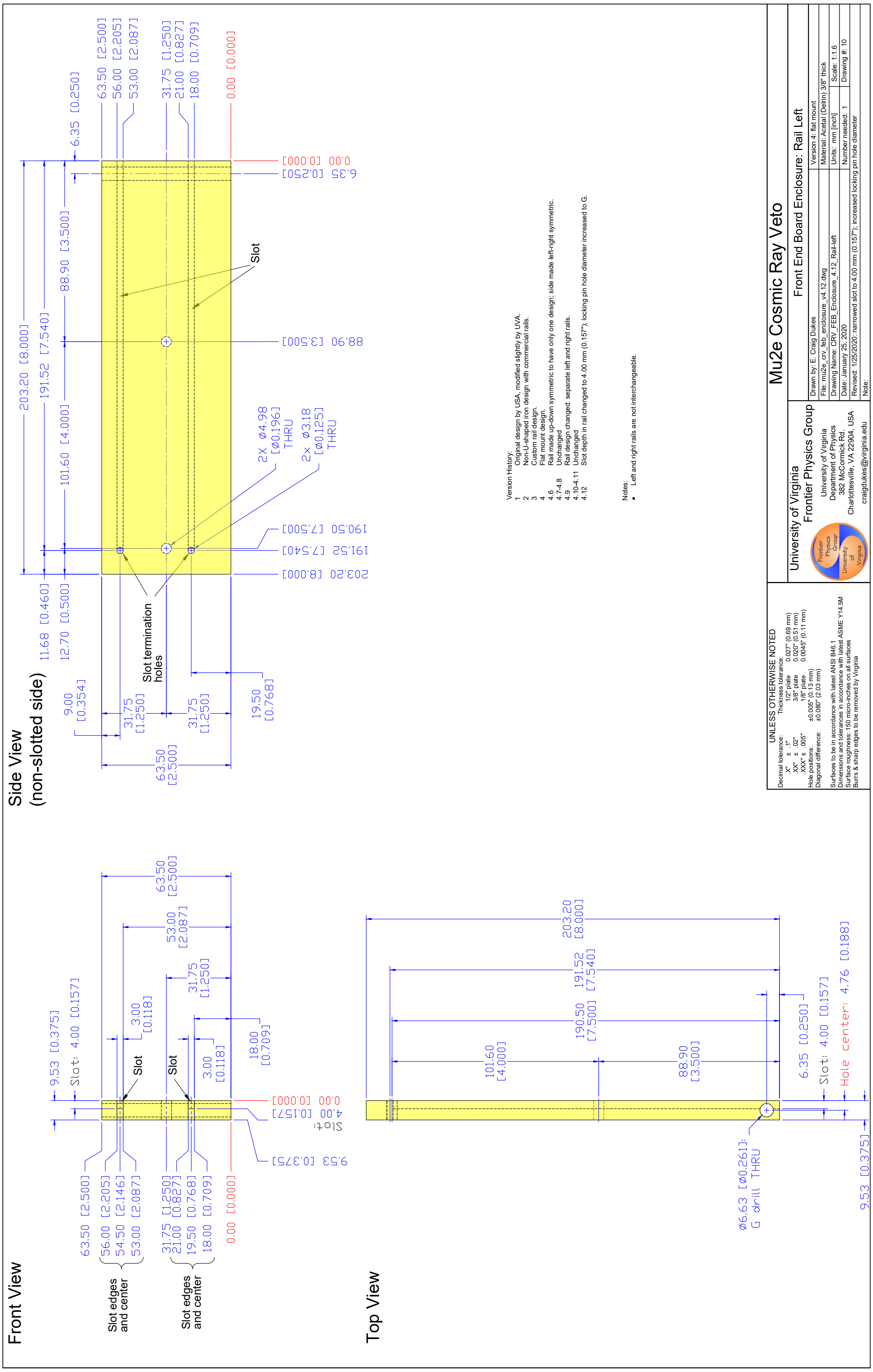

Figure J.10.: Drawing of FEBE left side FEB rail.

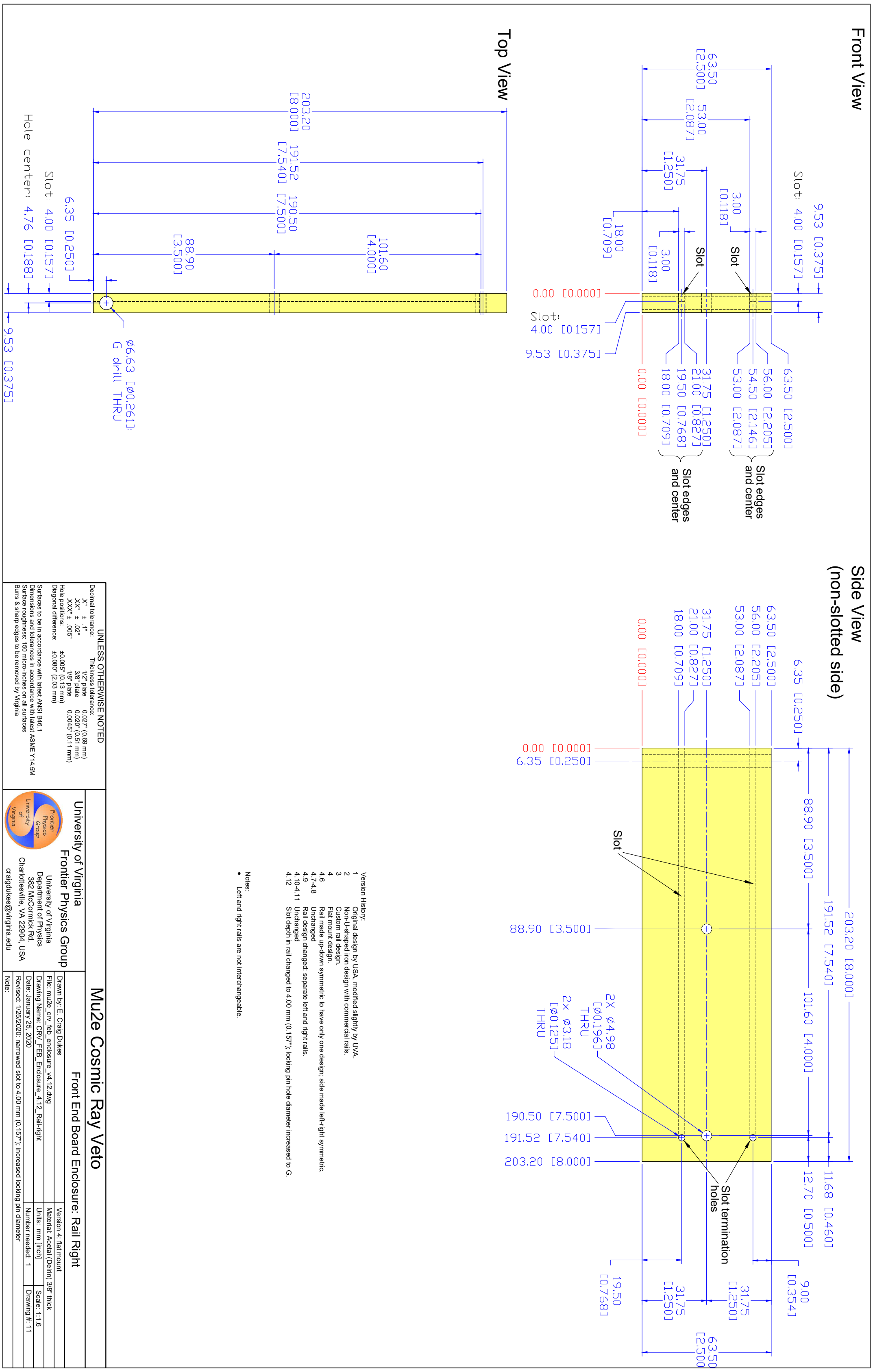

Figure J.11.: Drawing of FEBE right side FEB rail.

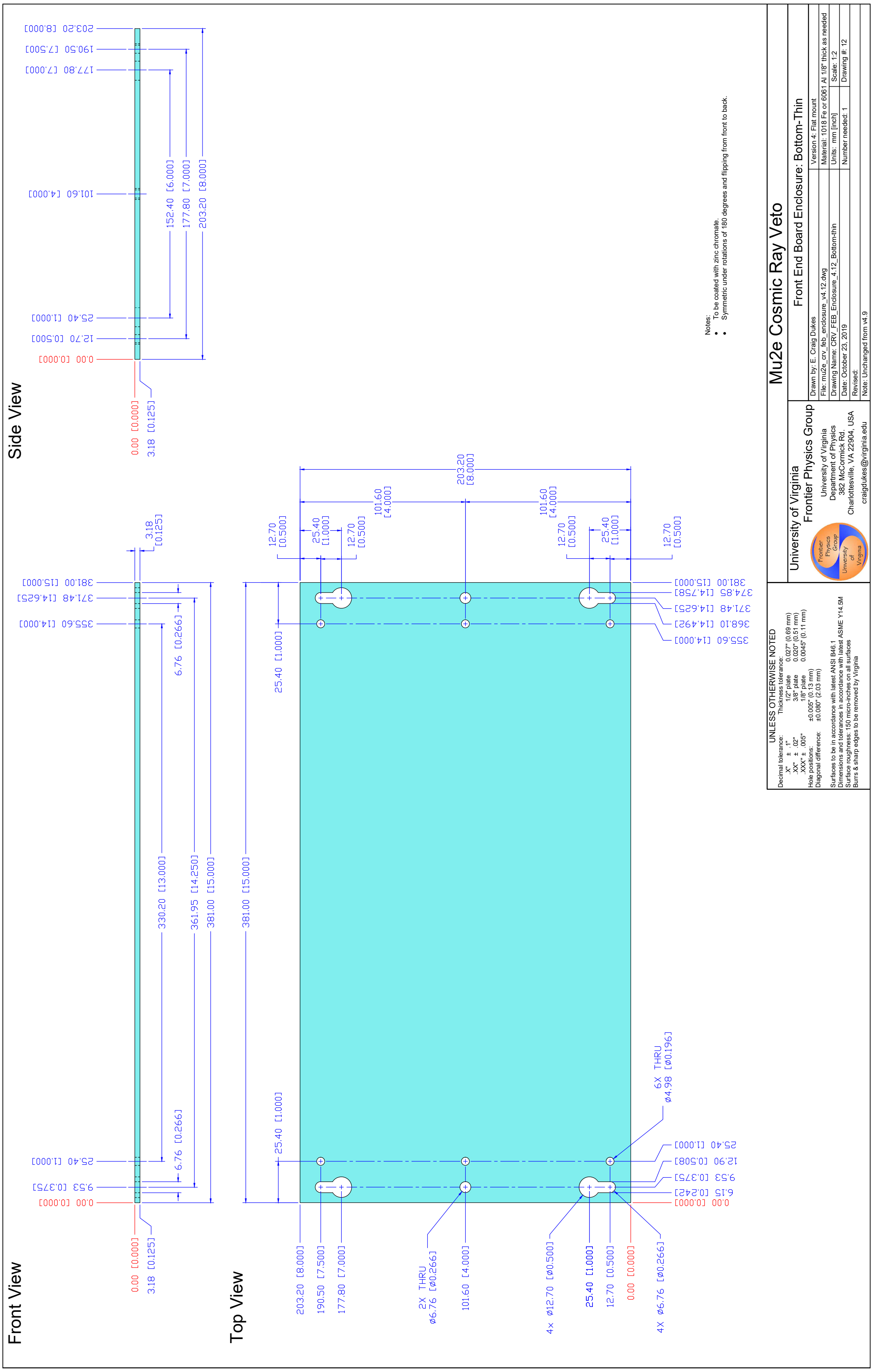

Figure J.12.: Drawing of FEBE thin bottom plate.

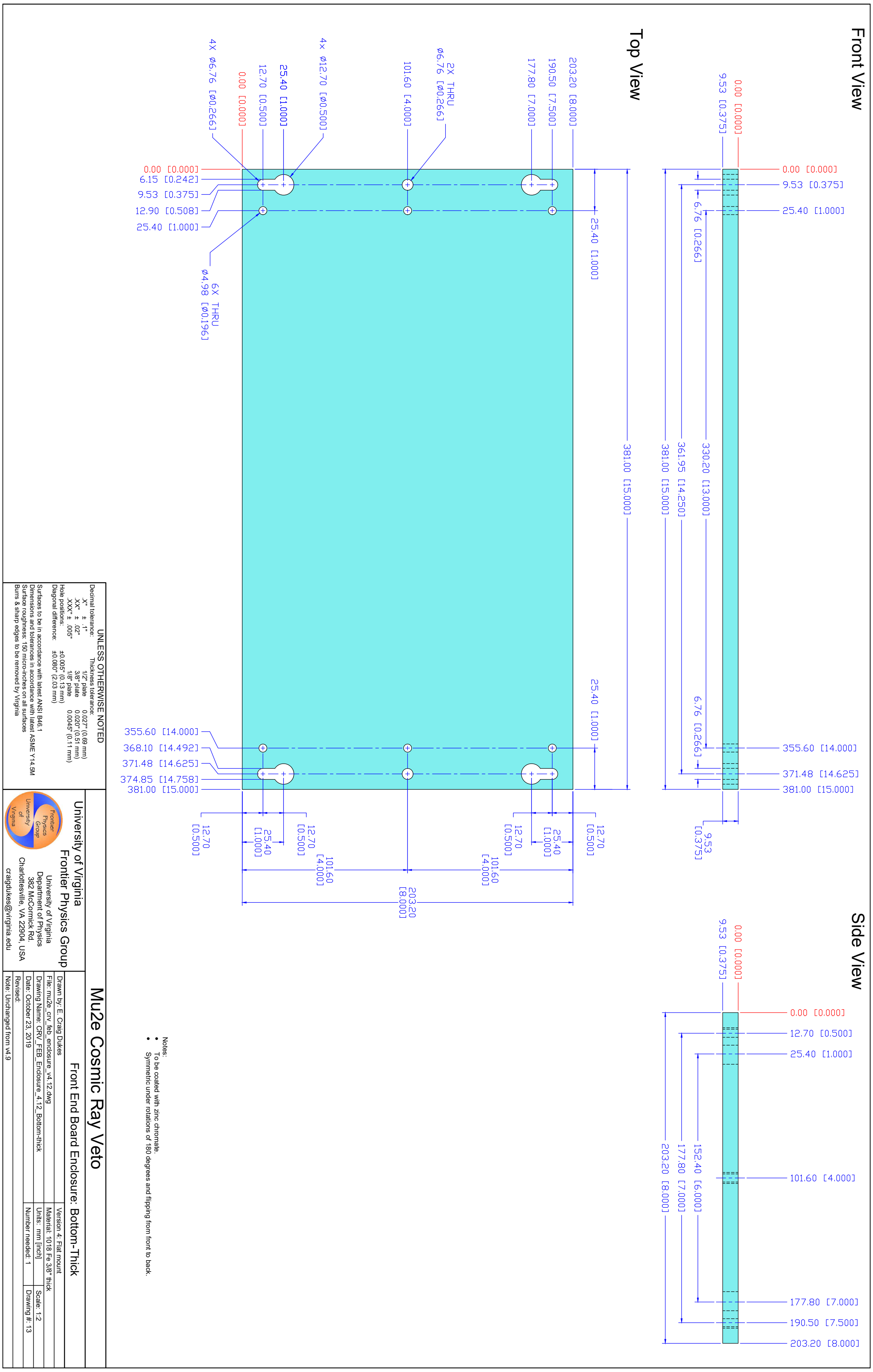

Figure J.13.: Drawing of FEBE thick bottom plate.

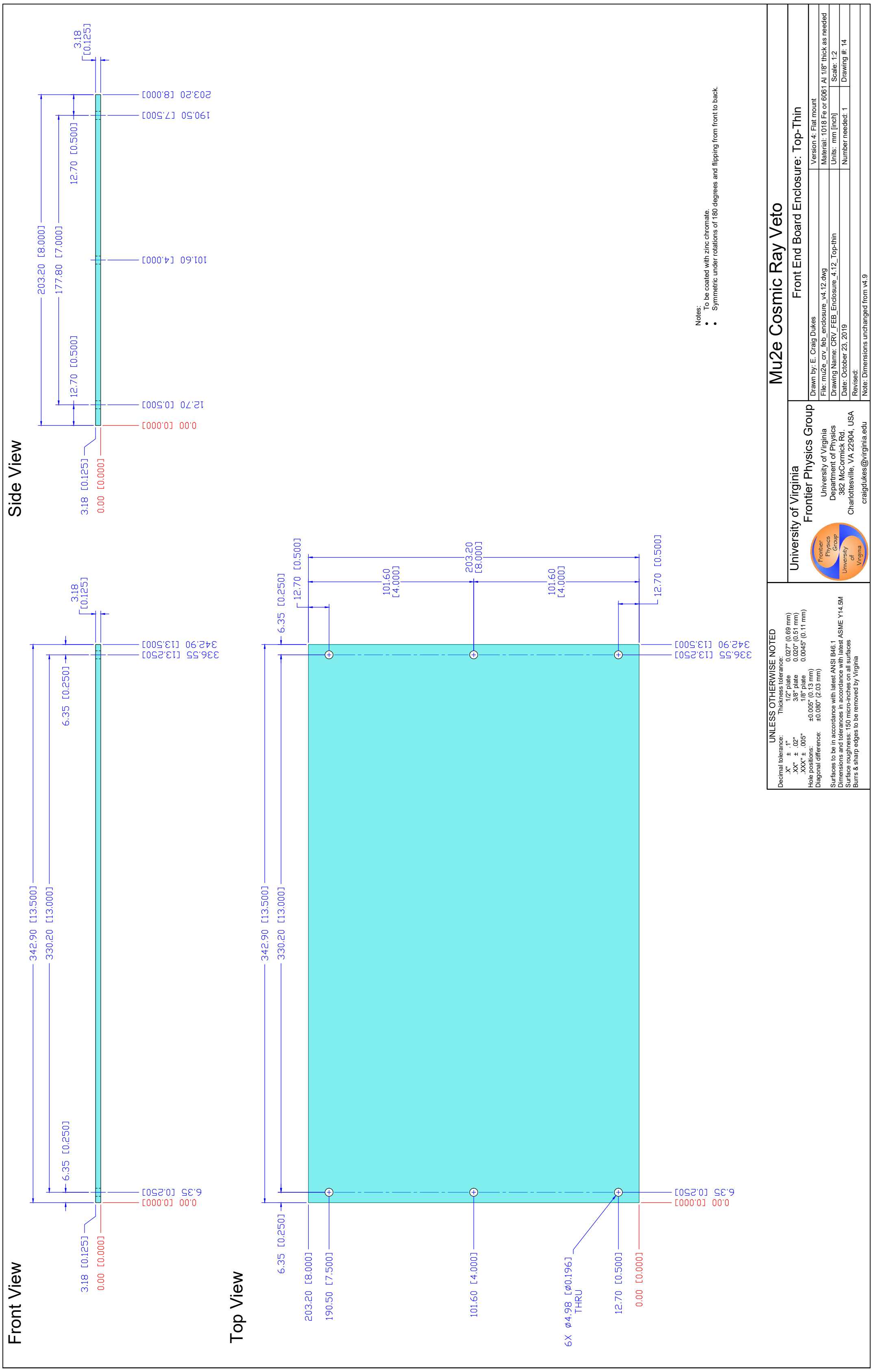

Figure J.14.: Drawing of FEBE thin top plate.

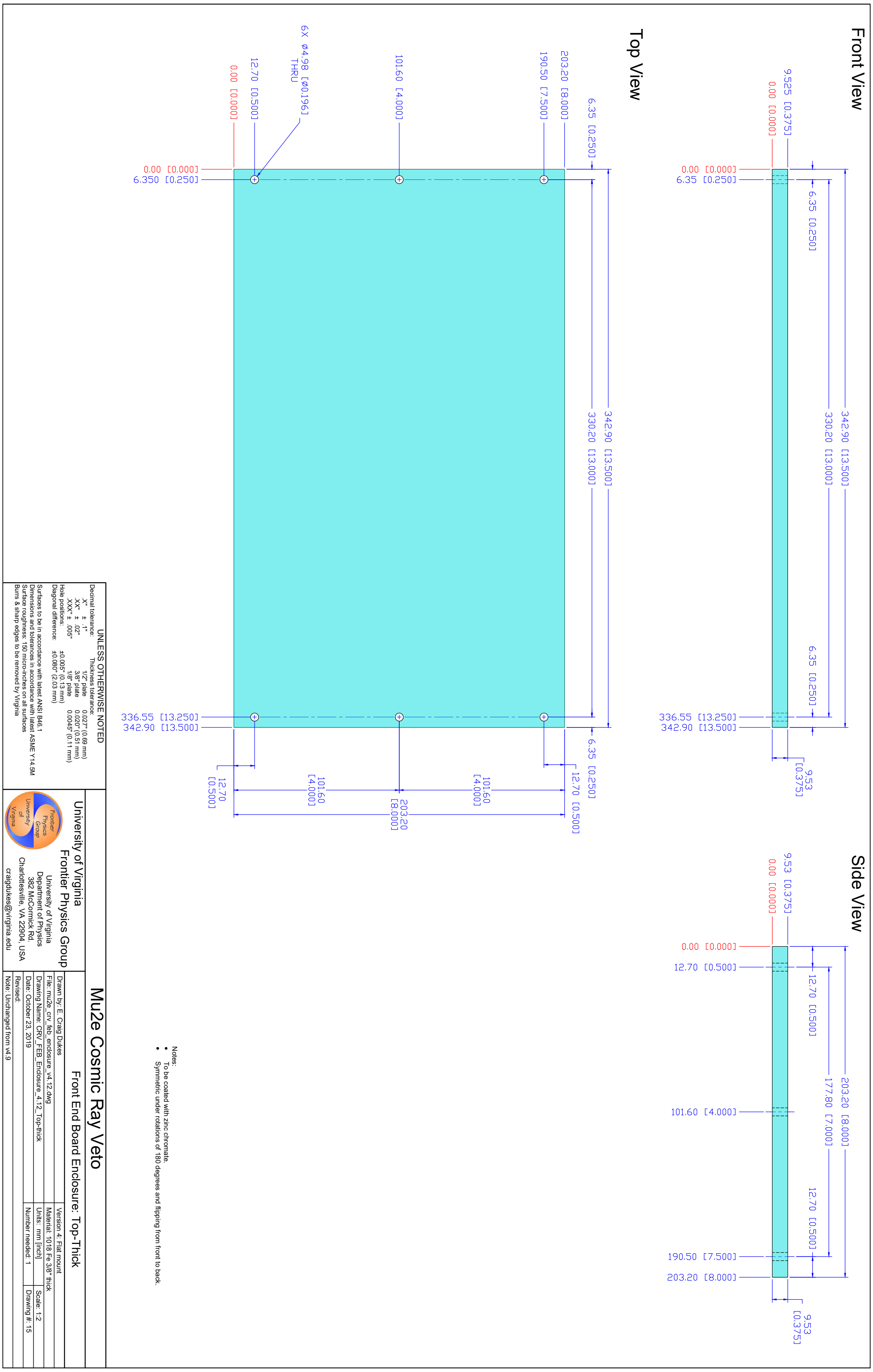

Figure J.15.: Drawing of FEBE thick top plate.

Appendix K.

Counter Motherboard Schematic

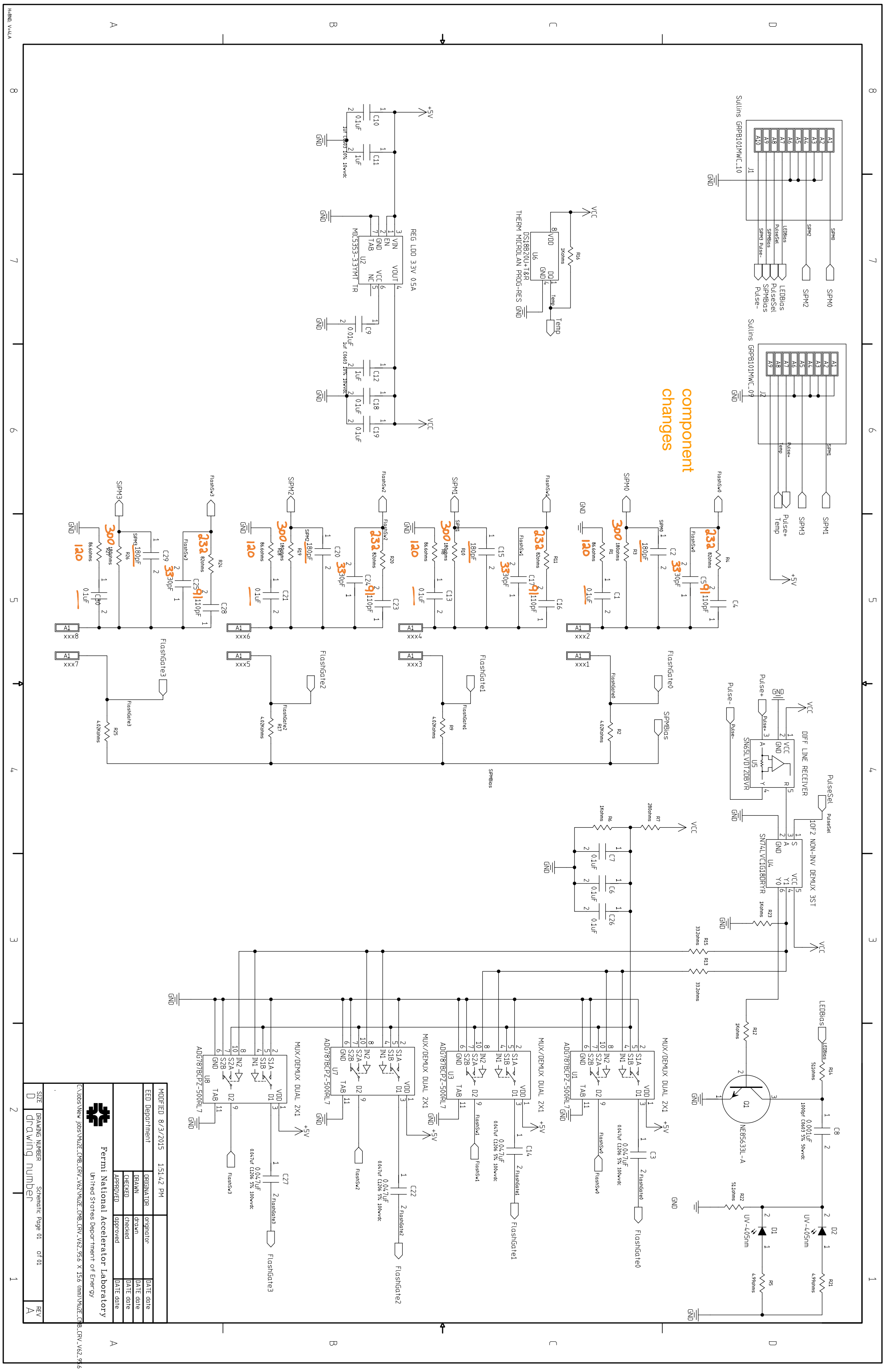

Figure K.1.: Schematic of the Counter Motherboard (CMB).

Appendix L.

Front End Board Schematic

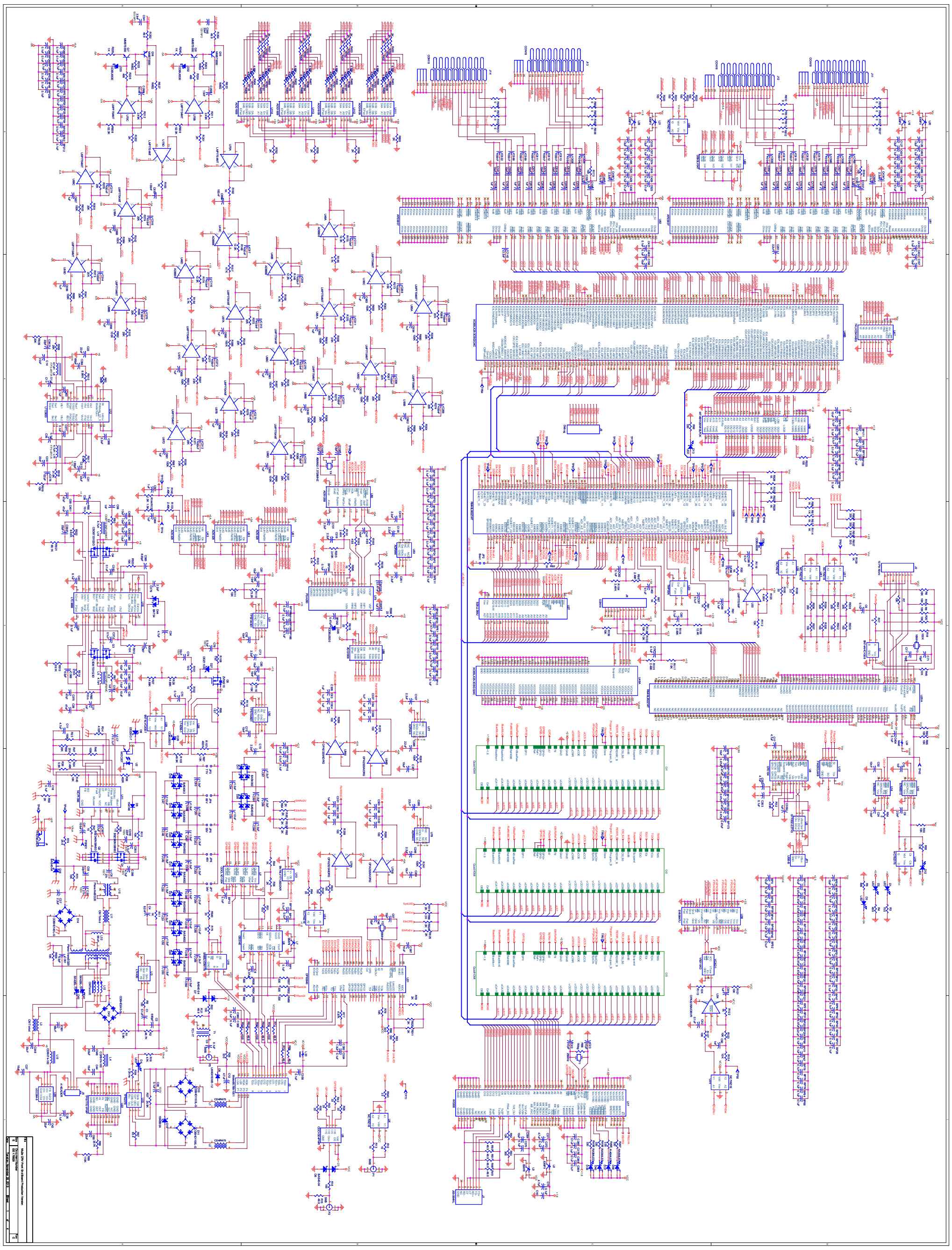

Figure L.1.: Schematic of the Front End Board (FEB).

Appendix M.

Front End Board Data Format

Table M.1.: For each spill there are multiple events/triggers. The FEB will send a header for each spill, followed by a header for every event. Each event contains, sequentially, each channel and its associated samples. The spill header is shown left, the event header in the middle, and the event data on the right. All words are 16 bits.

Spill Header:

Word #	Contents
1	Total Spill Word Count, Upper Bits
2	Total Spill Word Count, Lower Bits
3	Spill Trigger Count, Upper Bits
4	Spill Trigger Count, Lower Bits
5	Spill Count
6	Channel Mask
7	Board ID
8	Spill Status, Bits: [2..0]

Event Header:

Word #	Contents
1	Event Word Count
2	Event Time Stamp, Upper Bits
3	Event Time Stamp, Lower Bits
4	Trigger Count, Upper Bits
5	Trigger Count, Lower Bits
6	Number of ADC Samples Per Event, Bits[7..0]
7	Trigger Type, Bits [3..0]
8	Event Status, Bits: [2..0]

Event Data:

Word #	Contents
1	Channel 0, Bits: [5..0]
2	ADC Sample 1, Bits: [11..0]
...	...
N+1	ADC Sample N, Bits: [11..0]
(N+1)+1	Channel 1, Bits: [5..0]
(N+1)+2	ADC Sample 1, Bits: [5..0]
...	...
2N+1	ADC Sample N, Bits: [5..0]
...	...
M(N+1)+1	Channel M, Bits: [5..0]
M(N+1)+2	ADC Sample 1, Bits: [5..0]
...	...
(M+1)(N+1)	ADC Sample N, Bits: [5..0]

Appendix N.

Readout Controller Schematic

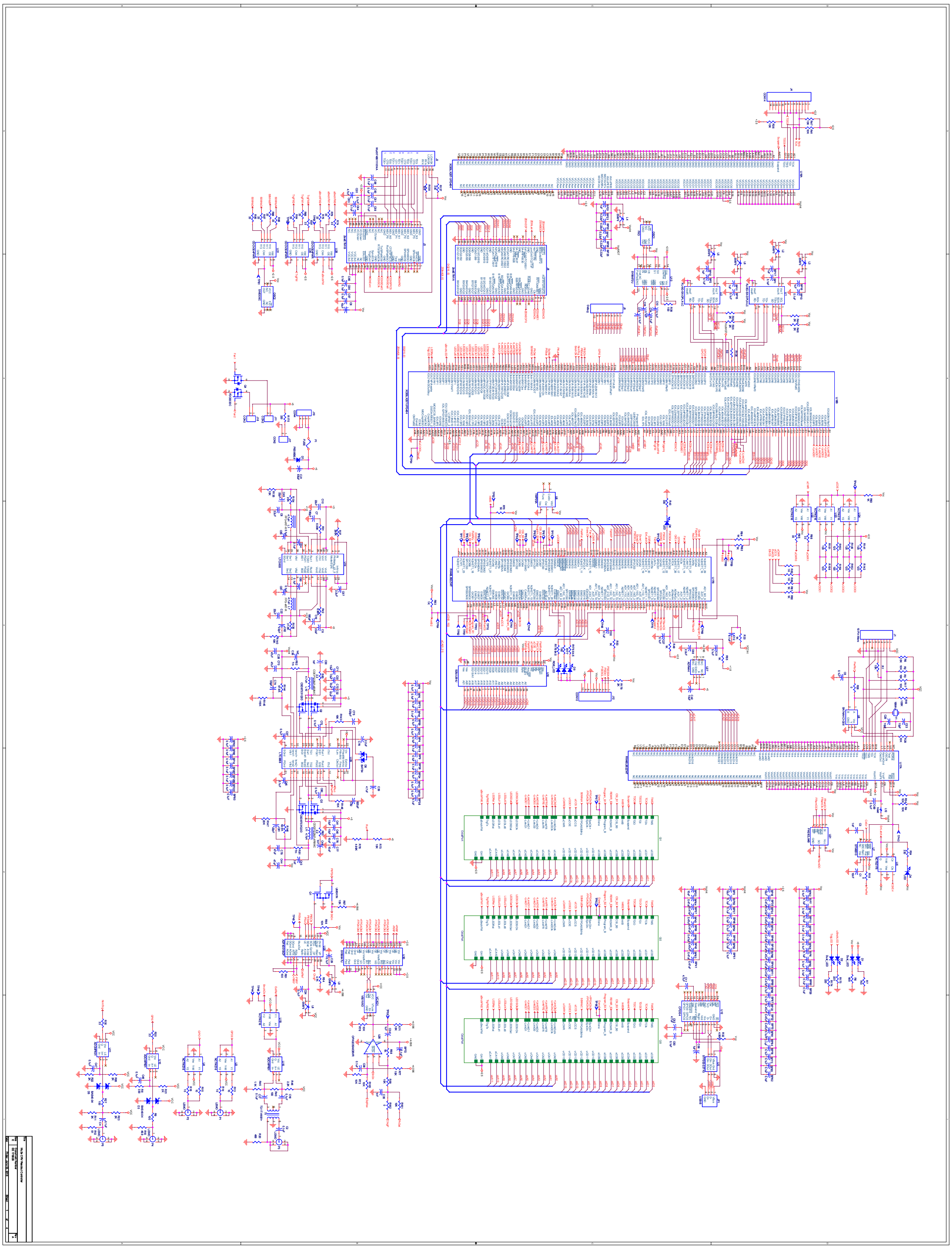

Figure N.1.: Schematic of the Readout Controller (ROC).

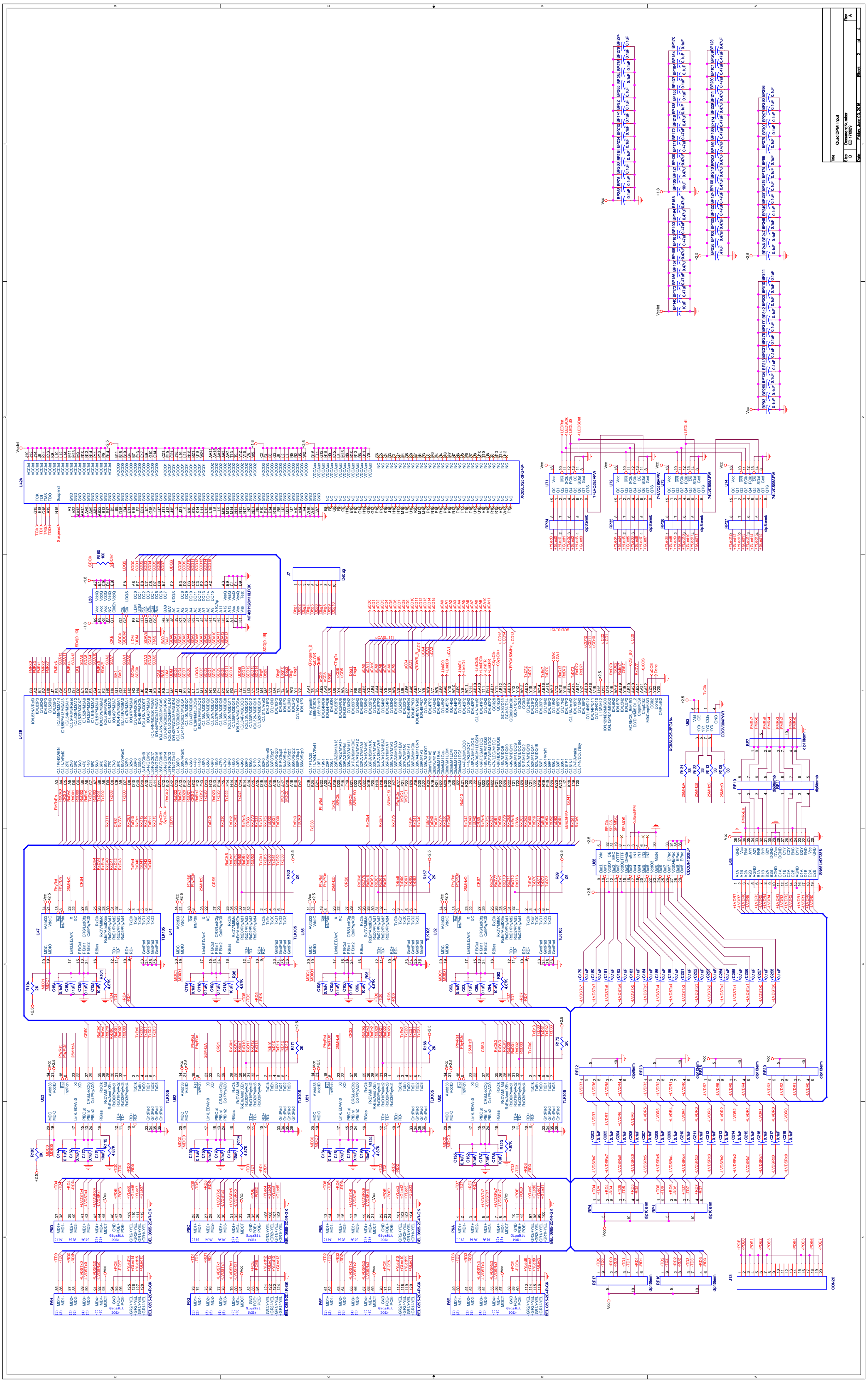

Figure N.2.: Schematic of one of the three octal ports of the Readout Controller (ROC).

Appendix O.

Readout Controller Status Format

Table O.1.: FEB status information. Each FEB sends status information to the ROC. Status information is broken up into five distinct blocks, the first of which contains general board information, shown in the left table, followed by information for each of the FPGAs, shown in the right table. All words are 16 bits. Specific units are shown alongside numeric quantities.

Word #	Contents
1	Board ID
2	Most Recent Spill Number
3	Board Temperature 0.1 °C
4	15 V supply monitor, mV
5	10 V supply monitor, mV
6	5 V supply monitor, mV
7	−5 V supply monitor, mV
8	3.3 V supply monitor, mV
9	2.5 V supply monitor, mV
10	1.8 V supply monitor, mV
11	1.2 V supply monitor, mV
12	SiPM Bias Bus0 monitor, 10 mV/count
13	SiPM Bias Bus1 monitor, 10 mV/count
...	...
19	SiPM Bias Bus7 monitor, 10 mV/count
20	Trigger Control register contents
21	Pipeline Length setting
22	Sample Length setting

Word #	Contents
1	Trim DAC 0 Setting
2	Trim DAC 1 Setting
...	...
15	Trim DAC 14 Setting
16	Trim DAC 15 Setting
17	LED Pulser DAC 0 Setting
...	...
20	LED Pulser DAC 3 Setting
21	Bias Bus0 DAC Setting
22	Bias Bus1 DAC Setting
23	AFE 0 Gain DAC Setting
24	AFE 1 Gain DAC Setting
25	CMB 0 Temperature 0.1 °C
...	...
28	CMB 3 Temperature 0.1 °C
29	AFE 0 Register 0x01
30	AFE 0 Register 0x02
31	AFE 0 Register 0x33
32	AFE 0 Register 0x34
33	AFE 0 Register 0x35
34	AFE 1 Register 0x01
35	AFE 1 Register 0x02
36	AFE 1 Register 0x33
37	AFE 1 Register 0x34
38	AFE 1 Register 0x35

Appendix P.

Cosmic Ray Test Stand Scintillator Counter Drawings

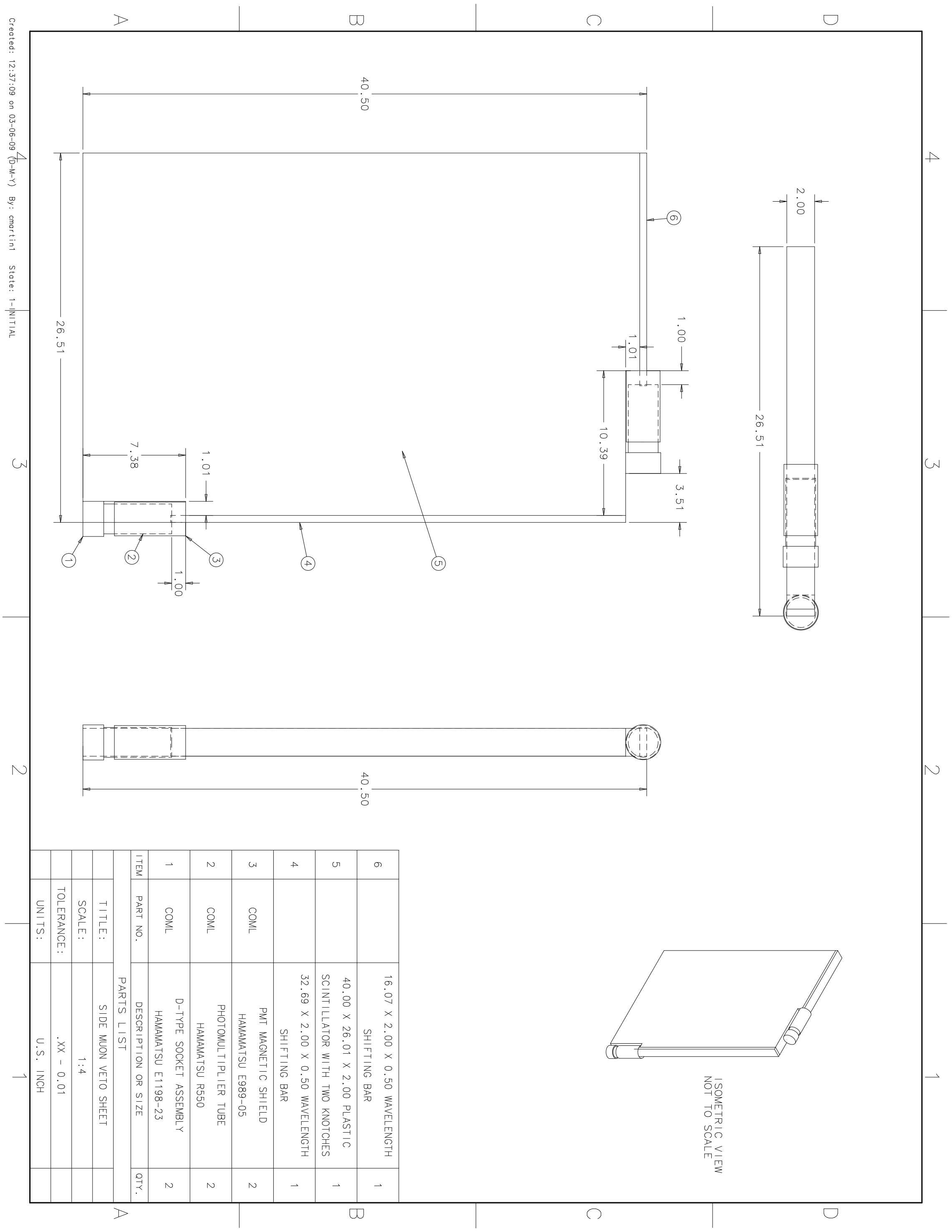

Figure P.1.: Drawing of the top scintillator counter used in the CRTS.

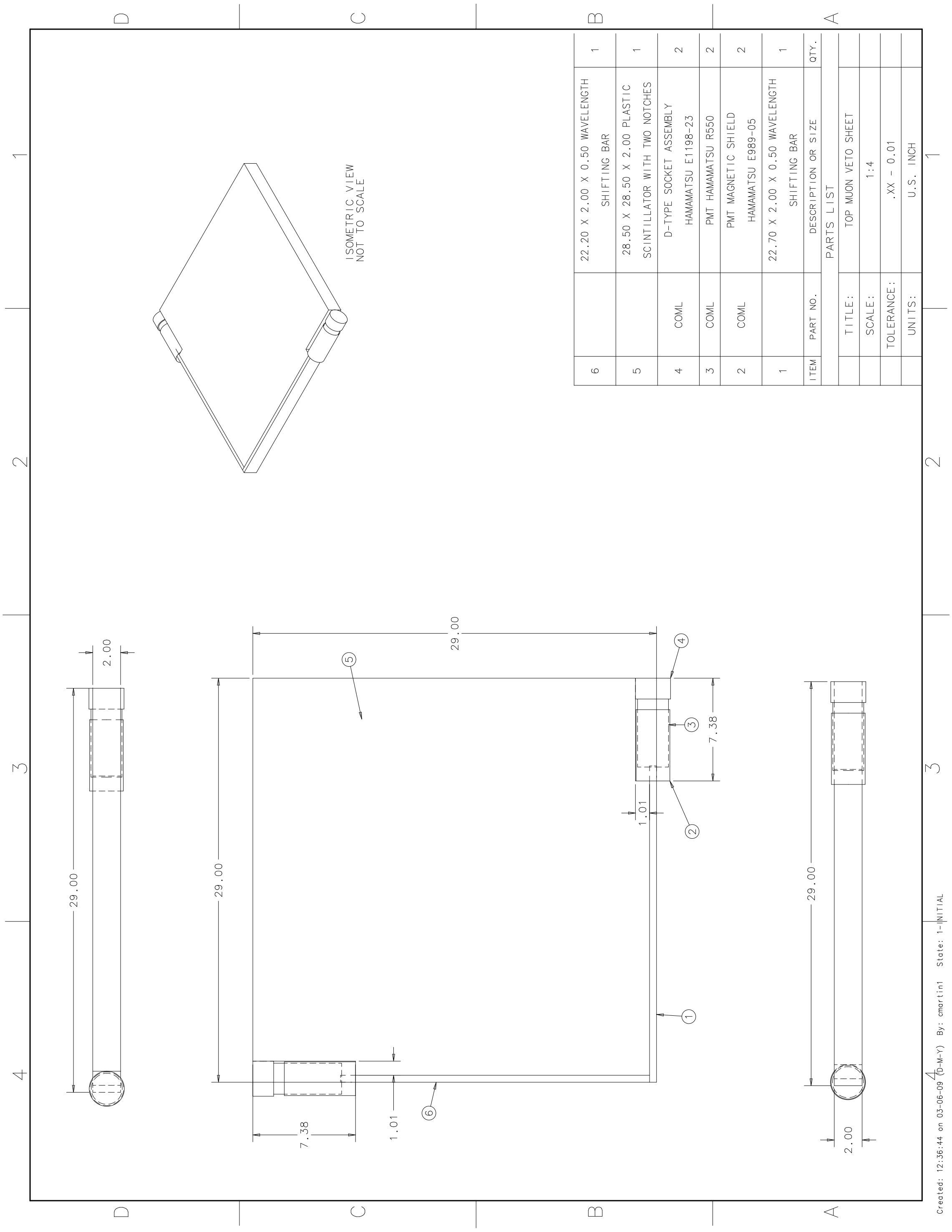

Figure P.2.: Drawing of the bottom scintillator counter used in the CRTS.

Appendix Q.

Cathode Strip Chamber Residuals

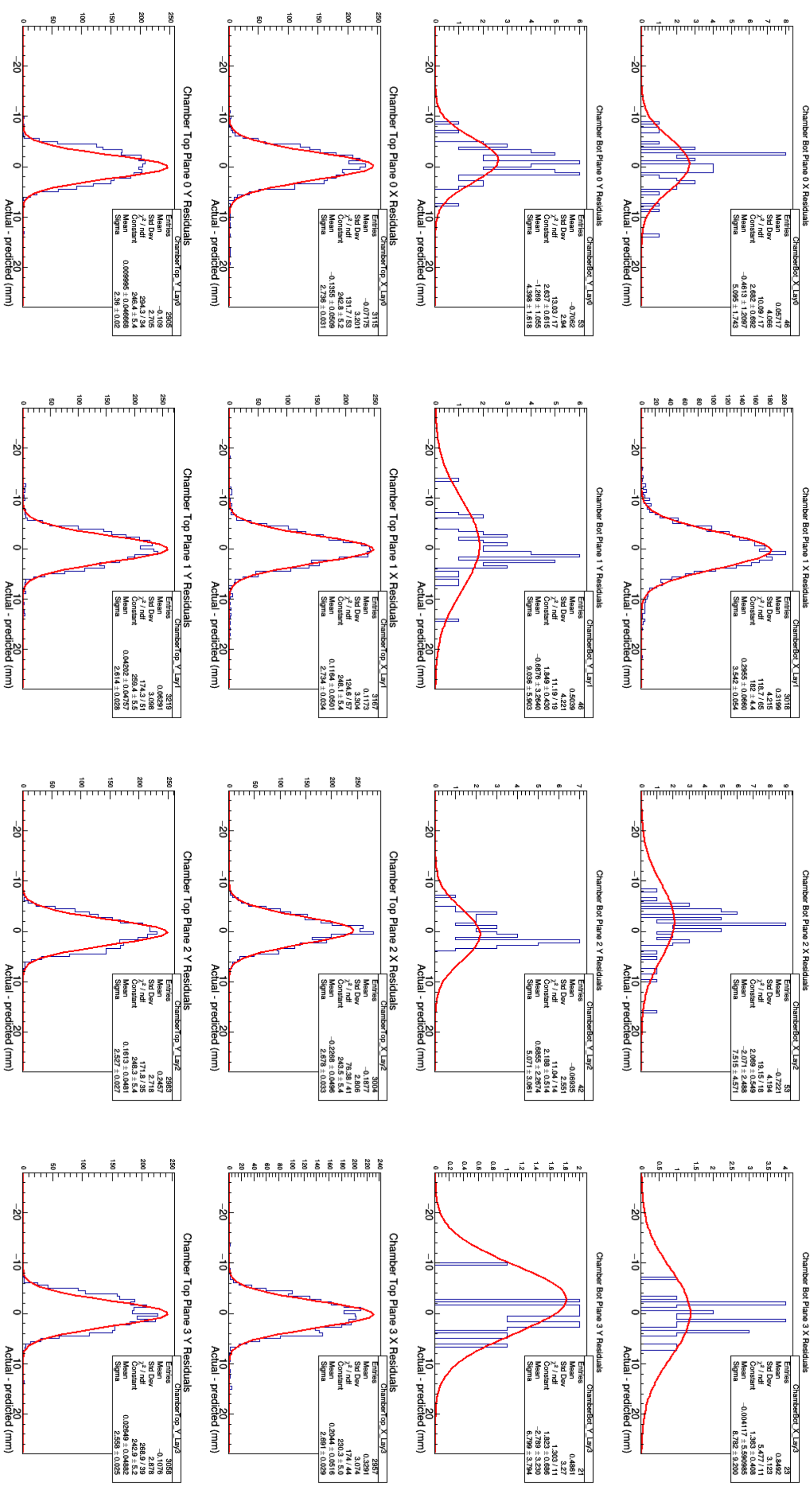

Figure Q.1.: Residuals for each plane of CSC1 (Top CSC) and CSC2 (Bottom CSC). Due to problems with the readout electronics, the statistics are very low, especially in the bottom CSC. The red lines are a Gaussian fit to the distributions.

Appendix R.

Module Light Yields

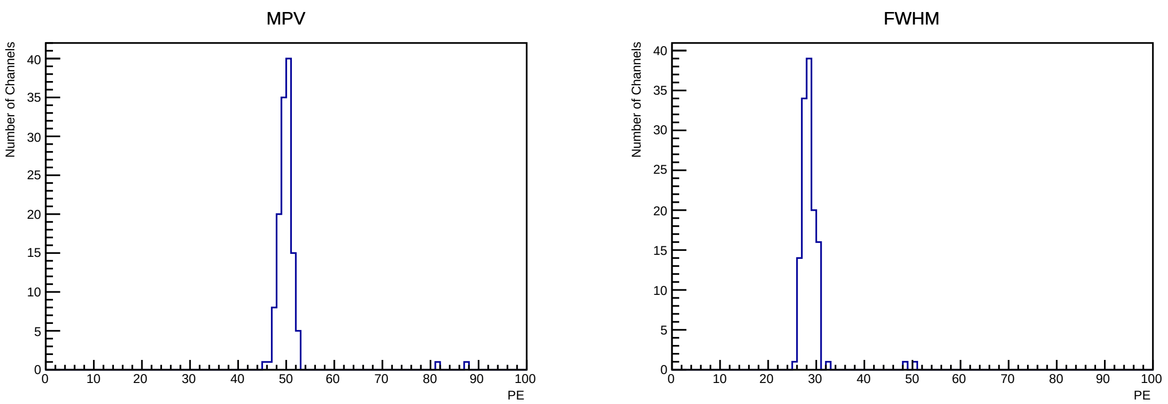

Figure R.1.: PE yield measured for Module 101 at $1.0 \pm 0.4\,\mathrm{m}$ from the readout end.

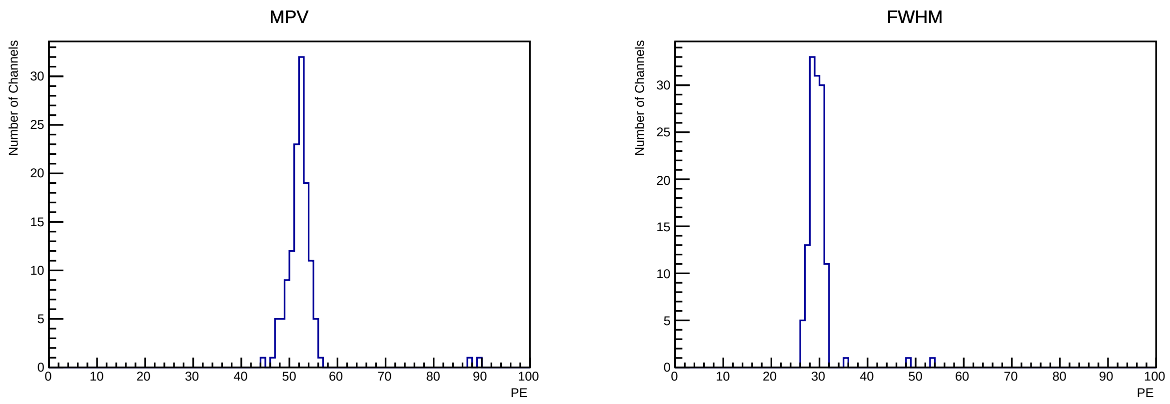

Figure R.2.: PE yield measured for Module 102 at $1.0 \pm 0.4\,\mathrm{m}$ from the readout end.

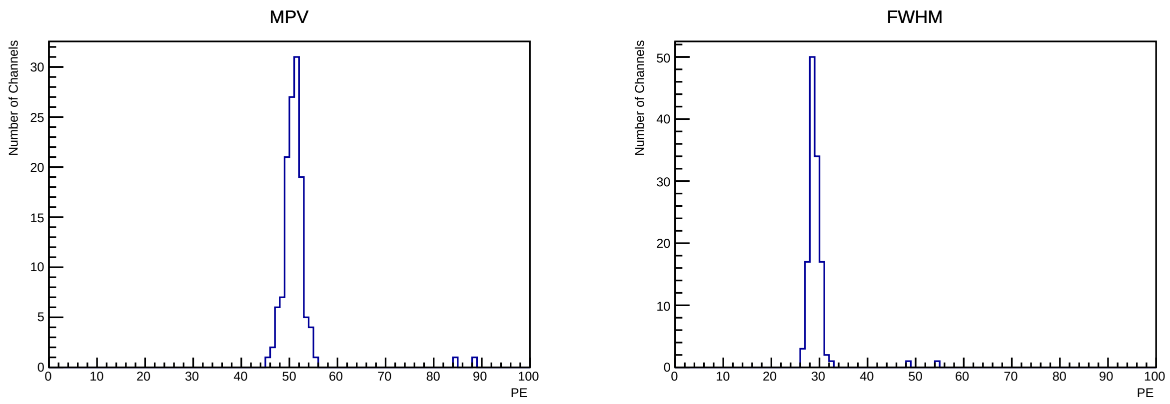

Figure R.3.: PE yield measured for Module 104 at $1.0 \pm 0.4\,\mathrm{m}$ from the readout end.

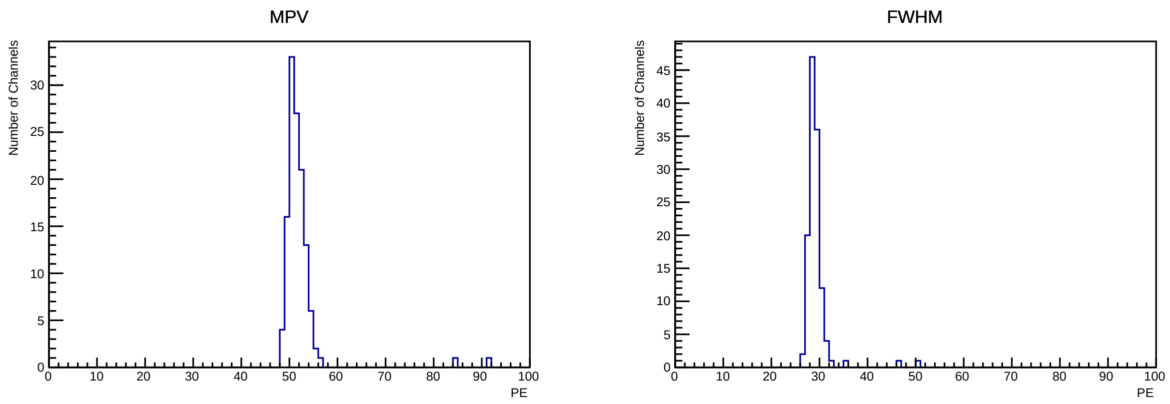

Figure R.4.: PE yield measured for Module 105 at $1.0 \pm 0.4\,\mathrm{m}$ from the readout end.

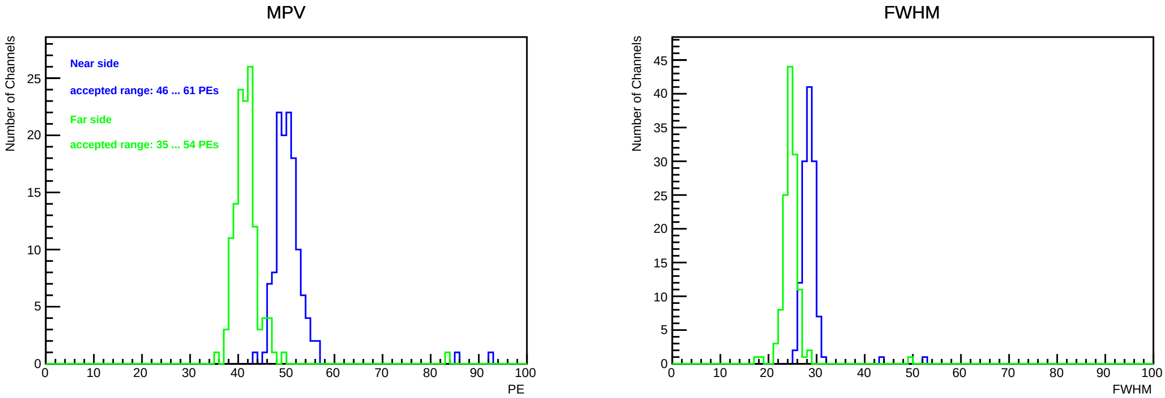

Figure R.5.: PE yield measured for Module 106 at $1.0 \pm 0.4\,\mathrm{m}$ from the readout end.

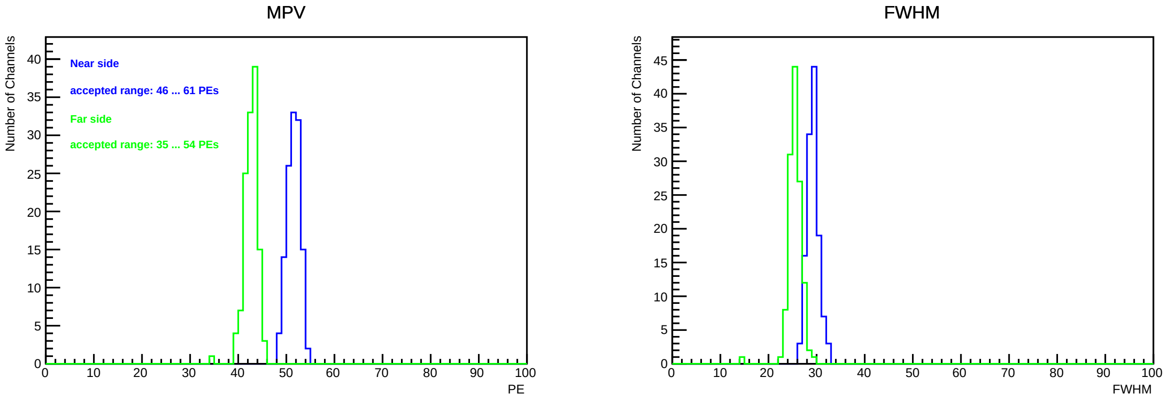

Figure R.6.: PE yield measured for Module 107 at $1.0 \pm 0.4\,\mathrm{m}$ from the readout end.

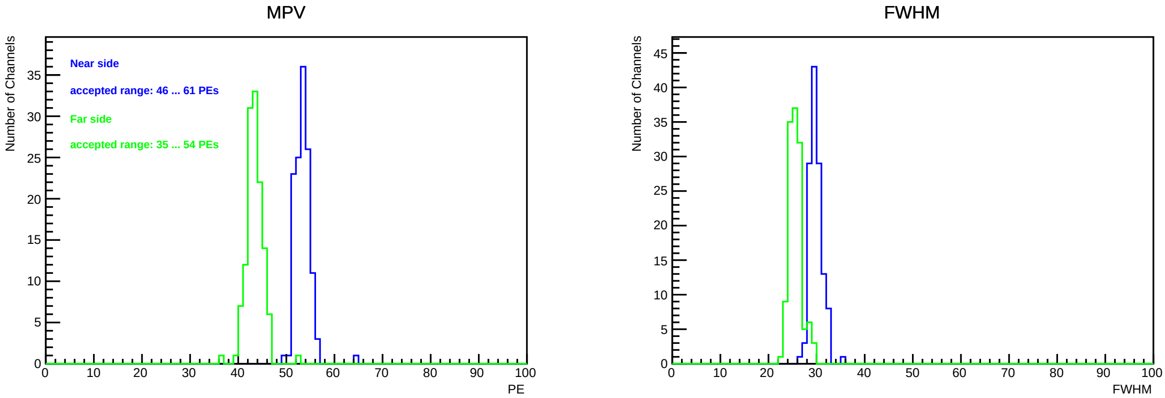

Figure R.7.: PE yield measured for Module 108 at $1.0 \pm 0.4\,\mathrm{m}$ from the readout end.

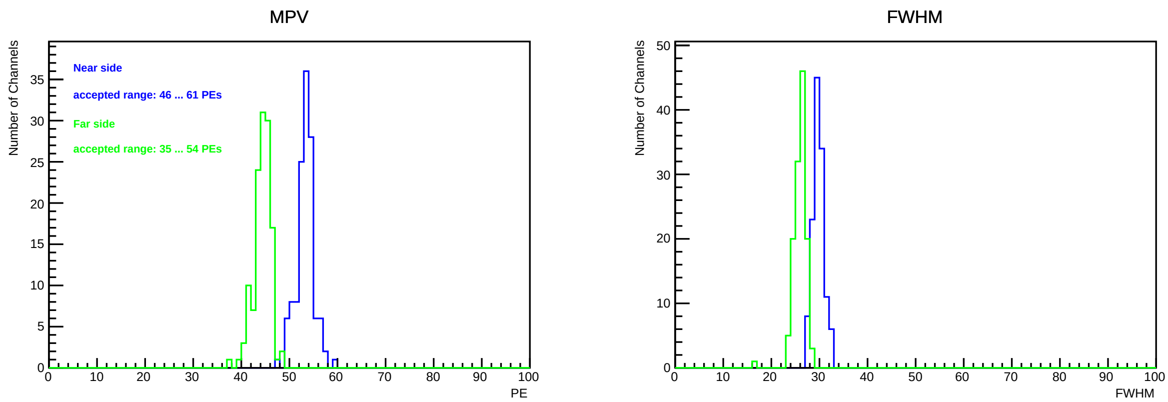

Figure R.8.: PE yield measured for Module 109 at $1.0 \pm 0.4\,\mathrm{m}$ from the readout end.

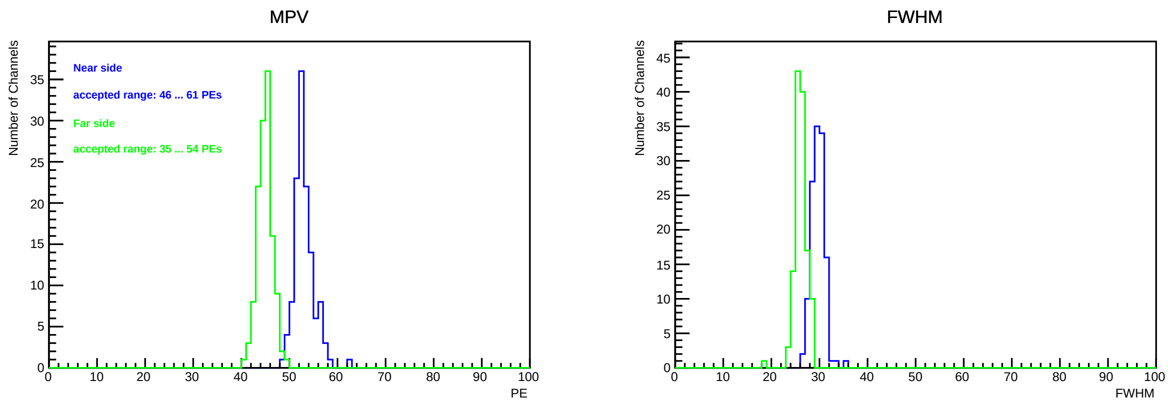

Figure R.9.: PE yield measured for Module 110 at $1.0 \pm 0.4\,\mathrm{m}$ from the readout end.

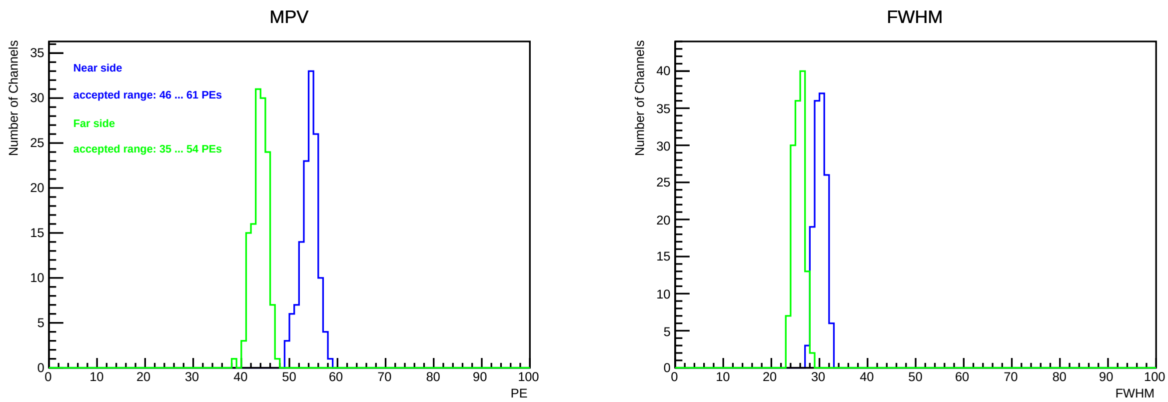

Figure R.10.: PE yield measured for Module 111 at $1.0 \pm 0.4\,\mathrm{m}$ from the readout end.

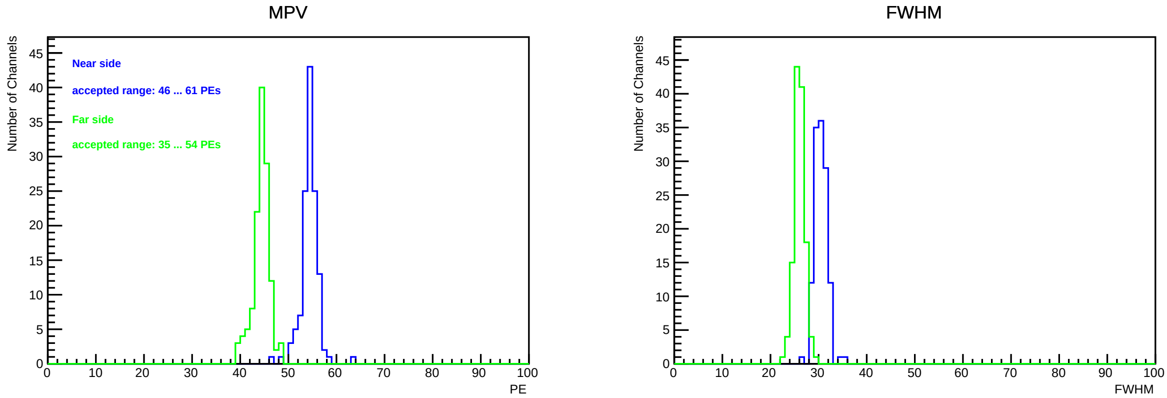

Figure R.11.: PE yield measured for Module 112 at 1.0 ± 0.4 m from the readout end.

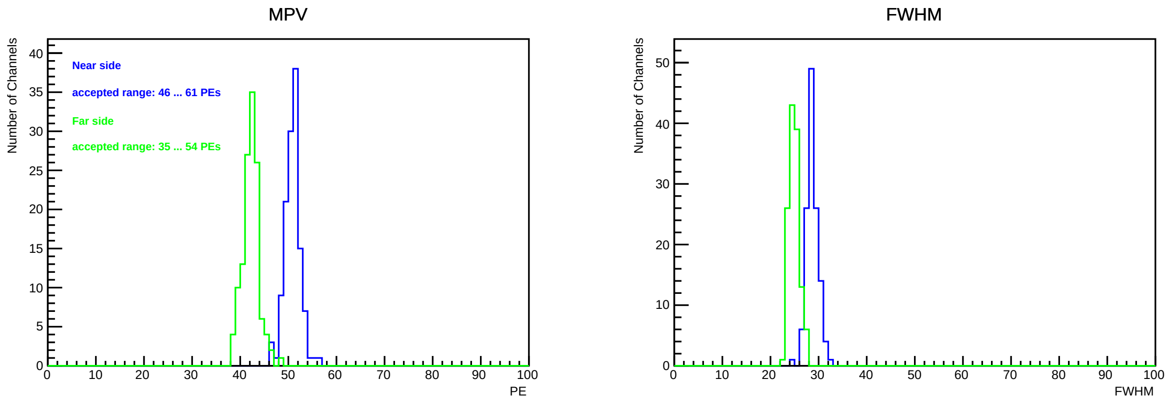

Figure R.12.: PE yield measured for Module 113 at 1.0 ± 0.4 m from the readout end.

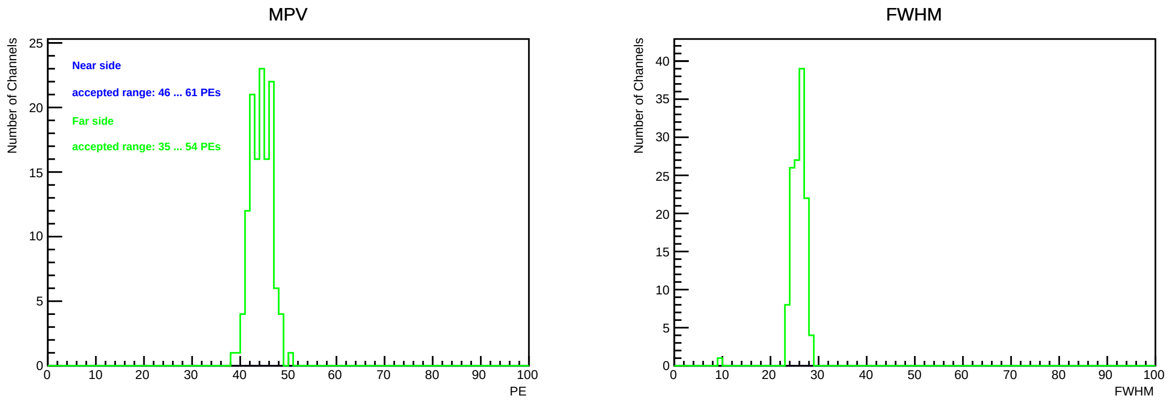

Figure R.13.: PE yield measured for Module 114 at 1.0 ± 0.4 m from the readout end.

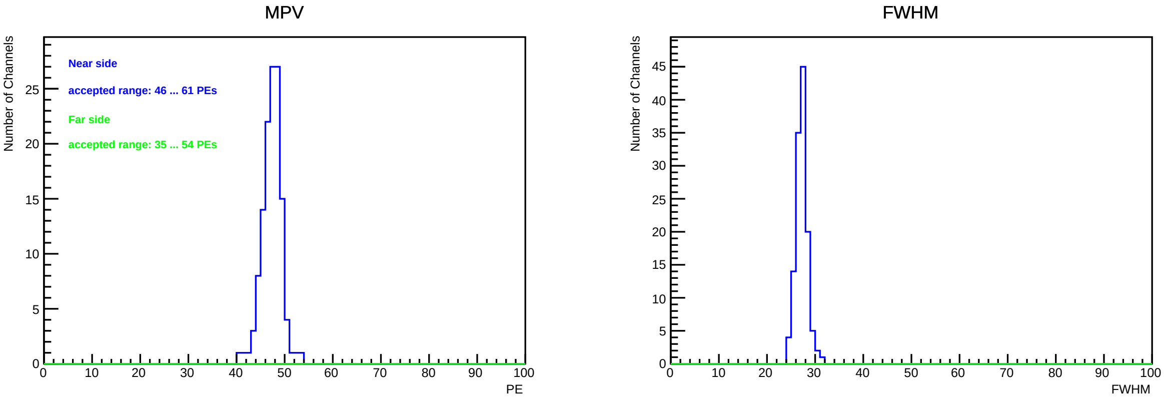

Figure R.14.: PE yield measured for Module 115 at 1.0 ± 0.4 m from the readout end.

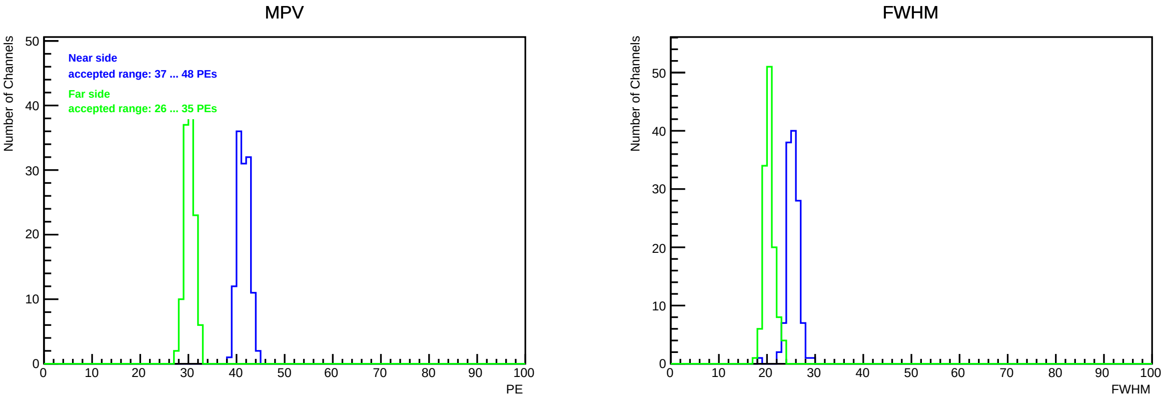

Figure R.15.: PE yield measured for Module 116 at 1.0 ± 0.4 m from the readout end.

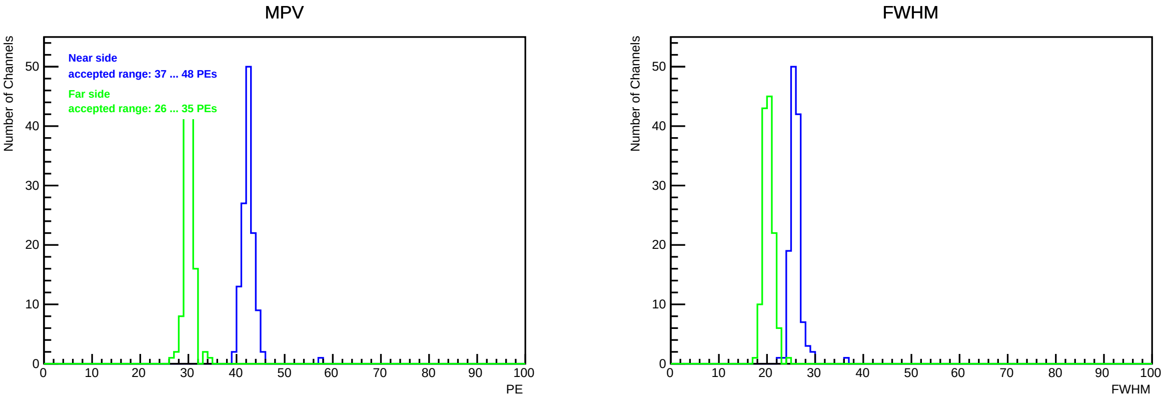

Figure R.16.: PE yield measured for Module 117 at 1.0 ± 0.4 m from the readout end.

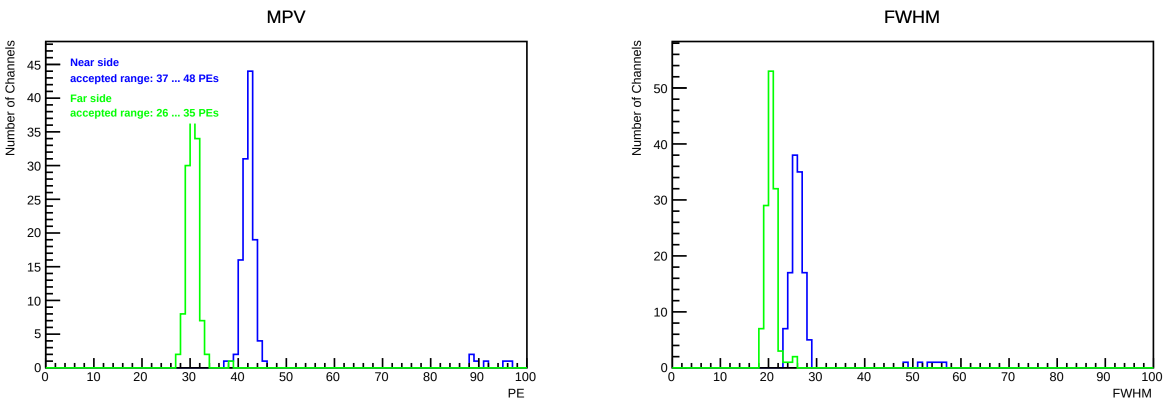

Figure R.17.: PE yield measured for Module 118 at $1.0 \pm 0.4\,\mathrm{m}$ from the readout end.

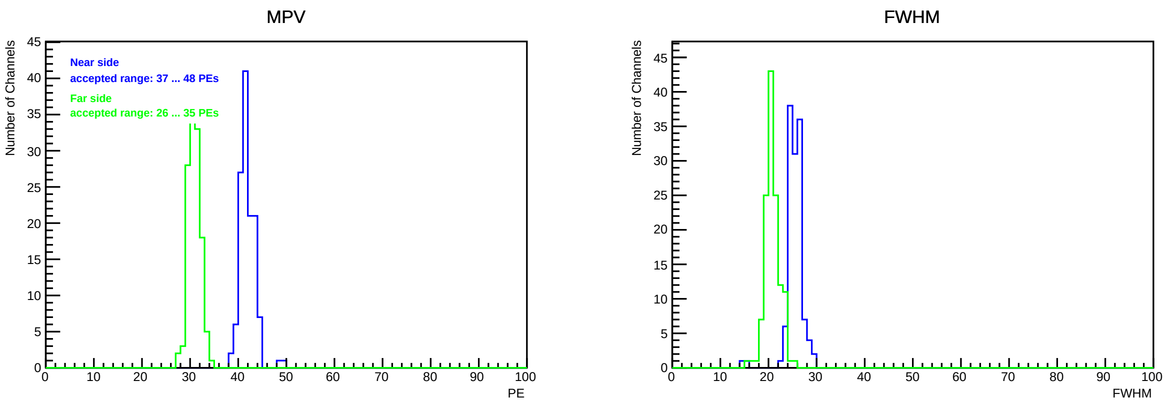

Figure R.18.: PE yield measured for Module 119 at $1.0 \pm 0.4\,\mathrm{m}$ from the readout end.

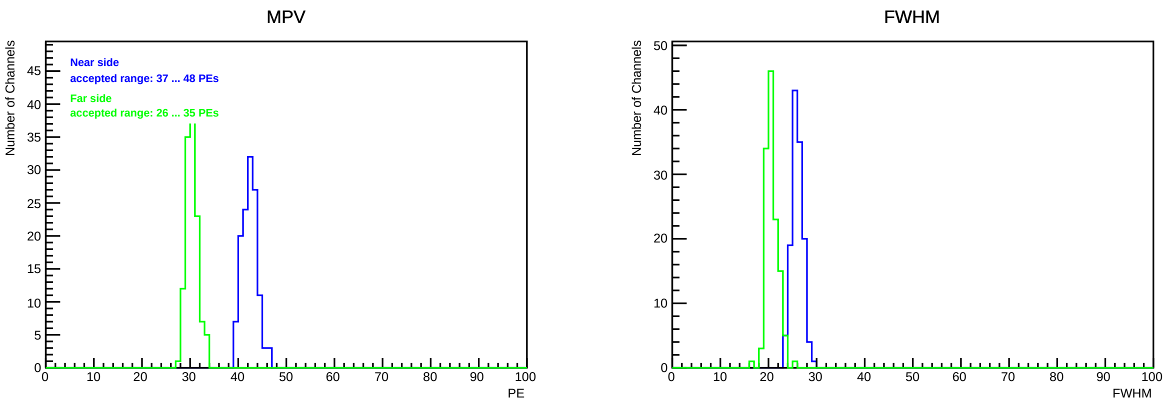

Figure R.19.: PE yield measured for Module 120 at $1.0 \pm 0.4\,\mathrm{m}$ from the readout end.

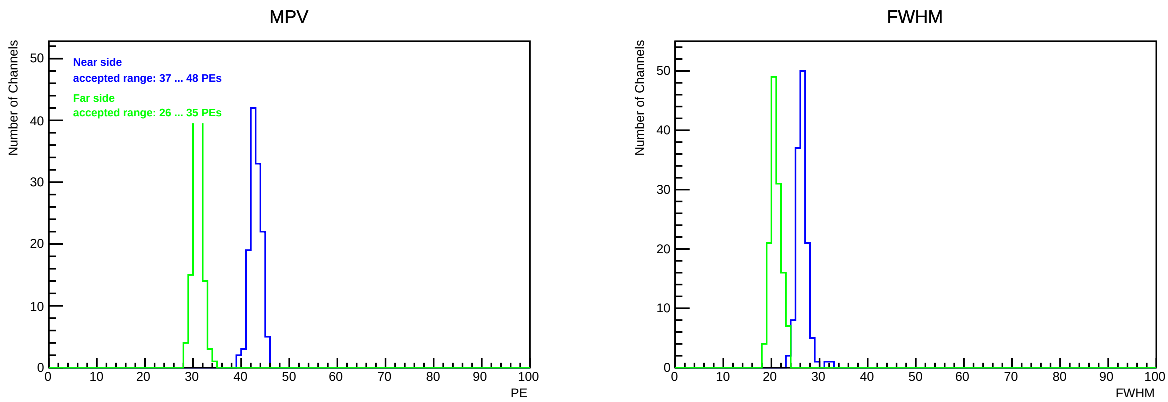

Figure R.20.: PE yield measured for Module 121 at $1.0 \pm 0.4\,\mathrm{m}$ from the readout end.

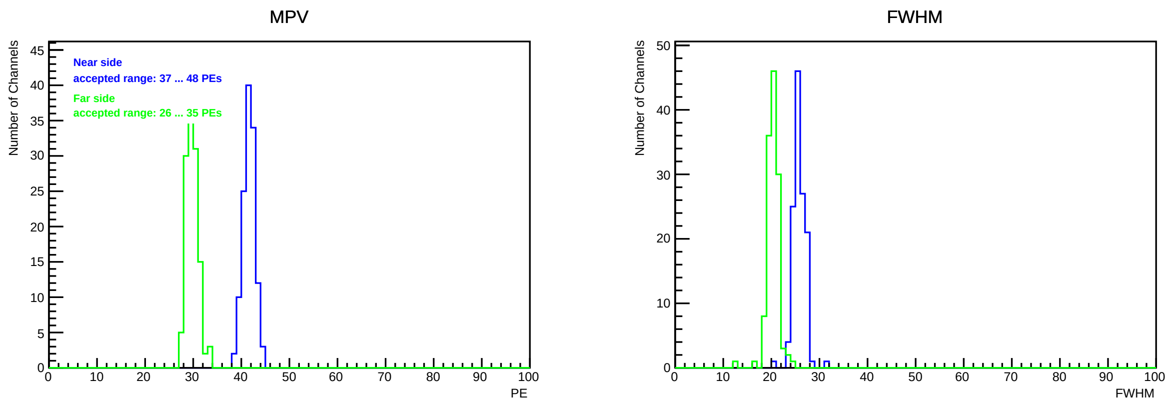

Figure R.21.: PE yield measured for Module 122 at $1.0 \pm 0.4\,\mathrm{m}$ from the readout end.

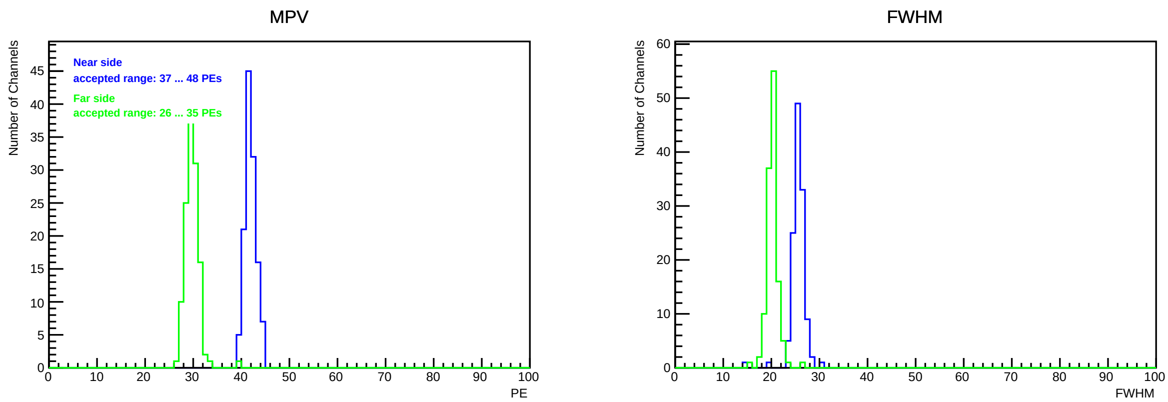

Figure R.22.: PE yield measured for Module 123 at $1.0 \pm 0.4\,\mathrm{m}$ from the readout end.

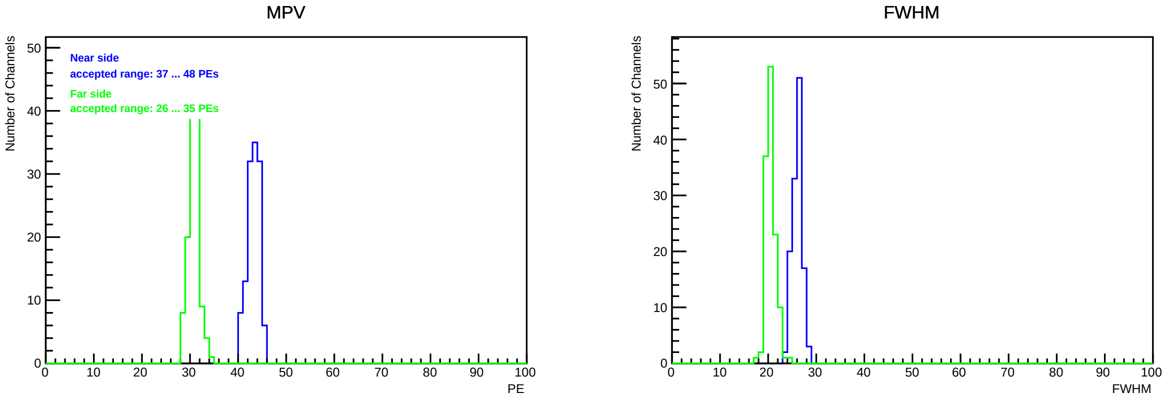

Figure R.23.: PE yield measured for Module 124 at $1.0 \pm 0.4\,\mathrm{m}$ from the readout end.

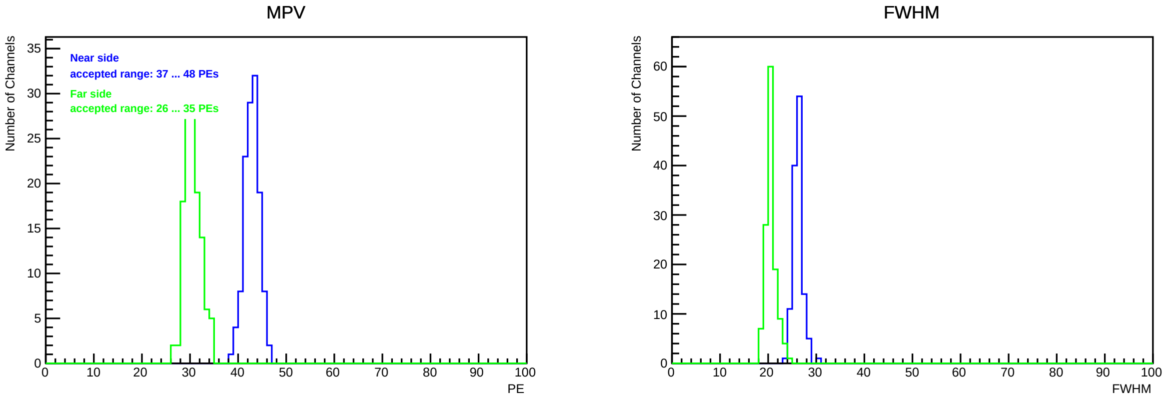

Figure R.24.: PE yield measured for Module 125 at $1.0 \pm 0.4\,\mathrm{m}$ from the readout end.

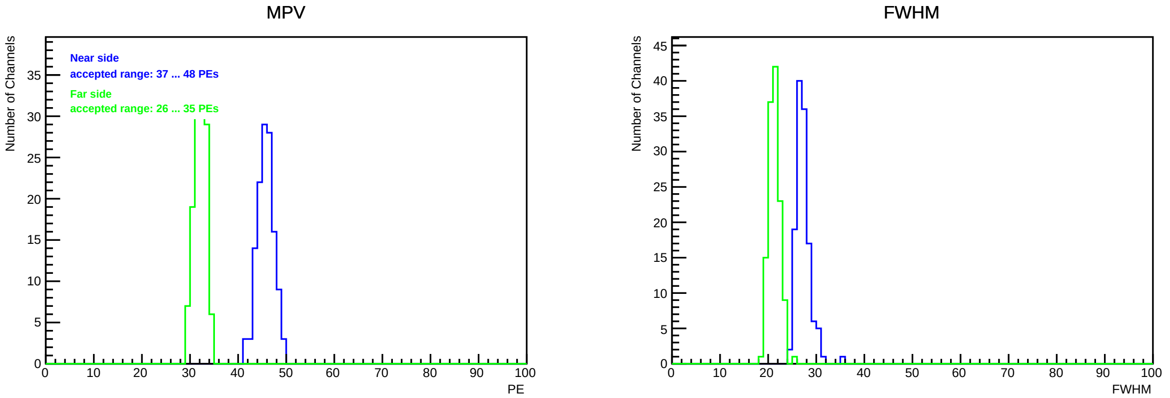

Figure R.25.: PE yield measured for Module 126 at $1.0 \pm 0.4\,\mathrm{m}$ from the readout end.

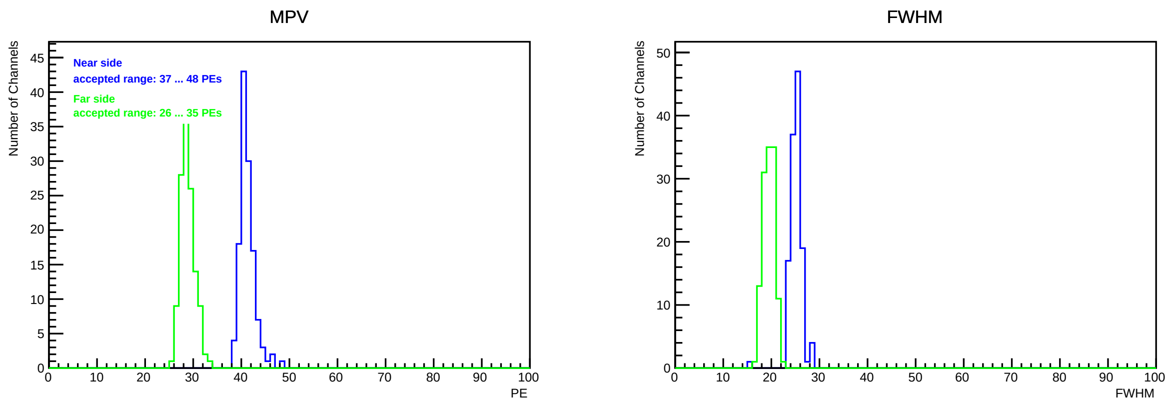

Figure R.26.: PE yield measured for Module 127 at 1.0 ± 0.4 m from the readout end.

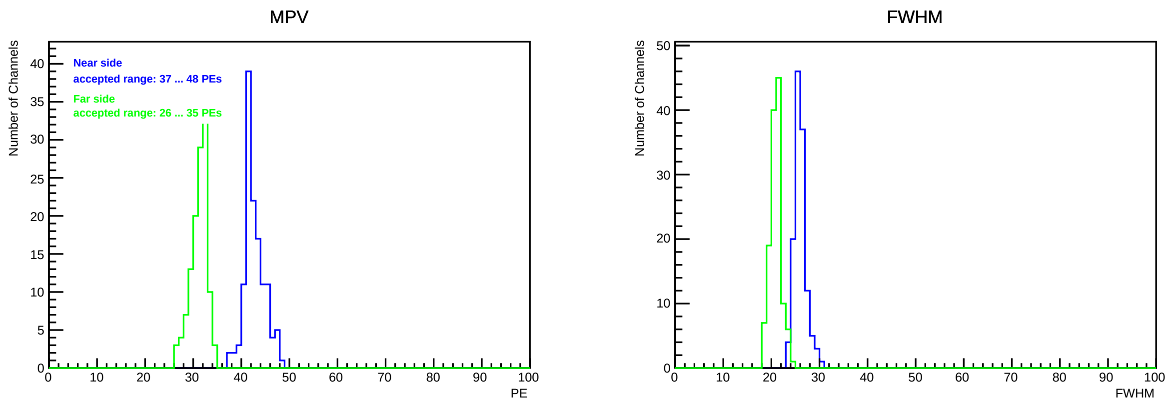

Figure R.27.: PE yield measured for Module 128 at 1.0 ± 0.4 m from the readout end.

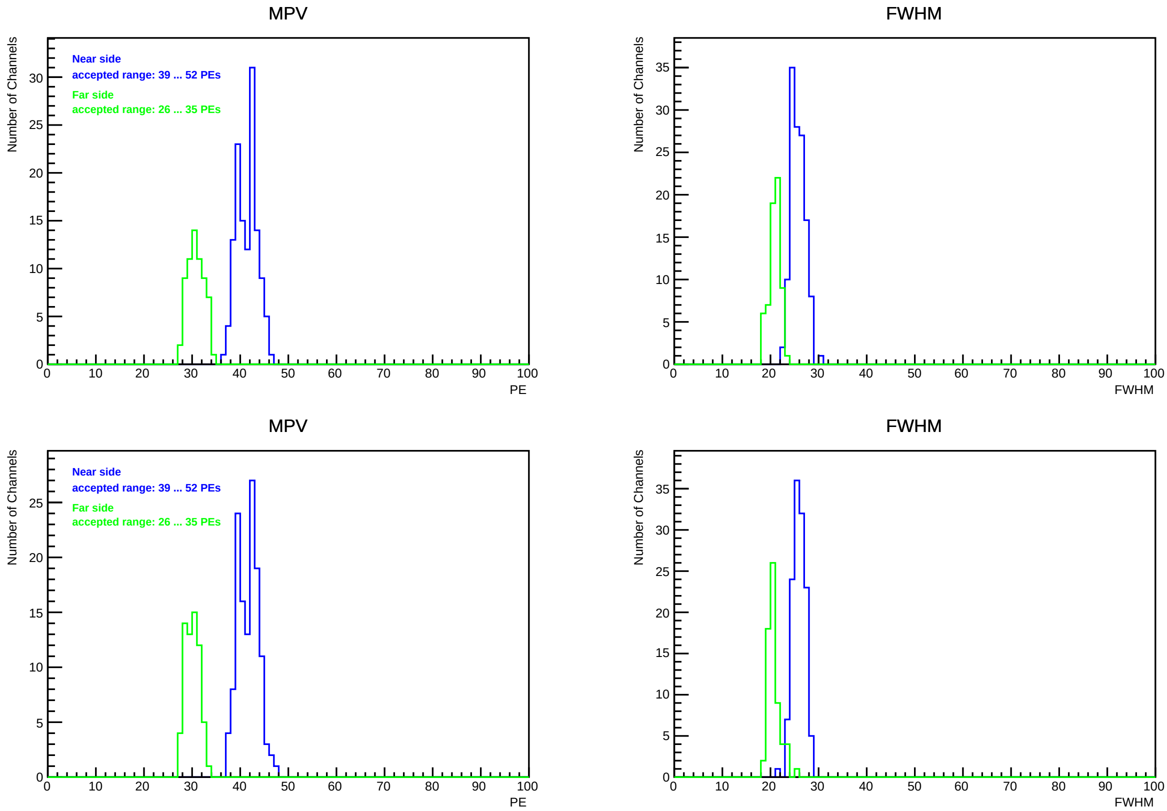

Figure R.28.: PE yield measured for Module 129 at 1.0 ± 0.4 m from the readout end. The upper plots are for the top half of the module while the lower plots are for the lower half of the module. The bifurcated distribution is the result of SiPMs with different breakdown voltages being biased at the same voltage of 53.7 V.

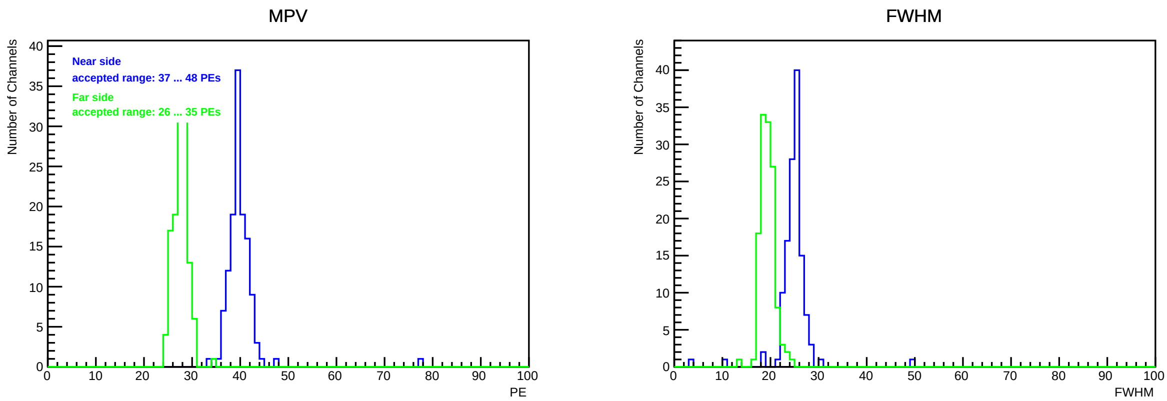

Figure R.29.: PE yield measured for Module 130 at 1.0 ± 0.4 m from the readout end.

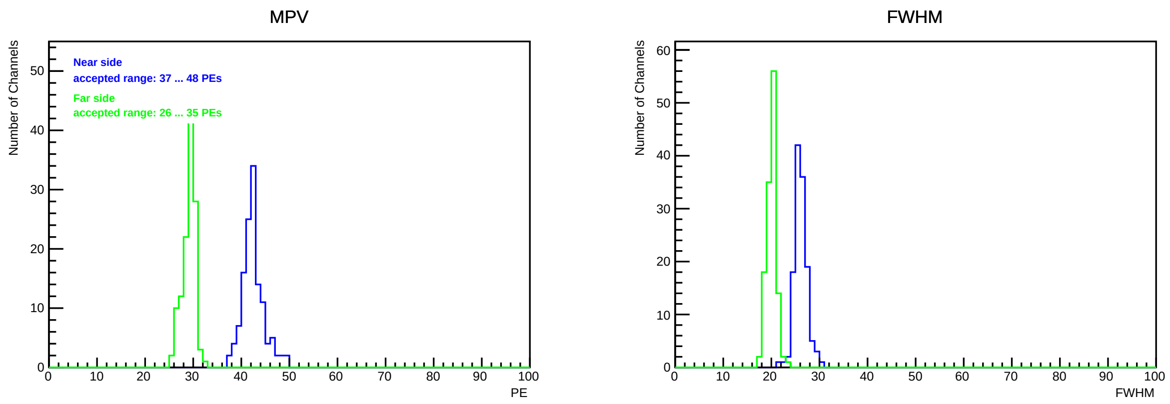

Figure R.30.: PE yield measured for Module 131 at $1.0 \pm 0.4\,\mathrm{m}$ from the readout end.

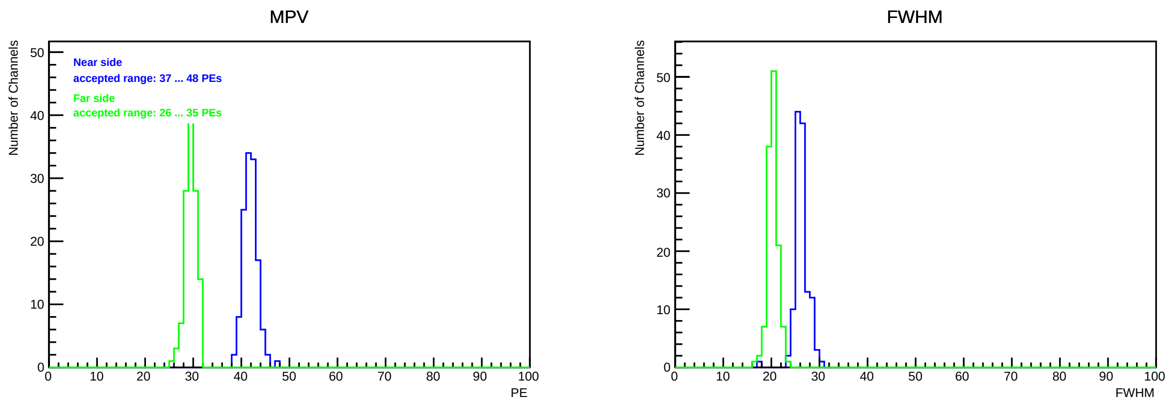

Figure R.31.: PE yield measured for Module 132 at $1.0 \pm 0.4\,\mathrm{m}$ from the readout end.

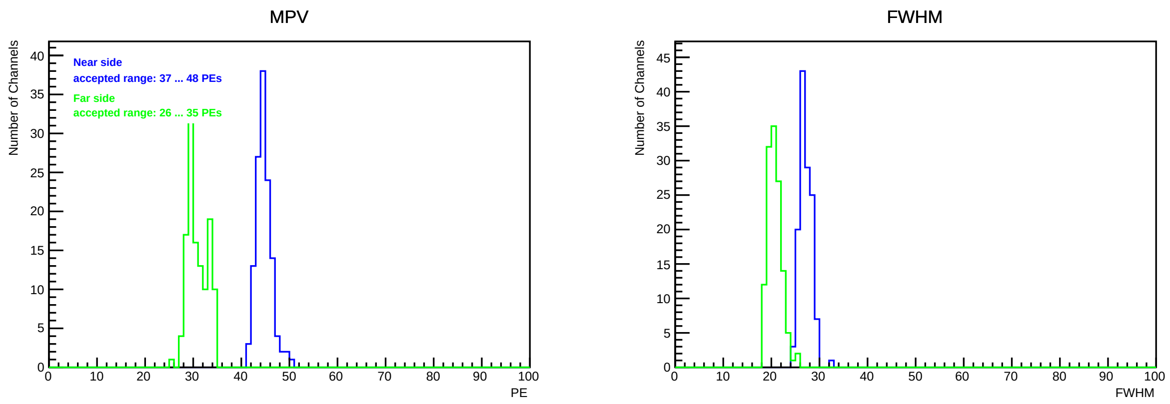

Figure R.32.: PE yield measured for Module 133 at $1.0 \pm 0.4\,\mathrm{m}$ from the readout end.

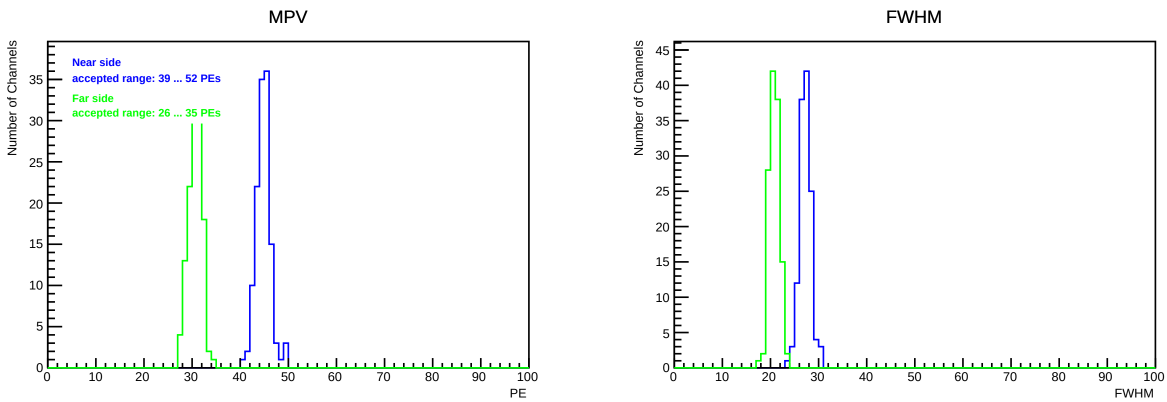

Figure R.33.: PE yield measured for Module 134 at $1.0 \pm 0.4\,\mathrm{m}$ from the readout end.

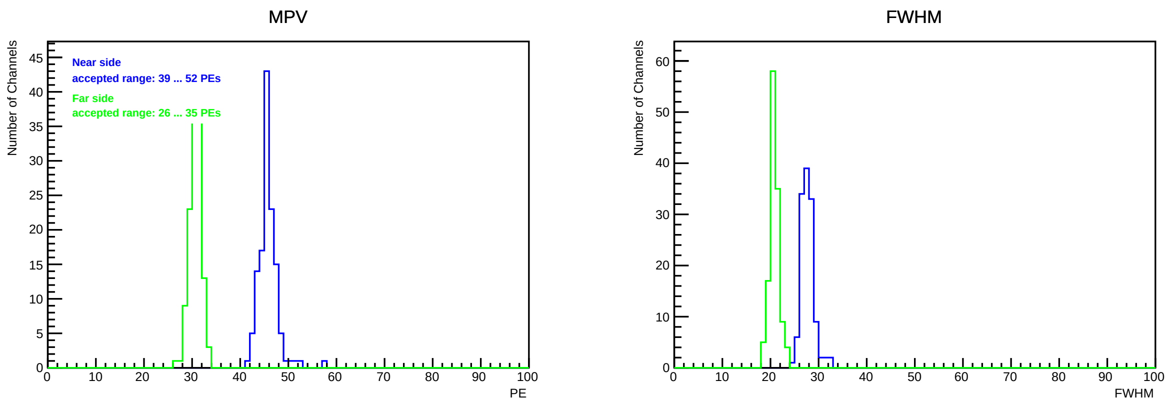

Figure R.34.: PE yield measured for Module 135 at $1.0 \pm 0.4\,\mathrm{m}$ from the readout end.

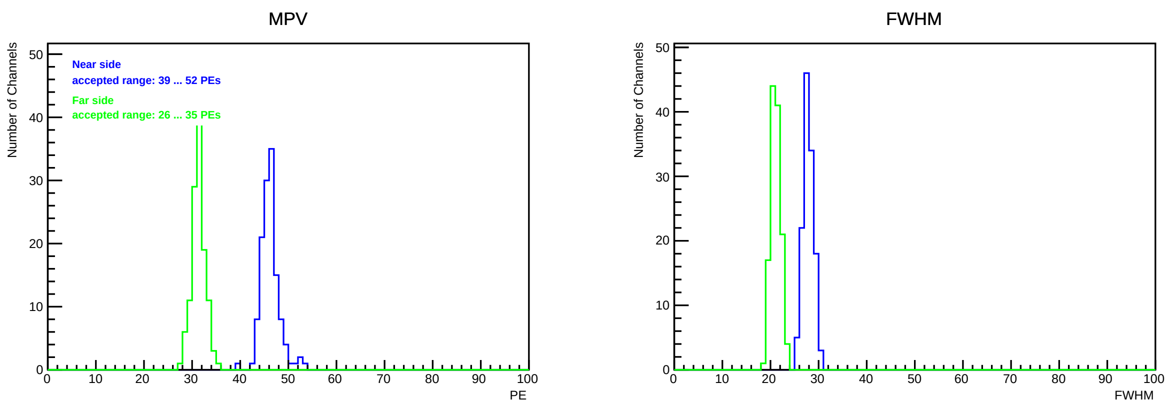

Figure R.35.: PE yield measured for Module 136 at $1.0 \pm 0.4\,\mathrm{m}$ from the readout end.

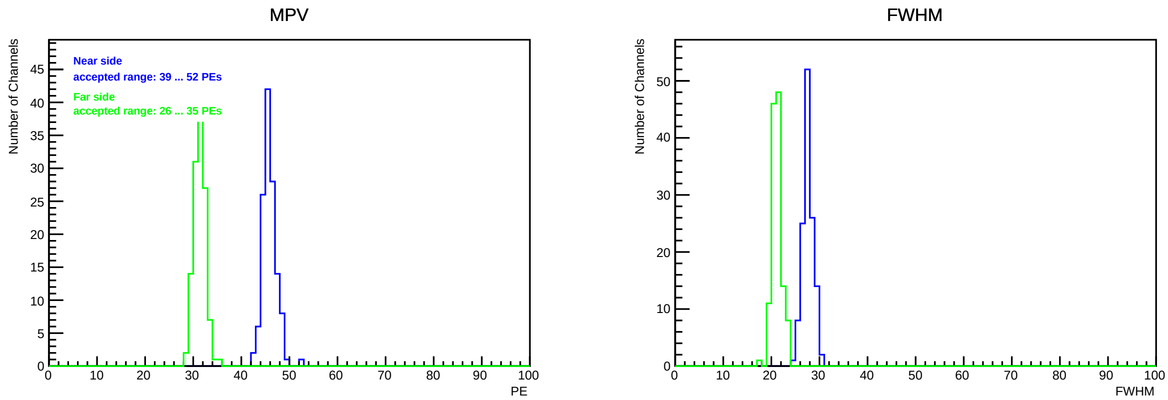

Figure R.36.: PE yield measured for Module 137 at 1.0 ± 0.4 m from the readout end.

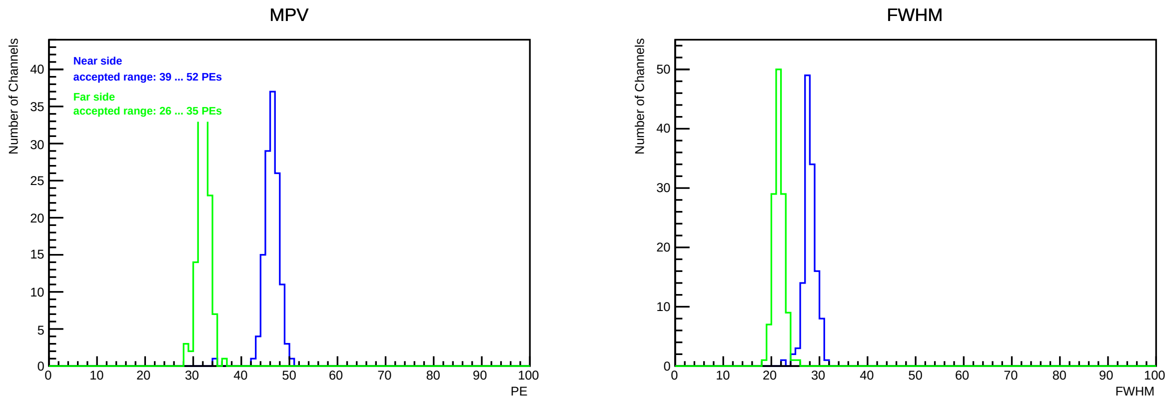

Figure R.37.: PE yield measured for Module 138 at 1.0 ± 0.4 m from the readout end.

Appendix S.

Module Crates

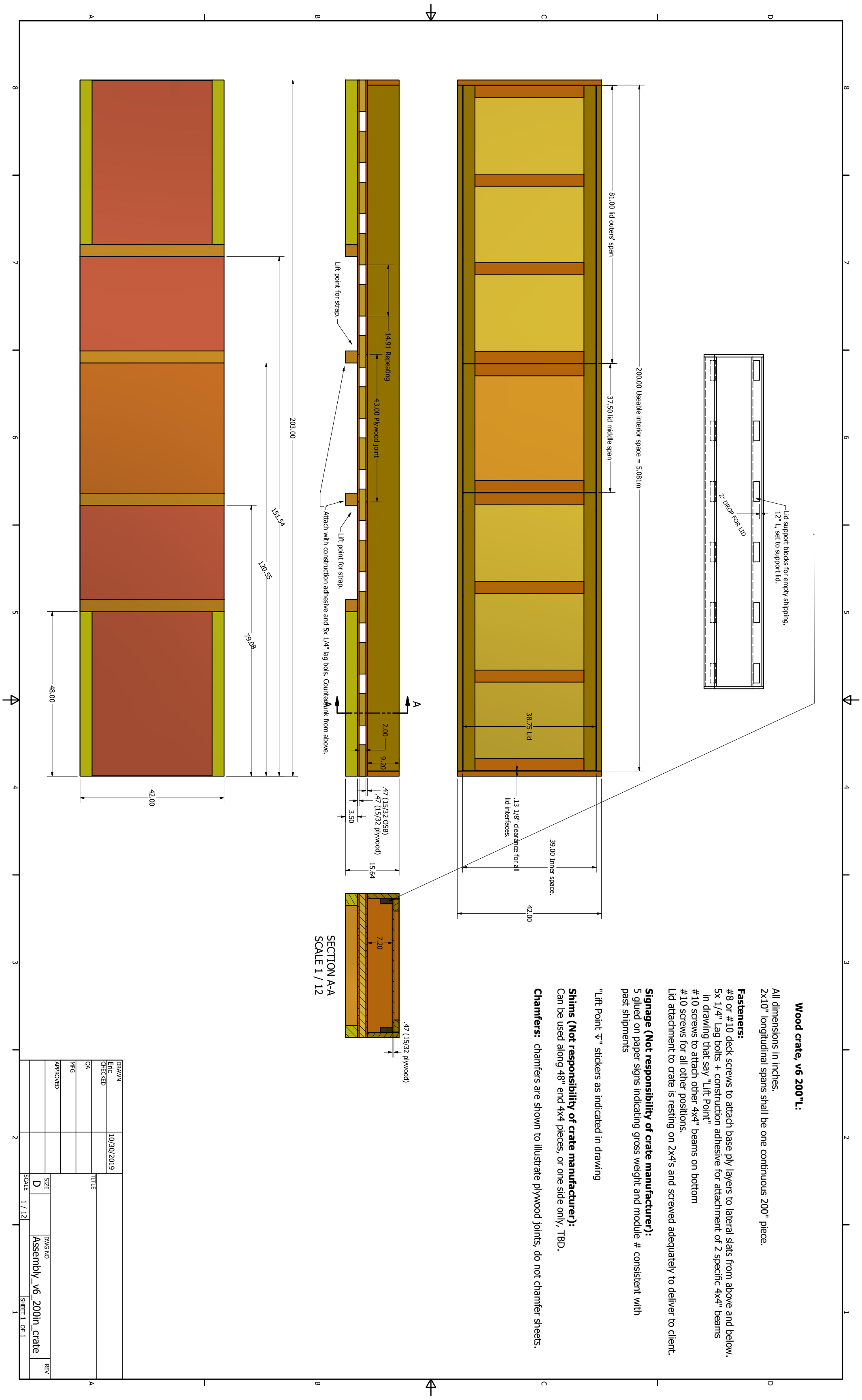

Figure S.1.: Module crate design 5.1 m (200 in).

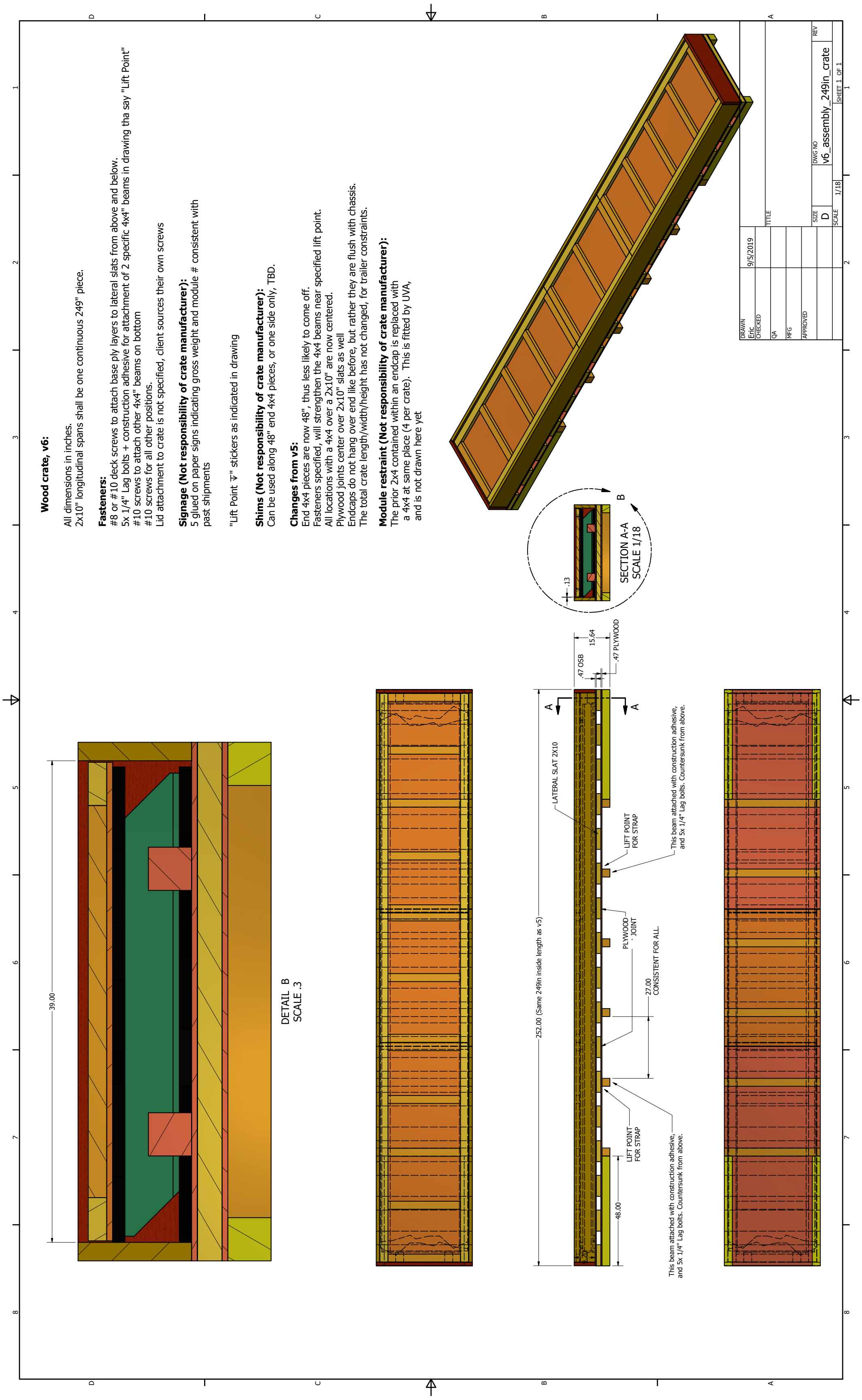

Figure S.2.: Module crate design 6.3 m (249 in).

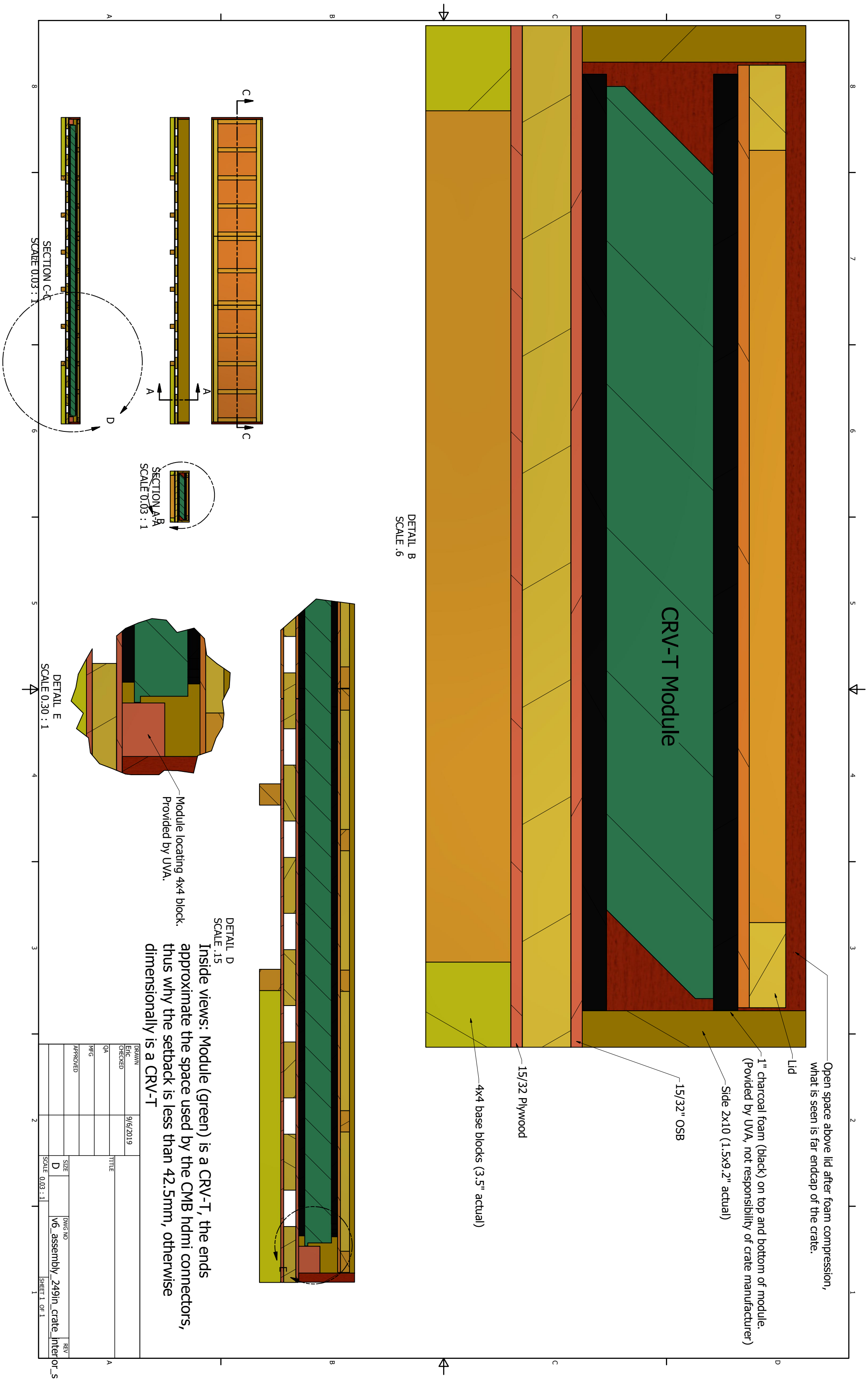

Figure S.3.: Module crate design interior 6.3 m (249 inch).